frontiers | Research Topics

Criticality in neural network behavior and its implications for computational processing in healthy and perturbed conditions

Edited by
Axel Sandvig, Matteo caleo and Ioanna Sandvig

Published in
Frontiers in Neural Circuits
Frontiers in Computational Neuroscience

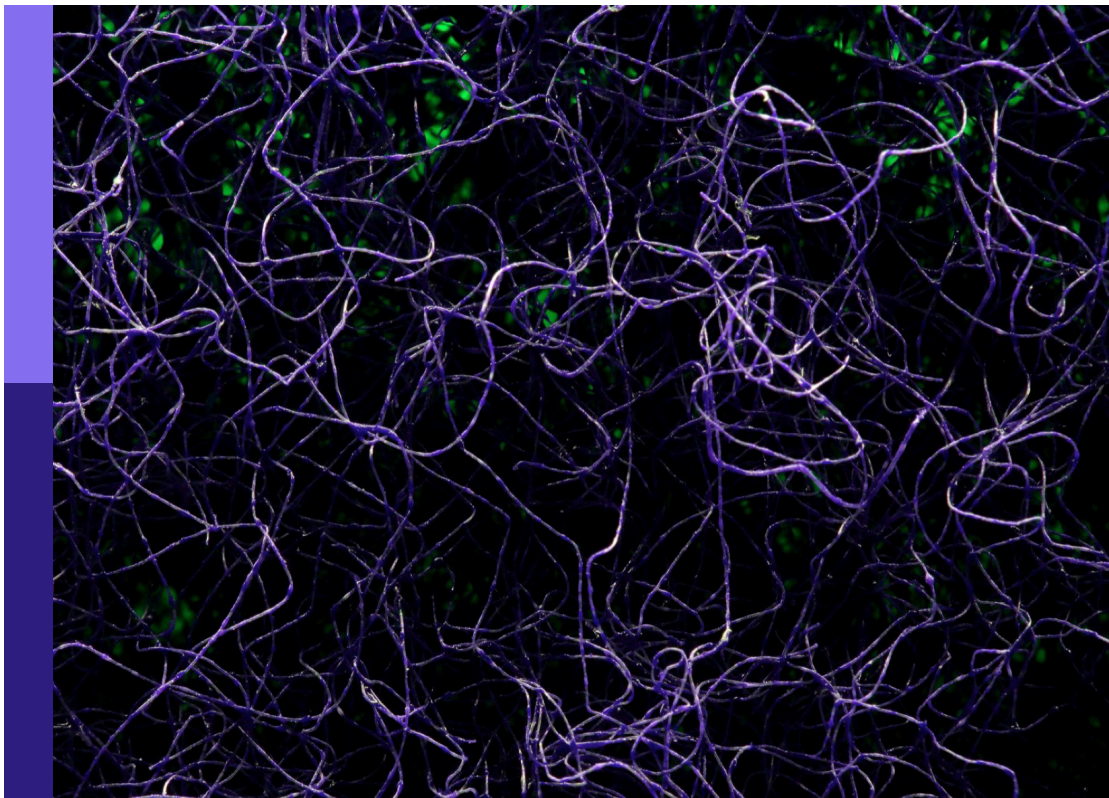

ISSN 1664-8714
ISBN 978-2-83251-324-8
DOI 10.3389/978-2-83251-324-8

About Frontiers

Frontiers is more than just an open access publisher of scholarly articles: it is a pioneering approach to the world of academia, radically improving the way scholarly research is managed. The grand vision of Frontiers is a world where all people have an equal opportunity to seek, share and generate knowledge. Frontiers provides immediate and permanent online open access to all its publications, but this alone is not enough to realize our grand goals.

Frontiers journal series

The Frontiers journal series is a multi-tier and interdisciplinary set of open-access, online journals, promising a paradigm shift from the current review, selection and dissemination processes in academic publishing. All Frontiers journals are driven by researchers for researchers; therefore, they constitute a service to the scholarly community. At the same time, the *Frontiers journal series* operates on a revolutionary invention, the tiered publishing system, initially addressing specific communities of scholars, and gradually climbing up to broader public understanding, thus serving the interests of the lay society, too.

Dedication to quality

Each Frontiers article is a landmark of the highest quality, thanks to genuinely collaborative interactions between authors and review editors, who include some of the world's best academicians. Research must be certified by peers before entering a stream of knowledge that may eventually reach the public - and shape society; therefore, Frontiers only applies the most rigorous and unbiased reviews. Frontiers revolutionizes research publishing by freely delivering the most outstanding research, evaluated with no bias from both the academic and social point of view. By applying the most advanced information technologies, Frontiers is catapulting scholarly publishing into a new generation.

What are Frontiers Research Topics?

Frontiers Research Topics are very popular trademarks of the *Frontiers journals series*: they are collections of at least ten articles, all centered on a particular subject. With their unique mix of varied contributions from Original Research to Review Articles, Frontiers Research Topics unify the most influential researchers, the latest key findings and historical advances in a hot research area.

Find out more on how to host your own Frontiers Research Topic or contribute to one as an author by contacting the Frontiers editorial office: frontiersin.org/about/contact

Criticality in neural network behavior and its implications for computational processing in healthy and perturbed conditions

Topic editors

Axel Sandvig — Norwegian University of Science and Technology, Norway
Matteo Caleo — University of Padua, Italy
Ioanna Sandvig — Norwegian University of Science and Technology, Norway

Citation

Sandvig, A., Caleo, M., Sandvig, I., eds. (2023). *Criticality in neural network behavior and its implications for computational processing in healthy and perturbed conditions*. Lausanne: Frontiers Media SA. doi: 10.3389/978-2-83251-324-8

Table of contents

frontiers | Frontiers in Neural Circuits

TYPE Editorial
PUBLISHED 14 October 2022
DOI 10.3389/fncir.2022.1041250

OPEN ACCESS

EDITED AND REVIEWED BY
Blake A. Richards,
Montreal Institute for Learning Algorithm (MILA), Canada

*CORRESPONDENCE
Ioanna Sandvig
ioanna.sandvig@ntnu.no

IN MEMORIAM
This paper is dedicated to the memory of Matteo Caleo (1970–2022)

RECEIVED 10 September 2022
ACCEPTED 05 October 2022
PUBLISHED 14 October 2022

CITATION
Sandvig I and Sandvig A (2022) Editorial: Criticality in neural network behavior and its implications for computational processing in healthy and perturbed conditions. *Front. Neural Circuits* 16:1041250. doi: 10.3389/fncir.2022.1041250

Editorial: Criticality in neural network behavior and its implications for computational processing in healthy and perturbed conditions

Ioanna Sandvig[1]* and Axel Sandvig[1,2,3]

[1]Department of Neuromedicine and Movement Science, Faculty of Medicine and Health Sciences, Norwegian University of Science and Technology (NTNU), Trondheim, Norway, [2]Department of Pharmacology and Clinical Neuroscience, Faculty of Medicine, Umeå University, Umeå, Sweden, [3]Department of Community Medicine and Rehabilitation, Faculty of Medicine, Umeå University, Umeå, Sweden

KEYWORDS

neural systems, emergence, self-organization, critical state, neuronal avalanche

Editorial on the Research Topic
Criticality in neural network behavior and its implications for computational processing in healthy and perturbed conditions

The aim of this Research Topic is to summarize the current state-of-the-art in the context of key conceptual, methodological, and analytical tools concerning criticality in neural networks within the context of the brain connectome. This includes emergent behavior such as memory and cognition, dynamic morphology-activity relationships at the micro, meso, and macroscale in response to perturbations, as for example, trauma or neurodegenerative disease. As such, the topic provides insights and perspectives on the relevance of criticality in the context of studying and understanding information processing in neural networks in health and disease in preclinical models and in the clinic.

Zimmern takes into consideration the clinical relevance of the topic and presents a comprehensive overview and explanation of central concepts and terminology in criticality, such as power laws, phase transitions, and the branching processes. The article provides a discussion and critique regarding the application of such concepts in the analysis of human neural data, with special focus on current controversies in the literature, and concludes with recommendations about how brain criticality may in the future add the diagnosis and treatment of diseases affecting the brain.

Carvalho et al. examine scaling relations observed in experimental data obtained from the anesthetized rodent cortex, which suggest a phase transition in firing rate variability that apparently differs from the canonical model of brain criticality and the branching process. The authors apply subsampling and two different models within the

same universality class as the branching process and demonstrate that the experimental results can be reproduced in this manner.

Bellay et al. investigate how single neuron activity contributes to avalanches observed in the primate cortex by comparing LFP recordings obtained from multiple sites with concomitant single neuron extracellular and intracellular activity. Their results support a selective contribution of single neurons to specific LFP-based avalanche patterns and thus align with the notion that information processing in the cortex is supported by Hebbian cell assemblies.

Heiney et al. discuss the role of criticality in neural systems taking into consideration the principles of self-organization and neuroplasticity, within the context of the dynamic, reciprocal relationships between underlying network topologies and function. The review highlights the relevance and application of criticality for experimental neuroscientists, especially in terms of how changes in underlying structure-function relationships, for example due to damage or disease, affect critical dynamics and neural computation. As such, the article also provides insights as to the role of criticality for clinical translation.

Gross presents a dynamical systems perspective and its implications on criticality and neural dynamics. The article provides a comprehensive overview of bifurcation theory concluding that several critical manifolds, rather than one critical state, can explain neural dynamics, such as self-organization and information processing. The article thus highlights the need for the development of new theoretical models that take the high-dimensional parameter into consideration.

Shaheen et al. present a mathematical model that can be applied in the investigation of altered neuron-glial interactions as an underlying neuropathology, such as Alzheimer's disease. The model proposes a shift of astrocytic function toward exosome-dependent release of Ca^{2+} that might contribute to the accumulation of pathological protein aggregates.

Arvin et al. examine how underlying network topology is associated with neural activity and critical dynamics. By applying the small-world model of Watts and Strogatz and Kuramoto's model of coupled oscillators, the authors demonstrate that the dynamics of the system are shaped by short-range connections, while the state of the system, for example its response to a perturbation, is driven by long-range connections. This differential but synergistic contribution of short- and long-range connections thus confers the required neuromodulation to the system.

Alamian et al. assess baseline cognitive function in schizophrenia patients using magnetoencephalography and reveal changes in self-similarity and multifractality values in affected brain regions consistent with altered criticality properties, thus illustrating the relevance and potential application of criticality in the evaluation of this patient group.

Finally, Beggs addresses controversies in the field regarding the criticality hypothesis, which poses that healthy biological neural networks demonstrate optimal information capacity when they operate at the near critical point. The author concludes that such controversies are an essential element of scientific discourse and, as such, they are valuable for the refinement of relevant research questions in the field.

Author contributions

Both authors listed have made a substantial, direct, and intellectual contribution to the work and approved it for publication.

Conflict of interest

The authors declare that the research was conducted in the absence of any commercial or financial relationships that could be construed as a potential conflict of interest.

Publisher's note

frontiers in Neural Circuits

REVIEW
published: 26 August 2020
doi: 10.3389/fncir.2020.00054

Why Brain Criticality Is Clinically Relevant: A Scoping Review

*Vincent Zimmern**

Division of Child Neurology, The University of Texas Southwestern Medical Center, Dallas, TX, United States

The past 25 years have seen a strong increase in the number of publications related to criticality in different areas of neuroscience. The potential of criticality to explain various brain properties, including optimal information processing, has made it an increasingly exciting area of investigation for neuroscientists. Recent reviews on this topic, sometimes termed brain criticality, make brief mention of clinical applications of these findings to several neurological disorders such as epilepsy, neurodegenerative disease, and neonatal hypoxia. Other clinicallyrelevant domains – including anesthesia, sleep medicine, developmental-behavioral pediatrics, and psychiatry – are seldom discussed in review papers of brain criticality. Thorough assessments of these application areas and their relevance for clinicians have also yet to be published. In this scoping review, studies of brain criticality involving human data of all ages are evaluated for their current and future clinical relevance. To make the results of these studies understandable to a more clinical audience, a review of the key concepts behind criticality (e.g., phase transitions, long-range temporal correlation, self-organized criticality, power laws, branching processes) precedes the discussion of human clinical studies. Open questions and forthcoming areas of investigation are also considered.

Keywords: criticality, brain, long-range temporal correlation, neurodevelopment, neurodegeneration, sleep, epilepsy, anesthesia

OPEN ACCESS

Edited by:
Ioanna Sandvig,
Norwegian University of Science and Technology, Norway

Reviewed by:
Adriano Barra,
University of Salento, Italy
Stephen M. Johnson,
University of Wisconsin-Madison, United States

***Correspondence:**
Vincent Zimmern
vincent.zimmern@utsouthwestern.edu

Received: *24 May 2020*
Accepted: *23 July 2020*
Published: *26 August 2020*

Citation:
Zimmern V (2020) Why Brain Criticality Is Clinically Relevant: A Scoping Review. Front. Neural Circuits 14:54. doi: 10.3389/fncir.2020.00054

INTRODUCTION

The brain criticality hypothesis suggests that neural networks and thus, many aspects of brain activity self-organize into a critical state (Wilting and Priesemann, 2019). Critical states are unique configurations of physical systems that have been a central focus of statistical physics for more than a century. Criticality, which is a synonymous term for "critical phenomena" or "critical states," marks the transition between ordered and disordered states. The theory of critical phenomena has found applications in many scientific fields, including neuroscience and clinical neurology (Sornette, 2004; Cocchi et al., 2017). In the neurosciences, criticality is appealing because theory and modeling suggest that neural networks at criticality exhibit optimal processing and computing properties (Beggs, 2008; Shew and Plenz, 2013). These properties include information transmission, information storage, dynamic range, metastable states, and computational power (Maass et al., 2002; Bertschinger and Natschläger, 2004; Latham and Nirenberg, 2004; Haldeman and Beggs, 2005; Kinouchi and Copelli, 2006; Tanaka et al., 2009; Boedecker et al., 2012; Shriki et al., 2013; Gautam et al., 2015; Shriki and Yellin, 2016; Hoffmann and Payton, 2018). The term "brain criticality" is used in this review as a catch-all term for the various manifestations of critical phenomena in human neuroscience.

This scoping review of the brain criticality literature will start with a section that reviews the physics-based ideas behind brain criticality, including a discussion of the Ising model. It will then review the brain criticality literature in each of seven domains (i.e., anesthesia, epilepsy, neurodegeneration, neurodevelopment, cognition, sleep medicine, and psychiatry), focusing on the clinical applications. This review should serve as an entry-point for clinicians and translational researchers interested in using this conceptual framework and its associated tools to advance patient care. Understandably, it is not possible to summarize nearly a century of developments in statistical physics − not to mention 30 years of applications of these physical concepts to neuroscience−in a single review paper. An excellent introductory paper for newcomers to criticality is Beggs and Timme, 2012. References are available for those interested in diving into the technical details of critical phenomena (Nishimori and Ortiz, 2011; Tomko et al., 2018), including two books on criticality in neural dynamics (Plenz and Niebur, 2014; Tomen et al., 2019). In this section, criticality is introduced from the perspective of phase transitions and is illustrated using the two-dimensional Ising model (see **Figure 1**). This is followed by a discussion of the various characteristics of critical phenomena and a brief discussion of self-organized criticality.

CRITICALITY AND ASSOCIATED CONCEPTS

In statistical physics, criticality refers to the behavior that is seen when a physical system undergoes a specific kind of phase transition. Typically, a macroscopic property of the system called the *order parameter* changes as a function of an underlying feature called the *control parameter*. In the example of a vapor-to-water phase transition, the order parameter is the macroscopic appearance reflective of the phase's entropy (i.e., water or vapor), and the control parameter is the temperature (Hesse and Gross, 2014). Generally, gradual changes in the control parameter lead to similarly gradual changes in the order parameter. However, at specific points, the order parameter changes abruptly. On a plot of the order parameter on the *y*-axis and the control parameter on the *x*-axis (i.e., a phase diagram), there is either a jump (i.e., a discontinuity) or a sharp corner (i.e., a non-differentiable point) at the transition point of a phase transition. If the change in the order parameter is a jump, the phase transition is known as first-order or discontinuous. If the change in the order parameter is a sharp corner, the phase transition is known as second-order or continuous. The second-order phase transition allows a system to be at the exact transition point at the interface between two very different states, with usually one state being more disordered than the other. The system is said to be "at criticality" or in the critical state (Nishimori and Ortiz, 2011; Hesse and Gross, 2014). The phase in which the control parameter is below the critical value is called the subcritical phase, while the phase in which the control parameter is above the critical value is called the supercritical phase. It is important to note that the theory of phase transitions usually involves systems at the thermodynamic limit, i.e. infinitelylarge volume. When not at the thermodynamic limit, phase transitions occur over a parameter range called a Griffiths phase rather than at a single critical point and are sometimes referred to as quasi-critical states (Moretti and Munoz, 2013). Quasi-critical states obey many of the properties of a critical system but are not entirely critical.

These concepts can be illustrated with the help of the two-dimensional Ising model, which is a classic example of a critical transition in ferromagnetism (Beggs and Timme, 2012). The Ising model consists of a lattice in a piece of iron, with each site of the lattice corresponding to a dipole moment (i.e., an up or down spin) (**Figure 1B**). Each dipole moment operates like a bar magnet and can influence its nearest neighbors to align in the same direction. At a low temperature, nearest-neighbor effects will dominate the system. At a fixed temperature below the critical temperature, a cluster of aligned spins will get larger and larger, and, with time, will take over the entire lattice to make a uniform dipole moment (**Figure 1A**). Thus, at this low temperature, the piece of iron will behave like a magnet because the spins will align throughout the lattice to yield a strong net magnetization (i.e., order parameter). However, as temperature (i.e., control parameter) increases, the energy from heat begins to jostle the spins. Past a critical temperature called the Curie temperature (Tc), the disordered spins from the added heat will overwhelm the ordering effect of the nearest-neighbor interaction, leading to a loss of the magnetization (**Figures 1A–C**). Heat, therefore, takes the system from a subcritical, magnetic phase through a critical phase transition and on to a supercritical, non-magnetic and disordered phase. At the critical temperature, a critical phase emerges where order and disorder are evenly matched (Nishimori and Ortiz, 2011; Beggs and Timme, 2012). The correlation length (i.e., how far a single spin change can propagate through the system) is maximized in this phase (**Figure 1D**), and in the infinitely large system, goes to infinity at the critical point. The order parameter (i.e., magnetization)−along with other observables like magnetization domain size and magnetic susceptibility−become power-law distributed with unique power-law exponents (**Figure 1F**). Power laws refer to a probability density function of the form of $p(x) = C\,x^{-\alpha}$ for some $x > x_o$ and with αcorresponding to the power-law exponent. Power laws exhibit scale invariance and are therefore called scale-free. A function $f(x)$ is scale invariant if $f(cx) \propto f(x)$, where α signifies "proportional to." In other words, scaling the argument of the function is equivalent to a proportional scaling of the function itself. In the case of the power-law, $f(cx) = (cx)^{-\alpha} = c^{-\alpha}\,x^{-\alpha} = c^{-\alpha}\,f(x) \propto f(x)$. Moreover, because $\log\left(f(x)\right) = \log \propto (x^{-\alpha}) = -\alpha \log(x)$, a log-log plot of a power-law distributed dataset should produce a straight line with slope −α. Caveats on using this log-log plot technique to extract the power-law exponent are addressed in a subsequent section.

The Ising model can lead to very complex behavior patterns and has been used to model neural networks (Fraiman et al., 2009; Beggs and Timme, 2012; Deco et al., 2012; Marinazzo et al., 2013; Stramaglia et al., 2017). The Ising model and several other well-characterized models have led to a better understanding of how critical systems behave. Nevertheless, critical systems remain difficult to identify because the relevant order and control parameters may not always be readily available

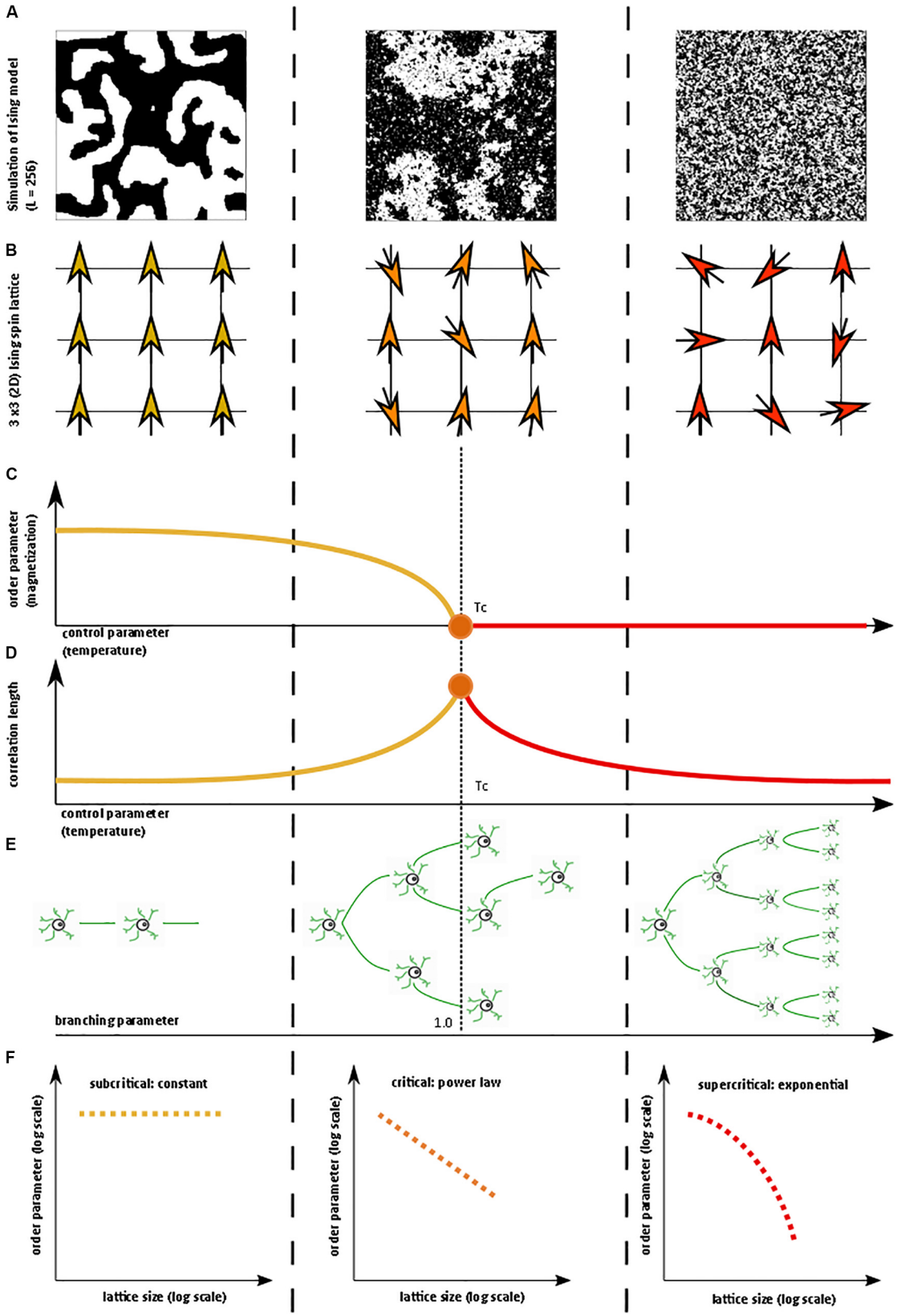

FIGURE 1 | Continued

FIGURE 1 | Illustration of critical phase transition using the two-dimensional (2D) Ising model. For more information on the Ising model, see Nishimori and Ortiz (2011), Beggs and Timme (2012). **(A)** Simulation of 2D Ising model with length = 256 in subcritical, critical, and super-critical states as temperature increases from left to right. Black and white areas represent magnetization domains with differing spins. Simulations were generated using open-source code from Matt Bierbaum (mattbierbaum.github.io/ising.js) using the Metropolis algorithm. **(B)** Illustration of 2D Ising spin lattice to show differing spin states during phase transition. Image adapted with permission from Beggs and Timme (2012). The organized spins in the subcritical state give way to random spin arrangements in the supercritical state, passing through an intermediate critical state with a complex arrangement of spins. **(C)** The order parameter of the system decreases smoothly as the control parameter increases, until it abruptly changes at the critical temperature (Tc or the Curie temperature). **(D)** The correlation length is maximized at the critical point. **(E)** A branching parameter of 1 allows an aggregate one-to-one transmission of neural signals. Branching parameter greater than 1 leads to supercritical, run-away neuronal excitation. Branching parameter less than 1 leads to subcritical dying-off of the neuronal transmission. **(F)** At the critical point, observables of the system, including the order parameter, obey a power-law or scale-free distribution, seen as a straight-line on a log-log plot. The order parameter remains constant in the subcritical case, while it drops off exponentially in the supercritical state.

for experimentation, making it difficult to construct a complete phase diagram. In the absence of a complete phase diagram, one can use several known markers of criticality, as follows:

Branching Parameter

A branching parameter σ, in the setting of brain criticality, is the ratio of downstream activated neurons to upstream activated neurons (Harris, 1963). In other words, as in **Figure 1E**, a branching parameter of 1 means that every activated neuron on average fires or activates one other downstream neuron (Hobbs et al., 2010). Branching parameter less than 1 indicates a subcritical phase that evolves with time to a quiescent, inactive state. On the other hand, a branching parameter greater than 1 indicates a supercritical phase of increasing activity. Of course, branching parameters are variable and dynamic. Caution is needed in the interpretation of the branching parameter, however, because a branching parameter of 1 can also be observed in certain supercritical states (Hesse and Gross, 2014).

Long-Range Temporal Correlation, Critical Slowing, and Flickering

In critical systems, the response of the system to external stimuli – called the dynamic range or dynamic correlation – is maximized. Small perturbations of the system at criticality lead to geometric (rather than exponential) returns to the steady-state (Hesse and Gross, 2014), leading to *long-range temporal correlation* (LRTC or long-memory). One can measure LRTC in multiple ways. Popular methods include the Hurst exponent (through various estimators) and detrended fluctuation analysis (DFA) (Peng et al., 1995a,b; Simonsen et al., 1998; Hardstone et al., 2012). DFA produces a *scaling exponent* over a defined time period (see **Figure 2** for an illustration of DFA). If that scaling exponent is between 0.5 and 1, with a good fit (see **Figure 2**), one can conclude that the time series exhibits LRTC over that time period.

This geometric rate of return to steady-state is also called *critical slowing down* (Scheffer et al., 2009; Van De Leemput et al., 2014). More generally, at the critical point, the dynamic correlation of the system diverges such that avalanches (i.e., network activity) occur at all scales of the system (Hesse and Gross, 2014). Another phenomenon seen at the critical transition is called *flickering*, which emerges when noise allows a system to migrate back-and-forth between two attractor basins (Wang et al., 2012). This phenomenon is not to be confused with flicker noise or *1/f* noise, which is discussed next.

The Emergence of Power-Law (1/*f*) Noise and Power-Law Observables

Critical systems, when perturbed by weak inputs, will exhibit superposed geometric responses to the inputs, which yields *1/f* noise, also called pink noise, power-law noise, or flicker noise (see **Figure 3C**). Many authors employ these terms synonymously with long-range dependence or long-memory, as these are identical phenomena. The term *1/f* noise refers to the phenomenon in which the power spectrum $S(f)$ of a time series obeys a power law of the form$S(f) = \alpha f^{-\beta}$. Historically, the cases of $\beta = 0$, $\beta = 1$, $\beta = 2$ are referred to as "white" noise, "pink" noise, and "brown" noise, respectively (Li et al., 2005). The range $0.5 < \beta < 1.5$ is commonly accepted as *1/f* noise. While all critical systems should exhibit *1/f* noise, not all *1/f* noise is indicative of criticality (Bédard et al., 2006; Hesse and Gross, 2014).

As mentioned earlier, multiple observables will follow a power-law distribution when in a critical state. However, power laws are necessary but not sufficient to prove the existence of criticality – many other processes can generate a power-law distribution. For more on this topic, see the following references (Mitzenmacher, 2004; Newman, 2005; Touboul and Destexhe, 2010). Demonstrating the existence of a power law is not straightforward. As a rule, power laws take the form of $Y = C\ x^{-\alpha}$ for some $x > x_o$. For many years, it was common practice to plot y against x (from the previous formula) in log-log coordinates – if a straight line emerged, the slope of that line was interpreted as the power-law exponent α (see **Figure 3B**). This approach led to many false claims of power-laws since many other finite datasets (e.g., from a log-normal distribution) can also approximate a straight line on a log-log plot. Since Clauset et al. (2009) and subsequent work, researchers have had access to more sophisticated statistical methodology to argue that their variable obeys a power law, as opposed to other heavy-tailed distributions. While definitions vary, heavy-tail distributions are probability distributions whose tails are "heavier" than the exponential distribution, of which the Gaussian is a sub-type. Examples include the Fisher-Tippett (double-exponential) distribution, the log-normal distribution, the Weibull distribution, among many others. An exhaustive review of several heavy-tailed distributions and their role in neuroscience can be found in Roberts et al. (2015). In this

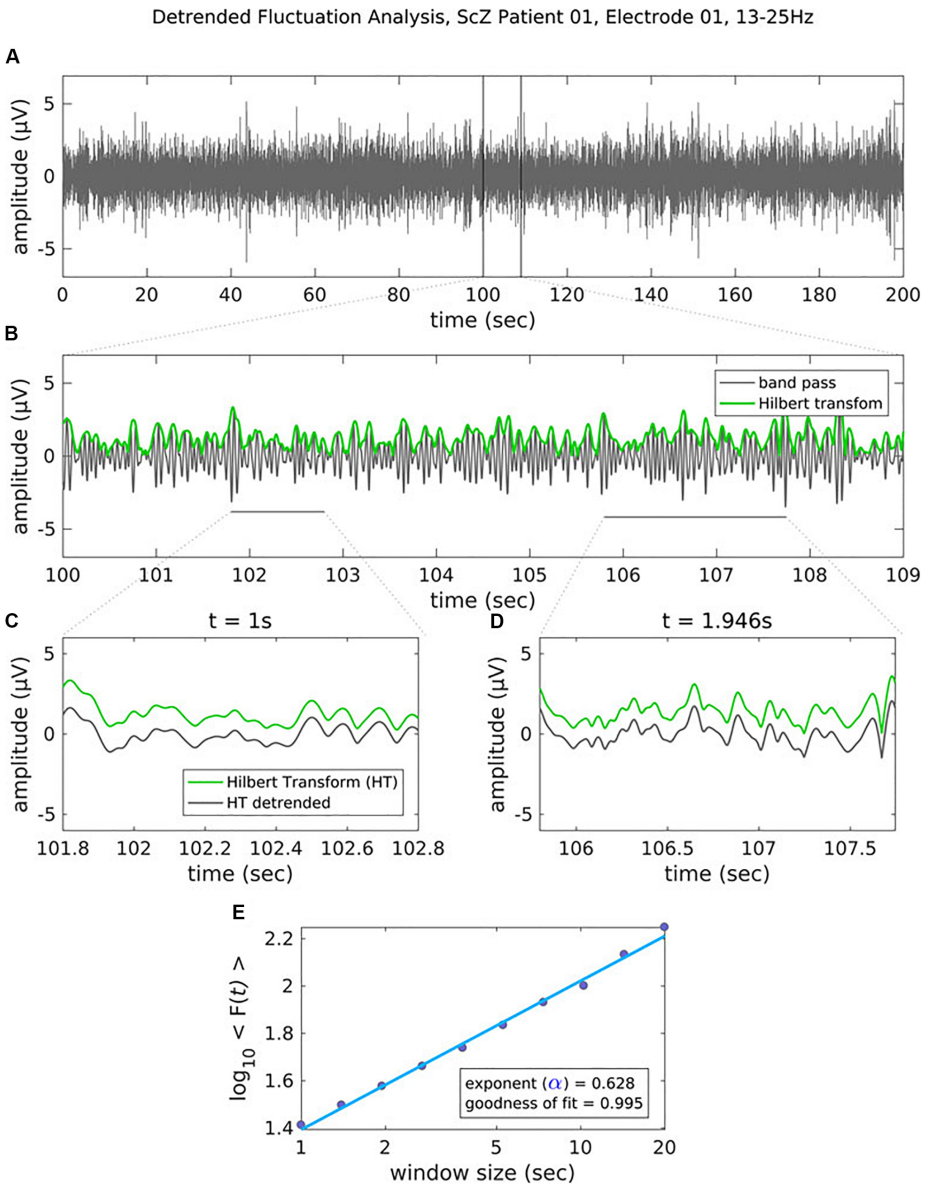

FIGURE 2 | Figure legend taken from Moran et al. (2019) and reproduced with permission. This figure depicts the steps of the detrended fluctuation analysis (DFA). **(A)** 200 s EEG recording that has been band-pass filtered (13–25 Hz, channel 01 = Cz) in a patient with schizophrenia. **(B)** A close-up view (9 s) of the band-pass filtered EEG along with the amplitude envelope derived from the Hilbert transformation (in green), which is used for estimating the scaling exponent. **(C–D)** Two examples of the amplitude envelope with two window sizes. In the left graph, no detrending (i.e., removal of the trend line) has been applied whereas in the right graph, detrending has been applied. For each time window size, the fluctuation of the detrended signal is calculated as the mean standard deviation over all identical sized segments **(E)** The DFA scaling exponent is given by the slope of the log-log plot between fluctuation F and window size. A DFA scaling exponent between 0.5 and 1 indicates the presence of LRTC – in this case, the correlation extends up to 20 s. In this example, the DFA scaling exponent for the beta-band-oscillations in this channel is $\alpha = 0.628$. It is common to report the R^2 value of the linear regression of the log-log plot as a goodness-of-fit score.

review, publications that claim a power-law distribution based on current practices are contrasted with publications that rely on the previously accepted "log-log approach."

Relationship of Power-Law Exponents to Each Other

In systems at criticality, many observable variables (e.g., correlation, size distribution) obey power laws. The different exponents of these power laws are inter-related. The details of these mathematical relationships are beyond the scope of this review but represent a fascinating topic in their own right. To give but one example, avalanche size distribution with power exponent α and avalanche lifetime distribution with power exponent β should be related to avalanche lifetime γ by the following equation: $\gamma = \frac{\beta-1}{\alpha-1}$. This relationship has been experimentally

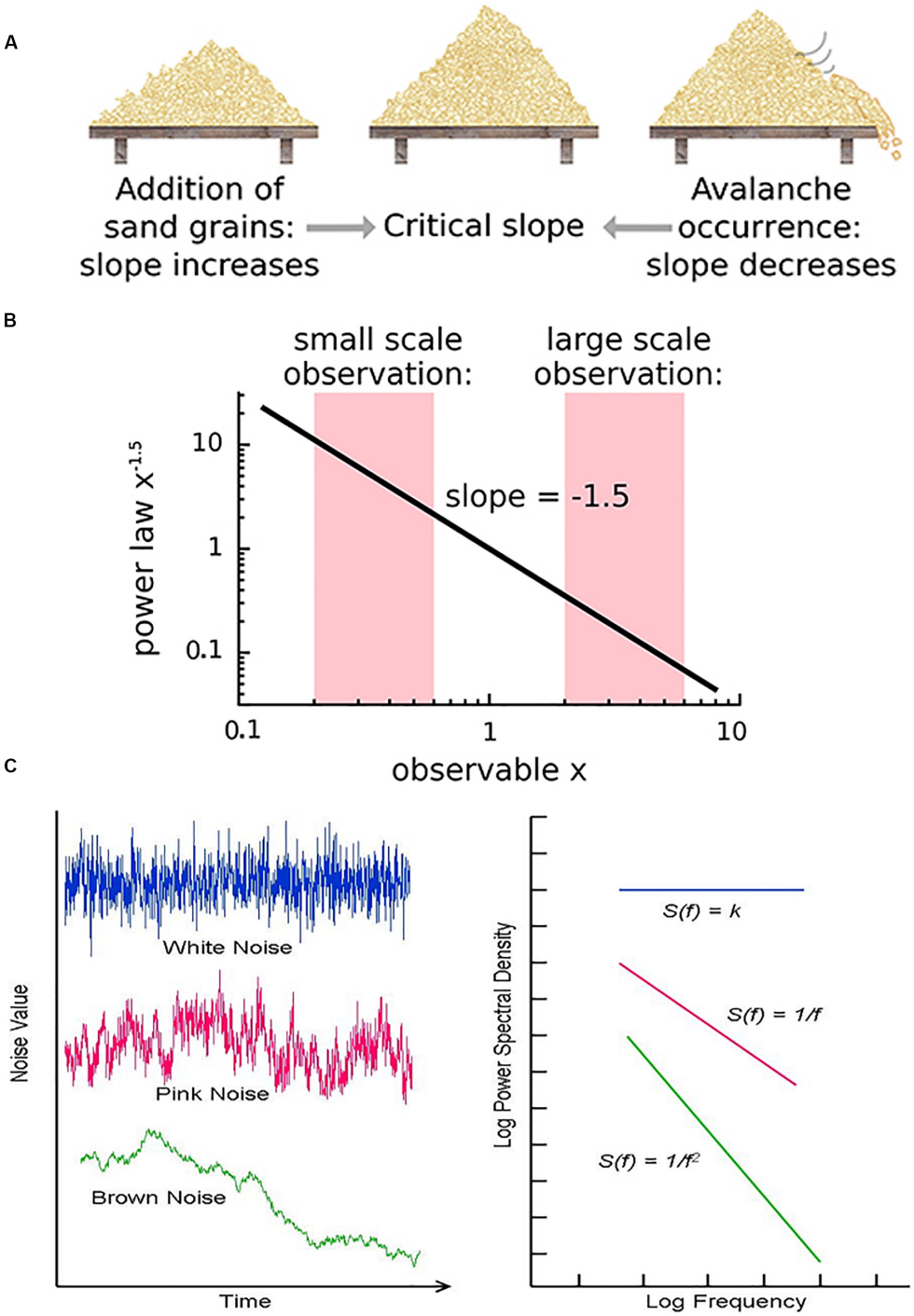

FIGURE 3 | (A) The sandpile model is a classic model of self-organized criticality (SOC), derived as a though experiment (Bak et al., 1988) and proven later with rice piles (Frette et al., 1996). Sand is dropped continuously at a fixed rate onto a flat surface. A sandpile forms. As the sand is added, the slope of the pile increases and avalanches of sand grains begin to occur. If the slope exceeds a "critical slope," small and large avalanches will decrease the slope back closer to the critical slope. **(B)** At the critical slope, the distribution of avalanche sizes (i.e., number of sand grains) is power-law distributed. On a log-log plot, the slope of a power-law-distributed variable gives the power-law exponent. Most avalanches are small but a non-negligible number are quite large, up to nearly the size of the entire system. **(A,B)** reused with permission from Hesse and Gross (2014). **(C)** Neurophysiologic measurements such as voltage from an EEG recording can be displayed as time series that exhibit characteristic spectral densities S(*f*). **(C)** Figure reused with permission from Scholarpedia and E. Izhikevich. Plot of different color-coded time series (left) and a log-log plot of their respective spectral densities (right). In Gaussian "white" noise, each frequency has equal energy, leading to a constant spectral density. "Pink" noise, which is characteristic of SOC but arises in many other settings, has a spectral density given by 1/f, thus the name "1/f noise." "Brown" noise refers to Brownian or random motion, whose spectral density is typically given by $1/f^2$.

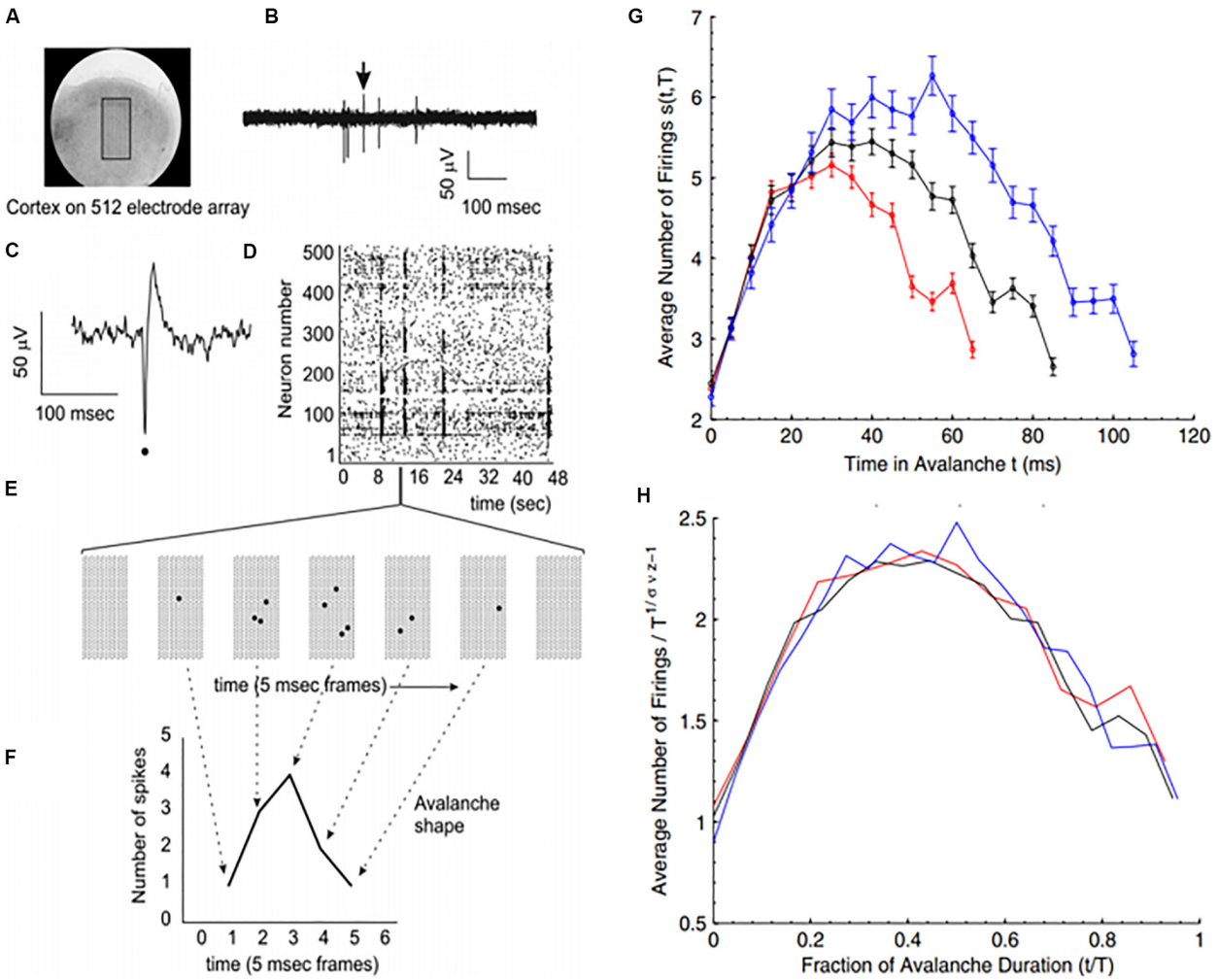

FIGURE 4 | Avalanches recorded from neural tissue. **(A)** Micrograph of a cortical slice on an electrode array, represented by a black rectangle. **(B)** Electrical potential recorded from an electrode. Arrow points to a spike from an individual neuron. The spike is expanded in panel **(C)** and marked by a black dot. **(D)** Raster plot of spike times (dots) from multiple neurons over time. **(E)** Expanding the view of the raster plot reveals an avalanche. Each frame represents the electrode array during a single 5 ms period. Black dots are spikes detected on the array. An avalanche is made up of consecutively active frames, beginning and ending with inactive frames. **(F)** Plotting the number of spikes in each frame versus time produces an avalanche shape. **(G)** Avalanche shapes are produced by averaging the temporal profiles of all avalanches of a particular duration from an experimental dataset close to criticality. Different colors here represent different durations. **(H)** The collapses are plotted by rescaling the horizontal and vertical axes. The tight overlap after rescaling is indicative of criticality. Images reproduced with permission Beggs and Timme (2012) and Friedman et al. (2012).

validated in individual neurons (Beggs and Timme, 2012; Friedman et al., 2012).

Scaling Function

Because of the self-similar or fractal nature of the avalanches of activity in critical systems, the "shape" of avalanche activity is also expected to behave as a fractal (see **Figures 4A–G**). Therefore, all cascades of activity at criticality ought to be re-scalable to a unique shape, as a function of time (or duration) and power exponents (see **Figure 4H**). This phenomenon of critical systems allows a "data collapse" or "shape collapse" of all activity onto a single unique shape (Friedman et al., 2012). In some neural avalanches, this shape takes the form of an inverted parabola (Beggs and Timme, 2012). This kind of shape collapse has been observed in many critical systems (Perković et al., 1995; Mehta et al., 2006; Papanikolaou et al., 2011).

There are various theories as to how physical systems can bring themselves to criticality. In the case of the brain, one of the popular theories is called *self-organized criticality* or *SOC* for short (Bak et al., 1987; Christensen et al., 1992; Hesse and Gross, 2014). It is also referred to as *self-organized quasi-criticality* (Bonachela and Muñoz, 2009) since, as mentioned earlier, true criticality occurs only in infinitelysized systems. Introduced initially by Bak et al. (1987), the idea of SOC is that the control parameter is constantly being adjusted to the critical value by a decentralized feedback mechanism. In other words, the control parameter spontaneously decreases when the system is in a supercritical phase and increases when in a subcritical phase.

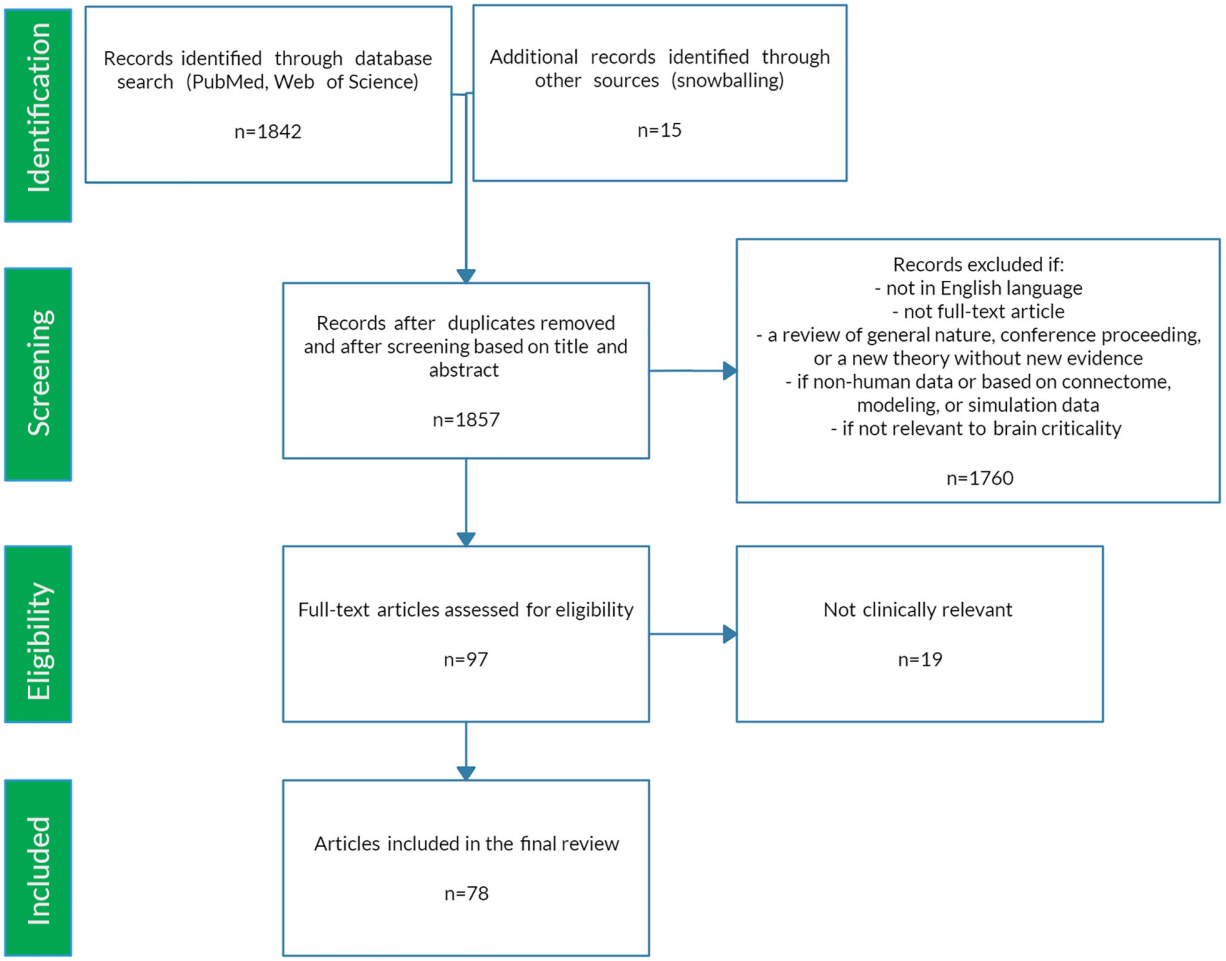

FIGURE 5 | PRISMA-ScR flow chart.

The use of the term "control parameter" is maintained, even if the parameter is not being controlled externally but rather by the system itself (Hesse and Gross, 2014). **Figure 3A** illustrates one of the earliest models of SOC, called the sandpile model (Bak et al., 1988; Frette et al., 1996). Imagine that sand is accumulating at a certain rate on a flat surface. As the sandpile rises, the slope of the sandpile increases. At a critical point, the distribution of sandpile avalanche sizes (i.e., a few grains of sand or the entire pile) obeys a power-law. With a power-law or scale-free distribution, avalanches of all scales can occur, but most avalanches will be small with a few being very large (**Figure 3B**). As sand continues to be added at the same rate, larger avalanches take place and the slope decreases back to the "critical slope." The criticality in this system is therefore self-organized and the control parameter does not have to be tuned externally, as it does for example in the Ising model.

The internal "tuning" of SOC models for the brain is reminiscent of the concept of homeostatic plasticity. Homeostatic plasticity refers to the capacity of neurons to regulate their excitability based on network activity (Turrigiano and Nelson, 2004). Criticality seems to be connected to homeostatic plasticity though the exact details remain unclear. A recent experiment, however, has cast some light on this question. Rat cortical networks exhibiting criticality in controlled circadian conditions lost their network criticality when deprived of visual inputs. However, signs of criticality resumed in under 48 h with neuronal firing rates being maximally inhibited. This finding suggests that homeostatic regulation of inhibition plays an important role in generating criticality (Ma et al., 2019).

ARTICLE SELECTION

The preceding review was conducted to set the stage for a scoping review of the literature (Colquhoun et al., 2014) using PRISMA-ScR methodology (Moher et al., 2009). A scoping review format was chosen since the nature of this literature is large, heterogeneous, and not amenable to a more precise systematic review. See **Figure 5** for a schematic of the article selection process. PubMed and Web of Science databases were searched from their inception until March 2020. The search terms were: "criticality anesthesia," "criticality brain," "criticality epilepsy,"

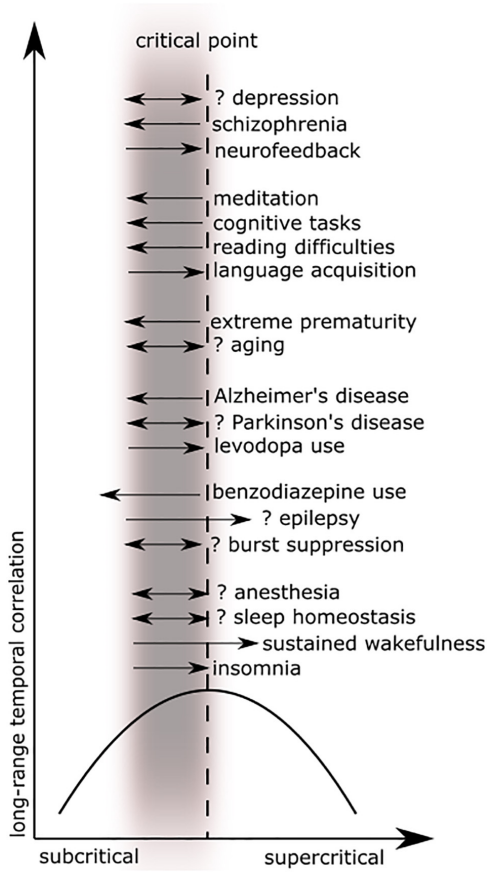

FIGURE 6 | These plots illustrate long-range temporal correlation (LRTC) in different clinical areas as a function of criticality. Figure adapted from Colombo et al. (2016) with permission. The black parabolic curve represents the dynamics of long-range temporal correlation from the subcritical state, reaching a theoretical maximum at the critical point, and decreasing in a supercritical state. The gray blurred rectangle represents the physiological range of brain dynamics, which is thought to be near or below the critical point. Black arrows (excluding the *x*- and *y*-axes) represent deviations toward subcriticality (to the left) or toward supercriticality (to the right) with associated decreases in correlation along the black parabolic curve. Double arrows imply that evidence for both increases and decreases (or absence) in LRTC have been reported in that disease process. See the relevant tables for further detail.

"criticality neural," "criticality neurology," "criticality seizure," and "criticality sleep." A snowball approach identified additional studies that were not captured by the search terms. The reviewer screened titles and abstracts for English language original articles with full-text availability. The following manuscripts were excluded: (1) reviews of a general nature, conference proceedings, and publications offering new theories but without empirical evidence, (2) papers based on non-human data, on connectome data, or mainly on modeling or simulation, (3) duplicates and studies not relevant to brain criticality. The remaining articles were then evaluated for eligibility based on clinical relevance. Ultimately, seventy-eight studies met study criteria for the scoping review. These articles were then analyzed according to seven major categories: anesthesia, epilepsy, neurodegeneration, neurodevelopment, cognition, psychiatry, and sleep medicine. **Figure 6** summarizes the changes in LRTC along a subcriticality–supercriticality spectrum that are thought to occur in disease states belonging to these seven clinical categories.

CLINICAL APPLICATIONS OF BRAIN CRITICALITY

Anesthesia

The literature on criticality in anesthesia is limited but has already shown signs of significant clinical promise. From this small body of research, one can extract two areas of clinical relevance: markers for the depth of anesthesia and predictors of recovery from a persistent comatose state. This literature harmonizes well overall with that of sleep medicine (see Sleep Medicine below).

Three studies have reported on criticality-based markers of the anesthesia depth (see **Table 1**). An electrocorticogram (ECoG) study of patients undergoing anesthesia for surgical removal of epileptic foci showed that the critical eigenvalues of matrices obtained from a vector auto-regressive (VAR) model could potentially serve as a marker of the depth of anesthesia (Alonso et al., 2014). A scalp electroencephalogram (EEG) study of patients under anesthesia found that LRTC, in combination with oscillation amplitude, could help differentiate between consciousness and anesthesia-induced unconsciousness (Thiery et al., 2018). The authors found that, under anesthesia, LRTC increases in the beta frequency range in frontocentral channels. This increase may reflect decreased neuronal excitability, leading to signal persistence and a resulting limitation on cognitive processes (He, 2014; Thiery et al., 2018). The results of this study contradict a previous study that had found a decrease in LRTC during anesthesia (Krzemiński et al., 2017). However, the contradiction may be secondary to significant differences between the experiments. Thiery et al. (2018) examined human subjects undergoing light anesthesia with sevoflurane, while Krzemiński et al. (2017) examined macaques undergoing deep anesthesia with different anesthetic agents. These differences suggest that future research should focus on identifying criticality-based metrics (e.g., power-law estimation, VAR eigenvalues, LRTC) that are specific to each anesthetic agent at different depths of anesthesia.

Another area of ongoing research is the use of criticality signatures to distinguish persistent coma from other forms of unconsciousness, including deep sleep and anesthesia-induced unconsciousness. A function magnetic resonance imaging (fMRI) study compared both blood oxygen level-dependent (BOLD) signals and brain networks between patients undergoing anesthesia and patients in unresponsive wakefulness syndrome (UWS or persistent coma) (Liu et al., 2014). While the node size in these brain networks was power-law distributed in both patient groups, the node degree distribution (i.e., the number of connections between nodes in the brain network) was only power-law distributed in the healthy patients undergoing anesthesia. The authors offer a helpful analogy from the world of airports and air traffic control. In patients under anesthesia, both the airport size and the air traffic follow a power-law distribution.

TABLE 1 | Summary of anesthesia-related criticality literature.

Study	Study population	Modality	Analysis	Main findings
Alonso et al., 2014	3 adult subjects with intractable epilepsy undergoing surgical removal of an epileptic focus	ECoG under propofol anesthesia	Vector auto-regressive (VAR) model; critical eigenvalues	• Eigenvalues of VAR matrices change significantly as anesthesia is induced. This finding is robust to changes in how data is normalized and could be used as a metric for depth of anesthesia. • As anesthesia is induced, high frequency modes are damped, suggesting that cognitive processes associated with higher frequencies are being tuned out while lower frequency processes are associated with maintaining the patient alive during anesthesia. • Self-organized criticality (SOC) could be result of synaptic adaptation. Disrupting synaptic adaptation should lead to loss of SOC.
Liu et al., 2014	8 healthy adults receiving propofol infusion; 5 adults with unresponsive wakefulness syndrome (UWS)	fMRI	Power-law estimation	• Node degree distribution was power-law distributed for healthy participants throughout all phases of anesthesia, but was never power-law distributed for patients with UWS, regardless of spatial scale. Node size distribution was power-law distributed for both. Study did not meet (Clauset et al., 2009)criteria for power law. • Criticality would not be needed for wakefulness alone but would underlie the brain's ability to recover from anesthesia or deep sleep. Future research should investigate whether power laws or other markers of SOC are helpful predictors of recovery from coma or other minimally conscious states
Thiery et al., 2018	7 adults receiving sevoflurane anesthesia	EEG	DFA	• Unconsciousness under sevoflurane was associated with increases in LRTC in beta amplitude over frontocentral channels and decrease in alpha amplitude over occipito-parietal channels. • LRTC and oscillation amplitude may reflect different properties of the brain that are impacted during anesthesia.

ECoG, electrocorticogram; fMRI, functional magnetic resonance imaging; EEG, electroencephalogram.

But in patients with UWS, the airport size remains power-law distributed while the air traffic loses its power-law distribution. This loss may reflect changes in underlying neuronal network topology that give UWS such a poor prognosis. However, more research in this area is required since the node degree distribution in this study does not meet the power-law criteria of Clauset et al. (2009) and, therefore, may follow a different distribution. In fact, another study found an exponentially truncated power law for both patients groups (anesthetized and UWS patients), which suggests the absence of a distinctive signature for the UWS group (Achard et al., 2012). Significant technical differences between Liu et al. (2014) and Achard et al. (2012) make a direct comparison difficult. Nevertheless, these studies raise the possibility that SOC underlies the brain's ability to rebound quickly from anesthesia or deep sleep, but not from UWS or other major brain insults. Future research in this area will benefit intensivists and neurologists looking for prognostic markers of irreversible brain damage.

Epilepsy

Epilepsy, a disorder characterized by multiple seizures and affecting 1% of the world's population, represents a significant clinical challenge (Fiest et al., 2017). There is a robust body of work examining the applications of critical phenomena to epilepsy, as summarized in **Table 2**. From this literature, the following four topics emerge as clinically relevant areas of ongoing research: seizure prediction, seizure localization, seizure characterization, and quantitative analysis of seizure genesis and termination.

Seizure prediction is an important goal in epileptology (Mormann et al., 2007). Efficient seizure prediction, even if only by a few seconds to minutes, may allow patients enough time to administer anti-epileptic medications before seizure onset, either by themselves or through automated implanted devices (Cook et al., 2013). To this end, several studies have identified criticality-based signatures that may help predict the onset of a seizure. For example, critical systems near a phase transition will exhibit signs of "critical slowing." A combined EEG and ECoG study of children with epilepsy found evidence of such critical slowing in synchronous fluctuations up to 1 h before seizure onset (Cerf et al., 2004). Other studies have taken advantage of an uncanny similarity between seizures and earthquakes. Seizures, like earthquakes, exhibit several properties that are characteristic of SOC (Bak and Tang, 1989; Bak et al., 2002). For example, both seizures and earthquakes cluster temporally, such that the likelihood of the next seizure or earthquake decreases the longer the seizure-free or earthquake-free interval (Omori, 1895; Sornette and Sornette, 1989; Osorio et al., 2009, 2010). Studies have identified other SOC properties in seizures. These include a power-law distribution of inter-seizure intervals (Osorio et al., 2009, 2010; Cook et al., 2014) and of time intervals between non-ictal epileptiform discharges, including burst suppression in neonatal hypoxia (Worrell et al., 2002; Roberts et al., 2014a). By better characterizing these properties, one could hope to identify parameters that can help predict a future seizure—much the same way that seismologists would like to predict the next earthquake (Meisel and Loddenkemper, 2019).

The predictability of these seizures may be related to increased temporal correlation or long memory. A study of long-term ECoG recordings found that epileptiform discharges and seizures in some patients were consistent with long-memory processes, with signal correlations going as far back as 40 days before seizure onset (Cook et al., 2014). Long memory suggests a decrease in signal complexity and, thus, more predictability.

TABLE 2 | Summary of epilepsy-related criticality literature.

Study	Study population	Modality	Analysis	Main findings
Worrell et al., 2002	7 adult patients with medication-resistant temporal lobe epilepsy	Interictal ECoG	Power-law estimation	• Study found evidence of SOC in interictal epileptiform discharges and suggested SOC-based method for identifying seizure focus.
Cerf et al., 2004	6 pediatric patients with presurgical epilepsy evaluation	Pre-ictal and inter-ictal ECoG, scalp EEG	Critical slowing-down of pre-ictal amplitude	• Study found evidence of criticality in synchronous fluctuations up to 1 h prior to seizure onset. • Root mean square amplitude or excess energy content were suggested as possible criticality order parameters.
Parish et al., 2004	5 adult patients with unilateral mesial temporal lobe epilepsy	Wake, sleep, pre-ictal and ictal/post-ictal ECoG	DFA	• LRTC in energy fluctuations over seconds to minutes was seen in both epileptogenic and non-epileptogenic hippocampus. • DFA exponents for non-epileptogenic regions were smaller compared to epileptogenic regions, but no difference in DFA exponents was noted between pre-ictal and baseline state.
Monto et al., 2007	5 adult patients with medication-resistant neocortical epilepsy; 2 patients received lorazepam	Inter-ictal ECoG	DFA	• LRTC was present near the seizure focus, and seen prominently in beta band (14−30 Hz). Lorazepam decreased beta-band LRTC near the focus and increased LRTC in other cortical areas. • Anti-epileptic mechanism of benzodiazepines may be related to normalization or reduction of LRTC in epileptic focus and may serve as biomarker during presurgical localization of epileptic foci.
Osorio et al., 2009	60 adult patients with mesial temporal and frontal lobe medication-resistant epilepsy	Pre-ictal and ictal ECoG	Power-law estimation	• Study finds evidence of power law distribution for seizure energy and inter-seizure interval time. Moreover, study found that seizures tend to occur in clusters, obeying an Omori-type law in which the likelihood of next seizure decreases the longer the seizure-free interval. These insights suggested a strong analogy between seizures and earthquakes, which behave in a self-organized critical way.
Osorio et al., 2010	60 adult patients with mesial temporal and frontal lobe medication-resistant epilepsy	Pre-ictal and ictal ECoG	Power-law estimation	• Five statistics from seismology (including energy, inter-event waiting time, direct and inverse Omori law, time to next earthquake) were compared to analogous statistics in seizures. Insights from SOC in earthquakes were applied to seizures.
Hobbs et al., 2010	6 pediatric epilepsy patients	LFPs from removed epileptic brain tissue	Branching parameter, correlation, power-law estimation	• Some epileptic brain tissue exhibited prolonged hyperactivity. Study found positive correlation between firing rate and critical branching parameter during this prolonged hyperactivity, suggesting possible existence of positive feedback loop in some forms of epilepsy.
Meisel et al., 2012	8 adult patients with focal epilepsy	Pre-ictal, ictal, post-ictal ECoG	Power-law estimation*	• Study found a robust power law distribution of phase-locking intervals and saw this as evidence of SOC. Variations in goodness-of-fit suggested that not all brain regions are tuned to criticality at the same time. • Significant deviation from power law during seizure suggested departure from critical state, in part due to excessive synchronization.
Meisel and Kuehn, 2012	8 adult patients with intractable epilepsy	Pre-ictal, ictal ECoG	Variance of signal amplitude	• The inverse of the signal variance followed a scaling law and decreased as a seizure approached. • Oscillations in variance leading toward seizure onset were suggestive of critical transition characterized by a Hopf bifurcation.
Kramer et al., 2012	19 adult patients with different epilepsy etiologies	ictal and post-ictal from scalp EEG, ECoG, LFP and MUA	Critical slowing down, temporal and spatial correlations, flickering	• Multi-scale analysis suggested seizure termination happens through a critical transition, modeled by a discontinuous fold bifurcation. • Status epilepticus may represent a system's inability to cross a critical transition, instead reverberating between ictal and post-ictal attractors.
Roberts et al., 2014a	13 term neonates with either birth hypoxia or circulatory collapse	Non-ictal EEG of burst suppression seen within 18 h of birth	Power-law estimation*, scaling relations, burst shape analysis (skewness, kurtosis)	• Power law relationship was seen between burst size and duration. The scaling exponent of that relationship increased as burst suppression gave way to normal EEG activity. • Shape analysis revealed leftward skewness, also seen in crackling noise like Barkhausen noise. Skewness resolved as burst suppression gave way to normal EEG activity. Leftward skewness may be related to state-dependent metabolite depletion. • Other signs of criticality include evidence of shape scaling function and inter-relationship of power-law exponents for burst area, duration, and area-duration relationship. There is evidence of critical phase transition from burst suppression to resumption of normal EEG.

(Continued)

TABLE 2 | Continued

Study	Study population	Modality	Analysis	Main findings
Cook et al., 2014	15 adult patients with refractory epilepsy	ECoG recorded over 0.5−1.8 years	Power-law estimation; Hurst exponent	• Study found evidence of a power law for inter-seizure interval in large human dataset, with scaling exponent −1.5 consistent with previous studies. Hurst analysis was consistent with a long-memory process in most subjects, with memory ranging from 3 to 40 days. • The presence of long-memory implies a less complex and more predictable system—epilepsy prediction may depend on the existence (or not) of long-memory in different types of epilepsy.
Minadakis et al., 2014	2 adult patients (iEEG); 6 adult patients (scalp EEG)	Pre-ictal and ictal ECoG and scalp EEG	Q-parameter, Tsallis entropy, volumetric energy density	• While seizures showed consistently elevated q-parameter in range 1.6−1.8, inter-ictal and pre-ictal EEG could not be readily distinguished by q-parameter alone. • There was evidence of intermittent criticality (IC), which may generalize to SOC on larger time scales. Tsallis entropy did not change significantly from pre-ictal to ictal, suggesting other forms of complexity may be involved in the ictal period. The concept of "fractures and faults in the brain," a continuation of the earthquake-seizure analogy, may be a fruitful framework for advancing seizure prediction.
Yan et al., 2016	3 adult patients with refractory temporal lobe epilepsy	Pre-ictal, ictal, post-ictal ECoG	Power-law of wavelet spectral density, Hurst exponent, linear correlation coefficient	• The pre-ictal to ictal transition was characterized by transition from anti-correlation to correlation as given by Hurst exponent and fractional Brownian motion (fBm) model. • Hurst exponent changes in ictogenesis happened throughout the brain and not just at epileptic foci. In posti-ical state, high Hurst exponents were seen throughout the brain, suggesting seizure was result of breakdown of global neuronal network. • Wavelet-based spectral density approach in setting of fBm model may be helpful tool for seizure prediction.
Arviv et al., 2016	12 adult and 8 pediatric patients with refractory epilepsy; 18 age-matched healthy controls	Inter-ictal MEG	Power-law estimation*, branching parameter, avalanche shape analysis	• Patients with drug-resistant epilepsy showed deviations from expected branching parameter at criticality, especially at interictal epileptiform discharges. • Quantitative analysis of MEG using criticality-related parameters may allow better evaluation of excitation-inhibition balance in sleep-related disorders and in epilepsy.
Witton et al., 2019	2 pediatric and 1 adult patients with medication-resistant epilepsy	MEG, beamformer source models, volumetric maps	Hurst exponent, rogue wave analysis, kurtosis of inter-ictal spikes	• Hurst exponent analysis, kurtosis, and rogue waves could serve as important parameters in automatic classifiers for epilepsy detection, as well as for patients referred for pre-surgical MEG evaluation who do not have interictal spikes. • Epileptiform activity was strongly persistent, suggesting that Grainger causality is not suitable for epilepsy data.

Asterisk (*) represents power-law estimations that meet criteria equivalent to or more stringent than Clauset et al. (2009). MEG, magneto-encephalography; ECoG, electrocorticogram; LFP, local field potential; MUA, multi-unit activity; DFA, detrended fluctuation analysis.

These studies open up the possibility of using LRTC and other correlation measures to predict impending seizures. While there is no gold-standard approach for seizure prediction at this time, the brain criticality framework offers new insights that will hopefully produce several candidates for effective seizure prediction. Some of these candidates include excess energy content of EEG signals (Cerf et al., 2004), heavy-tailed distributions of inter-ictal discharges (Osorio et al., 2010), signal variance (Meisel and Kuehn, 2012), Hurst exponent analysis (Cook et al., 2014; Yan et al., 2016), q-parameter, and volumetric energy density from Tsallis non-extensive statistical mechanics (Minadakis et al., 2014).

The surgical removal of epileptic foci for treating refractory epilepsy requires adequate localization of the source of epileptiform discharges (Mu et al., 2014). Localizing the epileptic focus remains a challenging part of this process. Epileptic foci exhibit many critical features, like power-law distributions and LRTC, that are useful for localization. In an ECoG study of patients with temporal lobe epilepsy, the epileptic foci produced a power-law-like behavior of seizure energy and inter-seizure intervals (Worrell et al., 2002). An ECoG study of epileptic patients found that both non-epileptic and epileptic foci in the hippocampus exhibited LRTC (Parish et al., 2004). However, the epileptic foci had larger scaling exponents compared to the non-epileptic foci. Another ECoG study found a similar result, namely stronger LRTC near the seizure focus (Monto et al., 2007). More recently, a magnetoencephalography (MEG) study found that the Hurst exponent – a metric of LRTC – improved the detection of seizure foci (Witton et al., 2019). These studies globally suggest that observables of critical phenomena, like power-law regimes and increased correlation, can improve seizure localization techniques.

The lens of criticality is also casting new light on the characteristics and dynamics of seizures themselves. Several publications have argued that seizures and inter-ictal epileptiform discharges, including burst suppression, represent a critical phenomenon that is power-law distributed (Worrell et al., 2002; Cerf et al., 2004; Osorio et al., 2009, 2010; Roberts et al., 2014a). If

this is correct and the reported power-law exponents for seizure energy are between 2 and 3 (as many are), then it follows that, at least mathematically, seizures ought to have a finite mean (energy, size, duration) but infinite (energy, size, duration) variance. Some have argued that this may account for status epilepticus, the phenomenon of prolonged seizures lasting hours to days. The theoretically infinite variance of seizure energy would lead to prolonged seizures that would ultimately resolve because of the finite metabolic supply available to neurons (Osorio et al., 2010; Roberts et al., 2014b). Moreover, if seizures represent a power-law distributed critical phenomenon, they cannot be described by their mean values, since, in a scale-free distribution, there is no "typical" value or mean. Thus, there may be no point in reporting mean seizure duration or energy in clinical publications. Rather, in future clinical and epidemiological studies, it may be more pertinent to report power-law exponents, which best characterize this distribution (Osorio et al., 2009).

However, other publications have argued that the normal brain at rest is in a critical state. Therefore, seizures and interictal epileptiform activity should represent a departure from criticality. This departure from criticality perhaps arises from synchronization effects and characteristic scales present in seizures that become dominant, thus diminishing the scale-free distribution (Osorio et al., 2009; Meisel et al., 2012; Arviv et al., 2016). This departure from a scale-free distribution has been confirmed visually with a "knee," "shoulder," or "bump" – different words for the same anomalous deviation—in the log-log plot of several probability density functions, including that of seizure energy (Osorio et al., 2009), phase-locking intervals (Meisel et al., 2012), neuronal avalanche size (Arviv et al., 2016) and burst area in burst suppression (Roberts et al., 2014a). The evidence suggesting that the resting brain is in a critical state is strong (Kitzbichler et al., 2009; He, 2011; Tagliazucchi et al., 2012; Daffertshofer et al., 2018), even if some of that evidence (Kitzbichler et al., 2009; Meisel et al., 2012) has been challenged (Botcharova et al., 2012). Seizures would logically seem to represent a departure from the resting state of the brain and thus from a critical state. How then can one reconcile this with all the evidence suggesting that seizures behave like a critical phenomenon?

Perhaps one way to reconcile this information is to look more closely at the types of variables (Milton, 2012). In cases that have identified power-laws in the resting brain (with departures during seizures), the variables studied were usually neuronal avalanche size and duration, in what could be called an "avalanche approach." On the other hand, studies that found power-law behaviors of seizures took more of an "earthquake approach" in which the variables were usually seizure energy and inter-seizure interval (Worrell et al., 2002; Osorio et al., 2009). Since different properties, or "laminar phases," are being examined in each case, it may not be reasonable to compare their power-law exponents (Milton, 2012).

Moreover, the range of power-law exponents found in both the avalanche and earthquake approaches is broad and overlapping. The exponents encompass the range of –3/2, which is expected for avalanche size in SOC, up to −5/3, characteristic in turbulent dynamical systems (Milton, 2012). This broad range may result from particular experimental conditions (including digitization rates of instruments). But this range may also reflect the reality that neurons, unlike earthquakes and sand-piles, learn and adapt (Bonachela et al., 2010). The existence of characteristic scales ("bumps") on log-log plots, which perturb the expected scale-free distribution, may also be due to characteristic scales from rare neurological events such as dragon-kings (Pisarenko and Sornette, 2012; Sachs et al., 2012). Finally, since many control parameters may be involved in governing these systems, the possibility of "double criticality" whereby critical regimes coexist with different order and control parameters may also be at work in this apparent disagreement (Hesse and Gross, 2014). Resolving this disagreement on both theoretical and experimental grounds will be an important area of future research.

Brain criticality also offers insights into seizure initiation. Epileptic foci removed from pediatric epilepsy patients exhibited neuronal hyperactivity, whose increased firing rate correlated with an increased branching parameter (Hobbs et al., 2010). This finding suggests that in some epileptic syndromes, a positive feedback loop between firing rate and branching parameter may be responsible for generating seizures as a super-critical state. An ECoG study found oscillations in signal variance in the lead-up to a seizure (Meisel and Kuehn, 2012). These pre-ictal oscillations were suggestive of a critical transition, characterized mathematically by a Hopf bifurcation. Despite the small number of studies in this area, research on seizure generation using criticality is promising.

Several studies suggest that seizure termination may also involve a critical transition. In one study by Kramer et al. (2012) the brain's inability to complete a critical transition results in status epilepticus, in which the brain dynamics constantly reverberate between the ictal and post-ictal state (i.e., attractor), without ever crossing the threshold that effectively ends a seizure. In a study of neonates with birth hypoxia, researchers found evidence of a critical phase transition in the shift from burst suppression to the resumption of normal EEG patterns (Roberts et al., 2014a). The role of benzodiazepines in seizure termination may also be related to criticality. In a small ECoG study of patients with epilepsy, study authors found that a decrease in LRTC in the ictal focus accompanied the clinical resolution of a seizure after benzodiazepine administration (Monto et al., 2007). These studies all suggest that criticality plays a role in seizure termination.

Neurodegeneration

A small number of studies (see **Table 3**) have examined the role of critical phenomena in neurodegenerative diseases, like Alzheimer's disease (AD) and Parkinson's disease (PD). These studies reveal new insights about the pathophysiology of these diseases and suggest novel markers for disease monitoring.

Cognition requires production and subsequent decay of synchronization in neural networks (Breakspear and Terry, 2002). Moreover, in healthy adults, spontaneous fluctuations in synchronization are known to follow a power-law distribution, suggestive of an underlying SOC state (Stam and de Bruin, 2004). Does AD represent a departure from critical dynamics? Is synchronization perhaps a control parameter given its

TABLE 3 | Summary of neurodegeneration-related criticality literature.

Study	Study Population	Modality	Analysis	Main Findings
Stam et al., 2005	24 adults with AD, 19 non-demented adults with subjective memory complaints	EEG during eyes-closed resting state	DFA	• Study examined mean synchronization in different frequency bands. Mean EEG synchronization and spontaneous fluctuations of synchronization were lower in AD in upper alpha and beta bands compared to non-AD patients. Mean synchronization level and DFA exponents were correlated to MMSE score. Both patients and controls showed scale-free patterns of synchronization fluctuations, extending to up to 10 s. • AD patients may have brain electrical pattern consistent with SOC but exhibit decreased processing speed from decreased fluctuations of synchronization.
Montez et al., 2009	19 adults with early-stage AD, 16 age-matched controls	MEG during eyes-closed resting state	DFA, burst statistics	• Using criticality-based "avalanche analysis," study found that AD patients had a strongly reduced incidence of alpha-band oscillation bursts over temporo-parietal regions and markedly weaker autocorrelations on long time scales (1–25 s). • Study suggested that criticality-related measurements of amplitude dynamics of oscillations may prove useful as neuroimaging biomarkers of early-stage AD.
Hohlefeld et al., 2012	10 adults with idiopathic PD	LFP from bilaterally implanted electrodes from STN DBS	DFA	• Study examined LRTC of the amplitude envelope of LFPs recorded from subthalamic nucleus, both on and off of levodopa. "On levodopa" state was characterized by stronger LRTC (up to 50 s) than the "off" state in beta and high-frequency oscillations. • Weaker LRTC in off state might indicate limited information processing in dopamine-depleted basal ganglia. Study suggests LRTC may serve as possible biomarker of pathological neuronal processes in PD.
Ruiz et al., 2014	1 adult with severe idiopathic PD, treated with STN DBS	Inter-onset interval (time between note onset of two subsequent notes) while playing piano, with STN DBS both on and off	DFA, spectral density	• Study investigated temporal deviations during skilled piano performance of a non-professional pianist with severe PD treated with STN DBS. In tremor-affected right hand, timing fluctuations of the performance exhibited random correlations while off DBS. When DBS was on, LRTC increased along with general motor improvement. • The authors remark that the presence of LRTC and *1/f* laws in performance (improved by DBS) can be related to the brain operating near criticality.
Vyšata et al., 2014	110 adults with moderate-to-severe AD, 110 healthy controls	EEG during resting-state	Power-law estimation, spectral density	• Study evaluated power-law exponents for power-law distribution of EEG spectrogram from patients with AD compared to healthy controls. Power-law exponent was found to be a specific marker of AD in the frontal EEG channels. Authors suggest that loss of functional connectivity may explain these differences in power-law exponents. Clinical utility of power-law exponent of spectrogram would require repeating the study on patients with mild cognitive impairment or early stages of AD.
West et al., 2016	12 adults with PD who received bilateral STN DBS	LFP while on and off dopaminergic medications	Spectral density, signal coherence, DFA	• Study examined LFPs from PD patients undergoing STN DBS surgery, on and off of dopaminergic medications. Authors demonstrated up-modulation of alpha-theta (5−12 Hz) band power with L-DOPA treatment, whilst low beta band power (15−20 Hz) band-power was suppressed. Using DFA adapted to phase synchrony (DFA-PS), study found LRTC in phase dynamics of coupled left and right STN region for low beta band. Low beta band DFA-PS scaling exponent magnitude for interhemispheric pairs was positively correlated with PD symptom severity in the off-medication state. Findings suggested that the more severe the motor impairment, the closer the subthalamic network was to onset of synchronization, implying shift of network toward supercritical regime.

AD, Alzheimer's disease; PD, Parkinson's disease; STN DBS, subthalamic nucleus deep brain stimulation; MMSE, Mini-Mental Status Examination; LFP, local field potential.

importance in cognition? To begin to answer these questions, researchers compared various measures of synchronization on EEG between patients with AD and non-demented patients with subjective memory problems (Stam et al., 2005). While both cohorts maintained a scale-free distribution of spontaneous fluctuations of synchronization, the mean synchronization and its fluctuations were both decreased in the upper alpha and beta frequency range in the AD patients compared to the non-demented patients. This finding is consistent with the view that AD patients maintain a SOC state but with decreased ability to generate and destroy synchronized neural networks. The authors go on to speculate that perhaps synchronization loss in the upper alpha and beta band is one of the first quantifiable changes in AD since it is statistically different from non-demented patients who report memory impairment. Moreover, the mean synchronization level and the DFA exponent of synchronization fluctuations were both correlated to the Mini-Mental State Examination (MMSE) score. Synchronization-based metrics may, therefore, prove helpful for diagnosis and monitoring of early-onset AD.

Other metrics inspired by brain criticality show promise for the diagnostic evaluation of early-onset AD. A MEG study discovered a decreased incidence of alpha-frequency oscillation bursts and weaker auto-correlations in patients with early-onset AD compared to controls (Montez et al., 2009). Its authors concluded that oscillation amplitude dynamics may be beneficial for early-onset AD detection. Operating from the framework of SOC, a large, resting-state EEG study of patients with moderate-to-severe AD compared to healthy controls also identified a possible marker for early AD detection (Vyšata et al., 2014). The power-law exponents for spectral densities (per brain region) were compared between AD and healthy patients. A statistically significant difference in the power-law exponent in the frontal and pre-frontal lobes was noted. This result is perhaps not so surprising given that frontal lobe atrophy typically accompanies AD dementia. Interestingly, the most highlyspecific and predictive area of the brain for AD in this study was the temporal region (Vyšata et al., 2014). Future studies using this approach and focusing on the temporal region may be able to validate this power-law approach as a diagnostic metric in patients with early manifestations of AD. To this point, a recent fMRI-connectome study showed that a combination of criticality-based metrics can help distinguish neurotypical adults from those with mild cognitive impairment or AD (Jiang et al., 2018).

Parkinson's disease (PD) may be a case of how deviation from a critical state in crucial motor circuits leads to motor symptoms like tremors, bradykinesia, and rigidity. Researchers have identified LRTC from the subthalamic nuclei (STN) of patients with PD undergoing deep brain stimulation (DBS) (Hohlefeld et al., 2012). These correlations increased with the administration of levodopa, one of the common medications for treating PD. In a rat model of PD, LRTC also increased following administration of apomorphine (Cruz et al., 2009), which suggests that restoration of LRTC may be related to symptomatic improvement in PD. A study of PD patients who underwent DBS surgery found LRTC in the dynamics of the bilateral STN, both on and off medications (West et al., 2016). Using an adaptation of DFA to study synchronization called DFA-PS (Botcharova et al., 2015), the authors found that the DFA-PS exponent was positively correlated with motor symptom severity when patients were not receiving dopaminergic medications. Therefore, these authors suggested that patients with more severe motor symptoms are closer to the onset of pathological synchronization, which may reduce effective information transfer in these important neural circuits (Hanslmayr et al., 2012; West et al., 2016). In this regard, PD may represent a situation of departure from a critical state toward perhaps a hyper-synchronized supercritical state.

Obtaining recordings from deep brain structures like the basal ganglia is not usually possible outside of DBS. Since DBS is not the first-line therapy for PD, it seems unlikely that LRTC will develop into a helpful marker of PD onset and progression. Gait analysis and related behavioral metrics, on the other hand, may offer a more convenient way to follow the clinical evolution of PD. Healthy human gait is characterized by *1/f* noise, which is known to be a feature of SOC systems (Hausdorff, 2009). This *1/f* noise disappears in PD but resumes with non-invasive auditory rhythmic stimulation (Hove et al., 2012). In a unique study, a single patient with idiopathic PD and right-handed tremor, who happened to be an accomplished pianist, received DBS and was subsequently asked to perform works of piano both with and without active DBS (Ruiz et al., 2014). Without DBS, correlations in the inter-onset interval (i.e., the time between note onset of subsequent piano notes) were random. But with active DBS, long-range correlations of inter-onset interval emerged, along with general motor improvement of the affected right hand on the Unified Parkinson's Disease Rating Scale (UPDRS) - III scale. The authors suspected that DBS provides a similar stimulus to the non-invasive rhythmic stimulation of Hove et al.'s (2012) experiment, which restores the *1/f* noise of gait, presumably by restoring a critical state in the motor basal ganglia circuit (Ruiz et al., 2014). Future research should focus on establishing whether restoration of *1/f* noise is necessary for motor improvement in PD and whether gait-based metrics can serve a clinical purpose in either diagnosing or monitoring PD.

Neurodevelopment

The brain criticality hypothesis also applies to the newborn brain that matures and ages across an average human lifespan. As it grows, the brain's electrical signature undergoes changes that are helpful markers of typical development. Research in this area has taken shape around two central themes (see **Table 4**). The first is the study of brain oscillations in premature infants or infants with birth asphyxia (hypoxemic-ischemic encephalopathy or HIE). The other is the study of brain oscillations in children, adolescents, and adults to characterize the electrical patterns that correlate with structural and anatomic changes of aging.

If the mature human brain exhibits signs of criticality, it seems reasonable to ask whether those signs are also present in the term or pre-term neonate. Studying burst activity on the EEG of pre-term infants, Hartley et al. identified LRTC and dynamics that were suggestive of a phase transition (Hartley et al., 2012). Despite several infants having intracranial hemorrhages, the Hurst exponents describing the LRTC were similar for infants with and without bleeding. This finding suggested that the brain maintains temporal complexity despite this vascular insult. Another EEG study showed that power-law exponents of electrical bursts were predictive of neurodevelopmental sequelae in term infants with HIE (Roberts et al., 2014a). This fascinating discovery led to a similar EEG study in extremely preterm infants, searching for criticality-based metrics that could predict long-term sequelae. A careful analysis of several parameters from shape analysis led to the identification of the slope of burst shape, among other parameters, that could serve as a sensitive and specific predictor of neurocognitive and motor sequelae in this unique population (Wikstro et al., 2015). In sum, shape analysis and power-law exponents predict clinical outcomes in preterm and term infants, respectively. Regardless of hemorrhage status, the brains of preterm infants exhibit LRTC. These findings suggest that criticality plays a vital role in the dynamics of the preterm and term infant brain.

How criticality or near-criticality emerges and evolves in the infant's brain through adolescence into adulthood is another crucial area of investigation. Jannesari et al. (2020) studied term

TABLE 4 | Summary of neurodevelopment-related criticality literature.

Study	Study population	Modality	Analysis	Main findings
Suckling et al., 2008	22 healthy adults (11 in the age range 20–25 years old, 11 in the age range 60–70 years old), matched for education.	Task and resting-state fMRI; double-blind, randomized administration of subcutaneous scopolamine or saline (placebo)	Hurst exponent, singularity spectrum using wavelet transform maximum modulus method, multifractal parameters	• Previous research had shown that healthy aging and cholinergic blockade with scopolamine were associated with increase in Hurst exponent, implying a marker of suboptimal neurophysiological dynamics (Wink et al., 2006). However, previous research had also shown that faster processing speed in certain tasks also led to increased Hurst exponent (Wink et al., 2008). This study used multifractal approach to tease apart the discrepancy and used (Castaing et al., 1990) algorithm to identify the role of turbulence. Authors conclude that turbulence has limited validity, while invariance of energy dissipation is better explained by critical phenomena.
Thatcher et al., 2009	458 healthy pediatric subjects (age 2 months to 16 years old)	resting-state EEG	Mean phase shift duration, phase-locking intervals, power-law estimation, spectral density analysis	• Study explored development of SOC as measured by EEG phase reset—a combination of phase shift followed by phase stability (or phase locking) – from infancy to adolescence. Mean duration of phase locking (150–450 s) and phase shift (45–67 s) increased as a function of age. Development and number of synaptic connections may be a possible order parameter for SOC during human brain maturation.
Berthouze et al., 2010	36 healthy subjects (age 0–55 years old)	EEG during wrist-extension task	Spectral density analysis, DFA	• In physical systems, SOC states take time to develop. Study found that there is a scale-free nature to EEG LRTCs from early childhood through to maturity but that the magnitude of these effects changed with age.
Smit et al., 2011	1433 healthy subjects (age 5–71 years old)	Resting-state EEG	DFA, spectral density, principal component analysis	• Study observed significant increases in LRTC from childhood to adolescence and into early adulthood. PCA of the spatial distribution of LRTC showed functional-anatomic segregation between frontal, occipito-temporal, and central regions that became more integrated with development. DFA scaling analysis may be useful as a biomarker of pathophysiology in neurodevelopmental disorders like ADHD and schizophrenia.
Hartley et al., 2012	11 pre-term newborns (23–30 weeks gestation)	EEG	Hurst exponent (Whittle estimator and DFA)	• LRTC were identified in very pre-term infants through two estimate of Hurst exponents of EEG bursts. The study found no difference in Hurst exponents between subjects with and without brain hemorrhages, indicating that despite lower burst event frequency for newborns with hemorrhages, signal complexity was maintained. Overall EEG pattern was suggestive of relaxation dynamics as can be seen near a phase transition.
Mares et al., 2013	17,722 healthy adults (ages 18–70 years old)	Resting-state EEG	Spectral density, power-law estimation	• Study investigated parameters of colored noise in EEG in healthy adults. Absolute value of power spectra exponent decreased significantly with age, perhaps indicative of age-related changes in self-organization of brain activity due to brain atrophy. Globally, there was a trend from pink noise to white noise with age that was seen consistently in beta and delta bands.
Fransson et al., 2013	fMRI: 18 term newborns and 17 healthy adults (ages 22–41 years old); EEG: 15 term or post-term newborns, 7 healthy adults (ages 14–53 years old)	EEG in stage 2 sleep, fMRI	power-law estimation	• Study found that newborn brain dynamics follow apparently scale-free frequency power distribution across several orders of magnitude in both fMRI and EEG signals. In newborns, primary sensory areas exhibit larger power-law exponents than higher associative cortical areas, in contrast with the adult brain. • High power-law exponents in newborns were likely due to spontaneous activity transients (SATs) or bursts that seem to underlie brain activity in the first neuronal networks in the human brain (Vanhatalo and Kaila, 2006).
Thatcher et al., 2014	70 healthy subjects (age 13–20 years old)	LORETA (EEG) of the Brodmann areas of the default mode network in the delta frequency band	Phase shift duration, phase lock duration	• Study found no significant correlation between age and phase shift and phase lock duration from EEG of the default mode network. Study findings were globally consistent with SOC.
Frohlich et al., 2015	39 preschool-age healthy subjects	EEG	Frequency variance, power-law estimation	• Study quantified variance of rate of change of signal phase (i.e. frequency variance) as a proxy for phase reset (or signal stability). Frequency variance increased with age in preschool age children. This method is helpful in pediatric studies because it does not require long recordings. Authors suggest that phase resets are critical fluctuations driven by SOC.
Iyer et al., 2015	43 preterm neonates (23–28 weeks gestation)	Resting-state single-channel EEG recorded at 12, 24, 48, and 72 h of life	Power-law estimation*, burst shape analysis, generalized linear model	• Study found scale-free properties of EEG bursts in extremely preterm infants as soon as 12 h after birth. Metrics of burst shape were predictive of neurodevelopmental outcomes using Bayley scales. Specifically, symmetric bursts that are relatively flat at long time scales suggested a favorable neurodevelopmental outcome. Conversely, skewed and highlykurtotic bursts in neonates shortly after birth were suggestive of long-term

(Continued)

TABLE 4 | Continued

Study	Study population	Modality	Analysis	Main findings
				disability. Low burst slope values, moderated by effect of gestational age, correlated with poor scores on the Bayley scales or early death.
Padilla et al., 2020	33 children born extremely prematurely and 29 children born term	fMRI and diffuse MRI at 10 years old	Ignition analysis, structural and connectivity matrices, whole-brain Hopf model	• Study compared 10 year-old children who were either born extremely pre-term (EPT) or born at term, using fMRI with ignition analysis. Intrinsic ignition events allow propagation of neuronal activity to other regions over time which drives global integration. Extremely pre-term children had reduced intrinsic ignition events, consistent with previous study that had shown reduced spontaneous neuromagnetic activity in pre-term children. Study found that the hierarchy of information processing based on the variability of intrinsic ignition events was predominantly driven by visual and sensory region in EPT children compared to the higher-order processing areas like the fronto-temporal region and the associative area in term children.
Jannesari et al., 2020	19 term infants	High-density EEG during an oddball auditory task	Power-law estimation*, DFA	• Study evaluated infants at 6 and 12 months of age during auditory odd-ball task to see if the bursting, scale-free activity of pre-term infants continues as scale-free avalanche activity outside the newborn period. Suprathreshold events organized as spatiotemporal clusters whose size and duration were power-law distributed while time series of these events showed significant LRTCs. Power law was a better distribution fit than log-normal and exponential. No significant differences were noted between 6 and 12 months, suggesting stability of avalanche dynamics and LRTCs in the first year after birth.

Asterisk (*) represents power-law estimations that meet criteria equivalent to or more stringent than Clauset et al. (2009). LORETA, low-resolution electromagnetic tomography; PCA, principal component analysis; ADHD, attention deficit hypersensitivity disorder; MDI, motor development index.

infants at 6 and 12 months of life using high-density EEG to see if scale-free brain activity that was already known to exist at birth (Fransson et al., 2013) continued in the first year of life (Jannesari et al., 2020). At both 6 and 12 months, the EEG organized spatiotemporally according to a power-law with significant LRTC. The authors found no significant differences between the 6- and 12-month data, suggesting a degree of stability in neuronal avalanche dynamics after the newborn period. But while there do not seem to be significant differences in LRTC and power-law distributions during the first year of life in term babies, a significant difference does exist between pre-term babies and term babies, even a decade after birth. Using functional and diffusion MRI, researchers examined the brain dynamics of 10-year-old children, roughly half of whom were born extremely premature, and the other half at term (Padilla et al., 2020). Extremely premature (EP) children generated fewer electrical events (i.e., decreased ignition) compared to the term children – suggesting decreased global integration from decreased firing to other important brain regions over time (Deco et al., 2017). EP children also exhibited abnormal hierarchical organization, which autistic children are also known to exhibit (Parr et al., 2018), further linking prematurity and autism (Padilla et al., 2017). EP children's brain dynamics showed decreased synchrony and sub-criticality compared to term children, mainly in brain areas with rich-club architecture (Ball et al., 2014). This difference in synchronization perhaps occurs due to abnormal development of white matter in EP children (Uhlhaas et al., 2010). Yet, whereas extreme prematurity seems to predispose to some degree of sub-critical brain dynamics, it seems from other studies that term infants go on to exhibit similar power-law-like brain dynamics as adults. In an EEG-fMRI study, newborn brain dynamics followed scale-free power (frequency) distributions across several orders of magnitude, with larger power-law exponents in primary sensory areas compared to associative cortical areas (Fransson et al., 2013). In contrast, power-law exponents for adult brain dynamics were highest in associative cortices. While both adults and term infants exhibit scale-free dynamics, the increased exponents in different brain areas suggest that development and aging control, to some degree, the cartography of near-criticality in the brain.

As for aging, the development of criticality and its suspected decay with age have been the subjects of several studies (see **Table 4**). Phase reset (PR), a combination of phase-shift followed by phase-locking of EEG signals, is a powerful marker of SOC used in many age-based studies of criticality. In a study of PR in close to 460 subjects in the age range of 2 months to 16 years old, PR followed a *1/f* distribution, with a longer mean duration of both phase-shift and phase-locking as a function of age (Thatcher et al., 2009). The presence of this distribution argues in favor of scale-invariant fluctuations in PR, consistent with SOC (Thatcher et al., 2009, 2014). In a study of pre-school children, EEG frequency variance, a proxy for PR, was also power-law distributed and increased with age (Frohlich et al., 2015). Like PR, frequency variance may reflect critical fluctuations driven by SOC.

LRTC has also been found to correlate with aging. A study of about 1430 subjects from ages 5 to 71 revealed significant increases in LRTC from childhood through adolescence into early adulthood (about age 25), after which LRTC stabilized (Smit et al., 2011). Scale-free modulations of resting-state oscillations, therefore, seem to reflect brain maturation. Moreover, principal component analysis (PCA) showed progressive integration of segregated functional-anatomic brain regions with age –

consistent with increased spatial correlation from critical dynamics. In a smaller study of subjects ages 0 to 55, EEG LRTC was present from early childhood into adulthood but with magnitudes that changed differently depending on age, EEG electrode, and frequency band (Berthouze et al., 2010). For example, LRTC magnitude increased with age in the beta band in central and parietal electrodes but decreased with age in the theta frequency range. But temporal correlation is not the only observable that appears to decrease with age in some frequency bands. A study of resting-state EEG in nearly 18,000 individuals ages 18 to 70 found a decrease in the power-law exponent of spectral density with age (Vyšata et al., 2014). The authors theorized that brain atrophy with age might lead to loss of neuronal connections (Morrison and Hof, 1997), which would shift the neural networks away from their scale-free topology (Barabási and Albert, 1999) and thus away from power-law dynamics.

While there may be some appearance of contradiction in these results (i.e., increased LRTC in one frequency range versus another with aging), there is precedent for contradictory results finding resolution when the right tool is applied. For example, both healthy aging and anticholinergic medications increase the Hurst exponent (Wink et al., 2006). Yet, faster processing speeds, which are not characteristic of aging, also lead to increases in the Hurst exponent (Wink et al., 2008). Suckling et al. (2008) reconciled these results with the introduction of a multi-fractal approach and demonstrated that criticality offered a better explanation than turbulence for these brain dynamics. This example highlights how the right methodology and tools can help make sense of disparate results. Methodological developments, like the index of functional criticality (Jiang et al., 2019), will hopefully generate more useful clinical results in this area. The applications of criticality to aging and geriatric medicine are still in their infancy but deserve more emphasis in a society with an increasingly elderly population.

Cognition, Attention, Learning, and Autism

In computational and theoretical models, criticality optimizes certain features of learning, including optimal information capacity and transmission (Shew et al., 2011; Shew and Plenz, 2013; Del Papa et al., 2017). Important aspects of human learning, including cognition and attention, have been analyzed through the lens of criticality (see **Table 5**). Studies on attention-deficit hypersensitivity disorder (ADHD) and autism, in which features of neurotypical cognition and attention are disrupted, are few in number but appear promising.

In the area of cognition, researchers have wondered whether criticality plays a role in the brain's response to increasing cognitive loads. In a study of healthy adults undergoing working memory and response tasks, Altamura et al. (2012) found power-law-like behavior in the upper tails of the cumulative distribution of response times. One possible interpretation of this result is the emergence of scale-free behavior in response to increased cognitive loads. In other words, increased cognitive load shifts random behavior toward scale-free behavior near a critical point. Another study of healthy adults undergoing a cognitive task also showed a power-law scaling of response time fluctuations (Simola et al., 2017). Furthermore, Simola et al. (2017) found autocorrelations and LRTC of response time fluctuations, with the LRTC scaling exponents correlating negatively with error rates and positively with executive function testing scores. As the authors pointed out, LRTC can originate in the setting of criticality but also exist in systems with a slow decay of memory. The negative correlation of LRTC scaling exponent with error rates suggests increased cognitive flexibility, which is more consistent with criticality than with a system that operates with slowlydecaying memory. Without criticality, LRTC would decrease cognitive flexibility because long-memory would not allow reconfigurations. Patients with ADHD are known to show increased response time variability in these kinds of tasks. However, in this study, the LRTC scaling exponents were not correlated to response time variability or mean response time, implying that another brain process may be involved in ADHD. Studies of behavioral dynamics (e.g., response times on tasks) in ADHD patients compared to neurotypical patients may grant further insights into the role of scale-free, critical dynamics in ADHD.

But while the behavioral response (i.e., response times) to increased cognitive load may be power-law-like, studies of the electrical brain response to increased cognitive load show more mixed results. A MEG study of neurotypical children and children with high-functioning autism undergoing executive function tasks demonstrated a decrease in power-law scaling of phase synchrony as cognitive tasks became more difficult, i.e., increased cognitive load (Tinker and Velazquez, 2014). Power-law distributions were uncommon in this study in both autistic and neurotypical children and were more likely to co-exist with other distributions (e.g., exponential). These results suggest that metastable, rather than purely critical, dynamics are at play in the brain's response to increased cognitive loads (Bressler and Kelso, 2001; Deco and Jirsa, 2012). Along similar lines, an EEG study of healthy adults during a working memory task found an inverse correlation between LRTC in the theta frequency range and memory performance (Euler et al., 2016). This result is perhaps the opposite of what one might have predicted from work that had found indications of criticality in behavioral dynamics (Altamura et al., 2012; Simola et al., 2017).

But not all brain studies of human cognition have argued against the existence of critical dynamics. An EEG study of 210 neurotypical adults undergoing an object recognition task showed that variation in *1/f* noise was a robust predictor of cognitive processing speed (Ouyang et al., 2020). Moreover, the power-law exponent of the *1/f* noise was most predictive of person-to-person processing speeds. While there are many non-critical sources of *1/f* noise, this study harmonizes well with the theoretical literature on criticality's optimization of information transmission. In an EEG study of healthy adults undergoing an action adjustment task, midfrontal theta – an electrical signature known to correlate with real-time error correction (Cavanagh and Frank, 2014) – displayed scale-free-like fluctuations over durations of up to tens of seconds (Cohen, 2016). The author suggested that fluctuations may modulate the midfrontal theta

TABLE 5 | Summary of cognition-related criticality literature.

Study	Study population	Modality	Analysis	Main findings
Lai et al., 2010	30 male adult subjects with autism or Asperger's syndrome, 33 age- and IQ-matched male adult controls	fMRI during resting-state	Hurst exponent	• Study examined complexity of endogenous, low-frequency neurophysiological processes in patients with ASD compared to control patients. Study confirmed that spontaneous BOLD signal fluctuations in the brain, specifically in regions implicated as atypical in previous autism neuroimaging studies, had small but significant decrease in Hurst exponents in the autistic compared with neurotypical group. This finding indicated a shift-to-randomness of brain oscillations in the autistic brain. • Though the meaning of the Hurst exponent ins limited by our understanding of neuronal and blood-supply sources to the measured BOLD signal, nevertheless fractal scaling may serve as indicator of organizational properties of local neural circuits.
Altamura et al., 2012	12 healthy adults	Response times to working memory and response tasks	Probability density functions, power-law estimation	• Power law-like behavior was noted in the upper tails of the CDF of response times for working memory tasks. This finding possibly reflects emergence of scale-free behavior in time series as an adaptation to increased cognitive requirements. Increasing cognitive load could shift random behavior to scale-free behavior near a critical point.
Dimitriadis et al., 2013	23 children with reading difficulties, 27 age- and IQ-matched children	MEG during resting-state	DFA	• Study examined MEG in children with reading difficulties compared to children without reading difficulties. Children with reading difficulties had decreased overall network organization across all frequency bands (global efficiency decrease) and a decrease in temporal correlations between sensors covering the left temporoparietal region. Study suggested that the specific parameters of SOC vary systematically in presence of reading difficulties. Both groups exhibited scale-free global network connectivity dynamics.
Tinker and Velazquez, 2014	15 children with high-functioning autism, 16 neurotypical children (ages 7–16 years old)	MEG during two executive function tasks	power-law estimation	• Study examined scaling of phase synchrony in MEG in patients with ASD compared to controls. Power-law scaling of phase synchrony was not common in either group. Its frequency of occurrence diminished with increased cognitive load/effort as children performed more difficult tasks. Power law distribution coexisted with other distributions (e.g., exponential) suggesting a sign of the metastability of brain dynamics.
Fagerholm et al., 2015	18 healthy adults	EEG-fMRI during rest and a visuomotor cognitive task	Power-law estimation*, shape analysis	• Study examined combined EEG and fMRI in healthy volunteers during rest and cognitive task. Resting-state EEG cascades were associated with approximate power-law distribution, while task state was associated with subcritical dynamics. Decreased response times during the cognitive task were associated with better approximation of a power-law form of cascade distribution. Findings suggest that resting-state was associated with near-critical dynamics while focused cognitive state induced subcritical dynamics with a lower dynamic range to reduce interference with task (i.e. promoting task performance).
Euler et al., 2016	54 healthy adults	EEG at rest and during a working memory task	DFA	• Study finds evidence of inverse relation between theta band LRTC and working memory performance—higher scaling exponent was related to poorer cognitive performance. Authors suggest that since elevated LRTC have been noted in epilepsy, increases in LRTC are not always beneficial.
Cohen, 2016	21 healthy adults	EEG during action adjustment task	Demeaned fluctuation analysis (DMA)	• Real-time error correction has been correlated to an idiosyncratic electrophysiological signature called midfrontal theta. This study found that midfrontal theta is a transient but non-phase-locked response modulated by task performance over three time scales, including scale-free-like fluctuations over many 10 s. The phasic midfrontal theta brain response to errors or error corrections is modulated by slow fluctuations in criticality.
Simola et al., 2017	27 healthy adults	Response times during a Go/NoGo task	Autocorrelation, spectral density, DFA	• Response time fluctuations in the Go/NoGO task exhibited a power law frequency scaling, autocorrelations and LRTCs, with LRTC scaling exponents negatively correlated with the commission error rates. Finding suggested that LRTCs co-exist with cognitive flexibility which is in line with the criticality hypothesis. LRTC scaling exponents were uncorrelated to the mean response time (MRT), suggesting that performance variables derive from distinct processes than brain criticality. Understanding the individual variation in scale-free behavioral dynamics may improve utility of neuropsychiatric assessment in ADHD.

(Continued)

TABLE 5 | Continued

Study	Study population	Modality	Analysis	Main findings
Irrmischer et al., 2018a	28 meditation-trained healthy adults, 21 meditation-naïve healthy adults	EEG during eyes-closed rest and meditation	Spectral density, DFA	• Study evaluated EEG from meditation practitioners and meditation-naive participants from independent labs. In practitioners, but not in controls, meditation strongly suppressed LRTC of oscillations relative to eyes-closed rest, across all frequency bands and scalp locations. Sustained practice led to reduction in LRTC during meditation after 1 year of additional training. Practice also impacted normal waking brain dynamics as reflected in increased LRTC during eyes-closed rest state, indicating an alteration beyond merely meditation. Authors suggested that meditation-induced release of GABA may lead to subcritical regime.
Irrmischer et al., 2018b	57 healthy adults	EEG during eyes-open, eyes-closed, and temporal expectancy task	Spectral density, DFA	• High levels of alpha band LRTC in sensorimotor region during rest predicted good reaction-time performance in attention task. During task execution, fast reaction times were associated with high-amplitude beta and gamma oscillations with low LRTC. • Authors hypothesize that focus and attention move the neural system from near-criticality optimized for environmental and internal demands, to a state of reduced input propagation but increased attentional stability, leading to suppression of LRTC.
Jia et al., 2018	35 children with ASD (ages 4−9 years old), 31 age- and gender-matched neurotypical children	Functional near-infrared spectroscopy (fNIRS) while watching a cartoon	DFA	• The hemoglobin concentration signals (i.e., oxy-Hb and deoxy-Hb) of young children with ASD and normal children were recorded via fNIRS while watching a cartoon. DFA exponents of young children with ASD were significantly smaller over left temporal region for oxy-Hb signal, and over bilateral temporo-occipital regions for deoxy-Hb signals, indicating a shift-to-random-ness of brain oscillations in children with ASD. Testing the relationship between age and DFA exponents revealed that this association could be modulated by autism. • Studying the temporal structure of brain activity via fNIRS technique may provide physiological indicators for autism. Authors speculated about a connection with SOC, though functional significance of DFA exponent is unclear. LRTC could play a role in evaluating disease progression in ASD.
Bongers et al., 2019	22 healthy university students	EEG during computerized learning and resting-state	Irregular Resampling Auto-spectral Analysis (IRASA), power-law estimation	• Study identified power law exponent of fractal signal during continuous EEG of computerized chemistry learning. Mixed power increase of broadband frequencies, which reflected an overall increase in fractal power, was seen during learning. A low power law exponent with increased band power of the fractal component seemed to correlate to high learning gains.
Kwok et al., 2019	41 healthy children (ages 4−6)	High-density EEG during eyes-open and eyes-closed	Spectral density, DFA	• Study used resting state EEG of children with typical development to explore relation between alpha (7−10 hz) oscillations and oral language ability. Higher language scores were correlated with lower alpha power and increased temporal correlations. Findings further demonstrated existence of critical state dynamics as important for language acquisition.
Ezaki et al., 2020	138 healthy adults	Resting-state fMRI; IQ scores	Correlation between spin-glass susceptibility and performance IQ score	• Study added support to criticality hypothesis by showing moderate but clear correlation between IQ scores and distance from criticality at an individual level using dynamic fMRI signals. A model of criticality using spin glasses was compared to data from healthy adults with a range of fluid intelligence IQs. Human fMRI data was found to be within paramagnetic phase close to the boundary with the spin-glass (SG) phase if using the framework of the Ising model. High fluid intelligence was associated with proximity to boundary between paramagnetic and SG phases. SG phase yields chaotic dynamics in spin systems, consistent with idea of enhanced computational performance "at the edge of chaos."
Ouyang et al., 2020	210 healthy adults	EEG during eyes-open, eyes-closed resting-state, and object recognition task	Structural equation modeling; fitting oscillations and one-over-f (FOOOF) methodology; IRASA	• The goal of this study was to investigate how individual differences in cognitive processing speeds could be predicted by the power spectrum of resting-state EEG signals. Alpha oscillations were not significantly associated with cognitive processing speed once the *1/f* noise was eliminated by SEM. Variation in *1/f* was revealed to robustly predict cognitive processing speed in eyes open and eyes closed. Slope of the power law decaying function was most predictive of between-person processing speed.

Asterisk (*) represents power-law estimations that meet criteria equivalent to or more stringent than Clauset et al. (2009). ASD, autism spectrum disorder; BOLD, blood oxygenation level-dependent; CDF, cumulative distribution function.

brain response to errors at a critical point (Cohen, 2016). In summary, evidence from both brain dynamics and behavioral dynamics points to some aspects of criticality in human cognition (Altamura et al., 2012; Cohen, 2016; Simola et al., 2017; Ouyang et al., 2020) while other studies do not (Tinker and Velazquez, 2014; Euler et al., 2016).

Studies of human attention have centered on the roles of criticality in meditation and its possible applications to ADHD, as mentioned earlier. There are many forms of meditation, and a commonly practiced form, called focused attention (FA) meditation, helps its practitioners improve their ability to focus (e.g., on their breath, on their bodily sensations). An EEG study of FA meditation-trained subjects compared to meditation-naïve subjects found that FA meditation in practitioners led to strong suppression of LRTC in oscillations across all frequency bands and electrodes, compared to the eyes-closed state (Irrmischer et al., 2018a). Meditation-naïve subjects did not show this suppression of LRTC. A year's worth of meditation practice led to more permanent changes since FA meditation practitioners had increased LRTC during eyes-closed rest state when they underwent EEG a year later. The authors hypothesized that meditation-related release of GABA might be contributing to excess inhibition and a subcritical regime as seen by decreased DFA exponent (i.e., LRTC suppression). In a similar EEG study of healthy subjects, high levels of alpha frequency LRTC in the sensorimotor region of the brain during rest predicted strong reaction-time performance in an attention task (Irrmischer et al., 2018b). During the execution of the task, on the other hand, suppressed LRTC in beta and gamma frequencies was associated with fast reaction-time performance. This study complements the results obtained in an earlier EEG-fMRI study of healthy adults during a visuomotor task and at rest. It found that the resting-state is associated with near-critical dynamics, while focused cognitive tasks induce subcritical dynamics that may reduce interference with the task at hand (Fagerholm et al., 2015). The upshot of these three studies is that focused attention – whether meditation-related (Irrmischer et al., 2018a) or visual attention (Fagerholm et al., 2015; Irrmischer et al., 2018b) – is associated with a reduction in criticality fluctuations. Generalized human attention at rest, on the other hand, balances a certain degree of focus with the ability to respond quickly to both internal and external stimuli. That balance should theoretically be optimal near criticality.

A handful of studies have examined the role of criticality in human learning, both in children and in adults. A MEG study of children with reading difficulties showed decreased temporal correlations in the left temporoparietal region compared to age and IQ matched children without reading difficulties (Dimitriadis et al., 2013). While this study examined subjects at rest instead of in a reading activity, its results dovetail well with previous studies that showed aberrant cortical activation in left posterior and temporal regions in children with severe reading difficulty during a reading assignment (Hoeft et al., 2007; Cao et al., 2008). Both groups of children exhibited scale-free global network connectivity, suggesting that local, rather than global, decreases in LRTC may be involved in reading difficulties and dyslexia. A high-density EEG study of neurotypical children found that lower alpha frequency power and increased LRTC correlated positively with language scores (Kwok et al., 2019). This study confirmed the findings of Dimitriadis et al. (2013) that critical state dynamics are important for language acquisition.

A recent resting-state fMRI study of neurotypical adults with a range of IQ scores found that high fluid intelligence is associated with proximity to a critical phase transition in a spin-glass model (Ezaki et al., 2020). This finding was consistent with previous work suggesting near-criticality as perhaps optimal for learning (Gisiger et al., 2014). From an EEG study of healthy university students learning organic chemistry, it is also known that a lower power-law exponent of the fractal component of EEG signals correlates with higher learning gains during a computerized learning task under EEG (Bongers et al., 2019). While this latter study makes no claims regarding criticality, one can infer that the scale-free behavior of neurons matters for the acquisition of complex new knowledge.

Only a few studies have examined the role of criticality-related markers in autism. A resting-state fMRI study of adult males with autism spectrum disorders, including high-functioning autism, detected a small but significant decrease in the Hurst exponent compared to controls in brain regions implicated in autism by previous neuroimaging studies (Lai et al., 2010). This decrease in the Hurst exponent indicates a shift toward randomness of fluctuations in blood oxygen level-dependent (BOLD) signals in the brain impacted by autism. Though the interpretation of the Hurst exponent in BOLD signals is challenging because of the unclear roles of blood supply and neural circuits among many others, the use of fractal scaling can serve as a barometer of underlying coordination and organization of neural circuits. In this study, the shift toward randomness in BOLD signals may indicate decreased coordination of small-scale circuits, to the disadvantage of larger brain circuitry. This hypothesis harmonizes well with one of many prevailing theories about the origins of autism, namely the local overconnectivity theory (Belmonte et al., 2004; Baron-Cohen and Belmonte, 2005). A more recent study of children with autism spectrum disorders (ASD) used functional near-infrared spectroscopy (fNIRS) to compare LRTC with age and gender-matched neurotypical children (Jia et al., 2018). Consistent with the findings of Lai et al. (2010) this study found that DFA exponents (i.e., LRTC scaling exponents) were significantly smaller over the left temporal region for the oxy-hemoglobin (oxy-Hb) signal in children with ASD compared to controls. DFA exponents were also significantly smaller over both temporo-occipital regions for deoxy-hemoglobin (deoxy-Hb) signals in children with ASD compared to controls. DFA exponents correlated well with age in neurotypical children, consistent with findings discussed previously (Smit et al., 2011). However, DFA exponents of oxy-Hb in the left temporal region correlated negatively with autism symptom severity on a parental questionnaire. This result dovetails nicely with a previouslyidentified negative correlation between cerebral blood flow to the left superior temporal gyrus and Autism Diagnostic Interview-Revised scores (Meresse et al., 2005). While the authors of this fNIRS study suspect that

autism may represent a departure from SOC, it seems further neuroimaging studies using criticality-based approaches will be needed before one can safely reach that conclusion.

Psychiatry

Researchers have turned to criticality-based tools to improve their understanding of common psychiatric conditions like depression, schizophrenia, anxiety, post-traumatic stress disorder (PTSD) (see **Table 6**). Insights from criticality theory have also helped describe the psychological effects of neurofeedback and psychedelics.

Studies of major depressive disorder (MDD) or unipolar depression have mostly relied on the search for temporal correlations (LRTC) using DFA. A small MEG study of patients with MDD and healthy controls found absent LRTC in the theta frequency band in patients with MDD compared to controls (Linkenkaer-Hansen et al., 2005). The study authors suggested that abnormal temporal structure of theta oscillations could reflect an underlying defect in limbic-cortical networks identified in anatomic-functional studies of MDD. Another small EEG study of patients with MDD and healthy controls did not reproduce this finding of absent theta LRTC (Lee et al., 2007). Instead, the study authors found that increased LRTC scaling exponents (i.e., slower decay of LRTC) correlated positively with the severity of depression over most EEG channels. This finding led the authors to speculate that rumination and psychomotor retardation – typical features of MDD – may be responsible for this persistence of LRTC.

Other studies have examined whether depression leads to alterations in LRTC during sleep. A small sleep EEG study of patients with untreated, acute episodes of MDD found a decrease in LRTC scaling exponents in NREM2, NREM3, and NREM4 compared to healthy controls (Leistedt et al., 2007b). However, this decrease was not statistically significant. A similar study by the same research team, this time with patients in remission from MDD, found no differences in LRTC through the stages of sleep (Leistedt et al., 2007a). In addition to demonstrating the existence of LRTC during sleep (see Sleep Medicine section for more details), these results argue against the "depressive scar" hypothesis, according to which depression leads to permanent residual defects.

Researchers have also taken an interest in negative emotional regulation as a precursor for MDD. A large EEG study of non-depressed undergraduate students found a positive linear correlation between LRTC scaling exponents of theta and broad-band frequencies and negative emotional regulation on various questionnaires (Bornas et al., 2013). Their research suggested that negative emotional control may anticipate full-blown MDD by several years. While this study broadly agreed with the findings of Lee et al. (2007), it disagreed with Linkenkaer-Hansen et al.'s (2005) conclusions with regards to the magnitude of scaling exponents with worsening rumination. A more recent, large EEG study found that, at baseline, patients with MDD have higher LRTC scaling exponents in the theta frequency range than healthy controls (Gärtner et al., 2017). After intervention with either mindfulness training or stress reduction training, both groups experienced a reduction in the strength of LRTC. This latter result suggests a new approach for examining the physiological mechanism by which psychotherapeutic interventions improve depressive symptoms. Given the inconsistencies in findings, more extensive studies will help clarify the nature of the LRTC in the various frequency bands and the multiple stages of depression (acute, treated, etc. . .). Future studies could assess whether LRTC changes significantly after initiation of first-line pharmacological intervention for MDD. Other criticality-based metrics could be useful to characterize the nature of brain dynamics in MDD as either sub-critical or, less likely, super-critical.

Criticality-based studies of schizophrenia are few but have opened up new horizons. An EEG study of around 30 patients with schizophrenia and schizoaffective disorders used a fractal analysis of *1/f* EEG rhythm fluctuations to try to distinguish the brain dynamics of schizophrenia from that of healthy controls (Slezin et al., 2007). A frontal electrode (F4) exhibited increased instability and randomness in the alpha band for patients with schizophrenia and schizoaffective disorders. The theta band, on the other hand, exhibited increased stability and decreased complexity in patients with schizophrenia compared to healthy controls. A subsequent fMRI study of patients with schizophrenia compared to healthy controls (Radulescu et al., 2012) also identified decreased complexity of brain dynamics, but different from that of Slezin et al's. (2007)study. In Radulescu et al's. (2012) study, a sophisticated analysis pipeline, including power spectrum scale invariance (PSSI) and Poincare maps (a measure of signal variance), found that signals coming from Brodmann area 10 (BA10) exhibited lower power-law exponents in schizophrenic patients than in healthy controls. In other words, schizophrenic patients displayed white (Gaussian or random) noise in this brain region, compared to pink (1/f) noise in healthy patients. This finding is consistent with previous research documenting the role of BA10 in executive function, working memory, and emotion regulation (Radulescu et al., 2012). This transition from pink noise to white noise in schizophrenia suggests, from the perspective of criticality, a loss of responsiveness to stimuli.

While the studies mentioned above took a fractal and power-law approach to signal analysis, others have taken the route of studying LRTC in schizophrenia. Their results complement and refine those obtained using fractal approaches. A high-density EEG study of LRTC in adults with schizophrenia and schizoaffective disorders found strong attenuation of LRTC scaling exponents in alpha and beta frequency bands in patients compared to healthy controls (Nikulin et al., 2012). While Slezin et al. (2007) did not study the beta frequency range, they did observe increased complexity in the alpha range, which is globally consistent with the findings in this study. These attenuated scaling exponents indicate decreased temporal correlation and a decrease in temporal precision of neuronal firing compared to healthy subjects. This interpretation fits well with at least two theories for the origins of schizophrenia, namely that of excessive neuronal noise and variability (Rolls et al., 2008) and the "disconnection hypothesis" of dysfunctional relationships between neural networks (Friston et al., 2016). A follow-up study found similar results (Moran et al., 2019). In this high-density

TABLE 6 | Summary of psychiatry-related criticality literature.

Study	Study population	Modality	Analysis	Main findings
Linkenkaer-Hansen et al., 2005	12 adults with MDD, 10 age-matched healthy controls	MEG during eyes-closed resting state	DFA, linear correlation of DFA exponent to Hamilton Depression Rating Scale	• This study recorded MEG data from patients with MDD compared to healthy controls during eyes-closed wakeful rest and quantified LRTC in amplitude fluctuations of different frequency bands. Temporal correlations in theta band were absent in the 5–100 s time range in patients but were prominent in controls. The magnitude of temporal correlations over left temporo-central region predicted severity of depression in patients. LRTCs in theta oscillations are a salient characteristic of healthy human brain and may have diagnostic potential in psychiatric disorders.
Lee et al., 2007	11 unmedicated adults with MDD per DSM-IV, 11 non-depressed age-matched controls	EEG during resting state	DFA	• Study compared LRTC in depressed subjects compared to controls. Study found a significant linear correlation between severity of depression and scaling exponent over most channels. There was slower decay of LRTC and persistence of LRTC in depressed patients associated with severity of depression over most cortical areas.
Slezin et al., 2007	33 patients with paranoid schizophrenia, schizotypal disorder, schizoaffective disorder per ICD-10, 23 healthy controls	EEG during resting state	Spectral density, power-law estimation	• Study applied multifractal analysis of *1/f* EEG rhythm fluctuations in patients with schizophrenia-related disorders compared to controls. Study found increased instability and randomness of alpha rhythm in the F4 electrodes in schizophrenia-related disorders. Theta rhythm, on the contrary, showed increased stability, regularity, and decreased complexity compared to normal/healthy controls in the same disorders.
Leistedt et al., 2007b	10 untreated inpatients with an acute episode of MDD per DSM-IV, 14 healthy controls	EEG during sleep	spectral density, DFA	• Major depressive episodes are characterized by modification in correlation structure of sleep EEG time series. Power law exponents were lower but not statistically significant in stage 2 and NREM3-4. These changes in scaling behavior could provide an explanation for why patients with acute depression have sleep fragmentation.
Leistedt et al., 2007a	10 untreated men in full or partial remission from MDD per DSM-IV; 14 healthy controls	EEG during sleep	DFA	• Goal of the study was to investigate the scaling properties of the sleep EEG in remitted depressed men and to see whether history of MDD could significantly alter dynamics of sleep EEG as a "scar marker." No significant differences were noted between the two groups during sleep. There were no functional sequelae of past history of one or more unipolar MDD episodes on fluctuation properties of sleep EEG. Study argued against "depressive scar hypothesis" in which some permanent residual defect is created by depressive disease. Study also confirmed LRTC in human sleep EEG.
Tolkunov et al., 2010	50 healthy adults without psychiatric history	fMRI during visual stimulus testing	power spectrum scale invariance (PSSI)	• Study examined whether patients with higher levels of trait anxiety would show less efficient regulation of limbic responses using a visual stimulus during fMRI. Significant positive correlations were found between beta frequency for limbic control circuit and trait anxiety. Dysregulated outputs from limbic system in trait anxiety also led to dysregulated inputs to the autonomic nervous system.
Radulescu et al., 2012	9 adults with schizophrenia per DSM-IV, 26 healthy controls	fMRI scan during affect-valent stimulus	Power spectrum scale invariance (PSSI), Poincare maps	• Study hypothesized that paranoid schizophrenia might be result of optimization abnormalities in the prefrontal-limbic circuit that regulates emotion. Patients and controls showed distinct PSSI in the orbitofrontal/medial prefrontal cortex (Brodmann 10). Poincare maps showed less variability in patients compared to controls. PSSI may be useful for psychiatric diagnoses, partly for the spatial localization it affords.
Nikulin et al., 2012	18 adults with schizophrenia, 3 with schizoaffective disorder per DSM-IV, 28 healthy age- and gender-matched controls	high-density EEG during resting state	DFA, cross-frequency correlations	• Study evaluated LRTC in schizophrenia-related disorders compared to healthy controls. LRTCs were significantly decreased in patients with schizophrenia in both alpha and beta frequency ranges. Authors hypothesize that decrease in LRTC arises from increased variability in neuronal activity in patients with schizophrenia. Haloperidol dosing and scaling exponent did not correlate in electrodes or frequency bands, which argues against the effects of anti-psychotics on the noted differences in LRTCs.
Bornas et al., 2013	56 healthy undergraduate students	EEG during eyes-open, eyes-closed resting state; Beck Depression	DFA, linear correlation between questionnaire scores and DFA exponents	• Goal of study was to look for possible differences in LRTC in brain signals from people with different negative emotion regulation strategies, including rumination, that lead to a depressed lifestyle. Study identified linear positive correlations between the scaling exponents of both broad band and theta band oscillations and negative emotion regulation strategies and depression

(Continued)

TABLE 6 | Continued

Study	Study population	Modality	Analysis	Main findings
		inventory and emotion regulation questionnaires		scores. Authors suggested that differences may exist between depressed and non-depressed even before depression manifests, though depressed mental state clearly impacts the degree of correlation.
Tagliazucchi et al., 2014	15 healthy adult subjects	fMRI before, during, and after IV psilocybin and placebo infusions	Variance and total spectral power	• Study aimed to quantify the repertoire of neural states under the influence of psychedelics like psilocybin. Changes in spectral scaling exponents and variance of BOLD signals exclusively affected higher brain systems. Authors found that psilocybin resulted in a larger repertoire of connectivity states at rest than in control conditions, consistent with brain criticality.
Zhigalov et al., 2016	9 healthy adult subjects (ages 18–23 years old)	EEG while resting with eyes-closed during closed-loop and sham NFB sessions	Spectral density, DFA	• Study hypothesized that LRTC could be manipulated by closed-loop NFB stimulation. Over multiple sessions, there emerged a significant difference in LRTCs of α-band oscillations, with LRTCs stronger during NFB than sham. Study served as a proof-of-concept that EEG LRTCs, and thus critical brain dynamics, could be modulated with closed-loop stimulation.
Ros et al., 2014	40 healthy adults; 21 adults with PTSD per DSM-IV, with 30 age- and gender-matched healthy controls	fMRI scan before NFB, EEG during NFB or sham-NFB, and fMRI scan after NFB	DFA	• Study aimed to evaluate possibility of manipulating LRTC in patients suffering from PTSD. Brain areas with low LRTCs in PTSD subjects normalized toward healthier population levels with application of neurofeedback compared to sham. Authors suggest that LRTC changes seen with NFB are due to fluctuations in excitation-inhibition balance.
Gärtner et al., 2017	71 depressed adult patients per DSM-IV, 25 healthy controls	EEG before and after mindfulness training or stress reduction training	DFA	• Study sought to understand whether neural dynamics improved in patients with MDD after psychological treatment. Depressed subjects exhibited stronger LRTC in theta oscillations (4–7 Hz) at baseline compared to controls. Following the psychological interventions both groups exhibited decreased LRTC in the theta band, with marginal numerical differences between the groups. Future of this research area will involve uncovering how psychological interventions effectively reduce LRTCs.
Moran et al., 2019	23 patients with schizophrenia per DSM-IV, 24 education-, handedness-, age-, and gender-matched healthy controls	EEG with eyes-open	DFA, LORETA	• Patients with schizophrenia showed area of significantly reduced beta-band LRTC over bilateral posterior regions compared to controls. Absence of alpha band differences (contrary to Nikulin et al., 2012) could be related to eyes-open EEG used in this study.

DSM-IV, Diagnostic and Statistical Manual, 4th edition; MDD, major depressive disorder; NFB, neurofeedback.

EEG and standardized low-resolution brain electromagnetic tomography (sLORETA) study of patients with schizophrenia compared to healthy controls, there was a significant reduction in LRTC in the beta-band over the bilateral posterior regions in patients compared to healthy controls. This study found no differences in the alpha frequency between patients and controls. However, the study authors suggested that the eyes-open state of their study (compared to the eyes-closed, resting state of Nikulin et al., 2012) may have eliminated an underlying difference in that frequency range. More importantly, both studies confirm the importance of LRTC as markers of network instability in schizophrenia.

A much smaller number of studies have examined the role of neurofeedback (NFB) as a treatment modality for psychiatric disorders. A small study of healthy adults randomized to either closed-loop NFB or sham NFB found that, after three sessions, LRTC in the alpha frequency band was stronger in the NFB group compared to the sham (Zhigalov et al., 2016). This difference was statistically significant and did not involve any statistically significant topographical changes in alpha power. The study provided proof-of-concept that closed-loop NFB can restore critical brain dynamics by altering the excitation-inhibition balance in psychiatric disorders with decreased LRTC. A larger EEG and fMRI study of healthy patients confirmed this improvement in LRTC after closed-loop NFB compared to sham. The study also involved a population of patients with PTSD, whose LRTC improved with closed-loop NFB (Ros et al., 2014). The study authors speculated that NFB leads to stronger excitation with an associated increase in temporal correlation and symptomatic improvement. While it is unclear whether NFB can help in disorders characterized by super-criticality (e.g., seizures), NFB has already shown benefit in several disorders characterized to some degree by sub-criticality, including schizophrenia (Surmeli et al., 2012) and major depression (Escolano et al., 2014).

A few criticality-based studies have taken an interest in the role of psychedelics in treating mental illnesses. Researchers have focused on psilocybin, the active ingredient in "magic mushrooms," and lysergic acid diethylamine (LSD). In an fMRI study of healthy patients receiving psilocybin versus a placebo, study authors found an increased variance in BOLD signals in the hippocampi of psychedelic recipients (Tagliazucchi et al., 2014). The increased variance implies increased synchronization, consistent with a super-critical state of brain dynamics. This

TABLE 7 | Summary of sleep-related criticality literature.

Study	Study population	Modality	Analysis	Main findings
Nikulin and Brismar, 2004	12 healthy adults	EEG with eyes-open and eyes-closed	DFA	• LRTC in alpha oscillations were not changed significantly by wakefulness level while beta oscillation scaling exponent significantly increased in the closed eye condition. Increased synaptic activity associated with arousal/wakefulness may interfere with dynamics of LRTC. Study confirmed existence of LRTC in both awake and closed eyes but more consistently in closed eye state and may be reflective of underlying SOC.
Weiss et al., 2011	22 healthy adults	EEG during REM, NREM2, NREM4 sleep	Hurst exponent, power spectral measures	• Study assessed various metrics of sleep EEG including monofractal, multifractal, and spectral power measures. Sleep stage discrimination with multifractal measure was superior to relative band powers, spectral edge frequency, or Hurst exponent. • Study found higher H exponent, DFA exponent, and fractal exponent in deep sleep, while multifractal measure was decreased. These findings indicate a decrease of multifractality and an increase in long memory in deep sleep.
Dehghani et al., 2012	2 adult patients with intractable epilepsy	iEEG from temporal gyrus in awake state, REM, and slow-wave sleep	Power-law estimation*	• Study investigated power-law distribution of neuronal avalanches (spikes) from iEEG data. Neuronal avalanches (spikes) did not clearly follow power-law in awake, SWS, or REM states and instead followed closer to exponential distribution. Positive and negative LFPs followed apparent power laws with log-log analysis but closer examination with CDF-based testing did not confirm power law and favored double exponential distribution. In cases where power laws were seen with log-log analysis, exponents were too high for SOC systems. • These results contradict those of prior studies (Petermann et al., 2009; Ribeiro et al., 2010) and perhaps could be harmonized with prior results by taking into account recording methods or volume conduction effects.
Meisel et al., 2013	8 healthy adults	EEG during 40 h of sustained wakefulness	Power-law estimation*, branching parameter, spectral density	• Study evaluated evolution of criticality parameters during prolonged wakefulness. At the start of sleep deprivation, coherence potentials were organized as neuronal avalanches in space and time with power law −3/2 and branching parameter 1.17, both of which suggest a system near criticality. With increased duration of wakefulness, size distributions of coherence potentials and PLIs developed larger tails, an increase in branching parameter, and an increase in mean synchronization while variability of synchronization decreased. • These findings suggested that, during sustained wakefulness, the neural networks move from a critical to a supercritical state, perhaps as a result of increased excitation and decreased inhibition (Shew et al., 2009; Yang et al., 2012). Sleep might serve to reorganize network dynamics to critical state in order to assure optimal computational capabilities while awake.
Priesemann et al., 2013	5 adults with refractory epilepsy	iEEG (depth electrode)	Power-law estimation*, branching parameter	• Neuronal avalanches were recorded from intracranial depth electrodes in 5 epilepsy patients over two nights through all sleep stages. Avalanches were described by power laws in all cases but with different dynamics depending on sleep stages. SWS showed the largest avalanches, wakefulness showed intermediate-sized, while REM showed smallest. Differences in avalanche distributions implied that not all vigilance states could be derived from SOC. • Modeling suggested that human brain operates within subcritical regime, near criticality where differences between vigilance states can be mediated by small changes in effective synaptic strength which allow the brain to tune closer to criticality (SWS) or farther away (REM). SWS showed increased correlations between cortical areas due to increased criticality, while REM sleep showed more fragmented dynamics than SWS and wakefulness.
Lo et al., 2013	48 healthy adults and 48 age-matched adults with obstructive sleep apnea (OSA)	Polysomnogram recorded for 2 consecutive nights	Probability transfer matrix, power-law estimation	• Study found a power law distribution of wake and arousal durations in sleep using log-log analysis. Power-law exponents were different between patients with OSA and healthy controls. • Using novel probability transfer matrix and SOC, authors revealed sleep transition pathways that could be reduced to two basic and independent transition paths. Study also found that sleep micro-architecture at scales from seconds to minutes exhibits a non-equilibrium behavior reminiscent of critical systems.
Tagliazucchi et al., 2013	63 healthy adults	fMRI and EEG during NREM sleep	DFA	• Study hypothesized that breakdown of LRTC would occur during descent into deep sleep. Authors found that Hurst exponent decreased during N2

(Continued)

TABLE 7 | Continued

Study	Study population	Modality	Analysis	Main findings
				sleep confined to DMN and attention networks. Study also discovered that autocorrelation in fronto-parietal areas diminish from wakefulness to deep sleep.
Allegrini et al., 2013	29 healthy adults	Polysomnogram	Random walks, DFA, fractal intermittency	• Study hypothesized that a renewal point process describing fractal intermittency could be a correlate of consciousness. Fractal intermittency can be seen in EEG data by sequence of global rapid transition processes (RTP) with power law distribution of waiting times. During sleep, Hurst exponent switched from 0.75 in wake and REM phases to 0.5 in deep sleep, suggesting fractal intermittency in wake and REM but short-time correlations in SWS.
Allegrini et al., 2015	29 healthy adults	Polysomnogram	Random walks, DFA, fractal intermittency	• Study evaluated fractal intermittency (see Allegrini et al., 2013) during sleep. While critical avalanches remained unchanged, there was a breakdown in intermittency and functional connectivity during shallow and deep NREM sleep. The authors provided a theory for fragmentation-induced intermittency breakdown. The possible role of critical avalanches in dreamless sleep is to provide rapid recovery of consciousness if stimuli arouse the person out of sleep.
Colombo et al., 2016	52 adults with insomnia disorder (ID), 42 age- and sex-matched controls	High-density EEG with eyes-open (EO) and eyes-closed (EC)	DFA	• There were no differences in DFA exponents between ID and controls in any frequency bands during EO or EC. However, during EO, individuals with worse sleep quality had stronger LRTC, suggesting that subjective insomnia complaints involve distinct processes in people with ID and controls. However, the measurement of insomnia severity was based on subjective report, not polysomnography. Future studies should examine polysomnographic data as well as examine frequency (rather than amplitude) fluctuations.
Meisel et al., 2017	8 healthy adults	EEG during 40 h of sustained wakefulness	DFA, autocorrelation function, spectral density	• Study evaluated LRTCs in resting state human EEG during 40-h sleep deprivation experiment. LRTCs declined as sleep deprivation progressed, even when taking into account changes in signal power. LRTCs naturally emerged in vicinity of critical state. Authors argued that the increased LRTCs seen in insomnia patients (Colombo et al., 2016) could be due to signal power changes associated with worse sleep quality.
Bocaccio et al., 2019	18 healthy adults	fMRI and EEG during wakefulness and all sleep stages	Power-law estimation*	• Study observed scale-free hierarchy of co-activated connected clusters using point-process transformation of fMRI data recorded during wake and NREM sleep. Sleep stage had significant impact on scaling parameter of power law, which was robust to spatial coarse-graining, alternative statistical models, and disappearing with phase shuffling of fMRI time series. These findings suggest the existence of larger clusters or avalanches during N2 sleep. Criticality may help with the "pretty hard problem of consciousness" by offering metrics that behave one way in conscious states and differently in another.

Asterisk (*) represents power-law estimations that meet criteria equivalent to or more stringent than Clauset et al. (2009). SWS, slow-wave sleep; REM, rapid eye-movement; NREM, non-rapid eye-movement; PLI, phase-locking interval; DMN, default mode network.

super-critical state could account for the hyper-associative cognition characteristic of psychedelics (Carhart-Harris et al., 2014; Carhart-Harris, 2018). While this review limits itself to non-connectomic data, the works of Atasoy et al. (2017, 2018) deserve mention here. Using a unique connectome-harmonic decomposition approach, her research team has found in several studies that infusions of psychedelics "push" brain dynamics out of baseline sub-criticality toward criticality (Atasoy et al., 2017, 2018). More and more studies are finding that psychedelics are helpful adjuncts to psychotherapy (Atasoy et al., 2017). A psychedelic-induced transition out of a sub-critical disorder like depression and closer to criticality may account for this benefit.

Sleep Medicine

Sleep medicine deals with human sleep and its associated disorders, including insomnia, sleep apnea, and narcolepsy. There are multiple stages of sleep, including rapid eye movement (REM), non-rapid eye movement (NREM), which is further divided into light sleep (NREM1 and NREM2) and deep sleep (NREM3 and NREM4). A typical night's sleep runs through several cycles of each of these sleep stages. The brain criticality literature centers on two key areas of sleep medicine – characterization of sleep stages and the physiology of sleeping disorders.

Researchers have tried improving the classification of sleep stages with the help of criticality-based metrics. The results of these studies seem, for now, largely inconsistent. An EEG study of healthy patients found LRTC in brain oscillations in both the open-eye and closed-eye states (Nikulin and Brismar, 2004). LRTC was more consistent, however, in the closed-eye state, with a significant difference in the scaling exponent between closed and open eye conditions in the beta frequency range. Building on this initial result for LRTC, an EEG study of healthy patients

examined the ability of various fractal and spectral metrics to distinguish REM, NREM2, and NREM4 (Weiss et al., 2011). The authors found that the multifractal metric was superior to other metrics for sleep stage classification. From wakefulness to deep sleep, multifractality decreased while monofractality (e.g., the Hurst exponent) increased. The loss of multifractality and disruptions in the *1/f* noise in the deep sleep stages suggested that sleep-specific brain rhythms (e.g., sleep spindles) disrupt the day-time self-similarity. Previous studies had shown an increase, not a decrease, in multifractality in deepening sleep (Ma et al., 2006). These differing results suggest that additional studies of multifractality are needed.

The increase in mono-fractality that accompanied deep sleep in the study by Weiss et al. (2011) suggested increased long-memory (LRTC) in sleep, similar to the increase in scaling exponent noted in the closed eye state by Nikulin and Brismar (2004). Subsequent studies, however, have produced results that seem to contradict these findings. Using EEG-fMRI data from healthy adults in NREM sleep, Tagliazucchi et al. (2013) found that a breakdown in LRTC happened as patients moved into the deeper sleep stages. Specifically, the Hurst exponent decreased in the default-mode network (DMN) and attention centers of the brain during NREM2 (Tagliazucchi et al., 2013). Two studies of polysomnogram data from a different cohort of healthy adults found a similar result (Allegrini et al., 2013, 2015). The monofractal metric (i.e., the Hurst exponent) decreased from ∼0.75 during wakefulness and REM, to ∼0.5 in NREM3 and NREM4. Recall that a Hurst exponent of 0.5 indicates random, white noise, while 0.75 suggests a moderate amount of positive correlation. This finding suggested the existence of a breakdown in LRTC when entering deep sleep. Complicating matters further is that studies showing decreases in LRTC during sleep did not control for changes in signal power that naturally occur during sleep (Meisel et al., 2017). More studies on the existence and changes of LRTC during sleep, taking into account fluctuations in signal power, are needed if these are to become useful in sleep stage classification or in understanding sleep microarchitecture.

There are also conflicting results in the literature when it comes to power-law distributions of various observables during sleep. In an EEG study, researchers noted that subjects in normal states of wakefulness exhibited a power-law distribution of coherence potentials and phase-locking intervals (PLI)(Meisel et al., 2013). Also, their EEG signals produced a branching parameter near one, which suggests a system at or near criticality (Yang et al., 2012; Meisel et al., 2013). As patients were kept awake longer and deprived of sleep, the distributions of coherence potentials and PLIs developed larger tails along with an increase in the branching parameter, a decrease in the variability of synchronization, and an increase in mean synchronization – all suggestive of a supercritical state. The authors suggested that prolonged wakefulness leads to a supercritical state through excess excitability of neurons (Shew et al., 2009), as is also thought to occur in epilepsy. Meisel et al. (2013) proposed that, during restorative sleep, a decrease in synaptic strength should lead to a shift away from super-criticality, back toward a critical regime. This view is in line with a similar theory that sleep is designed to restore brain dynamics to a slightly subcritical or near-critical regime to avoid the risk of run-away excitation in a supercritical state (Pearlmutter and Houghton, 2009, 2013).

An ECoG study of patients during sleep revealed power-law distributions of neuronal avalanches in local field potentials (LFPs), but with different exponents depending on the sleep stage (Priesemann et al., 2013). After making adjustments for the fact that LFP amplitude naturally increases from wakefulness to deep sleep, the study authors found that slow-wave sleep (SWS or NREM3) displayed large avalanches. Wakefulness and REM sleep, on the other hand, displayed intermediate and small avalanches, respectively. Because the study found a branching parameter less than one during wakefulness, the authors concluded that the awake human brain at rest is in a subcritical state rather than in a critical state as had been previously argued (Meisel et al., 2013). The authors suggest that brain dynamics shift closer to criticality during SWS and then back into sub-criticality during REM sleep (Priesemann et al., 2013). Their data and additional computational modeling found that small changes in effective synaptic strength could tune the brain closer to a critical state during SWS or closer to a subcritical state with fragmented dynamics during REM. Of note, this study did not find power-law distributions under the more stringent criteria of Clauset et al. (2009). Moreover, a small study of power-law distributions of cortical spikes and LFPs under awake, SWS, and REM sleep conditions could not confirm a power-law distribution of those brain signals using the Clauset et al. (2009) criteria (Dehghani et al., 2012).

While the study of Dehghani et al. (2012) casts doubt on these power-law findings, a recent study of EEG-fMRI data in healthy patients during sleep suggests that critical dynamics may be involved nonetheless (Bocaccio et al., 2019). A power-law distribution of co-activated connected clusters (voxel groups) from fMRI data during sleep was confirmed using the Clauset et al. (2009) criteria. As in Priesemann et al. (2013), this study found larger neuronal avalanches in NREM compared to REM or wakefulness. Moreover, each particular sleep stage impacted the power-law exponent significantly – a result that was independent of spatial coarse-graining of the fMRI data and which could not be accounted for by the presence of evoked neural bistabilities (e.g., K complexes).

All in all, while there are discrepancies in the results obtained from studies in this area, one can be optimistic about the role of criticality-based metrics in refining the understanding of sleep stages and their classification. Research into the role of LRTC (with adjustments made for signal power during sleep), branching parameters, power-law distributions of various metrics (coherence potential, PLI, LFP), mean synchronization, and other criticality parameters should lead to robust classifiers of sleep stages.

The conceptual framework of criticality is also helping researchers better understand various sleep pathologies (Iyer, 2018). Many animal and computational models show that critical dynamics play a central role in sleep stage transitions (Comte et al., 2006; Wang et al., 2019; Lombardi et al., 2020). Human studies are also beginning to capture this essential role by studying various sleep disorders. In the previouslymentioned EEG study of sleep deprivation (Meisel et al., 2013), there was

a progressive decline in markers of criticality and an increase in markers of supercriticality as the sleep deprivation worsened. This finding supports the idea that sleep restores healthy brain function by bringing dynamics back toward criticality. This study was followed up by an evaluation of LRTC in the same cohort under similar conditions of sleep deprivation (Meisel et al., 2017). After controlling for signal amplitude changes, LRTC strength declined as sleep deprivation progressed, consistent with the view that sleep restores brain criticality.

In contrast with forced sleep deprivation, insomnia disorder (ID) leads to chronic sleep deprivation despite the patient's attempts to fall asleep. In a study of patients with ID, there were no statistically significant differences in the LRTC during eyes-open and eyes-closed testing between patients and their age and sex-matched controls (Colombo et al., 2016). However, patients who subjectively reported lower quality sleep had increased LRTC during the eyes-open state. The study authors suggested that an increased excitation-inhibition ratio during wakefulness may translate into similar excitation during sleep, leading to lower sleep quality. Similar processes seem to be at work in obstructive sleep apnea (OSA), one of the most common sleep disorders. A polysomnogram study of patients with OSA and healthy controls found a power-law distribution of wakefulness durations during sleep in both groups (Lo et al., 2013). But the study did find a statistically significant difference between the power-law exponents. This finding reinforces the prospect that power-law exponents, perhaps in combination with other established metrics like the apnea-hypopnea index, could prove to be a helpful marker of diagnosis and monitoring of OSA. In the future, a study of LRTC in patients with OSA and ID compared to healthy patients in sleep could help determine whether the prevalent theory of sleep as a safety margin from supercriticality is correct. More broadly, the theory of brain criticality is likely to offer a different but complementary perspective on many sleep disorders (including narcolepsy, restless legs syndrome, and circadian disorders). See **Table 7** for a summary of findings from the sleep-related criticality literature.

CONCLUSION

This scoping review surveyed the brain criticality literature, focusing on seven major domains of clinical application. Wherever possible, an effort was made to emphasize areas of future research for those interested in pursuing a "critical approach" to these clinical questions. In this concluding section, controversies that continue to be problematic for the field of brain criticality as a whole are addressed.

Brain criticality is both an established area of neuroscience research and yet remains controversial in several regards (Wilting and Priesemann, 2019).

1. Diverse and inconsistent uses of the terms "critical" and "criticality" have led to confusion. In this review, criticality has mostly referred to avalanche dynamics that behave at the limit between stability and instability. But other variants of criticality exist (Wilting and Priesemann, 2019). These include criticality between ordered and chaotic phases called the "edge of chaos" (Boedecker et al., 2012), criticality between synchrony and asynchrony (Botcharova et al., 2014), and multiple paradigms for the time-evolution of a critical phase transition as in extended criticality, intermittent criticality, and self-organized criticality (Saleur et al., 1996; Huang et al., 1998; Sammis and Smith, 1999; Bowman and Sammis, 2004). These forms of dynamical criticality are also distinct from statistical criticality (Mora and Bialek, 2011; Tkačik et al., 2013). How these all inter-connect is a topic of ongoing research. Rigorously defining these states and enforcing a more consistent vocabulary would allow for better study comparison.
2. Proving the existence of a control parameter has been difficult. Candidates have included synchronization, excitation-inhibition balance, and synaptic conductance (Beggs and Timme, 2012). Feedback processes between these properties may make it difficult to prove that they behave as genuine control parameters in isolation.
3. Many of the publications that lay the groundwork for brain criticality did not have the benefit of a reliable statistical framework for verifying a power-law distribution. While publications since Clauset et al. (2009) have mostly implemented strong statistical testing of power laws, many of the initial papers and even some more recent publications suffer from this deficit. Establishing a standard pipeline of statistical analysis for common datasets (e.g., EEG, MEG, LFP) – a kind of statistical "best practices"—will eliminate a source of confusion and help clarify the clinical situations in which power-law regimes do and do not exist. Moreover, arguing for a mechanism that generates a power-law – whether criticality or another mechanism—may be as important as the discovery of the power-law distribution itself (Stumpf and Porter, 2012).
4. In many publications, the objects of study are defined differently from one paper to the next. Such is the case, for example, with neuronal avalanches (Wilting and Priesemann, 2019) and seizure energy (Worrell et al., 2002; Osorio et al., 2009). While flexibility in definitions may help with making discoveries or adjusting for specific experimental situations, frequent changes in definition make it difficult to compare results, which slows down the progress of the field as a whole.
5. A common strategy, especially since the invention of DFA, is to look for LRTC as an indication of criticality. However, recent research suggests there may be different types of LRTC at play in these various systems and not distinguishing them carefully may be leading to false conclusions about criticality. For example, the discovery of crucial events in the area of turbulence led to the identification of "crucial event LRTC" or CELRTC (Bohara et al., 2018; Culbreth et al., 2019). CELRTC emerges in critical systems, specifically self-organized temporal criticality (SOTC) and is based on a slowly-decaying, non-stationary correlation function (Mahmoodi et al., 2017). CELRTC is distinct from Hurst exponent LRTC (HLRTC)

which is based on a slowlydecaying but stationary correlation function, and which may not be indicative of underlying criticality. Future papers relying on detection of LRTC should incorporate this methodology in order to clarify the origin of the long-range correlation.

6. DFA was introduced for the study of non-stationary datasets. Yet there is evidence that this approach may not be adequate for that purpose (Bryce and Sprague, 2012). The introduction of a finite-size effect by DFA, leading to artifact, may have led to spurious results in many publications mentioned in this review. Future research should clarify the relevance of DFA-based methods for the purpose of LRTC detection.

Despite these challenges and controversies, there is also room for optimism. There has been rapid growth in the number of new articles published in this area. In fact, approximately two-thirds of the clinical articles discussed in this review were published in the last 8 years. The range of tools and concepts available from statistical physics and complexity science with which to tackle these problems is staggeringly broad and continually expanding. Determining how these tools and concepts inter-relate and in which research situation to use them should be an ongoing focus of research. Insights from other sciences—including geophysics, finance, applied physics, and signal processing, where these ideas are also commonly circulated – will undoubtedly shape the future of this already multidisciplinary field.

The future of criticality in the clinical arena will depend in large part on the formation of multidisciplinary teams in which physicists, mathematicians, data scientists, and clinicians collaborate to better answer a clinical question through the lens of criticality. While none of the applications mentioned in this review has yet to become mainstream or routine, it is conceivable that, under the broad umbrella of quantitative analysis of EEG, MEG, and fMRI, several of these techniques may transition to the bedside if they prove helpful in the diagnosis, prognosis, or treatment of diseases. In addition to more detailed studies in the clinical areas mentioned in this review, one can expect the next decade to see innovative studies, anchored in criticality, in areas like addiction medicine, stroke, neuro-immunology, traumatic brain injury, and headache medicine.

There are inevitable hurdles when concepts from one field (i.e., statistical physics) are translated into another (i.e., biomedicine). Still, there can be no doubt that these hurdles are worthwhile if they open up new horizons for both the understanding and the treatment of brain-related diseases.

AUTHOR CONTRIBUTIONS

VZ evaluated the literature and wrote the manuscript.

FUNDING

This study was supported by the Department of Pediatrics at the University of Texas Southwestern, which funded open access publication fees. No other funding was received for this research.

ACKNOWLEDGMENTS

The author would like to thank Lina Chalak, MD and Jeffrey McKinney, MD, Ph.D. for proposing the idea of this review. The author would also like to thank Mario Altamura, Ph.D. for kindly sending his manuscript as well as Didier Sornette, Ph.D., Gregory Worrell, MD, Ph.D., Luca Cocchi, Ph.D., John Beggs, Ph.D., Paolo Grigolini, Ph.D., and Michele Colombo, Ph.D. for sharing their insights.

REFERENCES

Achard, S., Delon-Martin, C., Vértes, P. E., Renard, F., Schenck, M., Schneider, F., et al. (2012). Hubs of brain functional networks are radically reorganized in comatose patients. *Proc. Natl. Acad. Sci. U.S.A.*109, 20608–20613. doi: 10.1073/pnas.1208933109

Allegrini, P., Paradisi, P., Menicucci, D., Laurino, M., Bedini, R., Piarulli, A., et al. (2013). Sleep unconsciousness and breakdown of serial critical intermittency: new vistas on the global workspace. *Chaos Solit. Fract.*55, 32–43. doi: 10.1016/j.chaos.2013.05.019

Allegrini, P., Paradisi, P., Menicucci, D., Laurino, M., Piarulli, A., and Gemignani, A. (2015). Self-organized dynamical complexity in human wakefulness and sleep: different critical brain-activity feedback for conscious and unconscious states. *Phys. Rev. E Stat. Nonlinear Soft Matt. Phys.*92:032808. doi: 10.1103/PhysRevE.92.032808

Alonso, L. M., Proekt, A., Schwartz, T. H., Pryor, K. O., Cecchi, G. A., and Magnasco, M. O. (2014). Dynamical criticality during induction of anesthesia in human ECoG recordings. *Front. Neural Circuits.*8:20. doi: 10.3389/fncir.2014.00020

Altamura, M., Elvevag, B., Campi, G., De Salvia, M., Marasco, D., Ricci, A., et al. (2012). Toward scale-free like behavior under increasing cognitive load. *Complexity*18, 38–43. doi: 10.1002/cplx.21407

Arviv, O., Medvedovsky, M., Sheintuch, L., Goldstein, A., and Shriki, O. (2016). Deviations from critical dynamics in interictal epileptiform activity. *J. Neurosci.*36, 12276–12292. doi: 10.1523/JNEUROSCI.0809-16.2016

Atasoy, S., Roseman, L., Kaelen, M., Kringelbach, M. L., Deco, G., and Carhart-Harris, R. L. (2017). Connectome-harmonic decomposition of human brain activity reveals dynamical repertoire re-organization under LSD. *Sci. Rep.*7:17661. doi: 10.1038/s41598-017-17546-0

Atasoy, S., Vohryzek, J., Deco, G., Carhart-Harris, R. L., and Kringelbach, M. L. (2018). Common neural signatures of psychedelics: frequency-specific energy changes and repertoire expansion revealed using connectome-harmonic decomposition. *Prog. Brain Res.*242, 97–120. doi: 10.1016/bs.pbr.2018.08.009

Bak, P., Christensen, K., Danon, L., and Scanlon, T. (2002). Unified scaling law for earthquakes. *Phys. Rev. Lett.*99, 2509–2513. doi: 10.1103/PhysRevLett.88.178501

Bak, P., and Tang, C. (1989). Earthquakes as a self-organized critical phenomenon. *J. Geophys. Res.*94, 15635–15637. doi: 10.1029/jb094ib11p15635

Bak, P., Tang, C., and Wiesenfeld, K. (1987). Self-organized criticality: an explanation of the 1/f noise. *Phys. Rev. Lett.*59, 381–384. doi: 10.1103/PhysRevLett.59.381

Bak, P., Tang, C., and Wiesenfeld, K. (1988). Self-organized criticality. *Phys. Rev. A*38, 364–374. doi: 10.1103/PhysRevA.38.364

Ball, G., Aljabar, P., Zebari, S., Tusor, N., Arichi, T., Merchant, N., et al. (2014). Rich-club organization of the newborn human brain. *Proc. Natl. Acad. Sci. U.S.A.*111, 7456–7461. doi: 10.1073/pnas.1324118111

Barabási, A. L., and Albert, R. (1999). Emergence of scaling in random networks. *Science*286, 509–512. doi: 10.1126/science.286.5439.509

Baron-Cohen, S., and Belmonte, M. K. (2005). AUTISM: a window onto the development of the social and the analytic brain. *Annu. Rev. Neurosci.*28, 109–126. doi: 10.1146/annurev.neuro.27.070203.144137

Bédard, C., Kröger, H., and Destexhe, A. (2006). Does the 1/f frequency scaling of brain signals reflect self-organized critical states?*Phys. Rev. Lett.*97:118102. doi: 10.1103/PhysRevLett.97.118102

Beggs, J. M. (2008). The criticality hypothesis: how local cortical networks might optimize information processing. *Philos. Trans. A Math. Phys. Eng. Sci.*366, 329–343. doi: 10.1098/rsta.2007.2092

Beggs, J. M., and Timme, N. (2012). Being critical of criticality in the brain. *Front. Physiol.*3:163. doi: 10.3389/fphys.2012.00163

Belmonte, M. K., Allen, G., Beckel-Mitchener, A., Boulanger, L. M., Carper, R. A., and Webb, S. J. (2004). Autism and abnormal development of brain connectivity. *J. Neurosci.*24, 9228–9231. doi: 10.1523/JNEUROSCI.3340-04.2004

Berthouze, L., James, L. M., and Farmer, S. F. (2010). Human EEG shows long-range temporal correlations of oscillation amplitude in Theta, Alpha and Beta bands across a wide age range. *Clin. Neurophysiol.*121, 1187–1197. doi: 10.1016/j.clinph.2010.02.163

Bertschinger, N., and Natschläger, T. (2004). Real-time computation at the edge of chaos in recurrent neural networks. *Neural Comput.*16, 1413–1436. doi: 10.1162/089976604323057443

Bocaccio, H., Pallavicini, C., Castro, M. N., Sanchez, S. M., De Pino, G., Laufs, H., et al. (2019). The avalanche-like behaviour of large-scale haemodynamic activity from wakefulness to deep sleep. *J. R. Soc. Interface*16:20190262. doi: 10.1098/rsif.2019.0262

Boedecker, J., Obst, O., Lizier, J. T., Mayer, N. M., and Asada, M. (2012). Information processing in echo state networks at the edge of chaos. *Theory Biosci.*131, 205–213. doi: 10.1007/s12064-011-0146-8

Bohara, G., West, B. J., and Grigolini, P. (2018). Bridging waves and crucial events in the dynamics of the brain. *Front. Physiol.*9:1174. doi: 10.3389/fphys.2018.01174

Bonachela, J. A., De Franciscis, S., Torres, J. J., and Muoz, M. A. (2010). Self-organization without conservation: are neuronal avalanches generically critical? *J. Stat. Mech. Theory Exp*. 2010. doi: 10.1088/1742-5468/2010/02/P02015

Bonachela, J. A., and Muñoz, M. A. (2009). Self-organization without conservation: true or just apparent scale-invariance?*J. Stat. Mech. Theory Exp.* 2009. doi: 10.1088/1742-5468/2009/09/P09009

Bongers, A., Flynn, A. B., and Northoff, G. (2019). Is learning scale-free? Chemistry learning increases EEG fractal power and changes the power law exponent. *Neurosci. Res.* doi: 10.1016/j.neures.2019.10.011 [Epub ahead of print]

Bornas, X., Noguera, M., Balle, M., Morillas-Romero, A., Aguayo-Siquier, B., Tortella-Feliu, M., et al. (2013). Long-range temporal correlations in resting EEG: its associations with depression-related emotion regulation strategies. *J. Psychophysiol.*27, 60–66. doi: 10.1027/0269-8803/a000087

Botcharova, M., Berthouze, L., Brookes, M. J., Barnes, G. R., and Farmer, S. F. (2015). Resting state MEG oscillations show long-range temporal correlations of phase synchrony that break down during finger movement. *Front. Physiol.*6:183. doi: 10.3389/fphys.2015.00183

Botcharova, M., Farmer, S. F., and Berthouze, L. (2012). Power-law distribution of phase-locking intervals does not imply critical interaction. *Phys. Rev. E. Stat. Nonlin. Soft Matter Phys.*86:51920. doi: 10.1103/PhysRevE.86.051920

Botcharova, M., Farmer, S. F., and Berthouze, L. (2014). Markers of criticality in phase synchronization. *Front. Syst. Neurosci.*8:176. doi: 10.3389/fnsys.2014.00176

Bowman, D. D., and Sammis, C. G. (2004). Intermittent criticality and the Gutenberg-Richter distribution. *Pure Appl. Geophys.*161, 1945–1956. doi: 10.1007/s00024-004-2541-z

Breakspear, M., and Terry, J. R. (2002). Detection and description of non-linear interdependence in normal multichannel human EEG data. *Clin. Neurophysiol.*113, 735–753. doi: 10.1016/S1388-2457(02)00051-2

Bressler, S. L., and Kelso, J. A. S. (2001). Cortical coordination dynamics and cognition. *Trends Cogn. Sci.*5, 26–36. doi: 10.1016/S1364-6613(00)01564-3

Bryce, R. M., and Sprague, K. B. (2012). Revisiting detrended fluctuation analysis. *Sci. Rep.*2:345. doi: 10.1038/srep00315

Cao, F., Bitan, T., and Booth, J. R. (2008). Effective brain connectivity in children with reading difficulties during phonological processing. *Brain Lang.*107, 91–101. doi: 10.1016/j.bandl.2007.12.009

Carhart-Harris, R. L. (2018). The entropic brain – revisited. *Neuropharmacology*142, 167–178. doi: 10.1016/j.neuropharm.2018.03.010

Carhart-Harris, R. L., Leech, R., Hellyer, P. J., Shanahan, M., Feilding, A., Tagliazucchi, E., et al. (2014). The entropic brain: a theory of conscious states informed by neuroimaging research with psychedelic drugs. *Front. Hum. Neurosci.*8:20. doi: 10.3389/fnhum.2014.00020

Castaing, B., Gagne, Y., and Hopfinger, E. J. (1990). Velocity probability density functions of high Reynolds number turbulence. *Phys. D Nonlinear Phenom.*46, 177–200. doi: 10.1016/0167-2789(90)90035-N

Cavanagh, J. F., and Frank, M. J. (2014). Frontal theta as a mechanism for cognitive control. *Trends Cogn. Sci.*18, 414–421. doi: 10.1016/j.tics.2014.04.012

Cerf, R., El Ouasdad, E. H., and Kahane, P. (2004). Criticality and synchrony of fluctuations in rhythmical brain activity: pretransitional effects in epileptic patients. *Biol. Cybern.*90, 239–255. doi: 10.1007/s00422-004-0463-9

Christensen, K., Olami, Z., and Bak, P. (1992). Deterministic 1/f noise in nonconservative models of self-organized criticality. *Phys. Rev. Lett.*68, 2417–2420. doi: 10.1103/PhysRevLett.68.2417

Clauset, A., Shalizi, C. R., andNewman, M. E. J (2009). Power-law distributions in empirical data. *SIAM Rev.*51, 661–703. doi: 10.1137/070710111

Cocchi, L., Gollo, L. L., Zalesky, A., and Breakspear, M. (2017). Criticality in the brain: a synthesis of neurobiology, models and cognition. *Prog. Neurobiol.*158, 132–152. doi: 10.1016/j.pneurobio.2017.07.002

Cohen, M. X. (2016). Midfrontal theta tracks action monitoring over multiple interactive time scales. *Neuroimage*141, 262–272. doi: 10.1016/j.neuroimage.2016.07.054

Colombo, M. A., Wei, Y., Ramautar, J. R., Linkenkaer-Hansen, K., Tagliazucchi, E., and Van Someren, E. J. W. (2016). More severe insomnia complaints in people with stronger long-range temporal correlations in wake resting-state EEG. *Front. Physiol.*7:576. doi: 10.3389/fphys.2016.00576

Colquhoun, H. L., Levac, D., O'Brien, K. K., Straus, S., Tricco, A. C., Perrier, L., et al. (2014). Scoping reviews: time for clarity in definition, methods, and reporting. *J. Clin. Epidemiol.*67, 1291–1294. doi: 10.1016/j.jclinepi.2014.03.013

Comte, J. C., Ravassard, P., and Salin, P. A. (2006). Sleep dynamics: a self-organized critical system. *Phys. Rev. E*73:056127. doi: 10.1103/PhysRevE.73.056127

Cook, M. J., O'Brien, T. J., Berkovic, S. F., Murphy, M., Morokoff, A., Fabinyi, G., et al. (2013). Prediction of seizure likelihood with a long-term, implanted seizure advisory system in patients with drug-resistant epilepsy: a first-in-man study. *Lancet Neurol.*12, 563–571. doi: 10.1016/S1474-4422(13)70075-9

Cook, M. J., Varsavsky, A., Himes, D., Leyde, K., Berkovic, S. F., O'Brien, T., et al. (2014). The dynamics of the epileptic brain reveal long-memory processes. *Front. Neurol.*5:217. doi: 10.3389/fneur.2014.00217

Cruz, A. V., Mallet, N., Magill, P. J., Brown, P., and Averbeck, B. B. (2009). Effects of dopamine depletion on network entropy in the external globus pallidus. *J. Neurophysiol.*102, 1092–1102. doi: 10.1152/jn.00344.2009

Culbreth, G., West, B. J., and Grigolini, P. (2019). Entropic approach to the detection of crucial events. *Entropy*21, 1–20. doi: 10.3390/e21020178

Daffertshofer, A., Ton, R., Kringelbach, M. L., Woolrich, M., and Deco, G. (2018). Distinct criticality of phase and amplitude dynamics in the resting brain. *Neuroimage*180, 442–447. doi: 10.1016/j.neuroimage.2018.03.002

Deco, G., and Jirsa, V. K. (2012). Ongoing cortical activity at rest: criticality, multistability, and ghost attractors. *J. Neurosci.*32, 3366–3375. doi: 10.1523/JNEUROSCI.2523-11.2012

Deco, G., Kringelbach, M. L., Jirsa, V. K., and Ritter, P. (2017). The dynamics of resting fluctuations in the brain: Metastability and its dynamical cortical core. *Sci. Rep.*7:3095. doi: 10.1038/s41598-017-03073-5

Deco, G., Senden, M., and Jirsa, V. (2012). How anatomy shapes dynamics: a semi-analytical study of the brain at rest by a simple spin model. *Front. Comput. Neurosci.*6:68. doi: 10.3389/fncom.2012.00068

Dehghani, N., Hatsopoulos, N. G., Haga, Z. D., Parker, R. A., Greger, B., Halgren, E., et al. (2012). Avalanche analysis from multielectrode ensemble recordings in

cat, monkey, and human cerebral cortex during wakefulness and sleep. *Front. Physiol.*3:302. doi: 10.3389/fphys.2012.00302

Del Papa, B., Priesemann, V., and Triesch, J. (2017). Criticality meets learning: criticality signatures in a self-organizing recurrent neural network. *PLoS One*12:e0178683. doi: 10.1371/journal.pone.0178683

Dimitriadis, S. I., Laskaris, N. A., Simos, P. G., Micheloyannis, S., Fletcher, J. M., Rezaie, R., et al. (2013). Altered temporal correlations in resting-state connectivity fluctuations in children with reading difficulties detected via MEG. *Neuroimage*83, 307–317. doi: 10.1016/j.neuroimage.2013.06.036

Escolano, C., Navarro-Gil, M., Garcia-Campayo, J., Congedo, M., De Ridder, D., and Minguez, J. (2014). A controlled study on the cognitive effect of alpha neurofeedback training in patients with major depressive disorder. *Front. Behav. Neurosci.*8:296. doi: 10.3389/fnbeh.2014.00296

Euler, M. J., Wiltshire, T. J., Niermeyer, M. A., and Butner, J. E. (2016). Working memory performance inversely predicts spontaneous delta and theta-band scaling relations. *Brain Res.*1637, 22–33. doi: 10.1016/j.brainres.2016.02.008

Ezaki, T., Fonseca Dos Reis, E., Watanabe, T., Sakaki, M., and Masuda, N. (2020). Closer to critical resting-state neural dynamics in individuals with higher fluid intelligence. *Commun. Biol.*3:52. doi: 10.1038/s42003-020-0774-y

Fagerholm, E. D., Lorenz, R., Scott, G., Dinov, M., Hellyer, P. J., Mirzaei, N., et al. (2015). Cascades and cognitive state: focused attention incurs subcritical dynamics. *J. Neurosci.*35, 4626–4634. doi: 10.1523/JNEUROSCI.3694-14.2015

Fiest, K. M., Sauro, K. M., Wiebe, S., Patten, S. B., Kwon, C. S., Dykeman, J., et al. (2017). Prevalence and incidence of epilepsy. *Neurology*88, 296–303. doi: 10.1212/WNL.0000000000003509

Fraiman, D., Balenzuela, P., Foss, J., and Chialvo, D. R. (2009). Ising-like dynamics in large-scale functional brain networks. *Phys. Rev. E Stat. Nonlinear, Soft Matt. Phys.*79(Pt 1):061922. doi: 10.1103/PhysRevE.79.061922

Fransson, P., Metsäranta, M., Blennow, M., Åden, U., Lagercrantz, H., and Vanhatalo, S. (2013). Early development of spatial patterns of power-law frequency scaling in fMRI resting-state and EEG data in the newborn brain. *Cereb. Cortex*23, 638–646. doi: 10.1093/cercor/bhs047

Frette, V., Christensen, K., Malthe-Sørenssen, A., Feder, J., Jøssang, T., and Meakin, P. (1996). Avalanche dynamics in a pile of rice. *Nature*379, 49–52. doi: 10.1038/379049a0

Friedman, N., Ito, S., Brinkman, B. A. W., Shimono, M., Deville, R. E. L., Dahmen, K. A., et al. (2012). Universal critical dynamics in high resolution neuronal avalanche data. *Phys. Rev. Lett.*108:208102. doi: 10.1103/PhysRevLett.108.208102

Friston, K., Brown, H. R., Siemerkus, J., and Stephan, K. E. (2016). The dysconnection hypothesis (2016). *Schizophr. Res.*176, 83–94. doi: 10.1016/j.schres.2016.07.014

Frohlich, J., Irimia, A., and Jeste, S. S. (2015). Trajectory of frequency stability in typical development. *Brain Imaging Behav.*9, 5–18. doi: 10.1007/s11682-014-9339-3

Gärtner, M., Irrmischer, M., Winnebeck, E., Fissler, M., Huntenburg, J. M., Schroeter, T. A., et al. (2017). Aberrant long-range temporal correlations in depression are attenuated after psychological treatment. *Front. Hum. Neurosci.*11:340. doi: 10.3389/fnhum.2017.00340

Gautam, S. H., Hoang, T. T., McClanahan, K., Grady, S. K., and Shew, W. L. (2015). Maximizing sensory dynamic range by tuning the cortical state to criticality. *PLoS Comput. Biol.*11:e1004576. doi: 10.1371/journal.pcbi.1004576

Gisiger, T., Linkenkaer-Hansen, K., Nikouline, V. V., Palva, J. M., Ilmoniemi, R. J., Worrell, G. A., et al. (2014). Spike avalanches in vivo suggest a driven, slightly subcritical brain state. *Front. Syst. Neurosci.*9:108. doi: 10.3389/fnsys.2014.00108

Haldeman, C., and Beggs, J. M. (2005). Critical branching captures activity in living neural networks and maximizes the number of metastable states. *Phys. Rev. Lett.*94:058101. doi: 10.1103/PhysRevLett.94.058101

Hanslmayr, S., Staudigl, T., and Fellner, M. C. (2012). Oscillatory power decreases and long-term memory: the information via desynchronization hypothesis. *Front. Hum. Neurosci.*6:74. doi: 10.3389/fnhum.2012.00074

Hardstone, R., Poil, S., Schiavone, G., Jansen, R., Nikulin, V. V., Mansvelder, H. D., et al. (2012). Detrended fluctuation analysis?: a scale-free view on neuronal oscillations. *Front. Physiol.*3:450. doi: 10.3389/fphys.2012.00450

Harris, T. (1963). *The Theory of Branching Processes*. Berlin and Heidelberg: Springer-Verlag OHG.

Hartley, C., Berthouze, L., Mathieson, S. R., Boylan, G. B., Rennie, J. M., and Farmer, S. F. (2012). Long-range temporal correlations in the EEG bursts of human preterm babies. *PLoS One7*:e0031543. doi: 10.1371/journal.pone.0031543

Hausdorff, J. M. (2009). Gait dynamics in Parkinson's disease: common and distinct behavior among stride length, gait variability, and fractal-like scaling. *Chaos*19:026113. doi: 10.1063/1.3147408

He, B. J. (2011). Scale-free properties of the functional magnetic resonance imaging signal during rest and task. *J. Neurosci.*31, 13786–13795. doi: 10.1523/JNEUROSCI.2111-11.2011

He, B. J. (2014). Scale-free brain activity: past, present, and future. *Trends Cogn. Sci.*18, 480–487. doi: 10.1016/j.tics.2014.04.003

Hesse, J., and Gross, T. (2014). Self-organized criticality as a fundamental property of neural systems. *Front. Syst. Neurosci.*8:166. doi: 10.3389/fnsys.2014.00166

Hobbs, J. P., Smith, J. L., and Beggs, J. M. (2010). Aberrant neuronal avalanches in cortical tissue removed from juvenile epilepsy patients. *J. Clin. Neurophysiol.*27, 380–386. doi: 10.1097/WNP.0b013e3181fdf8d3

Hoeft, F., Meyler, A., Hernandez, A., Juel, C., Taylor-Hill, H., Martindale, J. L., et al. (2007). Functional and morphometric brain dissociation between dyslexia and reading ability. *Proc. Natl. Acad. Sci. U.S.A.*104, 4234–4239. doi: 10.1073/pnas.0609399104

Hoffmann, H., and Payton, D. W. (2018). Optimization by self-organized criticality. *Sci. Rep.*8:2358. doi: 10.1038/s41598-018-20275-7

Hohlefeld, F. U., Huebl, J., Huchzermeyer, C., Schneider, G.-H., Schoenecker, T., Kuehn, A. A., et al. (2012). Long-range temporal correlations in the subthalamic nucleus of patients with Parkinson's disease. *Eur. J. Neurosci.*36, 2812–2821. doi: 10.1111/j.1460-9568.2012.08198.x

Hove, M. J., Suzuki, K., Uchitomi, H., Orimo, S., and Miyake, Y. (2012). Interactive rhythmic auditory stimulation reinstates natural 1/f timing in gait of parkinson's patients. *PLoS One*7:e32600. doi: 10.1371/journal.pone.0032600

Huang, Y., Saleur, H., Sammis, C., and Sornette, D. (1998). Precursors, aftershocks, criticality and self-organized criticality. *Europhys. Lett.*41, 43–48. doi: 10.1209/epl/i1998-00113-x

Irrmischer, M., Houtman, S. J., Mansvelder, H. D., Tremmel, M., Ott, U., and Linkenkaer-Hansen, K. (2018a). Controlling the temporal structure of brain oscillations by focused attention meditation. *Hum. Brain Mapp.*39, 1825–1838. doi: 10.1002/hbm.23971

Irrmischer, M., Poil, S.-S., Mansvelder, H. D., Intra, F. S., and Linkenkaer-Hansen, K. (2018b). Strong long-range temporal correlations of beta/gamma oscillations are associated with poor sustained visual attention performance. *Eur. J. Neurosci.*48, 2674–2683. doi: 10.1111/ejn.13672

Iyer, K. K. (2018). Sleep, wake, and critical brain states: corollaries from brain dynamics. *Front. Neurosci.*12:948. doi: 10.3389/fnins.2018.00948

Iyer, K. K., Roberts, J. A., Hellström-Westas, L., Wikström, S., Hansen Pupp, I., Ley, D., et al. (2015). Cortical burst dynamics predict clinical outcome early in extremely preterm infants. *Brain*138(Pt 8), 2206–2218. doi: 10.1093/brain/awv129

Jannesari, M., Saeedi, A., Zare, M., Ortiz-Mantilla, S., Plenz, D., and Benasich, A. A. (2020). Stability of neuronal avalanches and long-range temporal correlations during the first year of life in human infants. *Brain Struct. Funct.*225, 1169–1183. doi: 10.1007/s00429-019-02014-4

Jia, H., Li, Y., and Yu, D. (2018). Attenuation of long-range temporal correlations of neuronal oscillations in young children with autism spectrum disorder. *NeuroImage Clin.*20, 424–432. doi: 10.1016/j.nicl.2018.08.012

Jiang, L., Qiao, K., Sui, D., Zhang, Z., and Dong, H. (2019). Functional criticality in the human brain?: physiological, behavioral and neurodevelopmental correlates. *PLoS One*14:e0213690. doi: 10.1371/journal.pone.0213690

Jiang, L., Sui, D., Qiao, K., Dong, H.-M., Chen, L., and Han, Y. (2018). Impaired functional criticality of human brain during Alzheimer's disease progression. *Sci. Rep.*8:1324. doi: 10.1038/s41598-018-19674-7

Kinouchi, O., and Copelli, M. (2006). Optimal dynamical range of excitable networks at criticality. *Nat. Phys.*2, 348–351. doi: 10.1038/nphys289

Kitzbichler, M. G., Smith, M. L., Christensen, S. R., and Bullmore, E. (2009). Broadband criticality of human brain network synchronization. *PLoS Comput. Biol.*5:e1000314. doi: 10.1371/journal.pcbi.1000314

Kramer, M. A., Truccolo, W., Eden, U. T., Lepage, K. Q., Hochberg, L. R., Eskandar, E. N., et al. (2012). Human seizures self-terminate across spatial scales via a

critical transition. *Proc. Natl. Acad. Sci. U.S.A.*109, 21116–21121. doi: 10.1073/pnas.1210047110

Krzemiński, D., Kamiński, M., Marchewka, A., and Bola, M. (2017). Breakdown of long-range temporal correlations in brain oscillations during general anesthesia. *Neuroimage*159, 146–158. doi: 10.1016/j.neuroimage.2017.07.047

Kwok, E. Y. L., Cardy, O., Allman, B., Allen, P., and Herrmann, B. (2019). Dynamics of spontaneous alpha activity correlate with language ability in young children. *Behav. Brain Res.*359, 56–65. doi: 10.1101/679670

Lai, M. C., Lombardo, M. V., Chakrabarti, B., Sadek, S. A., Pasco, G., Wheelwright, S. J., et al. (2010). A shift to randomness of brain oscillations in people with autism. *Biol. Psychiatry*68, 1092–1099. doi: 10.1016/j.biopsych.2010.06.027

Latham, P. E., and Nirenberg, S. (2004). Computing and stability in cortical networks. *Neural Comput.*16, 1385–1412. doi: 10.1162/089976604323057434

Lee, J. S., Yang, B. H., Lee, J. H., Choi, J. H., Choi, I. G., and Kim, S. B. (2007). Detrended fluctuation analysis of resting EEG in depressed outpatients and healthy controls. *Clin. Neurophysiol.*118, 2489–2496. doi: 10.1016/j.clinph.2007.08.001

Leistedt, S., Dumont, M., Coumans, N., Lanquart, J. P., Jurysta, F., and Linkowski, P. (2007a). The modifications of the long-range temporal correlations of the sleep EEG due to major depressive episode disappear with the status of remission. *Neuroscience*148, 782–793. doi: 10.1016/j.neuroscience.2007.06.032

Leistedt, S., Dumont, M., Lanquart, J. P., Jurysta, F., and Linkowski, P. (2007b). Characterization of the sleep EEG in acutely depressed men using detrended fluctuation analysis. *Clin. Neurophysiol.*118, 940–950. doi: 10.1016/j.clinph.2007.01.003

Li, X., Polygiannakis, J., Kapiris, P., Peratzakis, A., Eftaxias, K., and Yao, X. (2005). Fractal spectral analysis of pre-epileptic seizures in terms of criticality. *J. Neural Eng.*2, 11–16. doi: 10.1088/1741-2560/2/2/002

Linkenkaer-Hansen, K., Monto, S., Rytsälä, H., Suominen, K., Isometsä, E., and Kähkönen, S. (2005). Breakdown of long-range temporal correlations in theta oscillations in patients with major depressive disorder. *J. Neurosci.*25, 10131–10137. doi: 10.1523/JNEUROSCI.3244-05.2005

Liu, X., Ward, B. D., Binder, J. R., Li, S.-J., and Hudetz, A. G. (2014). Scale-free functional connectivity of the brain is maintained in anesthetized healthy participants but not in patients with unresponsive wakefulness syndrome. *PLoS One*9:e92182. doi: 10.1371/journal.pone.0092182

Lo, C. C., Bartsch, R. P., and Ivanov, P. C. (2013). Asymmetry and basic pathways in sleep-stage transitions. *Europhys. Lett.*102:10008. doi: 10.1209/0295-5075/102/10008

Lombardi, F., Gómez-Extremera, M., Bernaola-Galván, P., Vetrivelan, R., Saper, C. B., Scammell, T. E., et al. (2020). Critical dynamics and coupling in bursts of cortical rhythms indicate non-homeostatic mechanism for sleep-stage transitions and dual role of VLPO neurons in both sleep and wake. *J. Neurosci.*40, 171–190. doi: 10.1523/JNEUROSCI.1278-19.2019

Ma, Q., Ning, X., Wang, J., and Bian, C. (2006). A new measure to characterize multifractality of sleep electroencephalogram. *Chinese Sci. Bull.*51, 3259–3264. doi: 10.1007/s11434-006-2213-y

Ma, Z., Turrigiano, G. G., Wessel, R., and Hengen, K. B. (2019). Cortical circuit dynamics are homeostatically tuned to criticality in vivo. *Neuron*104, 655–664.e4. doi: 10.1016/j.neuron.2019.08.031

Maass, W., Natschläger, T., and Markram, H. (2002). Real-time computing without stable states: a new framework for neural computation based on perturbations. *Neural Comput.*14, 2531–2560. doi: 10.1162/089976602760407955

Mahmoodi, K., West, B. J., and Grigolini, P. (2017). Self-organizing complex networks: individual versus global rules. *Front. Physiol.*8:478. doi: 10.3389/fphys.2017.00478

Mares, J., Vysata, O., Prochazka, A., and Valis, M. (2013). Age-dependent complex noise fluctuations in the brain. *Physiol. Meas.*34, 1269–1279. doi: 10.1088/0967-3334/34/10/1269

Marinazzo, D., Pellicoro, M., Wu, G.-R., Angelini, L., Cortes, J., and Stramaglia, S. (2013). Information transfer of an Ising model on a brain network. *BMC Neurosci.*14(Suppl. 1):376. doi: 10.1186/1471-2202-14-s1-p376

Mehta, A. P., Dahmen, K. A., and Ben-Zion, Y. (2006). Universal mean moment rate profiles of earthquake ruptures. *Phys. Rev. E Stat. Nonlinear, Soft Matter Phys.*73(Pt 2):056104. doi: 10.1103/PhysRevE.73.056104

Meisel, C., Bailey, K., Achermann, P., and Plenz, D. (2017). Decline of long-range temporal correlations in the human brain during sustained wakefulness. *Sci. Rep.*7, 1–11. doi: 10.1038/s41598-017-12140-w

Meisel, C., and Kuehn, C. (2012). Scaling effects and spatio-temporal multilevel dynamics in epileptic seizures. *PLoS One*7:e30371. doi: 10.1371/journal.pone.0030371

Meisel, C., and Loddenkemper, T. (2019). Seizure prediction and intervention. *Neuropharmacology*172:107898. doi: 10.1016/j.neuropharm.2019.107898

Meisel, C., Olbrich, E., Shriki, O., and Achermann, P. (2013). Fading signatures of critical brain dynamics during sustained wakefulness in humans. *J. Neurosci.*33, 17363–17372. doi: 10.1523/JNEUROSCI.1516-13.2013

Meisel, C., Storch, A., Hallmeyer-Elgner, S., Bullmore, E., and Gross, T. (2012). Failure of adaptive self-organized criticality during epileptic seizure attacks. *PLoS Comput. Biol.*8:e1002312. doi: 10.1371/journal.pcbi.1002312

Meresse, I. G., Zilbovicius, M., Boddaert, N., Robel, L., Philippe, A., Sfaello, I., et al. (2005). Autism severity and temporal lobe functional abnormalities. *Ann. Neurol.*58, 466–469. doi: 10.1002/ana.20597

Milton, J. G. (2012). Neuronal avalanches, epileptic quakes and other transient forms of neurodynamics. *Eur. J. Neurosci.*36, 2156–2163. doi: 10.1111/j.1460-9568.2012.08102.x

Minadakis, G., Ventouras, E., Gatzonis, S. D., Siatouni, A., Tsekou, H., Kalatzis, I., et al. (2014). Dynamics of regional brain activity in epilepsy: a cross-disciplinary study on both intracranial and scalp-recorded epileptic seizures. *J. Neural Eng.*11:026012. doi: 10.1088/1741-2560/11/2/026012

Mitzenmacher, M. (2004). A brief history of generative models for power law and lognormal distributions. *Internet Math.*1, 226–251. doi: 10.1080/15427951.2004.10129088

Moher, D., Liberati, A., Tetzlaff, J., Altman, D. G., Altman, D., Antes, G., et al. (2009). Preferred reporting items for systematic reviews and meta-analyses: the PRISMA statement. *PLoS Med.*6:e1000097. doi: 10.1371/journal.pmed.1000097

Montez, T., Poil, S. S., Jones, B. F., Manshanden, I., Verbunt, J. P. A., Van Dijk, B. W., et al. (2009). Altered temporal correlations in parietal alpha and prefrontal theta oscillations in early-stage Alzheimer disease. *Proc. Natl. Acad. Sci. U.S.A.*106, 1614–1619. doi: 10.1073/pnas.0811699106

Monto, S., Vanhatalo, S., Holmes, M. D., and Palva, J. M. (2007). Epileptogenic neocortical networks are revealed by abnormal temporal dynamics in seizure-free subdural EEG. *Cereb. Cortex*17, 1386–1393. doi: 10.1093/cercor/bhl049

Mora, T., and Bialek, W. (2011). Are biological systems poised at criticality?*J. Stat. Phys.*144, 268–302. doi: 10.1007/s10955-011-0229-4

Moran, J. K., Michail, G., Heinz, A., Keil, J., and Senkowski, D. (2019). Long-range temporal correlations in resting state beta oscillations are reduced in schizophrenia. *Front. Psychiatry*10:517. doi: 10.3389/fpsyt.2019.00517

Moretti, P., and Munoz, M. A. (2013). Griffiths phases and the stretching of criticality in brain networks. *Nat. Commun.*4:2521. doi: 10.1038/ncomms3521

Mormann, F., Andrzejak, R. G., Elger, C. E., and Lehnertz, K. (2007). Seizure prediction: the long and winding road. *Brain.*130(Pt 2), 314–333. doi: 10.1093/brain/awl241

Morrison, J. H., and Hof, P. R. (1997). Life and death of neurons in the aging brain. *Science*278, 412–419. doi: 10.1126/science.278.5337.412

Mu, J., Rampp, S., Carrette, E., Roessler, K., Sommer, B., Schmitt, F. C., et al. (2014). Clinical relevance of source location in frontal lobe epilepsy and prediction of postoperative long-term outcome. *Seizure*23, 553–559. doi: 10.1016/j.seizure.2014.04.006

Newman, M. E. J. (2005). Power laws, pareto distributions and Zipf's law. *Contemp. Phys.*46, 323–351. doi: 10.1080/00107510500052444

Nikulin, V. V., and Brismar, T. (2004). Long-range temporal correlations in alpha and beta oscillations: effect of arousal level and test-retest reliability. *Clin. Neurophysiol.*115, 1896–1908. doi: 10.1016/j.clinph.2004.03.019

Nikulin, V. V., Jönsson, E. G., and Brismar, T. (2012). Attenuation of long-range temporal correlations in the amplitude dynamics of alpha and beta neuronal oscillations in patients with schizophrenia. *Neuroimage*61, 162–169. doi: 10.1016/j.neuroimage.2012.03.008

Nishimori, H., and Ortiz, G. (2011). *Elements of Phase Transitions and Critical Phenomena*. Oxford: Oxford University Press, doi: 10.1093/acprof:oso/9780199577224.001.0001

Omori, F. (1895). On the aftershocks of earthquakes. *J. Coll. Sci. Imp. Univ. Tokyo* 7, 111–120.

Osorio, I., Frei, M. G., Sornette, D., and Milton, J. (2009). Pharmaco-resistant seizures: self-triggering capacity, scale-free properties and predictability?*Eur. J. Neurosci.*30, 1554–1558. doi: 10.1111/j.1460-9568.2009.06923.x

Osorio, I., Frei, M. G., Sornette, D., Milton, J., and Lai, Y. C. (2010). Epileptic seizures: quakes of the brain?*Phys. Rev. E Stat. Nonlinear, Soft Matter Phys.*82:021919. doi: 10.1103/PhysRevE.82.021919

Ouyang, G., Hildebrandt, A., Schmitz, F., and Herrmann, C. S. (2020). Decomposing alpha and 1/f brain activities reveals their differential associations with cognitive processing speed. *Neuroimage*205:116304. doi: 10.1016/j.neuroimage.2019.116304

Padilla, N., Eklöf, E., Mårtensson, G. E., Bölte, S., Lagercrantz, H., and Ådén, U. (2017). Poor brain growth in extremely preterm neonates long before the onset of autism spectrum disorder symptoms. *Cereb. Cortex*27, 1245–1252. doi: 10.1093/cercor/bhv300

Padilla, N., Saenger, V. M., Van Hartevelt, T. J., Fernandes, H. M., Lennartsson, F., Andersson, J. L. R., et al. (2020). Breakdown of whole-brain dynamics in preterm-born children. *Cereb. Cortex*30, 1159–1170. doi: 10.1093/cercor/bhz156

Papanikolaou, S., Bohn, F., Sommer, R. L., Durin, G., Zapperi, S., and Sethna, J. P. (2011). Universality beyond power laws and the average avalanche shape. *Nat. Phys.*7, 316–320. doi: 10.1038/nphys1884

Parish, L. M., Worrell, G. A., Cranstoun, S. D., Stead, S. M., Pennell, P., and Litt, B. (2004). Long-range temporal correlations in epileptogenic and non-epileptogenic human hippocampus. *Neuroscience* 125, 1069–1076. doi: 10.1016/j.neuroscience.2004.03.002

Parr, T., Rees, G., and Friston, K. J. (2018). Computational neuropsychology and bayesian inference. *Front. Hum. Neurosci.*12:61. doi: 10.3389/fnhum.2018.00061

Pearlmutter, B. A., and Houghton, C. J. (2009). A new hypothesis for sleep: tuning for criticality. *Neural Comput.*21, 1622–1641. doi: 10.1162/neco.2009.05-08-787

Pearlmutter, B. A., and Houghton, C. J. (2013). Dreams, mnemonics, and tuning for criticality. *Behav. Brain Sci.*36, 625–659. doi: 10.1017/S0140525X13001404

Peng, C. K., Buldyrev, S. V., Goldberger, A. L., Havlin, S., Mantegna, R. N., Simons, M., et al. (1995a). Statistical properties of DNA sequences. *Phys. A Stat. Mech. its Appl.*221, 180–192. doi: 10.1016/0378-4371(95)00247-5

Peng, C. K., Havlin, S., Stanley, H. E., and Goldberger, A. L. (1995b). Quantification of scaling exponents and crossover phenomena in nonstationary heartbeat time series. *Chaos*5, 82–87. doi: 10.1063/1.166141

Perković, O., Dahmen, K., and Sethna, J. P. (1995). Avalanches, Barkhausen noise, and plain old criticality. *Phys. Rev. Lett.*75, 4528–4531. doi: 10.1103/PhysRevLett.75.4528

Petermann, T., Thiagarajan, T. C., Lebedev, M. A., Nicolelis, M. A. L., Chialvo, D. R., and Plenz, D. (2009). Spontaneous cortical activity in awake monkeys composed of neuronal avalanches. *Proc. Natl. Acad. Sci. U.S.A.*106, 15921–15926. doi: 10.1073/pnas.0904089106

Pisarenko, V. F., and Sornette, D. (2012). Robust statistical tests of Dragon-Kings beyond power law distributions. *Eur. Phys. J. Spec. Top.*205, 95–115. doi: 10.1140/epjst/e2012-01564-8

Plenz, D., and Niebur, E. (2014). *Criticality in Neural Systems*. Hoboken, NJ: Wiley, doi: 10.1002/9783527651009

Priesemann, V., Valderrama, M., Wibral, M., and Le Van Quyen, M. (2013). Neuronal avalanches differ from wakefulness to deep sleep–evidence from intracranial depth recordings in humans. *PLoS Comput. Biol.*9:e1002985. doi: 10.1371/journal.pcbi.1002985

Radulescu, A. R., Rubin, D., Strey, H. H., and Mujica-Parodi, L. R. (2012). Power spectrum scale invariance identifies prefrontal dysregulation in paranoid schizophrenia. *Hum. Brain Mapp.*33, 1582–1593. doi: 10.1002/hbm.21309

Ribeiro, T. L., Copelli, M., Caixeta, F., Belchior, H., Chialvo, D. R., Nicolelis, M. A. L., et al. (2010). Spike avalanches exhibit universal dynamics across the sleep-wake cycle. *PLoS One*5:e0014129. doi: 10.1371/journal.pone.0014129

Roberts, J. A., Boonstra, T. W., and Breakspear, M. (2015). The heavy tail of the human brain. *Curr. Opin. Neurobiol.*31, 164–172. doi: 10.1016/j.conb.2014.10.014

Roberts, J. A., Iyer, K. K., Finnigan, S., Vanhatalo, S., and Breakspear, M. (2014a). Scale-free bursting in human cortex following hypoxia at birth. *J. Neurosci.*34, 6557–6572. doi: 10.1523/jneurosci.4701-13.2014

Roberts, J. A., Iyer, K. K., Vanhatalo, S., and Breakspear, M. (2014b). Critical role for resource constraints in neural models. *Front. Syst. Neurosci.*8:154. doi: 10.3389/fnsys.2014.00154

Rolls, E. T., Loh, M., Deco, G., and Winterer, G. (2008). Computational models of schizophrenia and dopamine modulation in the prefrontal cortex. *Nat. Rev. Neurosci.*9, 696–709. doi: 10.1038/nrn2462

Ros, T. J., Baars, B., Lanius, R. A., and Vuilleumier, P. (2014). Tuning pathological brain oscillations with neurofeedback: a systems neuroscience framework. *Front. Hum. Neurosci.*8:1008. doi: 10.3389/fnhum.2014.01008

Ruiz, M. H., Bin Hong, S., Hennig, H., Altenmueller, E., and Kuehn, A. A. (2014). Long-range correlation properties in timing of skilled piano performance: the influence of auditory feedback and deep brain stimulation. *Front. Psychol.*5:1030. doi: 10.3389/fpsyg.2014.01030

Sachs, M. K., Yoder, M. R., Turcotte, D. L., Rundle, J. B., and Malamud, B. D. (2012). Black swans, power laws, and dragon-kings: earthquakes, volcanic eruptions, landslides, wildfires, floods, and SOC models. *Eur. Phys. J. Spec. Top.*205, 167–182. doi: 10.1140/epjst/e2012-01569-3

Saleur, H., Sammis, C. G., and Sornette, D. (1996). Discrete scale invariance, complex fractal dimensions, and log-periodic fluctuations in seismicity. *J. Geophys. Res. Solid Earth.*101, 17661–17677. doi: 10.1029/96jb00876

Sammis, C. G., and Smith, S. W. (1999). Seismic cycles and the evolution of stress correlation in cellular automaton models of finite fault networks. *Pure Appl. Geophys.*155, 307–334. doi: 10.1007/s000240050267

Scheffer, M., Bascompte, J., Brock, W. A., Brovkin, V., Carpenter, S. R., Dakos, V., et al. (2009). Early-warning signals for critical transitions. *Nature*461, 53–59. doi: 10.1038/nature08227

Shew, W. L., and Plenz, D. (2013). The functional benefits of criticality in the cortex. *Neuroscientist*19, 88–100. doi: 10.1177/1073858412445487

Shew, W. L., Yang, H., Petermann, T., Roy, R., and Plenz, D. (2009). Neuronal avalanches imply maximum dynamic range in cortical networks at criticality. *J. Neurosci.*29, 15595–15600. doi: 10.1523/JNEUROSCI.3864-09.2009

Shew, W. L., Yang, H., Yu, S., Roy, R., and Plenz, D. (2011). Information capacity and transmission are maximized in balanced cortical networks with neuronal avalanches. *J. Neurosci.*31, 55–63. doi: 10.1523/JNEUROSCI.4637-10.2011

Shriki, O., Alstott, J., Carver, F., Holroyd, T., Henson, R. N. A., Smith, M. L., et al. (2013). Neuronal avalanches in the resting MEG of the human brain. *J. Neurosci.*33, 7079–7090. doi: 10.1523/JNEUROSCI.4286-12.2013

Shriki, O., and Yellin, D. (2016). Optimal information representation and criticality in an adaptive sensory recurrent neuronal network. *PLoS Comput. Biol.*12:e1004698. doi: 10.1371/journal.pcbi.1004698

Simola, J., Zhigalov, A., Morales-Munoz, I., Palva, J. M., and Palva, S. (2017). Critical dynamics of endogenous fluctuations predict cognitive flexibility in the Go/NoGo task. *Sci. Rep.*7:2909. doi: 10.1038/s41598-017-02750-9

Simonsen, I., Hansen, A., and Nes, O. M. (1998). Determination of the Hurst exponent by use of wavelet transforms. *Phys. Rev. E Stat. Physics, Plasmas, Fluids, Relat. Interdiscip. Top.*58:2779. doi: 10.1103/PhysRevE.58.2779

Slezin, V. B., Korsakova, E. A., Dytjatkovsky, M. A., Schultz, E. A., Arystova, T. A., and Siivola, J. R. (2007). Multifractal analysis as an aid in the diagnostics of mental disorders. *Nord. J. Psychiatry*61, 339–342. doi: 10.1080/08039480701643175

Smit, D. J. A., de Geus, E. J. C., van de Nieuwenhuijzen, M. E., van Beijsterveldt, C. E. M., van Baal, G. C. M., Mansvelder, H. D., et al. (2011). Scale-free modulation of resting-state neuronal oscillations reflects prolonged brain maturation in humans. *J. Neurosci.*31, 13128–13136. doi: 10.1523/JNEUROSCI.1678-11.2011

Sornette, A., and Sornette, D. (1989). Self-organized criticality and earthquakes. *Europhys. Lett.*9:197. doi: 10.1209/0295-5075/9/3/002

Sornette, D. (2004). *Critical Phenomena in Natural Sciences: Chaos*. Cham: Springer.

Stam, C. J., and de Bruin, E. A. (2004). Scale-free dynamics of global functional connectivity in the human brain. *Hum. Brain Mapp.*22, 97–109. doi: 10.1002/hbm.20016

Stam, C. J., Montez, T., Jones, B. F., Rombouts, S. A. R. B., van der Made, Y., Pijnenburg, Y. A. L., et al. (2005). Disturbed fluctuations of resting state EEG synchronization in Alzheimer's disease. *Clin. Neurophysiol.*116, 708–715. doi: 10.1016/j.clinph.2004.09.022

Stramaglia, S., Pellicoro, M., Angelini, L., Amico, E., Aerts, H., Cortés, J. M., et al. (2017). Ising model with conserved magnetization on the human connectome:

implications on the relation structure-function in wakefulness and anesthesia. *Chaos*.27:047407. doi: 10.1063/1.4978999

Stumpf, M. P. H., and Porter, M. A. (2012). Critical truths about power laws. *Science*335, 665–666. doi: 10.1126/science.1216142

Suckling, J., Wink, A. M., Bernard, F. A., Barnes, A., and Bullmore, E. (2008). Endogenous multifractal brain dynamics are modulated by age, cholinergic blockade and cognitive performance. *J. Neurosci. Methods*174, 292–300. doi: 10.1016/j.jneumeth.2008.06.037

Surmeli, T., Ertem, A., Eralp, E., and Kos, I. H. (2012). Schizophrenia and the efficacy of qEEG-guided neurofeedback treatment: a clinical case series. *Clin. EEG Neurosci.*43, 133–144. doi: 10.1177/1550059411429531

Tagliazucchi, E., Balenzuela, P., Fraiman, D., and Chialvo, D. R. (2012). Criticality in large-scale brain FMRI dynamics unveiled by a novel point process analysis. *Front. Physiol.*3:15. doi: 10.3389/fphys.2012.00015

Tagliazucchi, E., Carhart-Harris, R., Leech, R., Nutt, D., and Chialvo, D. R. (2014). Enhanced repertoire of brain dynamical states during the psychedelic experience. *Hum. Brain Mapp.*35, 5442–5456. doi: 10.1002/hbm.22562

Tagliazucchi, E., von Wegner, F., Morzelewski, A., Brodbeck, V., Jahnke, K., and Laufs, H. (2013). Breakdown of long-range temporal dependence in default mode and attention networks during deep sleep. *Proc. Natl. Acad. Sci. U.S.A.*110, 15419–15424. doi: 10.1073/pnas.1312848110

Tanaka, T., Kaneko, T., and Aoyagi, T. (2009). Recurrent infomax generates cell assemblies, neuronal avalanches, and simple cell-like selectivity. *Neural Comput.*21, 1038–1067. doi: 10.1162/neco.2008.03-08-727

Thatcher, R. W., North, D. M., and Biver, C. J. (2009). Self-organized criticality and the development of EEG phase reset. *Hum. Brain Mapp.*30, 553–574. doi: 10.1002/hbm.20524

Thatcher, R. W., North, D. M., and Biver, C. J. (2014). LORETA EEG phase reset of the default mode network. *Front. Hum. Neurosci.*8:529. doi: 10.3389/fnhum.2014.00529

Thiery, T., Lajnef, T., Combrisson, E., Dehgan, A., Rainville, P., Mashour, G. A., et al. (2018). Long-range temporal correlations in the brain distinguish conscious wakefulness from induced unconsciousness. *Neuroimage*179, 30–39. doi: 10.1016/j.neuroimage.2018.05.069

Tinker, J., and Velazquez, J. L. P. (2014). Power law scaling in synchronization of brain signals depends on cognitive load. *Front. Syst. Neurosci.*8:73. doi: 10.3389/fnsys.2014.00073

Tkačik, G., Marre, O., Mora, T., Amodei, D., Berry, M. J., and Bialek, W. (2013). The simplest maximum entropy model for collective behavior in a neural network. *J. Stat. Mech. Theory Exp.* 2013. doi: 10.1088/1742-5468/2013/03/P03011

Tolkunov, D., Rubin, D., and Mujica-Parodi, L. R. (2010). Power spectrum scale invariance quantifies limbic dysregulation in trait anxious adults using fMRI: adapting methods optimized for characterizing autonomic dysregulation to neural dynamic time series. *Neuroimage* 50, 72–80. doi: 10.1016/j.neuroimage.2009.12.021

Tomen, N., Ernst, U. A., and Herrmann, J. M. (2019). *The Functional Role of Critical Dynamics in Neural Systems*. Berlin: Springer International Publishing.

Tomko, G. J., Crapper, D. R., Wilson, K. G., Madison, D. V., Nicoll, R. A., Sauer, T., et al. (2018). The theory of critical phenomena: an introduction to the renormalization group. *Neuron*.46:671. doi: 10.1101/107185

Touboul, J., and Destexhe, A. (2010). Can power-law scaling and neuronal avalanches arise from stochastic dynamics?*PLoS One*5:e8982. doi: 10.1371/journal.pone.0008982

Turrigiano, G. G., and Nelson, S. B. (2004). Homeostatic plasticity in the developing nervous system. *Nat. Rev. Neurosci.*5, 97–107. doi: 10.1038/nrn1327

Uhlhaas, P. J., Roux, F., Rodriguez, E., Rotarska-Jagiela, A., and Singer, W. (2010). Neural synchrony and the development of cortical networks. *Trends Cogn. Sci.*14, 72–80. doi: 10.1016/j.tics.2009.12.002

Van De Leemput, I. A., Wichers, M., Cramer, A. O. J., Borsboom, D., Tuerlinckx, F., Kuppens, P., et al. (2014). Critical slowing down as early warning for the onset and termination of depression. *Proc. Natl. Acad. Sci. U.S.A.*111, 87–92. doi: 10.1073/pnas.1312114110

Vanhatalo, S., and Kaila, K. (2006). Development of neonatal EEG activity: from phenomenology to physiology. *Semin. Fetal Neonatal Med.*11, 471–478. doi: 10.1016/j.siny.2006.07.008

Vyšata, O., Procházka, A., Mareš, J., Rusina, R., Pazdera, L., Vališ, M., et al. (2014). Change in the characteristics of EEG color noise in alzheimer's disease. *Clin. EEG Neurosci.*45, 147–151. doi: 10.1177/1550059413491558

Wang, J. W. J. L., Lombardi, F., Zhang, X., Anaclet, C., and Ivanov, P. C. (2019). Non-equilibrium critical dynamics of bursts in Θ and δ rhythms as fundamental characteristic of sleep and wake micro-architecture. *PLoS Comput. Biol.*15:e1007268. doi: 10.1371/journal.pcbi.1007268

Wang, R., Dearing, J. A., Langdon, P. G., Zhang, E., Yang, X., Dakos, V., et al. (2012). Flickering gives early warning signals of a critical transition to a eutrophic lake state. *Nature*492, 419–422. doi: 10.1038/nature11655

Weiss, B., Clemens, Z., Bodizs, R., and Halasz, P. (2011). Comparison of fractal and power spectral EEG features: effects of topography and sleep stages. *BRAIN Res. Bull.*84, 359–375. doi: 10.1016/j.brainresbull.2010.12.005

West, T., Farmer, S., Berthouze, L., Jha, A., Beudel, M., Foltynie, T., et al. (2016). The parkinsonian subthalamic network: measures of power, linear, and non-linear synchronization and their relationship to L-DOPA treatment and OFF state motor severity. *Front. Hum. Neurosci.*10:517. doi: 10.3389/fnhum.2016.00517

Wikstro, S., Iyer, K. K., Roberts, J. A., Hellstro, L., Pupp, I. H., Ley, D., et al. (2015). Cortical burst dynamics predict clinical outcome early in extremely preterm infants. *Brain*138(Pt 8), 2206–2218. doi: 10.1093/awv147

Wilting, J., and Priesemann, V. (2019). 25 years of criticality in neuroscience - established results, open controversies, novel concepts. *Curr. Opin. Neurobiol.*58, 105–111. doi: 10.1016/j.conb.2019.08.002

Wink, A. M., Bernard, F., Salvador, R., Bullmore, E., and Suckling, J. (2006). Age and cholinergic effects on hemodynamics and functional coherence of human hippocampus. *Neurobiol. Aging.*27, 1395–1404. doi: 10.1016/j.neurobiolaging.2005.08.011

Wink, A. M., Bullmore, E., Barnes, A., Bernard, F., and Suckling, J. (2008). Monofractal and multifractal dynamics of low frequency endogenous brain oscillations in functional MRI. *Hum. Brain Mapp.*29, 791–801. doi: 10.1002/hbm.20593

Witton, C., Sergeyev, S. V., Turitsyna, E. G., Furlong, P. L., Seri, S., Brookes, M., et al. (2019). Rogue bioelectrical waves in the brain: the Hurst exponent as a potential measure for presurgical mapping in epilepsy. *J. Neural Eng.*16:56019. doi: 10.1088/1741-2552/ab225e

Worrell, G. A., Cranstoun, S. D., Echauz, J., and Litt, B. (2002). Evidence for self-organized criticality in human epileptic hippocampus. *Neuroreport*13, 2017–2021. doi: 10.1097/00001756-200211150-00005

Yan, J., Wang, Y., Ouyang, G., Yu, T., Li, Y., Sik, A., et al. (2016). Analysis of electrocorticogram in epilepsy patients in terms of criticality. *Nonlinear Dyn.*83, 1909–1917. doi: 10.1007/s11071-015-2455-9

Yang, H., Shew, W. L., Roy, R., and Plenz, D. (2012). Maximal variability of phase synchrony in cortical networks with neuronal avalanches. *J. Neurosci.*32, 1061–1072. doi: 10.1523/JNEUROSCI.2771-11.2012

Zhigalov, A., Kaplan, A., and Palva, J. M. (2016). Modulation of critical brain dynamics using closed-loop neurofeedback stimulation. *Clin. Neurophysiol.*127, 2882–2889. doi: 10.1016/j.clinph.2016.04.028

Conflict of Interest: The author declares that the research was conducted in the absence of any commercial or financial relationships that could be construed as a potential conflict of interest.

frontiers in Neural Circuits

ORIGINAL RESEARCH
published: 15 January 2021
doi: 10.3389/fncir.2020.576727

Subsampled Directed-Percolation Models Explain Scaling Relations Experimentally Observed in the Brain

*Tawan T. A. Carvalho[1], Antonio J. Fontenele[1], Mauricio Girardi-Schappo[2,3], Thaís Feliciano[1], Leandro A. A. Aguiar[4], Thais P. L. Silva[1], Nivaldo A. P. de Vasconcelos[5,6], Pedro V. Carelli[1] and Mauro Copelli[1]**

[1] Departamento de Física, Universidade Federal de Pernambuco, Recife, Brazil, [2] Department of Physics, University of Ottawa, Ottawa, ON, Canada, [3] Departamento de Física, Faculdade de Filosofia, Ciências e Letras de Ribeirão Preto, Universidade de São Paulo, Ribeirão Preto, Brazil, [4] Departamento de Ciências Fundamentais e Sociais, Universidade Federal da Paraíba, Areia, Brazil, [5] Life and Health Sciences Research Institute (ICVS), School of Medicine, University of Minho, Braga, Portugal, [6] Life and Health Sciences Research Institute/Biomaterials, Biodegradables and Biomimetics, Braga, Portugal

Recent experimental results on spike avalanches measured in the urethane-anesthetized rat cortex have revealed scaling relations that indicate a phase transition at a specific level of cortical firing rate variability. The scaling relations point to critical exponents whose values differ from those of a branching process, which has been the canonical model employed to understand brain criticality. This suggested that a different model, with a different phase transition, might be required to explain the data. Here we show that this is not necessarily the case. By employing two different models belonging to the same universality class as the branching process (mean-field directed percolation) and treating the simulation data exactly like experimental data, we reproduce most of the experimental results. We find that subsampling the model and adjusting the time bin used to define avalanches (as done with experimental data) are sufficient ingredients to change the apparent exponents of the critical point. Moreover, experimental data is only reproduced within a very narrow range in parameter space around the phase transition.

Keywords: subsampling, neuronal avalanches, brain criticality, scaling relations, cortex, urethane

OPEN ACCESS

Edited by:
Axel Sandvig, Norwegian University of Science and Technology, Norway

Reviewed by:
Dietmar Plenz, National Institute of Mental Health, National Institutes of Health (NIH), United States
Afshin Montakhab, Shiraz University, Iran

****Correspondence:***
Mauro Copelli
mauro.copelli@ufpe.br

Received: *26 June 2020*
Accepted: *30 November 2002*
Published: *15 January 2021*

Citation:
Carvalho TTA, Fontenele AJ, Girardi-Schappo M, Feliciano T, Aguiar LAA, Silva TPL, de Vasconcelos NAP, Carelli PV and Copelli M (2021) Subsampled Directed-Percolation Models Explain Scaling Relations Experimentally Observed in the Brain. Front. Neural Circuits 14:576727. doi: 10.3389/fncir.2020.576727

1. INTRODUCTION

In the first results that fueled the critical brain hypothesis, Beggs and Plenz (2003) observed intermittent bursts of local field potentials (LFPs) in *in vitro* multielectrode recordings of cultured and acute slices of the rat brain. Events occurred with a clear separation of time scales, and were named neuronal avalanches.

A neuronal avalanche can be characterized by its size S, which is the total number of significant voltage deflections recorded by electrodes between periods of silence, and by its duration T, which is the number of consecutive time bins spanned by an avalanche. Beggs and Plenz found power-law distributions for the sizes of avalanches,

$$P(S) \sim S^{-\tau} , \tag{1}$$

with $\tau \simeq 3/2$, and suggested, based on their data, a power-law distribution of avalanche duration,

$$P(T) \sim T^{-\tau_t} , \tag{2}$$

with $\tau_t = 2$. These scale-invariant distributions were interpreted as a signature that the brain could be operating at criticality—a second-order phase transition (Beggs and Plenz, 2003; Beggs, 2007; Chialvo, 2010; Shew and Plenz, 2013; Plenz and Niebur, 2014; Tomen et al., 2019).

In particular, these two critical exponents together are compatible with a branching process at its critical point (Harris, 1963), a conclusion that was further strengthened by the experimentally established critical branching parameter of 1 for neuronal avalanches (Beggs and Plenz, 2003). This points to a phase transition between a so-called absorbing phase (zero population firing rate) and an active phase (non-zero stationary population firing rate).

Due to its appeal, simplicity, and familiarity within the statistical physics community, the critical branching process has become a canonical model for understanding criticality in the brain. In fact, these exponents are compatible with a larger class of models, namely, any model belonging to the mean-field directed percolation (MF-DP) universality class (Muñoz et al., 1999). In the theory of critical phenomena, two models which can be different in their details are said to belong to the same universality class when the critical exponents which characterize their phase transition coincide (Binney et al., 1992). In general, probabilistic contagion-like models which have a unique absorbing state (all sites "susceptible" or in the neuroscience context, all neurons quiescent) and no further symmetries tend to belong to the directed-percolation universality class (Janssen, 1981; Grassberger, 1982; Marro and Dickman, 1999). If the network has topological dimension above 4 (such as random or complete graphs), the model usually belongs to the MF-DP universality class.

More recently, these ideas were tested with more advanced experimental techniques, highlighting the prospect of criticality in the awake brain. Two studies have shown that different types of anesthesia strongly affect avalanche statistics. In voltage imaging recordings of the mouse cortex, size distributions were more closely compatible with $\tau = 1.5$ for awake animals than for animals anesthetized with pentobarbital (Scott et al., 2014). A similar trend was observed in two-photon imaging of the rat cortex, where avalanche distributions become increasingly compatible with $\tau = 1.5$ and $\tau_t = 2$ as the animals recover from isoflurane anesthesia (Bellay et al., 2015).

Other experimental results, however, challenged the MF-DP scenario originally proposed by Beggs and Plenz (2003). For instance, avalanche exponents in *ex-vivo* recordings of the turtle visual cortex deviated significantly from $\tau = 3/2$ and $\tau_t = 2$ (Shew et al., 2015). Discrepancies in exponent values were also observed in spike avalanches of rats under ketamine-xylazine anesthesia (Ribeiro et al., 2010) and M/EEG avalanches in resting or behaving humans (Palva et al., 2013; Zhigalov et al., 2015), among others.

Furthermore, Touboul and Destexhe (2017) argued that the power-law signature alone in the distributions of size (Equation 1) and duration (Equation 2) of avalanches is insufficient to claim criticality, since power laws can be observed in non-critical models as well. They suggested that another scaling relation should be tested as a stronger criterion. This was based on the result that at criticality the average avalanche size $\langle S \rangle$ for a given duration T must obey

$$\langle S \rangle \sim T^{\frac{1}{\sigma \nu z}} , \tag{3}$$

where $1/(\sigma \nu z)$ is a combination of critical exponents that at criticality satisfy the so-called crackling noise scaling relation (Muñoz et al., 1999; Sethna et al., 2001; Friedman et al., 2012)

$$\frac{1}{\sigma \nu z} = \frac{\tau_t - 1}{\tau - 1} . \tag{4}$$

Equation (4) is a stronger criterion for criticality because it is expected not to be satisfied by non-critical models (Touboul and Destexhe, 2017). In the MF-DP case, the avalanche exponents obey $(\tau_t - 1)/(\tau - 1) = 2$ and $1/(\sigma \nu z) = 2$, independently. The absolute difference between the two sides of Equation (4) can even be employed as a metric for the distance to criticality (Ma et al., 2019), or to identify criticality in more general phase transitions of neuronal networks (Girardi-Schappo and Tragtenberg, 2018). Indeed, Ponce-Alvarez et al. (2018) have investigated the crackling noise relation in zebrafish whole-brain activity, obtaining $1/(\sigma \nu z) \simeq 2$ but values of τ and τ_t incompatible with MF-DP. Miller et al. (2019) have also found $1/(\sigma \nu z) \simeq 2$ in LFP avalanches from awake non-human primates, when the impact of ongoing gamma-oscillations was accurately taken into account.

Recently, cortical spike avalanches of urethane-anesthetized rats were investigated under this methodological lens by Fontenele et al. (2019). This experimental setup is known to yield spiking activity which is highly variable, ranging from very asynchronous to very synchronous population activity (Clement et al., 2008). These regimes can be characterized by different ranges of the coefficient of variation (CV) of the population firing rate (de Vasconcelos et al., 2017), which is thought of as a simple marker of cortical states (Harris and Thiele, 2011). By parsing the data according to levels of spiking variability, Fontenele et al. (2019) found that the scaling relation Equation (4) was satisfied at an intermediate value of CV, suggesting a phase transition away from both the synchronized and desynchronized ends of the spiking variability spectrum. In particular, the values of the avalanche exponents where the scaling relation was satisfied were not all compatible (within error bars) with MF-DP values: $\langle \tau \rangle \simeq 1.52 \pm 0.09$, $\langle \tau_t \rangle \simeq 1.7 \pm 0.1$ and $\langle 1/(\sigma \nu z) \rangle \simeq 1.28 \pm 0.03$ (Fontenele et al., 2019). This was interpreted as an incompatibility with the theoretical MF-DP scenario (Fontenele et al., 2019), thus requiring the formulation of models belonging to other universality classes and undergoing other phase transitions.

One hypothesis to explain this controversy is that the study of spike activity is strongly affected by subsampling effects, that is, the measured activity is based on a tiny fraction of the total number of neurons in a given area of the brain. Different groups have shown that subsampling indeed affects the apparent distribution of avalanches (Priesemann et al., 2009, 2014; Ribeiro et al., 2010, 2014; Girardi-Schappo et al., 2013; Levina and Priesemann, 2017; Wilting and Priesemann, 2019). For example,

an avalanche evaluated on all elements (full sampling) can be broken into smaller avalanches when recorded in a subset of the network (subsampling). In addition, we highlight that this effect is different from the well-studied phenomenon of finite-size scaling, which is the study of how statistical properties change as the size of the system increases and activity recorded in all sites is analyzed (see e.g., Levina and Priesemann, 2017).

Here, we revisit this issue by studying the data produced by two theoretical models in the MF-DP universality class. We start by showing that the models reproduce well-known analytical results, which however fail to reproduce the experimental data. Then we proceed to treat the model results under the same conditions as those of experimental data. Despite the large number of simulated neurons ($\sim 10^5$), we intentionally restrict the theoretical analysis to a small subset of cells ($\sim 10^2$), mimicking the fact that one can only record a few hundred neurons among the millions that comprise the rat's brain (the subsampling issue). Here we show that by combining the subsampling of the model with the analysis pipeline that has been applied to the experimental data (Fontenele et al., 2019), we can reconcile the empirical power-law avalanches with the theoretical MF-DP universality class.

2. METHODS

2.1. A Spiking Neuronal Network With Excitation and Inhibition

We used the excitatory/inhibitory network of Girardi-Schappo et al. (2020), where each neuron is a stochastic leaky integrate-and-fire unit with discrete time step equal to 1 ms, connected in an all-to-all graph. A binary variable indicates if the neuron fired $[X(t) = 1]$ or not $[X(t) = 0]$. The membrane potential of each cell i in either the excitatory (E) or inhibitory (I) population is given by

$$V_i^{E/I}(t+1) = \left[\mu V_i^{E/I}(t) + I_e + \frac{J}{N}\sum_{j=1}^{N_E} X_j^E(t) - \frac{gJ}{N}\sum_{j=1}^{N_I} X_j^I(t)\right]\left(1 - X_i^{E/I}(t)\right), \quad (5)$$

where J is the synaptic coupling strength, g is the inhibition to excitation (E/I) coupling strength ratio, μ is the leak time constant, and I_e is an external current. The total number of neurons in the network is $N = N_E + N_I = 10^5$, where the fractions of excitatory and inhibitory neurons are kept fixed at $p = N_E/N = 0.8$ and $q = N_I/N = 0.2$, respectively, as reported for cortical data (Somogyi et al., 1998). Note that the membrane potential is reset to zero in the time step following a spike.

At any time step, a neuron fires according to a piecewise linear sigmoidal probability $\Phi(V)$,

$$\Phi(V) \equiv P(X = 1|V) = \Gamma(V-\theta)\Theta(V-\theta)\Theta(V_S - V) + \Theta(V - V_S), \quad (6)$$

where $\theta = 1$ is the firing threshold, Γ is the firing gain constant, $V_S = 1/\Gamma + \theta$ is the saturation potential, and $\Theta(x > 0) = 1$ (zero otherwise) is the step function. For simplicity, the parameter $\mu = 0$ is chosen without lack of generality, since it does not change the phase transition of the model (Girardi-Schappo et al., 2020). The external current $I_e > V_S$ is used only to spark a new avalanche in a single excitatory neuron when the network activity dies off (it is kept as $I_e = \theta$ otherwise).

This model is known to present a directed percolation critical point (Girardi-Schappo et al., 2020) at $g_c = p/q - 1/(q\Gamma J) = 1.5$ (for $\Gamma = 0.2$ and $J = 10$), such that $g < g_c$ is the active excitation-dominated (supercritical) phase and $g > g_c$ corresponds to the inhibition-dominated absorbing state (subcritical). The synapses in the critical point g_c are dynamically balanced: fluctuations in excitation are immediately followed by counter fluctuations in inhibition (Girardi-Schappo et al., 2020). The initial condition of the simulations has all neurons quiescent except for a seed neuron to spark activity. This procedure was repeated whenever the system went back to the absorbing state.

2.2. Probabilistic Cellular Automaton Model

The spiking model described in section 2.1 is certainly not the simplest model to present a phase transition in the MF-DP universality class. Therefore, to probe the robustness of our findings, we also simulated a much simpler model: a network of probabilistic excitable cellular automata in a random graph (Kinouchi and Copelli, 2006). This model closely resembles a standard branching process and is known to mimic the changing inhibition-excitation levels of cortical cultures (Shew et al., 2009).

Each site i ($i = 1, \ldots, N$) has five states: the silent state, $s_i = 0$, the active state, $s_i = 1$, corresponding to a spike, and the remaining three states, $s_i = 2, 3, 4$, in which the site will not respond to incoming stimuli (absolute refractory states). Each site receives input from K presynaptic neighbors which are randomly selected at the start and kept fixed throughout the simulations. A quiescent site i becomes excited $[s_i(t) = 0 \to s_i(t+1) = 1]$ with probability p_{ij} if a presynaptic neighbor j is active at time t. All presynaptic neighbors are swept and independently considered at each time step, so that

$$P\left(s_i(t+1) = 1 | s_i(t) = 0\right) = 1 - (1 - h_i)\prod_{j \in \mathcal{N}(i)}^{K}\left[1 - p_{ij}s_j(t)\right], \quad (7)$$

where h_i is the probability of unit i spiking due to an external stimulus and $\mathcal{N}(i)$ is the set of presynaptic neighbors of i. The remaining transitions happen with probability 1, including the transition $4 \to 0$ that returns the site to its initial quiescent state. The time step of the model corresponds to 1 ms.

We initially chose the random variables $\{p_{ij}\}$ from a uniform distribution in the interval $[0, 2\lambda/K]$. The so-called branching ratio $\lambda = K\langle p_{ij}\rangle$ is the control parameter of the model. This model undergoes a MF-DP phase transition at $\lambda = \lambda_c = 1$ (Kinouchi and Copelli, 2006). For $\lambda < 1$, the system is in the subcritical phase and eventually reaches the absorbing state ($s_i = 0, \forall i$). For $\lambda > 1$, the system presents self-sustained activity, i.e., a non-zero stationary density of population firings

(the supercritical phase). The critical point is not affected by the number of refractory states (Kinouchi and Copelli, 2006).

In our simulations we used $K = 10$ neighbors for each of the $N = 10^5$ sites. Similarly to the spiking neuronal network model, a single random neuron was stimulated ($h_i = 1$) only when the system reached the absorbing state, sparking the network activity and subsequently being set back to $h_i = 0$. The initial condition was set with a single randomly chosen site active and the others in the silent state.

2.3. Experimental Data Acquisition

Urethane is a well-established drug that provides spontaneous changes of brain states that resemble sleep state alternations (Clement et al., 2008). In the last decade, experimental preparations using urethane have helped elucidate questions concerning mechanisms and the functional relevance of state-dependent patterns of brain activity (Curto et al., 2009; Renart et al., 2010; Mochol et al., 2015; de Vasconcelos et al., 2017). The property to promote spontaneous change in the levels of spiking variability cannot be achieved in other anesthesia approaches, such as pentobarbital and isoflurane.

The data used in this paper is original and corroborates the results of Fontenele et al. (2019). We used five rats Long-Evans (*Rattus norvegicus*) (male, 280–360 g, 2–4 months old). They were obtained from the animal house of the Laboratory of Computational and Systems Neuroscience, Department of Physics, Federal University of Pernambuco (UFPE). The animals were anesthetized with urethane (1.55 g/kg), diluted at 20% in saline, in three intraperitoneal (i.p.) injections, 15 min apart (Sakata and Harris, 2009). Some animals demanded supplement (max 5%) of urethane to reach the proper level of analgesia. In order to ensure that the animals are maintained at the correct depth of anesthesia, responses to painful stimuli (pinching the animal's toes, ears and tail) were always checked throughout the experiment. Once the anesthesia reached its proper level, the rats were placed in a stereotaxic frame and the coordinates to access the primary visual cortex (V1) were marked (Bregma: AP = −7.2, ML = 3.5) (Paxinos and Watson, 2007). A cranial window in the scalp was opened using this coordinate as center, with an area of ∼3 mm^2. We performed recordings of extra-cellular voltage of neuronal populations by using a 64-channel multielectrode silicon probe (Neuronexus technologies, Buzsaki64spL-A64). This probe has 60 electrodes disposed in six shanks separated by 200 μm, 10 electrodes per shank with impedance of 1–3 MOhm at 1 kHz. Each electrode has 160 μm^2 and they are in staggered positions 20 μm apart. We recorded from deeper layers of the rat cortex, similarly to what was previously done in Ribeiro et al. (2010) under ketamine-xylazine and Fontenele et al. (2019) under a setup similar to the one presented here.

Data was sampled at 30 KHz, amplified and digitized in a single head-stage (Intan RHD2164) (Siegle et al., 2017). We recorded spontaneous activity, during long periods (≥3 h). We used the open-source software Klusta to perform the automatic spike sorting on raw electrophysiological data (Rossant et al., 2016). The automatic part is divided in two major steps, spike detection and automatic clustering. The first step detects action potentials and the second one arrange those spikes into clusters according to their similarities (waveforms, PCA, refractory period). After the automatic part, all formed clusters are reanalyzed using the graphic interface phy kwikGUI[1]. Manual spike sorting allows the identification of each cluster of neuronal activity as single-unit activity (SUA) or multi-unit activity (MUA). We used both SUA and MUA clusters for our study.

2.4. Avalanche Analysis With CV Parsing

To study neuronal avalanches at different levels of spiking variability (Shadlen and Newsome, 1998), we segmented both the neurophysiological and simulated data in non-overlapping windows of width $w = 10$ s (unless otherwise stated) (Gervasoni et al., 2004). Each of these 10 s epochs was subdivided in non-overlapping intervals $\{\zeta_j\}$ of duration $\Delta T = 50$ ms (unless otherwise stated) in which we estimated the population spike-count rate R_j. We then calculated the coefficient of variation (CV) for the i-th 10 s window:

$$CV_i = \frac{\sigma_i}{\mu_i}, \tag{8}$$

where CV is dimensionless, and σ_i and μ_i correspond to the standard deviation and the mean of $\{R_j\}$, respectively.

For each 10 s window with a particular CV level, we proceeded with the standard avalanche analysis of Beggs and Plenz (2003). The summed population activity was sliced in non-overlapping temporal bins of width $\Delta t = \langle ISI \rangle$ (the average inter-spike interval). Ribeiro et al. (2010) and Yu et al. (2017) have shown that an adaptive bin, evaluated according to the current dynamical state, renders signatures of scale-free dynamics more robust. Following this strategy, we have separately computed $\Delta t = \langle ISI \rangle$ for each 10 s window. Population spikes preceded and followed by silence define a spike avalanche. The number of spikes correspond to the avalanche size S, whereas the number of time bins spanned by the avalanche is its duration T. Following this methodology, we associated each 10 s CV_i window with its corresponding set of n_i avalanche sizes $\mathbf{S_i} \equiv \{S_{i1}, S_{i2}, \ldots, S_{in_i}\}$ and durations $\mathbf{T_i} \equiv \{T_{i1}, T_{i2}, \ldots, T_{in_i}\}$.

To estimate the avalanche exponents τ and τ_t, we first ranked the sets $\{\mathbf{S_i}\}$ and $\{\mathbf{T_i}\}$ according to their CV values. Next, in order to increase the number of samples while preserving the level of spiking variability, we pooled NB consecutive ranked blocks of similar CV values ($NB = 50$ unless otherwise stated). For each set of NB blocks we calculated the average coefficient of variation $\langle CV \rangle$. The exponents of the size and duration distributions were obtained via a Maximum Likelihood Estimator (MLE) procedure (Deluca and Corral, 2013; Yu et al., 2014; Marshall et al., 2016) on a discrete power-law distribution

$$f(x) = \frac{1}{\sum_{x=x_{min}}^{x_{max}} (\frac{1}{x})^{\alpha}} \left(\frac{1}{x}\right)^{\alpha}. \tag{9}$$

The standard choice of fitting parameters, for both experimental and subsampled simulated data, was $S_{min} = 2$ and $S_{max} = 100$ for size distributions and $T_{min} = 2$ and $T_{max} = 30$ for duration

[1]https://github.com/cortex-lab/phy

TABLE 1 | Limits chosen for the calculation of the α exponent (Equation 9) via Maximum Likelihood Estimator (MLE) only for the model data shown in **Figures 4C,D** ($\Delta t = 1$ ms).

n	Size distribution		Duration distribution	
	S_{min}	S_{max}	T_{min}	T_{max}
100	2	30	2	15
200	2	100	2	50
500	2	200	2	70
1,000	2	200	2	70
2,000	2	300	3	100
5,000	2	500	4	100
10,000	5	3,000	5	150
20,000	5	5,000	5	200
30,000	10	10,000	10	200
40,000	10	10,000	10	250
50,000	10	10,000	10	300
100,000	10	20,000	10	300

See text for details.

distributions. The exceptions to this choice were for the data shown in **Figures 4C,D**, due to a change of orders of magnitude in the number of neurons sampled. The specific parameters for these cases are shown in **Table 1**.

After the MLE fit we used the Akaike Information Criterion (AIC) as a measure of the relative quality of a given statistical model for a data set:

$$AIC = 2k - 2\ln(\hat{L}) + \frac{2k^2 + 2k}{N - k - 1}\,, \tag{10}$$

where $\hat{L}$ is the likelihood at its maximum, k is number of parameters and N the sample size (Akaike, 1975). Starting from the principle that lower AIC indicates a more parsimonious model, we defined $\Delta \equiv AIC_{ln} - AIC_{pl}$, where AIC_{ln} and AIC_{pl} correspond to the AIC of a log-normal and a power-law model, respectively. Therefore, $\Delta > 0$ implies that a power-law model is a better fit to the data than a log-normal. Our scaling relation analyses were restricted to distributions that satisfied $\Delta > 0$.

2.5. Pairwise Correlations

Pairwise spiking correlations were estimated using only the SUA or the simulated data in the following way: first, for each cell k we obtained a spike count time series $R^{(k)}(t)$ at millisecond resolution ($\Delta T = 1$ ms), then each spike count time series $R^{(k)}$ was convolved with a kernel $h_{t_1,t_2}(t)$ to estimate the k-th mean firing rate $n^{(k)}(t)$:

$$n^{(k)}(t) = h_{t_1,t_2}(t) * R^{(k)}(t)\,, \tag{11}$$

where $h_{t_1,t_2}(t)$ is a Mexican-hat kernel obtained by the difference between zero-mean Gaussians with standard deviations $t_1 = 100$ ms and $t_2 = 400$ ms (Renart et al., 2010). The $n_k(t)$ were employed to calculate the spiking correlation coefficient between two units k and l:

$$r^{(k,l)} = \frac{\mathrm{Cov}\left(n^{(k)}, n^{(l)}\right)}{\sqrt{\mathrm{Var}\left(n^{(k)}\right)\mathrm{Var}\left(n^{(l)}\right)}}\,, \tag{12}$$

where Var and Cov are the variance and covariance over t, respectively.

3. RESULTS

3.1. Avalanches in the Fully Sampled Model

We start by illustrating the second order phase transition that the model undergoes at a critical value $g_c = 1.5$ of the inhibition parameter (Girardi-Schappo et al., 2020). As shown in **Figure 1A**, the stationary density of active sites $\bar{\rho}$ is positive for $g < g_c$ (the supercritical regime) and null for $g > g_c$ (the subcritical regime).

At the critical point $g = g_c$, the distribution of avalanche sizes and duration obey the expected power laws (Equations 1 and 2) with exponents $\tau = 3/2$ and $\tau_t = 2$ (Girardi-Schappo et al., 2020). Subcritical avalanches are exponentially distributed, whereas the supercritical distribution has a trend to display larger and longer avalanches (**Figures 1B,C**). Both sides of the scaling law in Equation (4) independently agree, since the fit to $\langle S\rangle(T)$ yields $1/(\sigma\nu z) = 2$ on the critical point (**Figure 1D**). **Figure 1E** shows typical time series of firing events for the three regimes. These exponents and dynamic behavior of the model are typical of a system undergoing a MF-DP phase transition.

3.2. Comparison of Subsampled Model and Experiments Stratified by CV

We now revisit the model by subjecting it to the same constraints that apply to experimental datasets (Fontenele et al., 2019) and compare the results between the two. More specifically: (1) data analysis necessarily uses only a tiny fraction of the total neurons in the system and (2) in urethane-anesthetized rats, cortical spiking variability is a proxy for cortical states (Harris and Thiele, 2011) and changes a lot during the hours-long recordings (Clement et al., 2008; de Vasconcelos et al., 2017).

Starting with the experimental results, **Figure 2A** shows the time series of the coefficient of variation (CV) of the population spiking activity. The lowest CV values correspond to asynchronous spiking activity, whereas the highest values correspond to more synchronized activity (both shown in **Figure 2B**). When we parsed the data by CV percentiles and evaluated neuronal avalanches for different percentiles, the distributions varied accordingly, with exponents τ, τ_t, and $1/(\sigma\nu z)$ varying continuously across the CV range (**Figure 2C**) as expected (Fontenele et al., 2019).

Can the MF-DP spiking network model reproduce these experimental results? We found that by sampling only a few neurons out of the entire network, indeed it can. Out of $N = 10^5$ simulated neurons, we sampled only $n = 100$, a number that is of the same order as the amount of neurons captured in our empirical data (Fontenele et al., 2019). Then, we applied to the

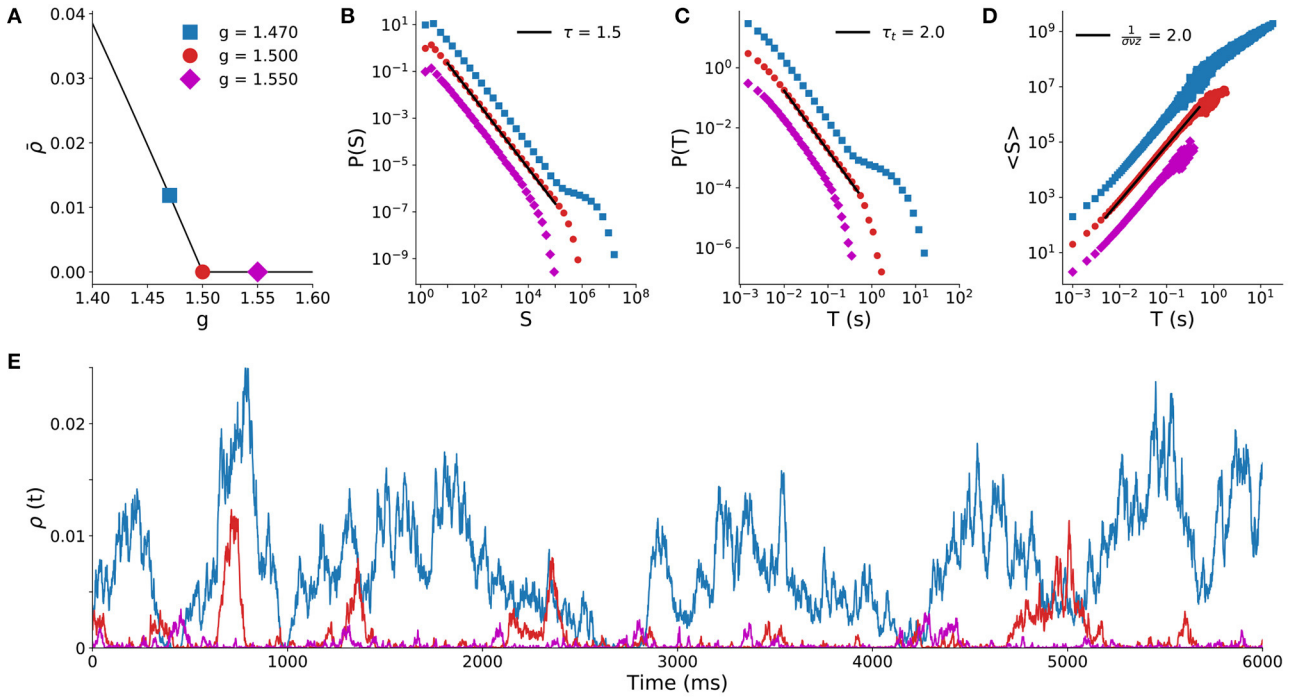

FIGURE 1 | Spiking model results with full sampling. Behavior of the spiking model ($N = 10^5$) for different values of the control parameter g. **(A)** Stationary density of firings $\bar{\rho}$ as a function of the inhibition strength g (critical point is the red circle at $g_c = 1.5$). Solid line is the mean-field solution (Girardi-Schappo et al., 2020), points are simulation results. Distribution of avalanche sizes **(B)** and duration **(C)** for the subcritical ($g > g_c$), critical ($g = g_c$) and supercritical ($g < g_c$) regimes. **(D)** Average avalanche size $\langle S \rangle$ of a given duration (T). **(E)** Time series of the density of active sites for the three regimes.

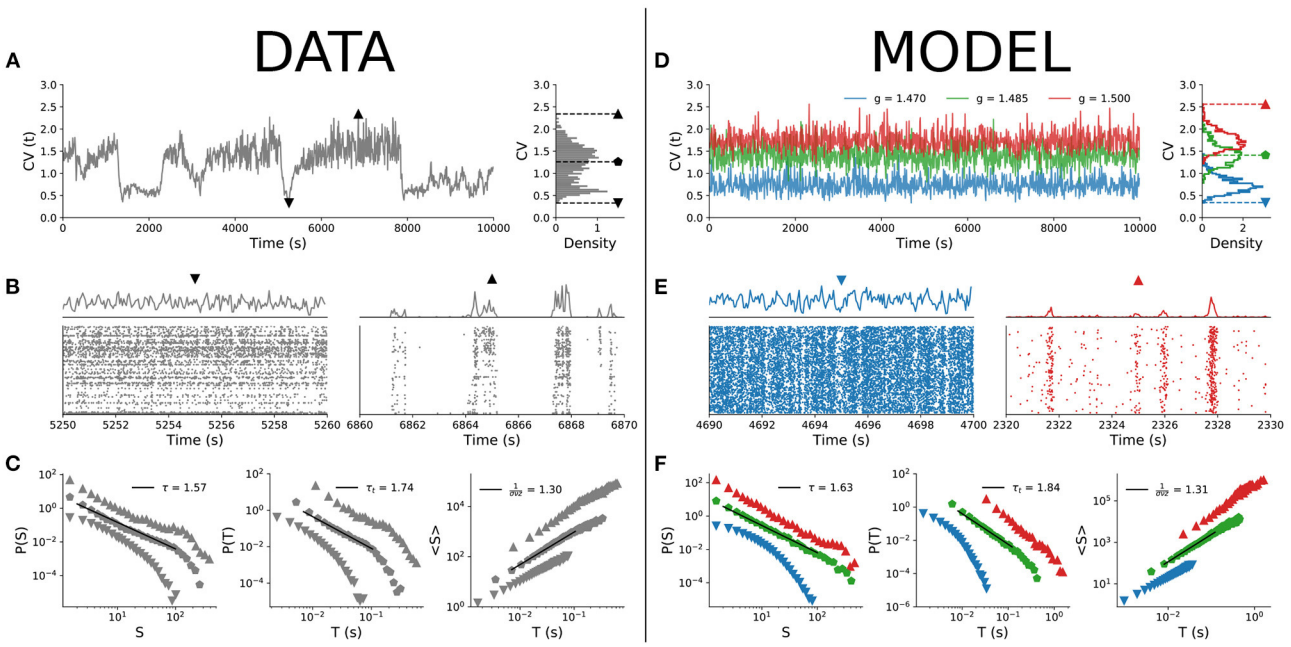

FIGURE 2 | Comparison between empirical data and subsampled spiking model. *CV* time series and distribution for **(A)** experimental data (single animal) and **(D)** model with $n = 100$. Raster plots and population firing rate in cases of low (▼) and high (▲) values of *CV* for **(B)** experimental data and **(E)** model. Scaling exponents τ, τ_t, and $1/(\sigma\nu z)$ for three different values of *CV* (denoted by different symbols): **(C)** experimental data and **(F)** model. For both experimental data and model, $w = 10$ s.

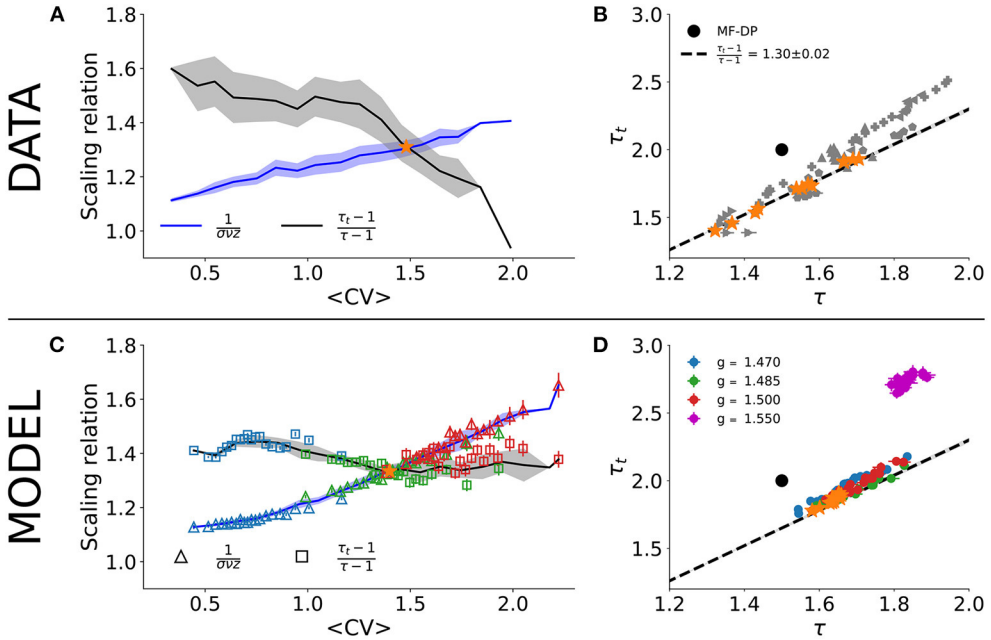

FIGURE 3 | Scaling relation and parametric plot of avalanche exponents. Right- and left-sides of Equation (4) (line and shade are average and standard deviation across the group) as a function of the average *CV* for **(A)** experimental data and **(C)** subsampled model ($n = 100$; note that color code and values of g are the same as in **Figures 2D,F**). Scatter plot in the (τ, τ_t) plane for **(B)** experimental data and **(D)** subsampled model. In both cases, $\Delta t = \langle ISI \rangle$ and $w = 10$ s. The star points in **(B,D)** indicate the values of τ and τ_t that satisfied Equation (4) in **(A,C)**. In **Supplementary Figure 2**, we show the same result in **(A)** for each rat separately.

subsampled simulation data exactly the same analysis pipeline used for experiments (section 2.4).

In the model, we changed the E/I level g to control for the spiking variability level CV. For a fixed value of parameter g, CV is a bell-shaped distribution with finite variance. The $CV(t)$ time series of the model for a single g does not present the dynamical complexity observed experimentally (compare **Figures 2A,D**). By varying g within a narrow interval around the critical point g_c, the CV distribution of the model covers the values observed experimentally (**Figure 2D**), with less synchronous behavior for low CV and more synchronous activity for high CV (**Figure 2E**; the full behavior of the CV distribution as a function of parameter g is shown in **Supplementary Figure 1A**). Parsing the data by CV and running the avalanche statistics for the subsampled model, we obtained scaling exponents that vary continuously, in remarkable similarity to what is observed in the experimental data (**Figure 2F**).

A critical system with an absorbing-active phase transition which satisfies Equations (1)–(3) is also expected to satisfy the so-called crackling noise scaling relation of Equation (4). **Figure 3A** shows the independent experimental fits for the left- and right-hand sides of Equation (4) as a function of CV. The crossing at $CV_* \simeq 1.46 \pm 0.08$ is consistent with the phase transition reported by Fontenele et al. (2019). In the crossing CV_*, we obtain $\tau_* = 1.54 \pm 0.12$, $\tau_{t*} = 1.73 \pm 0.18$, and $1/(\sigma\nu z)_* = 1.30 \pm 0.02$. Plotting τ vs. τ_t, the experimental data scatter along the line with slope given by $1/(\sigma\nu z)_*$ for different values of CV (**Figure 3B**). These results are in agreement with those of Fontenele et al. (2019), again suggesting an incompatibility with the MF-DP universality class.

The results for the subsampled spiking model, however, suggest otherwise. We did exactly the same procedure with the subsampled model and found a similar CV for the crossing of the critical exponents, $CV_*^{model} \simeq 1.41 \pm 0.05$, when controlling for the E/I ratio g very close to the critical point $g_c = 1.5$ (**Figure 3C**). On the crossing CV_*^{model}, we obtained $\tau_* = 1.65 \pm 0.02$, $\tau_{t*} = 1.87 \pm 0.03$, and $1/(\sigma\nu z)_* = 1.34 \pm 0.02$. Note that these critical exponents are not the true exponents of the model. In fact, they are apparent exponents generated by subsampling the network activity. The true critical exponents are $\tau = 3/2$, $\tau_t = 2$ and $1/(\sigma\nu z) = 2$ (as shown in **Figure 1**).

To reproduce the experimental results, the control interval of g was slightly biased toward the supercritical range: $g_{min} \simeq 1.47 \leq g \leq g_{max} \simeq 1.50$. Our model predicts, then, that the whole range of experimental results is produced by fluctuations of only about 2% around the critical point (**Figure 3D**). For instance, for $g = 1.55$ (3% above the critical point in the subcritical regime), the scaling relation is no longer satisfied and the measured exponents fall far away from the linear relation observed experimentally in the (τ, τ_t) plane (**Figure 3D**).

This result shows that the MF-DP phase transition under subsampling conditions is capable of reproducing a whole range of experimentally observed avalanches across a range of CV values. To test the robustness of our findings, we employed exactly the same procedure to a simpler model, a probabilistic cellular automaton (section 2.2). This model is also knowingly

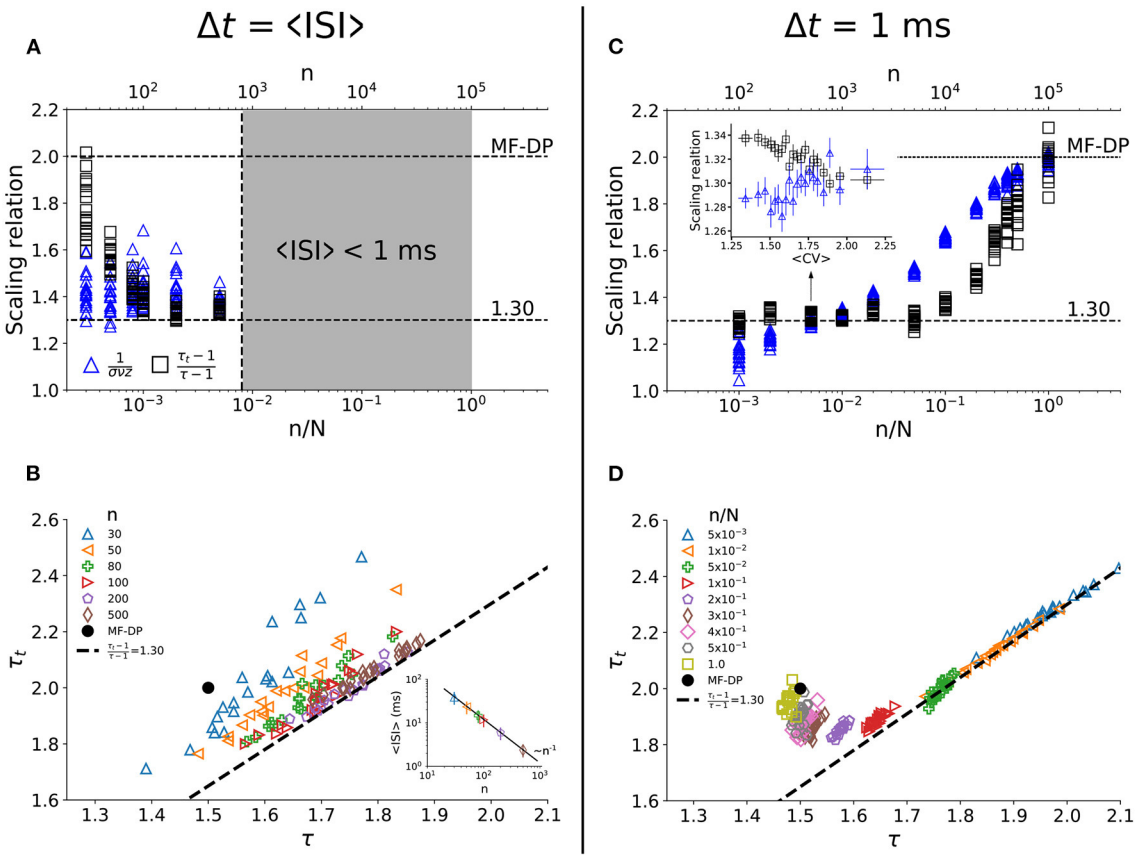

FIGURE 4 | Dependence of the apparent critical exponents on the sampling parameters at criticality. In **(A,C)**, we show both sides of the scaling relation (Equation 4) for *all* values of *CV* observed in the simulations. For each value of n/N, one has the equivalent of the projection of **Figure 3C** onto its vertical axis. For $\Delta t = \langle ISI \rangle$, **(A)** the scaling relation is satisfied for increasing number of sampled neurons **(B)** with exponents that agree with experimental data. Since $\langle ISI \rangle$ decreases with n [inset of **(B)**], this analysis breaks down when n is so large that $\langle ISI \rangle$ becomes smaller than 1 ms [gray region in **(A)**], which is the time step of the simulations. For $\Delta t = 1$ ms, **(C)** the scaling relation is satisfied for small n/N, within a relatively wide range of *CV* values [inset of **(C)**]. For $n/N \to 1$, results converge to MF-DP values **(C,D)**, as expected. Simulations with $N = 10^5$ and $g_c = 1.5$.

of the MF-DP type (Kinouchi and Copelli, 2006), but has a random network topology. All the results were similar (see **Supplementary Figure 3**), showing that the apparent exponents are a direct consequence of subsampling.

3.3. Dependence on Sampling Fraction and Time Bin Width

How robust are the results of the model at criticality against variation in the sampling size (n) and time bin width (Δt)? First, we considered the time bin width as the population interspike interval $\Delta t = \langle ISI \rangle$. The minimum sampling size we employed was $n = 30$ so that power laws still satisfied Akaike's Information Criterion. The agreement of both sides of the scaling law enhances with growing sampling fraction (**Figures 4A,B**). However, $\langle ISI \rangle$ decreases with the number of neurons sampled (inset of **Figure 4B**). When the natural bin decreases below 1 ms (the time step of the model), the analysis no longer makes sense. As n increases, the relation between τ and τ_t converges to the apparent critical scaling that fits experimental results (**Figure 4B**).

To check whether we could recover the MF-DP real exponents from their apparent values as n increases, we chose the smallest time bin possible, $\Delta t = 1$ ms. We observed that for a small fraction of sampled units [$n/N \sim \mathcal{O}(10^{-2})$] the scaling relation (Equation 4) is satisfied (**Figure 4C**) with apparent critical exponents that match the experimental results (**Figure 4D**). In fact, the scaling relation in Equation 4 is satisfied for a range of *CV* values (inset of **Figure 4C**). Increasing the sampling further [$n/N \sim \mathcal{O}(10^{-1})$], the scaling relation ceases to be satisfied (**Figure 4C**) and the avalanche exponents get separated from the experimental scaling relation (**Figure 4D**). But as $n \to N$, the MF-DP scaling relation is recovered (as it should).

We have further tested the robustness of these findings by varying the time bin width used to defined avalanches ($0.75 \leq \Delta t/\langle ISI \rangle \leq 2$). We observed that experiments and model have very similar behavior (**Supplementary Figures 4A,B**). Furthermore, both model

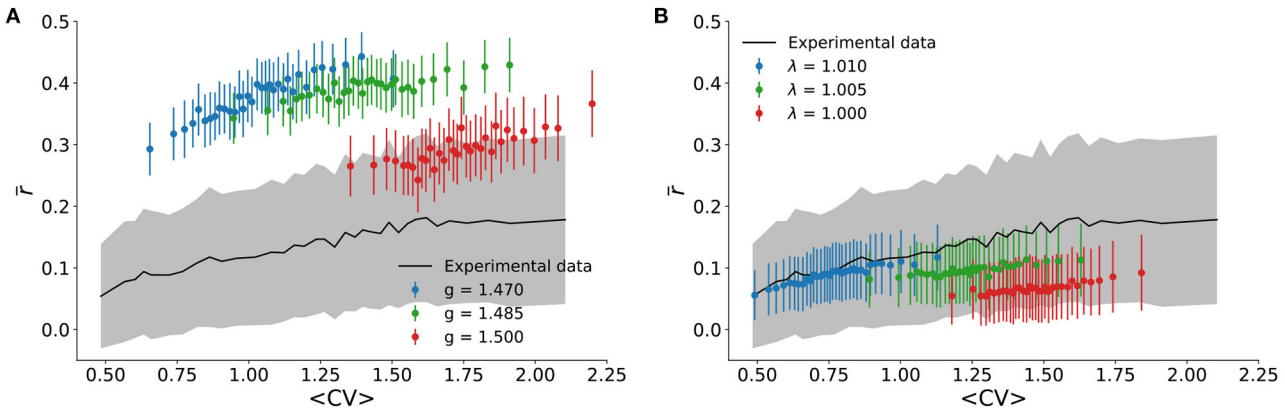

FIGURE 5 | Correlation structure. The experimental pairwise correlation of firing rates is shown as a function of $\langle CV \rangle$ (black line is the average $\bar{r}$, while gray shading is the standard deviation of the distribution). It is compared with theoretical results for **(A)** the spiking neuronal network with $n = 100$ sampled neurons, and **(B)** the cellular automaton model with $n = 500$ sampled sites.

and experiments are virtually insensitive to the width of the CV window w (**Supplementary Figures 4C,D**). Finally, we also tested whether allowing for small changes of g around g_c with $n = N$ would lead to apparent exponents compatible with experimental data. We observed in this case that the exponents and the scaling relation cluster around MF-DP values (**Supplementary Figure 5**), reinforcing the idea that subsampling is a necessary ingredient for the model to reproduce the experimental results.

3.4. Pairwise Correlation Structure

We also tested the correlation structure of the model and compared it to experimental results. In the literature on cortical states, asynchronous states are associated with pairwise spiking correlations $r^{(k,l)}$ which are distributed around an average $\bar{r}$ close to zero, whereas synchronous states have positive average (Harris and Thiele, 2011). This was quantified in **Figure 5A**, where $\bar{r}$ is shown to increase monotonically with CV. For the experimental data, $\bar{r}$ reaches zero within the standard deviation of the distribution for sufficiently small CV.

Compared with the experimental results, the spiking model with inhibition generally overestimates $\bar{r}$ (**Figure 5A**). This could be due to its all-to-all connectivity. The cellular automaton model on a random graph yields quantitatively better results (**Figure 5B**). In either case, we observed again that, just like for the scaling relation (**Figure 3**), the correlation structure of the experimental data was relatively well-reproduced by very small deviations around critical parameter values.

4. DISCUSSION AND CONCLUSIONS

We revisited the results recently published by Fontenele et al. (2019) by repeating their analyses on new experimental data and two different models. To test the idea that the urethanized cortex hovers around a critical point, we stratified the avalanche analyses across cortical states. For the new experimental data, we verified that the scaling relation combining the three exponents (Equation 4) was indeed satisfied at an intermediate value CV_*, away from the synchronous and asynchronous extremes. At this critical value, the three exponents differ from those of the MF-DP universality class, thus confirming previous findings (Fontenele et al., 2019).

We addressed whether the exponents of the MF-DP universality class and those observed experimentally could be reconciled, despite their disagreement. In other words, we returned to the question: if the brain is critical, what is the phase transition? Do the experimental results presented here and in Fontenele et al. (2019) refute branching-process-like models as explanations?

To answer these questions, we relied on two models: an E/I spiking neuronal network in an all-to-all graph; and a probabilistic excitable cellular automaton in a random graph. Despite the simplicity and limitations of these models (which we discuss below), they have a fundamental strength that led us to choose them: they are very well-understood analytically. In both cases, mean-field calculations agree extremely well with simulations, so that we are safe in locating the critical points of these models (Kinouchi and Copelli, 2006; Girardi-Schappo et al., 2020). This is very important for our purposes, because it allows us to test whether the models can reproduce the data, and if so, how close to the critical point they have to be. Besides, their universality class is also well-determined: the exponents shown in **Figures 1B–D** are those of with MF-DP.

The crucial point is that the results in **Figure 1** are based on avalanches which are measured by taking into account *all* simulated units of the model, a methodological privilege that is not available to an experimentalist measuring spiking activity of a real brain with current technologies. In fact, a considerable amount of work has shown that subsampling can have a drastic effect on the avalanche statistics of models (Priesemann et al., 2009, 2014; Ribeiro et al., 2010, 2014; Girardi-Schappo et al., 2013; Levina and Priesemann, 2017; Wilting and Priesemann,

2019). Therefore, here we set out to test whether MF-DP models could yield results nominally incompatible with that universality class if they were analyzed under the same conditions as the data, i.e., with *CV* parsing and severe subsampling.

Both subsampled models quantitatively and qualitatively reproduced the central features of the experimental results. The scaling relation (Equation 4) was satisfied at an intermediate value $\langle CV \rangle_*$, with the correct qualitative behavior of both sides of the equation: $1/(\sigma \nu z)$ increasing with *CV*, while $(\tau_t - 1)/(\tau - 1)$ decreasing (see **Figures 3A,C** and **Supplementary Figure 3D**). In fact, the values of $\langle CV \rangle_*$, and those of the apparent exponents of the subsampled MF-DP models, τ_*, τ_{t*}, and $1/(\sigma \nu z)_*$, agreed with the experiments within error bars. Moreover, even away from the point $\langle CV \rangle_*$ where Equation (4) was satisfied, the spread of the exponents τ and τ_t of the subsampled models followed an almost linear relation (**Figure 3D** and **Supplementary Figure 3E**), in good agreement with not only our experimental results (**Figure 3B**), but also with those of other experimental setups (Fontenele et al., 2019). When we sampled from the whole network, we recovered the true critical exponents of the model (**Figures 4C,D**), confirming that spatial subsampling and temporal binning are sufficient ingredients to push its critical exponents toward apparent values, hiding its true critical phase transition.

Knowing analytically the critical points of the models, we checked in which parameter range they successfully reproduced the experimental results. As it turns out, the scaling relation and the linear of spread of exponents are reproduced by the subsampled models only if they are tuned within a narrow interval around their critical points. The subsampled model still fits well the urethanized cortex data up to 3% off criticality, slightly biased toward the supercritical state. Note that if the model becomes too subcritical, the size and duration exponents fall very far apart from the experimentally observed linear relation (**Figure 3D**). If it is too supercritical, there are not enough silent windows to distinguish avalanches in the first place. Whether or not the fluctuations around the critical point of the model could be compatible with a scenario of self-organized-quasi-criticality (Buendía et al., 2020; Kinouchi et al., 2020) remains to be investigated.

Despite the small variation of the model E/I levels controlled by g, the variation of *CV* is large enough to essentially cover the range of experimentally observed values (**Figures 2A,D** and **Supplementary Figure 3B**). This is due in part to the fact that we evaluated *CV* within finite windows of width $w = 10$ s. In **Supplementary Figure 6** we show that, for the model, the standard deviation of *CV* is a decreasing function of the time used to estimate, all the way up to $w = 500$ s. For the data, on the other hand, a better resolution for *CV* can be obtained by increasing w up to about 20 s, above which the standard deviation no longer decreases. It is important to note, however, that in experiments one needs to reach a good trade-off between a better statistical definition of *CV* and not mixing different cortical states due to the non-stationarity characteristic of the urethane preparation (as depicted in **Figure 2A**).

Perhaps even more important than the range of *CV* values obtained around the critical point of the models is the richness of the experimentally observed temporal evolution of *CV* (**Figure 2A**). The model needs to be fine tuned to different values of E/I levels in order to get different average values of *CV*. This is one of the limitations of the models which would be worth addressing next. One possibility would be to replace static models (i.e., with fixed control parameters) with ones with plasticity, in which coupling parameters are themselves dynamic variables and the critical point is obtained via quasicritical self-organization (Costa et al., 2015, 2017; Brochini et al., 2016; Campos et al., 2017; Kinouchi et al., 2019, 2020; Buendía et al., 2020; Girardi-Schappo et al., 2020).

Moreover, both models failed to capture the steep drop of $(\tau_t - 1)/(\tau - 1)$ as a function of *CV* that is observed in the experimental data above CV_* (compare **Figure 3A** with **Figure 3C** and **Supplementary Figure 3D**). This region corresponds to high *CV*, where the models, which are entering their subcritical regimes, seem unable to quantitatively account for the statistics of the increasingly bursty behavior of the data. Whether different models (or a refinement of the ones presented here) could reproduce these results more accurately remains to be studied.

Another limitation of the models is their simple topology, which in future works could be improved to come closer to cortical circuitry (Potjans and Diesmann, 2014). This would likely come at the cost of foregoing analytical results to start with, thus augmenting the computational efforts involved. But it would certainly allow to probe the robustness of the results presented here against more realistic topologies. On the other hand, there is quantitative agreement between the apparent exponents of both models (each having a different topology) with the experimental exponents. This suggests that at the scale of the present phenomenology, the average topology should play a minor role.

It is also interesting to compare the performance of the two models in reproducing the experimental results. The cellular automaton model has the advantage of simplicity, corresponding essentially to a minimal model in the MF-DP universality class. The E/I balanced network, on the other hand, has the advantage of incorporating inhibition, which is an important ingredient for modeling cortical circuitry. As shown in detail in **Supplementary Figure 4**, the cellular automaton results generally agreed with experimental results, but those of the E/I balanced network had a consistently better agreement. The only exception in this trend was the correlation structure shown in **Figure 5**, in which the cellular automaton model fared better than the E/I balanced network. In this sense, the models complement each other.

Our model predicts that, for a fixed bin size, increasing the sampling of the data would eventually lead exponents to coincide with those of MF-DP (**Figure 4C**). However, below a sufficiently high sampling [see, e.g. $n/N \sim \mathcal{O}(10^{-1})$ in **Figure 4C**], the scaling relation would not be satisfied for any *CV* even if the system were critical (as the model is). An experimental verification of these predictions would require the recording of a much larger number of neurons than we have presented here.

The fact that subsampling seems to be a crucial ingredient for explaining the data is a double-edged sword. On the one hand, it allowed us here to reconcile MF-DP models with results for spiking data in the anesthetized rat cortex. On the other hand, note that even measurements which should in principle be less prone to subsampling, such as LFP results in the visual cortex of the turtle (Shew et al., 2015), still fall on the same scaling line of τ vs. τ_t (**Figure 3B**) as those of spiking data (Fontenele et al., 2019), both having apparent non-MF-DP critical exponents (note, however, that better controlled LFP results in Miller et al., 2019 are in line with MF-DP). This issue is not addressed by the current model and deserves further investigation. Our results point only to MF-DP models as sufficient, not as necessary, to explain the observed phenomenology. So it is at least conceivable that different models with different phase transitions (di Santo et al., 2018; Dalla Porta and Copelli, 2019; Pinto and Copelli, 2019) could also yield non-trivial true or apparent exponents compatible with the data, even without subsampling (Fontenele et al., 2019).

Finally, our simulation results underscore the methodological vulnerabilities of assessing criticality exclusively via avalanche analysis. Not only are MLE power-law fits sensitive to parameters, but even a more stringent analysis, requiring the crackling noise scaling relation, leads to non-trivial apparent exponents which are an artifact of subsampling, as we have shown. Therefore, the development of additional figures of merit, such as control and order parameters, susceptibilities and others (Tagliazucchi et al., 2012; Yang et al., 2012; Yu et al., 2013; Mora et al., 2015; Tkačik et al., 2015; Girardi-Schappo et al., 2016; Girardi-Schappo and Tragtenberg, 2018; Lotfi et al., 2020), remains a very important line of research to strengthen studies of brain criticality.

DATA AVAILABILITY STATEMENT

The raw data supporting the conclusions of this article will be made available by the authors, without undue reservation.

ETHICS STATEMENT

Housing, surgical and recording procedures were in strict accordance with the CONCEA-MCTI, and was approved by the Federal University of Pernambuco (UFPE) Committee for Ethics in Animal Experimentation (23076.030111/2013-95, 12/2015 and 20/2020).

AUTHOR CONTRIBUTIONS

TC, MG-S, PC, and MC designed the study, interpreted the results, and wrote the manuscript. TC ran the simulations. TC and AF analyzed the data. TF, LA, TS, and NV obtained the experimental data. All authors read and approved the submitted version.

FUNDING

The authors acknowledge Fundação de Amparo à Ciência e Tecnologia de Pernambuco (FACEPE) (grants APQ-0642-1.05/18, APQ-0826-1.05/15, and BFD-0013-1.05/20), Universidade Federal de Pernambuco, Conselho Nacional de Desenvolvimento Científico e Tecnológico (CNPq, grants 141579/2017-0, 425329/2018-6, and 301744/2018-1), Coordenação de Aperfeiçoamento de Pessoal de Nível Superior (CAPES), and FAPESP (grant 2018/09150-9). This paper was produced as part of the activities of Research, Innovation and Dissemination Center for Neuromathematics (grant No. 2013/07699-0, S. Paulo Research Foundation–FAPESP).

ACKNOWLEDGMENTS

We thank Osame Kinouchi for discussions and a critical read of this manuscript.

SUPPLEMENTARY MATERIAL

The Supplementary Material for this article can be found online at: https://www.frontiersin.org/articles/10.3389/fncir.2020.576727/full#supplementary-material

REFERENCES

Akaike, H. (1975). A new look at the statistical model identification. *IEEE Trans. Autom. Control.* 19, 716–723. doi: 10.1109/TAC.1974.1100705

Beggs, J. M. (2007). The criticality hypothesis: how local cortical networks might optimize information processing. *Philos. Trans. R. Soc. A* 366, 329–343. doi: 10.1098/rsta.2007.2092

Beggs, J. M., and Plenz, D. (2003). Neuronal avalanches in neocortical circuits. *J. Neurosci.* 23, 11167–11177. doi: 10.1523/JNEUROSCI.23-35-11167.2003

Bellay, T., Klaus, A., Seshadri, S., and Plenz, D. (2015). Irregular spiking of pyramidal neurons organizes as scale-invariant neuronal avalanches in the awake state. *eLife* 4:e07224. doi: 10.7554/eLife.07224

Binney, J. J., Dowrick, N. J., Fisher, A. J., and Newman, M. E. J. (1992). *The Theory of Critical Phenomena: An Introduction to the Renormalization Group*. Oxford: Oxford University Press.

Brochini, L., Costa, A. A., Abadi, M., Roque, A. C., Stolfi, J., and Kinouchi, O. (2016). Phase transitions and self-organized criticality in networks of stochastic spiking neurons. *Sci. Rep.* 6:35831. doi: 10.1038/srep35831

Buendía, V., di Santo, S., Bonachela, J. A., and Muñoz, M. A. (2020). Feedback mechanisms for self-organization to the edge of a phase transition. *Front. Phys.* 8:333. doi: 10.3389/fphy.2020.00333

Campos, J. G. F., Costa, A. A., Copelli, M., and Kinouchi, O. (2017). Correlations induced by depressing synapses in critically self-organized networks with quenched dynamics. *Phys. Rev. E* 95:042303. doi: 10.1103/PhysRevE.95.042303

Chialvo, D. R. (2010). Emergent complex neural dynamics. *Nat. Phys.* 6, 744–750. doi: 10.1038/nphys1803

Clement, E. A., Richard, A., Thwaites, M., Ailon, J., Peters, S., and Dickson, C. T. (2008). Cyclic and sleep-like spontaneous alternations of brain state under urethane anaesthesia. *PLoS ONE* 3:e2004. doi: 10.1371/journal.pone.0002004

Costa, A. A., Brochini, L., and Kinouchi, O. (2017). Self-organized supercriticality and oscillations in networks of stochastic spiking neurons. *Entropy* 19:399. doi: 10.3390/e19080399

Costa, A. A., Copelli, M., and Kinouchi, O. (2015). Can dynamical synapses produce true self-organized criticality? *J. Stat. Mech. Theory Exp.* 2015:P06004. doi: 10.1088/1742-5468/2015/06/P06004

Curto, C., Sakata, S., Marguet, S., Itskov, V., and Harris, K. D. (2009). A simple model of cortical dynamics explains variability and state dependence of sensory responses in urethane-anesthetized auditory cortex. *J. Neurosci.* 29, 10600–10612. doi: 10.1523/JNEUROSCI.2053-09.2009

Dalla Porta, L., and Copelli, M. (2019). Modeling neuronal avalanches and long-range temporal correlations at the emergence of collective oscillations: continuously varying exponents mimic M/EEG results. *PLoS Comput. Biol.* 15:e1006924. doi: 10.1371/journal.pcbi.1006924

de Vasconcelos, N. A. P., Soares-Cunha, C., Rodrigues, A. J., Ribeiro, S., and Sousa, N. (2017). Coupled variability in primary sensory areas and the hippocampus during spontaneous activity. *Sci. Rep.* 7:46077. doi: 10.1038/srep46077

Deluca, A., and Corral, Á. (2013). Fitting and goodness-of-fit test of non-truncated and truncated power-law distributions. *Acta Geophys.* 61, 1351–1394. doi: 10.2478/s11600-013-0154-9

di Santo, S., Villegas, P., Burioni, R., and Muñoz, M. A. (2018). Landau-Ginzburg theory of cortex dynamics: scale-free avalanches emerge at the edge of synchronization. *Proc. Natl. Acad. Sci. U.S.A.* 115, E1356–E1365. doi: 10.1073/pnas.1712989115

Fontenele, A. J., de Vasconcelos, N. A. P., Feliciano, T., Aguiar, L. A. A., Soares-Cunha, C., Coimbra, B., et al. (2019). Criticality between cortical states. *Phys. Rev. Lett.* 122:208101. doi: 10.1103/PhysRevLett.122.208101

Friedman, N., Ito, S., Brinkman, B. A. W., Shimono, M., DeVille, R. E. L., Dahmen, K. A., et al. (2012). Universal critical dynamics in high resolution neuronal avalanche data. *Phys. Rev. Lett.* 108:208102. doi: 10.1103/PhysRevLett.108.208102

Gervasoni, D., Lin, S., Ribeiro, S., Soares, E. S., Pantoja, J., and Nicolelis, M. A. L. (2004). Global forebrain dynamics predict rat behavioral states and their transitions. *J. Neurosci.* 24, 11137–11147. doi: 10.1523/JNEUROSCI.3524-04.2004

Girardi-Schappo, M., Bortolotto, G. S., Gonsalves, J. J., Pinto, L. T., and Tragtenberg, M. H. R. (2016). Griffiths phase and long-range correlations in a biologically motivated visual cortex model. *Sci. Rep.* 6:29561. doi: 10.1038/srep29561

Girardi-Schappo, M., Brochini, L., Costa, A. A., Carvalho, T. T. A., and Kinouchi, O. (2020). Synaptic balance due to homeostatically self-organized quasicritical dynamics. *Phys. Rev. Res.* 2:012042(R). doi: 10.1103/PhysRevResearch.2.012042

Girardi-Schappo, M., Kinouchi, O., and Tragtenberg, M. H. R. (2013). Critical avalanches and subsampling in map-based neural networks coupled with noisy synapses. *Phys. Rev. E* 88:024701. doi: 10.1103/PhysRevE.88.024701

Girardi-Schappo, M., and Tragtenberg, M. H. R. (2018). Measuring neuronal avalanches in disordered systems with absorbing states. *Phys. Rev. E* 97:042415. doi: 10.1103/PhysRevE.97.042415

Grassberger, P. (1982). On phase transitions in schlögl's second model. *Z. Phys. B Cond. Matter* 47, 365–374. doi: 10.1007/BF01313803

Harris, K. D., and Thiele, A. (2011). Cortical state and attention. *Nat. Rev. Neurosci.* 12:509. doi: 10.1038/nrn3084

Harris, T. E. (1963). *The Theory of Branching Processes*. Berlin: Springer.

Janssen, H. K. (1981). On the nonequilibrium phase transition in reaction-diffusion systems with an absorbing stationary state. *Z. Phys. B Cond. Matter* 42, 151–154. doi: 10.1007/BF01319549

Kinouchi, O., Brochini, L., Costa, A. A., Campos, J. G. F., and Copelli, M. (2019). Stochastic oscillations and dragon king avalanches in self-organized quasi-critical systems. *Sci. Rep.* 9:3874. doi: 10.1038/s41598-019-40473-1

Kinouchi, O., and Copelli, M. (2006). Optimal dynamical range of excitable networks at criticality. *Nat. Phys.* 2:348. doi: 10.1038/nphys289

Kinouchi, O., Pazzini, R., and Copelli, M. (2020). Mechanisms of self-organized quasicriticality in neuronal networks models. *Front. Phys.* 8:583212. doi: 10.3389/fphy.2020.583213

Levina, A., and Priesemann, V. (2017). Subsampling scaling. *Nat. Commun.* 8:15140. doi: 10.1038/ncomms15140

Lotfi, N., Fontenele, A. J., Feliciano, T., Aguiar, L. A., de Vasconcelos, N. A., Soares-Cunha, C., et al. (2020). Signatures of brain criticality unveiled by maximum entropy analysis across cortical states. *Phys. Rev. E* 102:012408. doi: 10.1103/PhysRevE.102.012408

Ma, Z., Turrigiano, G. G., Wessel, R., and Hengen, K. B. (2019). Cortical circuit dynamics are homeostatically tuned to criticality *in vivo*. *Neuron* 104, 655–664. doi: 10.1016/j.neuron.2019.08.031

Marro, J., and Dickman, R. (1999). *Nonequilibrium Phase Transition in Lattice Models*. Cambridge: Cambridge University Press.

Marshall, N., Timme, N. M., Bennett, N., Ripp, M., Lautzenhiser, E., and Beggs, J. M. (2016). Analysis of power laws, shape collapses, and neural complexity: new techniques and MATLAB support via the NCC toolbox. *Front. Physiol.* 7:250. doi: 10.3389/fphys.2016.00250

Miller, S. R., Yu, S., and Plenz, D. (2019). The scale-invariant, temporal profile of neuronal avalanches in relation to cortical γ-oscillations. *Sci. Rep.* 9:16403. doi: 10.1038/s41598-019-52326-y

Mochol, G., Hermoso-Mendizabal, A., Sakata, S., Harris, K. D., and De la Rocha, J. (2015). Stochastic transitions into silence cause noise correlations in cortical circuits. *Proc. Natl. Acad. Sci. U.S.A.* 112, 3529–3534. doi: 10.1073/pnas.1410509112

Mora, T., Deny, S., and Marre, O. (2015). Dynamical criticality in the collective activity of a population of retinal neurons. *Phys. Rev. Lett.* 114:078105. doi: 10.1103/PhysRevLett.114.078105

Muñoz, M. A., Dickman, R., Vespignani, A., and Zapperi, S. (1999). Avalanche and spreading exponents in systems with absorbing states. *Phys. Rev. E* 59, 6175–6179. doi: 10.1103/PhysRevE.59.6175

Palva, J. M., Zhigalov, A., Hirvonen, J., Korhonen, O., Linkenkaer-Hansen, K., and Palva, S. (2013). Neuronal long-range temporal correlations and avalanche dynamics are correlated with behavioral scaling laws. *Proc. Natl. Acad. Sci. U.S.A.* 110, 3585–3590. doi: 10.1073/pnas.1216855110

Paxinos, G., and Watson, C. (2007). *The Rat Brain in Stereotaxic Coordinates: Hard Cover Edition*. Amsterdam: Elsevier Science.

Pinto, I. L. D., and Copelli, M. (2019). Oscillations and collective excitability in a model of stochastic neurons under excitatory and inhibitory coupling. *Phys. Rev. E* 100:062416. doi: 10.1103/PhysRevE.100.062416

Plenz, D., and Niebur, E. (Eds.). (2014). *Criticality in Neural Systems*. Weinheim: Wiley.

Ponce-Alvarez, A., Jouary, A., Privat, M., Deco, G., and Sumbre, G. (2018). Whole-brain neuronal activity displays crackling noise dynamics. *Neuron* 100, 1446–1459. doi: 10.1016/j.neuron.2018.10.045

Potjans, T. C., and Diesmann, M. (2014). The cell-type specific cortical microcircuit: relating structure and activity in a full-scale spiking network model. *Cereb. Cortex* 24, 785–806. doi: 10.1093/cercor/bhs358

Priesemann, V., Munk, M. H. J., and Wibral, M. (2009). Subsampling effects in neuronal avalanche distributions recorded *in vivo*. *BMC Neurosci.* 10:40. doi: 10.1186/1471-2202-10-40

Priesemann, V., Wibral, M., Valderrama, M., Pröpper, R., Le Van Quyen, M., Geisel, T., et al. (2014). Spike avalanches *in vivo* suggest a driven, slightly subcritical brain state. *Front. Syst. Neurosci.* 8:108. doi: 10.3389/fnsys.2014.00108

Renart, A., de la Rocha, J., Bartho, P., Hollender, L., Parga, N., Reyes, A., et al. (2010). The asynchronous state in cortical circuits. *Science* 327, 587–590. doi: 10.1126/science.1179850

Ribeiro, T. L., Copelli, M., Caixeta, F., Belchior, H., Chialvo, D. R., Nicolelis, M. A. L., et al. (2010). Spike avalanches exhibit universal dynamics across the sleep-wake cycle. *PLoS ONE* 5:e14129. doi: 10.1371/journal.pone.0014129

Ribeiro, T. L., Ribeiro, S., Belchior, H., Caixeta, F., and Copelli, M. (2014). Undersampled critical branching processes on small-world and random networks fail to reproduce the statistics of spike avalanches. *PLoS ONE* 9:e94992. doi: 10.1371/journal.pone.0094992

Rossant, C., Kadir, S. N., Goodman, D. F. M., Schulman, J., Hunter, M. L. D., Saleem, A. B., et al. (2016). Spike sorting for large, dense electrode arrays. *Nat. Neurosci.* 19:634. doi: 10.1038/nn.4268

Sakata, S., and Harris, K. D. (2009). Laminar structure of spontaneous and sensory-evoked population activity in auditory cortex. *Neuron* 64, 404–418. doi: 10.1016/j.neuron.2009.09.020

Scott, G., Fagerholm, E. D., Mutoh, H., Leech, R., Sharp, D. J., Shew, W. L., et al. (2014). Voltage imaging of waking mouse cortex reveals emergence of critical neuronal dynamics. *J. Neurosci.* 34, 16611–16620. doi: 10.1523/JNEUROSCI.3474-14.2014

Sethna, J. P., Dahmen, K. A., and Myers, C. R. (2001). Crackling noise. *Nature* 410, 242–250. doi: 10.1038/35065675

Shadlen, M. N., and Newsome, W. T. (1998). The variable discharge of cortical neurons: implications for connectivity, computation, and information

coding. *J. Neurosci.* 18, 3870–3896. doi: 10.1523/JNEUROSCI.18-10-03870.1998

Shew, W. L., Clawson, W. P., Pobst, J., Karimipanah, Y., Wright, N. C., and Wessel, R. (2015). Adaptation to sensory input tunes visual cortex to criticality. *Nat. Phys.* 11, 659–663. doi: 10.1038/nphys3370

Shew, W. L., and Plenz, D. (2013). The functional benefits of criticality in the cortex. *Neuroscientist* 19, 88–100. doi: 10.1177/1073858412445487

Shew, W. L., Yang, H., Petermann, T., Roy, R., and Plenz, D. (2009). Neuronal avalanches imply maximum dynamic range in cortical networks at criticality. *J. Neurosci.* 29, 15595–15600. doi: 10.1523/JNEUROSCI.3864-09.2009

Siegle, J. H., López, A. C., Patel, Y. A., Abramov, K., Ohayon, S., and Voigts, J. (2017). Open Ephys: an open-source, plugin-based platform for multichannel electrophysiology. *J. Neural Eng.* 14:045003. doi: 10.1088/1741-2552/aa5eea

Somogyi, P., Tamás, G., Lujan, R., and Buhl, E. H. (1998). Salient features of synaptic organisation in the cerebral cortex. *Brain Res. Rev.* 26, 113–135. doi: 10.1016/S0165-0173(97)00061-1

Tagliazucchi, E., Balenzuela, P., Fraiman, D., and Chialvo, D. R. (2012). Criticality in large-scale brain fMRI dynamics unveiled by a novel point process analysis. *Front. Physiol.* 3:15. doi: 10.3389/fphys.2012.00015

Tkačik, G., Mora, T., Marre, O., Amodei, D., Palmer, S. E., Berry, M. J., et al. (2015). Thermodynamics and signatures of criticality in a network of neurons. *Proc. Natl. Acad. Sci. U.S.A.* 112, 11508–11513. doi: 10.1073/pnas.1514188112

Tomen, N., Herrmann, M. J., and Ernst, U. (2019). *The Functional Role of Critical Dynamics in Neural Systems*. Cham: Springer.

Touboul, J., and Destexhe, A. (2017). Power-law statistics and universal scaling in the absence of criticality. *Phys. Rev. E* 95:012413. doi: 10.1103/PhysRevE.95.012413

Wilting, J., and Priesemann, V. (2019). Between perfectly critical and fully irregular: a reverberating model captures and predicts cortical spike propagation. *Cereb. Cortex* 29, 2759–2770. doi: 10.1093/cercor/bhz049

Yang, H., Shew, W. L., Roy, R., and Plenz, D. (2012). Maximal variability of phase synchrony in cortical networks with neuronal avalanches. *J. Neurosci.* 32, 1061–1072. doi: 10.1523/JNEUROSCI.2771-11.2012

Yu, S., Klaus, A., Yang, H., and Plenz, D. (2014). Scale-invariant neuronal avalanche dynamics and the cut-off in size distributions. *PLoS ONE* 9:e99761. doi: 10.1371/journal.pone.0099761

Yu, S., Ribeiro, T. L., Meisel, C., Chou, S., Mitz, A., Saunders, R., et al. (2017). Maintained avalanche dynamics during task-induced changes of neuronal activity in nonhuman primates. *eLife* 6:e27119. doi: 10.7554/eLife.27119

Yu, S., Yang, H., Shriki, O., and Plenz, D. (2013). Universal organization of resting brain activity at the thermodynamic critical point. *Front. Syst. Neurosci.* 7:42. doi: 10.3389/fnsys.2013.00042

Zhigalov, A., Arnulfo, G., Nobili, L., Palva, S., and Palva, J. M. (2015). Relationship of fast- and slow-timescale neuronal dynamics in human MEG and SEEG. *J. Neurosci.* 35, 5385–5396. doi: 10.1523/JNEUROSCI.4880-14.2015

Conflict of Interest: The authors declare that the research was conducted in the absence of any commercial or financial relationships that could be construed as a potential conflict of interest.

frontiers in Neural Circuits

ORIGINAL RESEARCH
published: 22 January 2021
doi: 10.3389/fncir.2020.620052

Selective Participation of Single Cortical Neurons in Neuronal Avalanches

*Timothy Bellay[1,2†], Woodrow L. Shew[1†‡], Shan Yu[1‡], Jessica J. Falco-Walter[1‡] and Dietmar Plenz[1]**

[1]Section on Critical Brain Dynamics, National Institute of Mental Health, National Institutes of Health, Bethesda, MD, United States, [2]Department of Neuroscience, Brown University, Providence, RI, United States

OPEN ACCESS

Edited by:
Ioanna Sandvig,
Norwegian University of Science and Technology, Norway

Reviewed by:
Maximiliano Jose Nigro,
Norwegian University of Science and Technology, Norway
Yoshikazu Isomura,
Tokyo Medical and Dental University, Japan

***Correspondence:**
Dietmar Plenz
plenzd@mail.nih.gov

[†]These authors have contributed equally to this work

[‡]**Present address:**
Woodrow L. Shew,
Department of Physics, University of Arkansas, Fayetteville, AR, United States
Shan Yu,
Brainnetome Center, Institute of Automation, Chinese Academy of Sciences, Beijing, China
Jessica J. Falco-Walter,
Department of Neurology, Stanford University, Palo Alto, CA, United States

Received: 21 October 2020
Accepted: 21 December 2020
Published: 22 January 2021

Citation:
Bellay T, Shew WL, Yu S, Falco-Walter JJ and Plenz D (2021) Selective Participation of Single Cortical Neurons in Neuronal Avalanches. Front. Neural Circuits 14:620052. doi: 10.3389/fncir.2020.620052

Neuronal avalanches are scale-invariant neuronal population activity patterns in the cortex that emerge *in vivo* in the awake state and *in vitro* during balanced excitation and inhibition. Theory and experiments suggest that avalanches indicate a state of cortex that improves numerous aspects of information processing by allowing for the transient and selective formation of local as well as system-wide spanning neuronal groups. If avalanches are indeed involved with information processing, one might expect that single neurons would participate in avalanche patterns selectively. Alternatively, all neurons could participate proportionally to their own activity in each avalanche as would be expected for a population rate code. Distinguishing these hypotheses, however, has been difficult as robust avalanche analysis requires technically challenging measures of their intricate organization in space and time at the population level, while also recording sub- or suprathreshold activity from individual neurons with high temporal resolution. Here, we identify repeated avalanches in the ongoing local field potential (LFP) measured with high-density microelectrode arrays in the cortex of awake nonhuman primates and in acute cortex slices from young and adult rats. We studied extracellular unit firing *in vivo* and intracellular responses of pyramidal neurons *in vitro*. We found that single neurons participate selectively in specific LFP-based avalanche patterns. Furthermore, we show *in vitro* that manipulating the balance of excitation and inhibition abolishes this selectivity. Our results support the view that avalanches represent the selective, scale-invariant formation of neuronal groups in line with the idea of Hebbian cell assemblies underlying cortical information processing.

Keywords: nonhuman primate, rat, prefrontal cortex, primary motor cortex, high-density microelectrode array, local field potential, whole-cell patch recording, cell assemblies

INTRODUCTION

Understanding how the collective dynamics of the cortex emerges from neuronal interactions is a fundamental challenge in neuroscience. Given the limitations in accurately recording from many neurons simultaneously, this challenge is typically approached by studying how the activity of single neurons correlates with the dynamics of the network. Of particular interest in this context has been the discovery of "neuronal avalanches" in spontaneous (Beggs and Plenz, 2003; Petermann et al., 2009; Miller et al., 2019) and evoked cortical activity (Shew et al., 2015; Yu et al., 2017) in

which the collective dynamics of the cortex has been mapped using the local field potential (LFP). More specifically, it has been reliably found for slice cultures, acute slices, rodents, and nonhuman primates that the spatial and temporal spread of transient and fast deflections in the cortical LFP, when tracked using high-density microelectrode arrays (MEAs), obeys a power-law relationship in the size of LFP patterns, which is the hallmark of avalanches (Yu et al., 2014) and is in line with expectations for critical dynamics (for review see Plenz and Thiagarajan, 2007; Chialvo, 2010; Mora and Bialek, 2011; Plenz, 2012; Hesse and Gross, 2014; Marković and Gros, 2014; Muñoz, 2017).

The power law in avalanche size demonstrates that large avalanches, i.e., those that engage a large part of the cortical area monitored, are significantly more common than expected by chance (Yu et al., 2014). Hierarchical clustering *in vitro* further demonstrates that large avalanches exhibit diverse, yet distinct spatial patterns, i.e., families (Beggs and Plenz, 2004; Stewart and Plenz, 2006). This organization then raises the question of whether the activity of single neurons correlates selective with some avalanche families. Using 2-photon imaging, the spontaneous and evoked firing in groups of cortical neurons have been found to organize as scale-invariant avalanches (Bellay et al., 2015; Karimipanah et al., 2017; Bowen et al., 2019; Ribeiro et al., 2020). Similarly, extracellular unit recordings in the rodent during wakefulness, exploration, and sleep identified state-specific and repeated spike avalanche patterns (Ribeiro et al., 2016). Yet, it is currently not known how supra- and subthreshold activity of individual neurons relate to large and diverse avalanches encountered in the LFP.

Theory and experiment suggest that neuronal avalanches indicate a critical state of cortex at which numerous aspects of information processing are maximized such as dynamic range (Kinouchi and Copelli, 2006; Shew et al., 2009; Gautam et al., 2015; Shriki and Yellin, 2016; Clawson et al., 2017; Gollo, 2017) and information capacity (Shew et al., 2011; Yang et al., 2012; Fagerholm et al., 2016; Agrawal et al., 2018). Simulations suggest avalanche dynamics confer benefits as to how networks learn new input-output associations while staying adaptive (de Arcangelis et al., 2006; de Arcangelis and Herrmann, 2010; Rybarsch and Bornholdt, 2014; Stepp et al., 2015; Del Papa et al., 2017; Hernandez-Urbina and Herrmann, 2017; Michiels van Kessenich et al., 2018; Skilling et al., 2019; Zeng et al., 2019). An understanding of these beneficial aspects of avalanche dynamics concerning network properties requires insight into the cellular composition of avalanche activity.

Here, we studied the relationship between avalanche and single-neuron activity by comparing multi-site LFP recordings with simultaneously measured extra- and intracellular activity of single neurons. More specifically, when a spatial pattern of the LFP was found to repeat during a recording, we searched for reliable recruitment of single neurons during each repeated occurrence. First, we studied the extracellular unit activity and LFP signals recorded during ongoing activity from layers 2/3 of the premotor cortex in awake nonhuman primates. Since it is not feasible to separate the effects of local and distant sources of the LFP in awake animals, we next carried out complementary studies in acute slices of the rat cortex, for which the origins of the LFP signals are intrinsic to the cortex. For the slice studies, we combined intracellular whole-cell patch recordings of pyramidal neurons in layer 2/3 with multi-site LFP recordings. In line with our hypothesis, both *in vivo* and *in vitro*, we found that neurons participate selectively and reliably in particular avalanche patterns. We further demonstrate that this selective relationship between neurons and avalanches requires intact synaptic inhibition. Our findings suggest that the diversity of neuronal avalanches in the cortex emerges from diverse and distinct neuronal groups at the balance of excitation and inhibition.

MATERIALS AND METHODS

Nonhuman Primate Recordings

Two adult nonhuman primates (*Macaca mulatta*), one female (monkey 1; Victoria) and one male (monkey 2; Noma) were studied. High-density MEAs (96 electrodes, 10 × 10 grid configuration with no corner electrodes, 0.4 mm inter-electrode spacing, and 1.0 mm electrode length; from Blackrock Microsystems, Salt Lake City, UT, USA) were chronically implanted in the arm representation region of the left pre-motor cortex. Recordings were done at least 1 week following surgery within the context of a behavioral study during which the animals were trained to make a specific arm movement or perform a visual-motor mapping task (for details see Yu et al., 2017). Ongoing activity was recorded for 30 min during which the monkey was seated head-fixed and awake but did not perform any behavioral task. Extracellular signals were recorded at 30 kHz. In post-recording processing, LFP signals were down-sampled to 500 Hz and band-pass filtered at 1–100 Hz. One exception was the analysis presented in **Figure 1D**, for which the band-pass was set to 3–100 Hz.

Spike Sorting

Extracellular signals were band-pass filtered (0.3–3 kHz) to reveal unit activity. Potential extracellular spike waveforms were detected during recording by adaptive threshold crossing (Blackrock Microsystems, Salt Lake City, UT, USA). The 400 μs preceding and 1,200 μs following each threshold crossing were stored and used for spike sorting. Manual spike sorting was performed with Plexon Offline Sorter. The first three principal components, peak-to-trough amplitude, and non-linear energy were the waveform features used for sorting. The initial waveform detection was deliberately liberal, such that it detected most unit activity as well as some noise fluctuations. The noise fluctuations provided an important baseline comparison for strict spike sorting. The degree to which a unit was different from noise was quantified with a multivariate ANOVA test (dependent variables included at least two of the waveform features). A unit was considered well isolated if the null hypothesis (unit and noise waveforms drawn from distributions with the same mean) was rejected with $p < 0.001$. If more than one unit was detected from a single electrode, each pair of units was also required to pass the same test. Moreover, each unit was required to have less than 1% of its inter-spike-intervals (ISI) less than a 1 ms refractory period.

To compute the crosscorrelation in spike count between each pair of units recorded during the ongoing activity we followed established methods (e.g., Renart et al., 2010). First, to obtain spike count vectors, the spike time stamps of each unit were: (1) binned with 1 ms temporal resolution; and (2) convolved with a Gaussian window with 50 ms width. The crosscorrelation coefficient was computed between all pairs of spike count vectors (2,145 pairs for monkey 1,780 pairs for monkey 2).

Definition of LFP Avalanches

As established previously (Shew et al., 2009), we first detected negative LFP deflections (nLFPs) falling below a threshold of −3.5 standard deviation (SD) of ongoing fluctuations *in vivo* and −6 SD of noise *in vitro*. Unlike *in vivo*, periods of quiescence between population events were clear in the *in vitro* recordings and used to define the noise baseline. nLFPs were found to occur in clusters and their sizes were distributed according to a power law, the hallmark of neuronal avalanches. Two consecutive nLFPs (on any electrode) belonged to the same avalanche if the time interval between them was smaller than a threshold τ, which was determined using the probability distribution of inter-nLFP time intervals (Beggs and Plenz, 2003). We also repeated our analysis for different nLFP detection thresholds *in vivo*: 2.5, 3, 3.5, 4.25, and 5 SD, which has previously been demonstrated to not affect the power-law behavior in avalanche size distribution (Petermann et al., 2009). Our main findings were unchanged (see also "Definition of Avalanche Families" section). A complete scaling analysis of LFP avalanches for these two monkeys can be found in a recent publication (Miller et al., 2019).

Definition of Avalanche Families

First, each spatiotemporal avalanche was represented as a binary spatial pattern with one bit per MEA electrode (Yu et al., 2011). Bits were set to 1 if the corresponding electrode recorded an nLFP during the event and otherwise set to 0. Next, patterns that included only one active site were excluded to minimize the potential inclusion of noise events. Then we sorted the events into families with similar binary patterns. *K*-means sorting in MATLAB (Mathworks) was employed with randomly chosen seed patterns and a Euclidean distance metric. The number k of families to search for was decided based on the number N of population events being sorted $k = \sqrt{N/2}$ (Sánchez et al., 1979).

Family-Triggered Peri-Event Time Histograms

To characterize the relationship between every unit and every avalanche family, we computed family-triggered PETHs. If the family was comprised of N avalanches, then the trigger times for the PETH were the N timestamps of the first nLFPs in each avalanche. The PETHs included the 750 ms periods preceding and following the trigger times. The bins were 50 ms in width. A PETH peak was deemed "selective" if two conservative criteria were met. First, the integrated spike rate within a ±200 ms interval around the trigger time must be three times larger than the baseline spike rate computed in the two intervals −750 to −200 ms and 200 to 750 ms, relative to the trigger time. This criterion effectively reduces false positives but may classify units with very broad PETH peaks as non-selective. Second, the spike count in the ±200 ms interval around the trigger time must occur with a probability of less than 0.01 assuming Poisson spike generation of the neuron with rate λ. The rate λ was the mean spike rate calculated during the ±10 s intervals around the trigger times. The second criterion greatly reduces false positives for neurons with low firing rates, which can be common. As discussed in the main text, the number of expected false positives using these criteria was fewer than five times less than the observed number of selective unit-family pairs. To assess the delay t and width σ of significant PETH peaks, we fit the PETH with a four-parameter Gaussian function: $f(x) = A + B\ exp((-(x-t)^2)/2 * sigma^2)$. The fit parameters A, B, t, and σ were determined by minimizing the summed squared differences between spike counts in each bin and the fit function. The minimization was performed with a simplex search method (MATLAB function—*fminsearch*).

Acute Slice Preparation and Recording Media

Coronal slices from the medial prefrontal cortex (mPFC) or somatosensory cortex of Sprague–Dawley rats were cut at 400 μm thickness (VT1000S; Leica Microsystems, GmbH) in the chilled artificial cerebral spinal fluid (ACSF). In this study, we used two different types of ACSF during recordings, one for each of the two age groups. The first protocol, referred to as the *DA/NMDA* protocol in the main text, has been successfully used in prior studies (Beggs and Plenz, 2003; Stewart and Plenz, 2006) to induce avalanches in adult rats. Accordingly, slices were cut from adult rats (age 7–9 weeks) in ACSF saturated with 95% O_2 and 5% CO_2 (310 ± 5 mOsm) containing (in mM) 205 sucrose, 0.5 $CaCl_2$, 7 $MgSO_4$, 3.5 KCl, 26.2 $NaHCO_3$, 0.3 NaH_2PO_4, 10 D-glucose. Prior to recording, slices were stored submerged at room temperature in ACSF containing (in mM) 124 NaCl, 1.2 $CaCl_2$, 1 $MgSO_4$, 3.5 KCl, 26.2 $NaHCO_3$, 0.3 NaH_2PO_4, and 10 D-glucose. The recording was done in the same ACSF as used for storage, but with bath-application of 30 μM of dopamine (Sigma–Aldrich) and 5 μM of NMDA (Sigma–Aldrich). The second protocol, referred to as the *ACSF* protocol in the main text, induces neuronal avalanches in cortex slices from immature, young rats (Shew et al., 2010) in which we recorded under normal ACSF perfusion, but stored slices in a modified ACSF before recording. In the modified storage ACSF, Na was replaced with choline and spontaneous population activity arises without further pharmacological manipulation when switching to the recording ACSF. Moreover, this protocol may provide a practical *in vitro* model for the study of cortical regions that have reduced dopamine receptor density. For this protocol, slices were cut from young rats (ages 2–3 weeks) in modified ACSF containing (in mM) 124 choline-Cl (Sigma–Aldrich), 1.2 $CaCl_2$, 1 $MgSO_4$, 3.5 KCl, 0.3 NaH_2PO_4, 26.2 $NaHCO_3$, 10 D-glucose, and saturated with 95% O_2 and 5% CO_2 (310 ± 5 mOsm). Note that choline replaces the sodium of normal ACSF. The slices were stored submerged at room temperature in the same modified ACSF as used for slicing. MEA recordings were performed in normal ACSF.

All recordings were performed with ACSF saturated with 95% O_2 and 5% CO_2, perfused at 3–4 ml/min at 35.5 ± 0.5°C. Disinhibited activity was recorded by bath-application of picrotoxin (50 μM, Sigma–Aldrich) to the respective normal recording medium.

Recording LFP Avalanches *In vitro*

Spontaneous LFP activity was recorded with integrated planar MEAs (Multichannel Systems; GmbH) that contained 59 electrodes arranged on an 8 × 8 grid with an inter-electrode spacing of 200 and 30 μm electrode diameter (four corner electrodes and one ground electrode missing). Extracellular signals were recorded with a 1 kHz sample rate and low-pass filtered between 1 and 200 Hz to obtain the LFP. The activity was recorded for 20–45 min. Experiments with fewer than 100 nLFPs were not included in our analysis. Avalanches and avalanche families were defined as described above for the *in vivo* recordings.

Whole-Cell Patch Recordings

The intracellular patch solution contained (in mM) 132 K-gluconate, 6 KCl, 8 NaCl, 10 HEPES, 0.2 EGTA, 2.2 Mg-ATP, 0.39 Na-GTP (Sigma–Aldrich). The pH was adjusted to 7.2–7.4 with KOH. The final osmolarity of the pipette solution was 290 ± 10 mOsm. Biocytin hydrochloride (0.3%; Sigma–Aldrich) was added to the pipette for use in post-fixation (4% paraformaldehyde) anatomical reconstruction. A putative pyramidal cell (∼100 μm from the slice surface) was visually identified by its somatic shape and prominent apical dendrite and later confirmed by reconstructed morphology and/or electrophysiology. Intracellular membrane potentials were recorded in current-clamp mode (Axopatch 200B, Axon Instruments, Missouri City, TX, USA), pre-amplified and low-pass filtered at 10 kHz (Cyberamp380, Axon Instruments, Missouri City, TX, USA), and digitized at 25 kHz for voltage and 5 kHz for current using the CED 1401 (Cambridge Electronic Design, UK). Data were collected with Spike2 (CED) and analyzed off-line. Neurons were included in the analysis if their membrane potential was stable below −60 mV and if their action potential half-width was <2.5 ms (see **Table 2** for the presentation of more electrophysiological parameters). To visualize the morphology of patched cells (e.g., **Figure 5B**), a subset of slices (n = 9) was post-processed with streptavidin-conjugated Texas Red (Molecular Probes, Inc.), imaged with a Zeiss LSM 510 confocal microscope, and were stitched, projected and traced offline using Fiji ImageJ[1].

RESULTS

Extracellular Units and LFP During Ongoing Activity in Awake Nonhuman Primates

We first studied the relationship between LFP-based avalanches and single-neuron activity in the ongoing activity of nonhuman primates. LFP recordings (1–100 Hz) were performed with high-density MEAs chronically implanted towards superficial layers of the premotor cortex over the arm representation region in two macaque monkeys (**Figure 1A**). During the 30 min recordings, the monkeys were awake, but not engaged in a task. Spike sorting was used to identify 66 and 51 well-isolated extracellular units in monkeys 1 and 2, respectively (for details see "Materials and Methods" section). The firing rates of the units were 3.6 ± 9.4 Hz (mean ± SD) ranging from 0.03 to 52 Hz. The trough-to-peak time difference of unit waveforms was 345 ± 140 μs. We found average pairwise spike correlation coefficients of 0.050 ± 0.002 and 0.015 ± 0.001 for our monkeys 1 and 2, respectively consistent with previous reports (e.g., Ecker et al., 2010; Renart et al., 2010). In line with previous studies (Gray and Singer, 1989; Murthy and Fetz, 1996; Destexhe et al., 1999; Pesaran et al., 2002; Nauhaus et al., 2009; Petermann et al., 2009; Kelly et al., 2010; Okun et al., 2010), we observed a tendency for units to coincide with negative excursions in the LFP (**Figure 1A**). This was quantified by computing the spike rate as a function of LFP amplitude recorded within a 50 ms windows at the same site. In **Figure 1B**, which displays the average over all units and all times, we show that the rate increases with negative LFP amplitude as reported previously for high-density arrays based on tungsten electrodes (Petermann et al., 2009).

Averages Reveal Non-selective, Widely Distributed Unit-LFP Relationships *In vivo*

Having demonstrated that the LFP and extracellular units are related at individual electrodes, we next explored traditional spike-triggered and LFP-triggered relationships for our recordings to identify spatial selectivity in the LFP or unit activity concerning activity on the array. The example in **Figures 1C,D**, in which the location of the trigger unit is marked by the red triangle, draws attention to the spatially widespread, seemingly non-selective average nLFP activity related to local spiking. When slow LFP fluctuations were included in the analysis, i.e., band-pass filtering between 1 and 100 Hz, we found that the spike-triggered LFP waveform exhibited a broad (∼0.5 s negative deflection with a minimum close to the trigger time, **Figure 1C**). When very slow fluctuations were excluded, by band-pass filtering the LFP between 3 and 100 Hz, the spike-triggered average LFP waveform displayed a sharp (∼20 ms) negative peak with the largest amplitude at the recording site nearest the triggering unit, in line with previous studies (Nauhaus et al., 2009; Petermann et al., 2009), yet it systematically decayed with distance from the recorded unit (**Figure 1D**). This suggests a rather non-selective spatial relationship between low-frequency components in the LFP and single-unit activity. Next, we computed LFP-triggered averages of unit activity using the peak times of the nLFPs for triggers (**Figure 1E**). We considered all nLFPs that fell below −3.5 SD. For this and the remainder of the analysis in this article, we studied the 1–100 Hz frequency band of LFP signals. Consistent with previous studies in awake animals (Destexhe et al., 1999; Petermann et al., 2009), we found that peri-event time histograms (PETHs) of unit counts often indicated peak firing centered on the nLFP times. Consistent with **Figure 1C**, units that were distant from the nLFP recording

[1]https://imagej.net/Fiji

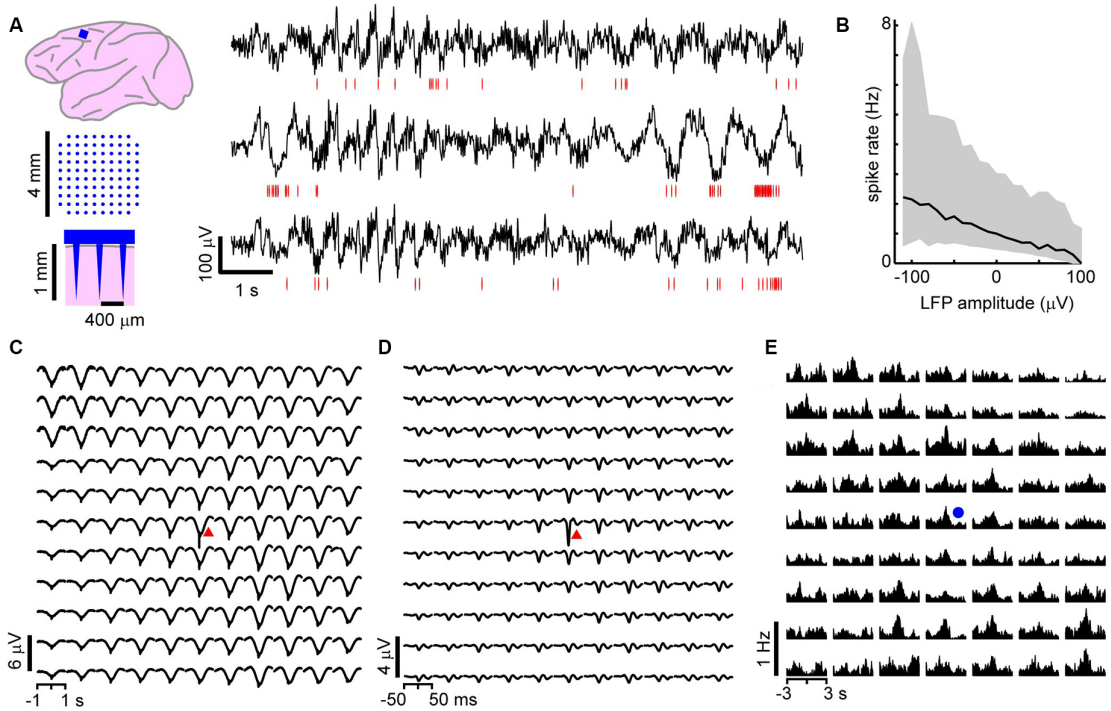

FIGURE 1 | On average, local unit activity associates with negative local field potential (LFP) deflections over the spatially extended cortical area in the monkey cortex. **(A)** Left: a 96 channel electrode array (blue) was implanted within superficial layers of the premotor cortex in two macaque monkeys. Right: simultaneous recordings of awake-state ongoing LFP (black) and single-unit activity (red—spike times) from three recording sites. Units exhibit increased firing around the time of negative LFP deflections. **(B)** Unit activity increases with negative LFP amplitude. Unit spike rate as a function of LFP amplitude computed for all times (in consecutive 50 ms windows). Units and LFP recorded at the same site were compared. Displayed is the average over all sites and units for both monkeys. Large deviations from the average relationship are typical (shaded region—lower to upper quartile, line—median). **(C)** Spike-triggered average LFP waveforms indicate that widespread, slow negative LFP fluctuations are associated with local spiking (red triangle indicates the site of the local unit). LFP was band-pass filtered between 1 and 100 Hz. **(D)** Same as in panel **(C)**, but with low-frequency components of the LFP removed (band-pass, 3–100 Hz), spike-triggered average LFP waveforms indicate that local, sharp negative LFP deflections are typically associated with spiking as reported previously (Petermann et al., 2009). **(E)** The peak times of large amplitude negative LFP deflections (nLFPs; bandpass filter, 1–100 Hz) were used to compute nLFP-triggered average spike count histograms. Consistent with **(C)**, units both near to and distant from the trigger site (blue dot) exhibited significant increases in firing with no clear decaying relationship over distance. For **(C–E)** all units were compared to all LFP recordings and then averaged together keeping track of relative locations of the unit concerning the LFP recording site.

site displayed a PETH peak that was comparable with that of nearby units, on average.

Figure 1 demonstrates that, on average, the spiking activity of single neurons is related to the LFP signal. However, the spike-triggered average LFP waveform for the average unit peaks around 1–10 μV (**Figures 1C,D**), which is much smaller than the 100 s of μV moment-to-moment fluctuations in the LFP (see **Figure 1A**; standard deviation over all electrodes was 35 ± 5 μV). Similarly, the nLFP-triggered spike histogram revealed an average increase in firing of less than 1 Hz (**Figure 1E**), which is a small change relative to ongoing 100 s of Hz fluctuations in spike rate. The coefficient of variation for the ISI distributions was 2.2 ± 0.5 and the standard deviation of instantaneous spike rates (1/ISI) was 75 ± 35 Hz.

Moment-to-Moment Fluctuations in the Spatial LFP Are Organized as Avalanche Families

These observations raise the question to what extent do average relationships faithfully represent the moment-to-moment relationships between spiking and LFP signals? The analysis that follows was designed to answer these questions and consisted of three main steps. First, we identified neuronal population events based on the spatial patterns of LFP signals afforded by multi-site recordings. Second, we sorted the population events into "families" of like events, based on which sites exhibited negative LFP deflections during each event. Third, we tested each unit individually for family-specific changes in the firing. If our hypothesis is correct, we should find that certain units fire selectively during certain families, while other units prefer other families.

Our definition of a population event is motivated by two observations: (1) nLFPs are associated with increased spiking activity; and (2) LFP signals recorded simultaneously from different sites are often highly correlated (e.g., **Figures 1A**, **2A**; Destexhe et al., 1999; Leopold and Logothetis, 2003; Nauhaus et al., 2009). Therefore, we define a population event to be a set of nLFPs (typically from many recording sites), which occur together sufficiently close in time. Specifically, if the time interval between two consecutive nLFPs is less than a threshold τ, we

assign them to the same population event. The threshold τ is chosen based on the inter-nLFP-interval distribution, which was bimodal; τ is between the peaks in the distribution, thus distinguishing the long time-scale which separates events and the short time-scale of within-event nLFPs (τ = 130, 114 ms for monkey 1, 2). In line with previous studies of ongoing activity in nonhuman primates (Leopold and Logothetis, 2003; Miller et al., 2019), slow timescale dynamics were dominant, although monkey 1 did show a slight increase in gamma-band power near 30 Hz compared to the 10–20 Hz range (**Figure 2B**). We recorded 1,308 and 2,016 population events for monkeys 1 and 2, respectively. Population events were diverse in spatial extent, spanning 9.6 ± 16.5 and 9.4 ± 16.2 electrodes (mean ± SD) for monkeys 1 and 2. We defined the size of a population event as the summed amplitudes of all the nLFPs comprising the event and demonstrate that the distribution of the population event sizes was close to a power-law with exponent −1.5 (**Figure 2C**). This power-law event size distribution indicates that the dynamics we study here are "neuronal avalanches" (Beggs and Plenz, 2003), in line with previous studies of ongoing activity in the cortex of awake monkeys (Petermann et al., 2009; Klaus et al., 2011; Miller et al., 2019). Next, for each avalanche, we generated a representative binary 10 × 10 pixel pattern (corner electrodes missing), which indicates which sites were active during the event (1 = active, 0 = inactive; Yu et al., 2011). **Figure 2A** exemplifies 3 s of simultaneous LFP recordings with an avalanche occurring about 1.5 s into the example (red dots mark nLFPs). The upper left in **Figure 2D** shows the corresponding binary pattern for this occurrence. We then used a *k*-means algorithm to find families of avalanches with similar activation patterns (Beggs and Plenz, 2004; Stewart and Plenz, 2006). Four example patterns from one family are shown in **Figure 2D**. The nLFP raster in **Figure 2E** shows all nLFP times and sites during a 30 min recording from monkey 1 with corresponding color-coded avalanche families. The occurrence-times of events in one family were typically scattered throughout the 30 min recording. **Figure 2F** displays the corresponding binary patterns derived from the nLFP raster sorted into families of similar patterns. The sorted raster of binary patterns for monkey 2 is shown in **Figure 2G**.

We note that *k*-means sorting resulted in spatially wide-spread patterns. It also results in one "misfit" family comprised of many small and local events that repeated rarely during the recording and will not be considered further for this analysis (e.g., family *a* in **Figure 2F**). Our objectives and the results of the *k*-means sorting were only to establish several families, within which events had similar spatial patterns of activation. Practically, as k is reduced, families include more population events and units become less selective for families. We quantified this trend by computing the ratio of the peri-event time histogram (PETH) peak height H_f of selective unit-family pairs to the nLFP-triggered PETH peak height H_{nf}, which disregards families. We found that for k = 30, 20, 10, 5, 4, 3, the ratio H_f/H_{nf} = 4.8, 4.4, 3.4, 3.2, 2.2, 1.0, respectively (monkey 1). Note that $\sqrt{N/2} = 20$ for monkey 1. Our main conclusions are not qualitatively affected by changes in k between 10 and 30. Higher values of k tended to reduce the number of events in each family, resulting in poor statistics. Moreover, using hierarchical clustering as reported previously (Beggs and Plenz, 2004; Stewart and Plenz, 2006) did not significantly change our results (data not shown). We also repeated this analysis for different nLFP thresholds and found that for thresholds of 2.5, 3, 3.5, 4.25, and 5 SD, the ratio H_f/H_{nf} = 2.6, 3.5, 4.4, 6.0, 4.7, respectively (monkey 1). Thus, for all thresholds, we found a greater than 100% increase in selectivity compared to nLFP-triggered PETHs which disregard families of population events.

Unit-Firing Is Selective for Avalanche Families

With the population events sorted into avalanche families, the next step was to determine whether units fired selectively for families. To accomplish this, we computed the family-triggered spike rate PETHs. One PETH was computed for each unit-family pair, triggered on the times of the first nLFP in each family. Examples for five units and a subset of families are displayed for monkey 1 in **Figures 3A–F**. The large spatial extent of each family is clearly visible in the family averages (**Figure 3A**) contrasted by the selectivity in family-triggered PETHs for units (**Figures 3B–F**; red histograms). Our main finding was that extracellular units were reliably and selectively active for avalanche families identified in the LFP. Some units were reliably active during multiple families (e.g., families *o* and *d* in **Figures 3B–D**), while other units (**Figures 3E,F**) fired reliably for only one family. The locations of the five units which fired reliably for families in **Figure 3A** were distributed diffusely over the majority of the 4 × 4 mm recording region (**Figure 3A**; right). The locations of all units in monkey 1 that were selectivity for the families displayed in **Figure 3A** are shown in **Figures 3G,H** for firing increase and decrease, respectively.

A closer inspection of the color-coded locations of the units reveals that spatial location is not predictive for family selectivity. For example, unit orange did not respond to family *r* who overlapped with its location but was selective for family *o* and *d*, who are most active at non-overlapping locations on the array.

All units and their respective family selectivity with corresponding negative or positive modulation are summarized in **Figure 4A** for both monkeys. In monkey 1, we found 124 selective unit-family pairs with a strong change in firing revealed by the family-triggered PETH. In monkey 2, we found 29 selective unit-family pairs. Here, we adopt a conservative definition of "selective," requiring a strong increase or decrease in firing compared to baseline. In both monkeys, the number of strong relationships was more than five times greater than the number expected by chance (nine and five for monkeys 1 and 2), demonstrated by repeating our analysis with randomized spike times—each time was shifted by a random amount between 1 and 10 s. Most units were selective for only one family as shown in the distribution of unit selectivity for families for both monkeys in **Figure 4B**. Units selective for multiple families could exhibit various combinations in the direction of modulation. Several units were positively modulated by some families but negatively

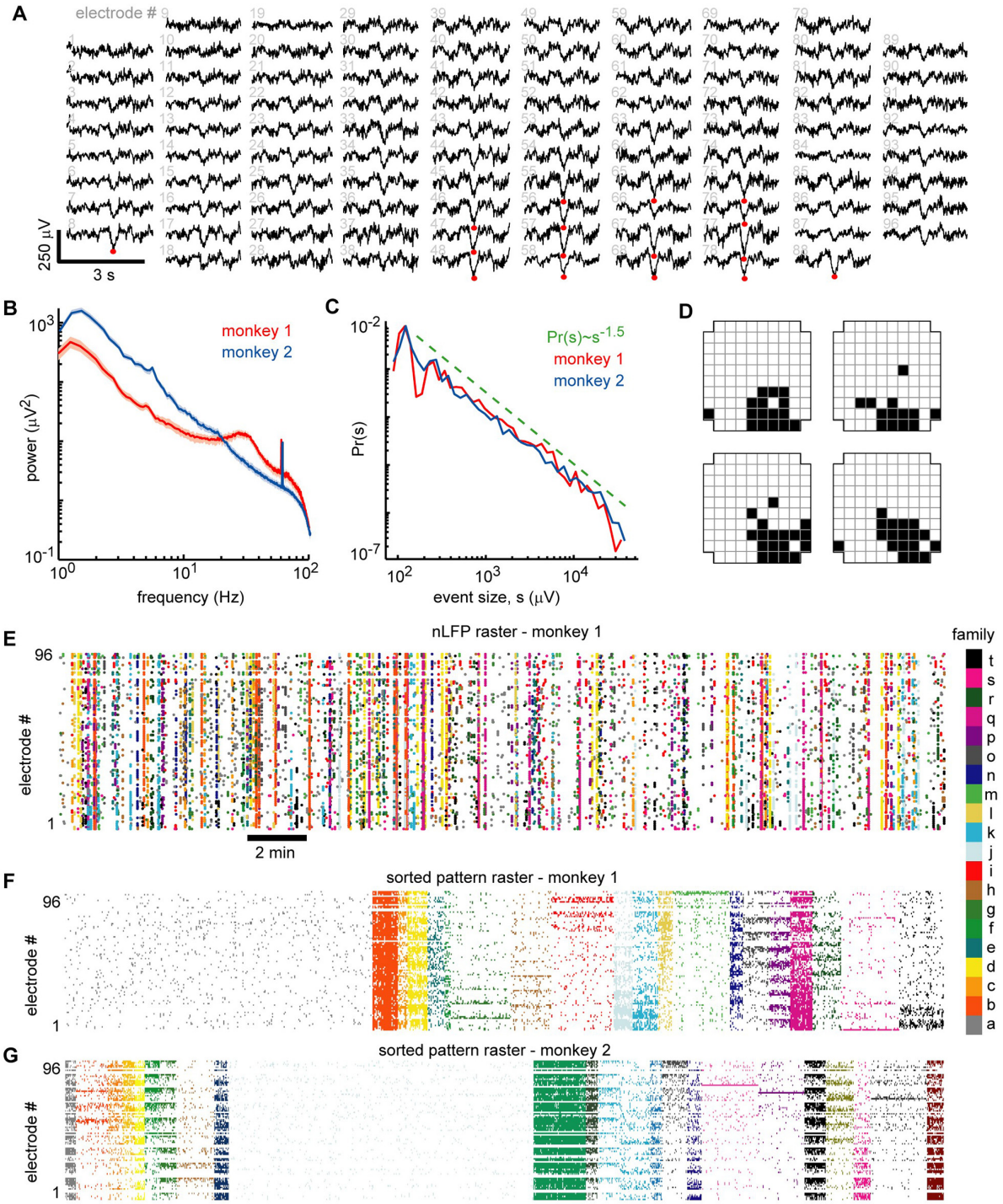

FIGURE 2 | Ongoing neuronal avalanches are composed of repeating spatial nLFP patterns. **(A)** Displayed are 3 s LFP recordings arranged to match the spatial layout of the 96 recordings sites. Multiple nLFPs (red dots) often occurred together within ∼100 ms across multiple sites—we defined such occurrences as "population events" (see Experimental Procedures). **(B)** Power spectra of LFP were broadband showing that low-frequency fluctuations dominate the signal. A prominent ∼30 Hz oscillation was present in monkey 1 (see also Miller et al., 2019). All recording sites were analyzed—median (line) and lower to upper quartile (shaded region) are shown. **(C)** Distributions of population event sizes *s* demonstrate that the activity is neuronal avalanches, defined by $Pr(s) \sim s^{-1.5}$ (Beggs and Plenz, 2003; Petermann et al., 2009). **(D)** The spatial locations of nLFP avalanches were represented with a binary pattern (Yu et al., 2011). The upper left pattern corresponds to population event in panel **(A)**. The other three patterns were similar but occurred at different times and are shown as typical like-examples extracted by our algorithm use. **(E)** Raster of all nLFP times and locations. Vertical clusters of nLFPs with matching color belong to one avalanche. **(F)** Avalanches were sorted into families with like patterns. The sorted avalanche raster of monkey 1 is shown. Color code identifies family and is same as in panel **(E)**. Note that family *a* (gray, left) is comprised of typically small avalanches that were not similar to many others. **(G)** Sorted avalanche raster of monkey 2.

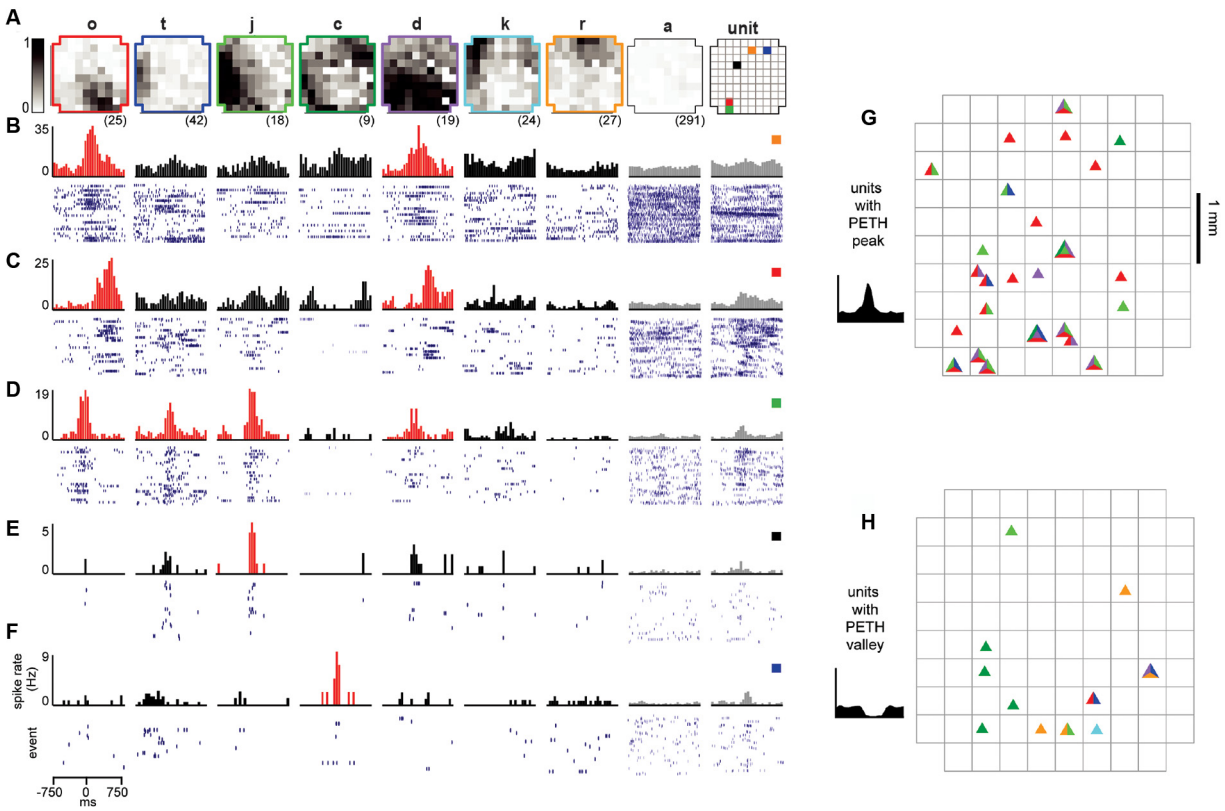

FIGURE 3 | Reliable ensembles of spiking units underlie avalanche families. **(A)** The average pattern for eight example avalanche families. Letter family labels correspond to **Figures 2E,F** of monkey 1. Grayscale indicates the fraction of events in which the site participated. Right: color code for locations of units in panels **(B–F)**. **(B–F)** Each column displays family-triggered spike rate PETHs (top) and spike rasters (bottom) for five example units. For example, the left-most PETH and spike raster in **(B)** indicates that this unit increases its firing rate selectively during the occurrence of family *o*. The temporal bin width for the PETHs was 50 ms. The second to right column shows the average response to avalanches of size 1 (pattern a), excluding large avalanche families. The right-most column includes PETHs and rasters triggered on all nLFPs recorded at the same site as the unit, disregarding family categorization. Red histograms indicate the family specificity of the unit. **(G,H)** Array location of units (triangles) that selectively increased **(G)** or decreases **(H)** their firing in response to families shown in panel **(A)**. The colors within each triangle indicate which families the unit was selective for.

modulated by other families (**Figure 4A**; units with at least 1 white and one black square in a row, M1 #1, 3, 17, 20, 28, 29 and M2 #8). On the other hand, some units were only negatively modulated by multiple families (**Figure 4A**; units with >1 black square in a row, M1 #35, 36 and M2 #19).

Among the units and families that were strongly related, we found that the temporal precision of unit participation in families was varied. For example, **Figures 3B,C** reveal PETH peaks that are broader than those in **Figures 3E,F**. Moreover, the latency from trigger time to PETH peak also varied. To quantify the width and latency of the PETH peaks, we fit a Gaussian function to the PETH (**Figure 4C**, inset, Experimental Procedures). We found that the PETH peak widths, i.e., standard deviation parameter of the Gaussian fit, were 140 ± 136 ms and 170 ± 110 ms and the latencies were broadly distributed 5 ± 107 ms (mean ± SD) and 0.4 ± 106 ms for monkeys 1 and 2 respectively (**Figures 4C,D**). Both width and latency variability suggest the temporal precision of unit-family relationships to be of the order of 10–100 ms.

The grand average nLFP-triggered spike histograms and spike-triggered average LFP shown in **Figure 1** conceals the richness of the relationship between different units and different families of LFP population events. For example, comparing the nLFP-triggered spike histograms in **Figure 1E** to the family-triggered PETHs in **Figure 3**, we see that family-triggered PETHS often had much larger or sharper peaks. This can also be seen by comparing the family-triggered PETHs to the rightmost PETHs in **Figure 3**, which were triggered on the times of all nLFPs that occurred on the electrode which recorded the unit. Quantitatively, we found that the selective unit-family pairs (as defined above) exhibited a PETH peak that was 4.4 ± 8.8 times larger than the nLFP-triggered PETH peak for monkey 1 and 4.3 ± 6.9 times larger for monkey 2. These results demonstrate that if all units and population events are averaged together as in **Figures 1B–E**, one underestimates the strength and spatiotemporal complexity of the relationship between unit activity and the LFP.

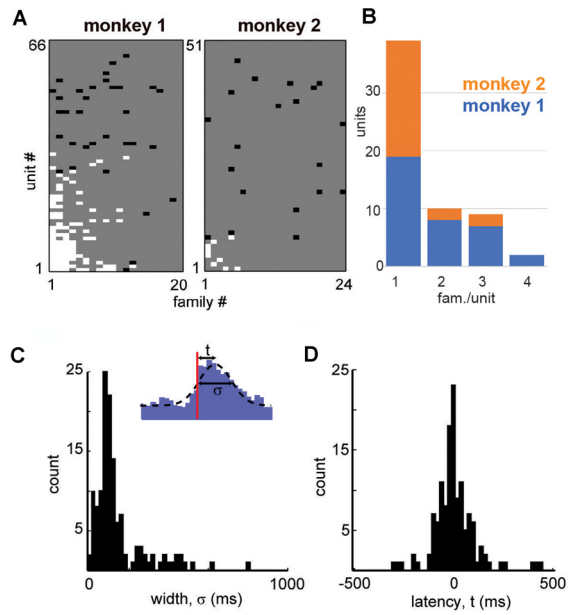

FIGURE 4 | Summary in family selectivity and temporal precision in a unit-family relationship. **(A)** Summary of all unit-family relationships for both monkeys. White pixels indicate firing increase, black pixels indicate a decrease in the firing. **(B)** Histogram of units and the number of selective families for both monkeys. **(C)** We estimated the latency *t* to peak firing and the width σ of the PETH peak for each strong unit-family pair, by fitting a Gaussian function with an offset (*inset*). The distribution in PETH widths peaked around 100 ms but was also widespread. **(D)** Peak unit firing centered near *t* = 0 but could precede or follow the occurrence of a family by up to 100 ms.

Synaptic Inputs to Layer 2/3 Pyramidal Neurons Selectively Occur During Avalanche Families in Rat Acute Slices

We have shown above that select ensemble of spiking neurons are closely related to LFP-based avalanche patterns in the cortex of awake monkeys. We next carried out combined whole-cell patch-clamp and multi-site LFP recordings in acute slices of rat somatosensory and medial prefrontal cortex (**Figure 5**). Since afferent fibers from distant regions are severed in the acute slice, this preparation allows us to investigate the selectivity of intrinsic dynamics in local cortical circuits. We focused on the role of layer 2/3 pyramidal neurons and carried out control experiments with pharmacologically blocked fast $GABA_A$-receptor-mediated synaptic inhibition.

In a first set of *in vitro* experiments, population activity was elicited in acute coronal slices from medial prefrontal cortex (mPFC) and motor cortex (M1) of adult rats (age 7–9 weeks) induced by continuous bath application of 30 μM dopamine (DA) and 3 μM NMDA in ASCF as reported previously (Beggs and Plenz, 2003; Stewart and Plenz, 2006). In the second set of experiments, slices were taken from mPFC and M1 of young rats (age 2–3 weeks) using a choline-based, protective slicing solution followed by recording spontaneous activity in normal ACSF only (for details see Experimental Procedures). Multi-site LFP was recorded using planar 60-electrode MEAs covering a 1.6 × 1.6 mm^2 region with an interelectrode distance of 200 μm (**Figure 5A**). There were several notable differences in basic parameters between these two protocols. Spontaneous LFP activity in normal ACSF of young slices was about 10 times higher in rate and aggregate LFP amplitude compared to the DA/NMDA induction protocol for slices from adult rats (**Table 1**). We identified all cells as putative pyramidal neurons based on a combination of morphology, I/V-responses, and action potential properties (**Figure 5B**; **Table 2**). For most cells, we also obtained extensive measures of action potential firing, which demonstrated that the increase in LFP activity for the younger slices correlated with a significantly longer action potential width for pyramidal neurons typical for immature neurons (**Table 2**). Thus, the two protocols allowed for examining avalanche and single-neuron activity under two largely different rates of activity. Except where noted, the following observations were found for both protocols. We defined neuronal avalanches as described previously (Beggs and Plenz, 2003; Stewart and Plenz, 2006) and sorted them into families exactly as in the *in vivo* data analysis.

An example of a simultaneously recorded intracellular membrane potential from a layer 2/3 pyramidal neurons and the spontaneous LFP on the MEA is shown in **Figures 5B,C**. Upon wash-in of DA/NMDA, ongoing LFP activity emerged and the intracellular membrane potential depolarized by ∼4.0 ± 3.5 mV (**Figures 5D,E**).

We note that, unlike our *in vivo* recordings in which the MEA matrix was placed horizontally within layer 2/3, the *in vitro* MEA spanned multiple cortical layers across the coronal slice with the uppermost row placed along the medial (mPFC) or dorsal/dorsolateral border of the cortex (M1). In line with our previous reports (Stewart and Plenz, 2006, 2007; Petermann et al., 2009), we found that LFP activity occurred predominantly in layer 2/3 (**Figure 6A**) for both protocols. In line with our *in vivo* observations, these predominantly layer 2/3 nLFP patterns distributed in sizes according to a power law that was sensitive to temporal shuffling, again as shown in our original article on neuronal avalanches in the acute cortex slice (Beggs and Plenz, 2003; **Figures 6A,B**).

As observed *in vivo*, LFP avalanche patterns were very diverse, but certain patterns tended to repeat during a recording. **Figure 7A** displays an unsorted nLFP raster of avalanches indicating the color-coded families and their time of occurrence. **Figure 7B** shows the corresponding sorted raster into avalanche families. Since action potential firing was very low in the patched neurons (<1 Hz), our goal here was to test whether neurons displayed significant subthreshold membrane potential changes concerning particular families. To this end, we performed family-triggered averages of the membrane potential recordings.

Our main finding from the *in vitro* recordings was that pyramidal neurons displayed reliable subthreshold membrane potential responses only from select avalanche families, in line with our selectivity results *in vivo*. Examples of family-triggered changes in membrane potentials for one neuron using the DA/NMDA protocol are shown in **Figure 7** below the average activity pattern for the corresponding families in **Figure 7C**. A corresponding example from

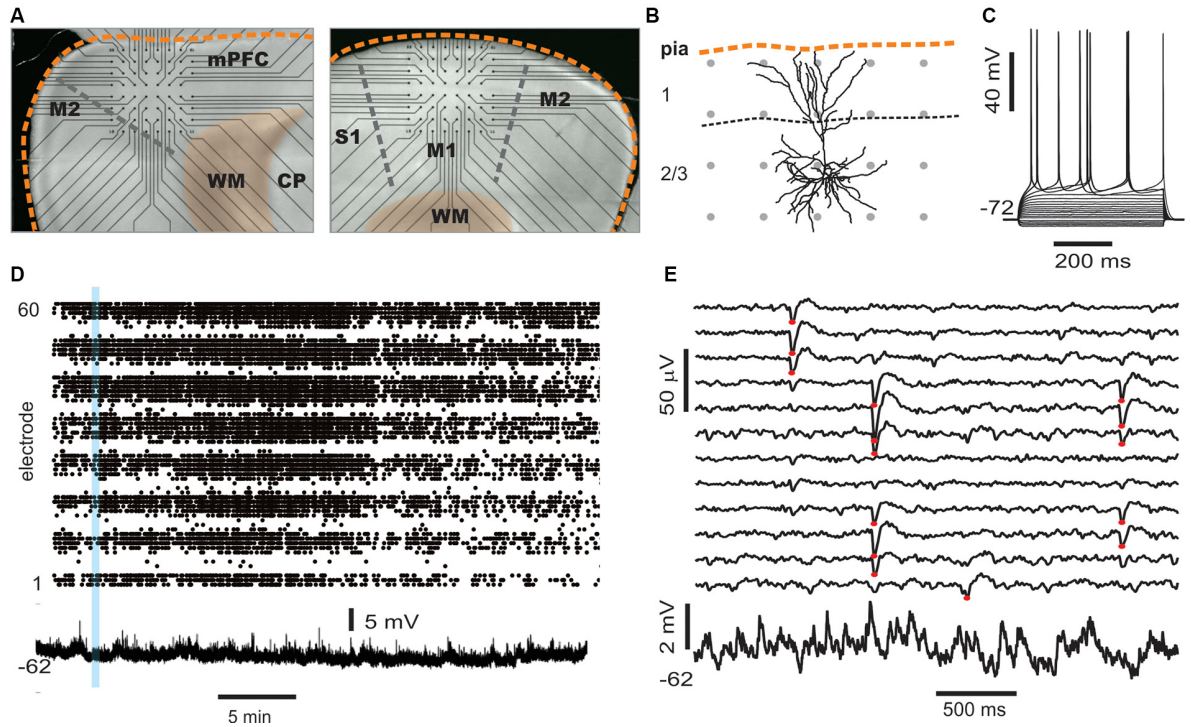

FIGURE 5 | Simultaneous multi-site LFP and whole-cell patch recordings *in vitro*. **(A)** Trans-illuminated pictures that display placement of acute coronal slices from rat cortex on a planar microelectrode array (MEA), visible as straight connection leads ending in recording electrodes (*black dots*). Left: example for medial prefrontal cortex (mPFC) recordings. The medial cortex border is oriented upwards. Right: example of somatosensory cortex (M1) recording. The dorsolateral axis is oriented upwards. Scale: inter-electrode distance is 200 µm. *Orange broken line*: cortical border. WM, white matter; CP, caudate-putamen. **(B)** Example of a reconstructed layer 2/3 pyramidal neuro (confocal image) to illuminate size relationships between single neurons and spacing of MEA electrodes (*gray dots*). **(C)** Sub- and suprathreshold voltage responses to step current injections of a whole-cell patched pyramidal cell. **(D)** Example of spontaneous nLFP activity on the full array (electrodes 1–60 ordered in groups of eight per row) in the presence of NMDA/DA, which typically lasts for >30 min (Stewart and Plenz, 2006). The time course of the simultaneously recorded intracellular membrane potential from a whole-cell patched neuron is displayed at the bottom. **(E)** Five seconds of ongoing LFP population activity recorded from a subset of MEA electrodes spanning layer 2/3 and intracellular membrane potential taken from the period in panel (**D**; *blue bar*) at higher spatiotemporal resolution. *Red dots* indicate suprathreshold nLFPs. Note the absence of any apparent, straightforward relationship between single-neuron activity and nLFPs.

the normal ACSF protocol for young slices is shown in **Figure 8**.

We identified neurons with significant input during families by comparing membrane potential fluctuations before (−500 to −50 ms; baseline) and after (50–250 ms) family triggers. An SD in deflections at least three times bigger than the SD in baseline fluctuations (−500 to −50 ms) was considered significant. Out of 84 recorded cells, only about 50% received input from just a few avalanche families (for a summary see **Figures 9A,B**). Thus, we conclude that the participation of single neurons in avalanche dynamics was typically selective.

As in our *in vivo* results, the relationship between the input to the neuron and the population activity in **Figures 7**, **8** would be missed or, at best, underestimated if one averaged over all avalanches and all neurons. Here we emphasize this point by computing the average membrane potential triggered on all avalanches except the selective family (**Figures 7C**, **8C**; *control*), which results in no significant average membrane deflection. These results indicate that accounting for the spatial pattern of avalanches is crucial to identify the relationships we present. LFP activity recorded with a randomly chosen single electrode from our multi-site recordings is likely to be uncorrelated to the input to any, particularly patched neuron.

Avalanche Diversity and Selectivity in Synaptic Input Is Abolished by Disinhibition

Finally, we investigated whether the selectivity encountered in our analysis might be due to a lack of excitability in the acute slice or might be maintained dynamically by the cortical network. To this end, we examined the role of fast $GABA_A$-receptor mediated synaptic inhibition. It is well established that suppression of inhibition destroys avalanche dynamics *in vitro* (Beggs and Plenz, 2003; Stewart and Plenz, 2006; Pasquale et al., 2008). Accordingly, we tested whether the diversity and selectivity for families of ongoing LFP patterns depend on inhibitory signaling. We added the $GABA_A$ receptor antagonist picrotoxin (50 µM) to our avalanche induction protocol for adult and young slices respectively. Under such disinhibited conditions, spontaneous nLFP count and rate increased by a factor of 10 in adult slices and by 50–100% in young slices (**Table 1**). Ongoing

TABLE 1 | Comparison of *in vitro* population activity for the three different recording conditions (mean ± SEM).

	DA/NMDA	ACSF	PTX
Number of slices (*n*)	85	42	9
Spontaneous activity duration (s)	1,486 ± 538	1,586 ± 667	1,306 ± 629
Total nLFP count from all sites (*n*)	596 ± 810	5,700 ± 9,130	4,733 ± 6,677
Rate of nLFPs at single site (Hz)	0.38 ± 0.46	3.7 ± 4.8	4.3 ± 5.1
Integrated nLFP amplitudes from all sites (mV)	−5.8 ± 7.1	−80 ± 113*	−158 ± 186
Number of families/ experiment *(n)*	14.9 ± 2.4	17.61 ± 5.4	6.6 ± 3.1*
Families w/neuron response (%)	6.7 ± 2.9	5.7 ± 2.9	42.9 ± 34.9*

*$p < 0.05$.

TABLE 2 | Action potential electrophysiological parameters for whole-cell patch recordings of pyramidal neurons (mean ± SEM).

	DA/NMDA	ACSF	PTX
Number of cells *(n)*	71	36	12
Resting potential (mV)	−71 ± 4	−68 ± 5	−71 ± 5
Action potential threshold (mV)	−35 ± 5	−38 ± 4	−34 ± 6
Action potential amplitude (mV)	88 ± 9	87 ± 9	87 ± 7
Action potential width (ms)	1.0 ± 0.4	1.68 ± 0.6*	1.0 ± 0.5
After hyper-polarization amplitude (mV)	8.8 ± 2.7	8.2 ± 2.5	10 ± 4
After hyper-polarization time (ms)	19 ± 7	21 ± 6	16 ± 11

*$p < 0.05$. *Only neurons for which reliable action potential measures were obtained are listed.*

activity was comprised of stereotyped population events with large LFP amplitude and spatial extent resulting in bimodal size distribution of population events (**Figure 6C**, arrow; **Figure 10**). About three times fewer families were observed and a single slice-spanning family dominated most of the activity when compared to intact inhibition (**Table 1**). On average, neurons exhibited a 10 times loss in selectivity, i.e., most neurons participated in about half of all families and neurons revealed membrane depolarization or action potentials during nearly every population event (**Figures 9C**, **10; Table 1**).

DISCUSSION

We simultaneously recorded single neuron and multi-site LFP activity from the cortex of awake monkeys and rat acute slices. In both preparations, spatiotemporal LFP patterns were distributed in sizes according to a power law, the hallmark of neuronal avalanches. The power-law quantifies a high incidence of large avalanches suggestive of a non-selective relationship between spatially extended LFP population signals and single-neuron activity. On the contrary, though, we found that diverse ensembles of extracellular units were selectively and reliably activated with particular avalanche patterns during ongoing activity in the premotor cortex of awake monkeys. We confirmed this selectivity in acute slices of rat cortex under two different activity levels, demonstrating reliable input to layer 2/3 pyramidal neurons during select and repeated

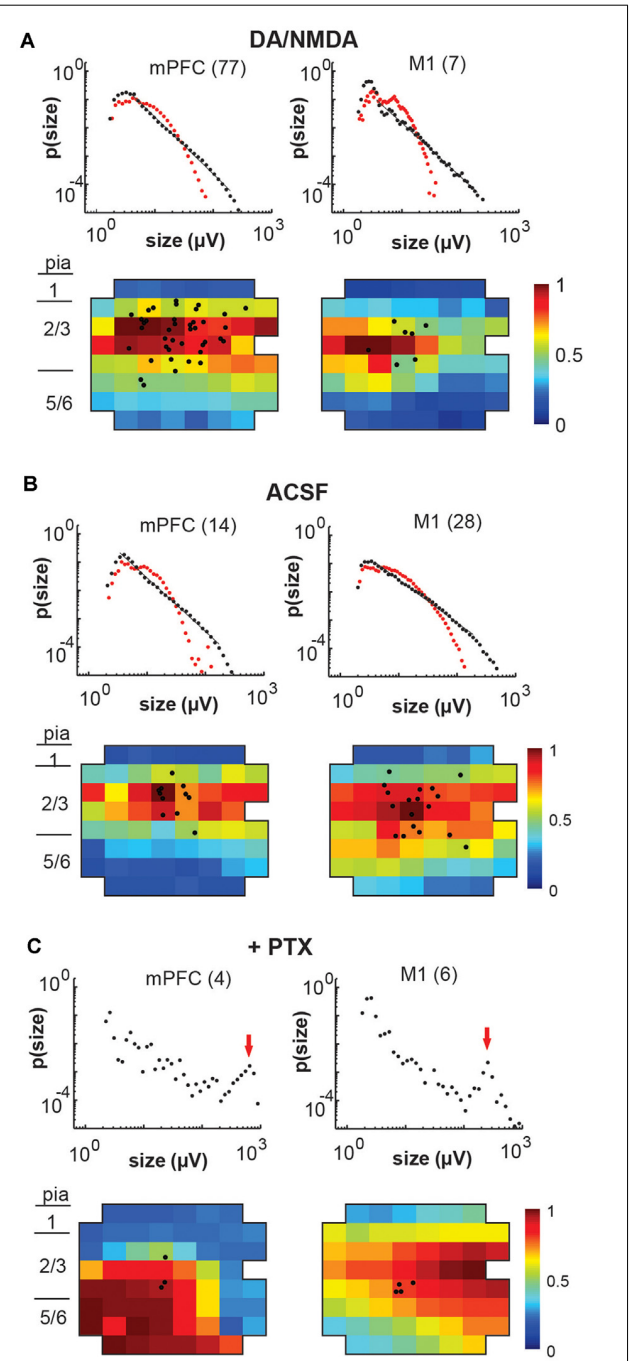

FIGURE 6 | Overview of total avalanche activity and location of whole-cell patched pyramidal neurons in layer 2/3 for all recording conditions. **(A)** Avalanche size distribution obtained under artificial cerebral spinal fluid (ACSF) + DA/NMDA conditions for mPFC and M1 acute slices from adult rats. Size distributions reveal power laws in line with neuronal avalanches, which are destroyed by shuffling (*red*). Numbers indicate the total number of slice experiments for each region. Bottom density plots indicate population activity measured on the MEA aligned to medial (mPFC) and dorsal (M1) border averaged over all slice experiments. Approximate layers as a visual guide indicated on the left (MEA, 8 × 8 electrodes, 200 μm interelectrode distance, corner electrodes missing, additional ground electrode in 4th row on the right). The color indicates the activation rate (averaged over experiments).

(*Continued*)

FIGURE 6 | Continued
Black markers indicate soma locations of patched neurons on the array. **(B)** Same as in panel **(A)** for ACSF condition in slices from young rats prepared under-protected choline condition. **(C)** Disinhibited condition due to the addition of picrotoxin (+PTX) for slices from adult and young rats combined. Red arrows point to the predominance of system size spontaneous activations.

LFP avalanches. We demonstrated that this selectivity breaks down during disinhibition and is not predicted by the spatially wide-spread correlation found with traditional spike-triggered or LFP-triggered average relationships. The selective participation of single neurons in repeated avalanches supports the view that avalanches are composed of highly diverse, yet selective neuronal ensembles.

Our work is related to previous studies in which multi-site recordings of LFP activity was compared to the activity of single-units (Destexhe et al., 1999; Rasch et al., 2008; Katzner et al., 2009; Nauhaus et al., 2009; Petermann et al., 2009; Kelly et al., 2010). Nauhaus et al. (2009) reported that the spiking activity of neurons generates negative LFP deflections near the neuron and decays with distance from the neuron. This conclusion was based on the spike-triggered average LFP recorded from anesthetized cats and monkeys. Our unit-triggered averages of LFP (**Figure 1D**) confirm these findings in awake monkeys. However, when lower frequency signals are not filtered out, i.e., 1–100 Hz is considered rather than 3–100 Hz as Nauhaus et al. (2009) did, the decay of the spike-triggered average LFP peak with distance is less prominent (**Figure 1C**). The converse relationship, i.e., LFP-triggered average spike histograms, revealed spatially widespread spiking during negative LFP deflections (**Figure 1E**). This observation is also consistent with previous observations of nLFP-triggered spike histograms (Destexhe et al., 1999; Petermann et al., 2009). Katzner et al. (2009) found that LFP signals originate from neurons within a 250 μm radius of the recording site. They reached this conclusion by comparing the orientation tuning of units and LFP signals in the visual cortex of anesthetized cats. Our results do not contradict this study, but we emphasize that neuronal avalanche dynamics is sensitive to anesthetics (Scott et al., 2014; Bellay et al., 2015) limiting extrapolations of previous findings to the current study in awake nonhuman primates. Indeed, previous studies have shown that LFP signals can be highly correlated over many millimeters of the cortex (Destexhe et al., 1999; Leopold and Logothetis, 2003; Nauhaus et al., 2009). When considered as a whole, our study demonstrates that large repeated population events involve selective ensembles of units distributed all across the 4 × 4 mm sized recording region. Some previous studies investigated the spike-LFP relationship by using spike trains to predict the LFP traces (Rasch et al., 2008) or vice versa (Kelly et al., 2010). Our work suggests that the success of such predictions would be substantially improved if algorithms take into account unit activity far from the LFP recording site as well the multi-site spatial pattern of the LFP.

Our analysis of population events are also related to previous studies using voltage-sensitive dye imaging (Tsodyks et al., 1999; Kenet et al., 2003; Han et al., 2008), which provides a spatially extended view of population activity similar to multi-site LFP recordings. As in our study, Kenet et al. (2003) and Han et al. (2008) found that population activity patterns repeat during ongoing cortical activity. Similar to our finding,

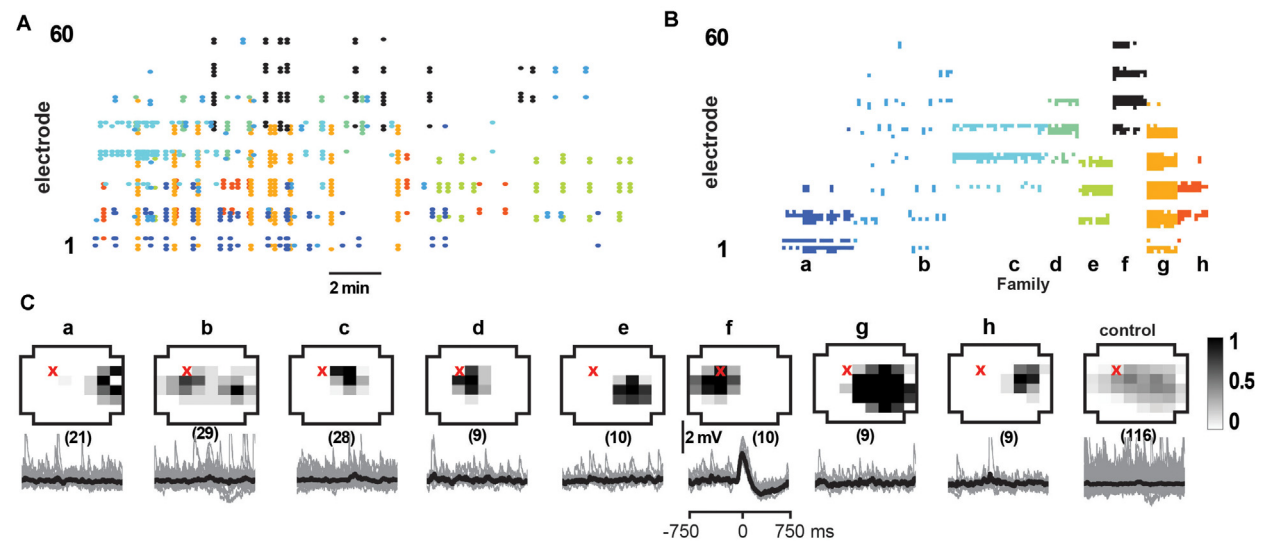

FIGURE 7 | Select responses in layer 2/3 pyramidal neurons to families of NMDA/DA induced LFP avalanches. **(A)** nLFP raster on the MEA with color-coded avalanche families and their temporal occurrences during spontaneous activity (15 min recording, mPFC). **(B)** Corresponding family-sorted avalanche raster. **(C)** Top: average spatial LFP pattern for all avalanche families. Grayscale indicates the fraction of site participation for each family. The red cross marks the soma location of the patched pyramidal neuron. *Control* includes all avalanches except those in family *f*. Bottom: family-triggered average intracellular membrane potential time course (*black*). *The number in brackets* indicates family members. Pre-averaged individual traces are shown in *gray*. Family *f* generated reliable input to the patched cell. Corresponding *control* demonstrates no reliable trigger with other family patterns outside *f*.

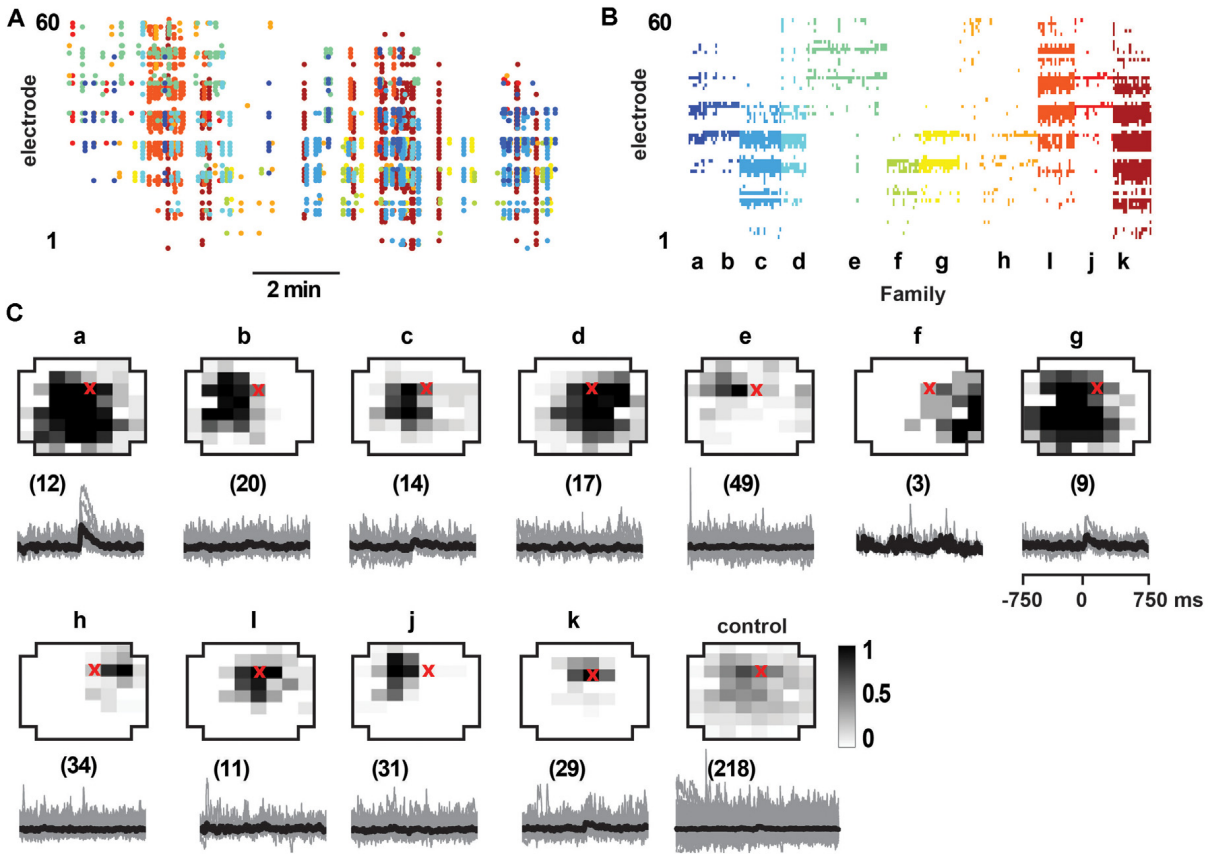

FIGURE 8 | Select responses in layer 2/3 pyramidal neurons to avalanche families in normal ACSF from young slices. **(A)** nLFP raster on the MEA with color-coded avalanche families and their temporal occurrences during spontaneous activity in young slices (10 min recording, M1). Note higher rate of avalanche occurrence compared to slices from adult rats (see **Figure 7**). **(B)** Corresponding family-sorted avalanche raster. **(C)** Top: average spatial LFP pattern for all avalanche families. Grayscale indicates the fraction of site participation for each family. The red cross marks the soma location of the patched pyramidal neuron. *Control* includes all avalanches except those in families *a, g*. Bottom: family-triggered average intracellular membrane potential time course (*black*). The number in brackets indicates family members. Pre-averaged individual traces are shown in *gray*. Note that families *d* and *i* do not reveal significant intracellular responses despite substantial spatial overlap with soma location. Families *a* and *g* correlated with reliable intracellular responses in the patched pyramidal neuron. Corresponding *control* demonstrates no reliable trigger with non-*a*, *g* families.

Tsodyks et al. (1999) showed that a single neuron may fire selectively during certain ongoing "preferred cortical states," which were defined by the spike-triggered average population pattern. However, our results indicate that single neurons are often selective for multiple different population events, specifically avalanche families, not just one "preferred cortical state." Moreover, Tsodyks et al. (1999) restricted their attention to population events that resemble those caused by sensory stimuli, which, unlike our study, excludes the possibility that a neuron might be selected for an internal cognitive process unrelated to sensory stimulation.

The present study exclusively analyzed periods of "ongoing" activity, during which the animals did not perform any specific task but remained seated, with their head fixed. We considered ongoing activity *in vivo* to be the most appropriate comparison with spontaneous activity induced in our *in vitro* experiments. In the absence of a behavioral read-out during these periods, the origins of fluctuations in nLFP rate during ongoing activity are not known but might include visual saccades, spontaneous posture adjustments, minor limb movements, and changes in arousal amongst others. In a recent study from our group (Yu et al., 2017), we demonstrated scale-free LFP-avalanches during a simple movement task and a visual-motor mapping task in nonhuman primates suggesting that spontaneous, non-monitored movements should not qualitatively change our results.

Our objectives and the results of the *k*-means sorting were: (1) to establish several avalanche families, within which events had similar spatial patterns of activation; and (2) to identify a comparable number of families with relatively large spatial extent for both *in vivo* and *in vitro* data to facilitate comparison between the two approaches. Typically the number of *in vitro* LFP avalanches was at the order of ∼10 lower than *in vivo*. In our view, there is no single "correct" choice of *k* for experimentally recorded cortical population events that are not likely to ever repeat exactly.

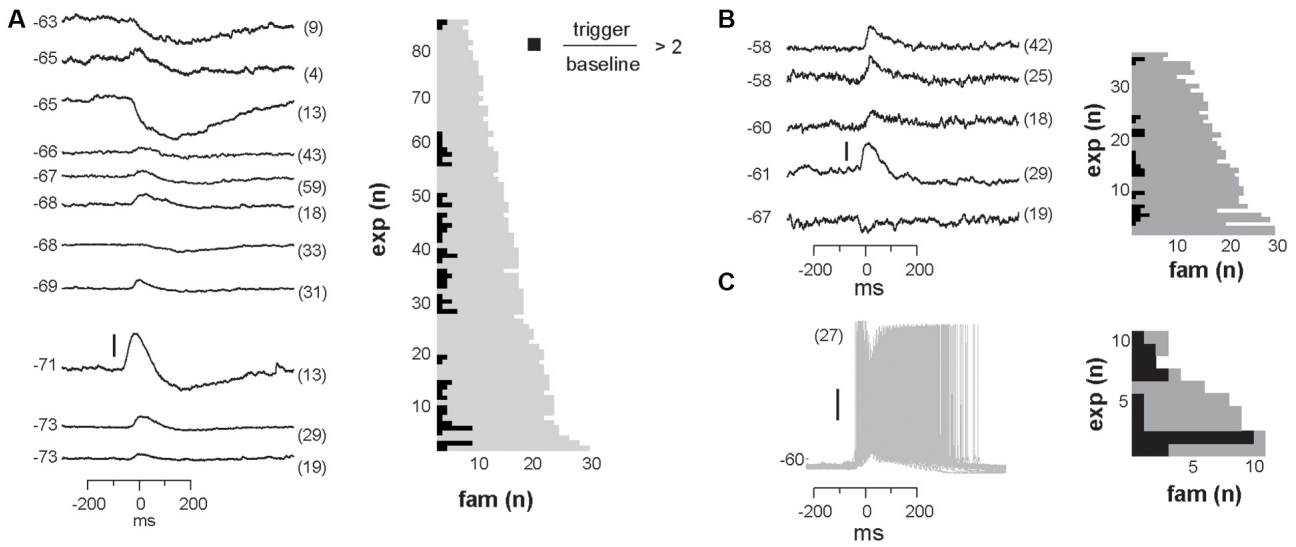

FIGURE 9 | Summary of significant membrane potential responses within each experimental group. **(A)** NMDA/DA condition in slices from adult rats: 42 neurons were found to receive reliable and selective input from particular avalanche families. Left: the subset of 11 family-triggered average membrane potential time courses with large amplitude changes ranked according to trigger-preceding average membrane potential shown at the left of each trace. The number of family triggers indicated by the number in brackets to the right. Note that responses could be depolarizing, hyperpolarizing or a depolarization followed by a hyperpolarization. Right: summary plot of the total number of avalanche families and the number of families with select intracellular responses. Note that most families will not trigger a response in a randomly recorded pyramidal neuron. **(B)** Summary for ACSF condition in slices from young rats. **(C)** Summary for PTX condition.

The Complementary *In vivo* and *In vitro* Approaches in Assessing Single-Neuron Selectivity During Avalanches

Here we measured the relationship between LFP-based avalanches and single-neuron activity using two very different approaches, each of which provided distinct advantages as well as profound limitations. The advantages of our *in vivo* recordings are: (1) the embedding of MEA tips in an intact three-dimensional cortical space biased towards superficial layers in an awake animal; (2) that single-neuron activity was measured near the electrode tip ensuring a close spatial relationship between maximal local LFP activity and single-neuron activity; and (3) the ability to simultaneously probe many neurons from the same network. Major disadvantages are: (1) the limitation to neuronal firing that is single neuron *output*; and (2) the ambiguity as to LFP contributions from remote, potentially extracortical sources. Our *in vivo* analysis demonstrates that single neuron output is selective for avalanche families.

The advantages of our *in vitro* recordings are: (1) intracellular whole-cell patch recordings that allow for studying the neuronal *input* during avalanching; and (2) that LFP avalanches must arise from sources that are part of the local microcircuit. Major disadvantages of this approach are: (1) recording from only a few, typically 1 randomly selected neuron per slice; and (2) LFP recording sites being distant from the site of single-neuron recording and neuronal activity generation. The latter problem arises from the fact that in the acute slice, oxygen diffusion is limited to about 150 μm from the slice surface leading to a ∼200 μm thick zone of hypoxic tissue separating the gas-impermeable planar MEA surface from the region of neuronal activity in the slice. With intracellular recording typically within the first 100 μm from the slice surface, we estimate that the typical distance between local LFP measurement sites and neuronal recording sites are of the order of 200–400 μm, much larger than *in vivo*. These spatial constraints should reduce the probability of finding tight coupling between the LFP and neuronal firing. This disadvantage as well as the low neuronal yield per experiment, though, is expected to be partially compensated for by dendritic arborizations of the recorded neurons which allow for subthreshold monitoring of remote network activity. Accordingly, our findings show that single neuron *input* is selective for avalanche families complementing our *in vivo* findings. Both approaches support the conclusion that the actual number of suprathreshold neurons during avalanching must be low even for large LFP patterns. Future experiments should target the selectivity encountered for single neurons during avalanches *in vivo*, for example using genetically encoded calcium indicators that monitor the neuronal firing, i.e., output, in combination with genetically encoded voltage indicators, which also monitor subthreshold activity (Knöpfel, 2012).

We note that when trying to assess the relationship between nLFP patterns and single-neuron activity, both extracellular and intracellular approaches naturally exhibit a bias against the identification of transient activity suppression. If extracellular unit firing is low, disfacilitation or active inhibition of firing is more difficult to identify because it can not be easily distinguished from unrelated quiet times in firing. For the intracellular membrane potential, active inhibition typically does not lead to a

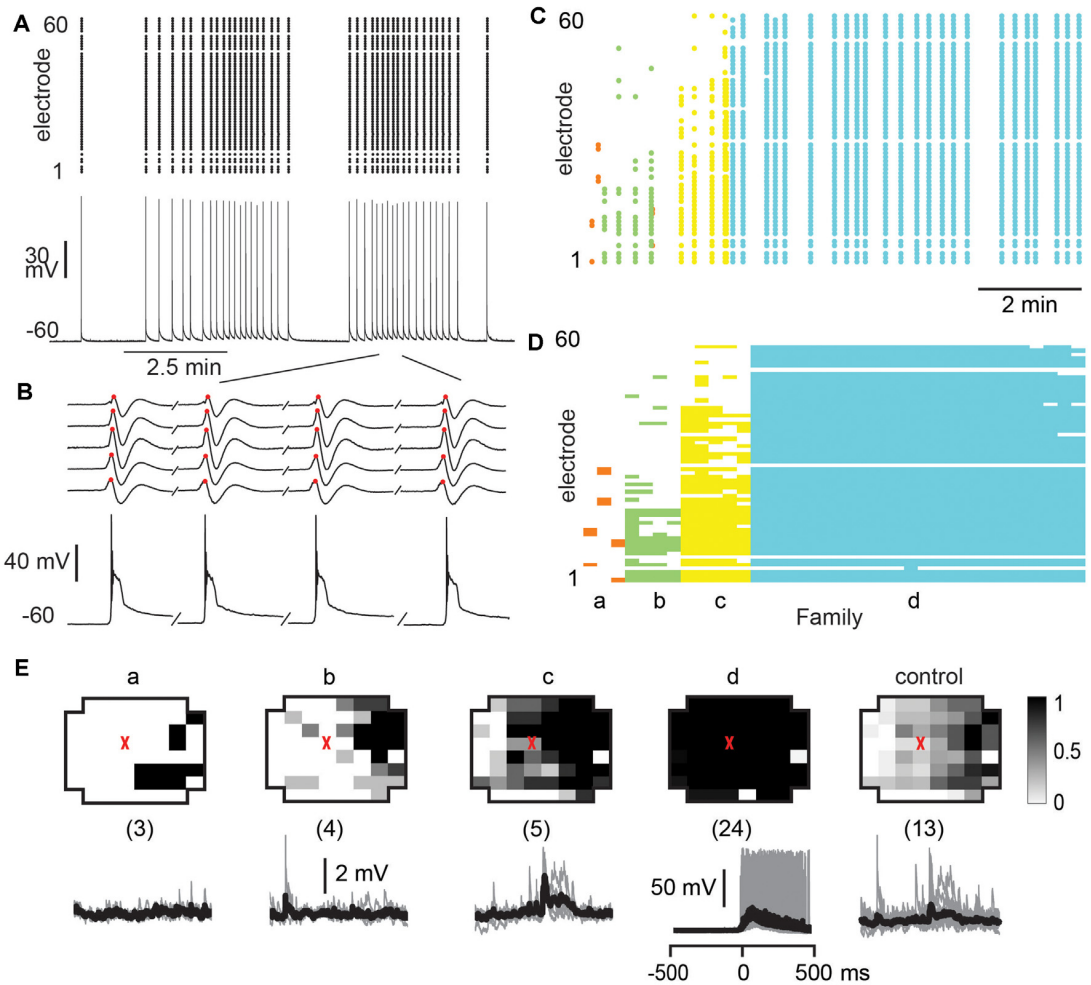

FIGURE 10 | Global disinhibition reduces family diversity uncovering system-wide synchronization and tightly coupled neuronal firing. **(A)** Disinhibition induces synchronous nLFP activity on the MEA time-locked with a single neuron firing. PTX (50 μM) was bath applied at the beginning to block fast $GABA_A$ receptor mediated inhibition. Top: nLFP raster. Bottom: intracellular membrane potential of a whole-cell patched pyramidal neuron. **(B)** Enlarged period in a demonstrating synchronous time course of nLFPs and corresponding large intracellular depolarization with spiking activity. Sequential occurrence of four population events grouped in time (discontinuity indicated by a forward slash). **(C)** nLFP raster on the MEA with color-coded avalanche families and their temporal occurrences. Note few families and tight firing for system-wide population event, identified as family *d*. **(D)** Corresponding family-sorted raster. **(E)** Most population events belong to family *d*, which spans most recording sites and always caused the patched cell to fire, i.e., the patched neuron was unselectively involved in network dynamics. Top: average patterns for each family. The red triangle marks the soma location of the patched neuron. The numbers of trigger events are shown in parentheses. Bottom: family-triggered average membrane potential waveforms (*black*). Pre-averaged individual traces are shown in gray. Vertical scale bars—2 mV (families *a*, *b*, and *c*), 50 mV (family *d*).

hyperpolarization unless the neuron is already depolarized. Both approaches thus bias detection of single-neuron—LFP relationships to transient excitation/depolarizations, potentially followed by suppression/hyperpolarization, in line with our experimental results.

The Change in Neuronal Response and Avalanche Patterns Under Global Disinhibition *In vitro*

Bath-application of the $GABA_A$-antagonist picrotoxin blocks inhibitory synaptic transmission in the cortical slice independent of the type of interneuron involved and subcellular location of the receptor. Non-selectively removing inhibition has been historically used *in vitro* (Beggs and Plenz, 2003; Pasquale et al., 2008) and in simulations (e.g., Tetzlaff et al., 2010) to collapse the power law in avalanche size into bimodal size distributions. Our study for the first time demonstrates this collapse to also drastically alter the relationship of single-neuron responses and spatially extended LFP patterns in the system. The non-selective reduction in $GABA_A$-mediated, i.e., fast synaptic transmission, uncovered one to two orders of magnitude higher spontaneous activity levels compared to DA/NMDA induced avalanches in the adult slice (see **Table 1**). Specifically, the nLFP rate increased by a factor of 10, and total activity increased by a factor of 100 for similar recording periods (∼20–25 min) besides expanding

into deep layers (see **Figure 6**). This remarkable difference demonstrates that: (1) fast synaptic inhibition is required to induce and maintain avalanche dynamics; (2) avalanche dynamics allows layer-wide events to be produced despite the circuit being orders of magnitude below its full capacity in excitability; and (3) spontaneous avalanche activity is biased towards superficial layers despite deep layers in principle being excitable. Disinhibition in young slices also increased activity, yet less dramatically than in the adult slice confirming the general immature state of $GABA_A$ mediated inhibition in the young cortex. These differences suggest developmental changes in the suppression of run-away excitation in the cortex and in the early support of avalanching in the neocortex.

Our family-triggered averages uncovered short-lasting depolarizations followed by hyperpolarization, or depolarizations and hyperpolarizations only. These subthreshold events and their respective order support the interpretation of inhibition being triggered by local recurrent excitation in the slice as an avalanche unfolds reminiscent of the synaptic "shadow" of a remotely propagating avalanche in the network.

To provide further insights into the inhibitory mechanisms involved in avalanche regulation, selective manipulation of distinct inhibitory microcircuit components e.g., interneuron cell types, will be required using e.g., optogenetical manipulation. Intracellular perfusion of whole-cell patched neurons with picrotoxin might allow for identifying excitatory inputs that underlie the selective sub- and suprathreshold responses of pyramidal neurons during avalanches.

LFP Based Avalanches and Their Composition of Selective Neuronal Ensembles *In vivo*

Our treatment of LFP population events was motivated by our studies of neuronal avalanches identified in the LFP *in vitro* (Beggs and Plenz, 2003, 2004; Stewart and Plenz, 2006, 2007; Shew et al., 2009, 2011; Yang et al., 2012), *ex vivo* turtle cortex (Shew et al., 2015) and *in vivo* in the rat (Gireesh and Plenz, 2008) and nonhuman primate (Petermann et al., 2009; Yu et al., 2017; Miller et al., 2019). Our observations that spatial nLFP patterns repeat during ongoing activity was shown previously for neuronal avalanches, but only *in vitro* (Beggs and Plenz, 2004; Stewart and Plenz, 2006). A common view of LFP signals is that their physiological origins are too poorly understood to provide concrete information about cortical dynamics. Our work suggests that this view is due for an update. We show that traditional spike- and LFP-triggered average relationships are much weaker than the fluctuating moment-to-moment spike-LFP relationships. Individual units are not well represented by the "average unit" and individual LFP population events are not well represented by the "average event." When these effects are accounted for, we show that diverse and reliable spiking ensembles underlie the cortical LFP-based avalanche.

Our work here demonstrates that neuronal avalanches are underpinned by selective, reliable spiking ensembles of neurons. This selectivity thus supports neuronal avalanches to be proposed (Plenz and Thiagarajan, 2007; Plenz, 2012) as a spatiotemporal organization of Hebbian cell assemblies (Hebb, 1949) lending strong experimental support to a large body of simulations on Hebbian plasticity, neuronal avalanches, and criticality (de Arcangelis et al., 2006; de Arcangelis and Herrmann, 2010; Rybarsch and Bornholdt, 2014; Stepp et al., 2015; Del Papa et al., 2017; Hernandez-Urbina and Herrmann, 2017; Michiels van Kessenich et al., 2018; Skilling et al., 2019; Zeng et al., 2019). By extension, the temporal organization of avalanches (Lombardi et al., 2014, 2016) or avalanches within avalanches (Petermann et al., 2009) and corresponding firing patterns of spike avalanches (Ribeiro et al., 2016) might provide a template for Hebb's "phase sequences."

DATA AVAILABILITY STATEMENT

The raw data supporting the conclusions of this article will be made available by the authors, without undue reservation.

ETHICS STATEMENT

The animal study was reviewed and approved by the Animal Care and Use Committee of the National Institute of Mental Health, USA.

AUTHOR CONTRIBUTIONS

DP, SY, WS, and TB designed the research. SY, TB, WS, and JF-W performed the experiments. SY, TB, WS, and DP analyzed the data. TB, WS, SY, and DP discussed the results and wrote the manuscript. All authors contributed to the article and approved the submitted version.

FUNDING

This research was supported by the Division of the Intramural Research Program (DIRP) of the National Institute of Mental Health (NIMH) ZIAMH002797.

ACKNOWLEDGMENTS

We thank members of the Plenz lab for discussions and Drs. Richard Saunders (NIMH) and Andy Mitz (NIMH) for help with the nonhuman primate surgery and electrophysiological recording.

REFERENCES

Agrawal, V., Cowley, A. B., Alfaori, Q., Larremore, D. B., Restrepo, J. G., and Shew, W. L. (2018). Robust entropy requires strong and balanced excitatory and inhibitory synapses. *Chaos* 28:103115. doi: 10.1063/1.5043429

Beggs, J. M., and Plenz, D. (2003). Neuronal avalanches in neocortical circuits. *J. Neurosci.* 23, 11167–11177. doi: 10.1523/JNEUROSCI.23-35-11167.2003

Beggs, J. M., and Plenz, D. (2004). Neuronal avalanches are diverse and precise activity patterns that are stable for many hours in cortical

slice cultures. *J. Neurosci.* 24, 5216–5229. doi: 10.1523/JNEUROSCI.0540-04.2004

Bellay, T., Klaus, A., Seshadri, S., and Plenz, D. (2015). Irregular spiking of pyramidal neurons organizes as scale-invariant neuronal avalanches in the awake state. *eLife* 4:e07224. doi: 10.7554/eLife.07224

Bowen, Z., Winkowski, D. E., Seshadri, S., Plenz, D., and Kanold, P. O. (2019). Neuronal avalanches in input and associative layers of auditory cortex. *Front. Syst. Neurosci.* 13:45. doi: 10.3389/fnsys.2019.00045

Chialvo, D. R. (2010). Emergent complex neural dynamics. *Nat. Phys.* 6, 744–750. doi: 10.1038/nphys1803

Clawson, W. P., Wright, N. C., Wessel, R., and Shew, W. L. (2017). Adaptation towards scale-free dynamics improves cortical stimulus discrimination at the cost of reduced detection. *PLoS Comput. Biol.* 13:e1005574. doi: 10.1371/journal.pcbi.1005574

de Arcangelis, L., and Herrmann, H. J. (2010). Learning as a phenomenon occurring in a critical state. *Proc. Natl. Acad. Sci. U S A* 107, 3977–3981. doi: 10.1073/pnas.0912289107

de Arcangelis, L., Perrone-Capano, C., and Herrmann, H. J. (2006). Self-organized criticality model for brain plasticity. *Phys. Rev. Lett.* 96:028107. doi: 10.1103/PhysRevLett.96.028107

Del Papa, B., Priesemann, V., and Triesch, J. (2017). Criticality meets learning: criticality signatures in a self-organizing recurrent neural network. *PLoS One* 12:e0178683. doi: 10.1371/journal.pone.0178683

Destexhe, A., Contreras, D., and Steriade, M. (1999). Spatiotemporal analysis of local field potentials and unit discharges in cat cerebral cortex during natural wake and sleep states. *J. Neurosci.* 19, 4595–4608. doi: 10.1523/JNEUROSCI.19-11-04595.1999

Ecker, A. S., Berens, P., Keliris, G. A., Bethge, M., Logothetis, N. K., and Tolias, A. S. (2010). Decorrelated neuronal firing in cortical microcircuits. *Science* 327, 584–587. doi: 10.1126/science.1179867

Fagerholm, E. D., Scott, G., Shew, W. L., Song, C., Leech, R., Knöpfel, T., et al. (2016). Cortical entropy, mutual information and scale-free dynamics in waking mice. *Cerebral Cortex* 26, 3945–3952. doi: 10.1093/cercor/bhw200

Gautam, H., Hoang, T. T., McClanahan, K., Grady, S. K., and Shew, W. L. (2015). Maximizing sensory dynamic range by tuning the cortical state to criticality. *PLoS Comput. Biol.* 11:e1004576. doi: 10.1371/journal.pcbi.1004576

Gireesh, E. D., and Plenz, D. (2008). Neuronal avalanches organize as nested theta- and beta/gamma-oscillations during development of cortical layer 2/3. *Proc. Natl. Acad. Sci. U S A* 105, 7576–7581. doi: 10.1073/pnas.0800537105

Gollo, L. L. (2017). Coexistence of critical sensitivity and subcritical specificity can yield optimal population coding. *J. R. Soc. Interface* 14:20170207. doi: 10.1098/rsif.2017.0207

Gray, C. M., and Singer, W. (1989). Stimulus-specific neuronal oscillations in orientation columns of cat visual cortex. *Proc. Natl. Acad. Sci. U S A* 86, 1698–1702. doi: 10.1073/pnas.86.5.1698

Han, F., Caporale, N., and Dan, Y. (2008). Reverberation of recent visual experience in spontaneous cortical waves. *Neuron* 60, 321–327. doi: 10.1016/j.neuron.2008.08.026

Hebb, D. (1949). *The Organization of Behavior. A Neuropsychological Theory*. New York, NY: Wiley.

Hernandez-Urbina, V., and Herrmann, J. M. (2017). Self-organized criticality *via* retro-synaptic signals. *Front. Phys.* 4:54. doi: 10.3389/fphy.2016.00054

Hesse, J., and Gross, T. (2014). Self-organized criticality as a fundamental property of neural systems. *Front. Syst. Neurosci.* 8:166. doi: 10.3389/fnsys.2014.00166

Karimipanah, Y., Ma, Z., Miller, J.-E. K., Yuste, R., and Wessel, R. (2017). Neocortical activity is stimulus- and scale-invariant. *PLoS One* 12:e0177396. doi: 10.1371/journal.pone.0177396

Katzner, S., Nauhaus, I., Benucci, A., Bonin, V., Ringach, D. L., and Carandini, M. (2009). Local origin of field potentials in visual cortex. *Neuron* 61, 35–41. doi: 10.1016/j.neuron.2008.11.016

Kelly, R. C., Smith, M. A., Kass, R. E., and Lee, T. S. (2010). Local field potentials indicate network state and account for neuronal response variability. *J. Comput. Neurosci.* 29, 567–579. doi: 10.1007/s10827-009-0208-9

Kenet, T., Bibitchkov, D., Tsodyks, M., Grinvald, A., and Arieli, A. (2003). Spontaneously emerging cortical representations of visual attributes. *Nature* 425, 954–956. doi: 10.1038/nature02078

Kinouchi, O., and Copelli, M. (2006). Optimal dynamical range of excitable networks at criticality. *Nat. Phys.* 2, 348–351. doi: 10.1038/nphys289

Klaus, A., Yu, S., and Plenz, D. (2011). Statistical analyses support power law distributions found in neuronal avalanches. *PLoS One* 6:e19779. doi: 10.1371/journal.pone.0019779

Knöpfel, T. (2012). Genetically encoded optical indicators for the analysis of neuronal circuits. *Nat. Rev. Neurosci.* 13, 687–700. doi: 10.1038/nrn3293

Leopold, D. A., and Logothetis, N. K. (2003). Spatial patterns of spontaneous local field activity in the monkey visual cortex. *Rev. Neurosci.* 14, 195–205. doi: 10.1515/revneuro.2003.14.1-2.195

Lombardi, F., Herrmann, H., Plenz, D., and de Arcangelis, L. (2014). On the temporal organization of neuronal avalanches. *Front. Syst. Neurosci.* 8:204. doi: 10.3389/fnsys.2014.00204

Lombardi, F., Herrmann, H. J., Plenz, D., and de Arcangelis, L. (2016). Temporal correlations in neuronal avalanche occurrence. *Sci. Rep.* 6:24690. doi: 10.1038/srep24690

Marković, D., and Gros, C. (2014). Power laws and self-organized criticality in theory and nature. *Phys. Rep.* 536, 41–74. doi: 10.1016/j.physrep.2013.11.002

Michiels van Kessenich, L., Luković, M., de Arcangelis, L., and Herrmann, H. J. (2018). Critical neural networks with short- and long-term plasticity. *Phys. Rev. E* 97:032312. doi: 10.1103/PhysRevE.97.032312

Miller, S. R., Yu, S., and Plenz, D. (2019). The scale-invariant, temporal profile of neuronal avalanches in relation to cortical γ-oscillations. *Sci. Rep.* 90:031001. doi: 10.1038/s41598-019-52326-y

Mora, T., and Bialek, W. (2011). Are biological systems poised at criticality? *J. Stat. Phys.* 144, 268–302. doi: 10.1007/s10955-011-0229-4

Muñoz, M. A. (2017). Colloquium: criticality and dynamical scaling in living systems. *Rev. Mod. Phys.* 90:031001. doi: 10.1103/RevModPhys.90.031001

Murthy, V. N., and Fetz, E. E. (1996). Synchronization of neurons during local field potential oscillations in sensorimotor cortex of awake monkeys. *J. Neurophysiol.* 76, 3968–3982. doi: 10.1152/jn.1996.76.6.3968

Nauhaus, I., Busse, L., Carandini, M., and Ringach, D. L. (2009). Stimulus contrast modulates functional connectivity in visual cortex. *Nat. Neurosci.* 12, 70–76. doi: 10.1038/nn.2232

Okun, M., Naim, A., and Lampl, I. (2010). The subthreshold relation between cortical local field potential and neuronal firing unveiled by intracellular recordings in awake rats. *J. Neurosci.* 30, 4440–4448. doi: 10.1523/JNEUROSCI.5062-09.2010

Pasquale, V., Massobrio, P., Bologna, L. L., Chiappalone, M., and Martinoia, S. (2008). Self-organization and neuronal avalanches in networks of dissociated cortical neurons. *Neuroscience* 153, 1354–1369. doi: 10.1016/j.neuroscience.2008.03.050

Pesaran, B., Pezaris, J. S., Sahani, M., Mitra, P. P., and Andersen, R. A. (2002). Temporal structure in neuronal activity during working memory in macaque parietal cortex. *Nat. Neurosci.* 5, 805–811. doi: 10.1038/nn890

Petermann, T., Thiagarajan, T., Lebedev, M. A., Nicolelis, M. A., Chialvo, D. R., and Plenz, D. (2009). Spontaneous cortical activity in awake monkeys composed of neuronal avalanches. *Proc. Natl. Acad. Sci. U S A* 106, 15921–15926. doi: 10.1073/pnas.0904089106

Plenz, D. (2012). Neuronal avalanches and coherence potentials. *Eur. Phys. J. Spec. Top.* 205, 259–301. doi: 10.1140/epjst/e2012-01575-5

Plenz, D., and Thiagarajan, T. C. (2007). The organizing principles of neuronal avalanches: cell assemblies in the cortex? *Trends Neurosci.* 30, 101–110. doi: 10.1016/j.tins.2007.01.005

Rasch, M. J., Gretton, A., Murayama, Y., Maass, W., and Logothetis, N. K. (2008). Inferring spike trains from local field potentials. *J. Neurophysiol.* 99, 1461–1476. doi: 10.1152/jn.00919.2007

Renart, A., de la Rocha, J., Bartho, P., Hollender, L., Parga, N., Reyes, A., et al. (2010). The asynchronous state in cortical circuits. *Science* 327, 587–590. doi: 10.1126/science.1179850

Ribeiro, T. L., Ribeiro, S., and Copelli, M. (2016). Repertoires of spike avalanches are modulated by behavior and novelty. *Front. Neural Circuits* 10:16. doi: 10.3389/fncir.2016.00016

Ribeiro, T. L., Yu, S., Martin, D. A., Winkowski, D., Kanold, P., Chialvo, D. R., et al. (2020). Trial-by-trial variability in cortical responses exhibits scaling in spatial correlations predicted from critical dynamics. *BioRxiv* [Preprint]. doi: 10.1101/2020.07.01.182014

Rybarsch, M., and Bornholdt, S. (2014). Avalanches in self-organized critical neural networks: a minimal model for the neural SOC universality class. *PLoS One* 9:e93090. doi: 10.1371/journal.pone.0093090

Sánchez, J., Mardia, K., Kent, J., and Bibby, J. (1979). *Multivariate Analysis*. New York, NY: Academic Press.

Scott, G., Fagerholm, E. D., Mutoh, H., Leech, R., Sharp, D. J., Shew, W. L., et al. (2014). Voltage imaging of waking mouse cortex reveals emergence of critical neuronal dynamics. *J. Neurosci.* 34, 16611–16620. doi: 10.1523/JNEUROSCI.3474-14.2014

Shew, W. L., Bellay, T., and Plenz, D. (2010). Simultaneous multi-electrode array recording and two-photon calcium imaging of neural activity. *J. Neurosci. Meth.* 192, 75–82. doi: 10.1016/j.jneumeth.2010.07.023

Shew, W. L., Clawson, W. P., Pobst, J., Karimipanah, Y., Wright, N. C., and Wessel, R. (2015). Adaptation to sensory input tunes visual cortex to criticality. *Nat. Phys.* 11, 659–663. doi: 10.1038/nphys3370

Shew, W. L., Yang, H., Petermann, T., Roy, R., and Plenz, D. (2009). Neuronal avalanches imply maximum dynamic range in cortical networks at criticality. *J. Neurosci.* 29, 15595–15600. doi: 10.1523/JNEUROSCI.3864-09.2009

Shew, W. L., Yang, H., Yu, S., Roy, R., and Plenz, D. (2011). Information capacity is maximized in balanced cortical networks with neuronal avalanches. *J. Neurosci.* 5, 55–63. doi: 10.1523/JNEUROSCI.4637-10.2011

Shriki, O., and Yellin, D. (2016). Optimal information representation and criticality in an adaptive sensory recurrent neuronal network. *PLoS Comput. Biol.* 12:e1004698. doi: 10.1371/journal.pcbi.1004698

Skilling, Q. M., Ognjanovski, N., Aton, S. J., and Zochowski, M. (2019). Critical dynamics mediate learning of new distributed memory representations in neuronal networks. *Entropy* 21:1043. doi: 10.3390/e21111043

Stepp, N., Plenz, D., and Srinivasa, N. (2015). Synaptic plasticity enables adaptive self-tuning critical networks. *PLoS Comput. Biol.* 11:e1004043. doi: 10.1371/journal.pcbi.1004043

Stewart, C. V., and Plenz, D. (2006). Inverted-U profile of dopamine-NMDA-mediated spontaneous avalanche recurrence in superficial layers of rat prefrontal cortex. *J. Neurosci.* 26, 8148–8159. doi: 10.1523/JNEUROSCI.0723-06.2006

Stewart, C. V., and Plenz, D. (2007). Homeostasis of neuronal avalanches during postnatal cortex development *in vitro*. *J. Neurosci. Meth.* 169, 405–416. doi: 10.1016/j.jneumeth.2007.10.021

Tetzlaff, C., Okujeni, S., Egert, U., Wörgötter, F., and Butz, M. (2010). Self-organized criticality in developing neuronal networks. *PLoS Comput. Biol.* 6:e1001013. doi: 10.1371/journal.pcbi.1001013

Tsodyks, M., Kenet, T., Grinvald, A., and Arieli, A. (1999). Linking spontaneous activity of single cortical neurons and the underlying functional architecture. *Science* 286, 1943–1946. doi: 10.1126/science.286.5446.1943

Yang, H., Shew, W. L., Roy, R., and Plenz, D. (2012). Maximal variability of phase synchrony in cortical networks with neuronal avalanches. *J. Neurosci.* 32, 1061–1072. doi: 10.1523/JNEUROSCI.2771-11.2012

Yu, S., Klaus, A., Yang, H., and Plenz, D. (2014). Scale-invariant neuronal avalanche dynamics and the cut-off in size distributions. *PLoS One* 9:e99761. doi: 10.1371/journal.pone.0099761

Yu, S., Ribeiro, T. L., Meisel, C., Chou, S., Mitz, A., Saunders, R., et al. (2017). Maintained avalanche dynamics during task-induced changes of neuronal activity in nonhuman primates. *eLife* 6:e27119. doi: 10.7554/eLife.27119

Yu, S., Yang, H., Nakahara, H., Santos, G. S., Nikolic, D., and Plenz, D. (2011). Higher-order interactions characterized in cortical activity. *J. Neurosci.* 31, 17514–17526. doi: 10.1523/JNEUROSCI.3127-11.2011

Zeng, G., Huang, X., Jiang, T., and Yu, S. (2019). Short-term synaptic plasticity expands the operational range of long-term synaptic changes in neural networks. *Neural Netw.* 118, 140–147. doi: 10.1016/j.neunet.2019.06.002

Conflict of Interest: The authors declare that the research was conducted in the absence of any commercial or financial relationships that could be construed as a potential conflict of interest.

frontiers in Computational Neuroscience

REVIEW
published: 10 February 2021
doi: 10.3389/fncom.2021.611183

Criticality, Connectivity, and Neural Disorder: A Multifaceted Approach to Neural Computation

Kristine Heiney[1,2*†], *Ola Huse Ramstad*[3*†], *Vegard Fiskum*[3], *Nicholas Christiansen*[3], *Axel Sandvig*[3,4,5], *Stefano Nichele*[1,6] *and Ioanna Sandvig*[3]

[1] Department of Computer Science, Oslo Metropolitan University, Oslo, Norway, [2] Department of Computer Science, Norwegian University of Science and Technology (NTNU), Trondheim, Norway, [3] Department of Neuromedicine and Movement Science, Norwegian University of Science and Technology (NTNU), Trondheim, Norway, [4] Department of Clinical Neuroscience, Umeå University Hospital, Umeå, Sweden, [5] Department of Neurology, St. Olav's Hospital, Trondheim, Norway, [6] Department of Holistic Systems, Simula Metropolitan, Oslo, Norway

OPEN ACCESS

Edited by:
Matjaž Perc,
University of Maribor, Slovenia

Reviewed by:
Dietmar Plenz,
National Institutes of Health (NIH), United States
Osame Kinouchi,
University of São Paulo, Brazil
Xiumin Li,
Chongqing University, China
Jean-Philippe Thivierge,
University of Ottawa, Canada

***Correspondence:**
Kristine Heiney
kristine.heiney@oslomet.no
Ola Huse Ramstad
ola.h.ramstad@ntnu.no

[†] These authors have contributed equally to this work

Received: 28 September 2020
Accepted: 18 January 2021
Published: 10 February 2021

Citation:
Heiney K, Huse Ramstad O, Fiskum V, Christiansen N, Sandvig A, Nichele S and Sandvig I (2021) Criticality, Connectivity, and Neural Disorder: A Multifaceted Approach to Neural Computation. Front. Comput. Neurosci. 15:611183. doi: 10.3389/fncom.2021.611183

It has been hypothesized that the brain optimizes its capacity for computation by self-organizing to a critical point. The dynamical state of criticality is achieved by striking a balance such that activity can effectively spread through the network without overwhelming it and is commonly identified in neuronal networks by observing the behavior of cascades of network activity termed "neuronal avalanches." The dynamic activity that occurs in neuronal networks is closely intertwined with how the elements of the network are connected and how they influence each other's functional activity. In this review, we highlight how studying criticality with a broad perspective that integrates concepts from physics, experimental and theoretical neuroscience, and computer science can provide a greater understanding of the mechanisms that drive networks to criticality and how their disruption may manifest in different disorders. First, integrating graph theory into experimental studies on criticality, as is becoming more common in theoretical and modeling studies, would provide insight into the kinds of network structures that support criticality in networks of biological neurons. Furthermore, plasticity mechanisms play a crucial role in shaping these neural structures, both in terms of homeostatic maintenance and learning. Both network structures and plasticity have been studied fairly extensively in theoretical models, but much work remains to bridge the gap between theoretical and experimental findings. Finally, information theoretical approaches can tie in more concrete evidence of a network's computational capabilities. Approaching neural dynamics with all these facets in mind has the potential to provide a greater understanding of what goes wrong in neural disorders. Criticality analysis therefore holds potential to identify disruptions to healthy dynamics, granted that robust methods and approaches are considered.

Keywords: criticality, connectivity, neural disorder, *in vitro* neural networks, complexity, neuronal avalanches, neural computation, plasticity

INTRODUCTION

Researchers have long grappled with the question of how the brain is able to process information, and many have recently turned to studying brain dynamics armed with tools from statistical physics and complexity science. In many physical systems, such as magnetic or gravitational systems, certain macroscopic features arise from the interactions of the constituent elements in a way that is unpredictable even from a perfect understanding of the behavior of each component; this is known as emergence (Chialvo, 2010). In the context of the brain, emergent phenomena encompass behavior and cognition, arising from the interaction of the vast number of neurons in the brain. Approaching the study of neural systems from this perspective entails studying neuronal behavior at the network or population level—observing and understanding emergent behaviors in the system rather than zeroing in on the behavior and connections of each individual neuron on its own. While exhibiting some computational power on their own, neurons are truly remarkable in their computational capacity when taken collectively.

It is hypothesized that the cortex may optimize its capacity for computation by self-organizing to a critical point (Beggs, 2008; Chialvo, 2010; Plenz, 2012; Shew and Plenz, 2013; Cocchi et al., 2017; Muñoz, 2018; Wilting and Priesemann, 2019a). Criticality is a dynamical state poised between order and disorder, or, more precisely, a transition between an absorbing phase in which activity gradually dies out and an active phase in which activity perpetuates indefinitely (Brochini et al., 2016). Critical systems must necessarily contain a large number of interacting non-linear components, though these conditions are not sufficient to ensure criticality; in the space of possible system states, criticality occupies a vanishingly small region, with chaotic and quiescent systems at the two opposite extremes (Brochini et al., 2016; Muñoz, 2018). A system operating in the critical state shows complex spatiotemporal behavior, and there is no scale, in space or time, that dominates the behavioral patterns of the system. That is, taking a closer or wider view of the system will show some variant of the same snapshot of the behavior. This mode of behavior is manifested by spatial and temporal correlations scaling as a power law over several orders of magnitude, giving rise to the presence of self-similar fractal-like structures over many scales. The brain exhibits complex spontaneous activity that crosses many time scales, a feature associated with criticality, and this activity is postulated to contribute to how the brain responds to stimuli and processes information.

In this review, we highlight network features evidenced to contribute to the emergence of critical dynamics in neural systems and discuss the benefits of experimentally studying the interplay between these features. Crucially, we also note here that care must be taken when extrapolating from theoretical findings on criticality to the more recent experimental research on criticality in neural systems observed at different scales. In particular, experimental explorations of criticality in neural systems point to the importance of considering the structures (Massobrio et al., 2015) and plastic mechanisms (Ma et al., 2019) that support this dynamical regime. Thus, critical dynamics in neuronal networks may be better understood by characterizing their connectivity and how this connectivity changes over time or in response to inputs and perturbations. Additionally, as discussed in detail by Shew and Plenz (2013), there is also much to be learned about the computational and functional benefits that criticality confers; thus, complementing graph theoretical and criticality metrics with an information theoretical approach can further shed light on the functional benefits of this dynamical regime.

Note that we aim here to focus on relevant considerations for empirical assessments of criticality in biological neural systems, particularly at the network level, and on how experimentalists may build upon the existing theoretical foundations to address the criticality hypothesis from a data-driven perspective. This review thus aims to provide the reader with basic insights on criticality and how it relates to neuroscience, rather than an in-depth discussion of the physics of criticality. Furthermore, we approach modeling studies with an eye on how they can inform our understanding of experimental systems but do not exhaustively review the vast field of model neural systems, as this is a topic of review unto itself.

In the remainder of this section, we present an overview of the theoretical benefits of criticality and experimental evidence supporting its emergence in living neural systems. The next section then focuses on the intersection between network neuroscience and criticality and discusses the connectivity features that can support critical dynamics. In the subsequent section, we consider the plasticity mechanisms that allow these networks to form, learn in response to inputs, and remain stable against perturbation or failures in the network. Finally, we conclude with a discussion of how approaching the study of criticality with a diversity of perspectives may prove more fruitful than any single directed approach.

Why Is Criticality Important?

The term self-organized criticality was coined as such to reflect the similarity of this phenomenon with the critical point observed in phase transitions in statistical mechanics, wherein a parameter, such as temperature, can be tuned to bring the system to a state between multiple phases of matter (Bak et al., 1988). However, a crucial point that distinguishes self-organized criticality from the conventional critical point in statistical mechanics is that the system tunes *itself* to criticality without the need for external tuning via a control parameter. In a self-organized critical system, the critical point is an attractor, meaning the system tends to evolve toward that point from a wide range of starting points; to again consider the parallel with thermodynamic criticality, if a thermodynamic system were to show self-organized criticality, intrinsic mechanisms would drive the system to return to the critical point between the liquid, solid, and gaseous phases. Obviously this is not the case, as matter in each of these phases can exist stably, but there are many fascinating properties conferred by criticality, as we will discuss in this section.

Many natural systems have been observed to show critical or critical-like behavior (Paczuski et al., 1996; Chialvo, 2010), including forest fires (Malamud et al., 1998; Buendía et al., 2020; Palmieri and Jensen, 2020) and flocks of birds (Cavagna et al., 2010), which has led researchers to explore the possibility

BOX 1 | Cellular automata at the "edge of chaos."

A binary cellular automaton (CA) is an n-dimensional array of binary cells whose states are updated synchronously in discrete time steps. The state of each cell at time $t + 1$ depends on the states of the cells in its neighborhood at time t. Such CAs are among the simplest systems to show complex behavior. Langton (1990) used the binary CA as a lens to assess the conditions under which a physical system may show the capacity to support computation. In a sweep of the possible rulesets for a one-dimensional binary CA, he demonstrated that a small subset of rules produce behavior compatible with the necessary tenets of computation, namely, the storage, transmission, and modification of information.

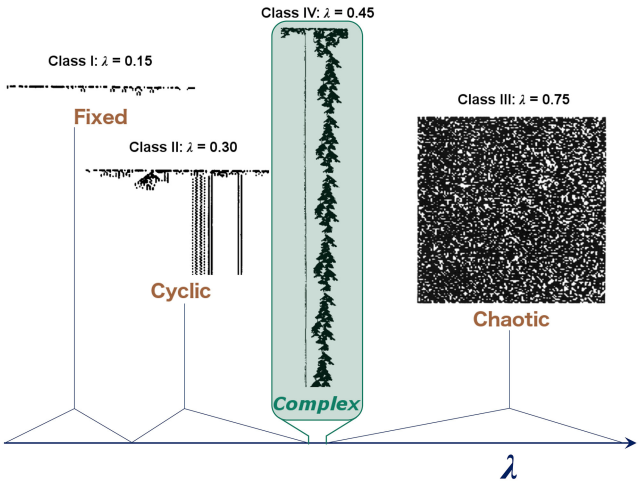

FIGURE 1 | Illustrative examples of the behavior observed in different classes of one-dimensional binary CAs. In these CAs, each row represents the CA at a given time step, and the two states of the cells are represented by black and white. Complex behavior arises in the critical regime, which becomes vanishingly small as the system increases in size. Langton (1990) characterized these CAs with the λ parameter, which represents the ratio of transitions to an arbitrary state selected as the "quiescent state." Adapted from Langton (1990).

Examples of different "classes" of CA (Wolfram, 1984) corresponding to different dynamical regimes are shown in **Figure 1**, with class IV representing a transitional state analogous to criticality. He also demonstrated that these CAs occupy a small region, where mutual information is maximized at a point of intermediate entropy. This maximal mutual information indicates that these CAs at the "edge of chaos" have struck a balance between the competing needs of information storage, which requires low entropy, and information transmission, which requires high entropy, thereby allowing complex patterns of activity to propagate through the system over time and space without rapidly dying out or overwhelming the system. Despite its simplicity, the CA demonstrates how some sets of rules balancing quiescence and transmission can lead to complex patterns that allow for the transfer of information, an appealing property for neural systems.

of a similar phenomenon in the brain in a conjecture known as the criticality hypothesis (Beggs and Plenz, 2003; Beggs, 2008). This hypothesis states that the brain self-organizes into the critical state in order to optimize its computational capabilities.

The canonical sandpile model by Bak et al. (1987, 1988) describes a system slowly driven by the addition of grains of sand until an instability occurs and the sand is redistributed to restabilize the system. Because of the dynamical minimal stability of the system, the chain reactions set off by the external drive, with sand traveling from site to site until the system restabilizes, called "avalanches," display the self-similar power-law scaling mentioned above. This means that the disruption of a single element in the system has a small but non-zero chance to change the state of the whole system. Work on emergent properties of dynamical systems has indicated that systems tuned to the critical regime show optimal information processing capabilities (Langton, 1990; Shew et al., 2009, 2011; Plenz, 2012; Shew and Plenz, 2013).

To provide a conceptual image of the complex behavior that can arise from even very simple parts and lay a foundation for how computation can emerge in such a system, we consider as an illustrative example the binary cellular automaton (CA), a system consisting of many stationary binary cells whose behavior is influenced by the states of the cells in their immediate neighborhood. **Box 1** gives a brief definition of the CA and summarizes the important findings obtained by Langton (1990) in his work on how computation may emerge in physical systems at the "edge of chaos." It should be noted, however, that although this regime was initially assumed to exhibit a continuous second-order phase transition, as classically described for critical dynamics, it has recently been found to show a discontinuous first-order transition (Reia and Kinouchi, 2014, 2015). In a vanishingly small region in the state of all possible CAs of the type Langton (1990) considered, quite interesting behavior emerges: complex patterns of activity are preserved over long distances in space and time. In the regime between the two extremes of quiescence and disorder (Kinouchi and Copelli, 2006), the system optimizes its capacity to perform the functions of information transmission, modification, and storage that are necessary to support computation.

Although the transition hypothesized to occur in neural systems is distinct from the "edge-of-chaos" transition shown in **Box 1**, the features captured in this simpler system can help us understand why the dynamics at phase transitions may be relevant for information processing in the brain. In the transitional regime, patterns of activity are preserved over space and time, which means that spatially disparate elements of the system can communicate with each other and that informational representations are propagated in time. Different inputs produce distinguishable outputs, allowing systems near criticality to respond to stimuli in a meaningful way. These concepts underlie how information is encoded and transmitted in dynamical systems at criticality and highlight how studying criticality in experimental studies on neural computation can inform our understanding of how the brain processes information.

What does this have to do with computation? In a general sense, computation is a process, either natural or artificial, by which information is communicated and manipulated to produce some kind of meaningful behavior in a system (Denning, 2007). More concretely, computation is the act of solving a "computational problem": a set of related questions with given information (input), each with its own distinct answer (output). Criticality has been found to optimize characteristics related to better performance at solving computational problems. For example, recurrent network models showing critical dynamics outperform their sub- and supercritical counterparts in terms of their input-to-output mappings; that is, the outputs produced from different inputs are more separable, or distinguishable, in critical networks (Bertschinger and Natschläger, 2004). Critical systems also show a maximal dynamic range (Kinouchi and Copelli, 2006; Gautam et al., 2015), which is the span of inputs distinguishable by the system. Additionally, the number of metastable states is maximized in networks with a critical branching ratio (Haldeman and Beggs, 2005), where a metastable state is defined as a cluster of similar output patterns produced by the same input. Information transfer and storage, represented, respectively, by the information shared between a source node and a destination node and that between a node's past and future states, is also optimized at criticality (Boedecker et al., 2012).

Although criticality is recognized to optimize many properties associated with computation, as discussed above, it should also be noted here that there are also some properties associated with criticality that may run counter to computational function in the sense described here (Wilting and Priesemann, 2019a). For example, the maximal dynamic range of a system in the critical state causes the specificity of the system to suffer; that is, a system that can sensitively respond to a wide range of inputs also shows more overlap between responses to similar inputs (Gollo, 2017). Thus, recent research has shifted from a singular focus on criticality to a broader realm of dynamical possibilities, including heterogenous networks composed of both critical and slightly subcritical subgroups (Gollo, 2017), the presence of a "reverberating regime," enabling the task-dependent switching or combining of critical and slightly subcritical dynamics to enjoy the benefits of both states (Wilting et al., 2018), and the concept of self-organized quasi-criticality, which accounts for non-conservative dynamics in systems that show critical-like behavior over a finite range of scales (Bonachela and Muñoz, 2009; Bonachela et al., 2010; Buendía et al., 2020; Kinouchi et al., 2020). These findings show promise for the advancement of a more detailed and physically accurate view of how criticality is realized in living neural systems; however, we refrain in this review from venturing too far into the details of these topics and direct the interested reader to the cited literature.

Experimental Evidence of Criticality in Neural Systems

Beggs and Plenz (2003) were the first to experimentally demonstrate that the spontaneous behavior of *in vitro* cortical networks displays features consistent with critical dynamics in their landmark study on neuronal avalanches in cortical slices interfaced with microelectrode arrays (MEAs). At its most general, a neuronal avalanche extends over the duration of persistent activity propagating through the network and is punctuated by silent periods preceding and following the active period, as shown in **Figure 2A**. In the case of *in vitro* systems (i.e., slices or dissociated cultures), "activity" may refer to either the higher-frequency spikes or the lower-frequency local field potentials (LFPs), as both modalities have been studied (e.g., Beggs and Plenz, 2003; Pasquale et al., 2008). Criticality has also been studied at the macroscale using electroencephalography (EEG) (e.g., Meisel et al., 2013; Lee et al., 2019).

Regardless of the scale or method of data collection, one main hallmark of criticality is that neuronal avalanches show power-law scaling in both space and time, with sub- and supercritical behavior being characterized by exponential and bimodal distributions, respectively. Beggs and Plenz (2004) demonstrated that neuronal avalanches show diverse spatiotemporal patterns that are stable over several hours, highlighting their capacity to represent a wide range of information in a reproducible manner. It should be noted that a simple power-law fitting alone is not sufficient to identify criticality (Goldstein et al., 2004; Priesemann and Shriki, 2018); in fact, this was far from the only approach used by Beggs and Plenz (2003), who also evaluated the branching ratio and the effect of using only a subset of all recording points. In addition to the methods first used by Beggs and Plenz (2003), a number of criticality measures have since been put forward. Providing empirical evidence of criticality is challenging, and it is suggested that a range of measures be applied (Priesemann and Shriki, 2018); we present a selection of some such measures in **Box 2**.

Avalanche behavior during development was first observed in organotypic cortical cultures by Stewart and Plenz (2008), and they found that avalanches persisted throughout development over periods of up to 6 weeks *in vitro*, despite large changes in activity levels, suggesting homeostatic regulation to maintain this mode of activity. It has also been demonstrated that dissociated cortical networks may self-organize into the critical state after a period of maturation, though not all such networks reach the critical state and reports on the time course of maturation differ (Pasquale et al., 2008; Tetzlaff et al., 2010; Yada et al., 2017). The reported results on dissociated networks suggest that after a period of low activity, networks tend to pass

BOX 2 | Experimental metrics of criticality.

To pursue further investigation of the criticality hypothesis, we must be armed with the appropriate tools for identifying a network's dynamic state. Power laws are notoriously challenging to handle in empirical data (Clauset et al., 2009) and can also arise in non-critical systems (Martinello et al., 2017; Touboul and Destexhe, 2017; Priesemann and Shriki, 2018). Thus, additional measures are needed to accurately identify when a network is in the critical state, and each measure should also be applied to appropriate null models for comparison. This box lists the main approaches currently used to identify criticality from empirical data, but it should be noted that the development of such methods remains an active area of research. Some of the measures listed below have been implemented in a freely available MATLAB toolbox called the Neural Complexity and Criticality Toolbox (Marshall et al., 2016), and detailed statistical analysis for fitting and analyzing power-law distributions can be performed with an open Python package called powerlaw (Alstott et al., 2014).

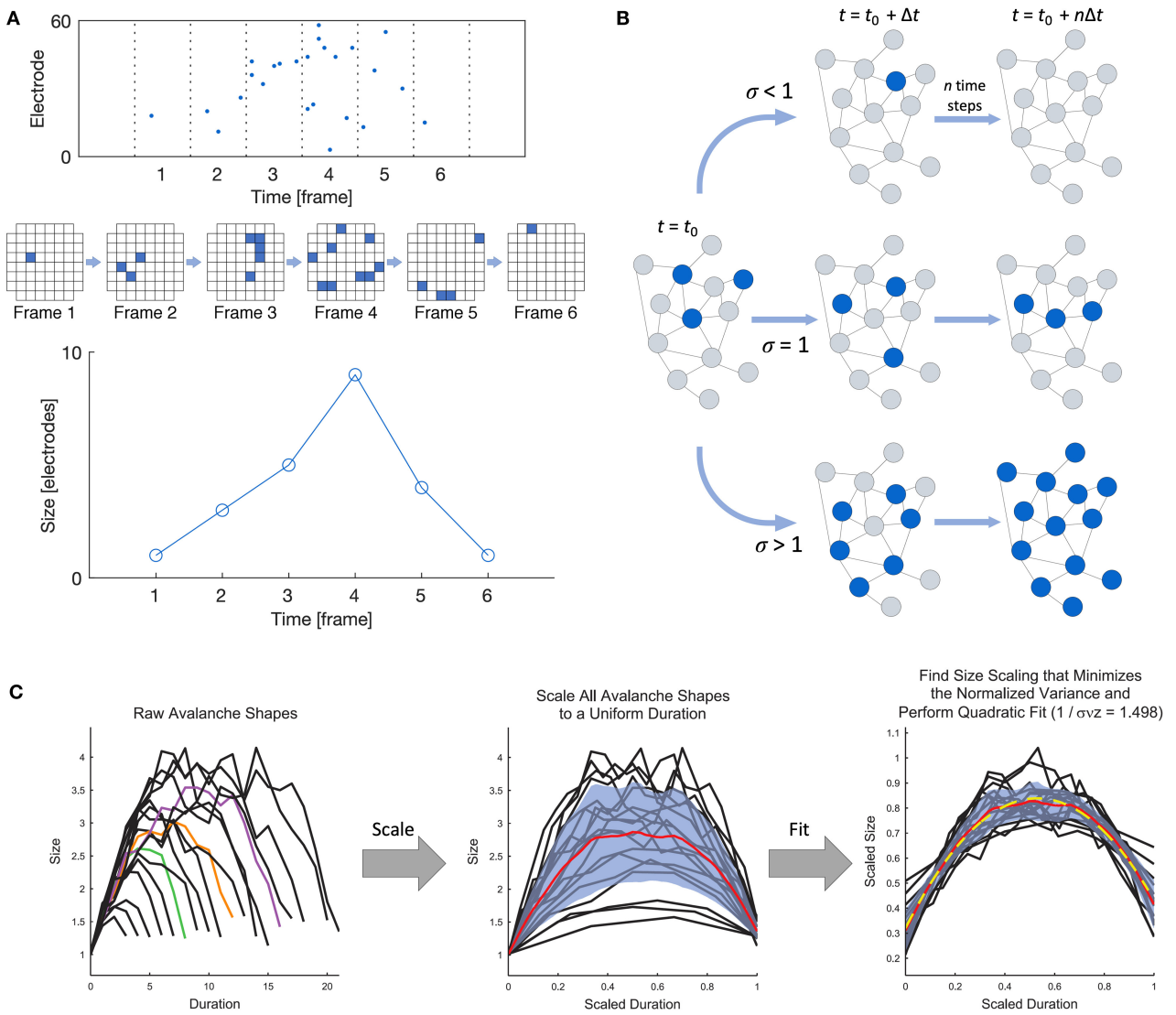

FIGURE 2 | Definition of a neuronal avalanche and examples of empirical measures of criticality. **(A)** Definition of a neuronal avalanche. The top panel shows a raster plot divided into time bins, and the avalanche in the plot spans six active frames preceded and followed by inactive frames. An alternate view of the activity in the six frames is shown below, where each square represents an active electrode in an 8 × 8 grid. The bottom panel shows the definition of the avalanche shape, which is obtained by taking the number of active electrodes in each frame. **(B)** Illustration of the branching ratio. Blue nodes are active, and gray are inactive. A branching ratio of 1 allows activity to persist without overwhelming the system. **(C)** Shape collapse. In a critical system, all avalanches should show the same mean temporal shape profile across different size scales. Adapted from Marshall et al. (2016).

- *Power-law scaling of neuronal avalanches*: One hallmark of criticality in neuronal networks is the power-law scaling of the size S and duration T of neuronal avalanches. That is, $P(S) \propto S^{-\alpha}$ and $P(T) \propto T^{-\beta}$, where $P(\cdot)$ is the probability distribution function. The size is generally defined as the number of activated electrodes or neurons, and the duration is the number of active time bins. When the time bin width is selected to correspond to the average inter-spike interval, the power law exponents of the size and duration have been shown to be approximately $\alpha = 1.5$ and $\beta = 2.0$. However, the power-law scaling should persist

(Continued)

BOX 2 | Continued

across a range of temporal resolutions close to the order of magnitude of the average inter-spike interval, with the exponent α changing systematically with the selected time bin size (Beggs and Plenz, 2003; Pasquale et al., 2008). Power-law scaling should also remain when a more coarse-grained spatial resolution is considered, by using only a subset of all recording points. As stated above, there is an open Python package called powerlaw that can be used for detailed statistical analysis of power-law distributions (Alstott et al., 2014). As an additional power-law related metric, the κ parameter (Shew et al., 2009) gives a quantitative measure of the difference between the experimental and fitted cumulative probability distributions when using power-law fitting.

- *Branching ratio*: The branching ratio σ is the ratio of the number of descendants to the number of ancestors, where activity on an ancestor electrode or neuron immediately precedes activity on a descendant electrode or neuron (Beggs and Plenz, 2003). A system in the critical state has a branching ratio of approximately 1, allowing activity to flow through the network without dying out ($\sigma < 1$) or overwhelming the entire network ($\sigma > 1$), as shown in **Figure 2B**. A modified version of the branching ratio that is specific to LFP data has also been introduced, where the ratio is instead taken between the baseline-to-baseline areas of the negative LFP deflections (nLFPs) in successive time bins, rather than the number of nLFPs (Plenz, 2012). The nLFP area is correlated with the number of neurons firing and thus provides a better measure of group activity during an avalanche than the nLFP count.
- *Shape collapse*: When a system is in the critical state, avalanches should show the same mean temporal profile across scales. The temporal profile of an avalanche represents the number of active sites as a function of time, and for a system in the critical state, the temporal profiles of all avalanches collapse onto the same profile shape when spatiotemporally scaled with a scaling exponent γ close to 2 (**Figure 2C**), as described by $\langle S \rangle(T) \propto T^{-\gamma}$, where $\langle S \rangle(T)$ is the average size of all avalanches of a given duration T. Details can be found in Sethna et al. (2001) and Friedman et al. (2012), and an experimental demonstration of shape collapse in non-human primates can be found in Miller et al. (2019). The deviation from criticality coefficient (DCC) by Ma et al. (2019) is related to the concept of shape collapse and is computed from the difference between the scaling exponent γ calculated from empirical data using linear regression and the expected value calculated from the power-law exponent α of the size distribution.
- *Spatial subsampling*: Because of the nature of observing neuronal systems, only a subset of the system components can be sampled. This spatial subsampling can sometimes lead to erroneous conclusions about the nature of the system's underlying dynamics. Methods involving the scaling of spatial subsampling (Levina and Priesemann, 2017) and a subsampling-invariant estimator (Wilting and Priesemann, 2018) have been developed to allow for the evaluation of dynamic states of subsampled systems.
- *Other measures*: Some researchers have developed other quantitative measures to describe the dynamical state of the system. One notable example is the use of statistical scaling laws related to a phenomenon called "critical slowing down," which refers to the tendency for systems to require more time to recover from a perturbation the closer they are to criticality (Meisel et al., 2015a). Additionally, detrended fluctuation analysis (DFA) offers a framework to understand scale-free oscillations in a range of systems (Hardstone et al., 2012).

through periods of first subcritical then supercritical behavior before settling into the critical state, though not all networks reach this state. This behavior has been hypothesized to stem from an initial overproduction of connections followed by a period of pruning excess connections (Pasquale et al., 2008; Yada et al., 2017). Additionally, experiments in which chemical perturbation is applied to increase excitation or inhibition in the network indicate that networks at criticality exhibit a balanced excitation-to-inhibition (E/I) ratio (Shew et al., 2009, 2011; Heiney et al., 2019). Together, these experimental findings point to the importance of a balance in both network structure and network dynamics to achieve criticality.

Shew et al. (2009, 2011) have explicitly linked the dynamic state of a cortical network with its information processing capacity by demonstrating that networks at criticality show maximal dynamic range, information transmission, and information capacity in comparison with their counterparts in the sub- and supercritical states. These properties harken back to the original requirements posed by Langton (1990) for a system to be capable of computation and further emphasize the role of the dynamical state in governing the functional behavior of a neuronal network. These studies highlight the functional benefits conferred by the critical state and give credence to the criticality hypothesis (Shew and Plenz, 2013). But how does a system organize itself to become capable of supporting critical dynamics? In the following sections we explore the relationship between the structure of a network and its dynamical behavior and consider the plasticity mechanisms that form and maintain target structures.

CRITICALITY AND NETWORKS

Biological neural networks are interconnected networks of individual information processing units (neurons). When considering how information is processed within the network, it is vital to understand the interactions of the individual units, the organization of the brain network, and the integration of activity of widely distributed neurons (Bressler and Menon, 2010; van den Heuvel and Sporns, 2013). Underlying the aggregate activity of groups of neurons are the structural and functional connectivity of the network, which determine where signals pass and which neurons act in consort (Sporns, 2002; Womelsdorf et al., 2007). This in turn influences the information processing capabilities of neural networks, and network structure therefore contributes to determining the emergence of critical properties in neural networks. The question is then how the organization of biological neural networks can support critical dynamics to optimize computational efficiency. This section examines a selection of experimental and simulation-based studies that address this question.

Network Neuroscience

The application of modern network science to the brain and networks of neurons has flourished over the past two decades. The complex network of the brain has information processing as its primary goal and attempts to maximize this capacity while under multiple constraining influences, such as availability of space, energy, and nutrients, and thus must strike a balance between computational capacity and wiring cost (Laughlin and

Sejnowski, 2003; Cuntz et al., 2010). These two factors are often in a tradeoff relationship; for example, direct connections facilitate the most effective signal transmission, but the long-range connections this requires are very costly to grow and maintain (Buzsáki et al., 2004). Additionally, the network must meet the changing demands of the organism while remaining resilient to damage to or failure of parts of the network, such as the loss of neurons or the connections between them (Pan and Sinha, 2007). Some of the basic network science principles that are commonly applied in neuroscience studies are highlighted in **Box 3**.

Multiple lines of evidence now show that brain networks have a small-world organization, with high local clustering and low average path length, which facilitates segregated local specialization and global integration. Low-cost, short-range connections dominate, while a smaller number of long-range connections allow for few intermediaries between distant components (Bullmore and Sporns, 2012). Brain networks also show evidence of link clustering, where strong connections preferentially form between nodes with similar neighborhoods (Pajevic and Plenz, 2012). Some evidence also indicates brain networks are scale-free, with a heavy-tail degree distribution that follows a power law (Eguíluz et al., 2005). Components with high degrees furthermore tend to connect to other high-degree components in a "rich club," which are hub regions of high connectivity that facilitate integration across distinct areas and wide propagation of signals and information (Sporns, 2013). The central nervous system (CNS) is also divided into specialized areas at multiple levels, from brain lobes to smaller but separate modules within these lobes, which can again be subdivided into further modules. This is characteristic of hierarchical modularity, which facilitates flexibility in adaptation because it can incorporate changes within a single module without affecting other, nearby modules. This makes the system at the same time robust and flexible (Meunier et al., 2010). The combination of these network architectures—small-world, scale-free, and modular—creates an efficient network well-suited for computation, as will be discussed in the following section.

Neural Network Topology Facilitates Criticality

Modeling work has provided evidence that the network features outlined above contribute to the emergence of critical dynamics as a means to support computation in networks of neurons. This provides some motivation to translate these findings into the experimental realm, but little work has been done thus far in this regard, despite the expanding experimental work on criticality, as already detailed above, and the large body of work on network neuroscience (Bassett and Sporns, 2017). However, one noteworthy methodological study has identified small-world organization in the effective (causal) connectivity of a cortical slice culture (Pajevic and Plenz, 2009). With further applications of such measures of connectivity to assess avalanche propagation *in vitro*, it will be possible to evaluate if network features found to be beneficial in modeling studies, such as small-worldness, can be experimentally confirmed. In this section, we will examine criticality and complex network features, but it should also be noted that criticality can also be demonstrated in random (Kinouchi and Copelli, 2006; Costa et al., 2015; Campos et al., 2017) and complete (Levina et al., 2007; Bonachela et al., 2010; Brochini et al., 2016; Costa et al., 2017; Kinouchi et al., 2019; Girardi-Schappo et al., 2020) networks. In a study specifically examining the impact of network structure on network dynamics *in silico*, Massobrio et al. (2015) showed that random network topology can only support power-law avalanche scaling under a narrow range of synaptic constraints and firing rates. Furthermore, of the topologies they investigated, only scale-free networks with a high average node degree and small-world features were able to display behavior consistent with experimental criticality.

Simulation studies on complex networks have found that features of criticality can emerge with biologically plausible regulatory mechanisms. Shin and Kim (2006) found that, for a network initialized as complete, i.e., fully connected, and allowed to change its connections over time by spike-timing-dependent plasticity (STDP), the network reorganizes into a scale-free network with small-world properties that shows evidence of self-organized criticality. Other studies have also found that concurrently scale-free and small-world networks recapture critical dynamics with exponents comparable to those found experimentally (Lin and Chen, 2005; Pellegrini et al., 2007; de Arcangelis and Herrmann, 2012). Complementary to this, Rubinov et al. (2011) demonstrated that a hierarchically modular structure with a preponderance of within-module connections, which have a relatively low wiring cost, produced a much broader critical regime than was observed in corresponding non-hierarchical networks. It has also been shown that in the Bak–Tang–Wiesenfield (BTW) model, also referred to as the "sandpile" model, self-organized criticality emerges as a result of the formation of modular clusters with biologically relevant dimensions, lending further evidence to the importance of modular network structures (Hoffmann, 2018).

When focusing on the activity of ensembles of neurons, it is common to consider bursting activity that encompasses multiple units and how these units coordinate their activity. In dissociated cortical neurons, networks that spontaneously develop critical dynamics display a level of synchrony higher than what is seen in uncoordinated subcritical activity but lower than that seen in highly regular supercritical activity (Pasquale et al., 2008; Valverde et al., 2015; Cocchi et al., 2017). This is also consistently reported in modeling studies and can be related to the branching ratio, or how many downstream neuronal responses are elicited by a single active neuron (**Box 2**). When the branching ratio is balanced near 1, the network is in a state of intermediate synchrony and tends to display critical avalanche dynamics in a way that maximizes the number of adaptive responses the network can produce to stimulus (Haldeman and Beggs, 2005; Shew and Plenz, 2013). However, despite bursting activity often being considered highly coordinated, critical networks *in vitro* have been observed to show more burst-dominated activity than their supercritical counterparts, with critical networks showing a higher proportion of spikes contained in bursts and an

BOX 3 | Benefits of network topology.

Network neuroscience encompasses an approach to studying brain function that considers the ways in which neurons communicate, anatomically and functionally, across multiple scales (Bassett and Sporns, 2017). It is informed by complex systems theory, which states that the emergent behavior of a system cannot necessarily be understood simply by the properties of its individual components. It further applies mathematical techniques such as graph theory and algebraic topology to describe networks (graphs) in terms of their individual units (nodes) and their connections (edges). A node in this context can be a brain area, a single neuron, a recording electrode, a voxel, pixel, or any unit which describes the activity of a discrete part of a neural network. Edges can be physical connections obtained from connectivity mapping or functional connectivity based on correlation or other measures (Bullmore and Sporns, 2009). This approach has yielded great insight into how the brain is organized and how communication within brain networks occurs (Newman, 2003). While numerous methods exist for extracting the structural, functional, effective, weighted, or binary networks from living neural systems (for a review see Bullmore and Sporns, 2009; Bastos and Schoffelen, 2016; Hallquist and Hillary, 2018), there are several features among these considered to play an important role in neuronal organization and function.

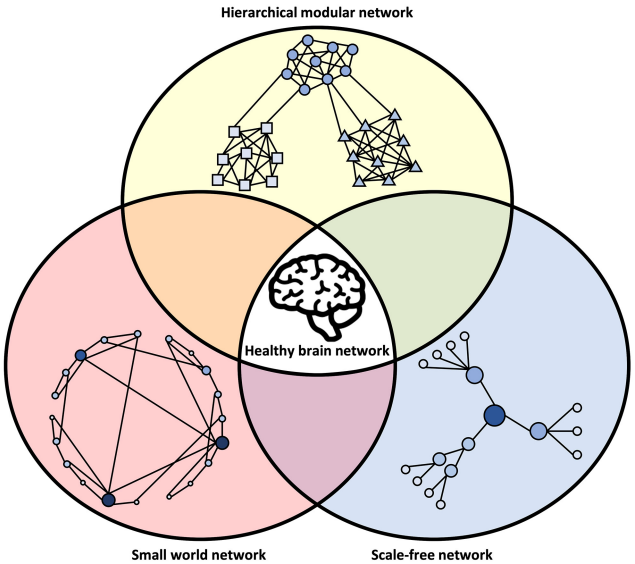

FIGURE 3 | Network characteristics associated with healthy brain networks. In normal conditions, brain networks show hallmarks of multiple network models. This includes an intermediate state between order and randomness in small-world organization, the power-law degree distribution of a scale-free network, and modular clusters organized in a hierarchical fashion. The integration of these different network types may be an evolutionary adaptation driven by the multi-constraint optimization of brain wiring. Deviations from the hallmarks of these network structures may be associated with abnormal brain function and disease.

Small-World Network: A small-world network is typically defined by how closely it approaches the small world ideal of high clustering and low characteristic path length (Watts and Strogatz, 1998). One way to produce a small-world network is to begin with a regular (or lattice) network, where each node is connected only with its nearest neighbors, and, with probability p, rewire each connection in the network to a randomly chosen node elsewhere in the network. When $p = 1$, every connection is rewired, and the result is a random network. However, at intermediate rewiring probabilities, the characteristic path length drops off drastically, showing that only a few long-range connections are necessary to facilitate the integration of the network. Additionally, the clustering of nodes remains high, retaining the local specialization of the original regular network. These properties make small-world networks highly advantageous for computation while reducing wiring cost (Chklovskii et al., 2002), essentially reducing the number of connections without sacrificing the capacity for network-wide communication (Bassett and Bullmore, 2017).

Scale-Free Network: In a scale-free network, the probability distribution of the node degree, which is the number of edges connected to each node in the network, follows a power law, meaning most nodes have a small number of edges and few nodes have many (Barabási and Albert, 1999; Eguíluz et al., 2005). These high-degree nodes are often called hubs, and they serve an important role in integration across the network (Sporns et al., 2004). Hubs make a scale-free network more robust to random deletion of nodes but susceptible to targeted damage of the hub nodes (Albert et al., 2000). Especially vulnerable (but not exclusive to scale-free networks) is the rich club (Zhou and Mondragón, 2004), a group of hubs with a high degree of interconnectivity between each other. While there is growing evidence for the presence of rich-club topology in the brain (Griffa and Van den Heuvel, 2018; Kim and Min, 2020) the presence of scale-free topology (Bonifazi et al., 2009) is still somewhat controversial, but it provides important insight in modeling studies of dynamics on network topology (Broido and Clauset, 2019).

Hierarchical Modularity: A modular network is characterized by the presence of clusters of nodes that are densely connected with each other and share few edges with nodes outside the cluster. In a hierarchically modular network, these clusters can be subdivided into other clusters according to the same principle, often over multiple scales (**Figure 3**). Modules are interconnected by connector nodes, which may or may not be hub nodes, allowing dissemination of signals and integration of information across the system. Modular networks may be more robust to dynamic change within the network. The intricacies of hierarchical modularity and its relation to other network topologies such as the rich club (McAuley et al., 2007) are extensive and, as such, beyond our scope here (for a review, see Meunier et al., 2010).

It is important to consider that the network models described above are not mutually exclusive. Rather, it appears that the brain displays hallmarks of all these network types (Bullmore and Sporns, 2009) and that deviations from their properties can be involved in disease (Stam, 2014), as illustrated in **Figure 3**.

intermediate level of synchrony within those bursts (Pasquale et al., 2008).

A biological constraint for the branching parameter is the level of inhibition present as mediated by inhibitory interneurons (Girardi-Schappo et al., 2020). In the human cortex, 15–30% of neurons provide local inhibition, and this E/I ratio is frequently replicated in *in silico* models by tuning the number of inhibitory nodes and their connectivity within the network (Rudy et al., 2011; Tremblay et al., 2016). In both models and biological networks, inhibitory nodes typically constrain their connectivity within modules or clusters. In examinations of this inhibitory connectivity, it has been found that local inhibitors are necessary for critical dynamics in systems combining modularity and plasticity (Rubinov et al., 2011). Furthermore, Massobrio et al. (2015) tested a wide range of E/I ratios on scale-free networks and were only able to achieve critical dynamics in networks with inhibitory nodes comprising 20–30% of all nodes. They also observed the effect of the E/I ratio of the hub nodes specifically and found that the same ratio of approximately 30% inhibition in the hubs was able to support critical dynamics across a wide range of mean degrees, whereas none of the fully excitatory hub networks displayed critical behavior. In models and in the brain, this balance of excitation and inhibition acts as a countermeasure against runaway excitation and stabilizes the network dynamics (Fingelkurts et al., 2004; Shin and Kim, 2006; Meisel and Gross, 2009; Naudé et al., 2013; Salkoff et al., 2015). Furthermore, through the careful tuning of the E/I balance, multiple dynamic states can also be achieved in the same model (Li and Shew, 2020).

The Brain May Operate in a Critical Region, Not at a Critical Point

While the criticality hypothesis of the brain is attractive because it provides a model for brain activity that optimizes information processing and storage, aspects of the model are difficult to reconcile with knowledge of the brain's activity. For instance, the brain's activity and dynamics are not constant but fluctuate widely depending on multiple factors. That this widely variable and adaptable dynamic system can be tuned to a specific critical *point* can therefore seem counterintuitive. However, a finite system at criticality does not have to be tuned to a specific point but rather exhibits critical behavior over a particular region. The phase transition can be continuous, such that there exists a range of states within the system that support critical dynamics (Hesse and Gross, 2014). This extended model of criticality appears much more compatible with our knowledge of the brain's dynamics than the notion of a strict critical point. One such form of critical range is referred to as the Griffith's phase and appears to be facilitated by hierarchical, modular network architectures, which are consistent with the previously investigated small-world architecture of the brain (Gallos et al., 2012; Moretti and Muñoz, 2013; Ódor et al., 2015; Girardi-Schappo et al., 2016). A wide critical range would appear to be advantageous for the network, making the critical dynamics more robust against failure or perturbation than in the case where criticality can only be achieved in a narrow range or single point (Li and Small, 2012; Wang and Zhou, 2012). This range appears to be dependent on the level of structural heterogeneity or disorder within the network, including variance in the node in-degree distribution (Muñoz et al., 2010; Wu et al., 2019).

Additionally, as mentioned in the section on the importance of criticality, recent evidence suggests that a strict adherence to criticality may not be the sole aim of network organization (Wilting and Priesemann, 2019a). On the basis of these findings, it has been hypothesized that some brain networks may self-organize to points in a slightly subcritical range, where they could then flexibly tune their dynamics in accordance with the demands of a given task (Wilting and Priesemann, 2018; Wilting et al., 2018). Following this hypothesis, certain tasks may benefit from a reduced dynamic range in the network to subsequently reduce interference from non-task-specific inputs. Networks may also show heterogeneous local dynamical states, with a mixture of critical and subcritical regions balancing the competing demands for specificity and sensitivity (Gollo, 2017).

Although we have highlighted in this review how the underlying network structure may influence the emergence of critical dynamics here, it is not evident that these topological features are in and of themselves necessary for a network to be considered critical. As mentioned, simulation studies have found that power-law avalanche scaling can be obtained in regular, random, and small-world networks (de Arcangelis and Herrmann, 2012; Michiels Van Kessenich et al., 2016), and regardless of the edge directedness or the presence of inhibitory edges (Ódor and Kelling, 2019). Furthermore, it is possible to achieve power-law avalanche scaling in networks with only weak pairwise correlations and not the more complex patterns of functional connectivity seen in biological networks (Thivierge, 2014). The relationship between critical dynamics in the brain and its underlying network structure may therefore reflect a balance between computational capacity, the metabolic cost of the network activity (Thivierge, 2014), wiring cost in network development (Laughlin and Sejnowski, 2003; Cuntz et al., 2010), and the resilience of the network against perturbations (Goodarzinick et al., 2018). Though certain complex network topologies may better accommodate and broaden the range of critical dynamics (Li and Small, 2012; Moretti and Muñoz, 2013), they are only one component of a neural system.

PLASTICITY IS NECESSARY TO ACHIEVE AND MAINTAIN CRITICALITY

How efficient network structures are formed in different dynamical systems varies widely from system to system, and numerous models have been developed to describe the growth of efficient networks. The first general model for scale-free network formation was proposed by de Solla Price (1965) and popularized by Barabási and Albert (1999). Through the addition of nodes as the network evolves, each new node is preferentially attached to an existing node with high connectivity, resulting in a "rich-get-richer" hub formation and power-law-distributed connectivity. However, such models cannot represent neural growth, as they forego an important consideration of neural network formation: self-organization

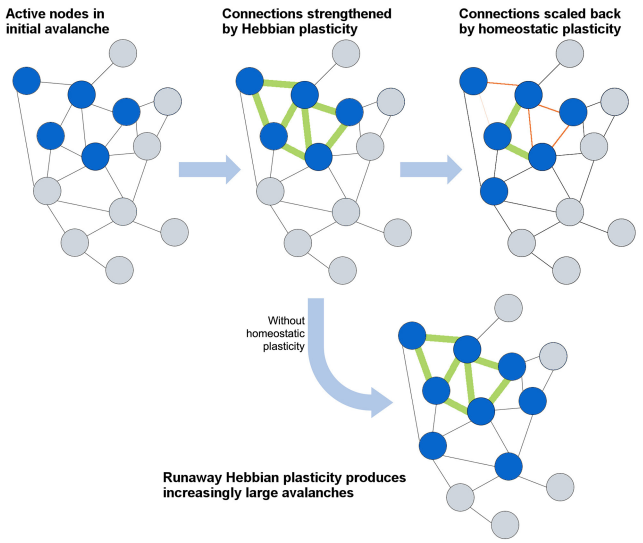

FIGURE 4 | Schematic overview of the interplay between Hebbian and homeostatic plasticity. Hebbian plasticity serves to strengthen and form connections between neurons that fire together, whereas homeostatic plasticity maintains a balance in connections and activity levels. The lowermost case demonstrates how an absence of homeostatic plasticity would allow runaway Hebbian plasticity to overwhelm the network with activity.

into an efficient topology depends not only on the connectivity but also on synaptic strength, E/I ratio, and, vitally, the plasticity that defines all of these network parameters. In this section, we will first focus on the role of plasticity in activity-dependent network formation and then consider how networks maintain the critical state through homeostatic plasticity (Stepp et al., 2015). The interplay between activity-dependent and homeostatic plasticity is schematically illustrated in **Figure 4**.

Establishing Critical Dynamics in Neuronal Networks

Whereas network models may be constructed in a variety of ways to display critical dynamics and scale-free structures, actual neuronal networks form and maintain connections under numerous constraints. It is generally acknowledged that during development, neurons overshoot the number of necessary connections and then go through a phase of pruning before reaching a relatively stable state of connectivity (Low and Cheng, 2006). There is also evidence that cortical networks *in vitro* go through this same sequence of overshoot and pruning as they mature, and after this stage they may exhibit critical dynamics, though not all networks do (Stewart and Plenz, 2006; Pasquale et al., 2008; Yada et al., 2017). Van Ooyen et al. (1995) and Okujeni and Egert (2019) showed that a simple axon growth model assuming activity-dependent radial growth could form a network similar to those found *in vitro* by utilizing activity spontaneously arising in the network. Even with only a simple activity-dependent growth rule applied to systems with random initial placement, these systems have been shown to grow into a state supporting avalanches with power-law scaling in the behavior of the final networks (Abbott and Rohrkemper, 2007; Kossio et al., 2018). Correspondingly, the trajectory of the dynamic state *in vitro* appears to move from a subcritical to a supercritical state before ultimately reaching criticality. As the supercritical state in this case produces network-wide synchrony, it is probable that plasticity mechanisms reduce the global excitation level as a result of this synchrony and drive the network toward criticality. To mimic some of this development, numerous models have attempted to generate critical networks using plasticity rules applied to random, small-world, and scale-free topologies (de Arcangelis et al., 2006; Rubinov et al., 2011; de Arcangelis and Herrmann, 2012; Teixeira and Shanahan, 2014; Michiels van Kessenich et al., 2018, 2019). These models typically apply local Hebbian mechanisms, such as STDP, to rewire the network into a weight distribution or topology capable of achieving critical dynamics, thus recapitulating certain facets of biological network development.

Simple plasticity mechanisms based on correlated firing, such as STDP, can shift the topology of networks by changing the connection weights, resulting in directed and more complex networks. In observations of activity-dependent neural development in computational models, a number of researchers have observed the same general trend: that these mechanisms tend to drive the dynamics toward criticality, with the resulting topologies showing scale-free organization (Bornholdt and Röhl, 2003; Meisel and Gross, 2009). The end result is robust against different initial topologies and changes to the underlying parameters, such as average connectivity. Even when initializing a network from a random topology, STDP is sufficient in some models to drive the network toward critical dynamics (Teixeira and Shanahan, 2014; Li et al., 2017; Khoshkhou and Montakhab, 2019). Li et al. (2017) have also investigated the computational benefit of these STDP-trained networks, which showed improved input-to-output transformation performance at criticality (see also Bertschinger and Natschläger, 2004; Siri et al., 2007, 2008 for the computational benefits of criticality and Hebbian plasticity in recurrent neural networks).

Recent studies have furthered this modeling approach with the addition of more neurobiologically relevant features, such as axonal delay and hierarchical modularity. The inclusion of a time or axonal delay between pre- and post-target activation can shift both the directionality and distribution of synaptic strengths from a bimodal to a unimodal distribution without a loss of critical dynamics (Khoshkhou and Montakhab, 2019). Note that the potential of Hebbian mechanisms to produce critical dynamics is still model-dependent and can also drive the network to supercritical states. Again, the complexity of the network topology plays a vital role in conjunction with these mechanisms, as modular and hierarchical topologies both can counteract this supercritical organization and broaden the critical regime once it arises (Rubinov et al., 2011). Though neural development is an immensely complicated and complex process, Hebbian mechanisms appear to be one of many aspects that play a vital role in the

self-organization of neural networks toward criticality and supporting topologies.

Homeostatic Maintenance of the Critical State

Although learning and developmental mechanisms, such as STDP, drive networks toward certain configurations, the network patterns formed in this way are not simply static structures but also undergo plastic changes to maintain homeostasis and in response to external stimuli. A number of researchers have investigated how different forms of plasticity influence the dynamical state of neuronal networks (Rubinov et al., 2011; Stepp et al., 2015; Zierenberg et al., 2018; Ma et al., 2019).

A network's resilience to damage necessitates a level of adaptability to restore dynamics following a perturbation beyond that offered by topologies that are robust against component failure (see **Box 3**). This adaptability is hypothesized to stem from homeostatic plasticity, which provides feedback to restore the overall excitability in local connections and the network. Whereas Hebbian plasticity is evidenced to give rise to critical dynamics, homeostatic plasticity is evidenced to maintain the network activity within this dynamic regime despite varying input levels and intrinsic activity (Levina et al., 2007; Naudé et al., 2013; Ma et al., 2019). This adaptive excitability can be exemplified through the branching ratio. A steadily increasing input level would produce branching parameters exceeding 1, given the increasing level of extrinsic excitation on the system. Yet by homeostatic scaling of the excitability in the network and the input connections, the branching parameter can be maintained, avoiding supercritical dynamics. The inverse also holds true in the absence of inputs. Homeostatic plasticity acts toward an intrinsic set point for the network's excitability and adjusts synaptic response to maintain input specificity (Turrigiano, 2017). In the absence of homeostatic plasticity mechanisms, such as synaptic scaling, Hebbian mechanisms create feedback loops of excitatory response that remove any specificity to synaptic input (Wu et al., 2020).

Michiels van Kessenich et al. (2018, 2019) have included global homeostatic plasticity mechanisms in their network models to observe if the networks are able to exhibit avalanches with power-law scaling and evaluate the performance of the network on classification tasks. By feeding error back into the network based on the desired outputs at certain readout sites, they were able to train the network to recognize different input patterns, including classifying handwritten digits. The response of the network to inputs after this training period showed a clear spatial organization, with distinct regions responding to different inputs. Although the network studied here is a simplified computational model, the results indicate that plasticity mechanisms are able to drive networks toward criticality and play a role in their capacity for learning and computation. Also, as shown by Girardi-Schappo et al. (2020), the use of *multiple* homeostatic mechanisms can generate highly diverse firing patterns and promote the self-organization of a network toward a critical point. Additionally, as with Hebbian plasticity and criticality, the application of homeostatic mechanisms can enhance the computational capabilities of the network by tuning it toward criticality, and increasing both the number of input patterns that can be distinguished by the network and the separability of these patterns (Naudé et al., 2013).

The role of homeostatic mechanisms in maintaining critical dynamics is exemplified experimentally in a study by Shew et al. (2015). There is growing evidence that homeostatic mechanisms such as synaptic depression aid in allowing the visual cortex to adapt to changes in sensory input and recover critical dynamics. Using *ex vivo* preparations of the visual cortex, Shew et al. (2015) demonstrated adaptation of the cortex to stimuli; upon first exposure to a stimulus, the network transiently showed non-critical dynamics, followed by a return to criticality via homeostatic plasticity. In a critically tuned model of their network, an external input similarly drove the network out of a critical state, and critical dynamics were then restored through the implementation of a synaptic scaling rule, indicating a likely mechanism for the homeostatic adaptation. While this provides evidence for short-term tuning toward criticality, there is also recent evidence of long-term homeostatic adaptation. Thus far, studies including homeostatic mechanisms in criticality experiments and models have largely been focused on such synaptic mechanisms or the E/I balance, with only scant focus on intrinsic plasticity (Naudé et al., 2013; Li X. et al., 2018; Zhang et al., 2019; Girardi-Schappo et al., 2020) or metaplasticity (Kinouchi et al., 2020, in preprint; Peng and Beggs, 2013).

The effect of E/I imbalance has been well-described in previous studies, as mentioned previously; however, manipulation of the intrinsic mechanisms underlying the E/I balance have largely been unexplored (Plenz, 2012). Ma et al. (2019) attempted to bridge this experimental gap by examining a well-established model of homeostatic plasticity in the context of criticality. By systematically exploring the space of possible E/I configurations, Ma et al. (2019) demonstrated that the balance achieved by critical networks may be struck with a number of configurations—specifically, they varied the E/I ratio, the number of excitatory neurons receiving input from each inhibitory neuron, and the ratio of inhibitory neurons receiving input. This shows that different possibilities exist for how networks may be configured to achieve criticality, though only a small fraction of the potential combinations yielded critical activity. Furthermore, when a combination of E/I parameters adjacent to one of the critical regimes was selected and further explored by allowing the network to evolve under synaptic scaling and STDP, it was unable to achieve critical dynamics regardless of the plasticity parameters, demonstrating the importance of local inhibitory dynamics in achieving criticality.

Crucially, when synaptic scaling was removed from the model by Ma et al. (2019), the model was no longer able to recover critical dynamics after a reduction in input. With synaptic scaling removed from the excitatory population, reduction in input resulted in runaway activity and increased synaptic strength due to uncompensated STDP; removing synaptic scaling from

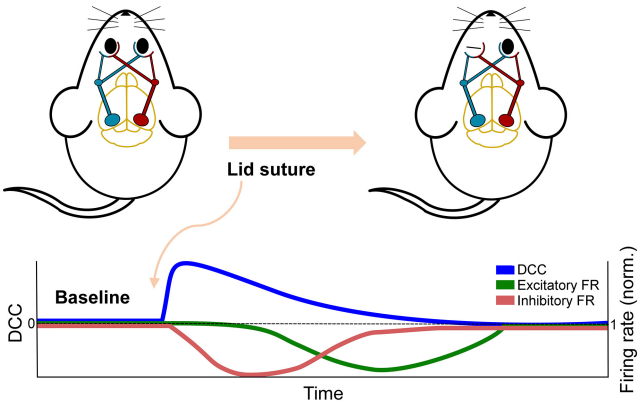

FIGURE 5 | Schematic overview of *in vivo* experiment from Ma et al. (2019). The overall firing rate of the network showed a delayed response to the perturbation of removing excitatory sensory input by monocular deprivation. In contrast, the DCC and other criticality-related measures showed an immediate response and a more rapid return to baseline.

inhibitory neurons also shifted the network out of the critical regime, though less dramatically, and was accompanied by a reduction in synaptic strength. In contrast, removal of STDP left the network unaffected by the reduction in input, indicating the necessity of this type of plasticity for the network to give a meaningful response to inputs.

BRAIN DISORDERS AND DISRUPTIONS TO CRITICALITY

Up to this point we have examined criticality's relationship to the network topology that supports it and the plastic mechanisms that organize and maintain it. Because of the intricate interplay of these underlying mechanisms, disruptions to either topology or plasticity can manifest as deviations in the dynamic state of the network, and as such, criticality analysis may aid in the identification of such disruptions and provide a better understanding of the mechanisms at play. In this section, we will detail studies that apply criticality analysis to the identification and prediction of diseases and disorders in the nervous system and propose suggestions for how to expand this work moving forward. Here we use the term "perturbation" in a medical sense to refer to disruptive and negative impacts to a network's baseline state, such as the severing of axons *in vitro* or epileptic states *in vivo*.

Criticality on Disrupted Foundations

The study by Ma et al. (2019) discussed above in the context of plasticity also provides substantial experimental insight into the effect of perturbations on the dynamic state of neuronal networks. By inducing monocular deprivation in rodents with chronic recording of the visual cortex, they were able to examine the effect of the perturbation on cortical activity. Despite the near complete removal of input to the cortex, the network's firing rate, or activity level, was initially maintained, providing no evidence of the sensory deprivation that had occurred. However, the neuronal avalanche behavior in the network revealed a deviation from criticality immediately following perturbation, despite the fact that the firing rate was maintained. Moreover, this deviation was sustained until homeostatic mechanisms restored it by upscaling inhibitory activity and subsequently reducing network firing (see **Figure 5**). The deviation from criticality and branching ratio measures (see **Box 2**) applied by Ma et al. (2019) exemplify the capacity for criticality analysis to identify perturbations. Additionally, this study emphasizes how multiple mechanistic underpinnings lend themselves to critical dynamics and the potential disparity between network dynamics and global activity levels. The effect of these mechanisms can be further emphasized through their disruptions during a critical state.

Modeling studies on disrupted network topology and impaired plasticity lend some insight into deviations from criticality following perturbation. Within scale-free and small-world networks, there exists a significant robustness against structural defects, as most nodes only connect to neighbors within a cluster or module. As a result, a large number of these low-degree nodes can be lesioned before critical dynamics are disrupted (Goodarzinick et al., 2018). Conversely, any removal of high-degree nodes or long-range connections can rapidly fragment the network structure and subsequently abolish any critical dynamics occurring (Callaway et al., 2000; Mizutaka and Yakubo, 2013; Valverde et al., 2015). The network-wide synchrony that occurs with efficient network topologies and at criticality may also enable the spread of disruptive states such as epilepsy. This synchrony is also dependent on a functioning and adaptive E/I balance, as discussed below.

In investigations of criticality in biological neural networks, it has been found that the simple addition of the GABA inhibitor bicuculline can shift the dynamics of a network from critical to supercritical by increasing synchrony within the network (Beggs and Plenz, 2003; Pasquale et al., 2008). Other studies have also shown that altering the balance of excitation and inhibition in biological networks can drive them into a different dynamic state. In self-organized critical networks, pharmacologically enhancing excitation can change the dynamics of the network from critical to supercritical, while reducing excitation promotes subcritical dynamics (Shew et al., 2009, 2011). Furthermore, it has been demonstrated that direct inhibitory action by addition of GABA to a network with supercritical dynamics can drive it into a critical state (Heiney et al., 2019). This points to GABAergic inhibition as important in disrupting highly synchronized activity where activity very frequently propagates throughout the entire network, driving it into a supercritical state. Multiple simulation studies have also shown that emergence of critical dynamics is dependent on a certain proportion of inhibition in the network, which conform to physiological levels of inhibitory neurons in the brain (de Arcangelis et al., 2006; Massobrio et al., 2015).

The Promise of Criticality Analysis in the Clinical Realm

Despite the rising interest in biological criticality in the last two decades, there has been a dearth of experimental and clinical studies connecting criticality to perturbations. Because criticality represents an optimal state for computation, one could expect departure from the critical state would entail a disruption unto itself (Shew et al., 2011); however, in practice, disruptions to network dynamics are likely more complicated than a transition away from criticality, as such transitions may be part of healthy activity (Stewart and Plenz, 2006; Pearlmutter and Houghton, 2009; Allegrini et al., 2015; Wilting and Priesemann, 2019b), though see also (Carvalho et al., 2020, in preprint) for a counterpoint to this. Given recent hypotheses concerning network computation in the slightly subcritical regime, quantifying the impact of perturbations on network dynamics necessitates rigorous analytical tools (see **Box 2**) (Priesemann et al., 2014; Wilting et al., 2018; Wilting and Priesemann, 2019a). The potential presence of heterogeneous local dynamics or global reverberating dynamics in the subcritical regime demands a combined and comparative approach for any medical application.

The existing literature detailing disorders as disrupted criticality largely pertain to the macroscale (see Zimmern, 2020 for a comprehensive review), as examined through (i)EEG (Thatcher et al., 2009), ECoG (Chaudhuri et al., 2018), and fMRI (Tagliazucchi et al., 2012). Even with the growing number of researchers examining the dynamics of mesoscale networks, there is still a lack of research turning these *in vitro* and *in vivo* methods toward the dynamics of perturbed networks. Given the growing sophistication of molecular and electrophysiological tools, the potential for experimental manipulation of network topology and homeostatic mechanisms is immense. In the absence of many mesoscale investigations into criticality perturbations (Stewart and Plenz, 2006; Gireesh and Plenz, 2008; Fekete et al., 2018), this section will focus on macroscale network dynamics and investigations into clinical disorders through the lens of criticality.

The majority of today's macroscale studies on disorders and criticality pertain to epilepsy disorder, which provides an example of how criticality analysis can benefit the clinical field (Worrell et al., 2002; Li et al., 2005; Meisel et al., 2015b, 2016; Arviv et al., 2016; Meisel and Loddenkemper, 2019; Rings et al., 2019). Given the absence of literature on other disorders in this context and the substantial literature that exists on network topology (Terry et al., 2012; Lopes et al., 2020) and E/I balance (Wei et al., 2017; Du et al., 2019) as they relate to epilepsy, we have chosen to examine this disorder here. An epileptic state, or seizure, is characterized by a departure from healthy dynamics to a hyper-synchronized or chaotic state. This epileptic state can be either focal and confined to cortical regions or circuits, or generalized and encompass the entire brain (Terry et al., 2012; Englot et al., 2016). Currently, diagnosing the presence of epilepsy is often based on the presence of overt structural deficits through MRI and CT, or through markers of infection and electrolyte testing (Stafstrom and Carmant, 2015). When the epilepsy is rooted in less overt factors, diagnosis becomes an issue of determining disruptive dynamics which has thus far proved to be a substantial problem (Stafstrom and Carmant, 2015; Meisel and Loddenkemper, 2019). To this end, the application of criticality analysis to epilepsy has been the focus of much recent research which we will discuss here (Meisel et al., 2015b, 2016; Arviv et al., 2016; Meisel, 2016; Beenhakker, 2019; Du et al., 2019; Meisel and Loddenkemper, 2019; Witton et al., 2019; Maturana et al., 2020).

Current literature links epileptogenesis to disruptions in network connectivity or neuronal excitability stemming from genetic pathologies, such as ion channel mutations, or acquired conditions, such as stroke (Terry et al., 2012; Wei et al., 2017). Predicting if and how these disruptions will lead to epileptogenesis has resulted in the development of measures of network excitability and synchrony and most recently the application of criticality analysis (Meisel, 2016). Diagnostically, criticality analysis has been applied as a biomarker in focal epilepsy patients, where critical slowing down, which is the stretching of activity patterns near a critical state, has been found to precede seizure onset (Maturana et al., 2020). Similarly, the presence of a Hopf bifurcation has been indicated as a diagnostic predictor based on modeled ECoG, neural field, and neural mass dynamics (Meisel and Kuehn, 2012; Buchin et al., 2018; Deeba et al., 2018); for a review on this topic, see Meisel and Loddenkemper (2019). In terms of treatment, the branching ratio computed from recordings of resting dynamics provides a quantitative measure to characterize the effect of anti-epileptic drugs (AEDs), as an alternative to the typically used absence of seizure or response to transcranial stimulation (Meisel et al., 2015b, 2016). A further study by Meisel (2020) also applied this to show an inverse correlation between network synchrony and AED dosage levels, indicating a shift toward a subcritical and away from a supercritical seizure state. However, we should note here that these promising results in the field also highlight some of the intricacies around criticality analysis. For example, when investigating critical slowing down and using a similar iEEG dataset as Maturana et al. (2020), Wilkat et al. (2019) conversely found no evidence of critical slowing down as an epileptic biomarker.

While these studies focus largely on neuronal excitability in isolation, the use of such analysis should also be integrated with the substantial work underway on epilepsy networks (Terry et al., 2012). Already, mapping of functional and structural connectivity in epileptic networks can identify the ictal, or seizure, onset zone and examine the spread from local to global seizure by means of effective connectivity (Yaffe et al., 2015). Indeed, models of seizure propagation and clinically recorded networks show rapid spread of disruptions through small-world networks as a result of their long-range connectivity and hub structure (Netoff et al., 2004; Ponten et al., 2007). With the reliance of seizure spread on network topology, epileptogenesis can occur as a result of disruptions to functional and structural connectivity (Avanzini and Franceschetti, 2009;

Terry et al., 2012; Fornito et al., 2015). Functional connectivity mapping in stroke patients often reveals hyperconnectivity, where functional network components paradoxically show an increase in connectivity post-stroke (Hillary and Grafman, 2017). Up to 10% of stroke patients suffer seizures either early or late in their recovery and currently there exists no reliable prognostic tool for determining if these will develop into epilepsy (Myint et al., 2006). Unfortunately, application of AEDs as a preventative measure has thus far proven ineffective, indicating that epileptogenesis is partially independent of neuronal excitability or subject to interference from complex homeostatic mechanisms (Gilad et al., 2011). These forms of acquired epilepsy highlight the heterogeneity of the disorder and the necessity of a combined network and dynamics analysis. The application of criticality analysis to epilepsy disorders can potentially act as both a trial and guideline for other neurological disorders, such as psychiatric (van Bokhoven et al., 2018), developmental (Tinker and Velazquez, 2014; Gao and Penzes, 2015; Li L. et al., 2018), and degenerative disorders (Jiang et al., 2018; Ren et al., 2018; Marcuzzo et al., 2019).

Still, caution must be taken when comparing these studies of macroscale dynamics to their underlying meso and microscale mechanisms (Meisel and Kuehn, 2012). Network scale is a crucial feature of these mechanisms, and node and edge descriptors at different scales substantially alter the relevant activity dynamics. Additionally, the highly divergent methods for avalanche detection between different assessment modalities [macroscale: fMRI, (i)EEG, MEG, ECoG; mesoscale: spikes and LFPs from tetrodes and MEAs] risk erroneous conflation of results between different scales. Each method of avalanche detection and definition requires a thorough investigation into its relevance and robustness to multiple tests. In the final section of this paper we will highlight steps to improve the accuracy and standardization of criticality analysis, as well as the relationship between structural and critical dynamics.

CONCLUSION

Network neuroscience has seen explosive growth in the clinical field within the past two decades, providing insight into pathophysiology and disease propagation. However, such rapid growth comes along with the challenge of standardizing the measures applied (Hallquist and Hillary, 2018). The current lack of standardized graph theory measures has created a widely dissimilar range of network definitions and graph metrics to the point where it precludes meta-analysis. Advancements in the empirical study of criticality in neural systems are also beginning to see rapid growth, and it can be a struggle to keep up with which measures are best to apply. The consolidation and standardization of metrics used in the study of critical dynamics and connectivity in neural networks thus remains a considerable challenge, yet the sooner this challenge is approached, the more it can be mitigated. Therefore, we have highlighted certain measures that have proven useful in the study of criticality in the context of neuroscience (see **Box 2**). Given the complex and multifaceted nature of criticality, we fully expect later studies will further expand upon and improve measures. However, applying and comparing the same measures across experiments will lessen the future burden of comparison.

Criticality holds the promise of bridging several scales of neural activity by its nature as a scale-free property. Yet as we have examined, the step from statistical models of criticality to experimental analysis is a difficult one, where constraints and complicating factors arising from experimental methods and the underlying biological mechanisms make themselves known. As we have discussed, the different recording modalities across scales apply disparate approaches to analyzing criticality, making any comparison fraught with analytical pitfalls, and this issue may be further exacerbated by more indirect measures such as fMRI with its different timescales. While there are some groups (Gireesh and Plenz, 2008; Miller et al., 2019) making substantial progress on these experimental issues, as more and more groups turn toward applying criticality-based measures in the clinic and laboratory they need to be cognizant of the intricacies inherent in these topics. Similarly, intuitions from theoretical work, the idea that epileptic systems are supercritical and thus should have branching ratios exceeding 1, can be counter to experimental findings (Hobbs et al., 2010; Plenz, 2012), necessitating a closer look at analytical techniques and theoretical understandings.

Throughout this review, we have attempted to highlight the multifaceted nature of criticality and the potential its analysis holds as a metric of network health. Criticality is closely tied to the efficiency of its underlying network structure, as this structure supports the propagation of dynamical activity through the system. The emergence of these efficient topologies in turn results from the dynamics of the structure itself: the changes in connectivity mediated by the local and global plasticity. This intertwining of criticality and structural dynamics is an essential feature of the critical state, and examining in isolation any single feature contributing to the behavior of a network may forgo the complex interplay that gives rise to critical dynamics. Neural networks organize into small-world and hierarchical modular topologies in part to support critical dynamics, and both structure and dynamics likely develop due to the computational benefits they afford. Furthermore, there is evidence that networks in the critical state display characteristics indicative of their optimal computational capacity, yet few studies have explicitly focused on highlighting these benefits conferred by criticality. A focus on this aspect of criticality would also aid in understanding what goes wrong—or what computational functions may be affected—when a network is damaged or diseased. In the future, we hope more studies take into consideration the interplay between structure and critical dynamics, as well as the functional benefits this confers, as criticality analysis and network neuroscience can provide significant insight into complexity, computation, and medicine.

AUTHOR CONTRIBUTIONS

KH and OH developed the focus and organization of the manuscript. KH and VF prepared the figures. All authors

contributed to the choice of review topic and the writing and review of the manuscript.

FUNDING

This work was conducted as part of the SOCRATES and DeepCA projects; the Liaison Committee for Education, Research and Innovation in Central Norway (Samarbeidsorganet HMN-NTNU); the Joint Research Committee between St. Olav's Hospital and the Faculty of Medicine and Health Sciences, NTNU; NTNU Enabling Technologies; and ALS Norge. The SOCRATES project was partially funded by the Norwegian Research Council (NFR) through their IKTPLUSS research and innovation action on information and communication technologies under the project agreement 270961. The DeepCA project was partially funded by NFR through their Young Research Talent program under the project agreement 286558.

REFERENCES

Abbott, L. F., and Rohrkemper, R. (2007). A simple growth model constructs critical avalanche networks. *Progress Brain Res.* 165, 13–19. doi: 10.1016/S0079-6123(06)65002-4

Albert, R., Jeong, H., and Barabási, A.-L. (2000). Error and attack tolerance of complex networks. *Nature* 406, 378–382. doi: 10.1038/35019019

Allegrini, P., Paradisi, P., Menicucci, D., Laurino, M., Piarulli, A., and Gemignani, A. (2015). Self-organized dynamical complexity in human wakefulness and sleep: different critical brain-activity feedback for conscious and unconscious states. *Phys. Rev. E Stat. Nonlin. Soft Matter Phys.* 92:032808. doi: 10.1103/PhysRevE.92.032808

Alstott, J., Bullmore, E., and Plenz, D. (2014). Powerlaw: a python package for analysis of heavy-tailed distributions. *PLoS ONE* 9:e85777. doi: 10.1371/journal.pone.0085777

Arviv, O., Medvedovsky, M., Sheintuch, L., Goldstein, A., and Shriki, O. (2016). Deviations from critical dynamics in interictal epileptiform activity. *J. Neurosci.* 36, 12276–12292. doi: 10.1523/JNEUROSCI.0809-16.2016

Avanzini, G., and Franceschetti, S. (2009). Mechanisms of epileptogenesis. *Treat. Epilepsy Third Edn.* 14, 67–79. doi: 10.1002/9781444316667.ch5

Bak, P., Tang, C., and Wiesenfeld, K. (1987). Self-organized criticality: an explanation of the 1/ f noise. *Phys. Rev. Lett.* 59, 381–384. doi: 10.1103/PhysRevLett.59.381

Bak, P., Tang, C., and Wiesenfeld, K. (1988). Self-organized criticality. *Phys. Rev. A* 38, 364–374. doi: 10.1103/PhysRevA.38.364

Barabási, A.-L., and Albert, R. (1999). Emergence of scaling in random networks. *Science* 286, 509–512. doi: 10.1126/science.286.5439.509

Bassett, D. S., and Bullmore, E. T. (2017). Small-world brain networks revisited. *Neuroscientist* 23, 499–516. doi: 10.1177/1073858416667720

Bassett, D. S., and Sporns, O. (2017). Network neuroscience. *Nat. Neurosci.* 20, 353–364. doi: 10.1038/nn.4502

Bastos, A. M., and Schoffelen, J. M. (2016). A tutorial review of functional connectivity analysis methods and their interpretational pitfalls. *Front. Syst. Neurosc.* 9:175. doi: 10.3389/fnsys.2015.00175

Beenhakker, M. P. (2019). Cracklin' fish brains. *Epilepsy Curr.* 19, 112–114. doi: 10.1177/1535759719835348

Beggs, J. M. (2008). The criticality hypothesis: how local cortical networks might optimize information processing. *Philos. Trans. R. Soc. A Math. Phys. Eng. Sci.* 366, 329–343. doi: 10.1098/rsta.2007.2092

Beggs, J. M., and Plenz, D. (2003). Neuronal avalanches in neocortical circuits. *J. Neuro Sci.* 23, 11167–11177. doi: 10.1523/JNEUROSCI.23-35-11167.2003

Beggs, J. M., and Plenz, D. (2004). Neuronal avalanches are diverse and precise activity patterns that are stable for many hours in cortical slice cultures. *J. Neurosci.* 24, 5216–5229. doi: 10.1523/JNEUROSCI.0540-04.2004

Bertschinger, N., and Natschläger, T. (2004). Real-time computation at the edge of chaos in recurrent neural networks. *Neural. Comput.* 16, 1413–1436. doi: 10.1162/089976604323057443

Boedecker, J., Obst, O., Lizier, J. T., Mayer, N. M., and Asada, M. (2012). Information processing in echo state networks at the edge of chaos. *Theory Biosci.* 131, 205–213. doi: 10.1007/s12064-011-0146-8

Bonachela, J. A., De Franciscis, S., Torres, J. J., and Muoz, M. A. (2010). Self-organization without conservation: are neuronal avalanches generically critical? *J. Stat. Mech. Theory Exp.* 10:P02015. doi: 10.1088/1742-5468/2010/02/P02015

Bonachela, J. A., and Muñoz, M. A. (2009). Self-organization without conservation: true or just apparent scale-invariance? *J. Stat. Mech. Theory Exp.* 9:P09009. doi: 10.1088/1742-5468/2009/09/P09009

Bonifazi, P., Goldin, M., Picardo, M. A., Jorquera, I., Cattani, A., Bianconi, G., et al. (2009). GABAergic hub neurons orchestrate synchrony in developing hippocampal networks. *Science* 326, 1419–1424. doi: 10.1126/science.1175509

Bornholdt, S., and Röhl, T. (2003). Self-organized critical neural networks. *Phys. Rev. E Stat. Phys. Plasmas Fluids Relat. Interdiscipl. Top.* 67:5. doi: 10.1103/PhysRevE.67.066118

Bressler, S. L., and Menon, V. (2010). Large-scale brain networks in cognition: emerging methods and principles. *Trends Cogn. Sci.* 14, 277–290. doi: 10.1016/j.tics.2010.04.004

Brochini, L., De Andrade Costa, A., Abadi, M., Roque, A. C., Stolfi, J., and Kinouchi, O. (2016). Phase transitions and self-organized criticality in networks of stochastic spiking neurons. *Sci. Rep.* 6, 1–15. doi: 10.1038/srep35831

Broido, A. D., and Clauset, A. (2019). Scale-free networks are rare. *Nat. Commun.* 10, 1–10. doi: 10.1038/s41467-019-08746-5

Buchin, A., Kerr, C. C., Huberfeld, G., Miles, R., and Gutkin, B. (2018). Adaptation and inhibition control pathological synchronization in a model of focal epileptic seizure. *ENeuro* 5, 1–14. doi: 10.1523/ENEURO.0019-18.2018

Buendía, V., di Santo, S., Bonachela, J. A., Muñoz, M. A., di Santo, S., Bonachela, J. A., et al. (2020). Feedback mechanisms for self-organization to the edge of a phase transition. *Front. Phys.* 8:333. doi: 10.3389/fphy.2020.00333

Bullmore, E., and Sporns, O. (2009). Complex brain networks: graph theoretical analysis of structural and functional systems. *Nat. Rev. Neurosci.* 10, 186–198. doi: 10.1038/nrn2575

Bullmore, E., and Sporns, O. (2012). The economy of brain network organization. *Nat. Rev. Neurosci.* 13, 336–349. doi: 10.1038/nrn3214

Buzsáki, G., Geisler, C., Henze, D. A., and Wang, X. J. (2004). Interneuron diversity series: circuit complexity and axon wiring economy of cortical interneurons. *Trends Neurosci.* 7, 446–451. doi: 10.1016/j.tins.2004.02.007

Callaway, D. S., Newman, M. E. J., Strogatz, S. H., and Watts, D. J. (2000). Network robustness and fragility: percolation on random graphs. *Phys. Rev. Lett.* 85, 5468–5471. doi: 10.1103/PhysRevLett.85.5468

Campos, J. G. F., Costa, A. D. A., Copelli, M., and Kinouchi, O. (2017). Correlations induced by depressing synapses in critically self-organized networks with quenched dynamics. *Phys. Rev. E* 95:042303. doi: 10.1103/PhysRevE.95.042303

Carvalho, T. T. A., Fontenele, A. J., Girardi-Schappo, M., Feliciano, T., Aguiar, L. A. A., Silva, T. P. L., et al. (2020). Subsampled directed-percolation models explain scaling relations experimentally observed in the brain. *arxiv [Preprint]* 1–15.

Cavagna, A., Cimarelli, A., Giardina, I., Parisi, G., Santagati, R., Stefanini, F., et al. (2010). Scale-free correlations in starling flocks. *Proc. Natl. Acad. Sci. U.S.A.* 107, 11865–11870. doi: 10.1073/pnas.1005766107

Chaudhuri, R., He, B. J., and Wang, X.-J. (2018). Random recurrent networks near criticality capture the broadband power distribution of human ECoG dynamics. *Cereb. Cortex* 28, 3610–3622. doi: 10.1093/cercor/bhx233

Chialvo, D. R. (2010). Emergent complex neural dynamics. *Nat. Phys.* 6, 744–750. doi: 10.1038/nphys1803

Chklovskii, D. B., Schikorski, T., and Stevens, C. F. (2002). Wiring optimization in cortical circuits. *Neuron* 34, 341–347. doi: 10.1016/S0896-6273(02)00679-7

Clauset, A., Shalizi, C. R., and Newman, M. E. J. (2009). Power-law distributions in empirical data. *SIAM Rev.* 51, 661–703. doi: 10.1137/070710111

Cocchi, L., Gollo, L. L., Zalesky, A., and Breakspear, M. (2017). Criticality in the brain: a synthesis of neurobiology, models and cognition. *Progress Neurobiol.* 158, 132–152. doi: 10.1016/j.pneurobio.2017.07.002

Costa, A. A., Brochini, L., and Kinouchi, O. (2017). Self-organized supercriticality and oscillations in networks of stochastic spiking neurons. *Entropy* 19, 1–16. doi: 10.3390/e19080399

Costa, A. D. A., Copelli, M., and Kinouchi, O. (2015). Can dynamical synapses produce true self-organized criticality? *J. Stat. Mech. Theory Exp.* 2015:P06004. doi: 10.1088/1742-5468/2015/06/P06004

Cuntz, H., Forstner, F., Borst, A., and Häusser, M. (2010). One rule to grow them all: a general theory of neuronal branching and its practical application. *PLoS Comput. Biol.* 6:e1000877. doi: 10.1371/journal.pcbi.1000877

de Arcangelis, L., and Herrmann, H. J. (2012). Activity-dependent neuronal model on complex networks. *Front. Physiol.* 3:62. doi: 10.3389/fphys.2012.00062

de Arcangelis, L., Perrone-Capano, C., and Herrmann, H. J. (2006). Self-organized criticality model for brain plasticity. *Phys. Rev. Lett.* 96:028107. doi: 10.1103/PhysRevLett.96.028107

de Solla Price, D. J. (1965). Networks of scientific papers. *Science* 149, 510–515. doi: 10.1126/science.149.3683.510

Deeba, F., Sanz-Leon, P., and Robinson, P. A. (2018). Dependence of absence seizure dynamics on physiological parameter evolution. *J. Theor. Biol.* 454, 11–21. doi: 10.1016/j.jtbi.2018.05.029

Denning, P. J. (2007). Computing is a natural science. *Commun. ACM* 50, 13–18. doi: 10.1145/1272516.1272529

Du, J., Vegh, V., and Reutens, D. C. (2019). Small changes in synaptic gain lead to seizure-like activity in neuronal network at criticality. *Sci. Rep.* 9, 1–15. doi: 10.1038/s41598-018-37646-9

Eguíluz, V. M., Chialvo, D. R., Cecchi, G. A., Baliki, M., and Apkarian, A. V. (2005). Scale-free brain functional networks. *Phys. Rev. Lett.* 94:018102. doi: 10.1103/PhysRevLett.94.018102

Englot, D. J., Konrad, P. E., and Morgan, V. L. (2016). Regional and global connectivity disturbances in focal epilepsy, related neurocognitive sequelae, and potential mechanistic underpinnings. *Epilepsia* 57, 1546–1557. doi: 10.1111/epi.13510

Fekete, T., Omer, D. B., O'Hashi, K., Grinvald, A., van Leeuwen, C., and Shriki, O. (2018). Critical dynamics, anesthesia and information integration: lessons from multi-scale criticality analysis of voltage imaging data. *NeuroImage* 183, 919–933. doi: 10.1016/j.neuroimage.2018.08.026

Fingelkurts, A. A., Fingelkurts, A. A., Kivisaari, R., Pekkonen, E., Ilmoniemi, R. J., and Kähkönen, S. (2004). Local and remote functional connectivity of neocortex under the inhibition influence. *NeuroImage* 22, 1390–1406. doi: 10.1016/j.neuroimage.2004.03.013

Fornito, A., Zalesky, A., and Breakspear, M. (2015). The connectomics of brain disorders. *Nat. Rev. Neurosci.* 16, 159–172. doi: 10.1038/nrn3901

Friedman, N., Ito, S., Brinkman, B. A. W., Shimono, M., Deville, R. E. L., Dahmen, K. A., et al. (2012). Universal critical dynamics in high resolution neuronal avalanche data. *Phys. Rev. Lett.* 108, 1–5. doi: 10.1103/PhysRevLett.108.208102

Gallos, L. K., Makse, H. A., and Sigman, M. (2012). A small world of weak ties provides optimal global integration of self-similar modules in functional brain networks. *Proc. Natl. Acad. Sci. U.S.A.* 109, 2825–2830. doi: 10.1073/pnas.1106612109

Gao, R., and Penzes, P. (2015). Common mechanisms of excitatory and inhibitory imbalance in schizophrenia and autism spectrum disorders. *Curr. Mol. Med.* 15, 146–167. doi: 10.2174/1566524015666150303003028

Gautam, S. H., Hoang, T. T., McClanahan, K., Grady, S. K., and Shew, W. L. (2015). Maximizing sensory dynamic range by tuning the cortical state to criticality. *PLoS Comput. Biol.* 11, 1–15. doi: 10.1371/journal.pcbi.1004576

Gilad, R., Boaz, M., Dabby, R., Sadeh, M., and Lampl, Y. (2011). Are post intracerebral hemorrhage seizures prevented by anti-epileptic treatment? *Epilepsy Res.* 95, 227–231. doi: 10.1016/j.eplepsyres.2011.04.002

Girardi-Schappo, M., Bortolotto, G. S., Gonsalves, J. J., Pinto, L. T., and Tragtenberg, M. H. R. (2016). Griffiths phase and long-range correlations in a biologically motivated visual cortex model. *Sci. Rep.* 6:29561. doi: 10.1038/srep29561

Girardi-Schappo, M., Brochini, L., Costa, A. A., Carvalho, T. T. A., and Kinouchi, O. (2020). Synaptic balance due to homeostatically self-organized quasicritical dynamics. *Phys. Rev. Res.* 2:012042. doi: 10.1103/PhysRevResearch.2.012042

Gireesh, E. D., and Plenz, D. (2008). Neuronal avalanches organize as nested theta- and beta/gamma-oscillations during development of cortical layer 2/3. *Proc. Natl. Acad. Sci. U.S.A.* 105, 7576–7581. doi: 10.1073/pnas.0800537105

Goldstein, M. L., Morris, S. A., and Yen, G. G. (2004). Problems with fitting to the power-law distribution. *Eur. Phys. J. B* 41, 255–258. doi: 10.1140/epjb/e2004-00316-5

Gollo, L. L. (2017). Coexistence of critical sensitivity and subcritical specificity can yield optimal population coding. *J. R. Soc. Interface* 14:20170207. doi: 10.1098/rsif.2017.0207

Goodarzinick, A., Niry, M. D., Valizadeh, A., and Perc, M. (2018). Robustness of functional networks at criticality against structural defects. *Phys. Rev. E* 98, 1–7. doi: 10.1103/PhysRevE.98.022312

Griffa, A., and Van den Heuvel, M. P. (2018). Rich-club neurocircuitry: function, evolution, and vulnerability. *Dialogues Clin. Neurosci.* 20, 121–132. doi: 10.31887/DCNS.2018.20.2/agriffa

Haldeman, C., and Beggs, J. M. (2005). Critical branching captures activity in living neural networks and maximizes the number of metastable states. *Phys. Rev. Lett.* 94, 1–4. doi: 10.1103/PhysRevLett.94.058101

Hallquist, M. N., and Hillary, F. G. (2018). Graph theory approaches to functional network organization in brain disorders: a critique for a brave new small-world. *Netw. Neurosci.* 3, 1–26. doi: 10.1162/netn_a_00054

Hardstone, R., Poil, S.-S., Schiavone, G., Jansen, R., Nikulin, V. V., Mansvelder, H. D., et al. (2012). Detrended fluctuation analysis: a scale-free view on neuronal oscillations. *Front. Physiol.* 3:450. doi: 10.3389/fphys.2012.00450

Heiney, K., Ramstad, O. H., Sandvig, I., Sandvig, A., and Nichele, S. (2019). "Assessment and manipulation of the computational capacity of *in vitro* neuronal networks through criticality in neuronal avalanches," in *2019 IEEE Symposium Series on Computational Intelligence (SSCI)* (Xiamen), 247–254. doi: 10.1109/SSCI44817.2019.9002693

Hesse, J., and Gross, T. (2014). Self-organized criticality as a fundamental property of neural systems. *Front. Syst. Neurosci.* 8:166. doi: 10.3389/fnsys.2014.00166

Hillary, F. G., and Grafman, J. H. (2017). Injured brains and adaptive networks: the benefits and costs of hyperconnectivity. *Trends Cogn. Sci.* 21, 385–401. doi: 10.1016/j.tics.2017.03.003

Hobbs, J. P., Smith, J. L., and Beggs, J. M. (2010). Aberrant neuronal avalanches in cortical tissue removed from juvenile epilepsy patients. *J. Clin. Neurophysiol.* 27, 380–386. doi: 10.1097/WNP.0b013e3181fdf8d3

Hoffmann, H. (2018). Impact of network topology on self-organized criticality. *Phys. Rev. E.* 97:022313. doi: 10.1103/PhysRevE.97.022313

Jiang, L., Sui, D., Qiao, K., Dong, H. M., Chen, L., and Han, Y. (2018). Impaired functional criticality of human brain during Alzheimer's disease progression. *Sci. Rep.* 8, 1–11. doi: 10.1038/s41598-018-19674-7

Khoshkhou, M., and Montakhab, A. (2019). Spike-timing-dependent plasticity with axonal delay tunes networks of izhikevich neurons to the edge of synchronization transition with scale-free avalanches. *Front. Syst. Neurosci.* 13:73. doi: 10.3389/fnsys.2019.00073

Kim, D. J., and Min, B. K. (2020). Rich-club in the brain's macrostructure: insights from graph theoretical analysis. *Comput. Struct. Biotechnol. J.* 18, 1761–1773. doi: 10.1016/j.csbj.2020.06.039

Kinouchi, O., Brochini, L., Costa, A. A., Campos, J. G. F., and Copelli, M. (2019). Stochastic oscillations and dragon king avalanches in self-organized quasi-critical systems. *Sci. Rep.* 9, 1–12. doi: 10.1038/s41598-019-40473-1

Kinouchi, O., and Copelli, M. (2006). Optimal dynamical range of excitable networks at criticality. *Nat. Phys.* 2, 348–352. doi: 10.1038/nphys289

Kinouchi, O., Pazzini, R., and Copelli, M. (2020). Mechanisms of self-organized quasicriticality in neuronal networks models. *arxiv*. doi: 10.3389/fphy.2020.583213

Kossio, F. Y. K., Goedeke, S., Van Den Akker, B., Ibarz, B., and Memmesheimer, R. M. (2018). Growing critical: self-organized criticality in a developing neural system. *Phys. Rev. Lett.* 121:58301. doi: 10.1103/PhysRevLett.121.058301

Langton, C. G. (1990). Computation at the edge of chaos: phase transitions and emergent computation. *Phys. D Nonlin. Phenomena* 42, 12–37. doi: 10.1016/0167-2789(90)90064-V

Laughlin, S. B., and Sejnowski, T. J. (2003). Communication in neuronal networks. *Science*. 301, 1870–1874. doi: 10.1126/science.1089662

Lee, H., Golkowski, D., Jordan, D., Berger, S., Ilg, R., Lee, J., et al. (2019). Relationship of critical dynamics, functional connectivity, and states of

consciousness in large-scale human brain networks. *NeuroImage* 188, 228–238. doi: 10.1016/j.neuroimage.2018.12.011

Levina, A., Herrmann, J. M., and Geisel, T. (2007). Dynamical synapses causing self-organized criticality in neural networks. *Nat. Phys.* 3, 857–860. doi: 10.1038/nphys758

Levina, A., and Priesemann, V. (2017). Subsampling scaling. *Nat. Commun.* 8, 1–9. doi: 10.1038/ncomms15140

Li, J., and Shew, W. L. (2020). Tuning network dynamics from criticality to an asynchronous state. *PLoS Comput. Biol.* 16:e1008268. doi: 10.1371/journal.pcbi.1008268

Li, L., Bachevalier, J., Hu, X., Klin, A., Preuss, T. M., Shultz, S., et al. (2018). Topology of the structural social brain network in typical adults. *Brain Connectivity* 8, 537–548. doi: 10.1089/brain.2018.0592

Li, X., Chen, Q., and Xue, F. (2017). Biological modelling of a computational spiking neural network with neuronal avalanches. *Philos. Trans. R. Soc. A Math. Phys. Eng. Sci.* 375:20160286. doi: 10.1098/rsta.2016.0286

Li, X., Polygiannakis, J., Kapiris, P., Peratzakis, A., Eftaxias, K., and Yao, X. (2005). Fractal spectral analysis of pre-epileptic seizures in terms of criticality. *J. Neural Eng.* 2, 11–16. doi: 10.1088/1741-2560/2/2/002

Li, X., and Small, M. (2012). Neuronal avalanches of a self-organized neural network with active-neuron-dominant structure. *Chaos* 22:023104. doi: 10.1063/1.3701946

Li, X., Wang, W., Xue, F., and Song, Y. (2018). Computational modeling of spiking neural network with learning rules from STDP and intrinsic plasticity. *Phys. A* 491, 716–728. doi: 10.1016/j.physa.2017.08.053

Lin, M., and Chen, T. (2005). Self-organized criticality in a simple model of neurons based on small-world networks. *Phys. Rev. E Stat. Nonlin. Soft Matter Phys.* 71:06133. doi: 10.1103/PhysRevE.71.016133

Lopes, M. A., Junges, L., Woldman, W., Goodfellow, M., and Terry, J. R. (2020). The role of excitability and network structure in the emergence of focal and generalized seizures. *Front. Neurol.* 11:74. doi: 10.3389/fneur.2020.00074

Low, L. K., and Cheng, H. J. (2006). Axon pruning: an essential step underlying the developmental plasticity of neuronal connections. *Philos. Trans. R. Soc. B Biol. Sci.* 361, 1531–1544. doi: 10.1098/rstb.2006.1883

Ma, Z., Turrigiano, G. G., Wessel, R., and Hengen, K. B. (2019). Cortical circuit dynamics are homeostatically tuned to criticality *in vivo*. *Neuron* 104, 655–664.e4. doi: 10.1016/j.neuron.2019.08.031

Malamud, B. D., Morein, G., and Turcotte, D. L. (1998). Forest fires: an example of self-organized critical behavior. *Science* 281, 1840–1842. doi: 10.1126/science.281.5384.1840

Marcuzzo, S., Terragni, B., Bonanno, S., Isaia, D., Cavalcante, P., Cappelletti, C., et al. (2019). Hyperexcitability in cultured cortical neuron networks from the G93A-SOD1 amyotrophic lateral sclerosis model mouse and its molecular correlates. *Neuroscience* 416, 88–99. doi: 10.1016/j.neuroscience.2019.07.041

Marshall, N., Timme, N. M., Bennett, N., Ripp, M., Lautzenhiser, E., and Beggs, J. M. (2016). Analysis of power laws, shape collapses, and neural complexity: new techniques and MATLAB support via the NCC toolbox. *Front. Physiol.* 7:250. doi: 10.3389/fphys.2016.00250

Martinello, M., Hidalgo, J., Maritan, A., Di Santo, S., Plenz, D., and Muñoz, M. A. (2017). Neutral theory and scale-free neural dynamics. *Phys. Rev. X* 7:041071. doi: 10.1103/PhysRevX.7.041071

Massobrio, P., Pasquale, V., and Martinoia, S. (2015). Self-organized criticality in cortical assemblies occurs in concurrent scale-free and small-world networks. *Sci. Rep.* 5:10578. doi: 10.1038/srep10578

Maturana, M. I., Meisel, C., Dell, K., Karoly, P. J., D'Souza, W., Grayden, D. B., et al. (2020). Critical slowing down as a biomarker for seizure susceptibility. *Nat. Commun.* 11:2172. doi: 10.1038/s41467-020-15908-3

McAuley, J. J., Da Fontoura Costa, L., and Caetano, T. S. (2007). Rich-club phenomenon across complex network hierarchies. *Appl. Phys. Lett.* 91, 2–5. doi: 10.1063/1.2773951

Meisel, C. (2016). Linking cortical network synchrony and excitability. *Commun. Integr. Biol.* 9, 1–3. doi: 10.1080/19420889.2015.1128598

Meisel, C. (2020). Antiepileptic drugs induce subcritical dynamics in human cortical networks. *Proc. Nat. Acad. Sci.* 117, 11118–11125. doi: 10.1073/pnas.1911461117

Meisel, C., and Gross, T. (2009). Adaptive self-organization in a realistic neural network model. *Phys. Rev. E Stat. Nonlin. Soft Matter Phys.* 80, 1–6. doi: 10.1103/PhysRevE.80.061917

Meisel, C., Klaus, A., Kuehn, C., and Plenz, D. (2015a). Critical slowing down governs the transition to neuron spiking. *PLoS Comput. Biol.* 11:e1004097. doi: 10.1371/journal.pcbi.1004097

Meisel, C., and Kuehn, C. (2012). Scaling effects and spatio-temporal multilevel dynamics in epileptic seizures. *PLoS ONE* 7:e30371. doi: 10.1371/journal.pone.0030371

Meisel, C., and Loddenkemper, T. (2019). Seizure prediction and intervention. *Neuropharmacology* 172, 107898. doi: 10.1016/j.neuropharm.2019.107898

Meisel, C., Olbrich, E., Shriki, O., and Achermann, P. (2013). Fading signatures of critical brain dynamics during sustained wakefulness in humans. *J. Neurosci.* 33, 17363–17372. doi: 10.1523/JNEUROSCI.1516-13.2013

Meisel, C., Plenz, D., Schulze-Bonhage, A., and Reichmann, H. (2016). Quantifying antiepileptic drug effects using intrinsic excitability measures. *Epilepsia* 57, e210–e215. doi: 10.1111/epi.13517

Meisel, C., Schulze-Bonhage, A., Freestone, D., Cook, M. J., Achermann, P., and Plenz, D. (2015b). Intrinsic excitability measures track antiepileptic drug action and uncover increasing/decreasing excitability over the wake/sleep cycle. *Proc. Natl. Acad. Sci. U.S.A.* 112, 14694–14699. doi: 10.1073/pnas.1513716112

Meunier, D., Lambiotte, R., and Bullmore, E. T. (2010). Modular and hierarchically modular organization of brain networks. *Front. Neurosci.* 4:200. doi: 10.3389/fnins.2010.00200

Michiels van Kessenich, L., Berger, D., de Arcangelis, L., and Herrmann, H. J. (2019). Pattern recognition with neuronal avalanche dynamics. *Phys. Rev. E* 99:010302. doi: 10.1103/PhysRevE.99.010302

Michiels Van Kessenich, L., De Arcangelis, L., and Herrmann, H. J. (2016). Synaptic plasticity and neuronal refractory time cause scaling behaviour of neuronal avalanches. *Sci. Rep.* 6:32071. doi: 10.1038/srep32071

Michiels van Kessenich, L., Luković, M., de Arcangelis, L., and Herrmann, H. J. (2018). Critical neural networks with short- and long-term plasticity. *Phys. Rev. E* 97:032312. doi: 10.1103/PhysRevE.97.032312

Miller, S. R., Yu, S., and Plenz, D. (2019). The scale-invariant, temporal profile of neuronal avalanches in relation to cortical γ-oscillations. *Sci. Rep.* 9, 1–14. doi: 10.1038/s41598-019-52326-y

Mizutaka, S., and Yakubo, K. (2013). Structural robustness of scale-free networks against overload failures. *Phys. Rev. E Stat. Nonlin. Soft Matter Phys.* 88:012803. doi: 10.1103/PhysRevE.88.012803

Moretti, P., and Muñoz, M. A. (2013). Griffiths phases and the stretching of criticality in brain networks. *Nat. Commun.* 4:2521. doi: 10.1038/ncomms3521

Muñoz, M. A. (2018). Colloquium: criticality and dynamical scaling in living systems. *Rev. Modern Phys.* 90:031001. doi: 10.1103/RevModPhys.90.031001

Muñoz, M. A., Juhász, R., Castellano, C., and Ódor, G. (2010). Griffiths phases on complex networks. *Phys. Rev. Lett.* 105:128701. doi: 10.1103/PhysRevLett.105.128701

Myint, P. K., Staufenberg, E. F. A., and Sabanathan, K. (2006). Post-stroke seizure and post-stroke epilepsy. *Postgraduate Med. J.* 82, 568–572. doi: 10.1136/pgmj.2005.041426

Naudé, J., Cessac, B., Berry, H., and Delord, B. (2013). Effects of cellular homeostatic intrinsic plasticity on dynamical and computational properties of biological recurrent neural networks. *J. Neurosci.* 33, 15032–15043. doi: 10.1523/JNEUROSCI.0870-13.2013

Netoff, T. I., Clewley, R., Arno, S., Keck, T., and White, J. A. (2004). Epilepsy in small-world networks. *J. Neurosci.* 24, 8075–8083. doi: 10.1523/JNEUROSCI.1509-04.2004

Newman, M. E. J. (2003). The structure and function of complex networks. *SIAM Rev.* 45, 167–256. doi: 10.1137/S003614450342480

Ódor, G., Dickman, R., and Ódor, G. (2015). Griffiths phases and localization in hierarchical modular networks. *Sci. Rep.* 5, 1–15. doi: 10.1038/srep14451

Ódor, G., and Kelling, J. (2019). Critical synchronization dynamics of the Kuramoto model on connectome and small world graphs. *Sci. Rep.* 9:19621. doi: 10.1038/s41598-019-54769-9

Okujeni, S., and Egert, U. (2019). Self-organization of modular network architecture by activity-dependent neuronal migration and outgrowth. *ELife* 8:e47996. doi: 10.7554/eLife.47996.031

Paczuski, M., Maslov, S., and Bak, P. (1996). Avalanche dynamics in evolution, growth, and depinning models. *Phys. Rev. E Stat. Phys. Plasmas Fluids Relat. Interdiscipl. Top.* 53, 414–443. doi: 10.1103/PhysRevE.53.414

Pajevic, S., and Plenz, D. (2009). Efficient network reconstruction from dynamical cascades identifies small-world topology of neuronal avalanches. *PLoS Comput. Biol.* 5:e1000271. doi: 10.1371/journal.pcbi.1000271

Pajevic, S., and Plenz, D. (2012). The organization of strong links in complex networks. *Nat. Phys.* 8, 429–436. doi: 10.1038/nphys2257

Palmieri, L., and Jensen, H. J. (2020). The forest fire model: the subtleties of criticality and scale invariance. *Front. Phys.* 8:257. doi: 10.3389/fphy.2020.00257

Pan, R. K., and Sinha, S. (2007). Modular networks emerge from multiconstraint optimization. *Phys. Rev. E Stat. Nonlin. Soft Matter Phys.* 76:045103. doi: 10.1103/PhysRevE.76.045103

Pasquale, V., Massobrio, P., Bologna, L. L., Chiappalone, M., and Martinoia, S. (2008). Self-organization and neuronal avalanches in networks of dissociated cortical neurons. *Neuroscience* 153, 1354–1369. doi: 10.1016/j.neuroscience.2008.03.050

Pearlmutter, B. A., and Houghton, C. J. (2009). A new hypothesis for sleep: tuning for criticality. *Neural Comput.* 21, 1622–1641. doi: 10.1162/neco.2008.05-08-787

Pellegrini, G. L., de Arcangelis, L., Herrmann, H. J., and Perrone-Capano, C. (2007). Activity-dependent neural network model on scale-free networks. *Phys. Rev. E* 76:016107. doi: 10.1103/PhysRevE.76.016107

Peng, J., and Beggs, J. M. (2013). Attaining and maintaining criticality in a neuronal network model. *Phys. A Statist. Mech. Appl.* 392, 1611–1620. doi: 10.1016/j.physa.2012.11.013

Plenz, D. (2012). Neuronal avalanches and coherence potentials. *Eur. Phys. J. Spec. Top.* 205, 259–301. doi: 10.1140/epjst/e2012-01575-5

Ponten, S. C., Bartolomei, F., and Stam, C. J. (2007). Small-world networks and epilepsy: graph theoretical analysis of intracerebrally recorded mesial temporal lobe seizures. *Clin. Neurophysiol.* 118, 918–927. doi: 10.1016/j.clinph.2006.12.002

Priesemann, V., and Shriki, O. (2018). Can a time varying external drive give rise to apparent criticality in neural systems? *PLoS Comput. Biol.* 14:e1006081. doi: 10.1371/journal.pcbi.1006081

Priesemann, V., Wibral, M., Valderrama, M., Pröpper, R., Le Van Quyen, M., Geisel, T., et al. (2014). Spike avalanches *in vivo* suggest a driven, slightly subcritical brain state. *Front. Syst. Neurosci.* 8:108. doi: 10.3389/fnsys.2014.00108

Reia, S. M., and Kinouchi, O. (2014). Conway's game of life is a near-critical metastable state in the multiverse of cellular automata. *Phys. Rev. E Stat. Nonlin. Soft Matter Phys.* 89, 1–5. doi: 10.1103/PhysRevE.89.052123

Reia, S. M., and Kinouchi, O. (2015). Nonsynchronous updating in the multiverse of cellular automata. *Phys. Rev. E Stat. Nonlin. Soft Matter Phys.* 91, 1–5. doi: 10.1103/PhysRevE.91.042110

Ren, S. Q., Yao, W., Yan, J. Z., Jin, C., Yin, J. J., Yuan, J., et al. (2018). Amyloid β causes excitation/inhibition imbalance through dopamine receptor 1-dependent disruption of fast-spiking GABAergic input in anterior cingulate cortex. *Sci. Rep.* 8, 1–10. doi: 10.1038/s41598-017-18729-5

Rings, T., von Wrede, R., and Lehnertz, K. (2019). Precursors of seizures due to specific spatial-temporal modifications of evolving large-scale epileptic brain networks. *Sci. Rep.* 9, 1–12. doi: 10.1038/s41598-019-47092-w

Rubinov, M., Sporns, O., Thivierge, J. P., and Breakspear, M. (2011). Neurobiologically realistic determinants of self-organized criticality in networks of spiking neurons. *PLoS Comput. Biol.* 7:e1002038. doi: 10.1371/journal.pcbi.1002038

Rudy, B., Fishell, G., Lee, S., and Hjerling-Leffler, J. (2011). Three groups of interneurons account for nearly 100% of neocortical GABAergic neurons. *Dev. Neurobiol.* 71, 45–61. doi: 10.1002/dneu.20853

Salkoff, D. B., Zagha, E., Yüzgeç, Ö., and McCormick, D. A. (2015). Synaptic mechanisms of tight spike synchrony at gamma frequency in cerebral cortex. *J. Neurosci.* 35, 10236–10251. doi: 10.1523/JNEUROSCI.0828-15.2015

Sethna, J. P., Dahmen, K. A., and Myers, C. R. (2001). Crackling noise. *Nature* 410, 242–250. doi: 10.1038/35065675

Shew, W. L., Clawson, W. P., Pobst, J., Karimipanah, Y., Wright, N. C., and Wessel, R. (2015). Adaptation to sensory input tunes visual cortex to criticality. *Nat. Phys.* 11, 659–663. doi: 10.1038/nphys3370

Shew, W. L., and Plenz, D. (2013). The functional benefits of criticality in the cortex. *Neuroscientist* 19, 88–100. doi: 10.1177/1073858412445487

Shew, W. L., Yang, H., Petermann, T., Roy, R., and Plenz, D. (2009). Neuronal avalanches imply maximum dynamic range in cortical networks at criticality. *J. Neurosci.* 29, 15595–15600. doi: 10.1523/JNEUROSCI.3864-09.2009

Shew, W. L., Yang, H., Yu, S., Roy, R., and Plenz, D. (2011). Information capacity and transmission are maximized in balanced cortical networks with neuronal avalanches. *J. Neurosci.* 31, 55–63. doi: 10.1523/JNEUROSCI.4637-10.2011

Shin, C. W., and Kim, S. (2006). Self-organized criticality and scale-free properties in emergent functional neural networks. *Phys. Rev. E Stat. Nonlin. Soft Matter Phys.* 74:045101. doi: 10.1103/PhysRevE.74.045101

Siri, B., Berry, H., Cessac, B., Delord, B., and Quoy, M. (2008). A mathematical analysis of the effects of Hebbian learning rules on the dynamics and structure of discrete-time random recurrent neural networks. *Neural Comput.* 20, 2937–2966. doi: 10.1162/neco.2008.05-07-530

Siri, B., Quoy, M., Delord, B., Cessac, B., and Berry, H. (2007). Effects of Hebbian learning on the dynamics and structure of random networks with inhibitory and excitatory neurons. *J. Physiol. Paris* 101, 136–148. doi: 10.1016/j.jphysparis.2007.10.003

Sporns, O. (2002). Network analysis, complexity, and brain function. *Complexity.* 8, 56–60. doi: 10.1002/cplx.10047

Sporns, O. (2013). Structure and function of complex brain networks. *Dialogues Clin. Neurosci.* 15, 247–262. doi: 10.31887/DCNS.2013.15.3/osporns

Sporns, O., Chialvo, D. R., Kaiser, M., and Hilgetag, C. C. (2004). Organization, development and function of complex brain networks. *Trends Cogn. Sci.* 8, 418–425. doi: 10.1016/j.tics.2004.07.008

Stafstrom, C. E., and Carmant, L. (2015). Seizures and epilepsy: an overview for neuroscientists. *Cold Spring Harbor Perspect. Med.* 5:a022426. doi: 10.1101/cshperspect.a022426

Stam, C. J. (2014). Modern network science of neurological disorders. *Nat. Rev. Neurosci.* 15, 683–695. doi: 10.1038/nrn3801

Stepp, N., Plenz, D., and Srinivasa, N. (2015). Synaptic plasticity enables adaptive self-tuning critical networks. *PLoS Comput. Biol.* 11:e1004043. doi: 10.1371/journal.pcbi.1004043

Stewart, C. V., and Plenz, D. (2006). Inverted-U profile of dopamine-NMDA-mediated spontaneous avalanche recurrence in superficial layers of rat prefrontal cortex. *J. Neurosci.* 26, 8148–8159. doi: 10.1523/JNEUROSCI.0723-06.2006

Stewart, C. V., and Plenz, D. (2008). Homeostasis of neuronal avalanches during postnatal cortex development *in vitro*. *J. Neurosci. Methods* 169, 405–416. doi: 10.1016/j.jneumeth.2007.10.021

Tagliazucchi, E., Balenzuela, P., Fraiman, D., and Chialvo, D. R. (2012). Criticality in large-scale brain fMRI dynamics unveiled by a novel point process analysis. *Front. Physiol.* 3:15. doi: 10.3389/fphys.2012.00015

Teixeira, F. P. P., and Shanahan, M. (2014). "Does plasticity promote criticality?" in *2014 International Joint Conference on Neural Networks (IJCNN)* (Beijing), 2383–2390. doi: 10.1109/IJCNN.2014.6889562

Terry, J. R., Benjamin, O., and Richardson, M. P. (2012). Seizure generation: the role of nodes and networks. *Epilepsia* 53, 166–169. doi: 10.1111/j.1528-1167.2012.03560.x

Tetzlaff, C., Okujeni, S., Egert, U., Wörgötter, F., and Butz, M. (2010). Self-organized criticality in developing neuronal networks. *PLoS Comput. Biol.* 6:e1001013. doi: 10.1371/journal.pcbi.1001013

Thatcher, R. W., North, D. M., and Biver, C. J. (2009). Self-organized criticality and the development of EEG phase reset. *Human Brain Mapp.* 30, 553–574. doi: 10.1002/hbm.20524

Thivierge, J. P. (2014). Scale-free and economical features of functional connectivity in neuronal networks. *Phys. Rev. E Stat. Nonlin. Soft Matter Phys.* 90:022721. doi: 10.1103/PhysRevE.90.022721

Tinker, J., and Velazquez, J. L. P. (2014). Power law scaling in synchronization of brain signals depends on cognitive load. *Front. Syst. Neurosci.* 8:73. doi: 10.3389/fnsys.2014.00073

Touboul, J., and Destexhe, A. (2017). Power-law statistics and universal scaling in the absence of criticality. *Phys. Rev. E* 95, 1–14. doi: 10.1103/PhysRevE.95.012413

Tremblay, R., Lee, S., and Rudy, B. (2016). GABAergic interneurons in the Neocortex: from cellular properties to circuits. *Neuron* 91, 260–292. doi: 10.1016/j.neuron.2016.06.033

Turrigiano, G. G. (2017). The dialectic of hebb and homeostasis. *Philos. Trans. R. Soc. B Biol. Sci.* 372, 4–6. doi: 10.1098/rstb.2016.0258

Valverde, S., Ohse, S., Turalska, M., West, B. J., and Garcia-Ojalvo, J. (2015). Structural determinants of criticality in biological networks. *Front. Physiol.* 6:127. doi: 10.3389/fphys.2015.00127

van Bokhoven, H., Selten, M., and Nadif Kasri, N. (2018). Inhibitory control of the excitatory/inhibitory balance in psychiatric disorders. *F1000Research* 7, 1–16. doi: 10.12688/f1000research.12155.1

van den Heuvel, M. P., and Sporns, O. (2013). Network hubs in the human brain. *Trends Cogn. Sci.* 17, 683–696 doi: 10.1016/j.tics.2013.09.012

Van Ooyen, A., Van Pelt, J., and Corner, M. A. (1995). Implications of activity dependent neurite outgrowth for neuronal morphology and network development. *J. Theor. Biol.* 172, 63–82. doi: 10.1006/jtbi.1995.0005

Wang, S. J., and Zhou, C. (2012). Hierarchical modular structure enhances the robustness of self-organized criticality in neural networks. *New J. Phys.* 14:023005. doi: 10.1088/1367-2630/14/2/023005

Watts, D. J., and Strogatz, S. H. (1998). Collective dynamics of 'small-world' networks. *Nature* 393, 440–442. doi: 10.1038/30918

Wei, F., Yan, L. M., Su, T., He, N., Lin, Z. J., Wang, J., et al. (2017). Ion channel genes and epilepsy: functional alteration, pathogenic potential, and mechanism of epilepsy. *Neurosci. Bull.* 33, 455–477. doi: 10.1007/s12264-017-0134-1

Wilkat, T., Rings, T., and Lehnertz, K. (2019). No evidence for critical slowing down prior to human epileptic seizures. *Chaos* 29:091104. doi: 10.1063/1.5122759

Wilting, J., Dehning, J., Pinheiro Neto, J., Rudelt, L., Wibral, M., Zierenberg, J., et al. (2018). Operating in a reverberating regime enables rapid tuning of network states to task requirements. *Front. Syst. Neurosci.* 12:55. doi: 10.3389/fnsys.2018.00055

Wilting, J., and Priesemann, V. (2018). Inferring collective dynamical states from widely unobserved systems. *Nat. Commun.* 9:2325. doi: 10.1038/s41467-018-04725-4

Wilting, J., and Priesemann, V. (2019a). 25 years of criticality in neuroscience — established results, open controversies, novel concepts. *Curr. Opin. Neurobiol.* 58, 105–111. doi: 10.1016/j.conb.2019.08.002

Wilting, J., and Priesemann, V. (2019b). Between perfectly critical and fully irregular: a reverberating model captures and predicts cortical spike propagation. *Cereb. Cortex* 29, 2759–2770. doi: 10.1093/cercor/bhz049

Witton, C., Sergeyev, S. V., Turitsyna, E. G., Furlong, P. L., Seri, S., Brookes, M., et al. (2019). Rogue bioelectrical waves in the brain: the Hurst exponent as a potential measure for presurgical mapping in epilepsy. *J. Neural Eng.* 16:056019. doi: 10.1088/1741-2552/ab225e

Wolfram, S. (1984). Universality and complexity in cellular automata. *Phys. D Nonlin. Phenomena* 10, 1–35. doi: 10.1016/0167-2789(84)90245-8

Womelsdorf, T., Schoffelen, J. M., Oostenveld, R., Singer, W., Desimone, R., Engel, A. K., et al. (2007). Modulation of neuronal interactions through neuronal synchronization. *Science* 316, 1609–1612. doi: 10.1126/science.1139597

Worrell, G. A., Cranstoun, S. D., Echauz, J., and Litt, B. (2002). Evidence for self-organized criticality in human epileptic hippocampus. *NeuroReport* 13, 2017–2021. doi: 10.1097/00001756-200211150-00005

Wu, S., Zhang, Y., Cui, Y., Li, H., Wang, J., Guo, L., et al. (2019). Heterogeneity of synaptic input connectivity regulates spike-based neuronal avalanches. *Neural Netw.* 110, 91–103. doi: 10.1016/j.neunet.2018.10.017

Wu, Y. K., Hengen, K. B., Turrigiano, G. G., and Gjorgjieva, J. (2020). Homeostatic mechanisms regulate distinct aspects of cortical circuit dynamics. *Proc. Natl. Acad. Sci. U.S.A.* 117, 24514–24525. doi: 10.1073/pnas.1918368117

Yada, Y., Mita, T., Sanada, A., Yano, R., Kanzaki, R., Bakkum, D. J., et al. (2017). Development of neural population activity toward self-organized criticality. *Neuroscience* 343, 55–65. doi: 10.1016/j.neuroscience.2016.11.031

Yaffe, R. B., Borger, P., Megevand, P., Groppe, D. M., Kramer, M. A., Chu, C. J., et al. (2015). Physiology of functional and effective networks in epilepsy. *Clin. Neurophysiol.* 126, 227–236. doi: 10.1016/j.clinph.2014.09.009

Zhang, A., Zhou, H., Li, X., and Zhu, W. (2019). Fast and robust learning in spiking feed-forward neural networks based on intrinsic plasticity mechanism. *Neurocomputing* 365, 102–112. doi: 10.1016/j.neucom.2019.07.009

Zhou, S., and Mondragón, R. J. (2004). The rich-club phenomenon in the internet topology. *IEEE Commun. Lett.* 8, 180–182. doi: 10.1109/LCOMM.2004.823426

Zierenberg, J., Wilting, J., and Priesemann, V. (2018). Homeostatic plasticity and external input shape neural network dynamics. *Phys. Rev. X* 8:031018. doi: 10.1103/PhysRevX.8.031018

Zimmern, V. (2020). Why brain criticality is clinically relevant: a scoping review. *Front. Neural Circuits* 14:54. doi: 10.3389/fncir.2020.00054

Conflict of Interest: The authors declare that the research was conducted in the absence of any commercial or financial relationships that could be construed as a potential conflict of interest.

frontiers in Neural Circuits

HYPOTHESIS AND THEORY
published: 02 March 2021
doi: 10.3389/fncir.2021.614268

Not One, but Many Critical States: A Dynamical Systems Perspective

Thilo Gross [1,2,3]*

[1] Helmholtz Institute for Functional Marine Biodiversity (HIFMB), Oldenburg, Germany, [2] Institute for Chemistry and Biology of the Marine Environment (ICBM), Carl-von-Ossietzky Universität Oldenburg, Oldenburg, Germany, [3] Helmholtz Center for Marine and Polar Research, Alfred-Wegener-Institute, Bremerhaven, Germany

The past decade has seen growing support for the critical brain hypothesis, i.e., the possibility that the brain could operate at or very near a critical state between two different dynamical regimes. Such critical states are well-studied in different disciplines, therefore there is potential for a continued transfer of knowledge. Here, I revisit foundations of bifurcation theory, the mathematical theory of transitions. While the mathematics is well-known it's transfer to neural dynamics leads to new insights and hypothesis.

Keywords: neural criticality, bifurcation, multi-criticality, critical brain, phase transition, criticality

1. INTRODUCTION

The critical brain hypothesis states that the brain operates in a state that is situated at or very near to a transition between qualitatively different dynamical regimes. Such "critical" states are thought to convey advantageous computational properties such as optimal information retention, signal detection and processing performance (Chialvo, 2010; Hesse and Gross, 2014; Zimmern, 2020).

The criticality hypothesis was first formulated based on the computational desirability of critical states (Chialvo, 2010) and a mathematical analogy between neural and earthquake dynamics (Herz and Hopfield, 1994). Subsequent works gradually build support for the hypothesis. For example Bornholdt and Rohlf (2000) showed that self-organized criticality can emerge from simple local rules, which was later confirmed in a more realistic models (Meisel and Gross, 2009; Kossio et al., 2018; Das and Levina, 2019). Beggs and Plenz (2004) provided early experimental evidence by demonstrating that *in-vitro* cultures of neurons sustain critical cascades of activity. Linkenkaer-Hansen et al. (2001), Kitzbichler et al. (2009), and Meisel et al. (2012) found signatures of criticality in MRI, MEG, and EEG recordings. More recently, Timme et al. (2016) confirmed the prediction that criticality maximizes information theoretic complexity and del Papa et al. (2017) shows that also learning behavior in recurrent neural networks leads to a state of criticality.

It has also been argued that brain could operate slightly below criticality. This is based on the analysis of experimental result on spike cascades (Priesemann et al., 2014) and is consistent with mathematical constraints on adaptive self-organization (Gross and Blasius, 2007; Kuehn, 2012; Droste et al., 2013). It has been argued that such an operation near critical states could allow the brain to control the desired degree of criticality (Wilting and Priesemann, 2014, 2018, 2019). Furthermore, in networks critical-like dynamics may be expected also in the neighborhood of the critical state in a so-called Griffith phase (Moretti and Munoz, 2013).

In the discussion of theoretical aspects of criticality many current authors resort to the toolkit of physics and its terminology and models, such as branching processes, correlation functions, critical exponents and the Ising model (Yaghoubi et al., 2018; Fontenele et al., 2019). However, critical

OPEN ACCESS

Edited by:
Ioanna Sandvig, Norwegian University of Science and Technology, Norway

Reviewed by:
Viola Priesemann, Max-Planck-Institute for Dynamics and Self-Organisation, Max Planck Society (MPG), Germany
Kenji Morita, The University of Tokyo, Japan

***Correspondence:**
Thilo Gross
thilo2gross@gmail.com

Received: *05 October 2020*
Accepted: *05 February 2021*
Published: *02 March 2021*

Citation:
Gross T (2021) Not One, but Many Critical States: A Dynamical Systems Perspective. Front. Neural Circuits 15:614268. doi: 10.3389/fncir.2021.614268

phenomena can also be studied from the perspective of dynamical systems theory, which offers a complementary perspective to physical theory. Dynamical systems theory is the mathematical theory of transitions between dynamical regimes. Phase transitions then appear as so-called *bifurcations* of system-level dynamical variables. In neuroscience bifurcation-based methods are widely used in the study of smaller-scale neural networks but are not often deeply discussed in the context of neural criticality (although, see Meisel and Gross, 2009; Kuehn, 2012; Droste et al., 2013).

In this paper I present a mathematical view of neural criticality, The mathematics is relatively elementary and much of the material presented here can be found in introductory textbooks to bifurcation theory, e.g., Kuznetsov, 2004. However, several insights that can be gained by leveraging this angle are, to my knowledge, presently not utilized in the study of brain criticality. Thus it is worthwhile to bridge the gap between the neural and mathematical literature. Below I have tried to provide a simple and accessible introduction to the most relevant parts of bifurcation theory.

One particular benefit of mathematics is that it deals gracefully with unknowns. As this ability extends to working with unknown models, the use of mathematics allows the researcher to make statements about criticality that hold irrespective of the specific model under consideration.

Some highlight are as follows: In section 2.1, we revisit the origin of power law behavior and critical slowing down that gives critical states the ability to retain memory of perturbations. Thereafter in section 2.2, we illustrate why critical states can be super sensitive to parameter change. In section 2.3, we take a closer look at super-sensitivity and find that remaining close to a super-sensitive state places strong constraints on the dynamics. This is further explored in the subsequent section, starting with section 2.4, where we discuss the transcritical bifurcation (the criticality of the SIS model). While we find that it may play some role in neural systems, it provides less benefits than other bifurcations. This lends weight to the hypothesis that the criticality observed *in-vitro* may be of a different form than the criticality observed *in-vivo* (Kanders et al., 2017). In section 2.5, I show that pitchfork bifurcations (the criticality of the Ising model), is an unlikely scenario for neural criticality as it requires a specific symmetry. By contrast, in section 2.6, we discover that the Hopf bifurcation (the criticality of the Kuramoto model) has several advantageous properties that make it a particularly attractive scenario for neural criticality. In this type of bifurcation, information would be encoded by the presence or absence of oscillations in populations of neurons, which agrees well with empirical evidence. Finally in section 2.7, I discuss that high-dimensional parameter spaces have on criticality. This points to some radical perspectives: Critical states of the brain are likely not isolated points but part of a large high-dimensional subset of parameter space, which could allow the brain to explore different parameter regions while remaining critical. It could also lead to multi-critical states, corresponding to bifurcations of high codimension, where the brain is critical in many different ways.

2. RESULTS

To gain insights it is useful to study a series of simple but general models. By keeping the models simple we make sure that the results we seek are easy to compute and intuitive to understand. By keeping them general we make sure that they are widely applicable and do not hinge on specific assumptions.
Consider a generic dynamical system of the form

$$\dot{x} = f(x, p), \tag{1}$$

where x is a dynamical variable and p is a parameter. For example we can imagine x to be the overall level of activity in the brain and p to be the average excitability. The dot on the left hand side denotes a time derivative. So, the change of excitation in time is described by some function f of the current excitation x and the parameter p. In the following we will explore what properties of f would be advantageous for information processing.

Let us assume that over some time (and in absence of external stimuli) the excitation will approach a steady homeostatic level, which we will call x^*. By definition a system that is in the *steady state* remains there indefinitely unless parameters are changed or it is subject to an external perturbation. That means in the state x^* there is no further change of x, which we can express as

$$f(x^*, p) = 0. \tag{2}$$

Although the model is very minimal, we can use it to study how dynamical systems respond to perturbations. Consider what happens after some external force pushes the variable x out of the steady state x^*, such that

$$x = x^* + \delta, \tag{3}$$

where δ is the deviation from the steady state caused by the perturbation. We assume that this deviation is initially small, but grows or diminishes in time according to the dynamics of the system. Substituting Equation (3) into Equation (1) we can write

$$\frac{\mathrm{d}}{\mathrm{d}t}(x^* + \delta) = f(x^* + \delta, p), \tag{4}$$

where we have indicated the time derivative as $\mathrm{d}/\mathrm{d}t$ instead of using the dot. Because the steady state x^* is constant in time, its time derivative vanishes, allowing us to return to the simpler notation,

$$\dot{\delta} = f(x^* + \delta, p). \tag{5}$$

To make further progress we need one mathematical tool: The Taylor expansion (James, 2015). The idea of a Taylor expansion is that we can approximate the function f by

$$f(x^* + \delta, p) = f(x^*, p) + \delta f_{\mathrm{x}}(x^*, p) + \frac{1}{2}\delta^2 f_{\mathrm{xx}}(x^*, p) + \ldots \tag{6}$$

where we used roman indices to indicate derivatives. So f_{x} is the derivative of f with respect to x and f_{xx} is the second derivative of f with respect to x.

While the Taylor expansion formula has an infinite number of terms on the right hand side, these terms include higher and higher powers of δ. If δ is a small number, say 0.01 then $\delta^2 = 0.0001$ is even smaller, and $\delta^3 = 0.000001$ is smaller yet. Hence, the terms in the Taylor formula represent smaller and smaller corrections.

If δ is sufficiently small then we can get an arbitrarily precise approximation by ignoring all but the first non-zero Taylor term. The first term $f(x^*, p)$ is always zero by virtue of Equation (2), hence in general the second term $\delta f_{rmx}(x^*, p)$ is the one we need to keep. We are left with

$$f(x^* + \delta, p) = \underbrace{f(x^*, p)}_{=0} + \delta f_x(x^*, p) + \underbrace{\frac{1}{2}\delta^2 f_{xx}(x^*, p) + \ldots}_{\approx 0}. \quad (7)$$

Substituting the remaining term into Equation (5) we find

$$\dot{\delta} = \delta f_x(x^*, p). \quad (8)$$

This equation tells us that the speed at which the deviation changes is proportional to the size of the current deviation. If f_x is less than zero, the change counteracts the current deviation such that we return to the steady state. By contrast if f_x is greater zero then the deviation grows over time.

Equation (8) is a so-called separable differential equation and thus can be solved by the method of separation of variables (James, 2015). The result is the size of the perturbation as a function of time

$$\delta(t) = \delta(0) \exp f_x t. \quad (9)$$

Here we have omitted the argument (x^*, p) behind the f_x for simplicity. The solution shows that starting from the initial perturbation, $\delta(0)$, the deviation of system from the steady state grows or declines exponentially in time. Specifically, we observe an exponential growth if $f_x > 0$ and an exponential decline if $f_x < 0$. In the former case, the system is fundamentally unstable; any small perturbation launches it into dynamics that lead away from the steady state, so finding the system in this state at all seems implausible. In the latter case the state is stable, but the exponential return after a perturbation means that the memory of the perturbation is lost from the system exponentially fast.

The reasoning above illustrates a fundamental dilemma. The system cannot operate in an unstable state, because the very instability of the state precludes it from remaining there. By contrast the system can be in a stable state indefinitely, but the very stability of this state means that any information received is quickly lost from the system because the system returns to its previous state exponentially fast.

2.1. Origin of Power Laws and Critical Slowing Down

Let's explore what happens just at the boundary between stability and instability, i.e., in a *critical state*. In such a state we have $f_x = 0$. This means that the second term in the Taylor expansion (Equation 7) vanishes, so we can no longer argue that the third term is negligible by comparison. Instead we keep the third term,

$$f(x^* + \delta, p) = \underbrace{f(x^*, p)}_{=0} + \underbrace{\delta f_x(x^*, p)}_{=0} + \frac{1}{2}\delta^2 f_{xx}(x^*, p) + \underbrace{\ldots}_{\approx 0}. \quad (10)$$

Substituting the remaining term into Equation (1) gives us

$$\dot{\delta} = \frac{\delta^2 f_{xx}}{2} \quad (11)$$

Now the speed at which the deviation changes is proportional to the square of the current size of the deviation. Solving the equation with separation of variables yields

$$\delta(t) = \frac{2}{\frac{2}{\delta(0)} - f_{xx} t} \quad (12)$$

The term $f_{xx}t$ in the denominator increases linearly in time, so after a sufficiently long time it will be much greater than $\delta(0)$. This means in the long run the $\delta(0)$ in the equation becomes negligible and the system behaves like $1/t$. Instead of rapid exponential decline we now have a much slower geometric return to the stationary state (**Figure 1**). Hence, information about the perturbation is retained much longer in the system, and thus potentially long enough for slower, higher-order mechanisms of information retention to be set in motion.

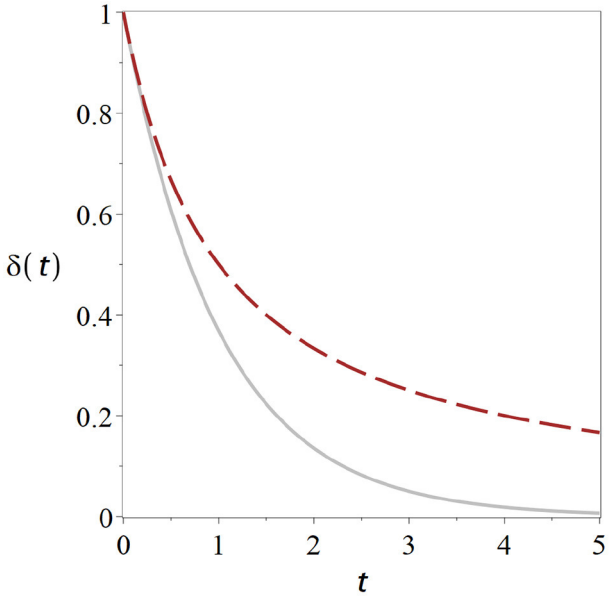

FIGURE 1 | Critical states retain memory of perturbations. Curves show the return to the homeostatic state after a perturbation for a non-critical state (solid gray) and for a critical state (dashed black). The distance δ from the homeostatic level declines significantly slower for the critical state. Parameters have been chosen such that the curves start from the same initial perturbation with identical slope Exponential. Exponential return: $\exp(-t)$ (cf. Equation 9). Geometric Return: $2/(2 + 2t)$ (Equation 12).

The geometric return observed in the critical state is the cause of the widely-discussed phenomenon of *critical slowing down* (van Nes and Scheffer, 2007): Picture a system which is subject to small perturbations from time to time. We start our system in the stable regime, where it returns to the steady state exponentially fast after a perturbation. If we change the parameter we may observe that the exponential return gets slower and slower until eventually it becomes a geometric return at the point were stability is lost. So the recovery from perturbations slows down as we approach criticality.

Physically speaking $\delta(t) \sim 1/t$ is a power-law, although the power is 1 in this case. This power-law in the response to perturbations is the root cause of some of the power-laws that are often observed at criticality. For example if there is some noise present that causes repeated small perturbations the $1/t$ responses to each of the perturbations add up to a power-law in the systems power spectrum.

This is a nice result but there is still a problem: The system will only return the to the steady state after perturbations in a certain direction. All is well if $\delta(0)$ and f_{xx} have opposite signs. However if f_{xx} and $\delta(0)$ have the same sign then there will be a time when the denominator in Equation (12) is zero and as we approach this point the deviation becomes arbitrarily large. Of course we won't expect infinite excitation to occur in the real world; after all, our model is only valid for small deviations from the steady state. Nevertheless the result shows that certain perturbation lead to a dramatic departure from the steady state, so the state is unstable.

Below we describe two ways out of this stability-sensitivity dilemma in sections 2.4, 2.6, respectively.

2.2. Sensitivity to Parameters

So far we have presented inputs into the system as short perturbations of the system, an ecologist would call this a *pulse perturbation*. There is however also another way in which information may enter a system, the *press perturbation*, a sustained change of the environment that we can model as a change in parameters.

For example think of the parameter p as a sustained input into the system and ask how sensitive our steady state x^* is to this input. We can measure this in terms of the derivative

$$\frac{\mathrm{d}}{\mathrm{d}p}x^* \tag{13}$$

The straight-d derivative that appears here denotes a differentiation where indirect effects are taken into account. By contrast the round-d partial derivative denotes a derivative where indirect effects are ignored.

A well-known trick to find this derivative is to differentiate the defining equation of the steady state Equation (2),

$$0 = f(x^*, p) \tag{14}$$

$$\frac{\mathrm{d}}{\mathrm{d}p}0 = \frac{\mathrm{d}}{\mathrm{d}p}f(x^*, p) \tag{15}$$

$$0 = \frac{\partial}{\partial p}f(x^*, p) + \left(\frac{\partial}{\partial x^*}f(x^*, p)\right)\left(\frac{\mathrm{d}}{\mathrm{d}p}x^*\right) \tag{16}$$

The differentiation of f in the second step results in two terms: The first captures the direct effect of change of p on f, whereas the second captures the indirect effect induced by the resulting change in x^*. This second term is the product of the actual change in x^* and the response of f to a change in x^*. Hence the derivative of x^* that we are looking for appears in the equation. Solving for it we obtain

$$\frac{\mathrm{d}x^*}{\mathrm{d}p} = -\frac{f_\mathrm{p}}{f_\mathrm{x}} \tag{17}$$

where we have again used roman indices to denote the partial (round-d) derivatives.

Now consider what happens to Equation (17) if we consider the critical state from the previous section. Above we found that this state is characterized by $f_\mathrm{x} = 0$, so that we have a infinitely sharp response to parameter change unless also $f_\mathrm{p} = 0$. In the following we call this phenomenon super-sensitivity of the critical state.

Super-sensitivity is another attractive property of critical states: While systems normally responds proportionally to parameter change, a critical system can, at least potentially, show an abrupt out-of-proportion response. To understand when such a response is observed we have to examine the actual transitions more closely which we do in the next section.

2.3. A Closer Look at Super-Sensitivity

Critical states lie on the edges been qualitatively different types of behavior (*phases*) of a system. In the language of dynamical systems the transition between phases that takes place at the critical state typically corresponds to a *bifurcation*, a qualitative transition in the dynamics of the system. To get a better understanding of the transition we need to explore what happens in the bifurcations in more detail. Instead of just considering a perturbation of the state of the system x, we now consider also a small perturbation ρ of the parameter, such that

$$p = p^* + \rho \tag{18}$$

where p^* is the *bifurcation point*, i.e., the critical parameter value where the bifurcation occurs.

To make progress we start again with our general system and Taylor expand with respect to both x and p:

$$\dot{x} = f(x, p) \tag{19}$$

$$= f(x^*, p^*) + f_\mathrm{x}(x^*, p^*)x + f_\mathrm{p}(x^*, p^*)p + \ldots \tag{20}$$

$$= f_\mathrm{x}\delta + f_\mathrm{p}\rho \tag{21}$$

In the second step we have used $f(x^*, p^*) = 0$ and omitted the arguments (x^*, p^*) for clarity.

The equation so far assumes that the two leading terms $f_\mathrm{p}, f_\mathrm{x}$ are non-zero such that we can neglect further terms $(\ldots)$ which contain higher powers of δ and ρ by comparison. While this is true in general, we are particularly interested in critical states where $f_\mathrm{x} = 0$. This means the first term vanishes and we have to add some higher terms of the Taylor expansion instead

$$\dot{x} = f_\mathrm{p}\rho + f_{xx}\delta^2/2 \tag{22}$$

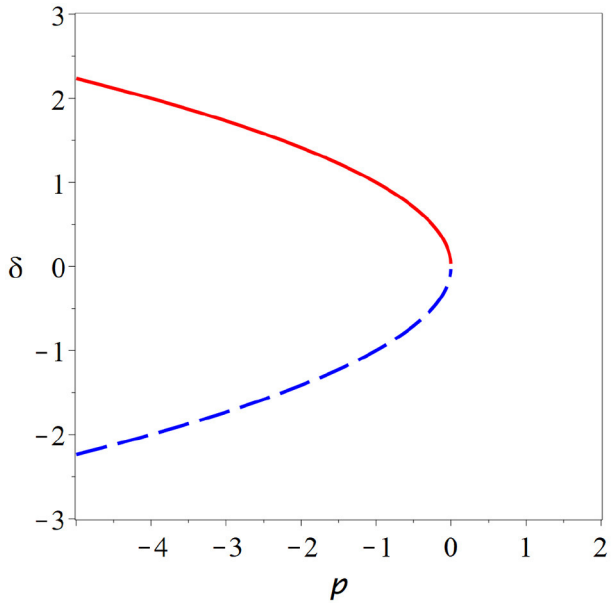

FIGURE 2 | Fold bifurcation. As parameter p is changed two steady states (red solid, blue dashed) collide and annihilate (cf. Equation 26). At the bifurcation point, where the steady states meet the system is supersensitive to parameter change. But due to the instability of the bifurcation point and the lack of states beyond the bifurcation point, it seems implausible that the brain could remain in such a state.

where the 2 appears due to the mechanics of the Taylor procedure. This expansion of the dynamical system is valid if

1. x^* is a steady state: $f(x^*, p^*) = 0$
2. The steady state is critical at p^*: $f_x(x^*, p^*) = 0$
3. We can neglect higher order terms if δ an ρ are small: $f_p \neq 0$, $f_{xx} \neq 0$

The three conditions are of a very different nature. To satisfy the first two, the *stationarity condition* and the *bifurcation condition*, we must chose x and p exactly right to be in a steady state and to be at a bifurcation. The third condition is a *genericity conditions*, it will typically be met except in special cases.

To understand what happens in the bifurcation we can now solve the expanded equation for the steady state, i.e.,

$$0 = \dot{x} \tag{23}$$

$$0 = f_p \rho + f_{xx} \delta^2 / 2 \tag{24}$$

$$\delta = \pm \sqrt{-\frac{f_p \rho}{f_{xx}}} \tag{25}$$

The result δ, shows us how much the steady state changes when we move the parameter p out of the critical point by an amount ρ. Equivalently we can write

$$x^*(p) = x^*(p^*) \pm \sqrt{-\frac{f_p}{f_{xx}}(p - p^*)} \tag{26}$$

The exact shape of the *branches* $x^*(p)$ depends on the values of the derivatives under the square root, but unless we are in a special case we always observe qualitatively the same picture. In the critical state two branches of steady states collide and annihilate each other (**Figure 2**).

At the point of collision the branches become vertical, which explains the super-sensitivity. One can show that for systems with one variable, one of the colliding steady states is stable whereas the other is unstable. Beyond the bifurcation both of the steady states involved have vanished, which means typically that the system departs the vicinity of the former steady states.

The bifurcation from **Figure 2** is known under many names including fold bifurcation, saddle-node bifurcation, and turning point, among others. It depicts the generic behavior that we expect to see whenever we encounter a critical state in a system with one variable. However, it seems implausible that the brain would operate at such a bifurcation as the critical point is an unstable state and a small parameter variation is sufficient to destroy steady states entirely.

One could imagine that the brain has some mechanisms to stabilize it's operating point to a saddle-node bifurcation. However, if such mechanisms exist they are part of the same system, and by their presence may change the type of bifurcation or remove it entirely. Let us therefore instead look at some critical states in other types of bifurcations.

2.4. Epidemic-Like Criticality

The criticality hypothesis has long been attacked for requiring that one parameter is tuned exactly right such that the system is at a bifurcation point. This has become a much smaller concern as several models have shown that the brain could reliably self-tune its parameters to this operating point, using widely described mechanisms of synaptic plasticity (e.g., Bornholdt and Rohlf, 2000; Meisel and Gross, 2009). However, we now make an additional demand. Not only are the parameters tuned exactly to the bifurcation point, but also the system is such that we do not see a generic bifurcation, but a special case. However, there are some well-known scenarios where fundamental physical constraints and/or symmetries make sure that a system must always be in such a special case.

For example in many physical systems some variables cannot be negative by design. A prominent example is the prevalence of an epidemic, e.g., described by the SIS model (Anderson and May, 1979; Keeling et al., 2016). In an epidemic there is typically a steady state when the number of infected reaches zero, and this steady state cannot be perturbed in the negative direction as such a perturbation would be *unphysical*, leading to a negative number of infected.

Because the steady state at zero is there for a fundamental reason (if there are no infected nobody can become infected), the location of this steady state does not depend on parameters, and if it undergoes a bifurcation it cannot simply vanish as we would normally expect. Mathematically, the physical constraints on the steady state implies $f_p = 0$ and thus, by-virtue of the physics of the epidemic system, it's bifurcations at zero must always be of a special case.

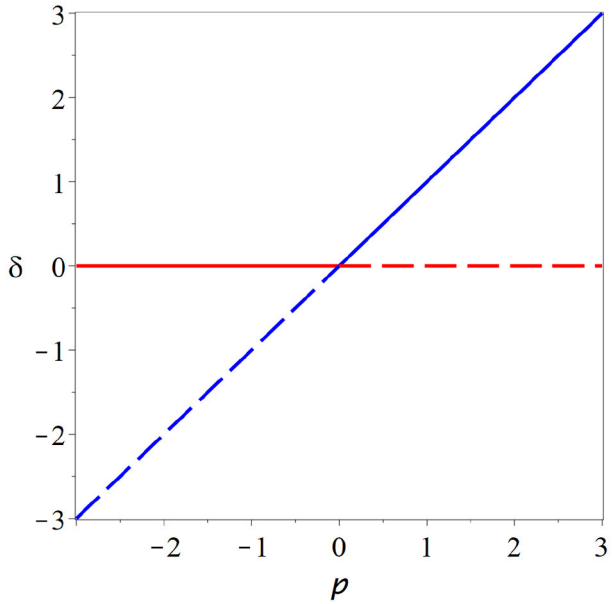

FIGURE 3 | Transcritical bifurcation. In the transcritical bifurcation two branches of steady states (red, blue) intersect and exchange their stability. This type of bifurcation might play a role in the *in-vitro* neural networks, but several caveats make it appear as an unlikely operating point for the brain.

For this case the Taylor expansion now reads

$$\dot{x} = f_{px}\rho\delta + f_{xx}\delta^2/2 \tag{27}$$

Note that every term that contains more than one ρ and one δ is negligible in comparison to $f_{px}\rho\delta$, moreover terms that contain more that two δ (e.g., δ^3) are negligible compared to $f_{xx}\delta^2/2$ and all terms that contain no δ are zero due to the physics of the system.

This expansion is valid if

1. x^* is a steady state: $f(x^*, p^*) = 0$
2. The steady state is critical at p^*: $f_x(x^*, p^*) = 0$
3. A genericity condition of the saddle-node bifurcation is violated $f_p = 0$ (also $f_{pp} = 0, \ldots$)
4. We can neglect higher order terms if δ an ρ are small: $f_{px} \neq 0$, $f_{xx} \neq 0$

The third condition plays the role of an additional genericity condition for this type of bifurcation.

We can solve for the steady state

$$0 = f_{px}\rho\delta + f_{xx}\delta^2/2, \tag{28}$$

which gives us two solutions, $\delta = 0$ and

$$\delta = -\frac{f_{px}}{f_{xx}}\rho, \tag{29}$$

a second branch that crosses the branch at zero in the bifurcation point. Stability analysis reveals that the branches exchange their stability in the bifurcation point (**Figure 3**). This *transcritcal* bifurcation is a typical scenario for the onset of epidemics. If the parameter is low enough, the disease-free state is stable, but once a threshold is crossed the disease-free state loses stability as a new steady enters the physical space in which the disease persists indefinitely.

Because the overall activity appears here as the order parameter of the bifurcation this is also the dimension in which computational benefits are reaped. It is therefore reasonable to expect this bifurcation to play a role when information is coded in terms of activitiy.

The transcritical bifurcation has some attractive features as a model for neural criticality. If we are willing to neglect spontaneous activity we can argue that the system should have a steady state at zero. Furthermore if the variable x represents a rate of spikes, we can argue that this variable can not be negative. Under these assumptions the state at a transcritical bifurcation is stable if $f_{xx} < 0$, and thus the system could plausibly remain there while profiting from the long memory that comes with criticality.

Note that the nature of the bifurcation has implications for information processing. If we are willing to accept that the brain operates at a transcritical bifurcation, then this would suggest that information is coded directly in terms of activity: After a perturbation causes increased activity, the system remains in a state of increased activity while slowly decaying back to the resting state where activity is zero.

There is indeed some evidence that points to transcritical-type criticality in the brain. The state at the transcritical bifurcation is characterized by activity cascades with branching ratio 1, which is in agreements with observations from *in-vitro* cultures (Beggs and Plenz, 2004; Hesse and Gross, 2014) and also direct measurements in life animals (Klaus et al., 2011; Hahn et al., 2017).

However, there are also some caveat regarding the transcritical bifurcation. It is subject to structural instability on which we discus in some more detail below. Additionally this bifurcation does not create super-sensitivity; because $f_p = 0$ the solution branches never become vertical (**Figure 3**). Thus this bifurcation scenario misses one of the two key features that make criticality attractive for computation.

In summary the transcritical bifurcation probably plays some role in systems of neurons. Particularly it is likely that this is the bifurcation that is encountered when one observed the onset of activity in neural networks and perhaps also in mature systems grown *in-vitro*. Moreover the observation of activity cascades and power-laws at in experiments supports this hypothesis. However, both evidence for other forms of information coding, and the caveats regarding transcritical bifurcations, suggest that other bifurcation scenarios also play significant and perhaps greater role for information processing in the brain.

2.5. Ising-Like Criticality

A very popular model system for criticality is the Ising model. The bifurcation that occurs in this model is the *pitchfork bifurcation*, another degenerate form of the fold bifurcation. In this case the degenerate bifurcation appears because the model is motivated by a physical system that has a mirror symmetry.

Due to this symmetry all terms of the Taylor expansion that are derivatives of even order with respect to x must be zero. This implies $f_p = 0$ and also $f_{xx} = 0$ so both genericity conditions of the fold bifurcation are violated.

In this case the expansion becomes

$$\dot{x} = f_{px}\rho\delta + f_{xxx}\delta^3 \tag{30}$$

which is valid if

1. x^* is a steady state: $f(x^*, p^*) = 0$
2. The steady state is critical at p^*: $f_x(x^*, p^*) = 0$
3. First fold genericity condition is violated: $f_p = 0$ (also $f_{pp} = 0, \ldots$)
4. Second fold genericity condition is violated: $f_{xx} = 0$
5. We can neglect higher order terms if δ an ρ are small: $f_{px} \neq 0$, $f_{xxx} \neq 0$

Solving for the steady state in the steady state in this case reveals three branches: the zero solution $\delta = 0$ and a pair of branches

$$\delta = \pm\sqrt{-\frac{f_{px}}{f_{xxx}}\rho} \tag{31}$$

If f_{px} and f_{xxx} have the same sign these two branches exist only for $\rho < 0$, otherwise they exist only for $\rho > 0$. Furthermore one can show that if $f_{px} > 0$ then the steady state at zero is stable for $\rho < 0$ (and vice versa).

In the *subcritical* form of the pitchfork bifurcation $f_{xxx} < 0$ the non-zero branches are unstable. In the bifurcation point they collide with the stable branch at zero and vanish as the zero becomes unstable. This leads to a *catastrophic* bifurcation after which no stable steady state is left. By contrast in the *supercritical* from of the pitchfork bifurcation f_{xxx} the steady state at zero becomes unstable as two stable non-zero branches emerge.

The supercritical pitchfork bifurcation is in principle an attractive model for neuroscience as the critical state is stable and has the desirable characteristics of long-term memory of perturbations and super sensitivity to parameter change.

The major problem with this sort of bifurcation is that it is hard to motivate why such dynamics should occur in the brain. The bifurcation requires a perfect mirror symmetry which is easy to motivate for the physical Ising model (spin up and spin down states are thought to be exactly symmetrical) but is hard to justify in a biological system.

All degenerate bifurcations, including transcritical and pitchfork suffer from structural instability (**Figure 5**). For example including even a low level of spontaneous activity destroys the transcritical bifurcation in SIS-type models model entirely. However, for multiple reasons we should not disregard degenerate bifurcations altogether. Also the transcritical bifurcation vanishes from the SIS model if spontaneous activity is included. However, it is replace by a region where the solution branch bends quickly, through not abruptly. This region of rapid change will retain some semblance to a critical state.

Moreover higher-level mechanisms may exist that drive the brain to degenerate bifurcations in a very similar way that to proposed primary self-organization to critical states (Seung, 1996; Feudel et al., 2018). For example Seung (1996) describes how neurons can approximate a degenerate line attractor, but also notes some caveats.

Even in absence of mechanisms that create degenerate situations over a broad range of operating conditions, the pitchfork bifurcation may play a role in information processing in decision making. Making decisions is only a challenge when different options appear almost exactly equally desirable. However, this equal desirability creates exactly the symmetry needed for pitchfork bifurcations.

For example the occurrence of a pitchfork bifurcation has been well-documented in collective decision making in fish faced with a binary choice task (Couzin et al., 2011).

The pitchfork-in-decision scenario is interesting because we get *criticality on demand*. The need for a decision, creates a situation in which the prerequisite symmetry for pitchfork criticality exists. The system can then be critical and profit from the super-sensitivity that this entails. Once the decision has been make the symmetry is broken, potentially leaving the system non-critical in this respect. This on-demand criticality is possible due to the difference between the slow timescale on which the need for the decision arises and the fast timescale of decision making processes.

2.6. Criticality at the Onset of Oscillations

In the previous sections, we have gone on a fairly exhaustive trawl of bifurcations of systems with one variable, but from the perspective of neuroscience none of the bifurcations scenarios we found was completely satisfactory. Of course there are other, even more degenerate bifurcations that we haven't discussed. For example there could be a transcritical-like bifurcation where three branches intersect or a pitchfork-like bifurcation where one branch splits into five. But essentially these are variations on a theme. If we want super sensitivity and memory in a stable critical state in a system we so far need to impose mirror symmetry.

An elegant way out of the dilemma is to consider systems with more than one variable. All the bifurcations that occur in systems with one variable (fold, transcritical, pitchfork,...) also occur in two-variable systems. Moreover, another type of long-term behavior is possible: sustained oscillations. The geometrical object in variable space on which such oscillations take place, a cycle, can undergo the same bifurcation as a steady state in one-variable systems, hence there can be a fold bifurcation of cycles, in which a stable and an unstable cycle collide and annihilate. However, all of these bifurcations present us with the same dilemma as the bifurcations in one-variable systems.

A genuinely new bifurcation of two-variable systems that does not have an equivalent in one-variable systems is the Hopf bifurcation. In this bifurcation a cycle emerges from (or is destroyed upon collision with) a steady state. The mathematical analysis of this bifurcation is slightly more complicated, hence I omit the expansion here (it can be found in Kuznetsov, 2004), but the key idea in this analysis is that one can transform the two variables of the system (say, x, y) near the bifurcation to obtain an

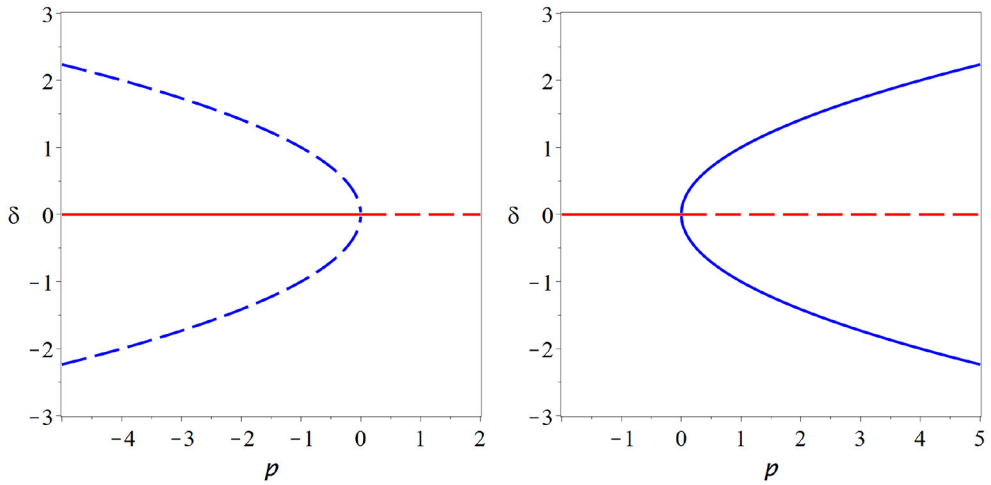

FIGURE 4 | Pitchfork bifurcation. In this bifurcation a steady state (red) loses stability as either two additional branches of steady states (blue dashed) are destroyed (subcritical case, **left**) or two branches of stable steady states (blue solid) emerge (supercritical, **right**). A system could plausibly operate at a supercritical pitchfork and profit from persistent memory and super-sensitivity that this bifurcation conveys. However, the pitchfork bifurcation requires a special symmetry that is hard to motivate for the brain, it therefore is an unlikely candidate for the operating point of neural criticality.

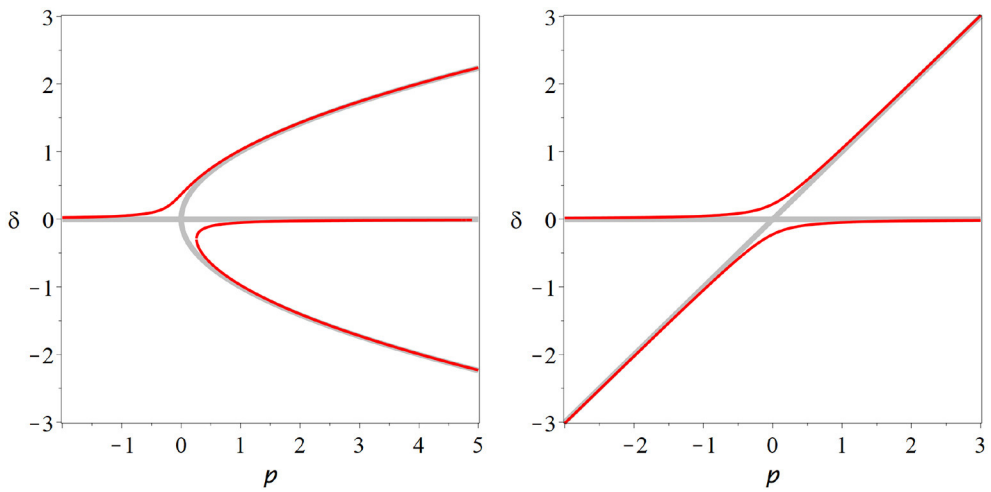

FIGURE 5 | Structural instability. The pitchfork **(left)** and transcritical **(right)** bifurcations are degenerate bifurcations: To observed their characteristic bifurcation diagrams (thick gray lines) special cases particular symmetries must exist in a model. If we break these symmetries, e.g., by adding a low level of spontaneous activity, then the degenerate bifurcation revert back to the generic fold bifurcation, or no bifurcation at all (red lines).

angle and radius variable,

$$r = \sqrt{(x - x^*)^2 + (y - y^*)^2} \tag{32}$$

$$\phi = \arctan((y - y^*)/(x - x^*)) \tag{33}$$

so r denotes the distance from the original steady state and the ϕ denotes the angle between the state of the system and the steady state. In these new variables the dynamical equations close to the bifurcation are captured by an expansion of the form

$$\dot{\phi} = a \tag{34}$$

$$\dot{r} = br\rho + cr^3 \tag{35}$$

where a, b, and c are constants that arise from derivatives of the dynamical equations (similarly to f_x etc.) and ρ is again our control parameter that measures the distance to the bifurcation point. Considering these equations we can see that the angle changes with a continuous angular velocity a. The equation for the radius is more interesting: The radius equation always has a stationary solution at $r = 0$. Even in this state the angle is constantly changing, but because the radius is 0 our original variables x, y remain stationary–this solution is our initial steady state. Stability analysis shows that it is stable if $b\rho \leq 0$ and unstable otherwise.

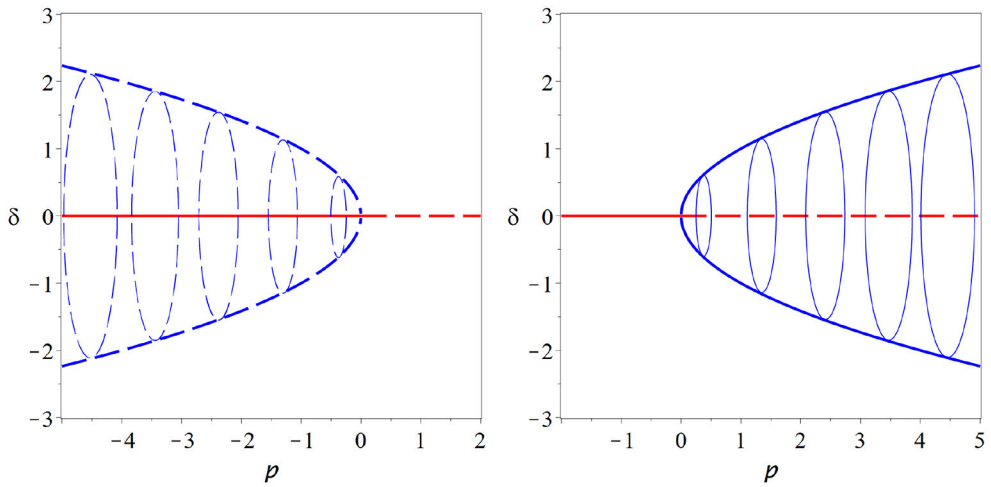

FIGURE 6 | Hopf bifurcation. The Hopf bifurcation marks the onset of at least transient oscillation in a dynamical system. It is in many ways similar to a pitchfork bifurcation and shares many of its attractive features. In contrast to the pitchfork, a stable cycle is created in the Hopf bifurcation (supercritical case, **right**) or an unstable cycle vanishes (subcritical case, **left**). Moreover, the Hopf bifurcation is a generic bifurcations and thus does not require hard-to-justify assumptions. These properties make it very attractive as an potential operating point for the brain (thin blue lines indicate some examples of the cycle, coming out of the plane of the paper).

Looking closely at the equation for r we note that this equation has the same form as the expansion of the pitchfork bifurcation, so at $\rho = 0$, where the initial steady state loses its stability, two new stationary solutions of r emerge. One is at negative radius and hence unphysical, whereas the other is at a positive radius. Due to the constant progression of the angle ϕ this stationary point of r is a cycle in the x, y coordinates (**Figure 6**).

The Hopf bifurcation inherits many properties from the pitchfork bifurcation. Like the pitchfork it has a subcritical and a supercritical form. In the supercritical case a stable limit cycle emerges as the initial steady state loses stability. The existence of stable dynamics on both sides of the bifurcation allows a system to operate in the vicinity of the bifurcation. Moreover, like the pitchfork, the Hopf bifurcation offers long memory of perturbations (perturbations create long-lasting oscillations) and super sensitivity to parameter change (quick rise of oscillation amplitude when the bifurcation point is crossed).

In contrast to the pitchfork, the Hopf bifurcation is a generic bifurcation. Thus we don't have to introduce hard-to-justify assumptions to observe this bifurcation.

In a complex system Hopf bifurcations typically occur when the microscopic parts of the system synchronize. At this point preexisting oscillations on the micro-level transition from oscillating asynchronously to a synchronous mutually reinforcing state such that detectable system-level oscillations are produced. Such a scenario is very plausible for the brain as the individual neurons already have oscillatory characteristics and have been illustrated in models (Brunel, 2000).

In this case the variables x and y typically relate to the microscopic variables of the individual oscillators. For example in a model x could be the number of neurons that are just spiking whereas y is the number of neurons that are currently refractory.

Seen in this light the Hopf bifurcation becomes an order-disorder transition in which disordered phases of oscillators become organized. It has been pointed out that systems can self-organized robustly using simple local rules (Droste et al., 2013). Moreover, spike-timing dependent plasticity observed in neurons is a rule that has the right characteristic to drive the system to such a transition (Meisel and Gross, 2009).

The assumption that the brain (or parts of the brain) operate at a Hopf bifurcation is consistent with information coding in terms of synchrony. The experimental evidence for this type of information coding (e.g., de Charms and Merzenich, 1996) thus lends further weight to this hypothesis.

Among all conceivable bifurcation scenarios on stationary states, and cycles the Hopf bifurcation is the only scenario that offers a stable operating point, super-sensitivity and structural stability. These properties make it extremely attractive for the use in computational systems.

Operating at a Hopf bifurcation point provides the advantageous properties of long information retention and super-sensitivity to parameter change. At the same time very plausible mechanism exist by which the brain could self-organize to this bifurcation and remain there indefinitely. These advantageous features highlight models of synchronization, such as networks of Kuramoto oscillators as promising conceptual models for neural dynamics.

2.7. The Critical Hypersurface

So far we have only studied bifurcations in diagrams with one parameter axis. The same is true for almost all papers that discuss bifurcations in the context of neural criticality. However, let's break this convention and consider what happens in systems with two or more parameters.

The bifurcations that we discussed so far are so-called bifurcations of *codimension 1*. This means that the bifurcations have a single bifurcation condition. To find the bifurcation we must change the parameters until we find a parameter set where the bifurcation condition is met. If we change one parameter we might eventually meet the condition and observe the bifurcation at a specific parameter value.

Mathematically speaking we can say if we have a one-dimensional parameter space (i.e., a parameter axis) then codimension-1 bifurcations occur in a zero-dimensional subset (i.e., specific points in parameter space).

Now suppose we have two parameters p_1, p_2. In the two-dimensional parameter space the bifurcation condition becomes a function of both parameters. Because we only have only one bifurcation condition we can (in general) satisfy it already by setting one of the parameters, say p_1 to the right value. That means (in a typical scenario) that for every value of p_2 we can find the bifurcation at some value of p_1: The bifurcation points fill a curve in the two-dimensional parameter plane.

The existence of this curves of critical point allows the system to move around in parameter space, while remaining at criticality all the time.

A system that has at least two parameters could self-organize to criticality and then start to drift on a curve of critical states. As we drift on the curve we can even encounter further bifurcations, so-called codimension-2 bifurcation points. In such a point the system is then critical in two different ways. For example it is conceivable that we reach a point where a Hopf and a transcritical bifurcation happen at the same time (a degenerate Takens-Bogdanov bifurcation). In a neural system that could be a point where we observe an onset of spontaneous activity (trancritical bif.) and at the same time the onset of synchronization of this activity (Hopf). Likewise we could imagine a higher-codimension bifurcation where the onset of oscillations takes place at the same time as changes in the number of synchronized clusters. Such higher a bifurcation would be very attractive for information processing.

In the real world much more than two parameters could be relevant. If our system has d parameters the bifurcation points of a codimension-1 bifurcation completely fill a $(d-1)$-dimensional subspace. We can say that the form *hyper-surfaces*. In a high-dimensional parameter space the existence of these hypersurfaces gives a self-organizing system potentially a huge parameter space to move around in while staying critical.

It is interesting to ask how many parameters exist in the brain. So far there are only partial answers to this question. On the one hand we might go down the list of network properties that are known to affect network dynamics: The include average connectivity, it's second moment, the spectral radius, the clustering coefficient and various other motif counts. While it is not clear that all of these affect the network dynamics independently we can say that there are at least several of these topological parameters are commonly found to affect dynamical processes on networks.

On the other hand, we could ask how many parameters are necessary to characterize the network structure of the brain completely. In this case the answer is at least one per synapse, which means the effective dimensionality d of the parameter space could be as high as the number of synapses.

So the best of the author's knowledge we can say that the effective dimensionality of the parameter space of the brain is somewhere between tens and billions of parameters. Any answer in this range means that the brain is not confined to a single critical point in parameter space, but has in-fact a huge high-dimensional space to explore, in which it could plausibly sit at the threshold of many different bifurcations at the same time. A particularly intriguing picture is to imagine the brain poised at the critical points of a large number of different Hopf bifurcations, each corresponding to the synchronization of a different community of neurons.

In summary the potentially very high effective dimensionality of the brain opens up some startling perspectives. We should not think of the brain as a system that sits stationarily in one point where a certain codimension-1 bifurcation happens. Instead the brain might be at some very high-codimension that is critical in many (and potentially very many) ways at the same time. Alternatively, mechanism of plasticity could take it on a self-organized journey that explores a high-dimensional critical hyper-surface. In the authors opinion, the most likely scenario is that both of these phenomena, drift on a critical manifold and high-codimension multi-criticality occur simultaneously in the brain.

3. CONCLUSIONS

In this paper I have reviewed some relatively basic and well-known dynamical systems theory, which nevertheless has profound implications for neural dynamics. Along the way we have discussed some side attractions (stability constraints, origins of power laws and critical slowing down, absence of super sensitivity in the transcritical bifurcation). However, perhaps the two most important messages are the ones that are hinted at in the title. There are many critical states in at least two ways:

1. There are many different types of bifurcations that can occur at critical points. And potentially all of the ones discussed here play some role in neural information processing. At the same time the supercritical Hopf bifurcation seems uniquely attractive for cortical information processing because it is the only scenario that allows criticality in a stable steady state, while providing super-sensitivity without requiring a specific degeneracy.
2. Even for a specific type of bifurcation, one should not think of the critical point as an isolated point in parameter space. In a high dimensional parameter space the critical points fill an almost equally high-dimensional hyper-surface. This means that mechanisms of self-organization can explore a large parameter space while maintaining criticality. It also means that the system can reach high-codimension points where the system is simultaneously critical in several, and potential many, different ways.

Particularly the second point highlights the need for future theoretical work to explore how self-organized critical systems drift on critical manifolds and assess the consequences of multi-criticality for information processing. So far such dynamics in high-dimensional parameter spaces remains largely unexplored.

DATA AVAILABILITY STATEMENT

The original contributions presented in the study are included in the article/supplementary material, further inquiries can be directed to the corresponding author/s.

AUTHOR CONTRIBUTIONS

The author confirms being the sole contributor of this work and has approved it for publication.

ACKNOWLEDGMENTS

The author acknowledges support by the HIFMB project of the Ministry for Science and Culture of Lower Saxony and the Volkswagen Foundation (grant ZN3285).

REFERENCES

Anderson, R. M., and May, R. M. (1979). Population biology of infectious diseases I. *Nature* 280, 361–367. doi: 10.1038/280361a0

Beggs, J., and Plenz, D. (2004). Neuronal avalanches are diverse and precise activity patterns that are stable for many hours in cortical slice cultures. *J. Neurosci.* 24:5216. doi: 10.1523/JNEUROSCI.0540-04.2004

Bornholdt, S., and Rohlf, T. (2000). Topological evolution of dynamical networks: global criticality from local dynamics. *Phys. Rev. Lett*. 84, 6114–6117. doi: 10.1103/PhysRevLett.84.6114

Brunel, N. (2000). Phase diagrams of sparsely connected networks of excitatory and inhibitory spiking neurons. *Neurocomputing* 32:307. doi: 10.1016/S0925-2312(00)00179-X

Chialvo, D. (2010). Emergent complex neural dynamics. *Nat. Phys*. 6, 744–750. doi: 10.1038/nphys1803

Couzin, I. D., Ioannou, C. C., Demirel, G., Gross, T., Torney, C. J., Hartnett, A., et al. (2011). Uninformed individuals promote democratic consensus in animal groups. *Science* 334, 1578–1580. doi: 10.1126/science.1210280

Das, A., and Levina, A. (2019). Critical neuronal models with relaxed timescale separation. *Phys. Rev. X* 9:021062. doi: 10.1103/PhysRevX.9.021062

de Charms, R. C., and Merzenich, M. M. (1996). Primary cortical representation of sounds by the coordination of action-potential timing. *Nature* 381, 610–613. doi: 10.1038/381610a0

del Papa, B., Priesemann, V., and Triesch, J. (2017). Criticality signatures in a self-organizing recurrent neural network. *PLoS ONE* 12:e0178683. doi: 10.1371/journal.pone.0178683

Droste, F., Do, A., and Gross, T. (2013). Analytical investigation of self-organized criticality in neural networks. *J. R. Soc. Interface* 10:20120558. doi: 10.1098/rsif.2012.0558

Feudel, U., Pisarchik, A. N., and Showalter, K. (2018). Multistability and tipping. *Chaos* 28:033501. doi: 10.1063/1.5027718

Fontenele, A. J., de Vasconcelos, N. A. P., Feliciano, T., Aguiar, L. A. A., Soares-Cunha, C., Coimbra, B., et al. (2019). Criticality between cortical states. *Phys. Rev. Lett*. 122:208101. doi: 10.1103/PhysRevLett.122.208101

Gross, T., and Blasius, B. (2007). Adaptive coevolutionary networks: a review. *J. R. Soc. Interface* 5, 259–271. doi: 10.1098/rsif.2007.1229

Hahn, G., Ponce-Alvarez, A., Monier, C., Benvenuti, G., and Kumar, A., Chavane, F., et al. (2017). Spontaneous cortical activity is transiently poised close to criticality. *PLoS Comput. Biol*. 13:e1005543. doi: 10.1371/journal.pcbi.1005543

Herz, A., and Hopfield, J. J. (1994). Earthquake cycles and neural reverberations: collective oscillations in systems with pulse-coupled threshold elements. *Phys. Rev. Lett*. 76, 1222–1226. doi: 10.1103/PhysRevLett.75.1222

Hesse, J., and Gross, T. (2014). Self-organized criticality as a fundamental property of neural systems. *Front. Syst. Neurosci*. 8:166. doi: 10.3389/fnsys.2014.00166

James, G. (2015). Modern engineering Mathematics. Pearson, Harlow, 5th edition.

Kanders, K., Lorimer, T., and Stoop, R. (2017). Avalanche and edge-of-chaos criticality do not necessarily co-occur in neural networks. *Chaos* 27:047408. doi: 10.1063/1.4978998

Keeling, M. J., House, T., Cooper, A., and Pellis, L. (2016). Systematic approximations to susceptible-infectious-susceptible dynamics on networks. *PLoS Comput. Biol*. 12:e1005296. doi: 10.1371/journal.pcbi.1005296

Kitzbichler, M., Smith, M., Christensen, S., and Bullmore, E. (2009). Broadband criticality of human brain network synchronization. *PLoS Comput. Biol*. 5:e1000314. doi: 10.1371/journal.pcbi.1000314

Klaus, A., Yu, S., and Plenz, D. (2011). Statistical analyses support power law distributions found in neuronal avalanches. *PLoS ONE* 6:0019779. doi: 10.1371/journal.pone.0019779

Kossio, F. Y. K., Goedeke, S., van den Akker, B., Ibarz, B., and Memmesheimer, R.-M. (2018). Growing critical: self-organized criticality in a developing neural system. *Phys. Rev. Lett*. 121:058301. doi: 10.1103/PhysRevLett.121.058301

Kuehn, C. (2012). Time-scale and noise optimality in self-organized critical adaptive networks. *Phys. Rev. E* 85:026103. doi: 10.1103/PhysRevE.85.026103

Kuznetsov, Y. A. (2004). *Elements of Applied Bifurcation Theory, 3rd Edn*. Heidelberg: Springer Verlag. doi: 10.1007/978-1-4757-3978-7

Linkenkaer-Hansen, K., Nikouline, V. V., Palva, J. M., and Ilmoniemi, R. J. (2001). Long-range temporal correlations and scaling behavior in human brain oscillations. *J. Neurosci*. 21, 1370–1377. doi: 10.1523/JNEUROSCI.21-04-01370.2001

Meisel, C., and Gross, T. (2009). Adaptive self-organization in a realistic neural network model. *Phys. Rev. E* 80:061917. doi: 10.1103/PhysRevE.80.061917

Meisel, C., Storch, A., Hallmeyer-Elgner, S., Bullmore, E., and Gross, T. (2012). Failure of adaptive self-organized criticality during epileptic seizure attacks. *PLoS Comput. Biol*. 8:e1002312. doi: 10.1371/journal.pcbi.1002312

Moretti, P., and Munoz, M. (2013). Griffiths phases and the stretching of criticality in brain networks. *Nat. Commun*. 4:2521. doi: 10.1038/ncomms3521

Priesemann, V., Wibral, M., Valderrama, M., Pröpper, R., Le Van Quyen, M., Geisel, T., et al. (2014). Why brain criticality is clinically relevant: a scoping review. *Front. Syst. Neurosci*. 8:108.

Seung, H. S. (1996). How the brain keeps the eyes still. *Proc. Natl. Acad. Sci. U.S.A*. 93, 13339–13344. doi: 10.1073/pnas.93.23.13339

Timme, N. M., Marshall, N. J., Bennett, N., Ripp, M., Lautzenhiser, E., and Beggs, J. M. (2016). Criticality maximizes complexity in neural tissue. *Front. Physiol*. 7:425. doi: 10.3389/fphys.2016.00425

van Nes, E. H., and Scheffer, M. (2007). Slow recovery from perturbations as a generic indicator of a nearby catastrophic shift. *Am. Nat*. 169, 738–747. doi: 10.1086/516845

Wilting, J., and Priesemann, V. (2014). 25 years of criticality in neuroscience-established results, open controversies, novel concepts. *Curr. Opin. Neurobiol*. 58, 105–111. doi: 10.1016/j.conb.2019.08.002

Wilting, J., and Priesemann, V. (2018). Operating in a reverberating regime enables rapid tuning of network states to task requirements. *Front. Syst. Neurosci*. 12:55. doi: 10.3389/fnsys.2018.00055

Wilting, J., and Priesemann, V. (2019). Between perfectly critical and fully irregular. *Cereb. Cortex* 29, 2759–2770. doi: 10.1093/cercor/bhz049

Yaghoubi, M., de Graaf, T., Orlandi, J. G., Girotto, F., Colicos, M. A., and Davidsen, J. (2018). Neuronal avalanche dynamics indicates different universality classes in neuronal cultures. *Sci. Rep*. 8:3417. doi: 10.1038/s41598-018-21730-1

Zimmern, V. (2020). Why brain criticality is clinically relevant: a scoping review. *Front. Neural Circ*. 14:54. doi: 10.3389/fncir.2020.00054

Conflict of Interest: The author declares that the research was conducted in the absence of any commercial or financial relationships that could be construed as a potential conflict of interest.

frontiers in Computational Neuroscience

ORIGINAL RESEARCH
published: 20 September 2021
doi: 10.3389/fncom.2021.653097

A Neuron-Glial Model of Exosomal Release in the Onset and Progression of Alzheimer's Disease

Hina Shaheen[1]*, *Sundeep Singh*[1] and *Roderick Melnik*[1,2]

[1] M3AI Laboratory, MS2Discovery Interdisciplinary Research Institute, Wilfrid Laurier University, Waterloo, ON, Canada,
[2] BCAM-Basque Center for Applied Mathematics, Bilbao, Spain

Exosomes are nano-sized extracellular vesicles that perform a variety of biological functions linked to the pathogenesis of various neurodegenerative disorders. In Alzheimer's disease (AD), for examples, exosomes are responsible for the release of $A\beta$ oligomers, and their extracellular accumulation, although the underpinning molecular machinery remains elusive. We propose a novel model for Alzheimer's $A\beta$ accumulation based on Ca^{2+}-dependent exosome release from astrocytes. Moreover, we exploit our model to assess how temperature dependence of exosome release could interact with $A\beta$ neurotoxicity. We predict that voltage-gated Ca^{2+} channels (VGCCs) along with the transient-receptor potential M8 (TRPM8) channel are crucial molecular components in Alzheimer's progression.

Keywords: brain, calcium channels, exosomes and biomarkers, molecular communication, temperature effects, astrocytes, dynamic models, Alzheimer's disease

OPEN ACCESS

Edited by:
Axel Sandvig,
Norwegian University of Science and Technology, Norway

Reviewed by:
Maurizio De Pittà,
Basque Center for Applied Mathematics, Spain
Jun Ma,
Lanzhou University of Technology, China

***Correspondence:**
Hina Shaheen
shah8322@mylaurier.ca

Received: *13 January 2021*
Accepted: *20 August 2021*
Published: *20 September 2021*

Citation:
Shaheen H, Singh S and Melnik R (2021) A Neuron-Glial Model of Exosomal Release in the Onset and Progression of Alzheimer's Disease. Front. Comput. Neurosci. 15:653097. doi: 10.3389/fncom.2021.653097

1. INTRODUCTION

Protein misfolding, oligomerization, and aggregation are responsible for the initiation of pathological disorders in the brain (Soto and Pritzkow, 2018). Nano-sized extracellular vesicles (exosomes) are believed to be key mediators in the transfer of cytotoxic proteins between the nerve cells, resulting in the spread of many neurodegenerative diseases, such as Alzheimer's disease (AD), Parkinson's disease (PD), Huntington's disease (HD), and Creutzfeldt-Jacob's disease (CJD) (Jiang et al., 2019; Luo et al., 2020; Zhang and Wang, 2020).

Exosome releases increased intracellular calcium (Ca^{2+}) (Jain, 2019). Specifically, Veletić et al. (2019) have shown that depolarization of neurons and glial cells, such as astrocytes, can trigger multivesicular exosome release therefrom. Because neurons interact with astrocytes and vice versa through a plethora of ion and molecular pathways that can reciprocally affect their membrane electrical potential (De Pittà, 2020), a question arises whether this interaction could be physiologically relevant for exosome release in the brain.

In AD etiology, oligomeric $A\beta$ can substantially affect intracellular Ca^{2+} homeostasis both in neurons and in astrocytes (Bezprozvanny and Mattson, 2008; Shigetomi et al., 2016), thereby potentially regulating exosome release too. The mechanism whereby this could happen and the relevant pathogenic factors are not known. The reason for this gap of knowledge is because of inherent limits in the available technology, and because the biophysical framework to account for exosomal release in the neuropil in the context of neuron-glial interactions is missing (De Pittà and Berry, 2019a). We introduce in this study, the first model for exosomal release leveraging on $A\beta$-dependent intracellular Ca^{2+} homeostasis.

Our model design emphasizes a well-documented pathway for $A\beta$ regulation of intracellular calcium that is amyloid-induced Ca^{2+} permeability through endogenous cation channels (Liu et al., 2010), such as L- and N-type voltage-gated calcium channels (VGCCs) and transient receptor potential melanostatin 8 (TRPM8) channels. These latter channels are prototypic temperature sensors and are emerging as possible key regulators in inflammation (Liu and Qin, 2011), often associated with Alzheimer's related neurodegeneration (Heppner et al., 2015).

This study is organized as follows. In section 2, we describe our model (the schematic representation of the model is given in **Figure 1**) in its different components: (i) Ca^{2+}-dependent exosomal release in neurons and in astrocytes, (ii) astrocytic exosome exocytosis mediated by $A\beta$ in AD, and (iii) temperature dependence of neuron models including *TRPM*8 currents. In section 3, we present numerical simulations based on the developed neuron-glial model. Finally, we discuss our results and outline future directions in section 4.

2. METHODS

2.1. Calcium-Dependent Exosome Release in Neurons

The calcium-mediated exosomal release is restricted to active zones that contain VGCCs that control Ca^{2+} from the extracellular domain, mediate and regulate exocytosis, leading to the exosomal release in the brain (Veletić et al., 2020). This mechanism can be conveniently modeled by combining the Watts-Sherman model for Ca^{2+} exosomal release and the Montefusco-Pedersen models for Ca^{2+}-regulated exocytosis, as originally put forth by Veletić et al. (2020). To link neuronal electrical activity and Ca^{2+}-mediated exocytosis, we first describe intracellular Ca^{2+} dynamics, paying special attention to microdomain Ca^{2+} concentrations surrounding high-voltage activated L-type Ca^{2+} channels (C_L) when the channels are opened ($C_{L|opened}$) and closed ($C_{L|closed}$), low-voltage activated T-type Ca^{2+} channels, as well as the characterization of Ca^{2+} below the plasma membrane (C_m) in the bulk cytosol (C_c), and in the endoplasmic reticulum (C_r). In this fashion, exosomal release can be expressed as a function of L-type Ca^{2+} microdomain concentrations and plasma membrane Ca^{2+} concentrations, respectively, are as follows:

$$R_{C_L} = m_{C_L}^2 h_{C_L} \cdot \mathcal{H}(C_{L|opened}, K_L, n_L) + (1 - m_{C_L}^2 h_{C_L}) \cdot \mathcal{H}(C_{L|closed}, K_L, n_L), \quad (1)$$

$$R_{C_m} = \mathcal{H}(C_m, K_m, n_m), \quad (2)$$

where $\mathcal{H}(x, K, n) = \frac{x^n}{x^n + K^n}$ is the Hill function, $C_{L|closed} = C_m$ (Montefusco and Pedersen, 2015), and the collective exosomal release rate in neurons is given by Veletić et al. (2020):

$$R_n = R_{C_L} + R_{C_m}. \quad (3)$$

The whole-cell intracellular Ca^{2+}dynamics ensues from the mass balance of Ca^{2+} fluxes across four different compartments: (i) C_L; (ii) C_m; (iii) C_c and (iv) C_r. The equations for compartment-specific Ca^{2+} concentrations (Veletić et al., 2020):

$$\frac{dC_{L|opened}}{dt} = -f\left(\alpha \frac{I_{C_L}}{\lambda_{ud}} - B_{ud}(C_L - C_m)\right), \quad (4)$$

$$\frac{dC_m}{dt} = \frac{f}{\lambda_m}\Big(- \alpha I_{C_T} + N_L \Gamma m_{C_L}^2 h_{C_L}(C_L - C_m) - \lambda_c k_{PMCA} C_m - \lambda_c B_m (C_m - C_c)\Big), \quad (5)$$

$$\frac{dC_c}{dt} = f(B_m(C_m - C_c) + p_{leak}(C_r - C_c) - k_{SERCA} C_c), \quad (6)$$

$$\frac{dC_r}{dt} = \frac{f\lambda_c}{\lambda_r}(p_{leak}(C_r - C_c) - k_{SERCA} C_c), \quad (7)$$

where the relevant parameters are provided in **Table 2**.

In terms of coefficients of the equations, f is the ratio of free-to-total Ca^{2+}, $\Gamma = \lambda_{ud} B_{ud}$, α is the constant that transfers current to flux, B_d is the constant that defines the flux from the microdomains to the sub-membrane, the flux from the sub-membrane compartment to the bulk cytosol is defined by B_m, while the volumes of a single microdomain, the sub-membrane compartment, the bulk cytosol, and the endoplasmic reticulum (r) are described by λ_d, λ_m, λ_c, and λ_r, respectively, k_{PMCA} is the rate of Ca^{2+} adenosine triphosphatase (ATPase) at the plasma membrane level, p_{leak} is the rate of the leak current from the r to the cytosol, and k_{SERCA} is the amount of Ca^{2+} sequestration into the r by the sarco/endoplasmic Ca^{2+} ATPase pump. The gating variables in the steady-state are defined in **Table 2**:

$$\frac{dm_x}{dt} = \frac{m_{x,\infty}(v_m) - m_x}{\tau_{mx(v_m)}}; \quad \frac{dh_x}{dt} = \frac{h_{x,\infty}(v_m) - h_x}{\tau_{hx(v_m)}}, \quad (8)$$

where $x = (C_L, C_T, C_N, Na, K)$ and $\mathcal{B}(x, v_{shift}, v_{scale}) = \frac{1}{1+\exp(-(x - v_{shift})/v_{scale})}$.

The experimental evidence reveals that Ca^{2+}-mediated exocytosis by neurons is regulated by intracellular Ca^{2+}, where electrical activity pattern determines the exocytosis Ca^{2+} threshold (Pedersen et al., 2017). Electrical activity is triggered by neuron depolarization, which entails the activation of VGCCs, resulting in increased intracellular Ca^{2+}concentration levels, which interfere with the mobilization of multivesicular bodies, resulting in the release of exosomes and evoking exocytosis (Shaheen et al., 2021). To describe the electrical activity of a depolarized neuron *via* membrane potential, we use the modified Hodgkin-Huxley neuron model, which includes voltage-gated potassium (K^+) channels, voltage-gated sodium (Na^+) channels, a leak current, and an induced control signal/current (I_{ind}) as Veletić et al. (2020):

$$\frac{dv_m}{dt} = \frac{1}{c_m}\Big(g_K(V_K - v_m) + g_{Na}(V_{Na} - v_m) + g_L(V_L - v_m) + I_{ind}\Big), \quad (9)$$

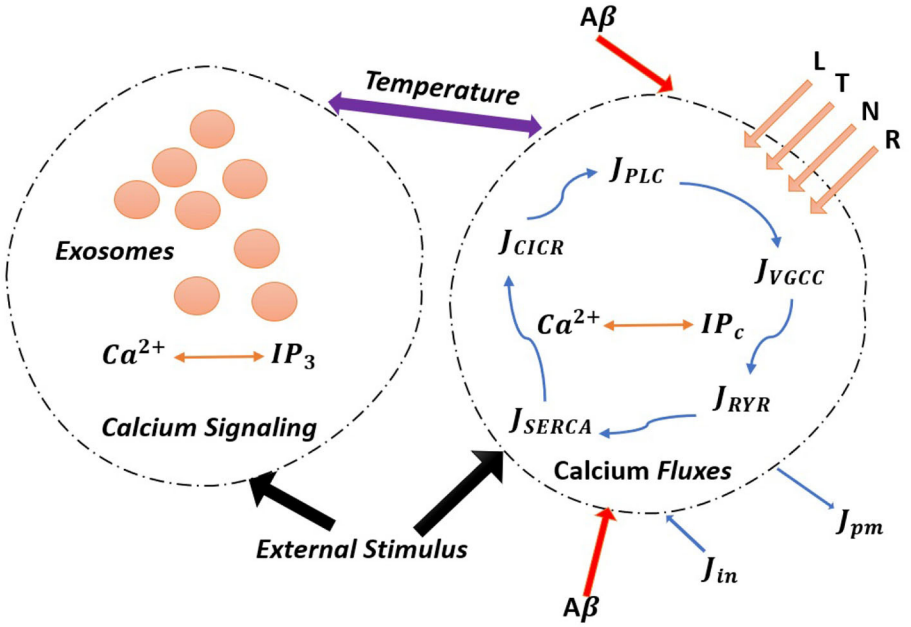

FIGURE 1 | (Color online) The model astrocyte with different Ca^{2+} fluxes and Ca^{2+} signals. External stimulus triggers exosome release in calcium-dependent exocytosis. Astrocytic exosome exocytosis mediated by $A\beta$ with the influence of the L-Type, T-Type, N-Type, and R-Type Ca^{2+} channels.

where c_m is the membrane capacitance, V_K, V_{Na}, and V_L are Nernst potentials for K^+, Ca^{2+}, and Na^+ ions and other ions were clustered together as a "leak" channel, respectively, and g_K, g_{Na}, and g_L are the corresponding membrane conductances. The external stimulus I_{ind} is the current pulses of 500 ms with varying length and amplitude from 10 to 20 $\mu A/cm^2$, voltage-gated conductances ($g_K = \overline{g_K} m_K^4$ and $g_{Na} = \overline{g_{Na}} m_{Na}^3 h_{Na}$) fluctuate over time as action potentials are initiated and propagated (Shaheen et al., 2021).

2.2. Calcium-Dependent Exosomal Release From Astrocytes

Traditionally, astrocytes were thought to be non-excitable brain cells that only provided structural and metabolic support to neurons (Valenza et al., 2011). However, in the last two decades, this viewpoint has shifted and it has been revealed that astrocytes react to neurotransmitters and neuromodulators by increasing cytosolic Ca^{2+} concentration levels (Di Garbo et al., 2007). Indeed, a significant amount of experimental evidence, describing the signaling processes between astrocytes and astrocyte neurons, revealed the potential role of glial cells in neural tissue dynamics (Escartin et al., 2021; Wang et al., 2021). Astrocytes have glutamate-sensitive and metabotropic glutamate receptors (mGluRs) on their plasma membranes (Veletić et al., 2020). The glutamate initiates the intracellular release of Ca^{2+} ions from the endoplasmic reticulum triggered by mGluRs. This is accomplished by chemical reactions involving IP_3, a secondary messenger molecule that is essential for Ca^{2+} mobilization into the cytosol. The IP_3 synthesis has been defined simply in tripartite synapses (a term introduced to emphasize the existence of an astrocyte in the vicinity of two neurons), with the hypothesis that a quantized amount of IP_3 molecules is released after glutamate levels rise due to pre-synaptic spiking activity (Veletić et al., 2019). We are interested in controlling IP_3 with a defined stimulation pattern in our scenario, where the astrocyte differentiated from CNS functions as a neuron-independent unit. Therefore, the IP_3 production rate (P), as a function of a generic control signal v_{ind} applied to depolarize the astrocyte, is given as follows (Veletić et al., 2020):

$$\frac{dP}{dt} = \frac{P_0 - P}{\tau_P} + r_P. \tag{10}$$

Next, combining (Equation 9) with Ca^{2+} dynamics we can propose a model with electrically silent astrocyte for IP_3 development and Ca^{2+}-dependent exocytosis. The Ca^{2+} dynamics surrounding L-Type and N-type Ca^{2+} channels delineate similarly to neurons. It is expected that L-type Ca^{2+}-channels in neurons and astrocytes have identical qualities (Veletić et al., 2020). Hence, C_L concentration in a single astrocytic microdomains is epitomized in Equation (4) by setting $v_m = V_m + v_{ind}$ in all corresponding equations, where $V_m = -70mV$ gives the resting astrocytic membrane potential. The Ca^{2+} concentrations in single microdomains surrounding high-voltage activate N-type Ca^{2+} channels when the channels are opened and closed, and the plasma membrane (C_m) lead to the following equations (Veletić et al., 2020):

$$\frac{dC_{N|opened}}{dt} = -f\left(\alpha \frac{i_{Ca_L}}{\lambda_{ud}} - B_{ud}(C_N - C_m)\right), \tag{11}$$

$$\frac{dC_m}{dt} = \frac{f}{\lambda_m}\Big(-\alpha i_{Ca_T} + N_L \Gamma m_{Ca_L}^2 h_{Ca_L} (C_L - C_m) - \lambda_c k_{PMCA} C_m - \lambda_c B_M (C_m - C_c) + N_N \Gamma m_{Ca_N} h_{Ca_N} (C_N - C_m)\Big), \tag{12}$$

with $C_{N|closed} = C_m$, where $i_{C_N} = g_{C_N}(V_m + v_{ind} - V_C)/N_N$ and g_{C_N} is the membrane conductance of N-type Ca^{2+} channels. In modeling exosomal release from astrocytes, by manipulating the Nadkarni-Jung model that is further based on the Li-Rinzel model (Li and Rinzel, 1994) to define Ca^{2+} concentrations in the bulk cytosol and in the endoplasmic reticulum coupled in astrocytes, we have:

$$\frac{dC_c}{dt} = -c_1 v_1 m_{P,\infty}^3 h_P^3 (C_c - \frac{c_0 - C_c}{c_1}) - c_1 v_2 (C_c - \frac{c_0 - C_c}{c_1}) - v_3 \cdot \mathcal{H}(C_c, k_3, n_4), \tag{13}$$

where the values of parameters used in the above equations are given in **Table 1** and the gating variable $m_{P,\infty} = \mathcal{H}(P, d_1, d_6) \cdot \mathcal{H}(C_c, d_5, d_6)$, $h_{P,\infty} = \mathcal{H}(Q, C_c, d_6)$ adopted from Veletić et al. (2020), moreover

$$\frac{dh_P}{dt} = \frac{h_{P,\infty} - h_P}{\tau_{h_P}}, \tag{14}$$

and $d_6 = 1$, $\tau_{h_P} = \frac{1}{a_2(Q+C_c)}$, $Q = d_2 \frac{P+d_1}{P+d_3}$. The IP_3 molecules bind to receptors on the surface of the endoplasmic reticulum, allowing Ca^{2+} to be released once they are generated *in situ* (or obtained from other cells through gap junction). Since internal Ca^{2+} stores are also responsive to Ca^{2+}, an increase in Ca^{2+} concentration deploys sufficient Ca^{2+} release. This biological process is known as Calcium-Induced Calcium Release (CICR) which shows the first term of Equation (12). Additional Ca^{2+} flow from the endoplasmic reticulum into the cytosol usually arises (leakage flow), while Ca^{2+} based ATPase pumps (SERCA) work in the opposite direction to uptake Ca^{2+} (second term of Equation 12) back into the stores for potential use (pump flow). The balance between passive leakage from the endoplasmic reticulum and SERCA uptake regulates Ca^{2+} concentration at rest. Sneyd and Li and Rinzel have identified analytically the Ca^{2+} dynamics and release/uptake processes triggered by IP_3 (Escartin et al., 2021). Further, the relative exosomal release rate feature in astrocytes based on N-type Ca^{2+} microdomain concentrations, as Watts and Sherman did for glucagon secretion in pancreatic alpha cells (Watts and Sherman, 2014):

$$R_{C_N} = m_{C_N}^2 h_{C_N} \cdot \mathcal{H}(C_{N|opened}, K_N, n_N) + (1 - m_{C_N}^2 h_{C_N}) \cdot \mathcal{H}(C_{N|closed}, K_N, n_N). \tag{15}$$

The relative exosomal release rate depending on C_L, C_m concentrations that is, R_{C_L} and R_{C_m}, follows Equations (1, 2), respectively, and the collective exosomal release rate in astrocytes is defined as follows (Veletić et al., 2020):

$$R_a = R_{C_L} + R_{C_m} + R_{C_N}. \tag{16}$$

2.3. Amyloid-Beta Peptide Modulation of Astrocytic Exosome Exocytosis

Alzheimer's disease is one of the most prominent neurodegenerative diseases with an unknown structure of amyloid-beta peptide ($A\beta$). The distribution of Ca^{2+} astrocyte signaling plays an important role in AD. We have modified our previously elaborated model of Ca^{2+}-mediated exosomal dynamics in neural cells to study spontaneous Ca^{2+}oscillations in astrocytes in order to investigate the impact of $A\beta$ on intracellular Ca^{2+} dynamics during AD. By activating the L-type VGCCs and metabolic glutamate receptors, or by increasing ryanodine receptor sensitivity and Ca^{2+}leakage, $A\beta$ will increase the resting concentration of intracellular $Ca^{2+}$and adjust the regime of Ca^{2+} oscillations. The primary target of $A\beta$ neurotoxicity is thought to be astrocytes (Gao et al., 2020). Astrocytes communicate with neurons and other brain cells in a functional way. Although astrocytes are not electrically excitable, they have a complex repertoire of intracellular Ca^{2+} signaling that changes across time and space within single astrocytes and through astrocytic networks (Semyanov et al., 2020). In an AD context, a computational model was recently used to investigate the effects of $A\beta$ on Ca^{2+}regulation (Latulippe et al., 2018).

In what follows, we provide further details of our new model to address the Ca^{2+}-mediated exosomal release in astrocytes mediated by $A\beta$ through four distinct pathways: VGCCs, metabotropic glutamate receptors 5, ryanodine receptor channels, and membrane leak (Gao et al., 2020). The $A\beta$ deposit and its neurotoxicity associated with AD is involved in the disruption of Ca^{2+} regulation in astrocytes. Based on our previously discussed model, we have carried out a comprehensive simulation on Ca^{2+}-mediated exosomal release in astrocytes mediated by $A\beta$, by also incorporating induced control signal/current. In the model of Ca^{2+}-mediated exosomal release in astrocytes, different types of VGCCs are responsible for Ca^{2+} influx J_{VGCC} from the extracellular to the intracellular space. The Hodgkin-Huxley equations were used to describe the electrophysiological properties of these VGCCs and the related parameters are given in **Tables 1**, **2**. Only the L-type VGCC current was thought to be mediated by $A\beta$ in this study (Gao et al., 2020). All forms of Ca^{2+} ionic currents through VGCCs shared the simplified HH form:

$$I = gmh(v_m - V_C), \tag{17}$$

where g represents membrane conductance, m and h represent the channel stimulation and inhibition (Zeng et al., 2009), respectively, whose values recover gradually to their steady-state values $\bar{m}$ and $\bar{h}$ given as

$$\frac{dy}{dt} = \frac{\bar{y} - y}{\tau_y}, \tag{18}$$

where $y = (m, h)$ and v_m is the membrane potential as given in Equation (9), V_C is the constant Nernst potential for calcium and other relevant parameters are given in **Table 1** (Veletić et al., 2019, 2020; Gao et al., 2020).

TABLE 1 | Parameter set for calcium-mediated exosomal dynamics.

Parameter	Value	Parameter	Value	Parameter	Value
V_K	$-70(mV)$	V_L	$-54.4(mV)$	$V_{h_{C_T}}$	$-52(mV)$
$V_{\tau_{h_{C_T}}}$	$-50(mV)$	$V_{\tau_{m_{C_T}}}$	$-50(mV)$	$V_{\tau_{h_{C_L}}}$	$0(mV)$
$V_{m_{C_T}}$	$-49(mV)$	$V_{h_{C_L}}$	$-33(mV)$	$V_{m_{C_L}}$	$-30(mV)$
$V_{\tau_{m_{C_L}}}$	-23(mV)	$S_{h_{C_L}}$	$-5(mV)$	$S_{h_{C_T}}$	$-5(mV)$
$\tau_{m0_{V_{C_T}}}$	$0(ms)$	λ_{ud}	$2.62 \times 10^{-19}(L)$	α	$5 \times 10^{-15}(\mu molpm/As)$
λ_m	$5 \times 10^{-14}(L)$	λ_c	$5.7 \times 10^{-13}(L)$	p_{leak}	$3 \times 10^{-4}(ms^{-1})$
f	0.01	$\tau_{m0_{V_{C_L}}}$	$0.05(ms)$	k_{SERCA}	$0.100(ms^{-1})$
B_m	$0.128(ms^{-1})$	g_L	$0.3(mS/cm^3)$	k_{PMCA}	$0.300(ms^{-1})$
g_{C_T}	$0.4(nS)$	g_{C_L}	$0.7(nS)$	c_m	$1(uF/cm^2)$
$\tau_{m_{V_{C_L}}}$	$1(ms)$	K_m	$2(uM)$	n_L	4
n_m	4	$S_{m_{C_T}}$	$4(mV)$	$\tau_{h0_{V_{CT}}}$	$5(ms)$
$S_{m_{C_L}}$	$10(mV)$	T	10^oC	$S_{\tau_{m_{C_T}}}$	$12(mV)$
$\tau_{m_{V_{CT}}}$	$15(ms)$	$S_{\tau_{h_{C_T}}}$	$15(mV)$	$S_{\tau_{m_{C_L}}}$	$20(mV)$
$S_{\tau_{h_{C_L}}}$	$20(mV)$	$\tau_{h_{V_{C_T}}}$	$20(ms)$	$\frac{\lambda_c}{\lambda_r}$	31
$\overline{g_K}$	$36(mS/cm^3)$	V_{Na}	$50(mV)$	K_L	$50(\mu M)$
$\tau_{h0_{V_{C_L}}}$	$51(ms)$	$\tau_{h_{V_{C_L}}}$	$60(ms)$	V_C	$65(mV)$
$\overline{g_{Na}}$	$120(mS/cm^3)$	N_L	200	B_{ud}	$264(ms^{-1})$
A_{VL}	1	A_{RYR}	1	A_m	1
A_{in}	1	l	0.4, 1	k_1	0.013
k_2	0.18	k_d	0.13	n_3	3
a_1	0.003	a_2	0.02	n_5	3.5
n_4	2	λ_{PM}	4.2	λ_{ast}	$3.49 * 1e - 13$
M_{SERCA}	$15\mu M/s$	M_{ClCR}	$10s^{-1}$	M_{PLC}	$0.05\mu M/s$
M_{PLC}	$0.05\mu M/s$	n_1	2.02	n_2	2.2
P_{SERCA}	$0.1\mu M/s$	P_{PC}	$0.3\mu M/s$	P_{CA}	$0.15\mu M/s$
P_{CI}	$0.15\mu M$	c_0	$2\mu M$	P_{IP3}	$0.1\mu M$
P_{deg}	$0.08s^{-1}$	P_f	$0.01s^{-1}$	$\bar{g}_T$	$0.0600pS$
$\bar{g}_L$	$3.5000pS$	$\bar{g}_N$	$0.3900pS$	$\bar{g}_R$	$0.2225pS$
V_C	$65mV$	ΔH	$-156KJ/mol$	ΔS	$-550J/molK$
z	0.87	R	$8.3144J/molK$	F	$96485C/mol$
c_1	0.185	v_1	$6s^{-1}$	v_2	$0.11s^{-1}$
v_3	$0.9\mu M/s$	k_3	$0.1\mu M$	d_1	0.13
d_2	1.049	d_3	0.943	d_5	0.082
a_2	$0.5/(\mu Ms)$	IP_{30}	$0.160\mu M$	r_P	$0.04\mu M/s$
τ_P	$1/0.000140ms$	V_m	$-70mV$	g_{C_N}	$0.6nS$
$V_{m_{C_N}}$	$-5mV$	$S_{m_{C_N}}$	$10mV$	$V_{h_{C_N}}$	$33mV$
$S_{h_{C_N}}$	$-5mV$	$\tau_{m_{V_{C_N}}}$	$1ms$	$\tau_{m0_{V_{C_N}}}$	$0.05ms$
$V_{\tau_{m_{C_N}}}$	$-23mV$	$S_{\tau_{m_{C_N}}}$	$20mV$	$\tau_{h_{V_{C_N}}}$	$60ms$
$\tau_{h0_{V_{C_N}}}$	$51ms$	$V_{\tau_{h_{C_N}}}$	$0mV$	$S_{\tau_{h_{C_N}}}$	$20mV$
N_N	200	n_N	4	K_N	$2\mu M$

We use parameter l to reflect a fixed amount of $A\beta$ concentration present in the environment to investigate the effects of $A\beta$. In addition, we use A_{VL} to monitor the strength of $A\beta$ effects on the L-type VGCC current pathway, resulting in a total Ca^{2+}current as follows:

$$I_{VGCC} = I_{C,T} + (1 + A_{VL}l)I_{C,L} + I_{C,N} + I_{C,R}, \tag{19}$$

where the corresponding flux is defined as

$$J_{VGCC} = -\frac{I_{VGCC}}{zF\lambda_{ast}}. \tag{20}$$

The concrete formula for each type of calcium current is given in detail in **Table 2** adopted from Zeng et al. (2009). The synthesis of IP_3 catalyzed by phospholipase (PLC) is enhanced by cytoplasmic Ca^{2+} in this model. The IP_3 receptors (IP_3R)

TABLE 2 | Details of voltage-gated calcium channels (VGCCs), time constants, and gating functions.

Channel type	Equation of channel kinetics
$m_{K/Na,\infty}$	$\frac{\alpha_{m_{K/Na}}}{\alpha_{m_{K/Na}}+\beta_{m_{K/Na}}}$
$h_{Na,\infty}$	$\frac{\alpha_{h_{Na}}}{\alpha_{h_{Na}}+\beta_{h_{Na}}}$
$\tau_{h_{Na}}$	$\frac{1}{\alpha_{h_{Na}}+\beta_{h_{Na}}}$
$\tau_{m_{K/Na}}$	$\frac{1}{\alpha_{m_{K/Na}}+\beta_{m_{K/Na}}}$
$\alpha_{m_{Na}}$	$0.1(v_m+40)\mathcal{B}(v_m,40,10)$
$\beta_{m_{Na}}$	$4*\exp\left(-(v_m+65)/18\right)$
α_{m_K}	$(0.01(v_m+55))\mathcal{B}(v_m,55,10)$
β_{m_K}	$0.125*\exp\left(-(v_m+65)/18\right)$
$\alpha_{h_{Na}}$	$0.07*\exp\left(-(v_m+65)/20\right)$
$\beta_{h_{Na}}$	$\mathcal{B}(v_m,35,10)$
$m_{C_x,\infty}$	$\mathcal{B}(v_m,V_{m_{C_x}},S_{m_{C_x}})$
$h_{C_x,\infty}$	$\mathcal{B}(v_m,V_{h_{C_x}},S_{h_{C_x}})$
$T-type$	$I_{C_T}=\bar{g}_T m_T(h_{Tf}+0.04h_{Ts})(v_m-V_C)$
	$\tilde{m}_T=\mathcal{B}(v_m,63.5,1.5)$
	$\tilde{h}_{Tf}=\mathcal{B}(v_m,76.2,3)$
	$\tilde{h}_{Ts}=\mathcal{B}(v_m,76.2,3)$
	$\tau_{h_{Tf}}=50*\exp(-((v_m+72)/10)^2)+10$
	$\tau_{h_{Ts}}=400*\exp(-((v_m+100)/10)^2)+400$
	$\tau_{m_T}=65*\exp(-((v_m+68)/6)^2)+12$
$L-type$	$I_{C_L}=\bar{g}_L m_L h_L(v_m-V_C)$
	$\tilde{m}_L=\mathcal{B}(v_m,50,3)$
	$\tilde{h}_L=(0.00045/(0.00045+C_c/1000))$
	$\tau_{m_L}=18\exp(-((v_m+45)/20)^2)+1.5$
$N-type$	$I_{C_N}=\bar{g}_N m_N h_N*(v_m-V_C)$
	$m_N=\mathcal{B}(v_m,45,7)$
	$h_N=0.0001/(0.0001+C_c/1000)$
	$\tau_{m_N}=18*\exp(-((v_m+70)/25)^2)+0.3$
$R-type$	$I_{C_R}=\bar{g}_R m_R h_R((v_m)-V_C)$
	$\tilde{m}_R=\mathcal{B}(v_m,10,10)$
	$\tilde{h}_R=\mathcal{B}(v_m,48,5)$
	$\tau_{h_R}=0.5*\exp(-((v_m+55.6)/18)^2)+0.5$
	$\tau_{m_R}=0.1*\exp(-((v_m+62)/13)^2)+0.05$
$\tau_{m_{C_x}}$	$\frac{\tau_{m_{V_{C_x}}}}{\exp(\frac{-(v_m-V_{\tau m_{C_x}})}{S_{\tau m_{C_x}}})+\exp(\frac{(v_m-V_{\tau m_{C_x}})}{S_{\tau m_{C_x}}})}+\tau_{m0_{V_{C_x}}}$
$\tau_{h_{C_x}}$	$\frac{\tau_{h_{V_{C_x}}}}{\exp(\frac{-(v_m-V_{\tau h_{C_x}})}{S_{\tau h_{C_x}}})+\exp(\frac{(v_m-V_{\tau h_{C_x}})}{S_{\tau h_{C_x}}})}+\tau_{h0_{V_{C_x}}}$

are mediated by cytoplasmic Ca^{2+} and IP_3, inducing Ca^{2+} flow out of the endoplasmic reticulum by CICR. Importantly, CICR from the endoplasmic reticulum is perhaps the most well-studied Ca^{2+} signaling pathway in astrocytes (De Pittà et al., 2019). $A\beta$ may mediate the L-type VGCC, metabotropic glutamate receptors 5 (mGluR5), ryanodine receptor (RyR) channels, and membrane leak J_{in} (Gao et al., 2020). Next, we define J_{SERCA} which represents the flux of calcium ions from the cytosol into the endoplasmic reticulum through the sarcoplasmic/endoplasmic reticulum calcium ATPase (SERCA). The leak flux due to the concentration gradient is indicated by the "leak" from the endoplasmic reticulum (J_r). The other Ca^{2+} fluxes $J_{CICR}, J_{SERCA}, J_{RyR}, J_r, J_{in}$, and J_{pm} are defined as follows:

$$J_{CICR}=4M_{CICR}\cdot\mathcal{H}(P_{CA},C_c,n_1).\mathcal{H}(C_c,P_{CI},n_1)\cdot\mathcal{H}(IP_c,P_{IP_3},n_2)((C_r-C_c) \quad (21)$$

$$J_{SERCA}=M_{SERCA}\cdot\mathcal{H}(C_c,P_{SERCA},n_4), \quad (22)$$

$$J_{RyR}=(k_1+k_2\cdot\mathcal{H}(C_c,k_d+A_{RyR}l,n_3)(C_r-C_c), \quad (23)$$

$$J_r=P_f(C_r-C_c), \quad (24)$$

$$J_{in}=a_1+a_2P_c+A_{in}l^{n_5}, \quad (25)$$

$$J_{pm}=\lambda_{PM}\cdot\mathcal{H}(C_c,K_{pm},n_4). \quad (26)$$

In J_{in}, J_{PLC}, and J_{RyR}, we also use A_{in}, A_{RyR}, A_m to monitor the intensity of these different effects, as well as l to represent the impact of $A\beta$. The essential parameters used in our analysis are listed in **Table 1**, they have been adopted from Gao et al. (2020). The modified Ca^{2+}concentrations in the cytosol, endoplasmic reticulum, and the IP_3 concentrations in the IP_c cell (P_c) are defined as follows:

$$\frac{dC_c}{dt}=J_{VGCC}+J_{in}+J_{RyR}+J_{CICR}+P_f(C_r-C_c)-J_{SERCA}-J_{pm}, \quad (27)$$

$$\frac{dC_r}{dt}=J_{SERCA}-J_{CICR}-J_{RyR}-P_f(C_r-C_c), \quad (28)$$

$$\frac{dP_c}{dt}=J_{PLC}-P_{deg}P_c, \quad (29)$$

where the initial concentrations are $C_c = 0.1\mu M, P_c = 0.1\mu M, C_r = 1.5\mu M$ at $t = 0$ motivated and validated by Gao et al. (2020) and P_{pC} is a half-saturation constant for calcium activation of PLC, J_{PLC} is the IP_3 production rate and defined as:

$$J_{PLC}=(1+A_ml)M_{PLC}\cdot\mathcal{H}(C_c,P_{pC},n_4). \quad (30)$$

In astrocytes, our model can replicate typical Ca^{2+} oscillations under the influence of $A\beta$. In addition, $A\beta$-containing exosomal release from astrocytes could be coupled by considering L-Type, N-type, and submembrane Ca^{2+} concentrations defined in Equations (4, 11–12). However, the bulk cytosol, endoplasmic reticulum, and P_c concentrations are the same as defined in Equations (27–29). Therefore, the relative exosomal release incorporating $A\beta$ would be the same as defined in Equation (16) by using the concrete formula for each type of calcium current is given in **Table 2**. Further, we recall that, in astrocytes, transient elevations in cytoplasm-free Ca^{2+} levels can be thought of as a form of Ca^{2+} excitability (Valenza et al., 2011). The astrocytic plasma membrane contains a variety of neurotransmitter receptors, and experimental findings show that astrocytes near synapses react to neurotransmitters (such as glutamate, GABA, ATP, and others) by increasing their

intracellular calcium levels (Di Garbo et al., 2007; Wang et al., 2012). The release of glutamate, ATP, and other neuromodulators substances is mediated by an increase in Ca^{2+}, which can regulate synaptic communication between neurons through a biological process. Furthermore, recent studies show that glutamate produced by astrocytes influences neuronal activity by stimulating a depolarizing current in neurons (De Pittà, 2020). Therefore, for modeling the effect of glutamate release of astrocytes we used the Nadkarni and Jung model (Nadkarni and Jung, 2004) that considers a minimal neural network model made up of two coupled units: a pyramidal neuron and an astrocyte, by means of the Ca^{2+} concentration to the additional current toward the post-synaptic neuron:

$$I_{astro} = A_{astro} \cdot H[1000 \cdot y] ln(y), \tag{31}$$

where $y = 1000 \cdot C_c - 196.69$, $A_{astro} = 2.11 \mu \text{A/cm}^2$, $H(x)$ is the Heaviside function (Valenza et al., 2011) and C_c is the cytosolic calcium concentration in the astrocyte defined in Equation (27). Therefore, the modified membrane potential for the neuron-astrocyte network model is defined as follows (Di Garbo et al., 2007):

$$\frac{dv_m}{dt} = \frac{1}{c_m}\Big(g_K(V_K - v_m) + g_{Na}(V_{Na} - v_m) + g_L(V_L - v_m) + I_{ind} + I_{astro}\Big). \tag{32}$$

2.4. TRPM8 Channel Kinetics

In the present section, we will construct a more realistic neuronal model where the main characteristics account for temperature effects on Ca^{2+}-dependant exosomal release in the neurons given in section 2.1. It is noteworthy to mention that in neurons potassium currents exceed sodium currents at higher temperatures, resulting in action potential failure. Thermal inhibition may, however, also be described by other temperature-dependent adjustments (Ganguly et al., 2019). Therefore, understanding the effects of temperature on Ca^{2+}-mediated exosomal release could be very useful for a more precise design of strategies to control neural activity in the brain. We will use the modified Hodgkin-Huxley model to capture the response of Ca^{2+}-mediated exosomal release in the neurons by varying the peak sodium and potassium conductances with temperature. It has been shown that the resting potential varies with the temperature (Ganguly et al., 2019). In the simplified neuronal model presented in section 2.1, the peak sodium and potassium conductances $\overline{g_{Na}}$ and $\overline{g_K}$, respectively, were considered to be constant and temperature independent as given in **Table 1**, but these values vary with temperature for a more realistic neuronal model, i.e., ($g_K = g_{Kmax}(T)m_K^4$ and $g_{Na} = g_{Namax}(T)m_{Na}^3 h_{Na}$), where $g_{Kmax}(T) = 1.60 \exp^{-\left(\frac{T-27.88}{12.85}\right)^2}$ and $g_{Namax}(T) = 0.42 \exp^{-\left(\frac{T-31.83}{31.62}\right)^2}$ (Ganguly et al., 2019). Thus, while modeling the temperature effects, only the membrane potential, given in Equation (9), will be modified and the peak conductances values will be computed from the temperature-dependent gating variables defined as follows:

$$\begin{cases} \frac{dm_{K/Na}}{dt} = \phi_{m_{K/Na}}(T)(\alpha_{m_{K/Na}}(1 - m_{K/Na}) - \beta_{m_{K/Na}} m_{K/Na}), \\ \frac{dh_{Na}}{dt} = \phi_{h_{Na}}(T)(\alpha_{h_{Na}}(1 - h_{Na}) - \beta_{h_{Na}} h_{Na}), \end{cases} \tag{33}$$

where the functional dependencies of ϕ_{m_K}, $\phi_{m_{Na}}$, and $\phi_{h_{Na}}$

$$\begin{cases} \phi_{m_K}(T) = 4.3518 \cdot 2.7^{\frac{T-20}{10}}, \\ \phi_{m_{Na}}(T) = 4.4288 \cdot 3^{\frac{T-20}{10}}, \\ \phi_{h_{Na}}(T) = 3.8923 \cdot 2.3^{\frac{T-20}{10}}, \end{cases} \tag{34}$$

are adopted from Ganguly et al. (2019) for the considered temperature of 25°C. Furthermore, we studied the somatosensory neuronal subset of cold thermosensors by creating a mathematical model of a cold sensing neuron in order to better understand the variety of ionic channels involved in Ca^{2+}-dependent exosomal dynamics in neurons. Cold insensitive sodium channels are thought to play a role at extremely low temperatures, while TRPM8 has been established as a basic channel in characterizing cold-sensing neurons (Luiz et al., 2019). Voltage-gated potassium channels, in addition to these cold-specific ion channels, have been proposed to influence the temperature threshold degree of activation (Teichert et al., 2014). This model, in particular, shows how TRPM8 controls temperature-dependent initiation and inhibition at the threshold level. Note that a general Hodgkin-Huxley neuronal model is used here, with an additional current flowing through the TRPM8 channel (McGahan and Keener, 2020). Therefore, the modified membrane potential is defined as follows:

$$\frac{dv_m}{dt} = \frac{1}{c_m}\Big(g_K(V_K - v_m) + g_{Na}(V_{Na} - v_m) + g_L(V_L - v_m) + I_{ind} + I_{m8}\Big). \tag{35}$$

To give a current (I_{m8}) for the cold sensing TRPM8 channel in contrast to the prior Hodgkin-Huxley model, prompted by McGahan and Keener (2020), with the current taking the following basic form:

$$I_{m8} = g_{m8} a_{m8} (v_m - V_{m8}), \tag{36}$$

where g_{m8} is the maximal conductance of TRPM8 and V_{m8} is the reversal potential for TRPM8 channels. In addition, a_{m8} is temperature-dependent and given by Madrid et al. (2009) and McGahan and Keener (2020).

$$a_{m8} = \mathcal{B}((T + 273.15)\Delta S, \Delta H - zFv_m, R(T + 273.15)), \tag{37}$$

where ΔH and ΔS are the enthalpy and entropy variations in between closed and open states, respectively, z is the gating charge, F and R are Faraday's and universal gas constants, respectively, T is the temperature in ^{o}C, and V_{m8}, as previously stated, is the reversal potential of the TRPM8 channels, which has been experimentally shown to be near 0 mV (McGahan

and Keener, 2020) and hence for all our analysis we set $V_{m8} = 0$. Furthermore, we will modify the neuronal model presented in section 2.3, where the main characteristics account for temperature effects on Ca^{2+}-mediated exosomal release in astrocytes mediated by $A\beta$. To quantify the effects of temperature in the developed model, the membrane potential and the temperature dependant gating variables given in Equations (33–35) will be used. Moreover, we will develop a biologically driven model of a Ca^{2+}-mediated exosomal release in astrocytes mediated by $A\beta$ of a specific cold thermosensor with the existence of TRPM8 channels. Therefore, we couple the developed neuronal model with TRPM8 channels for analyzing the temperature threshold dependence on cold-sensing neurons, utilizing (Equations 35–37).

3. RESULTS

3.1. Mechanism of Ca^{2+}-Dependant Exosome-Release Both in Astrocytes and in Neurons

We start by quantifying the influence of Ca^{2+} mediated exocytosis on the membrane potential with a focus on microdomain Ca^{2+} concentrations around high-voltage activated L-type and low-voltage activated T-type Ca^{2+} channels. Also, a definition of Ca^{2+} below the plasma membrane, in the bulk cytosol, and in the endoplasmic reticulum using the Ca^{2+}-mediated exosomal dynamics neuronal model. Moreover, the mechanism of Ca^{2+}-dependant exosome release in response to square pulses of DC input currents of different amplitudes, both in neurons and astrocytes on the Ca^{2+}-mediated exosomal dynamics is also investigated. The numerical results provided in this section are obtained by using the parameter values collected from Veletić et al. (2020), as presented in **Table 1**.

Motivated by Veletić et al. (2020), an external stimulus has been applied to excite the neurons by using the induced current pulses ranging from amplitudes of 10–20 μA/cm^2 for a duration of 500 ms, as depicted in **Figure 2A**. The effects of the induced pulse of 10–20 μA/cm^2 on the membrane potential have been presented in **Figure 2B**. As evident from this figure, the rate of generated sequences of the action potentials is proportional to both the magnitude and duration of the external stimuli. Not only this, but the spiking sequences are also significantly increased when the stimulus effect is incorporated within the numerical model. Importantly, these spiking sequences control the dynamics of the VGCCs in the membrane (Veletić et al., 2020). In addition, the rate of released exosomes from neurons with relative contributions of Ca^{2+} channels (evaluated by Equations 1–7) is shown in **Figure 2C** for the induced pulse of 10–20 μA/cm^2. As evident from **Figure 2C**, the applied external stimulus increases action potential mediated oscillations around the baseline, resulting in a linear increase in exosomal release concentrations from neurons. As for astrocytes, the IP_3 development rate is linearly proportional to the external stimuli v_{ind} adopted from Veletić et al. (2020).

The corresponding exosomal release rate in astrocytes with relative contributions of the Ca^{2+} channels are evaluated by Equations (10–16) and is shown in **Figure 2D** corresponding to $v_{ind} = 10 - 30$ mV (Veletić et al., 2020), where one can approximate the release rate as constant during the controlling phase. It is noteworthy to mention that for the considered parameter set, the total concentration of exosomal release rate in astrocytes is mainly made up of concentrations based on N-type Ca^{2+} concentrations (for heavy depolarization), L-type Ca^{2+} concentrations, and sub-membrane Ca^{2+} concentrations (for weak depolarization). Astrocytes, unlike neurons, are electrically silent and incapable of generating action potentials (De Pittà and Berry, 2019b). This implies a variety of mechanisms, including chemical processes involving IP_3, that cause astrocyte intracellular Ca^{2+} levels to rise. As shown in **Figures 2C,D**, these pathways have significantly slower dynamics than neuronal spiking, resulting in a significantly slower exosomal release by astrocytes as compared to the exosomal released by neurons. We detect an almost linear rise in the concentration of released exosomes from neurons for all stimuli intensities when non-depleted readily releasable exosomes are present in the cytosol throughout the stimulation period. We also found that three-quarters of the concentration of released exosomes in the considered scenario emanates from the concentration reliant on sub-membrane Ca^{2+} concentrations. As of exosomal release from astrocytes, we find that the concentration of released exosomes increases for all evaluated stimulus intensities when non-depleted readily releasable exosomes are present in the cytosol. Indeed, Ca^{2+} signaling is the most often observed readout of astrocyte activity in response to induced pulse, whether by synaptic activity, neuromodulators diffusing in the extracellular ambiance, or external chemical, mechanical, or visual stimuli. As shown by this interpretation, the individual astrocytic Ca^{2+} transient is viewed to some extent as an integration of the triggering external induced pulse and therefore is regarded as a demodulating of this pulse (De Pittà et al., 2019). It is worth noting that exosomes released by astrocyte activities demonstrated the capacity to specifically target neurons. Furthermore, the influence of the generated pulse/control signal presented in **Figure 2A** on the microdomain calcium concentrations is delineated in **Figure 3**. As evident, the increase in the amplitude of the control signal stimuli from 10 to 20 μA/cm^2 results in a corresponding increase in the concentrations of C_r, C_m, C_c, while the effect on the C_L concentration is quite negligible.

3.2. Characterization of Amyloid-Beta in Astrocytic-Calcium Signaling and Exosome Release

Calcium mediated exosomal release in astrocytes has been quantified for the membrane potential with particular attention given to microdomain Ca^{2+} concentrations surrounding L and T-type Ca^{2+} channels linked to a description of Ca^{2+} in the bulk cytosol, the endoplasmic reticulum, and the P_c concentrations. The numerical results presented in this section are based on the parameter values gathered (Ganguly et al., 2019; McGahan and Keener, 2020; Veletić et al., 2020) as presented in **Tables 1**, **2**. This newly developed model aimed to explore the

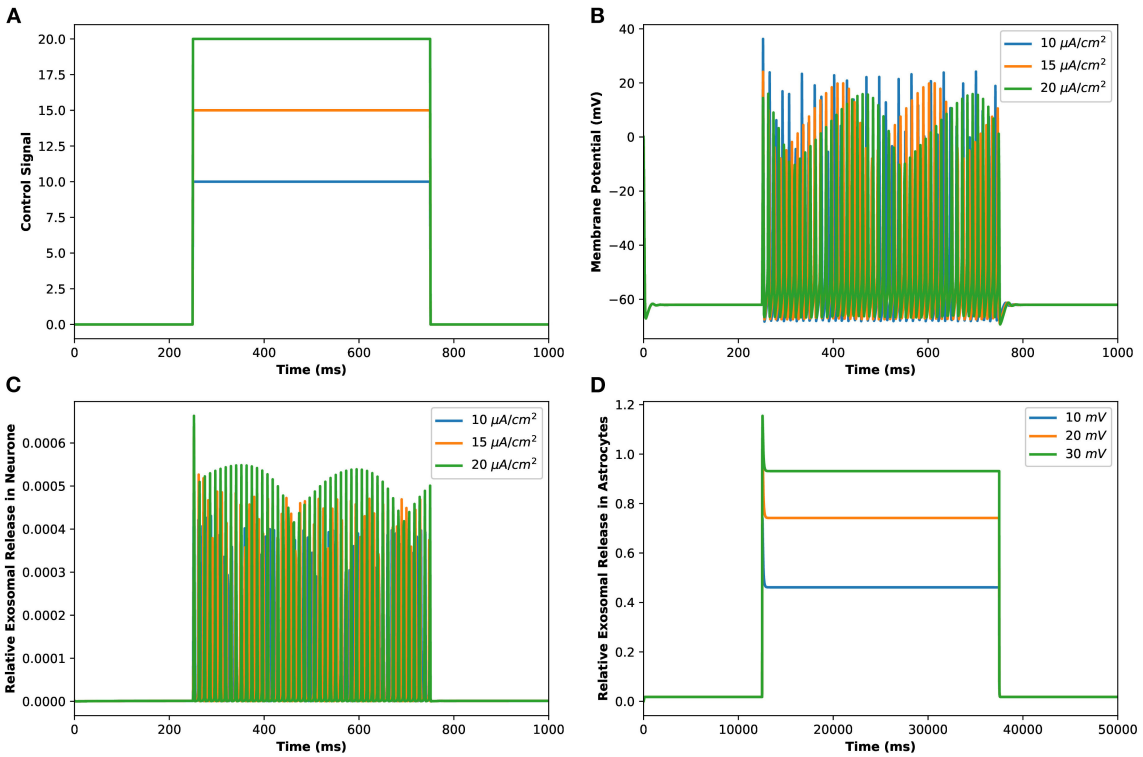

FIGURE 2 | (Color online) **(A)** Different amplitudes of induced control signals/currents ($I_{ind}(\mu A/cm^2)$) considered in the present study. **(B)** Responses/spiking sequence in the depolarized neurons, **(C)** the relative exosomal release rate in neurons, and **(D)** the relative exosomal release rate in astrocytes, for $I_{ind} = 20\ \mu A/cm^2$.

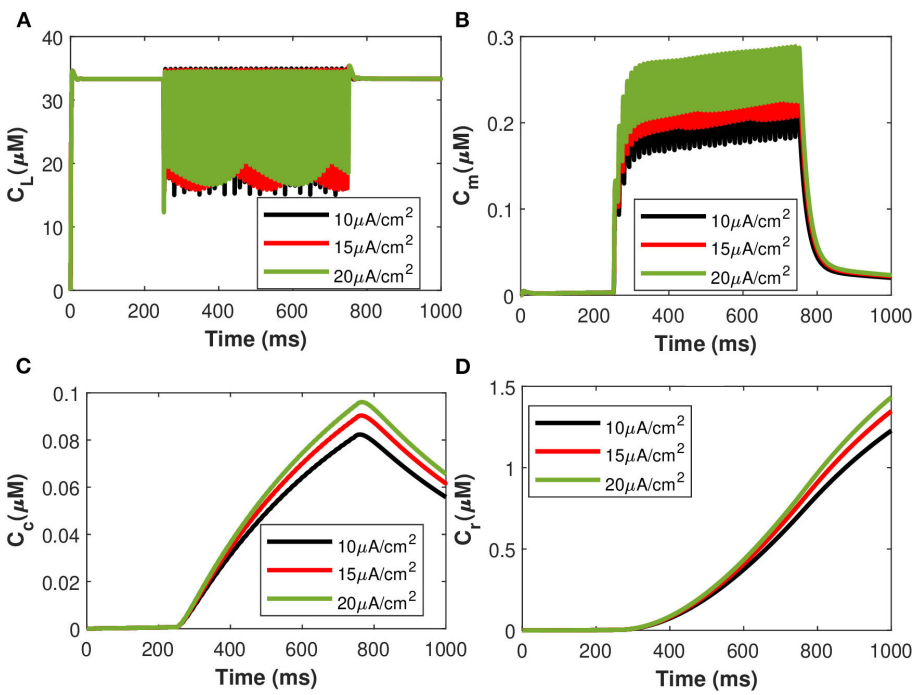

FIGURE 3 | (Color online) Microdomain calcium concentrations: **(A)** C_L, **(B)** C_m, **(C)** C_c, and **(D)** C_r corresponding to different values of control signals ranging from I_{ind} = 10 to 20 $\mu A/cm^2$.

importance of VGCCs in astrocytic Ca^{2+}-signaling and exosomal release mediated by $A\beta$. This study reproduced typical Ca^{2+} oscillations with the influence of $A\beta$ (i.e., setting $l = 0.4, 1$) by integrating different types of VGCCs (Latulippe et al., 2018) in astrocytes. However, the four separate pathways mediated by $A\beta$ (i.e., *VGCC*, *mGluR*5, *RyR*, and membrane leak J_{in}) act to harm astrocytes by raising the frequency of Ca^{2+} oscillations, lowering the membrane threshold for Ca^{2+} oscillations, and enhancing the stable state concentration of Ca^{2+}. Furthermore, by increasing J_{in}, $A\beta$ expands the membrane potential spectrum and raises resting Ca^{2+} concentrations to a low steady-state. The clustering of mGluR triggered by $A\beta$ causes the oscillating range to change to a lower potential, as demonstrated in Gao et al. (2020). The increasing sensitivity of the *RyR* channel is primarily responsible for the amplitude of the Ca^{2+} oscillations. By triggering L-type *VGCC*, $A\beta$ increases the resting Ca^{2+} at the high steady-state and moves the oscillating range to a lower potential. $A\beta$ will activate L-type channels, resulting in an increase in intracellular Ca^{2+} concentration. We emphasize only the transition of C_c and P_c (defined in section 2.3) by applying an external stimulus presented in **Figure 2A** which has been applied to excite the neurons in the presence of $A\beta$. The effects of different values of $A\beta$ on calcium concentrations for C_c and P_c without applying the induced/control signals stimulus is presented in **Figure 4**. It can be seen from **Figure 4** that the simulated results and trends are fully consistent with the studies reported by Gao et al. (2020). It is observed that $A\beta$ alters the membrane potential which in turn can enhance the regime of Ca^{2+} oscillations and increase the stable state concentration of Ca^{2+}. The Ca^{2+} oscillations demonstrate that astrocytes have ionic excitability mediated by $A\beta$, making them possible targets for $A\beta$ neurotoxicity. A pathological rise in $A\beta$ may cause functional and structural abnormalities in glial cells, including Ca^{2+} dysregulation. This calcium/gliotransmission alteration might route a key component in the pathophysiology of AD. The calcium hypothesis of AD proposes that activation of the amyloidogenic pathway retrofits neuronal Ca^{2+} signaling, affecting normal Ca^{2+} homeostasis and the processes involved in learning and memory. Our results show that the presence of $A\beta$ aggregates raises cytosolic Ca^{2+} levels. Exaggerated P_c concentrations evoked Ca^{2+} release with the influence of $A\beta$ raises the amplitude of a Ca^{2+}-activated hyperpolarizing current, which suppresses membrane excitability. Furthermore, as AD progresses, increasing the threshold for spike activation may have an effect on coincidence detection and local circuit activity. Additionally, the effect of the control signal presented in **Figure 2A** on the microdomain calcium concentrations has been depicted in **Figure 5**. It is evident from **Figure 5** that the increase in the amplitude of the control signal stimuli from 10 to 20 $\mu A/cm^2$ results in a corresponding increase in the concentration of P_c and C_c. Cytosolic buffering determines the presence of a control signal across the plasma membrane in response to an increase in free cytosolic Ca^{2+} concentration, the rate of removal from the cytosol by sequestration into organelles (primarily *r*), and cell extrusion over the plasma membrane. Furthermore, external stimuli leverage subsequent Ca^{2+} influx by inactivating voltage- or receptor-operated channels in the bulk cytosol, activating *K* channels that lower membrane excitability, or influencing Ca^{2+} release from intracellular depots. The spatial distribution of Ca^{2+} signals is greatly influenced by cytosolic Ca^{2+} buffering. One of the major pathways for Ca^{2+} release from the endoplasmic reticulum is through IP_3 receptors. The diffusion of IP_3 concentration in the IP_c cell can stimulate Ca^{2+} release from the endoplasmic reticulum in response to the activation of the firing of action potentials by external stimuli. Increased concentrations of P_c pathways may then encourage the transition to a low-threshold activated L-type Ca^{2+} current, causing additional disturbance of intracellular Ca^{2+} homeostasis which is a key phenomenon for AD (Bertsch et al., 2020).

Furthermore, the Ca^{2+}-dependant exosomal release from astrocytes in response to different representative values of extracellular $A\beta$ has been presented in **Figure 6** (Equation 16 used here and all relative equations found in sections 2.1, 2.2). As depicted in **Figure 6**, the relative contribution to Ca^{2+} signaling enhances the secretion of exosomal release in astrocytes from all components contributing to Ca^{2+} signaling in the cytoplasm (as defined in section 2.3). This means that astrocyte secretion will generate new synaptic connections for different values of $A\beta$, thus, increasing complexity of the neural network. Hence, increasing the values of $A\beta$ would lead to a significant increase in the spiking sequence of exosomal release from astrocytes, while the effect on the concentrations of exosomal release rate is quite negligible. In addition, the effect of the control signal presented in **Figure 2A** on the Ca^{2+}-dependent exosomal release from astrocytes has been presented in **Figure 7** with and without the influence of activity-dependent $A\beta$. **Figure 7** depicts that the exosomal release rate is substantially higher when the activity-dependent $A\beta$ is involved in the model. The external stimulus enhances the influence of activity-dependent $A\beta$ and the spiking sequences are significantly larger for the release of exosomes from astrocytes. The spiking sequences are also significantly reduced without the influence of activity-dependent $A\beta$ as depicted in **Figure 7**.

Our findings suggest that $A\beta$ enhances exosomal release from the astrocytes. Astrocytes, unlike neurons, are electrically quiet and cannot trigger action potentials. Because $A\beta$ triggers astrocytes and neurophysiological properties of selected neurons by shifting from a high-threshold to a low-threshold triggered L-type Ca^{2+} current, this hints that a variety of pathways, including chemical processes involving $A\beta$, cause an increase in astrocyte intracellular Ca^{2+} levels. It could be an underlying mechanism for the early metabolic and noncognitive symptoms of AD caused by hypothalamic dysfunction.

3.3. Characterization of Neural Activity in the Presence of Exosomal Release From Astrocytes

In this section, we will discuss the dynamics of neural activity in the presence of exosomal release from astrocytes by analyzing it with a model involving an astrocyte coupled to a single neuron, as developed in section 2.3. The biological processes involving astrocytes take place in close proximity to the synapses of neurons. They are sensitive to neuronal activity sensors

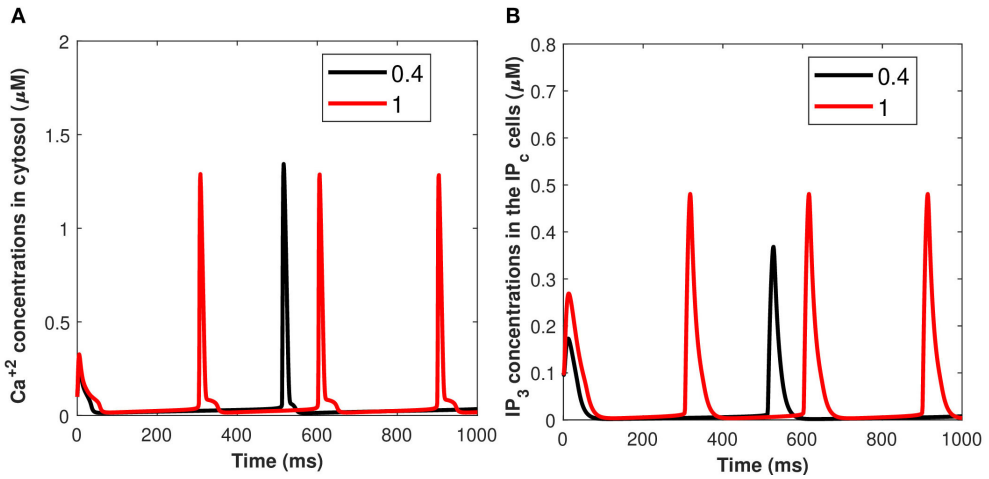

FIGURE 4 | (Color online) Microdomain calcium concentrations for: **(A)** C_c and **(B)** P_c with the influence of $A\beta$ (i.e., $I = 0.4, 1$) without induced/control signals.

that react to glutamate synaptic release with oscillations in intracellular calcium concentration. The concentration of P_c is triggered by glutamate elevations in the astrocyte domain, which activates intracellular Ca^{2+} dynamics. The amplitude, frequency, and propagation of intracellular Ca^{2+} oscillations produced in astrocytes are regulated by the intrinsic properties of both neuronal inputs and astrocytes. Astrocytes can distinguish between numerous forms of neuronal inputs and incorporate concomitant inputs in response to calcium elevations. Calcium dynamics are regulated by the interaction of CICR, which is a nonlinear amplification mechanism dependent on calcium channels opening to calcium stores, such as the endoplasmic reticulum. The action of active transporters causes a reverse flow (SERCA pumps). Signals impinging on the cell from an outside environment directly regulate the level of P_c (De Pittà, 2020). As a result, the calcium signal can be viewed as encoded information about the intensity of P_c. The release of glutamate from the astrocyte is triggered by an increase in intracellular calcium levels in astrocytes, which promotes a depolarizing current in neurons (I_{astro}), modulating pre-synaptic and post-synaptic neural activities. When a neuron fires, small quantities of neurotransmitters (glutamate) are released into the synaptic cleft. The release of intracellular P_c is triggered when neurotransmitters bind to glutamate receptors on astrocytes. The action potentials generated by the neuron injected with a constant current I_{ind}, trigger an increase of the internal Ca^{2+} concentration of the astrocyte. This event feedbacks an inward current to the neuron (I_{astro}).

The time course of the membrane potential and cytosolic Ca^{2+} concentrations in the presence of exosomal release from the astrocyte, when the neuron is injected with the current $I_{ind} = 20\ \mu\text{A/cm}^2$, are presented in **Figure 8**. The results presented in **Figure 8** show that the generation of firing activity in the exosomal release from neurons occurs during the stimulation phase alone. In this case, the elevation of the internal Ca^{2+} level in the astrocyte is not sufficient to trigger a feedback response in the neurons (see Equation 32). The increase of the production rate of P_c amplifies the Ca^{2+} response in the astrocyte and so leads to the generation of membrane potentials within a well-defined time window. The neural dynamics of membrane potential (v_m given in Equation 32) and C_c are altered by the surrounding activity, i.e., the astrocyte feedback. To illustrate the impact of the astrocytic feedback on neural excitability, we study the neural activity dynamics generated by our model both with and without $A\beta$. Numerical simulations of dynamical regimes in which neuronal firing is sustained indefinitely revealed that cytosolic Ca^{2+} concentration and membrane potential fluctuate rapidly under the control of $A\beta$ while spiking sequences are greatly decreased when $A\beta$ is not present (**Figure 8**). This pattern of activity is symptomatic of strong excitability of the neuronal system that can turn into hyperexcitability during a pathological crisis. In the time series generated by the model without $A\beta$ (**Figures 8A,C**), the neural activity and the glutamate concentration dynamics remain unchanged after the instantaneous increase of $I_{ind} = 20\ \mu\text{A/cm}^2$, which mimics glutamate release. In contrast, in the model with $A\beta$ i.e., $I = 0.4$ (**Figures 8B,D**), the strong increase in the spiking sequences of membrane potential and C_c enhance the glutamate release that halts neuronal activity. Once the action potentials have become sufficiently low, neural activity re-emerges and glutamate and concentrations come back to their respective basal values, oscillating with neural activity. Our results imply that neuronal activity controls the regional sensitivity of $A\beta$ formation. Although much of this discussion focuses on Ca^{2+}-regulated exosomal release from astrocytes in the presence of $A\beta$, we cover one transporter, in particular, the cystine/glutamate transporter, because it is important in neurodegenerative disorders, such as AD. Cytosolic Ca^{2+}-regulated glutamatergic gliotransmission activates neuronal extrasynaptic NMDA receptors, altering neuronal excitability and regulating synaptic transmission. Our findings point to a mechanism that might explain why neuronal activity in AD is susceptible to $A\beta$ deposition.

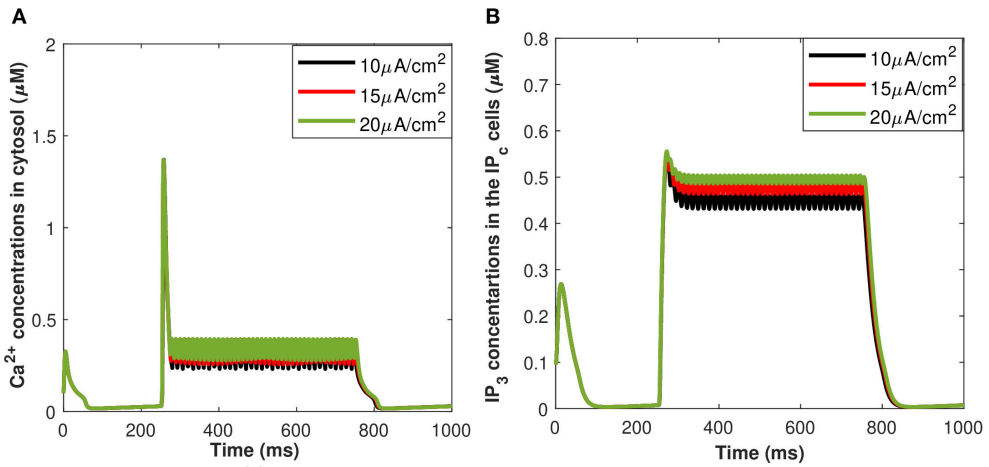

FIGURE 5 | (Color online) Microdomain calcium concentrations for: **(A)** C_c and **(B)** P_c corresponding to control signal shown in **Figure 1A** ranging as I_{ind} = 10–20 μA/cm^2.

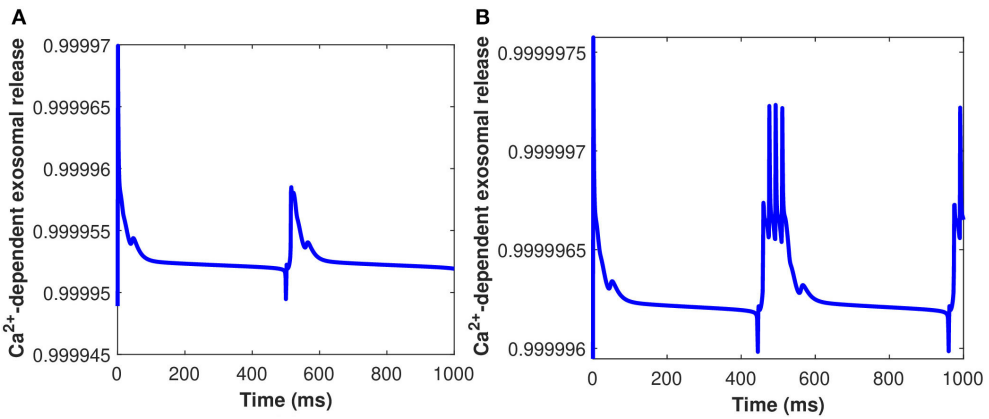

FIGURE 6 | (Color online) Ca^{2+}-dependent exosomal release (μ M) from astrocytes corresponding to different values of $A\beta$, i.e., **(A)** I = 0.4 and **(B)** I = 1 without the influence of I_{ind}.

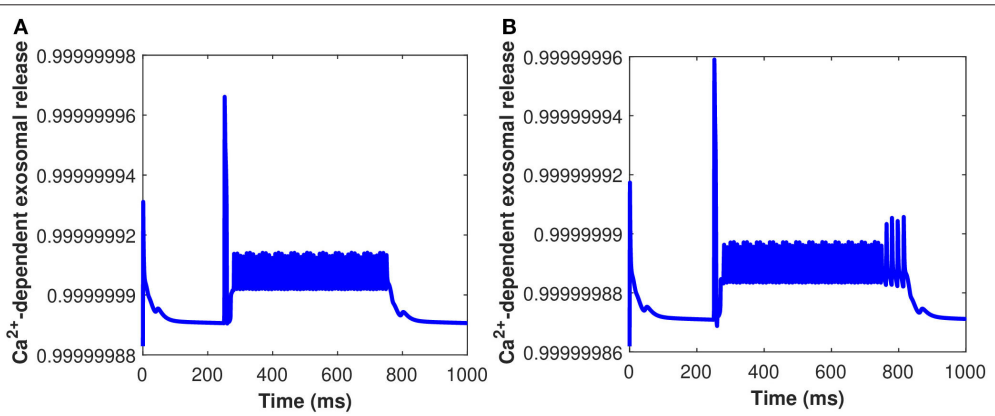

FIGURE 7 | (Color online) Ca^{2+}-dependent exosomal release from astrocytes corresponding with and without the influence of activity-dependent $A\beta$, i.e., **(A)** I = 0 and **(B)** I = 0.4 with the influence of I_{ind}.

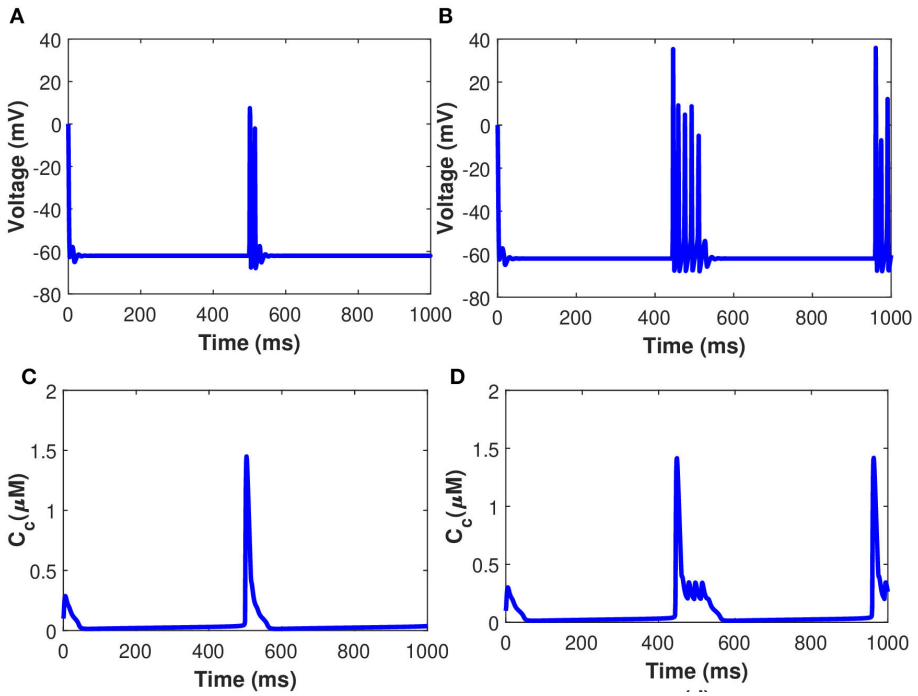

FIGURE 8 | (Color online) Behavior of membrane potential corresponding to $A\beta$ **(A)** $I = 0$, **(B)** $I = 0.4$, and C_c **(C)** $I = 0$, **(D)** $I = 0.4$ with $I_{ind} = 20\ \mu A/cm^2$.

3.4. Temperature Dependence, With Emphasis on TRPM8-Mediated Modulations of Membrane Potential

The excitability and response characteristics of a neuron might change depending on the temperature of the surroundings. The effects of the induced pulse of 20 $\mu A/cm^2$ on the membrane potential with temperature ($T = 25\ ^\circ C$) and without the temperature effects have been presented in **Figure 9**. As evident from **Figure 9**, the pace of produced sequences of action potentials is proportional to both the amplitude and length of the external stimuli. Not only that, but when temperature effects are included in the numerical model, the spiking sequences are considerably decreased. Importantly, these spiking sequences regulate the kinetics of VGCCs in the membrane (Veletić et al., 2020). Variations of membrane potential have been observed when the membrane temperature is increased/decreased, indicating that the cell membrane environment in neurons becomes more electronegative/electropositive. The amplitude of action potentials, defined as the voltage difference between the threshold and the peak, and their duration, assessed by the breadth of the action potential at the threshold, were both impacted by temperature changes.

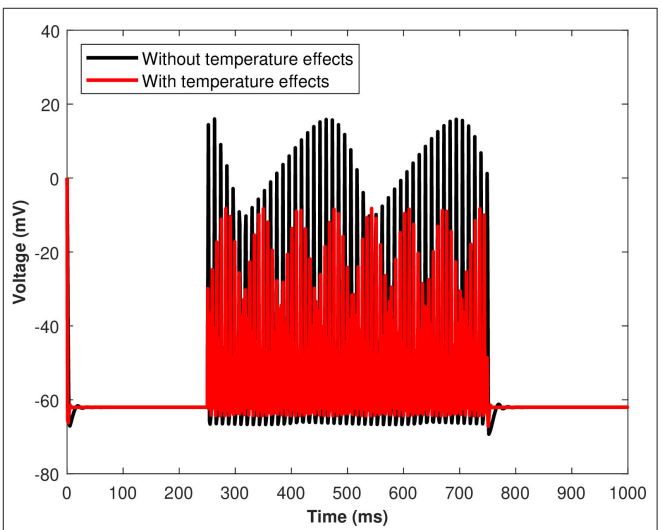

FIGURE 9 | (Color online) The effect of temperature on the responses/spiking sequence in the depolarized neurons for $I_{ind} = 20\ \mu A/cm^2$.

The effects of the temperature on the microdomain calcium concentrations have been presented in **Figure 10**. As seen from the analysis of this figure, the intracellular Ca^{2+} concentrations in the closed and open channels of L-type, plasma membrane, bulk cytosol, and endoplasmic reticulum are significantly overestimated if the effect of temperature is neglected and the spiking sequences are also significantly reduced. Indeed, incorporating temperature will result in a corresponding decrease in the concentration of C_r, C_m, C_c, and C_L concentrations, and the spiking sequences are also significantly reduced. The findings underpin Huxley's theory that thermally induced block is caused by increased activation of voltage-dependent potassium ion channels in

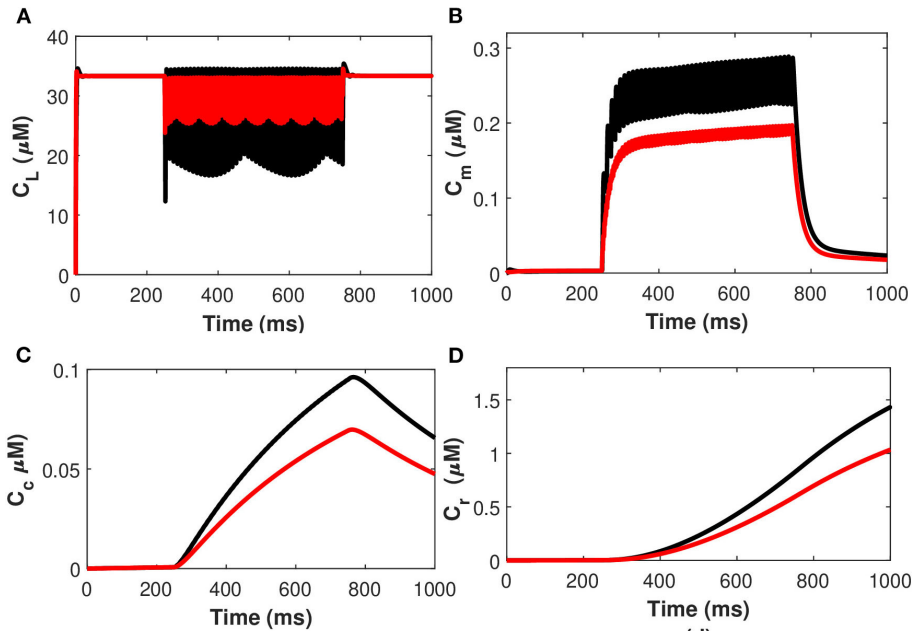

FIGURE 10 | (Color online) Microdomain calcium concentrations: **(A)** L-Type Ca^{2+} concentration, **(B)** Sub-membrane Ca^{2+} concentration, **(C)** Cytosolic Ca^{2+} concentration and **(D)** Endoplasmic reticulum Ca^{2+} concentration with (red color) and without (black color) temperature effects corresponding to control signal of $I_{ind} = 20\mu A/cm^2$.

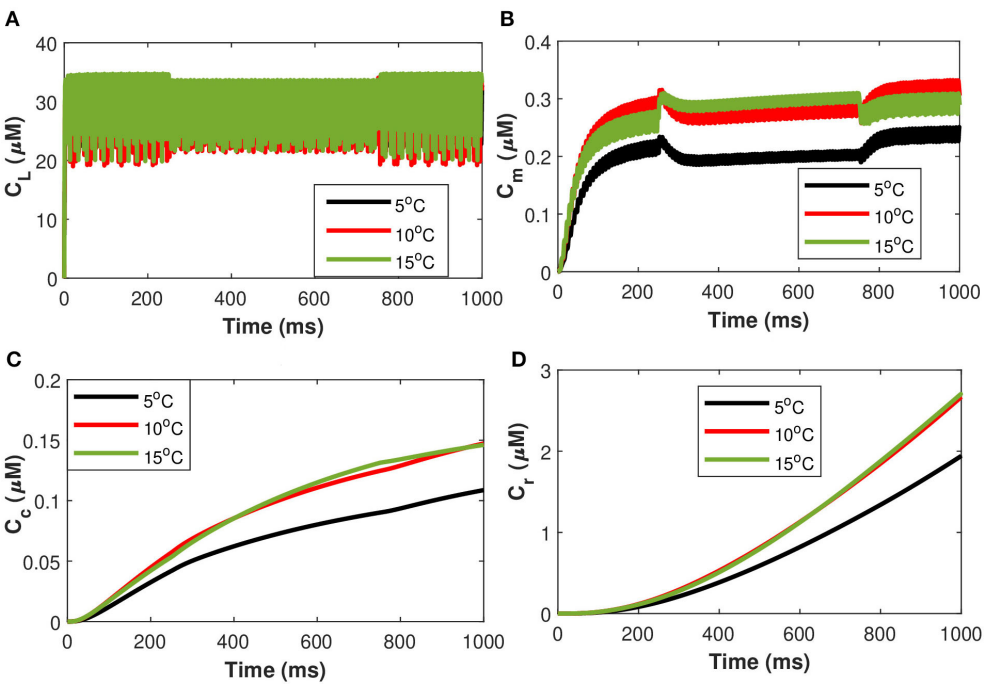

FIGURE 11 | (Color online) Microdomain calcium concentrations for: **(A)** L-Type Ca^{2+} concentration, **(B)** Sub-membrane Ca^{2+} concentration, **(C)** Cytosolic Ca^{2+} concentration and **(D)** Endoplasmic reticulum Ca^{2+} concentration corresponding to control signal of $I_{ind} = 20\ \mu A/cm^2$ and I_{m8} for different values of temperature.

response to depolarization, particularly at higher temperatures (Ganguly et al., 2019). The membrane depolarizes in response to depolarizing currents produced by an advancing action potential. The voltage-dependent potassium ion channels are activated, allowing potassium ions to flow out of the neuron, hyperpolarizing it. The depolarizing current that triggered these

channels is antagonized by the hyperpolarizing current that passes through them. As a result, this process efficiently and quickly stops the action potential from propagating. Since depolarizing current forms an advancing action potential, a hyperpolarizing current is more powerful than simply blocking all ion channels. Instead of being actively antagonized, this action potential will spread through the passive region of blocked ion channels, diminishing only as it leaked out through the passive components of the neuronal membrane, such as leak channels and capacitance. Moreover, the exosomal release rate in neurons is directly linked with the Ca^{2+} concentrations in different compartments. The exosomal release rate is relatively higher when temperature effects are incorporated within the model. This can be attributed to the fact that an increase in temperature values will lead to a corresponding increase in the net hyperpolarizing current. The sodium inward current became shorter and the potassium outward current became faster and larger due to the increased speed of sodium/potassium ions gated conductances. As the membrane was depolarized by the action potential, the net current in the neural network became steadily outward (hyperpolarizing) with increased temperature which enhances neural activity. Thus, the exosomal release rate of the targeted neuron is significantly affected by the changes in temperature.

Next, considering the state of cold sensing neurons we added the TRPM8 component in the present model by making g_{m8} nontrivial (i.e., $g_{m8} = 3$). We begin by using (Equation 36) of TRPM8 channels at different physiological voltages in response to temperature. **Figure 11** represents the variation of the TRPM8 current in response to temperature and voltage. We combined the Equation (36) of TRPM8 channels with the induced control signals/currents stimulation given in **Figure 2A** that helps describe the overall behavior of Ca^{2+} concentrations at different temperature levels (see Equation 35). From **Figure 11** we observe that as the fixed temperature level is raised, a few distinct characteristics occur. The stimulation-induced control signals/currents show decreasing amplitudes of the action potentials as the maximum voltage achieved for Ca^{2+} concentrations decreases with rising temperatures. Additionally, as the temperature rises, the average amplitude of the TRPM8 current grows. We should recognize that since $V_{m8} = 0$ (McGahan and Keener, 2020), the TRPM8 current will flow both inward and outward depending on the membrane potential, nonetheless, it is worth noting that at temperature effects ranging from $T = 5$ to 15°C there is an increase in outward current and concentration of C_r, C_m, C_c, and C_L that behave differently corresponding to each temperature prescribed in **Figure 11**. The amplitude of the action potential decreases and its duration decreases as the temperature rises. The temperature dependence of ion channel conductance as well as the time constants of channel activation/inactivation factors may have an effect on neuronal function. Thus, temperature variations significantly affect the Ca^{2+} concentrations, the rates of diffusion, the rates of conformational changes, and the rates of metabolic processes. Similarly, as before, it is seen that an increase in temperature will result in a corresponding increase in the concentrations of C_r, C_m, and C_c while the effect on C_L concentrations is quite negligible. The scenario considered in this study is the presence of cold neurons affecting the concentrations of Ca^{2+}-dependent exosomal release in neurons defined in section 2.1.

Examining the behavior of the established model as g_{m8} is increased in response to the simulated temperature ramp shown in **Figure 12A** is also instructive. There are two consistent features across the three different values of g_{m8}, as well as one that emerges as g_{m8} is increased. In **Figure 12**, we observe that when the neuron turns on and off, there are large amplitude jumps in the oscillations of membrane potential. Furthermore, in each of the **Figures 12B–D**, the neural activity is asymmetric on the down and up to temperature ramps, with the oscillations on the up temperature ramp lasting longer. Finally, when g_{m8} is increased, the neuron stops oscillating in the coldest part of the temperature ramp. The oscillations shrink in amplitude as the neuron is osed to lower temperatures, as seen in the plots with $g_{m8} = 5$ and $g_{m8} = 10$. While these voltage-time plots provide an overview of the role of TRPM8 channels in neuron activation and inactivation, they do not provide a complete picture. In particular, in the absence of induced control signals/currents, we wish to include a more complete description of the interactions between each of the ionic currents and temperature. The temperature ramp simulation with increasing TRPM8 maximal conductance provides a better picture of what the neurons are subjected to physiologically. The temperature-induced scaling of the rate constants, on the other hand, can have a significant impact on the length of the action potential. Temperature impacts the rate of neuron firing as well as the pace of action potential propagation. Variations in action potential frequencies with temperature are related to changes in resting potentials, but not in a straightforward manner. Cooling lowers the resting potential (depolarization), which leads to a rise in action potential frequencies, yet, when the temperature is increased, certain nerve cells exhibit an increase in frequency.

The effects of the induced pulse of 20 μA/cm^2 on the cytosolic calcium and the IP_3 concentrations in the IP_c cells in regards to astrocytic exosome exocytosis mediated by $A\beta$ in AD (see section 2.3), with temperature ($T = 25$°C) and without the temperature effects have been presented in **Figures 13A,B**. The kinetics of C_c and IP_3 was markedly accelerated by increasing temperature. At $T = 25$ °C, **Figures 13A,B** show that the rate of exosomal release of the astrocytes is proportional to both the magnitude and duration of the temperature and external stimuli. Therefore, increasing temperature will reduce the spiking sequences which enhance neural firing or promote neural activity. The temperature may increase exosomal release from neurons and glial cells, contributing to $A\beta$ accumulation and hyperexcitability. The effect of temperature has been examined on cytosolic Ca^{2+} concentrations and the IP_3 concentrations mediated by $A\beta$. Importantly, Ca^{2+} wave propagation is thought to be a reaction/diffusion system requiring several cycles of Ca^{2+} release from IP_3 clusters and diffusion to nearby clusters to trigger CICR. The study found that the concentrations of Ca^{2+} and IP_3 in the IP_c cells decrease monotonically with temperature which disturbs the brain dynamics and could lead to the pathophysiology of AD.

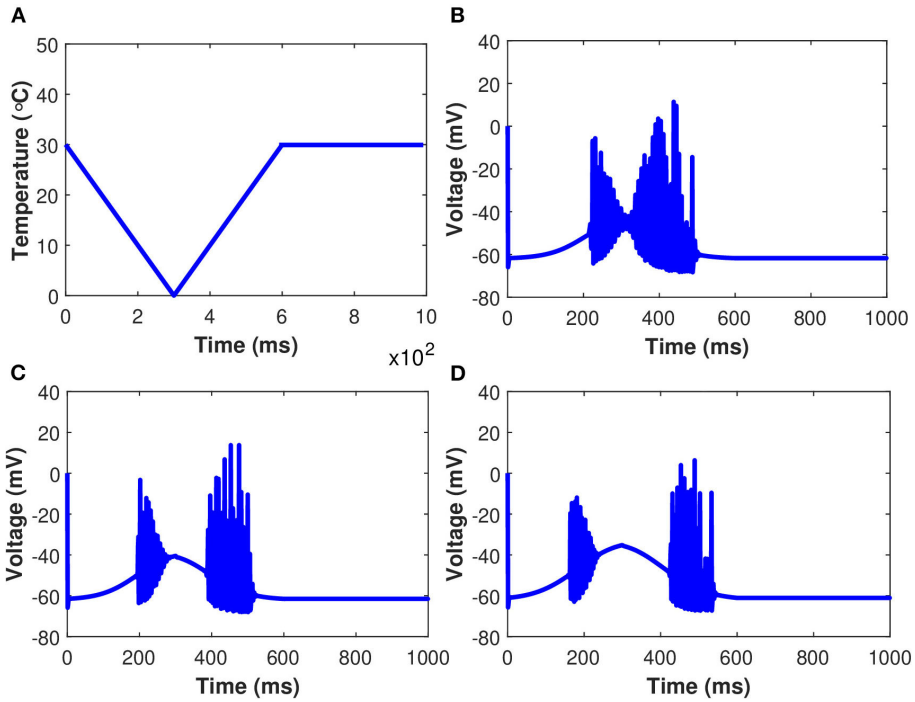

FIGURE 12 | (Color online) Membrane potential in response to an external temperature ramp. The periodic spiking activity of the neuron in response to temperature ramp **(A)** plotted against time with: **(B)** $g_{m8} = 3$, **(C)** $g_{m8} = 5$, and **(D)** $g_{m8} = 10$.

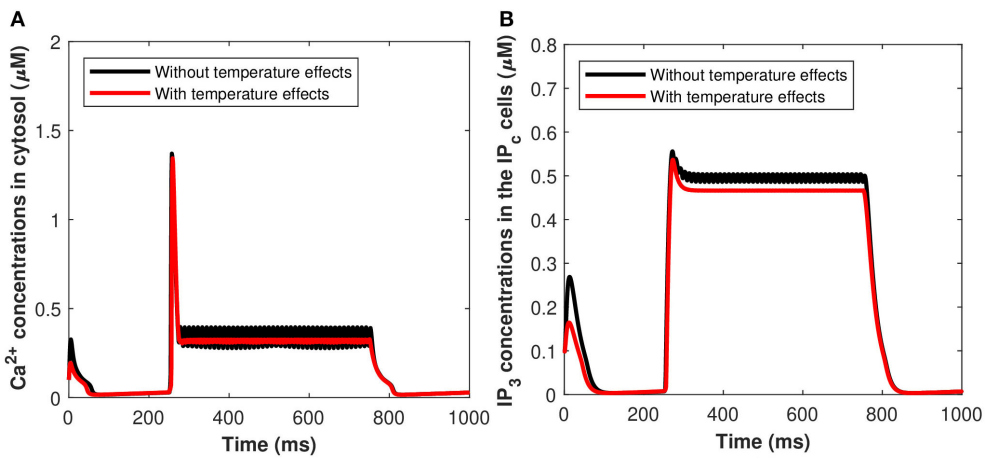

FIGURE 13 | (Color online) Microdomain calcium concentrations for **(A)** C_c, **(B)** P_c, with and without temperature effects corresponding to control signal shown in **Figure 2A**.

Moreover, a study has been conducted to quantify the effects of TRPM8 channels in the modeling of Ca^{2+}-mediated astrocytic exosome exocytosis mediated by $A\beta$ ($l = 0.4$) in AD. The TRPM8 part of the model is added by setting g_{m8} to nonzero. The open possibility of TRPM8 channels, a_{m8}, in response to temperature at various physiological voltages is first added. All other parameter values are set to Hodgkin-Huxley norms and $g_{m8} = 3$. As the fixed temperature level is raised, a few distinct features emerge that include the amplitudes of the action potentials increase, resulting in an increase in the maximum voltage reached. As a result, the current model emphasizes the importance of TRPM8 channels in determining temperature-dependent activation and inactivation thresholds. Furthermore, our findings shed light on what happens at the temperature levels at which these neurons shut down, as well as the role sodium and leak currents can play. It has been demonstrated by using both TRPM8 and the stimulus of induced control signal triggered the calcium concentrations of C_c and P_c defined in

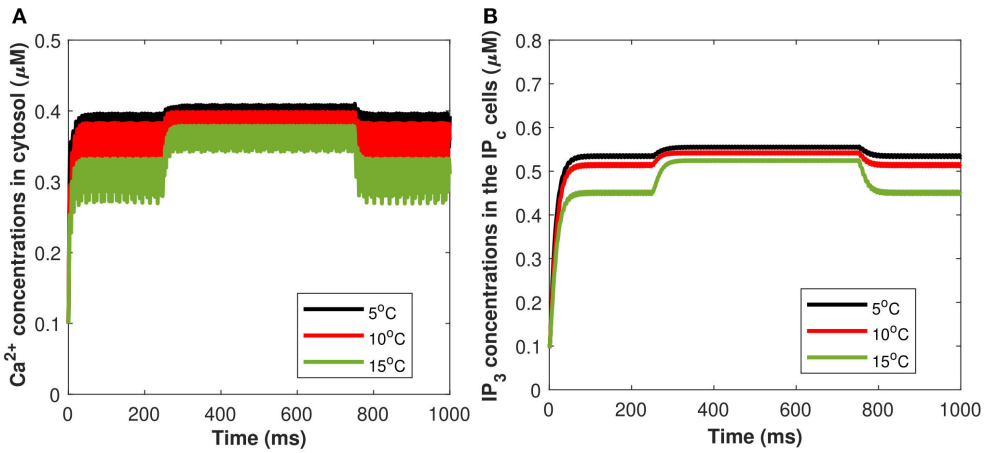

FIGURE 14 | (Color online) Microdomain calcium concentrations for **(A)** C_c, **(B)** P_c corresponding to I_{m8} and control signal shown in **Figure 2A** for different values of temperature, in presence of $A\beta$.

(Equations 27, 29). From **Figures 14A,B**, as the fixed temperature level is increased, a few distinct characteristics emerge in the presence of cold sensing neurons TRPM8 channels. The simulation shows that as the temperature rises, the amplitudes of the action potentials decrease as the maximum concentration of C_c and P_c declines. It can be seen from **Figures 14A,B** that increasing temperature from T = 5 to 15°C would result in a corresponding decrease in the concentration of C_c and P_c in the presence of $g_{m8} = 3$. However, TRPM8 channels were shown to be expressed in the endoplasmic reticulum where their modulation by activators and/or inhibitors was demonstrated to be crucial for intracellular Ca^{2+} signaling. The rise in inward flux is primarily responsible for the shift in the TRPM8 current amplitude, in fact, it is worth noting that from $T = 5$ to 15°C there is an increase in outward current. These findings imply that TRPM8 channels confer temperature sensitivity to the endoplasmic reticulum, which permits Ca^{2+} release by facilitating Ca^{2+} efflux into the cytosol and therefore contributing to CICR *via* IP_3 and ryanodine receptors. Although the IP_3 evoked Ca^{2+} signals were qualitatively comparable at 5–15 Ca^{2+}, this difference in temperature should take into account the temperature sensitivity of IP_3-mediated signal amplitudes. The transition temperature was 25°C in all cases, which might indicate a phase change in the lipids of the cytoplasmic membrane. Our findings demonstrate that using this temperature range (from $T = 5$ to 15°C) significantly increases the amplitude and lowers the frequency of global IP_3-mediated Ca^{2+} signals, which is consistent with findings from a variety of different cell types. For instance, fast cooling elicits strong oscillatory Ca^{2+}-activated leak currents when the IP_3 pathway is active and has been shown to enhance the amplitudes of IP_3-mediated Ca^{2+} signals in several cultured glial cells, including Schwann cells and olfactory ensheathing cells, as well as astrocytes. As a result, the temperature sensitivity of the cytosolic Ca^{2+} concentration underpinning global IP_3-mediated signals appears to be a common occurrence, which must be taken into account when extending data obtained at room temperature to body temperature.

4. CONCLUSION AND DISCUSSION

We presented an integrated mathematical model for therapeutic exosomal release modulated by an externally applied stimulus. The proposed model combines cell activation, intercellular signaling, and exocytosis and allows to shed light on the relative roles of different subcellular Ca^{2+} compartments and astrocytes in exosomal release regulation. We implemented a novel model for accurately quantifying the Ca^{2+}-mediated astrocytic exosome exocytosis mediated by amyloid-beta in AD. In addition, a comparative analysis has been conducted to quantify the effect of temperature and cold-sensitive neurons on the Ca^{2+}-dependent exosomal release mediated by VGCCs and amyloid-beta in AD. Moreover, we calculated the astrocytic current as a function of both the pre-synaptic neuron current and the astrocyte (Li-Rinzel model). This work describes the synapse and astrocyte couplings in a computationally efficient model. It is possible to simulate real-time spiking artificial neuron-glia networks using the model proposed in this study, revealing the mechanism that appears to be a necessary part of the regulation of spiking activities. We showed that this model can be used to simulate the neuron astrocyte interaction. The results obtained with the developed model suggest that cell depolarization in neurons is directly related to the exosomal release which is proportional to the applied stimulation. The novelty of the present research is in the development of the Ca^{2+}-mediated exosomal dynamics model of neurons accounting for the temperature effects with emphasis on TRPM8-mediated modulations of membrane potential. Further, it has been observed that Ca^{2+} concentrations in the respective compartments, and thus the overall Ca^{2+}-mediated exosomal dynamics are significantly affected by the changes in temperature and TRPM8 channels. The findings show that TRPM8 and VGCCs play an important role in determining temperature-dependent activation and inactivation at numerous threshold levels. Thermal effects caused by cold detecting neurons cause Ca^{2+} to be released from the endoplasmic reticulum of primary spiral ganglion neurons. The activation of TRPM8 channels causes Ca^{2+} release, which is amplified by CICR. TRPM8

channel that colocalizes with the endoplasmic reticulum, is immunostained in the neurons. Indeed, the original and modified Hodgkin/Huxley models have a high degree of qualitative agreement, and the findings of this study are a significant move toward a better understanding of a novel modality for altering neural activity. The developed neuronal model provides an important step not only for our better understanding of the exosomal dynamics in neurons and astrocytes but also paves the way for the generation of new models aiming at optimizing and designing exosome-based drug delivery systems for the treatment of brain pathologies and neurodegenerative disorders such as AD.

Our model supports the view that astrocytes normally serve as neuronal signaling events, but in AD, they transform into astrocyte-derived exosomes, which can disrupt neurons *via* unknown mechanisms (Goetzl et al., 2016). The development of methods for isolating Ca^{2+}-dependent exosome-release both in astrocytes and neuronally derived exosomes from plasma has enabled researchers to quantify neuronal proteins important in the pathogenesis of human neurodegenerative diseases. The astrocyte-derived exosomes were shown to be positive for neuroglobin, a protein that acts as a neuroprotectant against cell injury (Venturini et al., 2019); the notion that exosomes transmit neuroglobin to neurons would add another mechanism to the possible astrocytic neuroprotectant activity. Control signal microdomain Ca^{2+} concentrations unavoidably impact a wide range of neuronal activities, from the regulation of the overall cytosolic Ca^{2+} signal to the production of cell death. Multiple changes in this particular signaling pathway are prevalent in several neurodegenerative disorders, including AD, PD, and amyotrophic lateral sclerosis (ALS), emphasizing its importance. To further substantiate our findings presented on this study, a variety of future investigations into the astrocyte sources and cytotoxic mechanisms of complement proteins in astrocyte-derived exosomes will be needed. However, the definitive etiological relationships between the neuronal accumulation of primary neurotoxic proteins such as amyloid-beta, tau, and reductions in synaptic proteins that contribute to early synaptic dysfunction are now being discovered (Goetzl et al., 2018). It is worth noting that changes in intracellular Ca^{2+} signaling decrease neuronal interactions and enhance both acute and chronic degenerative diseases of the nervous system. In the present study, we found that due to the biophysical properties of voltage-gated and ligand-activated ion channels and receptors, Ca^{2+} fluxes through the neuronal membrane are strictly time-constrained. The neural activity could be enhanced by Ca^{2+}-dependent receptors and channels, constantly rearranged as they are embedded in the crowded dynamic environment of biological membranes, allowing for temporary interaction and the creation of transient signals. In a highly dynamic environment, efficient Ca^{2+}-mediated signal transduction necessitates mechanisms that support the very precise spatiotemporal alignment of the Ca^{2+} source and Ca^{2+}-dependent exosomal exocytosis (De Pittà, 2020). Neuroprotective strategies that target various aspects of the dynamic regulation of intracellular Ca^{2+} signaling are a promising avenue for pharmaceutical intervention in nervous system neurodegenerative diseases, such as AD. Moreover, several intracellular Ca^{2+} signaling regulators found on the plasma membrane and intracellular organelles have been implicated in many of these pathophysiological processes (Valori et al., 2019). Our current understanding sheds new light on the essential roles of Ca^{2+} channels in synapse formation and function in the healthy central nervous system. Importantly, the previous studies were focused on the effect of temperature and TRPM8 channels on Ca^{2+}-dependent exosome-release, where the temperature has been linked to dementia and may play a role in clinical phenotypes, particularly in the frontotemporal lobar degeneration continuum, but the cause of these symptoms has yet to be determined (Fletcher et al., 2015; De Pittà and Berry, 2019b; McGahan and Keener, 2020). Furthermore, altered neural activity and temperature perceptions may be expected in some neurodegenerative disorders, including AD, that can lead to impairments of the integrity of distributed and temperature processing networks. Alzheimer's syndrome is a notable test case. Future studies will be focused on the inclusion of other Ca^{2+} compartments linked to the integration of experimental mice model data of AD and on the development of a new stochastic model based on the ideas highlighted in this study.

DATA AVAILABILITY STATEMENT

The raw data supporting the conclusions of this article will be made available by the authors, without undue reservation.

AUTHOR CONTRIBUTIONS

HS: methods and materials, data curation, formal analysis, investigation, writing, and original draft preparation. SS and RM: designed research. SS: methodology, formal analysis, writing, review and editing, and supervision. RM: conceptualization, supervision, and reviews. All authors approved the final submitted version.

ACKNOWLEDGMENTS

This is an extended version of the work (Mathematical modeling of calcium-mediated exosomal dynamics in neural cells) that was presented at the Nodycon 2021 (Second International Nonlinear Dynamics Conference), February 16–19, 2021. The authors are grateful to the NSERC and the CRC Program for their support. RM is also acknowledging the support of the BERC 2018–2021 program and Spanish Ministry of Science, Innovation and Universities through the Agencia Estatal de Investigacion (AEI) BCAM Severo Ochoa excellence accreditation SEV-2017-0718, and the Basque Government fund AI in BCAM EXP. 2019/00432. Further possible developments of several ramifications from this work were discussed with Drs. A. B. Ali, M. Desroches, and S. Rodrigues, and the authors hope that new advances in those directions will stimulate the progress in integrating new experimental data from this field of research. Finally, the authors thank the referees for their careful reading of the manuscript, insightful comments, and suggestions that assisted in improving the initially submitted version of this work.

REFERENCES

Bertsch, M., Franchi, B., Meacci, L., Primicerio, M., and Tesi, M. (2020). The amyloid cascade hypothesis and Alzheimer's disease: a mathematical model. *Eur. J. Appl. Math*. 1–20. doi: 10.1017/S0956792520000339

Bezprozvanny, I., and Mattson, M. P. (2008). Neuronal calcium mishandling and the pathogenesis of alzheimer's disease. *Trends Neurosci*. 31, 454–463. doi: 10.1016/j.tins.2008.06.005

De Pittà, M. (2020). Neuron-glial interactions. *arXiv preprint arXiv*:2001.06881. doi: 10.1007/978-1-4614-7320-6_100691-1

De Pittà, M., Ben-Jacob, E., and Berry, H. (2019). "G protein-coupled receptor-mediated calcium signaling in astrocytes," in *Computational Glioscience* (New York, NY: Springer), 115–150.

De Pittà, M., and Berry, H. (2019a). *Computational Glioscience*. Switzerland: Springer.

De Pittà, M., and Berry, H. (2019b). "A neuron-glial perspective for computational neuroscience," in *Computational Glioscience* (Switzerland: Springer), 3–35.

Di Garbo, A., Barbi, M., Chillemi, S., Alloisio, S., and Nobile, M. (2007). Calcium signalling in astrocytes and modulation of neural activity. *Biosystems* 89, 74–83. doi: 10.1016/j.biosystems.2006.05.013

Escartin, C., Galea, E., Lakatos, A., O'Callaghan, J. P., Petzold, G. C., Serrano-Pozo, A., et al. (2021). Reactive astrocyte nomenclature, definitions, and future directions. *Nat. Neurosci*. 24, 312–325. doi: 10.1038/s41593-020-00783-4

Fletcher, P. D., Downey, L. E., Golden, H. L., Clark, C. N., Slattery, C. F., Paterson, R. W., et al. (2015). Pain and temperature processing in dementia: a clinical and neuroanatomical analysis. *Brain* 138, 3360–3372. doi: 10.1093/brain/awv276

Ganguly, M., Jenkins, M. W., Jansen, E. D., and Chiel, H. J. (2019). Thermal block of action potentials is primarily due to voltage-dependent potassium currents: a modeling study. *J. Neural Eng*. 16, 036020. doi: 10.1088/1741-2552/ab131b

Gao, H., Liu, L., and Chen, S. (2020). Simulation of Ca^2+ oscillations in astrocytes mediated by amyloid beta in Alzheimer's disease. *bioRxiv* 2020.03.18.996843. doi: 10.1101/2020.03.18.996843

Goetzl, E. J., Kapogiannis, D., Schwartz, J. B., Lobach, I. V., Goetzl, L., Abner, E. L., et al. (2016). Decreased synaptic proteins in neuronal exosomes of frontotemporal dementia and alzheimer's disease. *FASEB J*. 30, 4141–4148. doi: 10.1096/fj.201600816R

Goetzl, E. J., Schwartz, J. B., Abner, E. L., Jicha, G. A., and Kapogiannis, D. (2018). High complement levels in astrocyte-derived exosomes of alzheimer disease. *Ann. Neurol*. 83, 544–552. doi: 10.1002/ana.25172

Heppner, F. L., Ransohoff, R. M., and Becher, B. (2015). Immune attack: the role of inflammation in alzheimer disease. *Nat. Rev. Neurosci*. 16, 358–372. doi: 10.1038/nrn3880

Jain, K. K. (2019). "Neuroprotection in Alzheimer's disease," in *The Handbook of Neuroprotection* (New York, NY: Springer), 465–585.

Jiang, L., Dong, H., Cao, H., Ji, X., Luan, S., and Liu, J. (2019). Exosomes in pathogenesis, diagnosis, and treatment of Alzheimer's disease. *Med. Sci. Monit. Int. Med. J. Exp. Clin. Res*. 25:3329. doi: 10.12659/MSM.914027

Latulippe, J., Lotito, D., and Murby, D. (2018). A mathematical model for the effects of amyloid beta on intracellular calcium. *PLoS ONE* 13:e0202503. doi: 10.1371/journal.pone.0202503

Li, Y.-X., and Rinzel, J. (1994). Equations for InsP3 receptor-mediated $[Ca^2+]$i oscillations derived from a detailed kinetic model: a hodgkin-huxley like formalism. *J. Theor. Biol*. 166, 461–473. doi: 10.1006/jtbi.1994.1041

Liu, S.-J., Gasperini, R., Foa, L., and Small, D. H. (2010). Amyloid-β decreases cell-surface ampa receptors by increasing intracellular calcium and phosphorylation of glur2. *J. Alzheimers Dis*. 21, 655–666. doi: 10.3233/JAD-2010-091654

Liu, Y., and Qin, N. (2011). Trpm8 in health and disease: cold sensing and beyond. *Adv. Expe. Med. Biol*. 704, 185–208. doi: 10.1007/978-94-007-0265-3_10

Luiz, A., MacDonald, D., Santana-Varela, S., Millet, Q., Sikandar, S., Wood, J., et al. (2019). Cold sensing by nav1. 8-positive and nav1. 8-negative sensory neurons. *Proc. Natl. Acad. Sci. U.S.A*. 116, 3811–3816. doi: 10.1073/pnas.1814545116

Luo, S., Du, L., and Cui, Y. (2020). Potential therapeutic applications and developments of exosomes in parkinson's disease. *Mol. Pharm*. 17, 1447–1457. doi: 10.1021/acs.molpharmaceut.0c00195

Madrid, R., De La Pe na, E., Donovan-Rodriguez, T., Belmonte, C., and Viana, F. (2009). Variable threshold of trigeminal cold-thermosensitive neurons is determined by a balance between trpm8 and kv1 potassium channels. *J. Neurosci*. 29, 3120–3131. doi: 10.1523/JNEUROSCI.4778-08.2009

McGahan, K., and Keener, J. (2020). A mathematical model analyzing temperature threshold dependence in cold sensitive neurons. *PLoS ONE* 15:e0237347. doi: 10.1371/journal.pone.0237347

Montefusco, F., and Pedersen, M. G. (2015). Mathematical modelling of local calcium and regulated exocytosis during inhibition and stimulation of glucagon secretion from pancreatic alpha-cells. *J. Physiol*. 593, 4519–4530. doi: 10.1113/JP270777

Nadkarni, S., and Jung, P. (2004). Dressed neurons: modeling neural-glial interactions. *Phys. Biol*. 1, 35. doi: 10.1088/1478-3967/1/1/004

Pedersen, M. G., Tagliavini, A., Cortese, G., Riz, M., and Montefusco, F. (2017). Recent advances in mathematical modeling and statistical analysis of exocytosis in endocrine cells. *Math. Biosci*. 283:60–70. doi: 10.1016/j.mbs.2016.11.010

Semyanov, A., Henneberger, C., and Agarwal, A. (2020). Making sense of astrocytic calcium signals from acquisition to interpretation. *Nat. Rev. Neurosci*. 21, 551–564. doi: 10.1038/s41583-020-0361-8

Shaheen, H., Singh, S., and Melnik, R. (2021). "Mathematical modeling of calcium-mediated exosomal dynamics in neural cells," in *Proceedings of the Second International Nonlinear Dynamics Conference*, Rome: NODYCON, 1–10.

Shigetomi, E., Patel, S., and Khakh, B. S. (2016). Probing the complexities of astrocyte calcium signaling. *Trends Cell Biol*. 26, 300–312. doi: 10.1016/j.tcb.2016.01.003

Soto, C., and Pritzkow, S. (2018). Protein misfolding, aggregation, and conformational strains in neurodegenerative diseases. *Nat. Neurosci*. 21, 1332–1340. doi: 10.1038/s41593-018-0235-9

Teichert, R. W., Memon, T., Aman, J. W., and Olivera, B. M. (2014). Using constellation pharmacology to define comprehensively a somatosensory neuronal subclass. *Proc. Natl. Acad. Sci. U.S.A*. 111, 2319–2324. doi: 10.1073/pnas.1324019111

Valenza, G., Pioggia, G., Armato, A., Ferro, M., Scilingo, E. P., and De Rossi, D. (2011). A neuron-astrocyte transistor-like model for neuromorphic dressed neurons. *Neural Netw*. 24, 679–685. doi: 10.1016/j.neunet.2011.03.013

Valori, C. F., Guidotti, G., Brambilla, L., and Rossi, D. (2019). Astrocytes: emerging therapeutic targets in neurological disorders. *Trends Mol. Med*. 25, 750–759. doi: 10.1016/j.molmed.2019.04.010

Veletić, M., Barros, M. T., Arjmandi, H., Balasubramaniam, S., and Balasingham, I. (2020). Modeling of modulated exosome release from differentiated induced neural stem cells for targeted drug delivery. *IEEE Trans. Nanobioscience* 19, 357–367. doi: 10.1109/TNB.2020.2991794

Veletić, M., Barros, M. T., Balasingham, I., and Balasubramaniam, S. (2019). "A molecular communication model of exosome-mediated brain drug delivery," in *Proceedings of the Sixth Annual ACM International Conference on Nanoscale Computing and Communication* (Dublin), 1–7.

Venturini, A., Passalacqua, M., Pelassa, S., Pastorino, F., Tedesco, M., Cortese, K., et al. (2019). Exosomes from astrocyte processes: signaling to neurons. *Front. Pharmacol*. 10:1452. doi: 10.3389/fphar.2019.01452

Wang, F., Smith, N. A., Xu, Q., Fujita, T., Baba, A., Matsuda, T., et al. (2012). Astrocytes modulate neural network activity by Ca^2+-dependent uptake of extracellular K^+. *Sci. Signal*. 5:ra26-ra26. doi: 10.1126/scisignal.2002334

Wang, Y., Fu, A. K., and Ip, N. Y. (2021). Instructive roles of astrocytes in hippocampal synaptic plasticity: neuronal activity-dependent regulatory mechanisms. *FEBS J*. doi: 10.1111/febs.15878

Watts, M., and Sherman, A. (2014). Modeling the pancreatic α-cell: dual mechanisms of glucose suppression of glucagon secretion. *Biophys. J*. 106, 741–751. doi: 10.1016/j.bpj.2013.11.4504

Zeng, S., Li, B., Zeng, S., and Chen, S. (2009). Simulation of spontaneous Ca^2+ oscillations in astrocytes mediated by voltage-gated calcium channels. *Biophys. J*. 97, 2429–2437. doi: 10.1016/j.bpj.2009.08.030

Zhang, Y., and Wang, W. (2020). Mathematical analysis for stochastic model of Alzheimer's disease. *Commun. Nonlin. Sci. Numer. Simul.* 89:105347. doi: 10.1016/j.cnsns.2020.105347

Conflict of Interest: The authors declare that the research was conducted in the absence of any commercial or financial relationships that could be construed as a potential conflict of interest.

Publisher's Note: All claims expressed in this article are solely those of the authors and do not necessarily represent those of their affiliated organizations, or those of the publisher, the editors and the reviewers. Any product that may be evaluated in this article, or claim that may be made by its manufacturer, is not guaranteed or endorsed by the publisher.

frontiers in Computational Neuroscience

ORIGINAL RESEARCH
published: 25 January 2022
doi: 10.3389/fncom.2021.783474

Short- and Long-Range Connections Differentially Modulate the Dynamics and State of Small-World Networks

Simon Arvin[1,2*†], *Andreas Nørgaard Glud*[1†] *and Keisuke Yonehara*[2,3,4*]

[1] Department of Neurosurgery, Center for Experimental Neuroscience – CENSE, Institute of Clinical Medicine, Aarhus University Hospital, Aarhus C, Denmark, [2] Department of Biomedicine, Danish Research Institute of Translational Neuroscience – DANDRITE, Nordic-EMBL Partnership for Molecular Medicine, Aarhus University, Aarhus C, Denmark, [3] Multiscale Sensory Structure Laboratory, National Institute of Genetics, Mishima, Japan, [4] Department of Genetics, The Graduate University for Advanced Studies (SOKENDAI), Mishima, Japan

The human brain contains billions of neurons that flexibly interconnect to support local and global computational spans. As neuronal activity propagates through the neural medium, it approaches a critical state hedged between ordered and disordered system regimes. Recent work demonstrates that this criticality coincides with the small-world topology, a network arrangement that accommodates both local (subcritical) and global (supercritical) system properties. On one hand, operating near criticality is thought to offer several neurocomputational advantages, e.g., high-dynamic range, efficient information capacity, and information transfer fidelity. On the other hand, aberrations from the critical state have been linked to diverse pathologies of the brain, such as post-traumatic epileptiform seizures and disorders of consciousness. Modulation of brain activity, through neuromodulation, presents an attractive mode of treatment to alleviate such neurological disorders, but a tractable neural framework is needed to facilitate clinical progress. Using a variation on the generative small-world model of Watts and Strogatz and Kuramoto's model of coupled oscillators, we show that the topological and dynamical properties of the small-world network are divided into two functional domains based on the range of connectivity, and that these domains play distinct roles in shaping the behavior of the critical state. We demonstrate that short-range network connections shape the dynamics of the system, e.g., its volatility and metastability, whereas long-range connections drive the system state, e.g., a seizure. Together, these findings lend support to combinatorial neuromodulation approaches that synergistically normalize the system dynamic while mobilizing the system state.

Keywords: small-world, neuromodulation, neural oscillations, topology, simulation, network, criticality

OPEN ACCESS

Edited by:
Ioanna Sandvig,
Norwegian University of Science and Technology, Norway

Reviewed by:
Matjaž Perc,
University of Maribor, Slovenia
Claudia Battistin,
Norwegian University of Science and Technology, Norway
Alexander E. Hramov,
Innopolis University, Russia

***Correspondence:**
Simon Arvin
sarv@dandrite.au.dk
Keisuke Yonehara
keisuke.yonehara@dandrite.au.dk

†These authors share first authorship

Received: *26 September 2021*
Accepted: *03 December 2021*
Published: *25 January 2022*

Citation:
Arvin S, Glud AN and Yonehara K (2022) Short- and Long-Range Connections Differentially Modulate the Dynamics and State of Small-World Networks. Front. Comput. Neurosci. 15:783474. doi: 10.3389/fncom.2021.783474

INTRODUCTION

The human brain is thought to contain billions of neurons that densely interconnect across short and long spatial distances (von Bartheld et al., 2016). The pattern of neuronal activity hinges on the anatomical and functional medium by which it is generated, and in which it propagates (**Figure 1**) (Wolfram, 1984a,b; Perc, 2007; Wang et al., 2010). In a hypothetical lattice, where nodes are highly ordered and hold no long-range shortcuts, signals

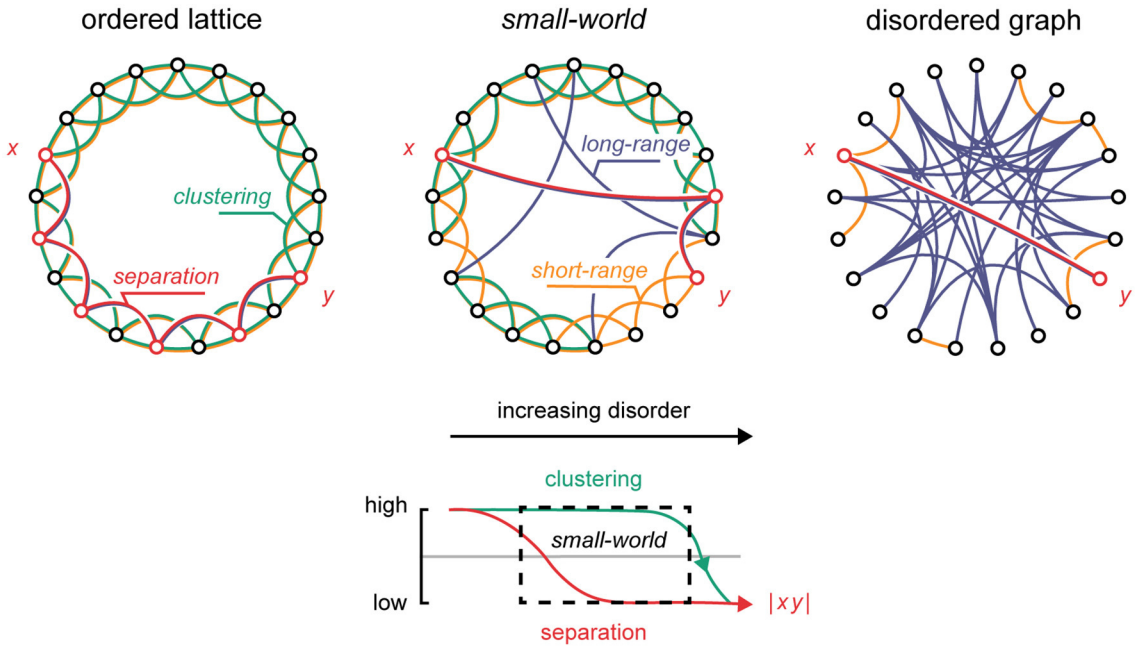

FIGURE 1 | The small-world topology. Upper panel: By randomly rewiring an ordered lattice, it gradually transitions to a disordered graph. Within this transition, the small-world arrangement defines a critical state. Green: clusters. Yellow: short-range connections. Blue: long-range connections. Red: the shortest path between nodes *x* and *y*. Lower panel: with increasing randomness, the degree of separation between nodes in the network rapidly decreases (red), while clustering remains practically unchanged within a wide limit (green). The small-world topology corresponds to the dashed area containing high-clustering and low-separation properties.

tend to fizzle out locally due to the resistance that high-nodal separation exerts on global transmission (Shew and Plenz, 2012). This contrast with more disordered graphs where signals tend to overwhelm the global network span through dense interconnectivity. Intermediately, in the "*small-world*" network formed by integrating just a few long-range shortcuts into an otherwise ordered lattice (Watts and Strogatz, 1998), signals tend to reverberate, perched on the edge of chaos in a so-called "*critical*" state (Shew and Plenz, 2012; Kim and Lim, 2015). Intriguingly, it is thought that the functional topology of the brain tends to this criticality (Takagi, 2018), flexibly maneuvering it based on an immediate operational needs; by dynamically recruiting or abandoning short- and long-range functional connections, e.g., through coherence of neuroelectric oscillations (Singer, 1999; Buzsáki, 2006; Akam and Kullmann, 2014), or neuroplasticity (Dan and Poo, 2004; Shin and Kim, 2006), the brain maneuvers clustered and disordered topological phases tuned to local and global operational spans, respectively. Within this theoretical framework, the dynamics of the brain essentially reflect a dialectic on one hand pulling the brain to its topological extremes (Poil et al., 2012; Shew and Plenz, 2012; Hesse and Gross, 2014), while, on the other hand, keeping it near the critical state (Shin and Kim, 2006; Hesse and Gross, 2014; Priesemann, 2015; Takagi, 2018). Operating near criticality is thought to offer several neurocomputational advantages, e.g., high-dynamic range, efficient information capacity, and information transfer fidelity. In turn, aberrations from criticality have been theorized to underpin distinct neuropathologies, such as post-traumatic epilepsy and consciousness disorders (Colombo et al., 2016). Certainly, the malfunction of long- and short-range functional connections, by injury or otherwise, could have disastrous effects on the dynamics of the brain (Pevzner et al., 2016). In this *Original Research* article, we investigate specifically how long- and short-range connections affect the topological and dynamical properties of the small-world network. Our results indicate that short-range connections shape the *dynamics* of the system, whereas long-range connections define its *state*. We discuss the implications of these differential effects on clinical neuromodulation.

METHODS

See **Table 1** for model parameters.

Network Generation

To keep a manageable number of free parameters, and to reduce the artifacts of boundary conditions, we restricted our analysis to a generative ring network model based on the small-world model of Watts and Strogatz (1998). These ring networks were generated using custom Python code based on the open-source module *networkx*. Briefly, $N = 1{,}000$ nodes were each wired to their h nearest neighbors, thus denoted "*short-range*" connections (for h well below saturation, $h << N$). Next, each node on average received an additional set of g random, yet unique, wires, which were denoted "*long-range*" connections (as wires of g did not equal those of h). Concretely, long-range

TABLE 1 | Model parameters.

Description	Notation	Notes
Network topology		
Short-range connections	h, H	[4–50]
Long-range connections	g, G	[0.001–10]
Adjacency matrix	A_{mn}	
Small-world coefficient	ω	[−1–+1]
Kuramoto-type simulation		
Oscillatory phase	θ_m	[0°–360°]
Network synchrony	r	[0–1]
Natural frequency	ϵ	Gaussian: $\mu = 0$, $\sigma = 1$
Total nodes	N	1,000

connectivity g was generated by a nested loop given by $g = T \times u$, where T is the maximum number of additional wires per node, and u is the average fraction of these actuated. To approximate biological gray-white matter ratios, while retaining a connected graph, we kept the range of short-range connectivity ∼10 times that of long-range connections (Bajada et al., 2019; Mota et al., 2019).

Finally, each network was defined by its adjacency matrix, A_{mn}, which was used for network simulation analysis (see Kuramoto's Model of Coupled Oscillators).

Small-World Coefficient

To quantify the extent to which a network resembled a small-world network, we computed the small-world coefficient ω (Telesford et al., 2011). Essentially, the small-world coefficient compares the resemblance of a network to a perfectly ordered vs. a perfectly disordered arrangement based on the extent to which the nodes of the network are clustered and the extent to which they are separated. The small-world coefficient is defined as:

$$\omega = \frac{L_{disordered}}{L} - \frac{C}{C_{ordered}},$$

where L is the average shortest path length between nodes in the network, and C is the degree of clustering (**Figure 1**). The disordered and ordered networks were generated based on the long-range connectivity given by $g = T \times u$ (see Network Generation). For the perfectly ordered network, no long-range connections were added, thus $u = 0$, and consequently $g = 0$. For the perfectly disordered network, the maximum number of long-range connections was introduced, thus $u = 1$, and consequently $g = T$.

The network parameters C and L were computed using common graph theory methods. Concretely, clustering C was computed as the network *transitivity*, such that:

$$C = \frac{3\nabla}{Tr}$$

where ∇ is the number of closed triplets in the network, and Tr is the maximum number of triplets. The average shortest path length L was given by:

$$L = \sum_{s,t \in V} \frac{D(s,t)}{N(N-1)},$$

where V is the set of nodes in the network, $D(s,t)$ is the shortest path length from node s to t, and N is the total number of nodes. Thus, when network separation $L \approx L_{disordered}$, and network clustering $C << C_{ordered}$, the small-world coefficient $\omega \approx +1$, meaning that the network approximates a perfectly disordered graph. Similarly, for the perfectly ordered lattice, when network clustering $C \approx C_{ordered}$ and network separation $L >> L_{disordered}$, the small-world coefficient approximates $\omega \approx -1$. Crucially, the small-world topology is defined as the critical state possessing both qualities, namely, network clustering similar to an ordered lattice $C \approx C_{ordered}$, and network separation similar to a disordered graph $L \approx L_{disordered}$; thus, the small-world coefficient tends to $\omega \approx 0$ as the network tends to the critical small-world arrangement.

Kuramoto's Model of Coupled Oscillators

Each node of the network was modeled as a coupled Kuramoto-type oscillator (Yamamoto et al., 2018), described by the set of N-coupled differential equations (Breakspear et al., 2010):

$$\dot{\theta}_n = \varepsilon_n + \frac{K}{N} \sum_{m=1}^{N} A_{mn} \sin(\theta_m - \theta_n),\ n = 1, \ldots, N,$$

where the n^{th} oscillator with a natural frequency ε_n adjusts its phase velocity $\dot{\theta}_n$ based on the pair-wise phase interactions with its coupled peers (provided by the adjacency matrix A_{mn}, see Network Generation). The internodal coupling was $K = 3$, and the natural frequencies were distributed according to the Gaussian probability density with mean $\varepsilon_0 = 0$. The state of the node ($n = 1, \ldots, N$) was thus defined by its phase θ, which was calculated by the Livermore Solver for Ordinary Differential Equations (LSODA) method with a dynamic time step.

The degree of synchrony in the network was quantified by the order parameter r, given by:

$$r(\theta_m) = re^{i\psi} = \frac{1}{N} \sum_{m=1}^{N} e^{i\theta_m},$$

where ψ is the mean phase of the set of oscillators N, and the scalar r represents the order, or phase uniformity, of the network. An open-source Python implementation of the Kuramoto oscillatory system is available online, which was used to generate the simulation data presented here (Damicelli, 2021).

Stability and Attractiveness Analysis

To compute the *stability* of different network states, we set the initial synchrony level of the network *via* the initial nodal phases

θ_{m0}. Thus, for initial synchrony $r_0 = 0.5$, on average 50% of the nodes of network had equal phases in the initial state. Then, at a predefined time-step $\Delta t = 250$, not necessarily in the steady-state, the deviation of the network from the initial synchrony level was computed, revealing the stability of the initial state. Specifically, larger deviations reflect weaker stability. Repeating this process for all combinations of initial synchrony levels and connectivity parameters produces the stability heat maps depicted in **Figure 4A**.

To calculate the *attractiveness* of different network states, we checked which synchrony levels the networks shifted to during the simulations and scored the end synchrony level based on the size of the shift. For instance, for initial synchrony $r_0 = 0.5$, and long-range connectivity $g = 0.001$, one network might end up in end synchrony level $r_1 = 0.0$. This adds a score of $s = |r_0 - r_1| = 0.5$ to the end synchrony state r_1. The synchrony states holding the highest cumulative scores had the highest attractiveness. Repeating this process for all the combinations of initial synchrony levels and connectivity parameters produces the attractiveness heat maps given in **Figure 4B**.

RESULTS

To examine the effects of long- and short-range connections on the topological and dynamical properties of the small-world network, we applied a variation on small-world model of Watts and Strogatz (1998) and the Kuramoto model of coupled oscillators (Kuramoto, 1984). Concretely, we generated an ordered ring lattice consisting of $N = 1{,}000$ nodes, each node connected to its h nearest neighbors. To this base, we added, on average, g *unique* long-range connections per node. Thus, by definition, long-range connections g were topologically distinct from their short-range correlates h, holding true for short-range connectivity well below network saturation, $h << N$. Then, to quantify the extent to which a network resembled a small-world network, we computed the small-world coefficient ω (Telesford et al., 2011). Essentially, the small-world coefficient compares the resemblance of a network to a perfectly ordered vs. a perfectly disordered arrangement based on the extent to which the nodes of the network are clustered and the extent to which they are separated. More specifically, ordered, *subcritical* lattices tend to $\omega \approx -1$, having high-clustering and high-separation parameters; disordered, *supercritical* graphs tend to $\omega \approx +1$, having low-clustering and low-separation parameters; and *critical* small-world topologies tend to $\omega \approx 0$, having both the ordered and disordered tendencies balanced out (see Methods). Within this definition, we visualized the topological behavior of the network by plotting the small-world coefficient ω as a function of the long- and short-range connectivity g and h, respectively (**Figure 2**). Finally, we used the same topological framework to generate networks of coupled Kuramoto-type oscillators (Kuramoto, 1984).

Long-Range Connections Dominate the Topological State

We first examined the roles of short- and long-range connections in defining the topological state of the network, specifically by keeping one parameter static (uppercase letters H and G) while modulating the other (lowercase letters h and g) (**Figure 2**). We found that modulations of the long-range connectivity g offered a near full topological range despite the underlying static short-range connectivity H (**Figure 2A**; ∼70% ± 0.05; mean ± SEM). Yet, the opposite was not the case: Invariant to the underlying long-range connectivity G, increases to the short-range connectivity h all converged to the critical state (**Figures 2A,B**). In general, less than half of the topological range was attainable by short-range modulation alone. Thus, short-range connections appear to be poorly suited as a modulator of the topological state.

For further examination, we computed the first derivative of the topological state to reveal the *state mobility* Δω of the network, i.e., how readily the network moved from one topological state to another *via* changes to its connectivity parameters h and g (**Figure 2C**). We found that across all underlying long-range connectivities G, modulation of the short-range connectivity h had near null effects on the topological state. Modulation of the long-range connectivity g of the network, however, offered potent state mobilization within the subcritical and critical regimes, but near null mobility approaching supercriticality. The dominant role of long-range connections on the topological state was confirmed by dominance analysis ($R^2 \sim 0.648$ for long-range vs. $R^2 \sim 0.003$ for short-range connections).

These results together indicate that the topological state of the small-world network is dominantly defined by the long-range connectivity (Watts and Strogatz, 1998) and that the topological mobility of the network is the most potent well below supercriticality (Carhart-Harris et al., 2014).

Short-Range Connections Shape the Topological Dynamics

Next, we evaluated how the underlying short-range connectivity H affects the topological behavior of the network, as reflected by the shape of the topological state curves (**Figure 2**). We found that as the static short-range connectivity H was reduced, the state curve steepened about the critical point, thus, contracting and "*right-shifting*" the critical regime to higher values of the long-range connectivity g (**Figure 2A**). This indicates that, to sustain the small-world criticality, poorly clustered networks (low H) must integrate long-range connections to a greater extent, yet within a narrower limit.

We then calculated the difference in state mobility of networks that had a high-static short-range connectivity ($H = 100$) and a low-static short-range connectivity ($H = 10$) (**Figure 2C**). In this difference plot, negative values reflect a reduction in the state mobility of the network, which essentially equates to a stabilization of the topological state (and oppositely for the positive values). Intriguingly, we found that, as the static short-range connectivity H was reduced, the stability of the topological state shifted to the subcritical regime, strongly destabilizing the small-world criticality (**Figure 2D**). This indicates that the short-range connectivity of the network has fundamental effects on the stability of the network across diverse topological regimes.

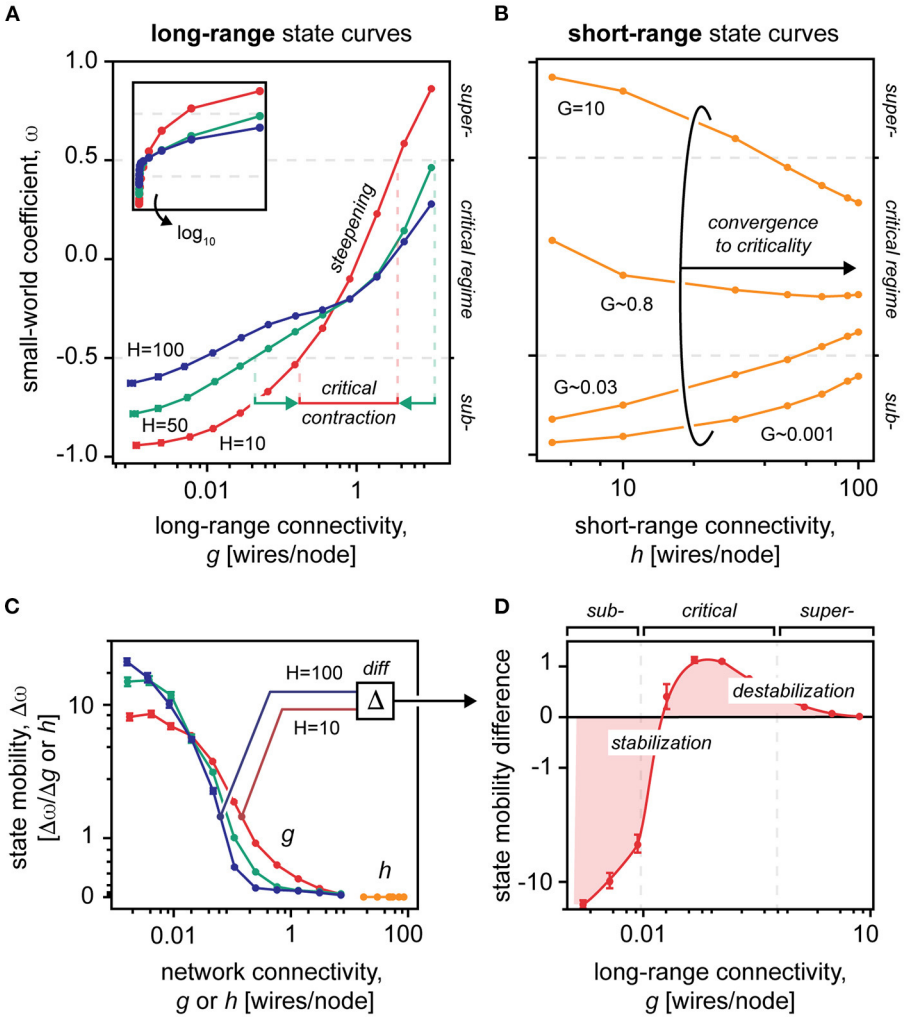

FIGURE 2 | The small-worldness of networks with varying long- and short-range connectivity values. **(A)** Small-world coefficients in a $N = 1{,}000$ graph with static short-range connectivity $H = 10$, 50, 100 averaged over 100 samples, shown in semilogarithmic x-axis. Inset, shown in non-logarithmic x-axis. The vertical dotted lines represent the bounds of the critical regime for networks $H = 10$ and $H = 100$. Note that the criticality contracts as the static short-range connectivity decreases. **(B)** Small-world coefficients in a $N = 1{,}000$ graph with static long-range connectivity G ($G \approx 0.001$, 0.03, 0.8, 10) averaged over 100 samples. Note that the short-range state curves converge to the critical state despite the underlying static long-range connectivity G. **(C)** The first derivative of the state curves, shown in A and B, constitutes state mobility of the network, i.e., how well it transitions from one topological state to another. Note that modulation of short-range connections h provides near null mobility of the topological state, vs. modulation of long-range connections g. Mobility of the topological state is mainly situated within subcritical and critical spaces, leaving near null mobility at high-connectivity values. **(D)** Difference in state mobility between networks with static short-range connectivity $H = 10$ and $H = 100$. The diagram shows that the topological state is stabilized in the subcritical space (negative values) and destabilized near criticality (positive values). Note that all plots have logarithmic x-axes. Data points are mean ± standard error of the mean.

Network Synchronizability

To extend our topological findings, we examined the synchronization properties offered by small-world networks of varying short- and long-range connectivity parameters (**Figure 3**). To this end, we quantified the global network synchrony at the steady-state using Kuramoto's order parameter r, which reflects that the global phase uniformity of the network nodes (see Methods).

By gradually integrating long-range connections into the network structure, our simulations show that the synchronizability abruptly reaches a critical point at which the network shifts from a state of low synchrony to near-complete synchrony (**Figure 3A**). Such "explosive synchronization," a critical transitioning, is characteristic for the Kuramoto-type coupled oscillators (Kuramoto, 1984; Gómez-Gardeñes et al., 2011; Boccaletti et al., 2016), and mirrors the topological criticality of small-world networks (**Figure 1**) (Watts and Strogatz, 1998).

Next, we modeled the synchronizability using four-parameter logistic regression (**Figure 3B**). Like in our topological findings,

we found that the slope of the critical transitioning b steepened as the static short-range connectivity H was reduced, indicating a destabilization and narrowing of the critical regime (**Figure 3B**, inset). The minimal synchronizability a of the network moreover related proportionally to the static short-range connectivity, indicating baseline synchronization hinged separately on short-range interactions. Indeed, as more short-range connections are introduced, the network ultimately reaches a point of saturation where global synchronization becomes deterministic, invariant to topological modulations (Barahona and Pecora, 2002).

Finally, by calculating the divergence of the network from a predefined initial synchrony level (see Methods), we examined the stability and attractiveness of different network states (**Figure 4**). First, these data confirm that the stability of the critical regime narrows as short-range connectivity decreases. Second, as short-range connections are removed, we find that the network becomes increasingly attracted to subcritical synchrony states (**Figure 4B**), which aligns with the topological destabilization that favors subcriticality presented earlier (*cf.* red curves in **Figures 2D**, **4D**, and inset).

Network Metastability Depends on Short-Range Connections

Our data show that the functional interactions of the network converge as the static short-range connectivity decreases (**Figure 3B**, note narrowing standard deviation). Accordingly, we found that the long-range connectivity g in the poorly clustered network (low H) had a very high predictive power (PPS) on the global synchrony r of the network, whereas highly clustered networks (high H) were generally poorly predictable ($H = 10$, PPS $= 0.93$; $H = 100$, PPS $= 0.43$) (Wetschoreck et al., 2020). Furthermore, as the short-range connectivity of the networks tends to saturation (H to $N = 1{,}000$), the PPS drops to 0. More specifically, we find that the PPS is linearly proportional to the short-range connectivity of the network (PPS $= -0.010\text{H} + 0.985$; $R^2 = 0.99$) (**Supplementary Figure 1**).

The PPS can be used to assess the *metastability* of the network. Thought to be inherent to cognition (Alderson et al., 2020), metastability defines a dynamical regime that accommodates flexible interactions of network nodes without stagnating in the fixed positions (Hellyer et al., 2015). Thus, our results show that metastability of the network depends linearly on the underlying short-range connectivity (by dominance analysis, $R^2 = 0.438$ for the short-range vs. $R^2 = 0.136$ for long-range connections). These simulation data altogether mirror our topological findings by suggesting that short-range connections are pivotal for the network's system dynamics (**Figure 4**).

DISCUSSION

We have investigated the effects of short- and long-range connections on the topological and dynamical properties of the small-world network. Converging with previous work (Watts and Strogatz, 1998), we demonstrate, first, that long-range connections determine the topological and functional state of the network. Second, we show that short-range connections shape the dynamics of the system, i.e., the stability of the system across diverse topological regimes (**Figures 2**, **4**). Our findings together provide evidence that short- and long-range connections play distinct roles in shaping the behavior of the small-world network.

The topological properties of a network have fundamental effects on the activity taking place on it (Strogatz, 2001). Several works have, for instance, analyzed the spread of infectious disease in small-world networks, finding fluctuations between sporadic endemic and self-sustaining epidemic infectious cycles based on network disorder (Kuperman and Abramson, 2001; Rüdiger et al., 2020). Others have examined the synchronizability of coupled oscillators on small-world graphs (Barahona and Pecora, 2002; Nishikawa et al., 2003). Later, such simulations have been expanded to examine cortical oscillations and neuroplasticity (Maistrenko et al., 2007; Breakspear et al., 2010).

The human brain is a complex system sustained by the interactions of billions of neurons across local and global spatial scales. Previous work has shown that the functional topology of the brain tends to a small-world-like criticality that accommodates both local (subcritical) and global (supercritical) system properties (Bassett and Bullmore, 2017; Takagi, 2018). The hypothesis that the brain maintains a proximity to the critical state stems from the premise of superior computational adaptability to rapidly changing operational demands (Massobrio et al., 2015a). Contention posits, however, that signatures for criticality, e.g., power-law distributions, could be artifacts of sampling (Touboul and Destexhe, 2010; Marsili et al., 2013), multiplicative noise (Sornette, 1998) or emerge from "hidden variables" not necessarily linked to network topology (Aitchison et al., 2016; Morrell et al., 2021). While an exhaustive review is beyond the scope of this discussion (Beggs and Timme, 2012), we note that diverse data supports the relationship between critical neural dynamics and small-world topologies (Massobrio et al., 2015b; Tan and Cheong, 2017; Takagi, 2018) and the presence of critical signatures in human fMRI (Kitzbichler et al., 2009), local field potentials (Petermann et al., 2009), spike data (Friedman et al., 2012), human brain oscillations (Poil et al., 2008), and artificial neural networks (Shin and Kim, 2006). Indeed, congruent with a near-critical regime (Priesemann, 2015), the brain operates within a wide dynamic range that accommodate high-level cognition through global neural coordination (Taylor et al., 2015), and low-activity states, such as anesthesia (Brown et al., 2010), and, to some extent, sleeping (Priesemann et al., 2013; Tagliazucchi and van Someren, 2017), marked by weaker, more fragmented interactions outside the local milieu.

It is believed that neural oscillations, or "brain waves," mediate short- and long-range neural connectivity through high- and low-frequency wavebands, respectively (Kopell et al., 2000; Buzsáki, 2006; Tiesinga and Sejnowski, 2009). In essence, the wave interference of oscillating neural populations facilitates the selective transfer of information (Singer, 1999; Buzsáki, 2006; Akam and Kullmann, 2010). Thus, it has been hypothesized that the malfunction of such neural interactions may have deleterious effects on the brain's system dynamics (Uhlhaas and Singer, 2006; Pevzner et al., 2016). In agreement with this premise, our results indicate that impairments to the network's short-range connectivity destabilize the small-world criticality in

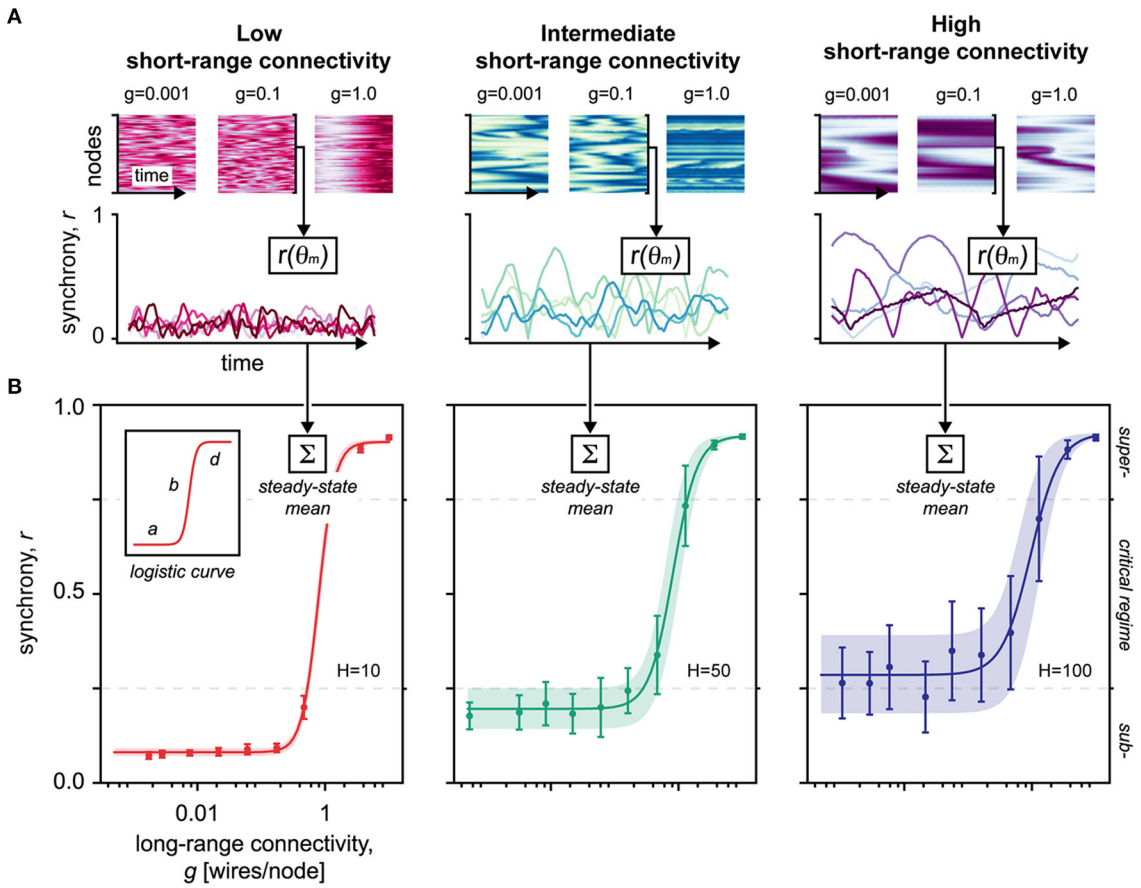

FIGURE 3 | Simulations of Kuramoto's coupled oscillators in small-world networks. **(A)** Upper panel shows the network activity over time. Colormap represents the phase of the nodes (faint: hyperpolarized–strong: depolarized). *g*, long-range connectivity. Lower panel shows the global synchrony of the network over time. The network activity, sampled in the upper panel, was mapped by $r(\theta_m)$ to reveal the network synchrony/order *r* given the set of oscillatory phases θ_m. The lines represent individual trials, color-shaded to increase visual separability. Red, $H = 10$, low short-range connectivity. Green, $H = 50$, intermediate short-range connectivity. Blue, $H = 100$, high short-range connectivity. **(B)** Averaged over 15 trials, this diagram shows the steady-state synchronizability of the network as the long-range connectivity *g* increases. Data points are mean ± SD of the mean. The shaded area corresponds to the SD of the mean, fitted to the logistic function. The SD of the mean is equivalent to metastability of the network, defining a dynamical regime that facilitates flexible nodal interactions without stagnating in fixed positions (Hellyer et al., 2015). Logistic curve parameters: *a*, minimum synchronizability; *b*, critical slope; *d*, maximum synchronizability; *H*, short-range connectivity. Red, $H = 10$, low short-range connectivity. Green, $H = 50$, intermediate short-range connectivity. Blue, $H = 100$, high short-range connectivity.

favor of extreme network regimes, i.e., sub- and supercriticality (**Figures 2D**, **4C**). Such departure from criticality has been linked to large-scale fMRI signatures of unconsciousness (Tagliazucchi et al., 2016).

Subcritical networks tend to be states of desynchronization and clustering that perturb global network processing, e.g., cognition (Roozenbeek et al., 2013). Congruently, our simulations show that sparsely clustered networks, with poor short-range connectivity, exhibit weak metastability (**Supplementary Figure 1**), which has been correlated with deficits in cognitive flexibility (Hellyer et al., 2015).

Notably, our stability analysis indicates that damage to the short-range connectivity of the network could produce a "repellant peak" that effectively barricades the critical regime, trapping the network activity in a subcritical trough (**Figure 4D**). Such "subcritical entrapment" aligns with the behavioral heterogeneity of persistent disorders of consciousness (Giacino et al., 2014), e.g., partial retainment of cognitive processing, and lends theoretical support to the rehabilitation of the system dynamic, e.g., through short-range neural potentiation.

The supercritical network, on the other hand, tends to hypersynchrony, broadly resembling the state of seizures (Szaflarski et al., 2014; Zimmern, 2020). Indeed, researchers have argued that epileptiform seizures reflect a critical–supercritical transition (Arviv et al., 2016; Bauer et al., 2017; Freestone et al., 2017), which was recently supported by a strong electroencephalographic sign in human patients (Scheffer et al., 2009; Maturana et al., 2020). Similarly, Gerster et al. report that artificial neuronal oscillators on supercritical small-world graphs mirror electroencephalographic epileptic patterns (Gerster et al., 2020). The refractoriness of some types of epilepsy could thus reflect an underlying destabilization of the critical regime by

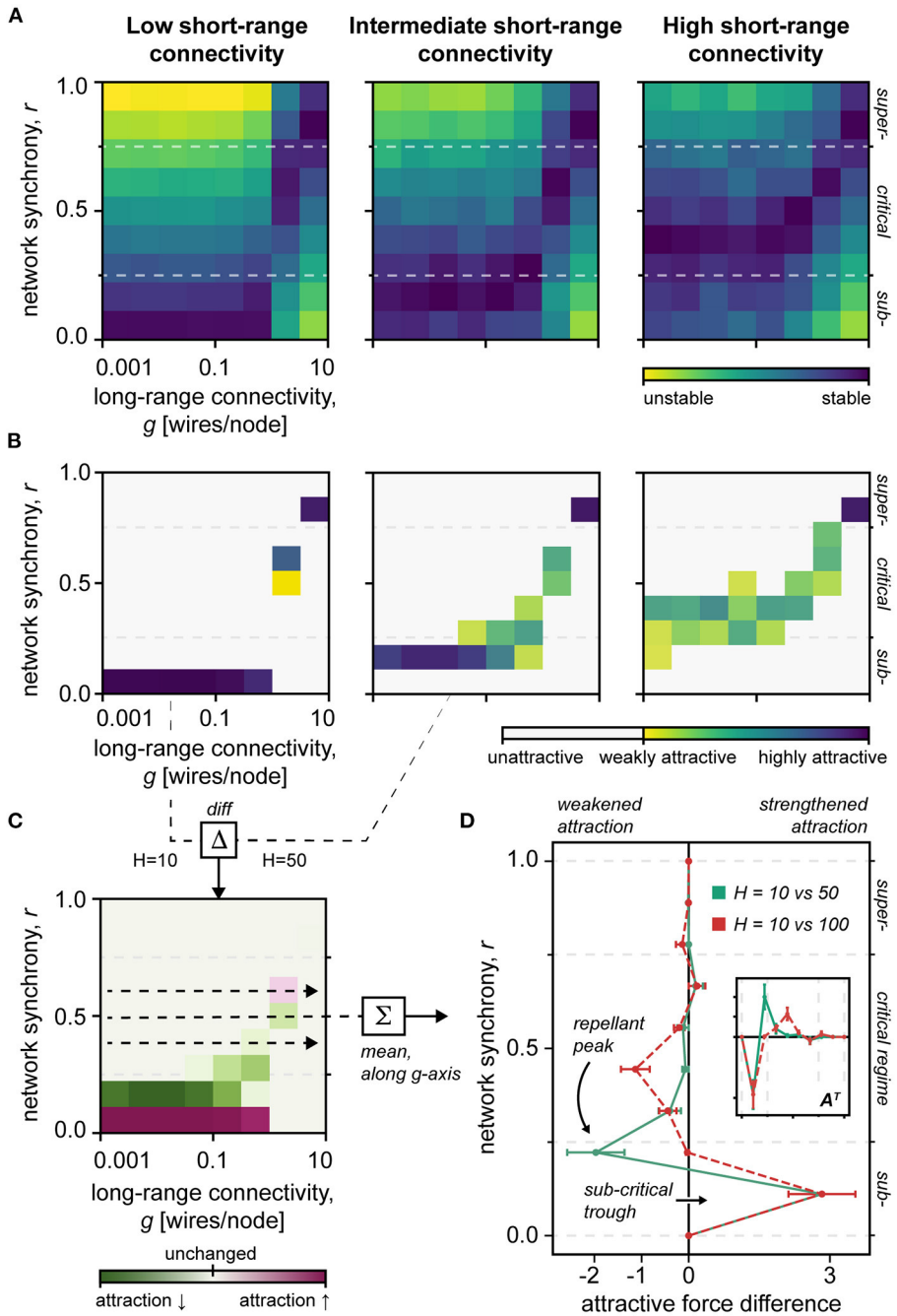

FIGURE 4 | Network stability. **(A)** Heat map of the stability of different network states. Note the narrowing stability of the critical regime in the sparsely clustered network $H = 10$, vs. $H = 50$, 100. *H*, short-range connectivity; *g*, long-range connectivity; *r*, network synchrony; Blue, stable; Yellow, unstable. **(B)** Heat map of the attractiveness of different network states. Note the increased attractiveness of extreme network regimes, particularly subcriticality, in the sparsely clustered network $H = 10$. *H*, short-range connectivity; *g*, long-range connectivity; *r*, network synchrony; Blue, highly attractive; Yellow, less attractive; White, unattractive. **(C)** Difference in state attractiveness between low ($H = 10$) and intermediate ($H = 50$) short-range connectivity networks. *H*, short-range connectivity; *g*, long-range connectivity; *r*, network synchrony; Red, increased attractiveness; Green, decreased attractiveness; Faint, unchanged attractiveness. **(D)** The difference in attractiveness between differently clustered networks, meaned along the long-range connectivity *g*-axis. Note the repellant peak at the critical–subcritical boundary, and the subcritical trough, which together could facilitate subcritical entrapment. Inset shows the main plot data in a transposed view A^T, which makes its similarity to the topological destabilization pattern clearer (**Figure 2D**). Red, dashed curve shows the attractiveness difference of sparsely clustered $H = 10$ and densely clustered $H = 100$ networks. Green, solid curve shows the attractiveness difference of sparsely clustered $H = 10$ and intermediately clustered $H = 100$ networks.

elimination of the short-range connections, such as through cortical dysgenesis or brain trauma (Semah et al., 1998). Interestingly, recent work on the Kuramoto model has shown that generalized resource constraints seed the network to self-terminating supercritical episodes (Frolov and Hramov, 2021), consistent with epileptic recurrences.

One potential mechanism for the disruption of short-range neural connectivity may be an injury to key brain hubs that contain a high-cumulative weight of short-range connections (Gratton et al., 2012; Zhou et al., 2012; Haimovici et al., 2016; Yuan et al., 2017). Indeed, hubs, e.g., the cingulate cortex, have been shown to be instrumental for cognitive performance (Fagerholm et al., 2015; Li et al., 2019), and have profound effects on the functional connectivity of simulated networks (Aerts et al., 2016). It is interesting to note that compensation to injury could thus predictably be offered by the recruitment, or hyperactivity, of dense hub regions, which has been widely hypothesized (Hillary et al., 2011, 2015; Tang et al., 2012; Iraji et al., 2016), e.g., in components of the default mode network (Zhou et al., 2012).

Our findings altogether lend support to combinatorial neuromodulation strategies that target short- and long-range neural connectivity differentially, to normalize the system dynamic and mobilize the system state, respectively. Future work will target components of short- and long-range neural communication, e.g., through pharmacological neurostimulation *via* amantadine to preferentially enhance low-frequency brain oscillations (Ott et al., 2018; Ma and Zafonte, 2020), direct current stimulation of deep brain structures, e.g., hippocampal theta (Lee et al., 2013), or modulation of cerebral cortex gamma (Pink et al., 2019), e.g., using cell-type-specific optogenetic or pharmacogenetic modulation (Liu et al., 2020), or non-invasive transcranial magnetic stimulation at low frequencies (Farzan et al., 2012).

STUDY LIMITATIONS

There are several limitations to this study. First, while providing a useful conceptual framework, Watts and Strogatz's ring model does not reflect real brain connectivity known to contain non-random edge distributions, e.g., "rich hubs" (van den Heuvel and Sporns, 2011), and a scale-free degree distribution (Eguíluz et al., 2005). Still, reduced topologies, e.g., generative small-worlds (Netoff et al., 2004; Perc, 2007; Tekin and Tagluk, 2017), and randomized graphs (van Vreeswijk and Sompolinsky, 1996; Tsodyks et al., 2000) remain valuable to neural network analysis by offering a controlled computational environment with manageable parameters and optimized network conditions.

Second, Kuramoto's oscillatory model represents a reduction of the complex interactions of distributed neural populations (Singer, 1999; Buzsáki, 2006). It is plausible that fuller physiological models would provide deeper insights into the precise mechanisms of such neural interactions. In support of the applicability of Kuramoto's equations, however, simulations have previously been applied to macaque (Honey and Sporns, 2008), and human brain research (Kitzbichler et al., 2009; Cabral et al., 2014), showing high congruence between simulation data and resting-state activity (Cabral et al., 2014; Vuksanović and Hövel, 2014). More broadly, reduced models (Siettos and Starke, 2016), such as two-state units (van Vreeswijk and Sompolinsky, 1996), and the *FitzHugh–Nagumo* model (Perc, 2007; Gerster et al., 2020), have been used extensively to examine complex network behaviors, such as self-organized balanced states (van Vreeswijk and Sompolinsky, 1996). Similarly, the abstraction offered by Kuramoto's model allows tractable simulations and analyses, holding high value for the investigation of more fundamental principles of oscillatory dynamics (Breakspear et al., 2010), such as the functional division of network connectivity examined here.

Despite these limitations, this study provides important insights into the relationship between network connectivity and critical system dynamics, which are broadly consistent with empirical reports and previous work (Haimovici et al., 2016). Future research should apply brain connectomic data and fuller network simulations to extend these findings.

DATA AVAILABILITY STATEMENT

The datatsets presented in this study can be found in the online repository: https://github.com/simonarvin/connectivity_smallworld.

AUTHOR CONTRIBUTIONS

SA and AG conceived the project. SA designed the project, performed the computations, and analyzed the data. SA, AG, and KY interpreted the data and wrote the manuscript. All authors contributed to the article and approved the submitted version.

FUNDING

We acknowledge the following grants: Lundbeck Foundation (DANDRITE-R248-2016-2518; R344-2020-300; and R351-2020-1095), Novo Nordisk Foundation (NNF20OC0064395), and European Research Council Starting (638730) grants to KY.

SUPPLEMENTARY MATERIAL

The Supplementary Material for this article can be found online at: https://www.frontiersin.org/articles/10.3389/fncom.2021.783474/full#supplementary-material

Supplementary Figure 1 | Predictive power of long-range connectivity *g* on network synchrony *r*. The predictive power of long-range connections on the synchrony state of the network is linearly proportional to short-range connectivity of the network. In fact, as short-range connectivity *H* tends to saturation $N = 1{,}000$, the predictive power tends to 0. *g*, long-range connectivity; *r*, network synchrony; *H*, short-range connectivity; *N*, total nodes; *PPS*, predictive power.

REFERENCES

Aerts, H., Fias, W., Caeyenberghs, K., and Marinazzo, D. (2016). Brain networks under attack: robustness properties and the impact of lesions. *Brain* 139, 3063–3083. doi: 10.1093/brain/aww194

Aitchison, L., Corradi, N., and Latham, P. E. (2016). Zipf's law arises naturally when there are underlying, unobserved variables. *PLoS Comput. Biol.* 12, e1005110. doi: 10.1371/journal.pcbi.1005110

Akam, T., and Kullmann, D. M. (2010). Oscillations and filtering networks support flexible routing of information. *Neuron* 67, 308–320. doi: 10.1016/j.neuron.2010.06.019

Akam, T., and Kullmann, D. M. (2014). Oscillatory multiplexing of population codes for selective communication in the mammalian brain. *Nat. Rev. Neurosci.* 111–122. doi: 10.1038/nrn3668

Alderson, T. H., Bokde, A. L. W., Kelso, J. A. S., Maguire, L., and Coyle, D. (2020). Metastable neural dynamics underlies cognitive performance across multiple behavioural paradigms. *Hum. Brain Mapp.* 41, 3212–3234. doi: 10.1002/hbm.25009

Arviv, O., Medvedovsky, M., Sheintuch, L., Goldstein, A., and Shriki, O. (2016). Deviations from critical dynamics in interictal epileptiform activity. *J. Neurosci.* 36, 12276–12292. doi: 10.1523/JNEUROSCI.0809-16.2016

Bajada, C. J., Schreiber, J., and Caspers, S. (2019). Fiber length profiling: a novel approach to structural brain organization. *Neuroimage* 186, 164–173. doi: 10.1016/j.neuroimage.2018.10.070

Barahona, M., and Pecora, L. M. (2002). Synchronization in small-world systems. *Phys. Rev. Lett.* 89, 054101. doi: 10.1103/PhysRevLett.89.054101

Bassett, D. S., and Bullmore, E. T. (2017). Small-world brain networks revisited. *Neuroscientist* 23, 499–516. doi: 10.1177/1073858416667720

Bauer, P. R., Thijs, R. D., Lamberts, R. J., Velis, D. N., Visser, G. H., Tolner, E. A., et al. (2017). Dynamics of convulsive seizure termination and postictal generalized EEG suppression. *Brain* 140, 655–668. doi: 10.1093/brain/aww322

Beggs, J. M., and Timme, N. (2012). Being critical of criticality in the brain. *Front. Physiol.* 3, 163. doi: 10.3389/fphys.2012.00163

Boccaletti, S., Almendral, J. A., Guan, S., Leyva, I., Liu, Z., Sendiña-Nadal, I., et al. (2016). Explosive transitions in complex networks' structure and dynamics: percolation and synchronization. *Phys. Rep.* 660, 1–94. doi: 10.1016/j.physrep.2016.10.004

Breakspear, M., Heitmann, S., and Daffertshofer, A. (2010). Generative models of cortical oscillations: neurobiological implications of the Kuramoto model. *Front. Hum. Neurosci.* 4, 190. doi: 10.3389/fnhum.2010.00190

Brown, E. N., Lydic, R., and Schiff, N. D. (2010). General anesthesia, sleep, and coma. *N. Engl. J. Med.* 363, 2638–2650. doi: 10.1056/NEJMra0808281

Buzsáki, G. (2006). *Rhythms of the Brain*.O xford, UK; New York: Oxford University Press.

Cabral, J., Kringelbach, M. L., and Deco, G. (2014). Exploring the network dynamics underlying brain activity during rest. *Prog. Neurobiol.* 114, 102–131. doi: 10.1016/j.pneurobio.2013.12.005

Carhart-Harris, R. L., Leech, R., Hellyer, P. J., Shanahan, M., Feilding, A., Tagliazucchi, E., et al. (2014). The entropic brain: a theory of conscious states informed by neuroimaging research with psychedelic drugs. *Front. Hum. Neurosci.* 8, 20. doi: 10.3389/fnhum.2014.00020

Colombo, M. A., Wei, Y., Ramautar, J. R., Linkenkaer-Hansen, K., Tagliazucchi, E., and Van Someren, E. J. W. (2016). More severe insomnia complaints in people with stronger long-range temporal correlations in wake resting-state EEG. *Front. Physiol.* 7, 576. doi: 10.3389/fphys.2016.00576

Damicelli, F. (2021). kuramoto: Python implementation of the Kuramoto model on graphs. *Github*. Available online at: https://github.com/fabridamicelli/kuramoto (accessed August 4, 2021).

Dan, Y., and Poo, M.-M. (2004). Spike timing-dependent plasticity of neural circuits. *Neuron* 44, 23–30. doi: 10.1016/j.neuron.2004.09.007

Eguíluz, V. M., Chialvo, D. R., Cecchi, G. A., Baliki, M., and Apkarian, A. V. (2005). Scale-free brain functional networks. *Phys. Rev. Lett.* 94, 018102. doi: 10.1103/PhysRevLett.94.018102

Fagerholm, E. D., Hellyer, P. J., Scott, G., Leech, R., and Sharp, D. J. (2015). Disconnection of network hubs and cognitive impairment after traumatic brain injury. *Brain* 138, 1696–1709. doi: 10.1093/brain/awv075

Farzan, F., Barr, M. S., Sun, Y., Fitzgerald, P. B., and Daskalakis, Z. J. (2012). Transcranial magnetic stimulation on the modulation of gamma oscillations in schizophrenia. *Ann. N. Y. Acad. Sci.* 1265, 25–35. doi: 10.1111/j.1749-6632.2012.06543.x

Freestone, D. R., Karoly, P. J., and Cook, M. J. (2017). A forward-looking review of seizure prediction. *Curr. Opin. Neurol.* 30, 167–173. doi: 10.1097/WCO.0000000000000429

Friedman, N., Ito, S., Brinkman, B. A. W., Shimono, M., DeVille, R. E. L., Dahmen, K. A., et al. (2012). Universal critical dynamics in high resolution neuronal avalanche data. *Phys. Rev. Lett.* 108, 208102. doi: 10.1103/PhysRevLett.108.208102

Frolov, N., and Hramov, A. (2021). Extreme synchronization events in a Kuramoto model: the interplay between resource constraints and explosive transitions. *Chaos* 31, 063103. doi: 10.1063/5.0055156

Gerster, M., Berner, R., Sawicki, J., Zakharova, A., and Škoch, A., Hlinka, J., et al. (2020). FitzHugh-Nagumo oscillators on complex networks mimic epileptic-seizure-related synchronization phenomena. *Chaos* 30, 123130. doi: 10.1063/5.0021420

Giacino, J. T., Fins, J. J., Laureys, S., and Schiff, N. D. (2014). Disorders of consciousness after acquired brain injury: the state of the science. *Nat. Rev. Neurol.* 10, 99–114. doi: 10.1038/nrneurol.2013.279

Gómez-Gardeñes, J., Gómez, S., Arenas, A., and Moreno, Y. (2011). Explosive synchronization transitions in scale-free networks. *Phys. Rev. Lett.* 106, 128701. doi: 10.1103/PhysRevLett.106.128701

Gratton, C., Nomura, E. M., Pérez, F., and D'Esposito, M. (2012). Focal brain lesions to critical locations cause widespread disruption of the modular organization of the brain. *J. Cogn. Neurosci.* 24, 1275–1285. doi: 10.1162/jocn_a_00222

Haimovici, A., Balenzuela, P., and Tagliazucchi, E. (2016). Dynamical signatures of structural connectivity damage to a model of the brain posed at criticality. *Brain Connect.* 6, 759–771. doi: 10.1089/brain.2016.0455

Hellyer, P. J., Scott, G., Shanahan, M., Sharp, D. J., and Leech, R. (2015). Cognitive flexibility through metastable neural dynamics is disrupted by damage to the structural connectome. *J. Neurosci.* 35, 9050–9063. doi: 10.1523/JNEUROSCI.4648-14.2015

Hesse, J., and Gross, T. (2014). Self-organized criticality as a fundamental property of neural systems. *Front. Syst. Neurosci.* 8, 166. doi: 10.3389/fnsys.2014.00166

Hillary, F. G., Roman, C. A., Venkatesan, U., Rajtmajer, S. M., Bajo, R., and Castellanos, N. D. (2015). Hyperconnectivity is a fundamental response to neurological disruption. *Neuropsychology* 29, 59–75. doi: 10.1037/neu0000110

Hillary, F. G., Slocomb, J., Hills, E. C., Fitzpatrick, N. M., Medaglia, J. D., Wang, J., et al. (2011). Changes in resting connectivity during recovery from severe traumatic brain injury. *Int. J. Psychophysiol.* 82, 115–123. doi: 10.1016/j.ijpsycho.2011.03.011

Honey, C. J., and Sporns, O. (2008). Dynamical consequences of lesions in cortical networks. *Hum. Brain Mapp.* 29, 802–809. doi: 10.1002/hbm.20579

Iraji, A., Chen, H., Wiseman, N., Welch, R. D., O'Neil, B. J., Haacke, E. M., et al. (2016). Compensation through functional hyperconnectivity: a longitudinal connectome assessment of mild traumatic brain injury. *Neural Plast.* 2016, 4072402. doi: 10.1155/2016/4072402

Kim, S.-Y., and Lim, W. (2015). Effect of small-world connectivity on fast sparsely synchronized cortical rhythms. *Phys. A Stat. Mech. Appl.* 421, 109–123. doi: 10.1016/j.physa.2014.10.019

Kitzbichler, M. G., Smith, M. L., Christensen, S. R., and Bullmore, E. (2009). Broadband criticality of human brain network synchronization. *PLoS Comput. Biol.* 5, e1000314. doi: 10.1371/journal.pcbi.1000314

Kopell, N., Ermentrout, G. B., Whittington, M. A., and Traub, R. D. (2000). Gamma rhythms and beta rhythms have different synchronization properties. *Proc. Nat. Acad. Sci. U.S.A.* 97, 1867. doi: 10.1073/pnas.97.4.1867

Kuperman, M., and Abramson, G. (2001). Small world effect in an epidemiological model. *Phys. Rev. Lett.* 86, 2909–2912. doi: 10.1103/PhysRevLett.86.2909

Kuramoto, Y. (1984). Cooperative dynamics of oscillator community: a study based on lattice of rings. *Progr. Theoret. Phys.* 79, 223–240. doi: 10.1143/PTPS.79.223

Lee, D. J., Gurkoff, G. G., Izadi, A., Berman, R. F., Ekstrom, A. D., Muizelaar, J. P., et al. (2013). Medial septal nucleus theta frequency deep brain stimulation improves spatial working memory after traumatic brain injury. *J. Neurotrauma* 30, 131–139. doi: 10.1089/neu.2012.2646

Li, F., Lu, L., Chen, H., Wang, P., Chen, Y.-C., Zhang, H., et al. (2019). Disrupted brain functional hub and causal connectivity in acute mild

traumatic brain injury. *Aging* 11, 10684–10696. doi: 10.18632/aging.102484

Liu, L., Xu, H., Wang, J., Li, J., Tian, Y., Zheng, J., et al. (2020). Cell type-differential modulation of prefrontal cortical GABAergic interneurons on low gamma rhythm and social interaction. *Sci. Adv.* 6, eaay4073. doi: 10.1126/sciadv.aay4073

Ma, H. M., and Zafonte, R. D. (2020). Amantadine and memantine: a comprehensive review for acquired brain injury. *Brain Inj.* 34, 299–315. doi: 10.1080/02699052.2020.1723697

Maistrenko, Y. L., Lysyansky, B., Hauptmann, C., Burylko, O., and Tass, P. A. (2007). Multistability in the Kuramoto model with synaptic plasticity. *Phys. Rev. E Stat. Nonlin. Soft Matter Phys.* 75, 066207. doi: 10.1103/PhysRevE.75.066207

Marsili, M., Mastromatteo, I., and Roudi, Y. (2013). On sampling and modeling complex systems. *arXiv* arXiv:1301.3622. doi: 10.1088/1742-5468/2013/09/P09003

Massobrio, P., de Arcangelis, L., Pasquale, V., Jensen, H. J., and Plenz, D. (2015a). Criticality as a signature of healthy neural systems. *Front. Syst. Neurosci.* 9, 22. doi: 10.3389/fnsys.2015.00022

Massobrio, P., Pasquale, V., and Martinoia, S. (2015b). Self-organized criticality in cortical assemblies occurs in concurrent scale-free and small-world networks. *Sci. Rep.* 5, 10578. doi: 10.1038/srep10578

Maturana, M. I., Meisel, C., Dell, K., Karoly, P. J., D'Souza, W., Grayden, D. B., et al. (2020). Critical slowing down as a biomarker for seizure susceptibility. *Nat. Commun.* 11, 2172. doi: 10.1038/s41467-020-15908-3

Morrell, M. C., Sederberg, A. J., and Nemenman, I. (2021). Latent dynamical variables produce signatures of spatiotemporal criticality in large biological systems. *Phys. Rev. Lett.* 126, 118302. doi: 10.1103/PhysRevLett.126.118302

Mota, B., Dos Santos, S. E., Ventura-Antunes, L., Jardim-Messeder, D., Neves, K., Kazu, R. S., et al. (2019). White matter volume and white/gray matter ratio in mammalian species as a consequence of the universal scaling of cortical folding. *Proc. Natl. Acad. Sci. USA.* 116, 15253–15261. doi: 10.1073/pnas.1716956116

Netoff, T. I., Clewley, R., Arno, S., Keck, T., and White, J. A. (2004). Epilepsy in small-world networks. *J. Neurosci.* 24, 8075–8083. doi: 10.1523/JNEUROSCI.1509-04.2004

Nishikawa, T., Motter, A. E., Lai, Y.-C., and Hoppensteadt, F. C. (2003). Heterogeneity in oscillator networks: are smaller worlds easier to synchronize? *Phys. Rev. Lett.* 91, 014101. doi: 10.1103/PhysRevLett.91.014101

Ott, T., Westendorff, S., and Nieder, A. (2018). Dopamine receptors influence internally generated oscillations during rule processing in primate prefrontal cortex. *J. Cogn. Neurosci.* 30, 770–784. doi: 10.1162/jocn_a_01248

Perc, M. (2007). Effects of small-world connectivity on noise-induced temporal and spatial order in neural media. *Chaos Solit. Fract.* 31, 280–291. doi: 10.1016/j.chaos.2005.10.018

Petermann, T., Thiagarajan, T. C., Lebedev, M. A., Nicolelis, M. A. L., Chialvo, D. R., and Plenz, D. (2009). Spontaneous cortical activity in awake monkeys composed of neuronal avalanches. *Proc. Natl. Acad. Sci. U.S.A.* 106, 15921–15926. doi: 10.1073/pnas.0904089106

Pevzner, A., Izadi, A., Lee, D. J., Shahlaie, K., and Gurkoff, G. G. (2016). Making waves in the brain: what are oscillations, and why modulating them makes sense for brain injury. *Front. Syst. Neurosci.* 10, 30–30. doi: 10.3389/fnsys.2016.00030

Pink, A. E., Williams, C., Alderman, N., and Stoffels, M. (2019). The use of repetitive transcranial magnetic stimulation (rTMS) following traumatic brain injury (TBI): a scoping review. *Neuropsychol. Rehabil.* 31, 479–505. doi: 10.1080/09602011.2019.1706585

Poil, S.-S., Hardstone, R., Mansvelder, H. D., and Linkenkaer-Hansen, K. (2012). Critical-state dynamics of avalanches and oscillations jointly emerge from balanced excitation/inhibition in neuronal networks. *J. Neurosci.* 32, 9817–9823. doi: 10.1523/JNEUROSCI.5990-11.2012

Poil, S.-S., van Ooyen, A., and Linkenkaer-Hansen, K. (2008). Avalanche dynamics of human brain oscillations: relation to critical branching processes and temporal correlations. *Hum. Brain Mapp.* 29, 770–777. doi: 10.1002/hbm.20590

Priesemann, V. (2015). Self-organization to sub-criticality. *BMC Neurosci.* 16, O19. doi: 10.1186/1471-2202-16-S1-O19

Priesemann, V., Valderrama, M., Wibral, M., and Le Van Quyen, M. (2013). Neuronal avalanches differ from wakefulness to deep sleep–evidence from intracranial depth recordings in humans. *PLoS Comput. Biol.* 9, e1002985. doi: 10.1371/journal.pcbi.1002985

Roozenbeek, B., Maas, A. I. R., and Menon, D. K. (2013). Changing patterns in the epidemiology of traumatic brain injury. *Nat. Rev. Neurol.* 9, 231–236. doi: 10.1038/nrneurol.2013.22

Rüdiger, S., Plietzsch, A., Sagués, F., Sokolov, I. M., and Kurths, J. (2020). Epidemics with mutating infectivity on small-world networks. *Sci. Rep.* 10, 5919. doi: 10.1038/s41598-020-62597-5

Scheffer, M., Bascompte, J., Brock, W. A., Brovkin, V., Carpenter, S. R., Dakos, V., et al. (2009). Early-warning signals for critical transitions. *Nature* 461, 53–59. doi: 10.1038/nature08227

Semah, F., Picot, M. C., Adam, C., Broglin, D., Arzimanoglou, A., Bazin, B., et al. (1998). Is the underlying cause of epilepsy a major prognostic factor for recurrence? *Neurology* 51, 1256–1262. doi: 10.1212/WNL.51.5.1256

Shew, W. L., and Plenz, D. (2012). The functional benefits of criticality in the cortex. *Neuroscientist* 19, 88–100. doi: 10.1177/1073858412445487

Shin, C.-W., and Kim, S. (2006). Self-organized criticality and scale-free properties in emergent functional neural networks. *Phys. Rev. E Stat. Nonlin. Soft Matter Phys.* 74, 045101. doi: 10.1103/PhysRevE.74.045101

Siettos, C., and Starke, J. (2016). Multiscale modeling of brain dynamics: from single neurons and networks to mathematical tools. *Wiley Interdiscip. Rev. Syst. Biol. Med.* 8, 438–458. doi: 10.1002/wsbm.1348

Singer, W. (1999). Neuronal synchrony: a versatile code for the definition of relations? *Neuron* 24, 49–65, 111–25. doi: 10.1016/S0896-6273(00)80821-1

Sornette, D. (1998). Multiplicative processes and power laws. *Phys. Rev. E* 57, 4811–4813. doi: 10.1103/PhysRevE.57.4811

Strogatz, S. H. (2001). Exploring complex networks. *Nature* 410, 268–276. doi: 10.1038/35065725

Szaflarski, J. P., Nazzal, Y., and Dreer, L. E. (2014). Post-traumatic epilepsy: current and emerging treatment options. *Neuropsychiatr. Dis. Treat.* 10, 1469–1477. doi: 10.2147/NDT.S50421

Tagliazucchi, E., Chialvo, D. R., Siniatchkin, M., Amico, E., Brichant, J.-F., Bonhomme, V., et al. (2016). Large-scale signatures of unconsciousness are consistent with a departure from critical dynamics. *J. R. Soc. Interface* 13, 20151027. doi: 10.1098/rsif.2015.1027

Tagliazucchi, E., and van Someren, E. J. W. (2017). The large-scale functional connectivity correlates of consciousness and arousal during the healthy and pathological human sleep cycle. *Neuroimage* 160, 55–72. doi: 10.1016/j.neuroimage.2017.06.026

Takagi, K. (2018). Information-based principle induces small-world topology and self-organized criticality in a large scale brain network. *Front. Comput. Neurosci.* 12, 65. doi: 10.3389/fncom.2018.00065

Tan, T. L., and Cheong, S. A. (2017). Statistical complexity is maximized in a small-world brain. *PLoS ONE* 12, e0183918. doi: 10.1371/journal.pone.0183918

Tang, C. Y., Eaves, E., Dams-O'Connor, K., Ho, L., Leung, E., Wong, E., et al. (2012). Diffuse disconnectivity in tBi: a resting state fMri anD Dti stuDy. *Transl. Neurosci.* 3, 9–14. doi: 10.2478/s13380-012-0003-3

Taylor, P., Hobbs, J. N., Burroni, J., and Siegelmann, H. T. (2015). The global landscape of cognition: hierarchical aggregation as an organizational principle of human cortical networks and functions. *Sci. Rep.* 5, 18112. doi: 10.1038/srep18112

Tekin, R., and Tagluk, M. E. (2017). Effects of small-world rewiring probability and noisy synaptic conductivity on slow waves: cortical network. *Neural Comput.* 29, 679–715. doi: 10.1162/NECO_a_00932

Telesford, Q. K., Joyce, K. E., Hayasaka, S., Burdette, J. H., and Laurienti, P. J. (2011). The ubiquity of small-world networks. *Brain Connect.* 1, 367–375. doi: 10.1089/brain.2011.0038

Tiesinga, P., and Sejnowski, T. J. (2009). Cortical enlightenment: are attentional gamma oscillations driven by ING or PING? *Neuron* 63, 727–732. doi: 10.1016/j.neuron.2009.09.009

Touboul, J., and Destexhe, A. (2010). Can power-law scaling and neuronal avalanches arise from stochastic dynamics? *PLoS ONE* 5, e8982. doi: 10.1371/journal.pone.0008982

Tsodyks, M., Uziel, A., and Markram, H. (2000). Synchrony generation in recurrent networks with frequency-dependent synapses. *J. Neurosci.* 20, RC50. doi: 10.1523/JNEUROSCI.20-01-j0003.2000

Uhlhaas, P. J., and Singer, W. (2006). Neural synchrony in brain disorders: relevance for cognitive dysfunctions and pathophysiology. *Neuron* 52, 155–168. doi: 10.1016/j.neuron.2006.09.020

van den Heuvel, M. P., and Sporns, O. (2011). Rich-club organization of the human connectome. *J. Neurosci.* 31, 15775. doi: 10.1523/JNEUROSCI.3539-11.2011

van Vreeswijk, C., and Sompolinsky, H. (1996). Chaos in neuronal networks with balanced excitatory and inhibitory activity. *Science* 274, 1724. doi: 10.1126/science.274.5293.1724

von Bartheld, C. S., Bahney, J., and Herculano-Houzel, S. (2016). The search for true numbers of neurons and glial cells in the human brain: a review of 150 years of cell counting. *J. Comp. Neurol.* 524, 3865–3895. doi: 10.1002/cne.24040

Vuksanović, V., and Hövel, P. (2014). Functional connectivity of distant cortical regions: role of remote synchronization and symmetry in interactions. *Neuroimage* 97, 1–8. doi: 10.1016/j.neuroimage.2014.04.039

Wang, Q., Perc, M., Duan, Z., and Chen, G. (2010). Impact of delays and rewiring on the dynamics of small-world neuronal networks with two types of coupling. *Phys. A Stat. Mech. Appl.* 389, 3299–3306. doi: 10.1016/j.physa.2010.03.031

Watts, D. J., and Strogatz, S. H. (1998). Collective dynamics of "small-world" networks. *Nature* 393, 440–442. doi: 10.1038/30918

Wetschoreck, F., Krabel, T., and Krishnamurthy, S. (2020). *8080labs/ppscore: zenodo release*. doi: 10.5281/zenodo.4091345

Wolfram, S. (1984a). Cellular automata as models of complexity. *Nature* 311, 419–424. doi: 10.1038/311419a0

Wolfram, S. (1984b). Universality and complexity in cellular automata. *Physica D* 10, 1–35. doi: 10.1016/0167-2789(84)90245-8

Yamamoto, H., Kubota, S., Shimizu, F. A., Hirano-Iwata, A., and Niwano, M. (2018). Effective subnetwork topology for synchronizing interconnected networks of coupled phase oscillators. *Front. Comput. Neurosci.* 12, 17. doi: 10.3389/fncom.2018.00017

Yuan, B., Fang, Y., Han, Z., Song, L., He, Y., and Bi, Y. (2017). Brain hubs in lesion models: Predicting functional network topology with lesion patterns in patients. *Sci. Rep.* 7, 17908. doi: 10.1038/s41598-017-17886-x

Zhou, Y., Milham, M. P., Lui, Y. W., Miles, L., Reaume, J., Sodickson, D. K., et al. (2012). Default-mode network disruption in mild traumatic brain injury. *Radiology* 265, 882–892. doi: 10.1148/radiol.12120748

Zimmern, V. (2020). Why brain criticality is clinically relevant: a scoping review. *Front. Neural Circuits* 14, 54. doi: 10.3389/fncir.2020.00054

Conflict of Interest: The authors declare that the research was conducted in the absence of any commercial or financial relationships that could be construed as a potential conflict of interest.

Publisher's Note: All claims expressed in this article are solely those of the authors and do not necessarily represent those of their affiliated organizations, or those of the publisher, the editors and the reviewers. Any product that may be evaluated in this article, or claim that may be made by its manufacturer, is not guaranteed or endorsed by the publisher.

frontiers in Neural Circuits

ORIGINAL RESEARCH
published: 28 March 2022
doi: 10.3389/fncir.2022.630621

Altered Brain Criticality in Schizophrenia: New Insights From Magnetoencephalography

Golnoush Alamian[1], Tarek Lajnef[1], Annalisa Pascarella[2], Jean-Marc Lina[3,4,5], Laura Knight[6], James Walters[7], Krish D. Singh[6] and Karim Jerbi[1,5,8]*

[1] CoCo Lab, Department of Psychology, Université de Montréal, Montréal, QC, Canada, [2] Institute for Applied Mathematics Mauro Picone, National Research Council, Roma, Italy, [3] Department of Electrical Engineering, École de Technologie Supérieure, Montréal, QC, Canada, [4] Mathematical Research Center, Université de Montréal, Montréal, QC, Canada, [5] Centre UNIQUE, Union Neurosciences et Intelligence Artificielle - Québec, Montréal, QC, Canada, [6] CUBRIC, School of Psychology, College of Biomedical and Life Sciences, Cardiff University, Cardiff, United Kingdom, [7] Division of Psychological Medicine and Clinical Neurosciences, MRC Centre for Neuropsychiatric Genetics and Genomics, School of Medicine, College of Biomedical and Life Sciences, Cardiff University, Cardiff, United Kingdom, [8] MEG Center, Université de Montréal, Montréal, QC, Canada

Schizophrenia has a complex etiology and symptomatology that is difficult to untangle. After decades of research, important advancements toward a central biomarker are still lacking. One of the missing pieces is a better understanding of how non-linear neural dynamics are altered in this patient population. In this study, the resting-state neuromagnetic signals of schizophrenia patients and healthy controls were analyzed in the framework of criticality. When biological systems like the brain are in a state of criticality, they are thought to be functioning at maximum efficiency (e.g., optimal communication and storage of information) and with maximum adaptability to incoming information. Here, we assessed the self-similarity and multifractality of resting-state brain signals recorded with magnetoencephalography in patients with schizophrenia patients and in matched controls. Schizophrenia patients had similar, although attenuated, patterns of self-similarity and multifractality values. Statistical tests showed that patients had higher values of self-similarity than controls in fronto-temporal regions, indicative of more regularity and memory in the signal. In contrast, patients had less multifractality than controls in the parietal and occipital regions, indicative of less diverse singularities and reduced variability in the signal. In addition, supervised machine-learning, based on logistic regression, successfully discriminated the two groups using measures of self-similarity and multifractality as features. Our results provide new insights into the baseline cognitive functioning of schizophrenia patients by identifying key alterations of criticality properties in their resting-state brain data.

Keywords: complexity, criticality, multifractal analysis, machine-learning, magnetoencephalography, resting-state, scale-free dynamics

OPEN ACCESS

Edited by:
Axel Sandvig, Norwegian University of Science and Technology, Norway

Reviewed by:
Ken-ichi Amemori, Kyoto University, Japan
Riccardo Iandolo, Norwegian University of Science and Technology, Norway

****Correspondence:***
Golnoush Alamian
golnoush.alamian@ubc.ca

Received: *18 November 2020*
Accepted: *03 March 2022*
Published: *28 March 2022*

Citation:
Alamian G, Lajnef T, Pascarella A, Lina J-M, Knight L, Walters J, Singh KD and Jerbi K (2022) Altered Brain Criticality in Schizophrenia: New Insights From Magnetoencephalography. Front. Neural Circuits 16:630621. doi: 10.3389/fncir.2022.630621

INTRODUCTION

The global prevalence of schizophrenia is reported to be close to 21 million individuals (Charlson et al., 2018). The symptoms and poor prognosis of those affected can deeply impact their daily functioning, and weigh on those close to them. Unfortunately, progress in therapeutic development is slow in the field of psychiatry due to the extreme complexity of the brain, the heterogeneity of patients' symptoms and difficulties in translational research. More knowledge is needed to better understand what alterations occur in the neural activity of patients. Among the missing pieces, further characterization of the resting neural dynamics of schizophrenia, and their relationship to patients' symptoms, is needed. Alterations in the rhythmic (oscillatory) neural activity of schizophrenia patients have been widely reported in the neuroimaging literature (reviews: Uhlhaas and Singer, 2010; Maran et al., 2016; Alamian et al., 2017). In addition, an emerging body of research has reported changes in the arrhythmic properties of brain dynamics in schizophrenia (Breakspear, 2006; Fernández et al., 2013). A powerful concept that has so far remained under-exploited and poorly understood in neuropsychiatry is criticality.

What Is Criticality?

The dynamics of many complex systems, such as the human brain, appear to reside around the critical point of a phase transition (Beggs and Plenz, 2003; Stam and De Bruin, 2004; Fraiman and Chialvo, 2012; Palva and Palva, 2018). At this point of criticality, these systems are in a wavering state, at the cusp of a new phase, between the states of order and disorder (Beggs and Timme, 2012; Cocchi et al., 2017; Souza França et al., 2018). The brain requires such a balance of regularity (i.e., structure) on the one hand, to maintain coherent behavior, and flexibility (i.e., local variability) on the other hand, to adapt to ongoing changes in the environment (Chialvo, 2004; Beggs and Timme, 2012). Indeed, critical brain dynamics have been shown to be optimal for fast switching between metastable brain states, for maximizing information transfer and information storage within neural networks (Socolar and Kauffman, 2003; Haldeman and Beggs, 2005), and for optimizing phase synchrony (Yang et al., 2012). Importantly, it is within a critical state that neural communication can span the greatest distance and achieve maximal correlational length (Fraiman and Chialvo, 2012). Thus, the brain's state of criticality is thought to affect the functional properties of oscillations, local synchronization and signal processing (Palva and Palva, 2018). Changes to this state, due to psychiatric illness for instance, can alter certain properties of this balance (e.g., in terms of strength and number of synaptic connections) (Beggs and Timme, 2012). Some of the tuning parameters of criticality appear to be embedded in the balance between neural excitation and inhibition (e.g., through NMDA receptors; Mazzoni et al., 2007; Shew et al., 2009; Hobbs et al., 2010; Poil et al., 2012), in neural network connection strengths, and synaptic plasticity (Rubinov et al., 2011; Beggs and Timme, 2012).

Measures of Criticality

Self-Similarity and Multifractality

Within the framework of criticality, local and large-scale fluctuations arise from excitatory post-synaptic potentials (EPSPs) and modulate brain states by facilitating or suppressing neuronal firing (Palva and Palva, 2018), with long-range spatial spread (He et al., 2010; Zilber, 2014). Systems in this state are characterized by power-law distributions, fractal geometry and fast metastable state transitions (Plenz and Chialvo, 2009; Cocchi et al., 2017; Chialvo, 2018; Palva and Palva, 2018). These features of a critical state are said to be scale-free or scale invariant. Power-law distributions of a given signal can be recognized as a linear slope in the log-log plot of the feature distribution, and they imply that the signal's statistics and structural characteristics are preserved across spatiotemporal scales—in other words, that the signal has fractal properties (Beggs and Plenz, 2003; Chialvo, 2018). Fractal architectures describe objects that contain identical, or statistically equivalent, repetitive patterns at different magnifying scales (Mandelbrot, 1983, 1985; Van Orden et al., 2012; Fetterhoff et al., 2015).

Scale invariant dynamics of systems at criticality (i.e., power-law distributions and fractal architecture) have often been described using a $1/f^{\beta}$ power law fitted to Fourier-based spectral estimations. On the other hand, self-similarity is a well-accepted model for scale-free dynamics and is richer than the sole measure of β, as it captures fractional Gaussian noise and fractional Brownian motion. Self-similarity can be measured by the Hurst exponent, *H*. In the brain, *H* is thought to index how well neural activity is temporally structured (via its autocorrelation). The smoother the signal, the higher the value of *H* (Zilber, 2014). However, self-similarity alone does not fully account for scale-free dynamics or criticality, since it can only capture additive processes (La Rocca et al., 2018). Combining self-similarity with multifractality improves on this framework to better capture criticality in a system. Multifractality can account for the remaining non-additive, non-Gaussian processes. The multifractality parameter, *M,* quantifies the diversity of *H*'s (singularities) and the overarching geometry of spatiotemporal fluctuations (Leonarduzzi et al., 2016; La Rocca et al., 2018). Generally, fractals are evaluated using the topological dimension, *D*, which describes the complexity and structure of an object by measuring the change in detail based on the change in scale (Di Ieva, 2016). In multifractal analysis, the local regularity of a signal is quantified using the *Hölder exponent, D(h)* (Jaffard et al., 2016), allowing a more realistic characterization of phenomena that are too complex to be explained solely by Euclidian models. In sum, the brain's degree of criticality is defined by its scale-free dynamics, which are best quantified by combining measures of self-similarity and multifractality.

Common Measures of Criticality

Numerous metrics have been developed to measure the scale-free properties that define criticality, such as Detrended Fluctuation Analysis (DFA) applied to oscillatory envelopes (Linkenkaer-Hansen et al., 2001; Hardstone et al., 2012) and neuronal avalanche detection (Beggs and Plenz, 2003). Non-linear dynamics, and specifically multifractal analysis,

has been used to address questions of self-similarity and multifractality. Multifractal analysis can characterize both the amount of global self-similarity in a system and the amount of local fluctuations (i.e., number of singularities) (Zilber et al., 2012). This approach allows for more in-depth interpretations of the electrophysiological data compared to more conventional analytical approaches. A number of mathematical frameworks have tapped into this, such as the Multifractal Detrended Fluctuation Analysis (MFDFA; Kantelhardt et al., 2002; Ihlen, 2012) and the Wavelet Leaders-based Multifractal Analysis (WLMA; Wendt and Abry, 2007; Serrano and Figliola, 2009). For reviews of scale-free and multifractal analytical approaches (see Lopes and Betrouni, 2009; Zilber, 2014).

Application to Psychiatry

A scoping review of alterations of brain criticality changes in clinical populations was recently discussed in Zimmern (2020). An insightful illustration of reported changes to the state of criticality across multiple neurological and psychiatric disorders, from the perspective of self-similarity, are illustrated in **Figure 6** of that article (Zimmern, 2020). The application of criticality models to psychiatry, and in particular to the study of schizophrenia (SZ), is well in line with leading theories for this pathology, which are centered around dysconnectivity and altered information processing and transfer (Weinberger et al., 1992; Friston and Frith, 1995; Fernández et al., 2013). So far, most of the empirical evidence for dysconnectivity theory in SZ has come from functional magnetic resonance imaging studies, which highlight several important alterations in anatomical and functional connectivity that exist in SZ patients, as well as from electroencephalography (EEG) and magnetoencephalography (MEG) connectivity studies (review: Alamian et al., 2017). However, we still lack a complete, in-depth understanding of the brain alterations inherent to this pathology in the temporal domain.

In terms of scale-free analyses in psychiatry, power spectral densities (PSD) of resting-state fMRI scans have shown SZ patients to have reduced complexity and disrupted scale invariant dynamics compared to controls in the precuneus, inferior frontal gyrus and temporal gyrus, and these changes correlated with their symptoms (Lee et al., 2021). Electrophysiological studies have found altered dimensional complexity and increased variability in SZ patients' signal (Koukkou et al., 1993). A number of studies have applied different versions of multifractal analysis on electrophysiological (Slezin et al., 2007; Racz et al., 2020) or white-matter MRI data in SZ (Takahashi et al., 2009). One of these used the multifractal analysis on resting-state EEG data, and found increased long-range autocorrelation and multifractality in patients compared to controls (Racz et al., 2020).

In addition, two insightful reviews have examined how non-linear methods could improve our understanding of SZ (Breakspear, 2006; Fernández et al., 2013). They highlighted conflicting results among studies reporting on complexity changes in SZ, which they proposed were attributable to participants' symptomatic state, the method of imaging or medication. Complexity as measured by Lempel–Ziv complexity (LZC) or correlation dimension (D2) was typically found to be increased in SZ in studies that recruited younger, first-episode patients who were drug-naïve and symptomatic, while studies reporting SZ-related reductions in complexity tended to recruit older, chronic, patients who were on medication and hence less symptomatic (Lee et al., 2008; Fernández et al., 2013). Although these measures have been widely applied to neuroscientific data, they each come with caveats that affect their precision or generalizability. Moreover, these reviews highlight the importance of controlling for factors such as age and medication when studying complex pathologies, such as SZ.

Goals of the Study

The brain is functionally optimal when in a state of criticality—in other words, when neural activity can spread equally well at long and short distances in time and space and information is processed and stored efficiently (Shew et al., 2009)—and multifractality analysis is an efficient indicator of criticality. Meanwhile, leading neural theories of SZ emphasize a pathological connectivity among neural signals across both space and time. It follows that multifractal analysis of brain signals in SZ may provide important insights into the nature of the pathological alterations that are associated with the disease and that underlie the severity of its symptoms.

Based on previous research that used self-similarity metrics (e.g., DFA) among the SZ population (Nikulin et al., 2012; Alamian et al., 2020), we expected altered self-similarity and multifractality values compared to healthy controls. Moreover, based on the literature on altered complexity in SZ (e.g., Lee et al., 2008, 2021; Fernández et al., 2013) we hypothesize that our patient group would show reduced multifractality compared to controls. We also predict significant correlations between measures of criticality and patients' clinical symptom scores. The aim of the present study is to test these hypotheses by examining how criticality is altered in the neural activity of chronic SZ patients. More specifically, we set out to address this question by using a multimodal neuroimaging approach, combining resting-state MEG and structural MRI, and wavelet-based estimations of multifractality and self-similarity.

MATERIALS AND METHODS

Participants

Participant data collection was conducted at the Cardiff University Brain Research Imaging Centre in Wales, United Kingdom., and the data analyses were conducted at the University of Montreal, QC, Canada. Ethical approval was obtained for the data collection according to the guidelines of the United Kingdom National Health Service ethics board, and the Cardiff University School of Psychology ethics board (EC.12.07.03.3164). Ethical approval was also obtained for these analyses from the research committee of the University of Montréal (CERAS-2018-19-069-D).

Behavioral and neuroimaging data from 25 chronic SZ patients (average age = 44.96 ± 8.55, 8 females) and 25 healthy controls (average age = 44.04 ± 9.20, 8 females) were included

in this study. Healthy controls had no history of psychiatric or neurological disorders. The collected demographic information from all participants included: age, gender, depression score on the Beck Depression Inventory—II (BDI-II, Beck et al., 1996), and mania score on the Altman Self-Rating Mania Scale (ASRM, Altman et al., 1997). For the SZ patient group, additional information was collected: scores on the Scale of the Assessment of Positive Symptoms (SAPS) and the Scale of the Assessment of Negative Symptoms (SANS) (Kay et al., 1987), and information on antipsychotic doses standardized using olanzapine equivalents (Gardner et al., 2010). All of these data were anonymized, such that no identifiable information of participants was associated with their data nor with data from subsequent analyses. Patients were overall fairly asymptomatic on the testing day. No statistically significant group differences were observed across these demographic and clinical metrics, except for BDI-II scores, where SZ patients had on average mild depression (14.83 ± 9.11), compared to controls (4.50 ± 4.67). Additional details on participant information (i.e., recruitment procedure, exclusions, inclusions, and sample size calculation) can be found in Alamian et al. (2020).

Magnetoencephalography Experimental Design

The brain imaging data used for this study comes from 5-min of resting-state MEG recorded during an eyes-closed condition, with a 275-channel CTF machine. Reference electrodes were placed on each participant to account for cardiac, ocular, and other potential artifacts (Messaritaki et al., 2017). The MEG signal was initially recorded at a sampling frequency of 1,200 Hz. A 3 Tesla General Electric Signa HDx scanner with an eight-channel receive-only head RF coil was used to acquire MRI data. Each participant had a 5-min weighted 3D T1 anatomical scan (TR/TE/TI = 7.8/3.0/450 ms, flip angle = 20°FOV = 256*192*172 mm, 1 mm isotropic resolution) that was later used for source-reconstruction of the MEG data.

Data Preprocessing and Magnetoencephalography Source Reconstruction

Reference electrodes were placed on each participant above and below the center of the left eye, on the left and right pre-auricular, under the left and right temples and behind the left ear, to account for cardiac, ocular, and other potential artifacts (Messaritaki et al., 2017). The MEG signal was initially recorded at a sampling frequency of 1,200 Hz. NeuroPycon (Meunier et al., 2020), an open-source python toolbox, was used for the preprocessing and source-reconstruction analyses. First, the continuous raw data was down-sampled from 1,200 to 600 Hz, and band-pass filtered between 0.1 and 150 Hz using a finite impulse response filtering (FIR 1, order = 3) and a Hamming window. Next, independent component analysis (ICA) was used to remove artifacts (i.e., blinks, horizontal eye movements, heartbeat) from the MEG signal using MNE-python (Hyvarinen, 1999; Gramfort et al., 2013). ICs related to heart and ocular artifacts were identified based on the correlation with ECG and EoG channels. ICs were visually inspected to check the reliability of the automatic procedure implemented in MNE. On average we removed 1–2 ICs related to cardiac artifacts and 1–2 ICs related to ocular artifacts.

Since it has been reported that the values of the Hurst exponent, *H,* are unusually low in sensor-space, and tend to increase when moving from sensor to source space (based on simulations and real data: Blythe et al., 2014), source-reconstruction steps were taken to present cortical-level results in multifractal analysis. To generate individual anatomical source-spaces, the anatomical T1-MRI information of each subject was segmented with FreeSurfer (Fischl, 2012). However, given that this process would produce different source-space dimensions for each participant, individual source spaces were morphed and projected onto a standardized space from FreeSurfer (*fsaverage*) (Greve et al., 2013). The resulting source-space comprised 8,196 nodes on the cortical surface, where dipoles were 5 mm apart. The single layer model boundary element method implemented in MNE-python was used to compute the lead field matrix (Gramfort et al., 2013). Weighted Minimum Norm Estimate (Dale and Sereno, 1993; Hämäläinen and Ilmoniemi, 1994; Hincapié et al., 2016), implemented in the MNE-python package (Hyvarinen, 1999; Gramfort et al., 2013), was used to compute the inverse solution with a Tikhonov regularization parameter of *lambda* = 1.0 (Hincapié et al., 2016). Dipoles of the source-space were constrained to have an orientation perpendicular to the cortical surface. Thus, for this study, 8,196 time series were extracted at the cortical level.

Characterization of Criticality Through Self-Similarity and Multifractality

Measuring Self-Similarity and Multifractality

The singularity spectrum is a concise way to summarize information about scale-free dynamics. It allows the plotting of the Hölder exponents (h) about local variability in a time series, against the Fractional (Hausdorff) Dimensions, $D(h)$, as can be seen in **Figure 1**.

Multifractal analysis builds on measures of self-similarity (e.g., slope of the PSD, DFA) to provide information about local fluctuations (singularities) in time. The multifractality spectrum and the scaling function ζ(q) (in terms of statistical moments q) are related, and can be described using the Legendre transformation:

$$D\left(h\right) \ \leq \ \underset{q\neq 0}{min}(1 \ + \ qh - \ \zeta\left(q\right)).$$

When a signal is monofractal, this becomes a linear function, where ζ(q) = qH, as it would only have a single singularity (one unique property, **Figure 1A**). Here, the self-similarity parameter would be equal to H, the Hurst exponent (Wendt and Abry, 2007). When a signal is multifractal, the function ζ(q) has a curvature, as in **Figure 1B**, which shows the global spectrum of singularities. The Hölder exponent (h) with the largest Fractal dimension, D (apex of the curve), is said to be the most common singularity in the time-series. The width of the curve can be described with the multifractality parameter, M (Wendt and Abry, 2007).

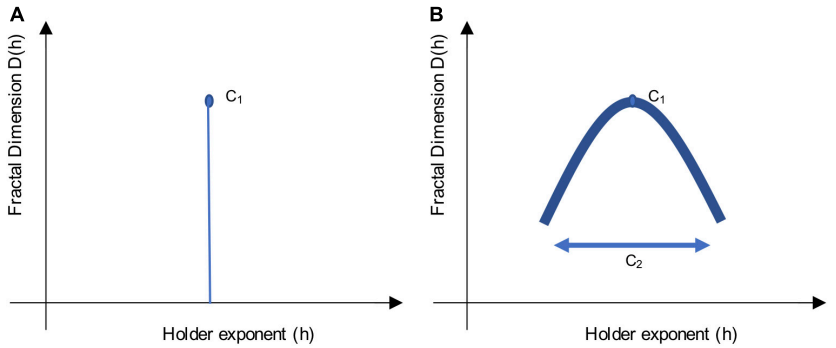

FIGURE 1 | Sketch of a singularity spectrum. These sketches illustrate the multifractal scaling function, which depicts a singularity spectrum. Local variability in the signal is represented by Hölder exponents, h, on the *x*-axis, while the amount of singularities is represented by the Fractal Dimension, D(h), on the *y*-axis. The apex of the curve reveals the most common h exponent, while the width of the curve reveals the multifractal spectrum. Using log-cumulants from the WLBMF (described in section "Defining Parameters of Log-Cumulants") to describe the singularity spectrum, C1 informs on the apex, while C2 informs on the width of the function. **(A)** Shows a monofractal function, where C1 = H, the Hurst exponent, and C2 = 0. **(B)** Shows a multifractal function, where the concavity shows the distribution of h singularities.

In this study, to meaningfully estimate self-similarity and multifractality, we used the Wavelet p-Leader and Bootstrap based MultiFractal analysis (WLBMF). This approach builds on the Wavelet leaders-based multifractal analysis (WLMA) method that has been thoroughly described elsewhere (Wendt and Abry, 2007; Wendt et al., 2007; Serrano and Figliola, 2009; Ciuciu et al., 2012; Fetterhoff et al., 2015). Briefly, this WLMA method of estimating the singularity spectrum was shown to be efficient in untangling the scaling properties of neuronal signal, and more robust than other algorithms in addressing non-stationarity issues (Wendt, 2008). The curved shape of the scaling function ζ(q) can be written in its polynomial expansion around its maximum to allow the evaluation of C_p, log-cumulants:

$$\zeta(q) = \sum_{p=1}^{\infty} C_p\left(\frac{q^p}{p!}\right).$$

The singularity spectrum can be thus derived from the series-expansion of C_p. The first two log-cumulants are the most informative, with C1, the first log-cumulant, reflecting self-similarity [and the location of the maximum of *D(h)*, similar to *H*]. Its values approximate those of the *H*, and typically range between 0 and 1, although values above 1 have been observed (Samoradnitsky and Taqqu, 1994). C1 values above 0.5 indicate positive correlation (signal has memory), values below 0.5 indicate negative correlation, and a value of 0.5 indicates lack of correlation (random signal). Meanwhile, C2, the second log-cumulant, reflects multifractality (and the width of the singularity spectrum, like *M*) (Wendt and Abry, 2007; Wendt et al., 2009; Zilber, 2014; Diallo and Mendy, 2019). Given the concavity of the scaling function, C2 is always negative, and when C2 equals 0, it is said to indicate monofractality. Typically, the few studies that have applied this novel analytical approach have observed values between 0 and −0.02 (Zilber, 2014) or 0 and −0.07 (Ciuciu et al., 2012).

Hölder exponents cannot take on negative values. Thus, most multifractal analyses are constrained to scaling functions that have only positive local regularities, implying that there is a continuous temporal positive correlation in the signal (i.e., locally bound everywhere in the function). However, this is not true of all brain signals, which can present with discontinuities in the signal and can thus take on negative regularities. Thus, p-leaders have been proposed as a way to circumvent this limitation (Jaffard et al., 2016). The p-leader formalism has been proposed as an extension of and improvement on older mathematical frameworks of multifractal analysis (e.g., MFDFA) using wavelet-projections, by allowing the analysis of negative local regularities and by providing more accurate and detailed characterization of singularities in the signal. Different p-leader values change the regularity exponents, where p = infinity corresponds to the original wavelet-leaders analysis, p = 2 brings about similar exponents as observed using DFA. For a deeper understanding of the mathematical details, we refer the reader to Jaffard et al. (2016) and Leonarduzzi et al. (2016).

Defining Parameters of Log-Cumulants

One method to detect criticality in the brain is through the Wavelet p-Leader and Bootstrap based MultiFractal (WLBMF) analysis and, more specifically, through the evaluation of log-cumulants (Wendt and Abry, 2007; Wendt et al., 2007). This MATLAB-implemented technique uses the discrete wavelet domain for the analysis of self-similarity and multifractality in signals. In order to compute C1 and C2 in our study, we first plotted the PSD of each participant group (SZ patients, controls) in log-log space and identified the portion of the PSD function exhibiting a log-linear relationship. In our data, the log-linear portion of the PSD belonged to j1 = 7 and j2 = 10, which correspond to 3.5 and 0.4 Hz, respectively, as deduced by the following equation: Scale = $\frac{3 \times Sf}{4 \times 2^j}$, where Sf represents the sampling frequency, j1 and j2 represent the start and end points of the log-linear portion, respectively, and the scale represents the frequency bin to which it corresponds. This frequency range is similar to those of other researchers who have used the same multifractal analysis (Zilber, 2014). For a step-by-step illustration

of the method, we direct the reader to **Figure 7.1** in Zilber (2014) for an illustration of these steps. The PSD was calculated at the overall cortical level and also at the ROI level, using the Destrieux Atlas (Destrieux et al., 2010), to ensure that the linear part of the spectrum was comparable across brain regions. For the purposes of this study, we used second order statistics in the evaluation of the log-cumulants (i.e., p-leader of $p = 2$), which is comparable to long-range temporal correlations computed with DFA (Leonarduzzi et al., 2016). For the ROI-based investigations, the C1 and C2 log-cumulants were first computed for each node (n = 8,196 sources) in cortical source-space, and then averaged across ROIs (n = 148 ROIs based on the Destrieux atlas, Destrieux et al., 2010). Although we calculate group differences across all individual nodes, we chose to also run ROI based analysis to help with the interpretability of the brain regions involved.

Statistics and Machine-Learning Analyses

Conventional Statistics and Correlation Analyses

Group statistical analyses were conducted between SZ patients and matched-controls to test for group-level differences in C1, C2, and demographic and clinical data. This was done at the ROI and source levels. To do so, we used non-parametric statistical tests (two-tailed, unpaired, pseudo t-tests), corrected with maximum statistics using permutations (n = 1000, $p < 0.001$) (Nichols and Holmes, 2001; Pantazis et al., 2005).

Moreover, Pearson correlations with False Discovery Rate (FDR) correction (Genovese et al., 2002) were used to explore the relationship between cortex-level C1/C2 values and scores on the SANS, SAPS and medication-dosage, in patients. FDR correction (Benjamini-Hochberg) was applied to each p-value (computed for each of the 8,196 nodes) to account for the multiple comparisons in order to achieve a significance threshold of $p < 0.05$, corrected.

Machine Learning Analyses

MEG signal classification was conducted using a logistic regression model and a stratified 10-fold cross-validation scheme to evaluate the discriminative power of the log-cumulants C1 and C2 in classifying SZ patients and controls. First, at each of the 8,196 nodes, the feature vector (either C1 or C2 values), computed for each participant, was split into 10-folds, while maintaining a balance between the two classes (SZ and controls). Next, the classifier was trained on the data from nine of the 10-folds and tested on the remaining fold (test set). The classification performance was assessed using the decoding accuracy (DA) on the test set (i.e., percentage of correctly classified participants across the total number of participants in the test set). This operation was repeated iteratively until all the folds were used as test sets. The mean DA was used as the classification performance metric. In order to infer the statistical significance of the obtained DAs, permutation tests were applied to derive a statistical threshold as described in Combrisson and Jerbi (2015). This method consists of generating a null-distribution of DAs obtained by running multiple instances of the classification (n = 1,000), and randomly shuffling class labels each time. Maximum statistics were applied in order to control for multiple comparisons across all the nodes (Nichols and Holmes, 2001; Pantazis et al., 2005). Visbrain was used for all the ROI and cortical-level visualizations (Combrisson et al., 2019).

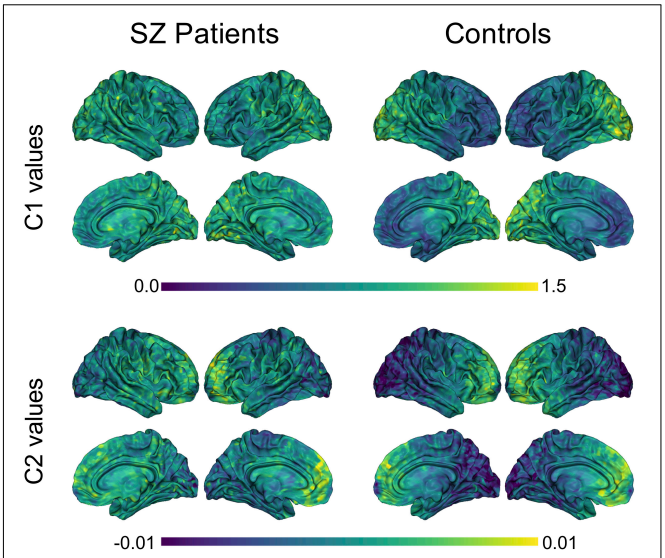

FIGURE 2 | Group averages of C1 and C2 values in SZ patients and controls. Averaged C1 and C2 values were computed for each of the 8,196 nodes, within each group. P-leader p = 2 was used. SZ, schizophrenia.

RESULTS

Alterations in Self-Similarity and Multifractality

The group averages of C1 and C2 values for SZ patients and healthy controls can be seen in **Figure 2**. Across both participant groups, a clear gradient in C1 values was observed, where self-similarity values increase gradually from the frontal lobe to the occipital lobe. Interestingly, a similar gradient, but in the opposite direction, is observed in terms of C2 values in both groups, with C2 values gradually increasing from the occipital lobe to the frontal lobe. Moreover, the magnitude of this gradient appears less pronounced in patients than in controls.

Conventional unpaired t-tests between the two subject groups did not yield any statistically significant differences in terms of C1 or C2 values ($p < 0.05$, two-tailed t-test). **Figure 3A** shows t-values for the direction and magnitude of group differences for C1 and C2 values, where positive (red) t-values indicate brain areas where SZ patients have smaller C1 or C2 values compared to controls, and negative (blue) t-values indicate brain areas where patients have larger C1 or C2 values compared to controls.

By contrast, when using a machine-learning approach to test for out-of-sample generalization in the same data, we found that C1 and C2 in multiple brain regions led to statistically significant classification of the two subject groups, with up to 77% decoding accuracy (**Figure 3D**, max statistics correction, $p < 0.05$). More specifically, using source-space C1 values as a decoding feature led to statistically significant discrimination of SZ and controls

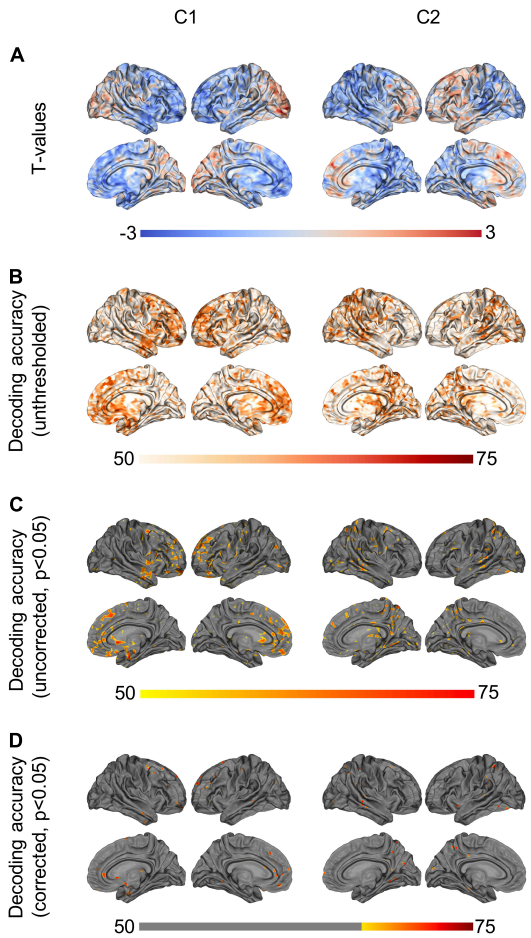

FIGURE 3 | Group differences and machine-learning results. **(A)** Shows *t*-values from the unpaired *t*-tests (non-significant), showing (controls—patients). Positive (red) *t*-values illustrate brain regions where patients show smaller C1/C2 values than controls, while negative (blue) *t*-values illustrate regions where patients have larger C1/C2 values than controls. **(B)** Shows unthresholded DA values based on logistic regression, using C1/C2 as a single feature. **(C)** Shows the same DA values, thresholded at $p < 0.05$. **(D)** Shows the DA values corrected for multiple comparisons using maximum statistics ($p < 0.05$), thresholded at the chance level of 70%. P-leader $p = 2$ was used. DA, decoding accuracy.

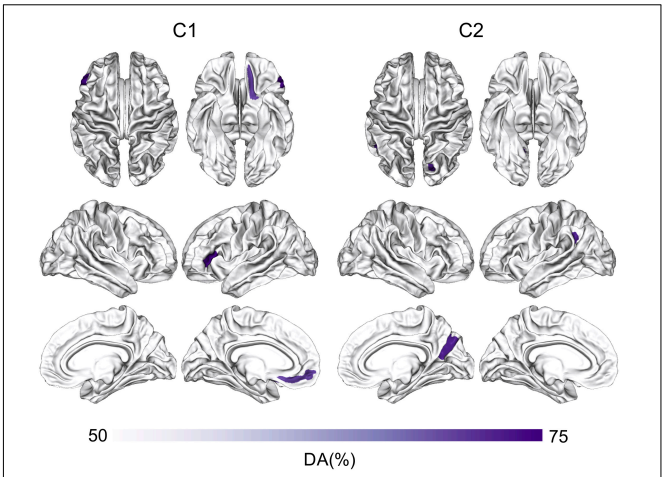

FIGURE 4 | ROI-based classification of SZ and controls using C1 and C2. Machine-learning classification of SZ patients and healthy controls using logistic regression and the features of C1 or C2 at the ROI-level. The ROI analysis was based on the Destrieux Atlas, $p < 0.05$, corrected for multiple comparisons. DA, decoding accuracy; SZ, schizophrenia.

in the subcallosal gyrus, middle fontal gyrus and anterior part of the cingulate gyrus, bilaterally. The left superior frontal gyrus, the left inferior frontal gyrus and sulci, and the right orbital, straight and frontomarginal gyri were also significant. The maximum decoding occurred in the left superior frontal gyrus (77%, compared to the chance level of 70%). Meanwhile, using source-space C2 values as a decoding feature led to statistically significant classification of SZ patients and controls in the superior parietal lobule, precuneus and posterior-ventral part of the cingulate gyrus in the right hemisphere. The left post-central gyrus, and superior temporal gyrus and occipital gyrus, bilaterally, were also significant. The maximum decoding accuracy took place in the right temporal gyrus (76%, compared to the chance level of 70%). **Figures 3B–D** show the unthresholded DA values for C1 and C2, as well as the uncorrected results at $p < 0.05$, and the corrected classification results at $p < 0.05$, with multiple comparisons correction using max statistics.

Figure 4 shows the classification results based on C1 and C2 values computed at the ROI-level ($p < 0.05$, corrected for multiple comparisons). The ROIs involved in the significant discrimination of patients and controls were the left straight gyrus, the triangular part of the inferior frontal gyrus and the medial transverse frontopolar gyrus and sulcus for C1, and the superior occipital gyrus, the right cuneus and the left angular gyrus for C2. To illustrate how the classifier was able to successfully separate SZ patients from healthy controls, individual C1 and C2 values were computed and averaged across all brain sites that had shown significant decoding at the source-level. These values are presented in a scatter plot in **Figure 5**. The distribution of the individual C1 and C2 values (averaged over all sources with significant decoding accuracy) shows that C1 values are higher in patients than in controls (i.e., a trend toward more self-similarity) and C2 values also shift upwards in patients (i.e., a trend toward less multifractality).

It is noteworthy that this scatter plot reveals the presence of positive C2 values in the dataset, primarily in patients. Although mathematically ill-defined, the observation of positive C2 is not unprecedented. Positive C2 values in some individuals can be attributed to numerical instabilities (and might be statistically undistinguishable from 0) or to the fact that the data in these participants cannot be modeled using the multifractal formalism. The safest interpretation for the positive C2 values observed in **Figure 5** (primarily in patients), is that data in these individuals were neither multifractal ($C2 < 0$) nor monofractal ($C2 = 0$). Given that this specific type of multifractal analysis has never been conducted on clinical data before, we explored how the results would change when using a p-leader of $p = 4$ (as opposed to the $p = 2$ we have used up to now). This analysis found fewer

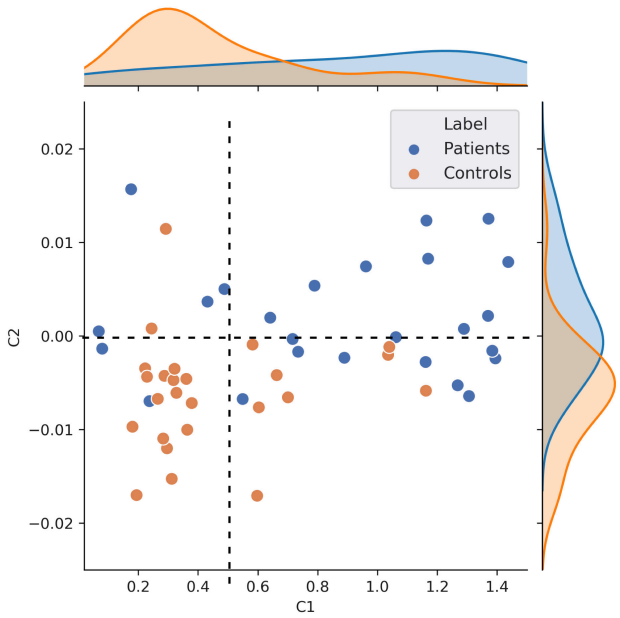

FIGURE 5 | Scatter plot visualization of individual C1 and C2 values. This figure shows individual C1 and C2 values, averaged across all the nodes that showed statistically significant patient vs. controls decoding ($n = 50$). This scatter plot illustrates that patients exhibit overall higher self-similarity (higher C1) and less multifractality (higher, less negative, C2).

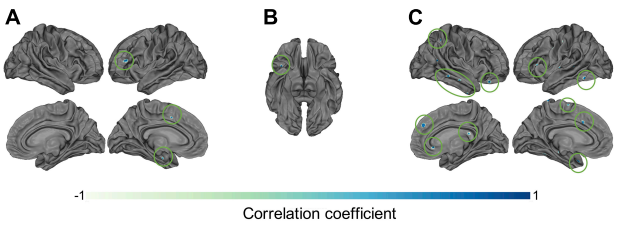

FIGURE 6 | Correlational results between C1 and C2 values and patients' clinical information. Pearson correlation results between patients' **(A)** C1 values and negative symptom scores on the SANS ($p < 0.05$), **(B)** C2 values and positive symptom scores on the SAPS ($p < 0.05$), and **(C)** C1 values and medication dosages (olanzapine equivalent in mg), $p < 0.05$.

participants to have positive C2 values compared to $p = 2$, and generally allowed for a better modeling of multifractality in the resting neuromagnetic signal of participants. Figures of C1/C2 group averages and classification patterns based on $p = 4$ can be found in **Supplementary Material 1**. In summary, we observed a similar albeit stronger decoding of patients and controls based on C2 values in $p = 4$ than $p = 2$. Interestingly, C1 values were smaller (**Supplementary Figure 1**), and the strong frontal lobe classification results based on C1 values at $p = 2$ diminished at $p = 4$ (**Supplementary Figures 2C,D**). Taken together, the results of C1 estimation (self-similarity) were more reliable in our data when using a p-leader of $p = 2$, while C2 estimation (multifractality) provided more robust results with $p = 4$. Most importantly, the trends in terms of increasing C1 and C2 values in patients compared to controls was present irrespective of the choice of p.

Correlations With Clinical Scores/Information

The investigation of potential correlations between C1/C2 and clinical information resulted in a number of interesting results. Specifically, the correlations between C1 values and patients' SANS scores (maximum $r = 0.78$, $p < 0.05$) in the left inferior frontal gyrus and sulcus (**Figure 6A**), and between C2 values and patients' SAPS scores (maximum $r = 0.78$, $p < 0.05$) in the circular sulcus of the insula (**Figure 6B**) were statistically significant. In addition, the relationship between C1 and medication dosage yielded a statistically significant positive correlation (maximum $r = 0.79$, $p < 0.05$, after correcting across all nodes). **Figures 6C**, **7C** illustrate that patients with higher medication dosage exhibited higher C1 values. This was especially significant in the superior frontal gyri, the right middle temporal gyrus, left mid-anterior cingulate gyrus and left inferior temporal sulcus (see **Figure 6C**). The positive correlations in these analyses are shown in the scatter plots in **Figures 7A–C**. These plots depict the relationship between individually averaged C1 and C2 values (based on the significant nodes), and patients' symptom severity and medication dosages. To further clarify the C1 × SANS correlational results, a Pearson correlation was conducted between SANS scores and medication dosage, revealing a low-to-moderate correlation coefficient. The r2 of the regression model suggested that this relationship explained 27–40% of the data, meaning that the correlation of C1 × SANS was only partially mediated by medication.

Uncorrected Spearman correlations were also computed and reasonable overlap was observed between the Pearson-based correlations and the Spearman findings. Similar to the Pearson correlations, the Spearman analysis revealed a positive correlation between C1 values and patients' SANS scores in the left mid-anterior part of the cingulate gyrus and sulcus ($r = 0.65$, $p < 0.0005$), in the left precentral gyrus ($r = 0.67$, $p < 0.0005$), in the left temporal pole ($r = 0.66$, $p < 0.0005$), and in the right middle frontal sulcus ($r = 0.71$, $p < 0.0005$). Future studies with larger cohorts would be critical to probe the robustness of these results and should take into account covariates such as age, sex and illness duration.

DISCUSSION

The central goal of this study was to examine and characterize criticality features in the baseline neural dynamics of schizophrenia. To do so, we evaluated the first two log-cumulants of the Wavelet p-Leader and Bootstrap based MultiFractal (WLBMF) analysis on the resting-state neuromagnetic signals of chronic SZ patients and healthy controls. This allowed us to determine the values of C1 (reflective of self-similarity) and C2 (reflective of multifractality) on the linear, scale-free portion of participants' arrhythmic MEG signal in source-space. In brief, our findings partially supported our initial hypotheses about

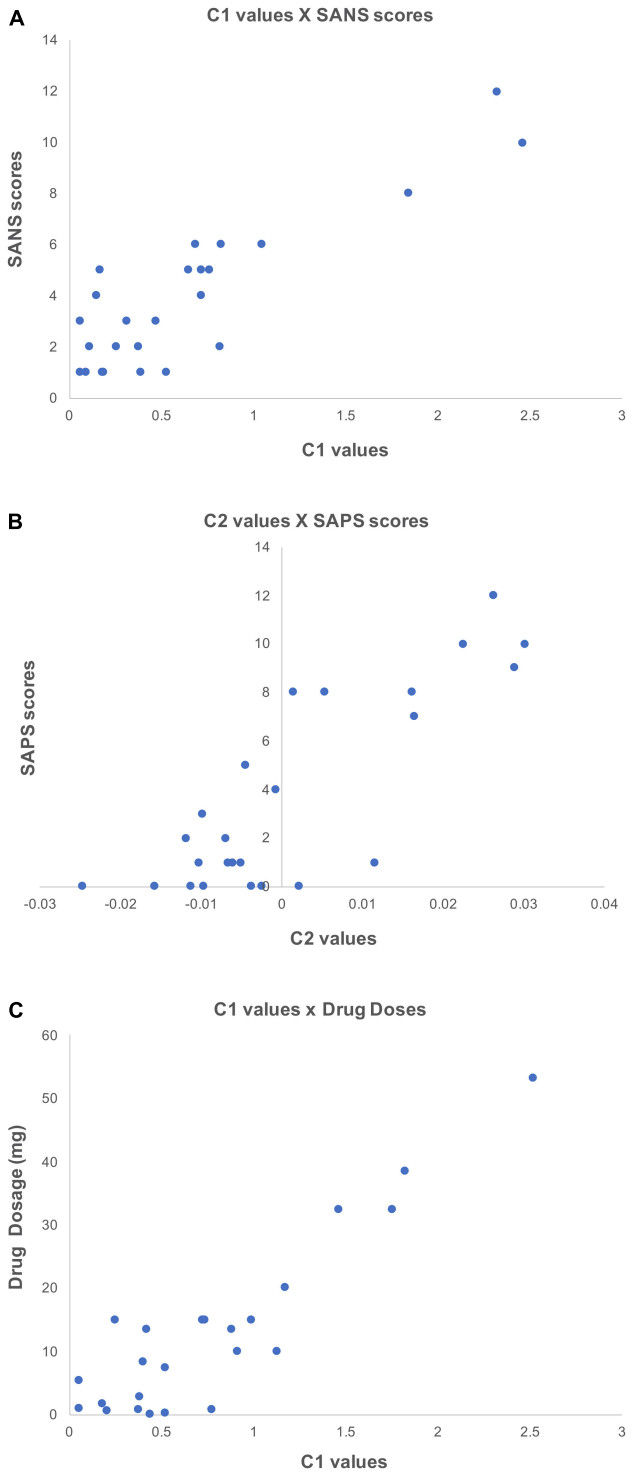

FIGURE 7 | Scatter plots showing the positive correlations between C1/C2 values and clinical information. These scatter plots depict correlations ($p < 0.05$) between individually averaged C1 and C2 values and subjects' clinical information. The averaging of C1 and C2 values was over significant nodes. **(A)** Shows the correlation between C1 values and patients' SANS scores, **(B)** shows the correlation between C2 values and SAPS scores, and **(C)** shows the correlation between C1 values and patients medication dosage (olanzapine equivalent in mg).

self-similarity and multifractality changes in SZ, whilst also revealing unexpected alterations in criticality.

Specifically, the findings of this study show that there are clear opposite gradients in the values of C1 and C2, along the rostro-caudal axis. A progression from low to high values of C1 were observed from anterior to posterior poles (i.e., frontal to occipital lobes), while C2 values showed the reverse progression. For both of these metrics, the gradient was less clear in SZ patients than in healthy controls. The *t*-values of the unpaired *t*-tests showed that patients had higher C1 values in the fronto-temporal area, and lower C1 values in the parieto-occipital areas compared to controls. In contrast, patients appeared to have higher C2 values in the temporal, parietal, and occipital areas than controls. Conventional *t*-test statistics failed to reach significance after multiple comparisons correction. However, a machine-learning approach based on logistic regression yielded statistically significant decoding (up to 77%) of patients and controls in a number of brain regions. Indeed, SZ patients and controls were categorized using C1 values in the anterior part of the cingulate gyrus (ACC), the left inferior gyrus, and the mid and superior frontal gyri, among other brain regions. Meanwhile, using C2 as a feature, we were able to statistically significantly classify patients and controls in the right temporal gyrus, precuneus, and occipital gyrus, among other brain regions.

In terms of the first log-cumulant, patients had a range of C1 values of [0.07, 1.44] in significant regions. In controls, this range was of [0.18, 1.16]. Typically, C1 (and thus H) values would be expected to be between 0 and 1 (where $0 < C1 < 0.5$ implies negatively autocorrelated signal, $C1 = 0.5$ implies uncorrelated signal, and $0.5 < C1 < 1$ implies positively autocorrelated signal), although values above 1 have been observed within the theory of *generalized processes and tempered distributions* (Samoradnitsky and Taqqu, 1994). In terms of the second log-cumulant, patients had a range of C2 values of [−0.01, 0.015] in significant brain regions, while controls had a range of [−0.02, 0.011]. These values fall within the same ranges reported by previous researchers (e.g., Zilber, 2014). As a reminder, higher C1 values are indicative of more self-similarity and memory in the signal, while lower (more negative) C2 values are indicative of more complexity in the form of multifractality. From our results, we infer that SZ patients exhibited more self-similar neural dynamics than healthy controls, and thus more regularity in the frontal and temporal brain areas. In addition, patients had fewer singularities (less diverse *h)* in the parietal and occipital brain regions, compared to healthy controls whose neural signals were more multifractal.

Further investigation of this analysis revealed that a subportion of participants (predominantly patients) had some positive C2 values. Theoretically, only [$C2 < 0$] (multifractal signals) or [$C2 = 0$] (monofractal signals) are expected. Observing positive C2 values implies that the multifractal formalism could not properly model the neuromagnetic data recorded in these patients. So, what does this tell us about the success of the classifier in using C2 to distinguish between patients and controls? The simplest explanation is that individuals with more negative C2 (stronger multifractal properties) were identified as healthy, whereas individuals with C2 values closer to zero (monofractal), or even higher than zero (neither multifractal no

monfractal), were classified as patients. As a side note, we found that using an alternate p-leader of $p = 4$ improved C2 values, and the classifier reaffirmed the diminished multifractality characteristics of patients' resting neuromagnetic signal. Taken together, we observe clear rostro-caudal gradients of ascending self-similarity and multifractality across both participant groups, albeit more clearly in controls. The reduced multifractality and increased self-similarity might reflect a certain rigidity in the temporal dynamics of SZ patients' neural activity.

Our findings are consistent with recent publications that have characterized complexity in SZ in the same regions in which we observed alteration in the log-cumulants C1 and C2 [i.e., precuneus, inferior frontal gyrus and temporal gyrus, (e.g., Lee et al., 2021)]. Interestingly, a recent resting-state MEG-based study of SZ patients by La Rocca et al. (2018) also found a gradient in C1 values along the longitudinal axis; however, in contrast to our own finding of an ascending anterior-posterior gradient, they instead found an opposite, descending anterior-posterior gradient (La Rocca et al., 2018). In addition, La Rocca et al. (2018) compared how criticality features changed during a perceptual task. They reported that in healthy individuals, global self-similarity decreased, while focal multifractality increased when switching from rest to task. Moreover, the changes in multifractality correlated with brain regions implicated in the task. This finding could suggest that the metric of C2 has a functional role in cognitive processes (La Rocca et al., 2018). Of note, there are some methodological differences between our studies, such as the choice of scale (j1 and j2) for the linear portion of the PSD. Differences could also be due to age differences. Indeed, the authors reported the mean age of their participants to be 22 years old, while our group's mean age was of 44 years old. In the complexity literature, it has been often reported that the properties of scale-free dynamics change with age (e.g., Fernández et al., 2011; Churchill et al., 2016), and so it is possible that there is a reversal of the self-similarity gradient with age. More work is needed to elucidate this.

Positive correlations were observed between the metrics of self-similarity and multifractality and patients' clinical information. In particular, we observed an increase in C1 values in patients with increasing severity of scores on the negative symptoms scale (SANS) in the inferior frontal gyrus, as well as with patient's medication dosage, the latter of which was especially strong ($r = 0.79$). The left frontal gyrus plays an important role in cognitive functioning (Swick et al., 2008) and language (Klaus and Hartwigsen, 2019). At the structural level, cortical thinning has been observed in the inferior frontal gyrus in SZ patients compared to healthy controls, which correlated with cognitive dysfunction (Kuperberg et al., 2003; Oertel-Knöchel et al., 2013). Correlation between inferior frontal gyrus volume and negative symptoms in SZ patients have been previously observed, but not in their non-affected siblings (Harms et al., 2010). At the functional level, higher cluster coefficients have been observed in the left inferior frontal compared to bipolar patients or controls (Kim et al., 2020), as well as weaker connectivity within the language network (Jeong et al., 2009). In addition to the reported structural alterations in this language processing center, the reduction in the temporal flexibility and enhanced regularity in the signal might explain why patients' have poorer speech understanding, such as difficulty detecting metaphors, sarcasm or jokes (Rossetti et al., 2018). A correlational trend was also observed between multifractality and patients' scores on the positive symptom scale (SAPS) in the circular sulcus of the insula. In past studies, negative correlations have been observed between reduced gray matter volume of the insula and SZ patients' positive symptoms (Wylie and Tregellas, 2010; Cascella et al., 2011). It is interesting to note that self-similarity and multifractality were oppositely (and perhaps complementarily) correlated with symptom severity scores.

Taking into account the correlational findings, it is not surprising that, in our dataset of chronic and medicated patients, antipsychotic medication dosage was related to symptom severity, which itself was related to scale-free neural properties. Psychiatrists typically increase pharmaceutical dosage, gradually and as needed, to help manage symptoms. Sometimes, certain drug combinations that help manage positive symptoms (hallucinations, delusions) can worsen negative symptoms (Schooler, 1994; Goff et al., 1996). Evidence from other studies (Koukkou et al., 1993; Saito et al., 1998; Raghavendra et al., 2009) suggests that drug-naïve and first-episode patients may display a different pattern of criticality, thus the generalizability of our results is limited to other medicated, chronic SZ patients.

Another parallel can be drawn between this study's results and findings from DFA analyses. The log-cumulants (C1 and C2) derived from WLBMF analysis using a p-leader of $p = 2$, as was used in the present study, are similar to scaling exponents obtained using DFA (Leonarduzzi et al., 2016), in that they both reflect temporal autocorrelations. In one of our recent publications, we computed DFA exponents on oscillatory envelopes in this same dataset of SZ patients and healthy controls (Alamian et al., 2020). The scale used for the computation of the log-cumulants (j1,2: 0.4–3.5 Hz) overlaps with the delta oscillatory band (0.5–3.5 Hz). Comparing delta DFA exponents and C1 between the studies reveals a good agreement: DFA exponents were reduced in patients compared to controls in the occipital and parietal lobes and increased values in the prefrontal and temporal lobes, similar to the C1 topology. The overlap was remarkably good considering that DFA was computed on band-limited rhythmic brain signal, while the log-cumulants of the singularity spectrum were computed on the arrhythmic raw brain signal. This comparison shows that while DFA is an adequate measure of the self-similarity aspect of criticality, it does not, however, provide any information on the multifractality of a signal, as does the second log-cumulant, C2. In this respect, they capture different properties of the neural signal, and should be treated as such. Several studies have examined the alterations of DFA across a number of psychiatric and neurological disorders. They found that a drop in DFA exponents occurs in SZ as well as in Alzheimer's and Parkinson's disease, whereas other conditions, such as depression, insomnia and epilepsy are typically associated with increases in DFA exponents (Zimmern, 2020). These findings reveal that reduced temporal autocorrelations observed in SZ are not disease-specific, but capture alterations that might be common to multiple psychiatric or neurological conditions. This again highlights the need for more elaborate measures of

brain criticality, such as through the WLBMF analysis carried out in the present manuscript.

Criticality in the brain likely informs on the spatiotemporal organization and functioning of neural networks at the micro- and macroscopic levels (Hesse and Gross, 2014; Cocchi et al., 2017). While the origins of criticality are still debated, many agree that scale-free neural fluctuations are the signature of a brain in a state of criticality. A right balance of scale invariant properties (self-similarity, multifractality) is thought to be needed to adapt and respond to ever changing environments (Linkenkaer-Hansen et al., 2001; Plenz and Chialvo, 2009; Beggs and Timme, 2012; Palva et al., 2013; Shew and Plenz, 2013). Consequently, we propose that a change in this equilibrium could disrupt optimal brain functioning. When self-similarity is strong in a signal, as in the brain signals of our SZ cohort, the signal's temporal autocorrelation decays slowly, such that signal memory lasts a long time. While still the subject of debate, it has been proposed that this enhanced temporal persistence (or redundancy) may make the brain less efficient in information processing (Zilber et al., 2013). Lower levels of self-similarity in signals, as in those of our healthy controls, are thought to reflect enhanced neural excitability and more efficient processing (He, 2011, 2014; Zilber et al., 2013). Interpretations of multifractality are still unclear, but it appears that a richer repertoire of singularities (multifractality > monofractality) suggests more variability and flexibility in the neural signal (Beggs and Timme, 2012), and thus in behavior. In our dataset, patients exhibited reduced multifractality in certain areas, thus suggesting a decrease in complexity and flexibility in their resting neuromagnetic signal. The observed alterations in these criticality metrics in SZ could explain the long, sustained nature of patients' positive symptoms (delusions, hallucinations) and their difficulty in breaking away from them.

CONCLUSION

The overarching scale invariance of brain activity is thought to be a useful indicator of its organization across both temporal and anatomical scales (Werner, 2007; Zilber, 2014). Indeed, many have suggested that biological systems optimally process, adapt to and communicate information over long neural distances when in a state of criticality. This critical state involves a balance between regularity (structure) and flexibility (variability, local fluctuations). Disruption of this equilibrium may reduce the efficiency with which the system responds to changes in the environment. In this study, we applied WLBMF analysis to resting MEG signals and observed clear deviations in both the self-similarity and multifractality of these signals in chronic SZ patients compared to healthy controls. These changes in the state of criticality of patients lend further support to the theory of dysconnectivity in SZ from the perspective of temporal dynamics, as it characterizes a different way in which information interruption occurs in patients. This study also demonstrated that alterations in neural criticality can be used to accurately differentiate between chronic SZ patients and controls. We expect that these findings will fuel the search for strong biomarkers in SZ, borrowing a new, largely uncharted path.

DATA AVAILABILITY STATEMENT

The datasets presented in this article are not readily available because the dataset for this manuscript is not publicly available due to ethical restrictions. Requests to access the datasets should be directed to corresponding author.

ETHICS STATEMENT

The studies involving human participants were reviewed and approved by the United Kingdom National Health Service Ethics Board, Cardiff University School of Psychology, and CERAS of University of Montreal. The patients/participants provided their written informed consent to participate in this study.

AUTHOR CONTRIBUTIONS

GA wrote the manuscript, designed and performed the analyses, and interpreted the results. TL designed the analyses and edited the manuscript. AP designed the analyses. J-ML provided theoretical background and edited the manuscript. LK and JW designed the data collection protocol and acquired the data. KS designed the data collection protocol and edited the manuscript. KJ conceptualized the study, interpreted the data, and edited the manuscript. All authors contributed to the article and approved the submitted version.

FUNDING

This research was supported in part by the FRQNT Strategic Clusters Program (grant no. 2020-RS4-265502—Centre UNIQUE—Union Neurosciences and Artificial Intelligence—Quebec). The scanning was supported by CUBRIC and the Schools of Psychology and Medicine at Cardiff University, together with the MRC/EPSRC funded United Kingdom MEG Partnership Grant (grant no. MR/K005464/1). GA was supported by the Fonds de Recherche du Québec en Santé. TL was supported by the postdoctoral fellowship from IVADO. KJ was supported by funding from the Canada Research Chairs Program and a Discovery Grant (grant no. RGPIN-2015-04854) from NSERC (Canada), a New Investigators Award from FRQNT (grant no. 2018-NC-206005), and the IVADO-Apogée fundamental research project grant.

ACKNOWLEDGMENTS

We would like to thank Herwig Wendt for helping with the interpretations of our findings, and Jordan O'Byrne for helpful comments on the manuscript.

SUPPLEMENTARY MATERIAL

The Supplementary Material for this article can be found online at: https://www.frontiersin.org/articles/10.3389/fncir.2022.630621/full#supplementary-material

REFERENCES

Alamian, G., Hincapié, A.-S., Pascarella, A., Thiery, T., Combrisson, E., Saive, A.-L., et al. (2017). Measuring alterations in oscillatory brain networks in schizophrenia with resting-state MEG: state-of-the-art and methodological challenges. *Clin. Neurophysiol.* 128, 1719–1736. doi: 10.1016/j.clinph.2017.06.246

Alamian, G., Pascarella, A., Lajnef, T., Knight, L., Walters, J., Singh, K. D., et al. (2020). Patient, interrupted: MEG oscillation dynamics reveal temporal dysconnectivity in schizophrenia. *Neuroimage Clin.* 28:102485. doi: 10.1016/j.nicl.2020.102485

Altman, E. G., Hedeker, D., Peterson, J. L., and Davis, J. M. (1997). The altman self-rating mania scale. *Biol. Psychiatry* 42, 948–955. doi: 10.1016/S0006-3223(96)00548-3

Beck, A. T., Steer, R. A., and Brown, G. K. (1996). *Manual for the Beck Depression Inventory-II*. San Antonio, TX: Psychological Corporation.

Beggs, J. M., and Plenz, D. (2003). Neuronal avalanches in neocortical circuits. *J. Neurosci.* 23, 11167–11177. doi: 10.1523/JNEUROSCI.23-35-11167.2003

Beggs, J. M., and Timme, N. (2012). Being critical of criticality in the brain. *Front. Physiol.* 3:163. doi: 10.3389/fphys.2012.00163

Blythe, D. A. J., Haufe, S., Müller, K. R., and Nikulin, V. V. (2014). The effect of linear mixing in the EEG on Hurst exponent estimation. *Neuroimage* 99, 377–387. doi: 10.1016/j.neuroimage.2014.05.041

Breakspear, M. (2006). The nonlinear theory of schizophrenia. *Aust. N. Z. J. Psychiatry* 40, 20–35. doi: 10.1111/j.1440-1614.2006.01737.x

Cascella, N. G., Gerner, G. J., Fieldstone, S. C., Sawa, A., and Schretlen, D. J. (2011). The insula-claustrum region and delusions in schizophrenia. *Schizophr. Res.* 133, 77–81. doi: 10.1016/j.schres.2011.08.004

Charlson, F. J., Ferrari, A. J., Santomauro, D. F., Diminic, S., Stockings, E., Scott, J. G., et al. (2018). Global epidemiology and burden of schizophrenia: findings from the global burden of disease study 2016. *Schizophr. Bull.* 44, 1195–1203. doi: 10.1093/schbul/sby058

Chialvo, D. R. (2004). Critical brain networks. *Phys. A Stat. Mech. Appl.* 340, 756–765. doi: 10.1016/j.physa.2004.05.064

Chialvo, D. R. (2018). Life at the edge: complexity and criticality in biological function. *Acta Phys. Pol. B* 49, 1955–1979. doi: 10.5506/APhysPolB.49.1955

Churchill, N. W., Spring, R., Grady, C., Cimprich, B., Askren, M. K., Reuter-Lorenz, P. A., et al. (2016). The suppression of scale-free fMRI brain dynamics across three different sources of effort: aging, task novelty and task difficulty. *Sci. Rep.* 6:30895. doi: 10.1038/srep30895

Ciuciu, P., Varoquaux, G., Abry, P., Sadaghiani, S., and Kleinschmidt, A. (2012). Scale-free and multifractal time dynamics of fMRI signals during rest and task. *Front. Physiol.* 3:186. doi: 10.3389/fphys.2012.00186

Cocchi, L., Gollo, L. L., Zalesky, A., and Breakspear, M. (2017). Criticality in the brain: a synthesis of neurobiology, models and cognition. *Prog. Neurobiol.* 158, 132–152. doi: 10.1016/j.pneurobio.2017.07.002

Combrisson, E., and Jerbi, K. (2015). Exceeding chance level by chance: the caveat of theoretical chance levels in brain signal classification and statistical assessment of decoding accuracy. *J. Neurosci. Methods* 250, 126–136. doi: 10.1016/J.JNEUMETH.2015.01.010

Combrisson, E., Vallat, R., O'Reilly, C., Jas, M., Pascarella, A., Saive, A., et al. (2019). Visbrain: a multi-purpose GPU-accelerated open-source suite for multimodal brain data visualization. *Front. Neuroinform.* 13:14. doi: 10.3389/fninf.2019.00014

Dale, A. M., and Sereno, M. I. (1993). Improved localization of cortical activity by combining EEG and MEG with MRI cortical surfarce reconstruction: a linear approach. *J. Cogn. Neurosci.* 5, 162–176. doi: 10.1162/jocn.1993.5.2.162

Destrieux, C., Fischl, B., Dale, A., and Halgren, E. (2010). Automatic parcellation of human cortical gyri and sulci using standard anatomical nomenclature. *Neuroimage* 53, 1–15. doi: 10.1016/j.neuroimage.2010.06.010

Di Ieva, A. (2016). *The Fractal Geometry of the Brain* (Springer Series in Computational Neuroscience). New York, NY: Springer.

Diallo, O. K., and Mendy, P. (2019). Wavelet leader and multifractal detrended fluctuation analysis of market efficiency: evidence from the WAEMU market index. *World J. Appl. Econ.* 5, 1–23. doi: 10.22440/wjae.5.1.1

Fernández, A., Gómez, C., Hornero, R., and López-Ibor, J. J. (2013). Complexity and schizophrenia. *Prog. Neuro Psychopharmacol. Biol. Psychiatry* 45, 267–276. doi: 10.1016/j.pnpbp.2012.03.015

Fernández, A., López-Ibor, M.-I., Turrero, A., Santos, J.-M., Morón, M.-D., Hornero, R., et al. (2011). Lempel–Ziv complexity in schizophrenia: a MEG study. *Clin. Neurophysiol.* 122, 2227–2235. doi: 10.1016/j.clinph.2011.04.011

Fetterhoff, D., Opris, I., Simpson, S. L., Deadwyler, S. A., Hampson, R. E., and Kraft, R. A. (2015). Multifractal analysis of information processing in hippocampal neural ensembles during working memory under δ9-tetrahydrocannabinol administration. *J. Neurosci. Methods* 244, 136–153. doi: 10.1016/j.jneumeth.2014.07.013

Fischl, B. (2012). FreeSurfer. *Neuroimage* 62, 774–781. doi: 10.1016/j.neuroimage.2012.01.021

Fraiman, D., and Chialvo, D. R. (2012). What kind of noise is brain noise: anomalous scaling behavior of the resting brain activity fluctuations. *Front. Physiol.* 3:307. doi: 10.3389/fphys.2012.00307

Friston, K. J., and Frith, C. D. (1995). Schizophrenia: a disconnection syndrome? *Clin. Neurosci.* 3, 89–97.

Gardner, D., Murphy, A., O'Donnell, H., Centorrino, F., and Baldessarini, R. (2010). International consensus study of antipsychotic dosing. *Am. J. Psychiatry* 167, 686–693. doi: 10.1176/appi.ajp.2009.09060802

Genovese, C. R., Lazar, N. A., and Nichols, T. (2002). Thresholding of statistical maps in functional neuroimaging using the false discovery rate. *Neuroimage* 15, 870–878. doi: 10.1006/NIMG.2001.1037

Goff, D. C., Tsai, G., Manoach, D. S., Flood, J., Darby, D. G., and Coyle, J. T. (1996). D-cycloserine added to clozapine for patients with schizophrenia. *Am. J. Psychiatry* 153, 1628–1630. doi: 10.1176/ajp.153.12.1628

Gramfort, A., Luessi, M., Larson, E., Engemann, D. A., Strohmeier, D., Brodbeck, C., et al. (2013). MEG and EEG data analysis with MNE-Python. *Front. Neurosci.* 7:267. doi: 10.3389/fnins.2013.00267

Greve, D. N., Van der Haegen, L., Cai, Q., Stufflebeam, S., Sabuncu, M. R., Fischl, B., et al. (2013). A surface-based analysis of language lateralization and cortical asymmetry. *J. Cogn. Neurosci.* 25, 1477–1492. doi: 10.1162/jocn_a_00405

Haldeman, C., and Beggs, J. M. (2005). Critical branching captures activity in living neural networks and maximizes the number of metastable states. *Phys. Rev. Lett.* 94:058101. doi: 10.1103/PhysRevLett.94.058101

Hämäläinen, M. S., and Ilmoniemi, R. J. (1994). Interpreting magnetic fields of the brain: minimum norm estimates. *Med. Biol. Eng. Comput.* 32, 35–42. doi: 10.1007/BF02512476

Hardstone, R., Poil, S.-S., Schiavone, G., Jansen, R., Nikulin, V. V., Mansvelder, H. D., et al. (2012). Detrended fluctuation analysis: a scale-free view on neuronal oscillations. *Front. Physiol.* 3:450. doi: 10.3389/fphys.2012.00450

Harms, M. P., Wang, L., Campanella, C., Aldridge, K., Moffitt, A. J., Kuelper, J., et al. (2010). Structural abnormalities in gyri of the prefrontal cortex in individuals with schizophrenia and their unaffected siblings. *Br. J. Psychiatry* 196, 150–157. doi: 10.1192/bjp.bp.109.067314

He, B. J. (2011). Scale-free properties of the functional magnetic resonance imaging signal during rest and task. *J. Neurosci.* 31, 13786–13795. doi: 10.1523/JNEUROSCI.2111-11.2011

He, B. J. (2014). Scale-free brain activity: past, present, and future. *Trends Cogn. Sci.* 18, 480–487. doi: 10.1016/j.tics.2014.04.003

He, B. J., Zempel, J. M., Snyder, A. Z., and Raichle, M. E. (2010). The temporal structures and functional significance of scale-free brain activity. *Neuron* 66, 353–369. doi: 10.1016/j.neuron.2010.04.020

Hesse, J., and Gross, T. (2014). Self-organized criticality as a fundamental property of neural systems. *Front. Syst. Neurosci.* 8:166. doi: 10.3389/fnsys.2014.00166

Hincapié, A.-S., Kujala, J., Mattout, J., Daligault, S., Delpuech, C., Mery, D., et al. (2016). MEG connectivity and power detections with minimum norm estimates require different regularization parameters. *Comput. Intell. Neurosci.* 2016:3979547. doi: 10.1155/2016/3979547

Hobbs, J. P., Smith, J. L., and Beggs, J. M. (2010). Aberrant neuronal avalanches in cortical tissue removed from juvenile epilepsy patients. *J. Clin. Neurophysiol.* 27, 380–386. doi: 10.1097/WNP.0b013e3181fdf8d3

Hyvarinen, A. (1999). Fast and robust fixed-point algorithms for independent component analysis. *IEEE Trans. Neural Netw.* 10, 626–634. doi: 10.1109/72.761722

Ihlen, E. A. F. (2012). Introduction to multifractal detrended fluctuation analysis in Matlab. *Front. Physiol.* 3:141. doi: 10.3389/fphys.2012.00141

Jaffard, S., Melot, C., Leonarduzzi, R., Wendt, H., Abry, P., Roux, S. G., et al. (2016). P-exponent and p-leaders, part I: negative pointwise regularity. *Phys. A Stat. Mech. Appl.* 448, 300–318. doi: 10.1016/j.physa.2015.12.061

Jeong, B., Wible, C. G., Hashimoto, R. I., and Kubicki, M. (2009). Functional and anatomical connectivity abnormalities in left inferior frontal gyrus in schizophrenia. *Hum. Brain Mapp.* 30, 4138–4151. doi: 10.1002/hbm.20835

Kantelhardt, J. W., Zschiegner, S. A., Koscielny-Bunde, E., Havlin, S., Bunde, A., and Stanley, H. E. (2002). Multifractal detrended fluctuation analysis of nonstationary time series. *Phys. A Stat. Mech. Appl.* 316, 87–114. doi: 10.1016/S0378-4371(02)01383-3

Kay, S. R., Fiszbein, A., and Opler, L. A. (1987). The positive and negative syndrome scale (PANSS) for schizophrenia. *Schizophr. Bull.* 13, 261–276. doi: 10.1093/schbul/13.2.261

Kim, S., Kim, Y.-W., Shim, M., Jin, M. J., Im, C.-H., and Lee, S.-H. (2020). Altered cortical functional networks in patients with schizophrenia and bipolar disorder: a resting-state electroencephalographic study. *Front. Psychiatry* 11:661. doi: 10.3389/fpsyt.2020.00661

Klaus, J., and Hartwigsen, G. (2019). Dissociating semantic and phonological contributions of the left inferior frontal gyrus to language production. *Hum. Brain Mapp.* 40, 3279–3287. doi: 10.1002/hbm.24597

Koukkou, M., Lehmann, D., Wackermann, J., Dvorak, I., and Henggeler, B. (1993). Dimensional complexity of EEG brain mechanisms in untreated schizophrenia. *Biol. Psychiatry* 33, 397–407. doi: 10.1016/0006-3223(93)90167-C

Kuperberg, G. R., Broome, M. R., McGuire, P. K., David, A. S., Eddy, M., Ozawa, F., et al. (2003). Regionally localized thinning of the cerebral cortex in schizophrenia. *Arch. Gen. Psychiatry* 60, 878–888. doi: 10.1001/archpsyc.60.9.878

La Rocca, D., Zilber, N., Abry, P., van Wassenhove, V., and Ciuciu, P. (2018). Self-similarity and multifractality in human brain activity: a wavelet-based analysis of scale-free brain dynamics☆. *bioRxiv* [Preprint] 315853. doi: 10.1101/315853

Lee, S. H., Choo, J. S., Im, W. Y., and Chae, J. H. (2008). Nonlinear analysis of electroencephalogram in schizophrenia patients with persistent auditory hallucination. *Psychiatry Investig.* 5, 115–120. doi: 10.4306/pi.2008.5.2.115

Lee, Y. J., Huang, S. Y., Lin, C. P., Tsai, S. J., and Yang, A. C. (2021). Alteration of power law scaling of spontaneous brain activity in schizophrenia. *Schizophr. Res.* 238, 10–19. doi: 10.1016/j.schres.2021.08.026

Leonarduzzi, R., Wendt, H., Abry, P., Jaffard, S., Melot, C., Roux, S. G., et al. (2016). P-exponent and p-leaders, part II: multifractal analysis. Relations to detrended fluctuation analysis. *Phys. A Stat. Mech. Appl.* 448, 319–339. doi: 10.1016/j.physa.2015.12.035

Linkenkaer-Hansen, K., Nikouline, V. V., Palva, J. M., and Ilmoniemi, R. J. (2001). Long-range temporal correlations and scaling behavior in human brain oscillations. *J. Neurosci.* 21, 1370–1377. doi: 10.1523/JNEUROSCI.21-04-01370.2001

Lopes, R., and Betrouni, N. (2009). Fractal and multifractal analysis: a review. *Med. Image Anal.* 13, 634–649. doi: 10.1016/j.media.2009.05.003

Mandelbrot, B. B. (1983). *Fractals and the Geometry of Nature*. New York, NY: WH freeman.

Mandelbrot, B. B. (1985). Self-affine fractals and fractal dimension. *Phys. Script.* 32, 257–260. doi: 10.1088/0031-8949/32/4/001

Maran, M., Grent-'t-Jong, T., and Uhlhaas, P. J. (2016). Electrophysiological insights into connectivity anomalies in schizophrenia: a systematic review. *Neuropsychiatr. Electrophysiol.* 2:6. doi: 10.1186/s40810-016-0020-5

Mazzoni, A., Broccard, F. D., Garcia-Perez, E., Bonifazi, P., Ruaro, M. E., and Torre, V. (2007). On the dynamics of the spontaneous activity in neuronal networks. *PLoS One* 2:e439. doi: 10.1371/journal.pone.0000439

Messaritaki, E., Koelewijn, L., Dima, D. C., Williams, G. M., Perry, G., and Singh, K. D. (2017). Assessment and elimination of the effects of head movement on MEG resting-state measures of oscillatory brain activity. *Neuroimage* 159, 302–324. doi: 10.1016/j.neuroimage.2017.07.038

Meunier, D., Pascarella, A., Altukhov, D., Jas, M., Combrisson, E., Lajnef, T., et al. (2020). NeuroPycon: an open-source Python toolbox for fast multi-modal and reproducible brain connectivity pipelines. *Neuroimage* 219:117020. doi: 10.1016/j.neuroimage.2020.117020

Nichols, T. E., and Holmes, A. P. (2001). Nonparametric permutation tests for functional neuroimaging: a primer with examples. *Hum. Brain Mapp.* 15, 1–25. doi: 10.1002/hbm.1058

Nikulin, V. V., Jönsson, E. G., and Brismar, T. (2012). Attenuation of long-range temporal correlations in the amplitude dynamics of alpha and beta neuronal oscillations in patients with schizophrenia. *Neuroimage* 61, 162–169. doi: 10.1016/j.neuroimage.2012.03.008

Oertel-Knöchel, V., Knöchel, C., Rotarska-Jagiela, A., Reinke, B., Prvulovic, D., Haenschel, C., et al. (2013). Association between psychotic symptoms and cortical thickness reduction across the schizophrenia spectrum. *Cereb. Cortex* 23, 61–70. doi: 10.1093/cercor/bhr380

Palva, J. M., Zhigalov, A., Hirvonen, J., Korhonen, O., Linkenkaer-Hansen, K., and Palva, S. (2013). Neuronal long-range temporal correlations and avalanche dynamics are correlated with behavioral scaling laws. *Proc. Natl. Acad. Sci. U.S.A.* 110, 3585–3590. doi: 10.1073/pnas.1216855110

Palva, S., and Palva, J. M. (2018). Roles of brain criticality and multiscale oscillations in temporal predictions for sensorimotor processing. *Trends Neurosci.* 41, 729–743. doi: 10.1016/j.tins.2018.08.008

Pantazis, D., Nichols, T. E., Baillet, S., and Leahy, R. M. (2005). A comparison of random field theory and permutation methods for the statistical analysis of MEG data. *Neuroimage* 25, 383–394. doi: 10.1016/j.neuroimage.2004.09.040

Plenz, D., and Chialvo, D. R. (2009). Scaling properties of neuronal avalanches are consistent with critical dynamics. *arXiv* [Preprint]. arXiv:0912.5369

Poil, S.-S., Hardstone, R., Mansvelder, H. D., and Linkenkaer-Hansen, K. (2012). Critical-state dynamics of avalanches and oscillations jointly emerge from balanced excitation/inhibition in neuronal networks. *J. Neurosci.* 32, 9817–9823. doi: 10.1523/JNEUROSCI.5990-11.2012

Racz, F. S., Stylianou, O., Mukli, P., and Eke, A. (2020). Multifractal and entropy-based analysis of delta band neural activity reveals altered functional connectivity dynamics in schizophrenia. *Front. Syst. Neurosci.* 14:49. doi: 10.3389/fnsys.2020.00049

Raghavendra, B. S., Dutt, D. N., Halahalli, H. N., and John, J. P. (2009). Complexity analysis of EEG in patients with schizophrenia using fractal dimension. *Physiol. Meas.* 30, 795–808. doi: 10.1088/0967-3334/30/8/005

Rossetti, I., Brambilla, P., and Papagno, C. (2018). Metaphor comprehension in schizophrenic patients. *Front. Psychol.* 9:670. doi: 10.3389/fpsyg.2018.00670

Rubinov, M., Sporns, O., Thivierge, J. P., and Breakspear, M. (2011). Neurobiologically realistic determinants of self-organized criticality in networks of spiking neurons. *PLoS Comput. Biol.* 7:e1002038. doi: 10.1371/journal.pcbi.1002038

Saito, N., Kuginuki, T., Yagyu, T., Kinoshita, T., Koenig, T., Pascual-Marqui, R. D., et al. (1998). Global, regional, and local measures of complexity of multichannel electroencephalography in acute, neuroleptic-naive, first-break schizophrenics. *Biol. Psychiatry* 43, 794–802. doi: 10.1016/S0006-3223(97)00547-7

Samoradnitsky, G., and Taqqu, M. S. (1994). *Stable Non-Gaussian Random Processes: Stochastic Models with Infinite Variance*, 1st Edn. New York, NY: Chapman and Hall/CRC.

Schooler, N. R. (1994). Deficit symptoms in schizophrenia: negative symptoms versus neuroleptic-induced deficits. *Acta Psychiatr. Scand.* 89, 21–26. doi: 10.1111/j.1600-0447.1994.tb05827.x

Serrano, E., and Figliola, A. (2009). Wavelet leaders: a new method to estimate the multifractal singularity spectra. *Phys. A Stat. Mech. Appl.* 388, 2793–2805. doi: 10.1016/j.physa.2009.03.043

Shew, W. L., and Plenz, D. (2013). The functional benefits of criticality in the cortex. *Neuroscientist* 19, 88–100. doi: 10.1177/1073858412445487

Shew, W. L., Yang, H., Petermann, T., Roy, R., and Plenz, D. (2009). Neuronal avalanches imply maximum dynamic range in cortical networks at criticality. *J. Neurosci.* 29, 15595–15600. doi: 10.1523/JNEUROSCI.3864-09.2009

Slezin, V. B., Korsakova, E. A., Dytjatkovsky, M. A., Schultz, E. A., Arystova, T. A., and Siivola, J. R. (2007). Multifractal analysis as an aid in the diagnostics of mental disorders. *Nord. J. Psychiatry* 61, 339–342. doi: 10.1080/08039480701643175

Socolar, J. E. S., and Kauffman, S. A. (2003). Scaling in ordered and critical random Boolean networks. *Phys. Rev. Lett.* 90:068702. doi: 10.1103/PhysRevLett.90.068702

Souza França, L. G., Vivas Miranda, J. G., Leite, M., Sharma, N. K., Walker, M. C., Lemieux, L., et al. (2018). Fractal and multifractal properties of electrographic recordings of human brain activity: toward its use as a signal feature for machine learning in clinical applications. *Front. Physiol.* 9:1767. doi: 10.3389/fphys.2018.01767

Stam, C. J., and De Bruin, E. A. (2004). Scale-free dynamics of global functional connectivity in the human brain. *Hum. Brain Mapp.* 22, 97–109. doi: 10.1002/hbm.20016

Swick, D., Ashley, V., and Turken, A. U. (2008). Left inferior frontal gyrus is critical for response inhibition. *BMC Neurosci.* 9:102. doi: 10.1186/1471-2202-9-102

Takahashi, T., Kosaka, H., Murata, T., Omori, M., Narita, K., Mitsuya, H., et al. (2009). Application of a multifractal analysis to study brain white matter abnormalities of schizophrenia on T2-weighted magnetic resonance imaging. *Psychiatry Res. Neuroimaging* 171, 177–188. doi: 10.1016/j.pscychresns.2008.03.009

Uhlhaas, P. J., and Singer, W. (2010). Abnormal neural oscillations and synchrony in schizophrenia. *Nat. Rev. Neurosci.* 11, 100–113. doi: 10.1038/nrn2774

Van Orden, G., Hollis, G., and Wallot, S. (2012). The blue-collar brain. *Front. Physiol.* 3:207. doi: 10.3389/fphys.2012.00207

Weinberger, D. R., Berman, K. F., Suddath, R., and Fuller Torrey, E. (1992). Evidence of dysfunction of a prefrontal-limbic network in schizophrenia: a magnetic resonance imaging and regional cerebral blood flow study of discordant monozygotic twins. *Am. J. Psychiatry* 149, 890–897. doi: 10.1176/ajp.149.7.890

Wendt, H. (2008). Contributions of Wavelet Leaders and Bootstrap to Multifractal Analysis: Images, Estimation Performance, Dependence Structure and Vanishing Moments. Confidence Intervals and Hypothesis Tests. Available online at: http://citeseerx.ist.psu.edu/viewdoc/download?doi=10.1.1.372.8718&rep=rep1&type=pdf (accessed September 1, 2020).

Wendt, H., and Abry, P. (2007). Multifractality tests using bootstrapped wavelet leaders. *IEEE Trans. Signal Process.* 55, 4811–4820. doi: 10.1109/TSP.2007.896269

Wendt, H., Abry, P., and Jaffard, S. (2007). Bootstrap for empirical multifractal analysis. *IEEE Signal Process. Mag.* 24, 38–48. doi: 10.1109/MSP.2007.4286563

Wendt, H., Abry, P., Jaffard, S., Ji, H., and Shen, Z. (2009). "Wavelet leader multifractal analysis for texture classification," in *Proceedings of the International Conference on Image Processing, ICIP* (Washington, DC: IEEE Computer Society), 3829–3832. doi: 10.1109/ICIP.2009.5414273

Werner, G. (2007). Brain dynamics across levels of organization. *J. Physiol.* 101, 273–279. doi: 10.1016/j.jphysparis.2007.12.001

Wylie, K. P., and Tregellas, J. R. (2010). The role of the insula in schizophrenia. *Schizophr. Res.* 123, 93–104. doi: 10.1016/j.schres.2010.08.027

Yang, H., Shew, W. L., Roy, R., and Plenz, D. (2012). Maximal variability of phase synchrony in cortical networks with neuronal avalanches. *J. Neurosci.* 32, 1061–1072. doi: 10.1523/JNEUROSCI.2771-11.2012

Zilber, N. (2014). *ERF and Scale-Free Analyses of Source-Reconstructed MEG Brain Signals During a Multisensory Learning Paradigm*. Available online at: https://tel.archives-ouvertes.fr/tel-00984990 (accessed July 6, 2020).

Zilber, N., Ciuciu, P., Abry, P., and Van Wassenhove, V. (2012). "Modulation of scale-free properties of brain activity in MEG," in *Proceedings of the International Symposium on Biomedical Imaging*, Barcelona, 1531–1534. doi: 10.1109/ISBI.2012.6235864

Zilber, N., Ciuciu, P., Abry, P., and Van Wassenhove, V. (2013). "Learning-induced modulation of scale-free properties of brain activity measured with MEG," in *Proceedings of the 10th IEEE International Symposium on Biomedical Imaging*, San Francisco, CA, 998–1001. doi: 10.1109/ISBI.2013.6556645

Zimmern, V. (2020). Why brain criticality is clinically relevant: a scoping review. *Front. Neural Circuits* 14:54. doi: 10.3389/fncir.2020.00054

Conflict of Interest: The authors declare that the research was conducted in the absence of any commercial or financial relationships that could be construed as a potential conflict of interest.

Publisher's Note: All claims expressed in this article are solely those of the authors and do not necessarily represent those of their affiliated organizations, or those of the publisher, the editors and the reviewers. Any product that may be evaluated in this article, or claim that may be made by its manufacturer, is not guaranteed or endorsed by the publisher.

frontiers | Frontiers in Computational Neuroscience

TYPE Review
PUBLISHED 15 September 2022
DOI 10.3389/fncom.2022.703865

OPEN ACCESS

EDITED BY
Axel Sandvig,
Norwegian University of Science and Technology, Norway

REVIEWED BY
Lucilla de Arcangelis,
University of Campania Luigi Vanvitelli, Italy
CM,
Charité - University Medicine Berlin, Germany
Klaus Linkenkaer-Hansen,
Vrije Universiteit Amsterdam, Netherlands

*CORRESPONDENCE
John M. Beggs
jmbeggs@iu.edu

RECEIVED 30 April 2021
ACCEPTED 08 August 2022
PUBLISHED 15 September 2022

CITATION
Beggs JM (2022) Addressing skepticism of the critical brain hypothesis.
Front. Comput. Neurosci. 16:703865.
doi: 10.3389/fncom.2022.703865

Addressing skepticism of the critical brain hypothesis

John M. Beggs[1,2]*

[1]Department of Physics, Indiana University Bloomington, Bloomington, IN, United States, [2]Program in Neuroscience, Indiana University Bloomington, Bloomington, IN, United States

The hypothesis that living neural networks operate near a critical phase transition point has received substantial discussion. This "criticality hypothesis" is potentially important because experiments and theory show that optimal information processing and health are associated with operating near the critical point. Despite the promise of this idea, there have been several objections to it. While earlier objections have been addressed already, the more recent critiques of Touboul and Destexhe have not yet been fully met. The purpose of this paper is to describe their objections and offer responses. Their first objection is that the well-known Brunel model for cortical networks does not display a peak in mutual information near its phase transition, in apparent contradiction to the criticality hypothesis. In response I show that it does have such a peak near the phase transition point, provided it is not strongly driven by random inputs. Their second objection is that even simple models like a coin flip can satisfy multiple criteria of criticality. This suggests that the emergent criticality claimed to exist in cortical networks is just the consequence of a random walk put through a threshold. In response I show that while such processes can produce many signatures criticality, these signatures (1) do not emerge from collective interactions, (2) do not support information processing, and (3) do not have long-range temporal correlations. Because experiments show these three features are consistently present in living neural networks, such random walk models are inadequate. Nevertheless, I conclude that these objections have been valuable for refining research questions and should always be welcomed as a part of the scientific process.

KEYWORDS

neuronal avalanche, criticality, hypothesis, phase transition, temporal correlations

Introduction

> *"I am that gadfly which God has attached to the state, all day long. . .arousing and persuading and reproaching. . .You will not easily find another like me."*
>
> -Socrates, in Plato's Apology

The "criticality hypothesis" states that the brain operates near a phase transition point for optimal information processing (Beggs, 2008; Chialvo, 2010; Shew and Plenz, 2013; Cocchi et al., 2017). The origins of this idea trace back over several decades and derive from many investigators: Kauffman (1969); Wilson and Cowan (1972); Kelso (1984); Freeman (1987); Dunkelmann and Radons (1994); Bienenstock (1995); Herz and Hopfield (1995); Bak (1996); Chialvo and Bak (1999); De Carvalho and Prado (2000); Greenfield and Lecar (2001); Linkenkaer-Hansen et al. (2001); Eurich et al. (2002); Worrell et al. (2002).

To illustrate this hypothesis, consider the three possible ways that activity could propagate in a neural network. First, it could be damped so that activity in one neuron would, on average, lead to activity in less than one neuron in the next time step. This is the subcritical phase. To quantify this, we can use the branching ratio, σ, which gives the average number of descendant neurons from a single active parent neuron. Thus, the subcritical phase has a branching ratio of less than one ($\sigma < 1$). Second, activity could be amplified so that one active neuron would, on average, activate more than one neuron in the next time step. This is the supercritical phase, characterized by a branching ratio greater than one ($\sigma > 1$). Third, activity could be balanced so that one active neuron would, on average, activate one neuron in the next time step. This is a critical point, poised between the damped and amplified phases, and characterized by a branching ratio exactly equal to one ($\sigma = 1$). When a network operates near a critical point ($\sigma \approx 1$), it produces avalanches of neural activity whose size distributions approximately follow power laws (Beggs and Plenz, 2003; Petermann et al., 2009; Shew et al., 2015; Ponce-Alvarez et al., 2018).

In addition, near a critical point, information processing functions like the dynamic range (Kinouchi and Copelli, 2006; Shew et al., 2009) and the amount of information that can be transmitted through a network (Greenfield and Lecar, 2001; Beggs and Plenz, 2003; Shew et al., 2011) are maximized. Very briefly, this is because communication between neurons is extremely weak in the subcritical phase when activity dies out, and it is saturated in the supercritical phase when it is amplified (Beggs, 2008; Shew and Plenz, 2013). Between these extremes, near a critical point, information transmission is greatest. Both models and experimental data are consistent with this picture. Other functions that are predicted to be optimized near the critical point include computational power (Bertschinger and Natschlager, 2004; Legenstein and Maass, 2007), information storage (Haldeman and Beggs, 2005), sensitivity to changes in inputs (Williams-Garcia et al., 2014), and controllability of dynamics without instability (Chialvo et al., 2020; Finlinson et al., 2020). Many of these functions are nicely reviewed in Shew and Plenz (2013).

Evidence for nearly critical dynamics now has been found in a wide range of species including zebrafish (Ponce-Alvarez et al., 2018), turtles (Shew et al., 2015), rodents (Fontenele et al., 2019), monkeys (Petermann et al., 2009), and humans (Priesemann et al., 2013; Shriki et al., 2013).

In this paper we will cover ideas and models that are positioned as rivals to the criticality hypothesis. Such rivals are extremely useful, as they become dialog partners, helping us to refine what we really mean when we say a network is critical, or what falsifiable predictions need to be addressed in experiments. These rivals may even be right, and objective science should always leave open the possibility that a hypothesis, however beautiful or psychologically dear, might be wrong. In the interest of such rational discussion, and to guard against becoming too subjective, it is vitally important to examine these alternative ideas–to not kill the gadfly but let it bite. One way to do this is by presenting the opposition in the strongest way possible, and not as a weakened straw man that can be easily knocked down. What are the best counterarguments? Can the criticality hypothesis meet them, or does it survive only if opposing ideas arrive pre-damaged before doing battle?

Let us overview several waves of criticism so far. Briefly, an early wave argued that many neural data sets that were claimed to follow power laws did not pass appropriate statistical tests. The field responded by consistently applying more statistical rigor. This revealed that while some neural data sets were not best fit by power laws, many in fact were (Klaus et al., 2011; Bellay et al., 2015; Shew et al., 2015; Timme et al., 2016; Ponce-Alvarez et al., 2018). Another early issue raised as criticism was that several non-critical processes, like successive fragmentation or random combinations of exponentials, could also produce power laws (Reed and Hughes, 2002; Mitzenmacher, 2004). Here, the field responded by developing additional tests for criticality that went beyond power laws. These included the exponent relation (Sethna et al., 2001; Friedman et al., 2012), avalanche shape collapse, evidence of long-range temporal correlations (Hardstone et al., 2012) and a more accurate measure of the branching ratio (Wilting and Priesemann, 2018), improvements that are now widely adopted. A summary of many of these critiques and how they were met can be found in Beggs and Timme (2012). Toolboxes for implementing these improvements can be found in Hardstone et al. (2012); Ihlen (2012); Alstott et al. (2014); Marshall et al. (2016); Spitzner et al. (2020).

Another issue that has been raised is that there may be no critical phase transition at all. For example, (Martinello et al., 2017) argue that neutral drift can account for many of the observations seen in experiments, like scale-free power

laws. However, this idea of neutral drift is difficult to reconcile with experimental evidence of homeostasis actively working to restore perturbed networks back toward the critical point (Meisel et al., 2013; Shew et al., 2015; Ma et al., 2019; Meisel, 2020).

A more recent wave of criticism has come through the work of Touboul and Destexhe (Touboul and Destexhe, 2017; Destexhe and Touboul, 2021). Their first claim is that operating near the critical point does not necessarily optimize information processing. To demonstrate their point, they investigated the well-known model of spiking cortical networks developed by Brunel (2000). In their hands, they showed that response entropy (which can also be called the information capacity) did not have a peak, but rather a step-like transition, as the model was moved from the synchronous irregular (SI) phase of firing to the asynchronous irregular (AI) phase (Touboul and Destexhe, 2017). The lack of a peak in information capacity, they claim, demonstrates that operating near a phase transition does not optimize information processing. This would be a clear contradiction of the criticality hypothesis. Their second claim is that when a Brunel model with no internal synaptic connections is driven by a very simple random process like a coin flip or a modified random walk, it can show many signatures of criticality (Touboul and Destexhe, 2017; Destexhe and Touboul, 2021). If random noise passed through a threshold can mimic the power laws and exponent relation seen in the data, then why do we need to hypothesize that the apparent criticality in living neural networks is anything more than this? The contradiction with the criticality hypothesis here is somewhat less obvious. The claim is that signatures of criticality present in living neural networks are not a result of collective interactions among neurons. In other words, neuronal criticality is not emergent like the criticality observed in an ensemble of water molecules or in a sample of iron.

Before going further, let us revisit and update the criticality hypothesis to explain it in more detail. This will allow us to respond to the two critiques more specifically. I take the criticality hypothesis to mean the following:

When a network of neurons operates near a critical phase transition point, multiple information processing functions (e.g., information transmission and storage, dynamic range, susceptibility to inputs and computational power) are simultaneously optimized through collective interactions among neurons.

I want to emphasize three facets of this hypothesis. First, the network needs to be near a critical point. This will lead us to consider multiple signatures of criticality. Second, near a critical point, information processing will be optimized. This will lead us to search for a peak in information transmission (objection 1). Third, both a critical point and optimal information processing emerge through the collective interactions of many neurons in a network. This will lead us to distinguish collective models with interacting neurons from simple, random walk models without interactions (objection 2).

In what follows, I first review the criteria that we will apply to determine if a system is operating near the critical point. I next explain the claims of Touboul and Destexhe with more detail so they can be assessed by the reader. I then present computational demonstrations to challenge their claims. To streamline the presentation, methodological details of these simulations are contained in the **Supplementary material**. I conclude by noting that their arguments against the criticality hypothesis do not constitute a refutation. However, they are still very useful in refining our interpretations of criticality experiments.

Signatures of criticality

An intuitive description of criticality

In the most simplified terms, a system that exhibits criticality must be a tunable system. For example, at a particular pressure, water can be tuned from its gas phase to its liquid phase as the temperature is reduced. To take another example, when a piece of iron is cooled, it is tuned from a phase where its spins were pointing equally up and down, to a phase where they are all pointing in the same direction. Similarly, as the strength of synaptic connections is increased, a neural network can be tuned from a phase where neurons are firing independently to a phase where they are all firing synchronously. In these examples, the variable that tunes the system is called the control parameter; for water and iron this is the temperature, while for neural networks it is the connection strengths.

Notice also the differences between the two phases. One phase is random, high in energy and has symmetry, while the other is ordered, lower in energy and is associated with some breaking of symmetry. For the water example, the high energy phase is the gas, where molecules are equally likely to be in any location within the volume. The low energy phase is the liquid, where the molecules coalesce into a reduced volume. For the iron example, the high energy phase consists of spins pointing equally up and down, while the low energy phase breaks this symmetry and has all the spins pointing the same way. For neural networks, disconnected, randomly firing neurons visit a broad range of network states, while strongly coupled synchronous neurons are confined to a relatively small region of state space.

The critical point in such tunable systems occurs right between these phases, when the control parameter is at its critical value. At the critical point, these systems are a mixture of randomness and order. They have neither the complete symmetry associated with randomness nor the order associated with symmetry-breaking. Rather, they have both variety and structure across all scales.

The most common way to identify this scale-invariant structure has been to observe power law distributions. At the critical point, spatial and temporal correlations fall off slowly with power law tails; distributions of avalanche sizes and durations also follow a power law. When the system is sufficiently far away from the critical point, power law distributions disappear. The power laws at criticality indicate that spatial and temporal correlations diverge–which means that their average values become infinite. This also allows information to pass through the system most readily at the critical point. As a result, plots of mutual information or temporal correlations should show a peak when the control parameter is tuned to its critical value.

As mentioned earlier, power laws by themselves are insufficient to determine whether a system operates near a critical point–additional criteria are needed. Some phenomena like successive fractionation and the summation of many exponential processes can produce power law distributions. Yet these are not clearly tunable systems that exhibit phase transitions or symmetry breaking. How then can we distinguish between critical and non-critical systems that both produce power laws?

Moving beyond power laws

Fortunately, critical phase transitions have been studied extensively in physics, and the literature there provides guidance on how to proceed. In a seminal paper published in 2001, Sethna et al. (2001) argued that to move beyond power laws alone, we should examine scaling functions. Perhaps the easiest way to describe a scaling function is by giving an example of it from neural data.

Consider a toy raster plot of activity from a neural network, shown in **Figure 1A**. In the avalanche there, we can plot the number of neurons active in each time bin to produce an avalanche shape that describes how the activity unfolds over time (**Figure 1B**). When this is done for an actual data set, we see shapes that look like inverted parabolas (**Figure 1C**). More generally, such shapes could be semicircular or skewed parabolas (Laurson et al., 2013). No matter what the shapes, if they are rescaled, they can be made to collapse onto each other (**Figure 1D**) in systems near the critical point. This rescaling is done for both the time and the height of the avalanche. For time, each avalanche is divided by its duration, so that all avalanche shapes to be compared will have a length of 1. For height, each avalanche is rescaled by dividing it by its maximum height, so all avalanches will have the same height. To get the maximum height, h_{max}, we realize that the size S of the avalanche (its area under the curve) is proportional to ($\propto$) its duration T times h_{max}. This means h_{max} is proportional to S divided by T: $h_{max} \propto S/T$. As we see in **Figure 1E**, there is a scaling relation ($\sim$) between avalanche size and duration: $S \sim T^{\gamma}$. Thus, we have $h_{max} \propto T^{\gamma-1}/T = T^{\gamma-1}$. If we divide each average avalanche shape by $T^{\gamma-1}$, then they will all have the same heights. Note that this is possible only if they follow a scaling relation like the one shown in **Figure 1E**.

When this avalanche shape collapse occurs, it shows that the avalanche shapes are all similar, no matter what their sizes. In other words, they are fractal copies of each other, each merely being a version of an inverted parabola that is either scaled up for larger avalanches or scaled down for smaller ones. Because all the average avalanches can be made to follow this shape by rescaling, it is called a universal scaling function.

You might think that such a function should always occur, but it does not. For example, consider what would happen if a network produced tent-like avalanche shapes (**Figure 1B**), but with different slopes. Say the longer avalanches had shallower slopes and the shorter avalanches has steeper ones. While it might be possible to rescale all of them to the same length, they would not then all have the same heights, and so they would not collapse on top of each other. Likewise, one could rescale all their heights, but then they would not all have the same lengths. Avalanche shape collapse is only possible if the system in question has scale-free properties in many domains, and this is empirically found to occur only when near a critical phase transition point.

By scale-free, we mean that some relationships between numbers will be the same across scales. To illustrate, consider the Gutenberg-Richter law for earthquakes. Here, there is a power law relationship between the frequency of an earthquake occurring and its energy. An earthquake with a magnitude of 7 on the Richter scale has 10 times the energy of a Richter scale 6 earthquake; it also occurs only 1/10 as often as Richter scale 6 earthquake. Thus, there is an inverse relationship, by powers of 10, between earthquake magnitude and frequency per year. This relationship occurs again between Richter scale 3 earthquakes and Richter scale 2 earthquakes. The former have 10 times the energy but occur 1/10 as often. For any pair of adjacent magnitudes, this type of relationship will apply–at the smallest scales and also at the largest scales. This is why power laws are often called scale-free.

When a system is operating very close to a critical point, its activity is expected to be scale free. By this, we mean that many variables of the system will follow power law relationships. With the neuronal avalanches we discussed previously, this was shown in the distribution of avalanche sizes and in the distribution of avalanche lengths. Recall also **Figure 1E**, where there is a relationship between avalanche size and duration. Without this relationship, avalanche shape collapse would not be possible. Shape collapse is thus an indicator that the network is operating near a critical point. The existence of a universal scaling function, in our case the inverted parabola, is evidence that even the shapes of things replicate across different scales. Because a parametric description of this shape would require not just a single number, but several, it is considered by physicists

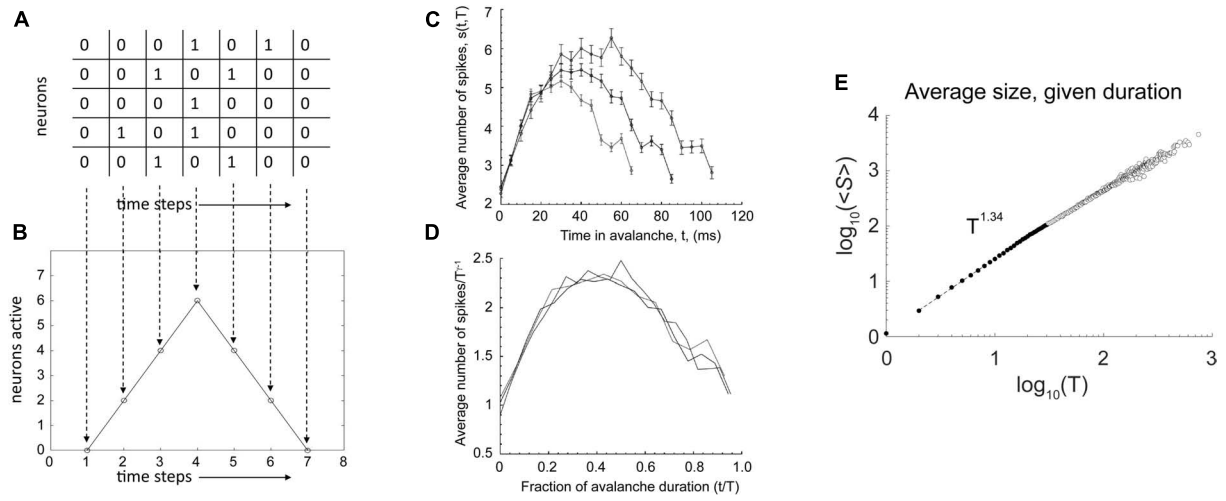

FIGURE 1
Additional signatures of criticality. **(A)** A toy raster plot where spikes are represented by 1 s and no activity by 0 s. Here, five neurons are recorded over seven time bins. An avalanche is a sequence of consecutively active time bins, bracketed by time bins with no activity. **(B)** The raster can be used to construct the avalanche shape, which is just the number of active neurons at each time bin. Here, we have a tent shape. **(C)** Average avalanche shapes for three different lengths, taken from microelectrode array recordings of cortical slice cultures. Here, the shapes are like inverted parabolas. **(D)** With appropriate rescaling of avalanche duration and height (explained in text), these avalanche shapes collapse on top of each other, demonstrating that the inverted parabola is a scaling function for this network. Such a scaling function is expected to exist only very close to a critical point. **(E)** Avalanche size is related to avalanche duration by a power law. The *y*-axis is the average avalanche size, <S>, for a given duration, T. The *x*-axis is the avalanche duration, T. Because these data nearly follow a straight line in log-log axes, we can say that they approximate a power law. We can estimate the exponent, γ, of the power law by the slope of the line. In this case, it is 1.34. Thus, avalanche size scales with the duration according to this relationship: $<S>(T) \sim T^{1.34}$. A scaling relationship between size and duration is necessary for avalanche shape collapse. Data from Fosque et al. (2021). The portion of the data used for estimating the power law is shown as filled circles with dashed line. Fitting was performed using software from Marshall et al. (2016). Panels **(C,D)** adapted from Friedman et al. (2012).

to be an excellent indicator that a system is near a critical point (Spasojević et al., 1996; Papanikolaou et al., 2011). Power laws, in contrast, are typically described by only one number, their slope.

Let us now discuss another indicator of proximity to a critical point. Each of the power laws we mentioned has its own slope, given by its exponent: τ for avalanche size, α for avalanche duration, and γ for avalanche size vs. duration. The values of these exponents cannot be arbitrary if everything is scale-free; they must interlock in just the right proportions if they are to describe avalanches whose sizes and durations are all fractal copies of each other. By simple reasoning, described in Scarpetta et al. (2018), one can show that they must be related by this exponent relation equation:

$$\frac{\alpha - 1}{\tau - 1} = \gamma$$

This then is another signature of a neural network operating near a critical point–the exponents obtained from empirical data must satisfy this equation within some statistical limits (Ma et al., 2019). This relationship has been adopted by experimenters using cortical slice cultures (Friedman et al., 2012), zebrafish (Ponce-Alvarez et al., 2018), turtles (Shew et al., 2015), mice (Fontenele et al., 2019), rats (Ma et al., 2019), monkeys (Miller et al., 2019), and humans (Arviv et al., 2015) to assess closeness to a critical point. There is currently much work exploring why so many data sets follow this relation (Carvalho et al., 2020; Fosque et al., 2021; Mariani et al., 2021).

Criticality can also be suggested by long-range temporal correlations, and these have often been reported in neuronal data (Linkenkaer-Hansen et al., 2001; Lombardi et al., 2012, 2014, 2021; Meisel et al., 2017a,b). As we mentioned earlier, when a system is brought to the critical point, both spatial and temporal correlations can become scale-invariant.

A common way to quantify temporal correlations is through the Hurst exponent, *H*. This describes how the standard deviation scales with the duration of the data. See Hardstone et al. (2012) and Ihlen (2012) for excellent tutorial reviews with software. For example, consider a random walker on the number line whose position, x, is known over time (**Figure 2A**). It starts at the origin and takes either a step forward (+1) or backward (−1) with equal probability.

To illustrate how to calculate *H*, let's consider a simulation of this process. We observe that after $t = 131{,}072$ time steps, the standard deviation is measured to be 70.26. Next, we expand the recording length by a factor of $L = 8$. By how much will the standard deviation, *STD*(x), increase? We want to know if the standard deviation is somehow related to the duration of the recording in a scale-free manner. In other words, the standard deviation should scale with the duration by some exponent. To continue our example, we observe that over

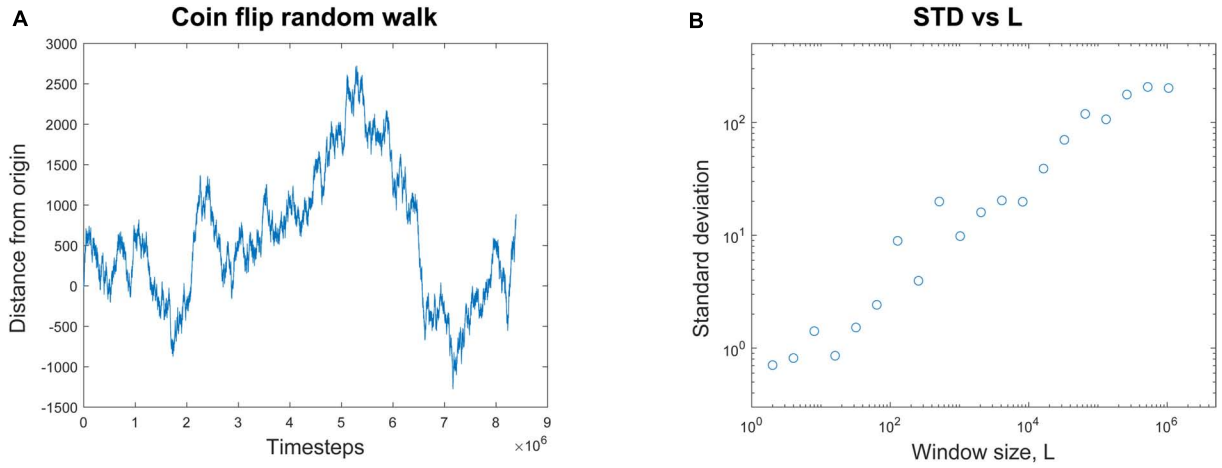

FIGURE 2
Calculating the Hurst exponent from a random walk. **(A)** A random walk process is started at the origin. At each time step, it randomly moves either forward (+1) or backward (−1) by one step. The position of the walker is plotted against the number of time steps. **(B)** The average standard deviation of the random walk is plotted for window lengths, L, of many different sizes. If $L = 8$, for example, the entire random walk is broken up into segments of eight time steps each and the average standard deviation from them all is calculated. When the average standard deviation for each window size is plotted against window size, a nearly linear relationship is revealed in these log-log coordinates. The Hurst exponent, H, is the slope of the best fit line through these data. In this case, $H = 0.47$. This linear relationship is evidence of scaling; when $H > 0.5$, it is evidence of long-range temporal correlations (LRTCs), often found in systems operating near the critical point.

$L \times 131{,}072 = 1{,}048{,}576$ time steps the standard deviation is now measured to be 202.13. We can relate these numbers through the equations below to find the scaling exponent H. Recall that in our example, $t = 131{,}072$, $L = 8$, and the standard deviation when $t = 131{,}072$ is just 70.26 ($STD(131{,}072) = 70.26$). We now want to find H:

$$STD(Lt) = L^H STD(t)$$

$$STD(8 \times 131,072) = 8^H STD(131,072)$$

$$STD(1,048,576) = 8^H STD(131,072)$$

$$202.13 = 8^H 70.26$$

$$\frac{202.13}{70.26} = 8^H$$

$$\log_8(2.88) = \log_8(8^H)$$

$$0.51 = H$$

Here the Hurst exponent is approximately 0.5, which matches the analytic results for a random walk (Tapiero and Vallois, 1996). For any window of length L, the standard deviation of the random walk will be L^H. If we plot the standard deviation for each window length L against the window length, we can get several data points (**Figure 2B**). The slope of the best fit line through these points will give an estimate of the Hurst exponent H; in this case it is $H = 0.47$. This is then a scale-free relationship, like what we saw with avalanche shapes, where the duration and height of the avalanches had the same relationship across all scales.

The Hurst exponent can also tell us things about long-range temporal correlations. In the case of the random walk, there is no temporal memory. This means that each step taken is independent of all the previous steps. For memoryless processes like these, the Hurst exponent is known to be about 0.5 (Hu et al., 2013).

But there are processes where some temporal memory is present. What happens if each successive step is influenced by previous steps? For example, in a correlated random walk, we could make it such that a step in one direction would slightly increase the odds of drawing another step in the same direction. This would cause the random walker to move away from the origin more rapidly than in the balanced, uncorrelated situation. In this case, the standard deviation would grow more quickly with the recording duration and so the Hurst exponent would be greater than 0.5. Conversely, if we made it such that a step in one direction would slightly decrease the odds of drawing another step in the same direction (anticorrelated), the walker would remain closer to the origin and the Hurst exponent would be less than 0.5 (Hu et al., 2013). In EEG data from humans, H has been reported to be in the range of $0.55 \leq H \leq 0.85$ over several frequency bands (Colombo et al., 2016). These data show that neuronal processes near the critical point are not memoryless–they are correlated. Experiments have shown that temporal correlations in systems near the critical point do not decay as exponentials but as power laws (Linkenkaer-Hansen et al., 2001). Thus, long-range temporal correlations are another signature of criticality that have been consistently reported in neural data.

Continuing with signatures of being near the critical point, it is important to mention the recent advancements made by Wilting and Priesemann in estimating the branching ratio σ under conditions of sparse data sampling (Wilting and Priesemann, 2018). Recall that σ should be very close to one when the network is near a critical point. When they applied their method to data sets of spiking activity recorded *in vivo* from monkeys (n = 8), cats (n = 1), and rats (n = 5), they found the average value to be $\sigma = 0.9875 \pm 0.0105$ (Wilting and Priesemann, 2019). In our own data from hundreds of measurements taken from networks of primary cultured neurons, we find the mode of the branching ratio to be $\sigma = 0.98$ (Timme et al., 2016). While there is still some discussion as to whether the networks are exactly at a critical point or slightly below it, there is now growing consensus they are very near it. Being near a critical point to optimize information processing would still be consistent with the criticality hypothesis.

Taken together, these advancements show that the field has tools beyond power laws to assess proximity to a critical point. When the control parameter in a tunable system is moved, we can now tell with confidence when the system is near criticality. These criteria for assessing criticality will be useful later when we examine systems based on random walks.

Objection one: The Brunel network model is not critical and does not show a peak in information processing at the phase transition. Reply: When properly tuned and stimulated, the Brunel model shows a critical phase transition and a peak in mutual information

We will now consider the first objection, raised by Jonathan Touboul and Alain Destexhe in their paper entitled "Power law statistics and universal scaling in the absence of criticality," (Touboul and Destexhe, 2017). There, they claim that the well-known Brunel model (Brunel, 2000) of spiking cortical networks does not show critical dynamics. Further, they claim that this model does not show a peak in information capacity. As the model is expected to represent cortical network dynamics, these results would seem to refute the criticality hypothesis.

We can begin by describing the Brunel model (Brunel, 2000). Briefly, it consists of leaky integrate-and-fire neurons that are sparsely connected so that 10% of all possible connections are present. It contains 80% excitatory neurons and 20% inhibitory neurons; there is also an external input to simulate thalamic drive (**Figure 3A**). Nicolas Brunel showed that by tuning the parameters of this model, like the relative strength of inhibition compared to excitation, he could cause it to display different phases of activity commonly reported in experimental studies of cortical networks (**Figure 3B**). For example, the synchronous regular (SR) phase was characterized by neurons firing synchronously in a rhythmic, or regular, manner reminiscent of cortical oscillations. Recordings of cortical neurons *in vivo* have been typically thought to fire with AI activity, where neurons do not tend to fire at the same time and there is no pronounced rhythm, while those *in vitro* have been thought to fire with SI patterns characterized by simultaneous firings but not at regular intervals. However, a recent report of *in vivo* activity in awake behaving rodents has shown that over several hours activity often switches between AI and SI phases, with signatures of criticality found between them (Fontenele et al., 2019). The Brunel model can capture all these activity phases.

In Touboul and Destexhe's implementation, they made the external random drive equal in strength to the drive from excitatory neurons within the model. With this, they showed that as the model was tuned from the SR phase to the AI and SI phases by increasing the relative strength of inhibition, there was a jump in the entropy of the network activity, also known as the information capacity. The information capacity did not drop back down after the transition; rather it stayed high throughout the AI and SI phases (**Figure 4**, red arrow). They did not observe a peak near the transition to the SI phase, where they found power law distributions. Yet this should be expected by the criticality hypothesis. In addition, as they increased the external drive by raising the ratio ν_{ext}/ν_{thresh} for a fixed value of g, they did not observe a peak in response entropy either (**Figure 4**, blue arrow). They claimed that the lack of a peak in the information capacity argued against the critical brain hypothesis, which would predict a peak near a phase transition. They stated "...we observe no difference between entropy levels in the SI or AI states, Therefore, we conclude that the maximality of entropy is not necessarily related to the emergence of power-law statistics" (Touboul and Destexhe, 2017, pages 7–8).

To investigate these issues, I modified the Matlab code used to simulate the Brunel model that was freely provided by Destexhe and Touboul in their most recent paper on this subject (Destexhe and Touboul, 2021). I explored the model under more controlled conditions, where I could deliver stimulation pulses and observe the response of the network without random background activity. I brought the external drive to zero and, for example, activated 320 randomly chosen neurons (out of 1,000) only at one given time step. The results of these experiments are shown in **Figure 5**. When the parameter g, which controls the relative strength of inhibition, is low, then activity is quickly amplified (**Figures 5A,D**). When g is at an intermediate value, stimulation produces very slowly decaying activity (**Figures 5B,E**). When g is large, strong inhibition quickly dampens activity from the stimulus (**Figures 5C,F**). This shows that the network can be tuned from an active, amplifying

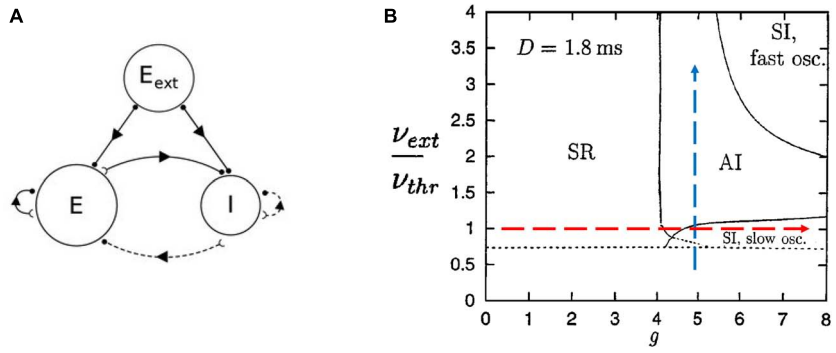

FIGURE 3
The Brunel model and its phase space. **(A)** Schematic of the Brunel model. It consists of an excitatory population of neurons (E), an inhibitory population (I), and a source of external excitatory drive (E_{ext}). Excitatory connections are given by solid lines and inhibitory connections are given by dashed lines. **(B)** The phase space of the model is plotted as a function of two parameters, the ratio of external drive to the drive needed to exceed threshold (ν_{ext}/ν_{thr}), and the relative strength of inhibitory connections (g). There are four main regions, or phases: SR for synchronous regular; AI for asynchronous irregular; SI with slow oscillations; SI with fast oscillations. The dashed arrows represent the types of paths we will take in parameter space to explore the model. We will increase inhibition while keeping external drive fixed (red horizontal arrow) and we will increase external drive while keeping inhibition fixed (blue vertical arrow). Delays between neurons were 1.8 ms (D = 1.8 ms). Panel **(A)** is adapted from Nordlie et al. (2009); panel **(B)** is adapted from Brunel (2000).

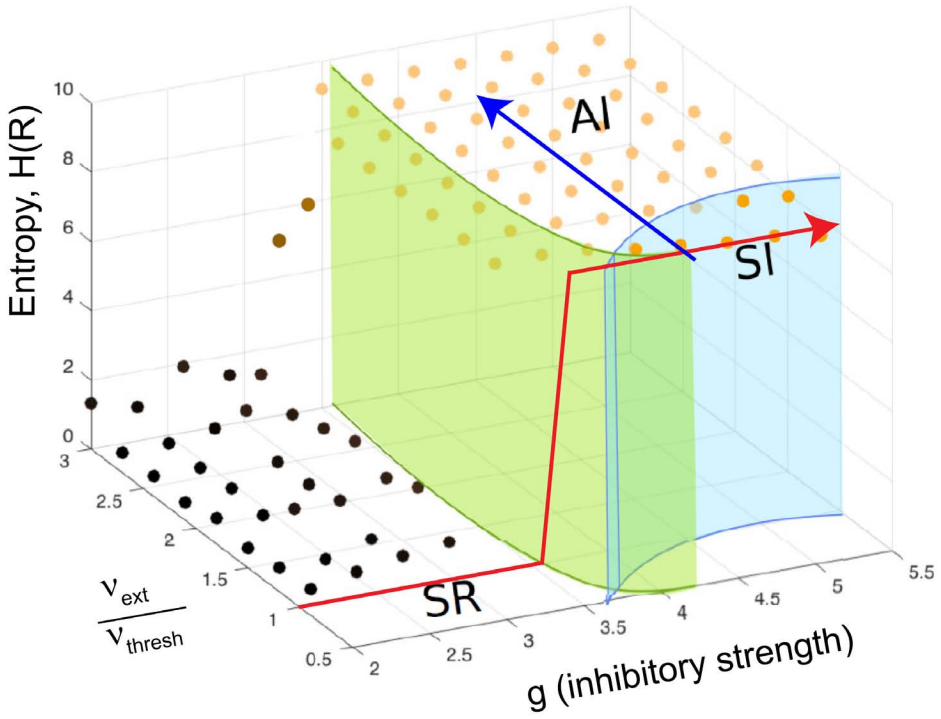

FIGURE 4
The continuously driven Brunel model does not show a peak in response entropy. The diagram shows the phase space of the model as a function of two parameters: g, the relative strength of inhibition, and the ratio of external drive to drive required to exceed threshold, ν_{ext}/ν_{thresh}, similar to what was shown previously in **Figure 3B**. The z-axis gives the entropy of the activity produced by the network in response to this drive, H(R). Each dot shows a location in parameter space that was sampled with the model by Touboul and Destexhe (2017). As described earlier, there are multiple phases: SR, synchronous regular; AI, asynchronous irregular; SI, synchronous irregular. One phase transition could occur at the boundary between regular (SR) and irregular (AI/SI) activity. For a given ratio of ν_{ext}/ν_{thresh}, the entropy increases in a step-like manner as g is increased through this transition. This is shown by the red line, which jumps upward near g = 3.5 and stays elevated. It does not drop back down as expected from the critical brain hypothesis. Another phase transition could occur as the model is moved from the SI phase to the AI phase at a constant value of g (blue line). Along either path, the response entropy does not show a peak as the model transitions from one phase to another. The model here is being constantly driven by random external input whose strength is equal to the strength of internal feedback connections within the network. Adapted from Touboul and Destexhe (2017).

phase to an inactive, dampening phase as g is increased. Here, g serves as the control parameter for tuning the network while the average firing rate serves as the order parameter giving the phase of the system. This path through phase space, changing g while keeping the amount of external drive fixed, is like the path shown by the red arrow in **Figures 3B**, **4**. The phase plot shown in **Figure 5G** looks just like what we should expect for a system with a critical phase transition.

If this really is a critical phase transition, then we should also expect to see peaks in some functions near the phase transition point. To examine this, I extracted time constants from a Brunel model with 8,000 neurons with activity curves like those shown in **Figure 5D** through **Figure 5F**. As the relative strength of inhibition was increased, the model showed a transition from an active phase to an inactive phase (**Figure 6A**). When the 8,000 neuron network was near the phase transition point (g = 3) activity decayed quite slowly. But away from the phase transition point this was not the case. In the amplified network, activity quickly saturated so the time constant was short; in the dampened network, activity quickly died so the time constant was also short. Plotting the time constants against the control parameter revealed a sharp peak near the phase transition (**Figures 6B,C**). This showed that temporal correlations were maximized, just as we would expect in a critical system.

Next, I turned to examine the mutual information. Here, I stimulated a network at one time step with eight different numbers of randomly chosen neurons (thus giving 8 = 2^3 or 3 bits of input entropy) and used the number of neurons active in the network as a measure of the response. As many readers may know, the mutual information can be written as a difference between two quantities, the entropy of the response, H(R), and the entropy of the response conditioned on the stimulus, H(R| S). Thus we have: MI(S;R) = H(R)–H(R| S). For mutual information to be high there should be a wide variety of responses, making H(R) large, and a narrow and reliable set of responses for each given stimulus, making H(R| S) low. The information capacity is merely the H(R) term and does not include the H(R| S) term. Note it is possible to have a high information capacity but low mutual information if H(R| S) is large. This would occur if the network had highly variable output and rarely gave the same response to a given stimulus. When Touboul and Destexhe measured the information capacity, they were only measuring H(R) and were not delivering stimuli. Thus, they did not measure information transmitted through the network. When the mutual information MI(S;R) was measured in the stimulated Brunel networks, I found a peak near g = 3, in agreement with the peak for the time constants (**Figure 7**). For smaller networks this peak occurred for lower values of g, but as network sizes were increased, the peak value of g asymptotically approached g = 2.952, in good agreement with the peak value of g for the time constant measurements (g = 2.99). These findings suggest that the Brunel model indeed has a phase transition and that information transmission is maximized there. This all agrees with the criticality hypothesis stated earlier.

Given this result, one might wonder why Touboul and Destexhe reported only that there was no peak in information capacity. First, as we just explained, information capacity is not the same thing as mutual information. The criticality hypothesis predicts a peak in information transmission through a network when it is at a critical point. To assess this, one must measure mutual information, which is the difference between the information capacity, H(R), and the conditional entropy, H(R| S). Second, the Brunel model tested by Touboul and Destexhe was receiving external input that had a total synaptic weight equal to the weight of all the excitatory neuron synapses within the network. This arrangement made the network activity very dependent on the random external drive and made the internal network dynamics more difficult to observe. Interestingly, experiments in cortical slice networks have shown that limited thalamic stimulation does not seem to disrupt ongoing cortical network activity (MacLean et al., 2005). However, more recent work has shown that an intrinsically critical network will be pushed away from the critical point as external drive is increased (Fosque et al., 2021). This makes it reasonable to explore how the network functions under conditions of reduced external drive. To see how influential strong random drive can be, let us move on to the second objection.

Objection two: Very simple unconnected models can show signatures of criticality when randomly driven. Reply: Such models have many of these signatures, but the signatures largely arise from the noise source itself. Such models also fail to account for experiments showing neuronal criticality: (1) Processes information, (2) depends on connections between neurons, and (3) produces long-range temporal correlations

In their 2017 paper, entitled "Power law statistics and universal scaling in the absence of criticality," Touboul and Destexhe continued their computational experiments by exploring the behavior of an ensemble of neurons without internal connections that received strong, correlated, randomly varying external drive. They first showed that this model could produce power law distributions of avalanches that satisfied avalanche shape collapse (**Figure 8**;

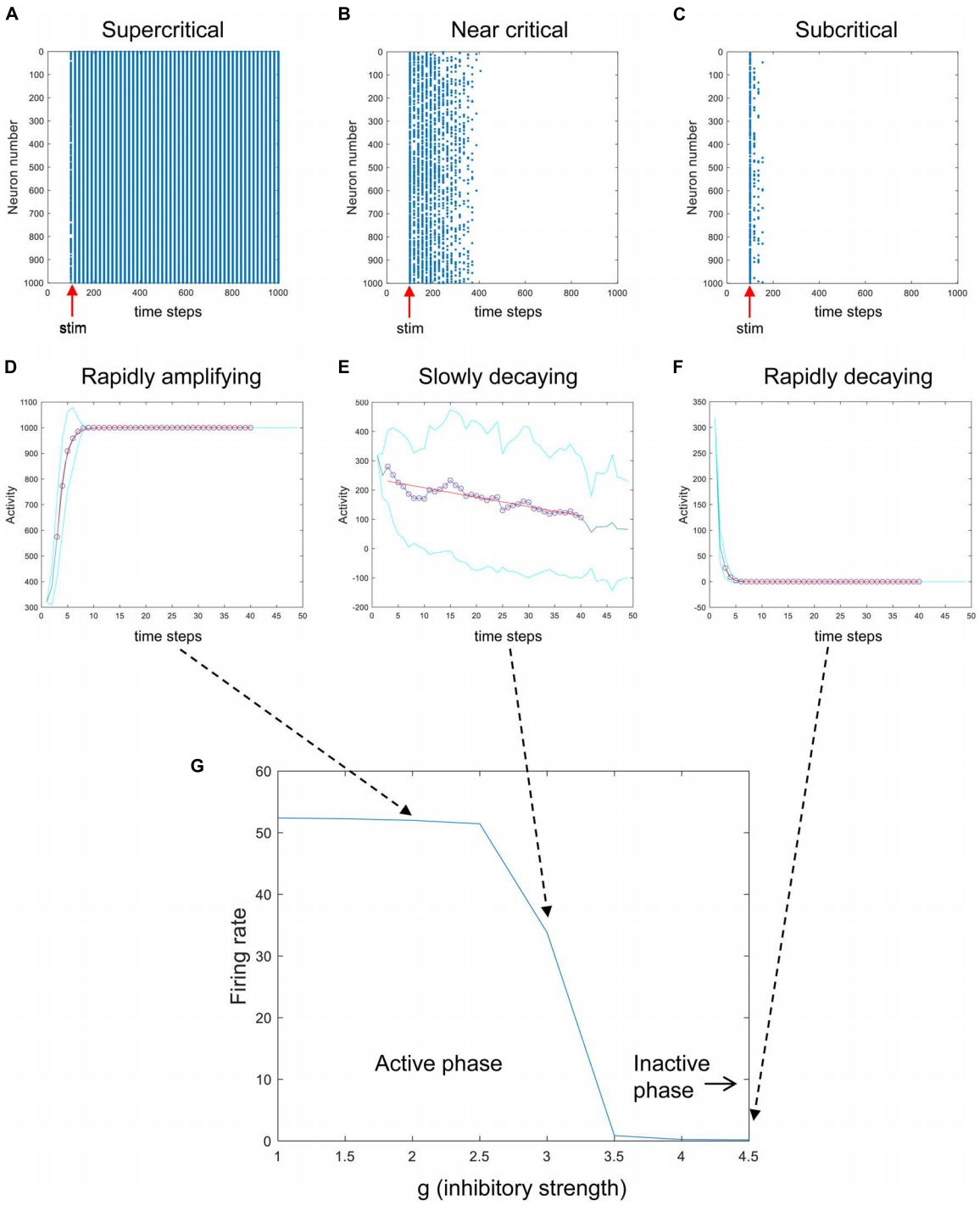

FIGURE 5
A phase transition in the Brunel model. Here, the random external drive was turned off and stimulation was delivered once at a prescribed time. The top row shows raster plots of activity produced by the Brunel model when it was stimulated once at the 100th time step (red arrows). Stimulation consisted of randomly activating 320 out of 1,000 neurons. Each spike is given by a blue dot. **(A)** When the inhibitory connection strength, g, was low, activity rapidly increased. **(B)** When g was at an intermediate value, activity died out slowly. **(C)** When g was large, activity was quickly damped. The middle row shows the average number of neurons activated after stimulation for the three conditions **(D–F)**. Each curve shows an average of 30 trials. Cyan curves show one standard deviation. Exponential curves in red were fit to time steps 3 through 40, shown in circles. Note that while conditions **(D,F)** have opposite directions of growth, they both have short time constants (sharply bending curves). Condition **(E)**, in contrast, has a long time constant (gradually bending curve). **(G)** The average firing rate for the model is plotted against different values of g, showing a clear transition from an active phase to an inactive phase. Matlab code for producing all these plots is given in the **Supplementary material**.

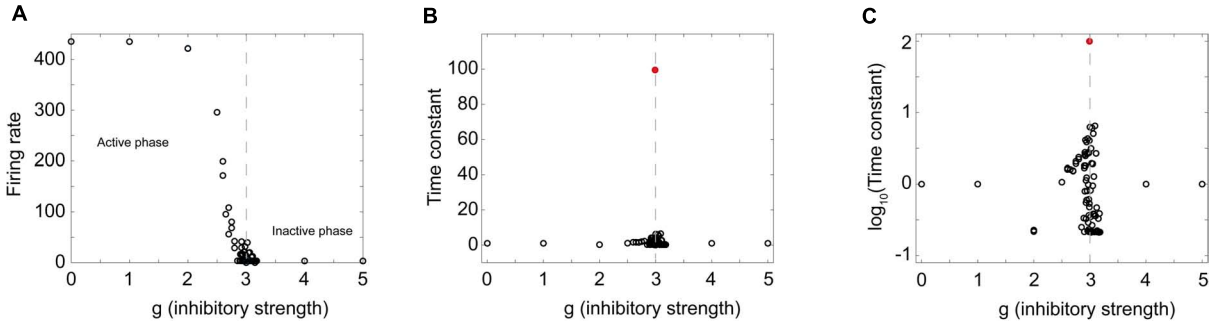

FIGURE 6
A sharp peak in the time constant near the phase transition point. **(A)** The firing rate in a Brunel model with 8,000 neurons is plotted as a function of the inhibitory strength g. The model was stimulated by randomly activating 20% of the neurons; the number of spikes divided by the total number of time steps was taken to be the firing rate. Note active phase on the left and inactive phase on the right. Dashed gray line denotes approximate border between them. **(B)** Time constant for exponential decay of activity after stimulation shows a sharp peak near the phase transition. Peak value of time constant occurred at $g = 2.99$ and is indicated by the red circle. Dashed gray line again drawn at transition. **(C)** Same plot as shown in panel **(B)**, but with the time constant measured in log scale, showing transition region in more detail. A total of 93 different values of g were probed. Probing was densest near the transition region; each probe consisted of 30 stimulations of the network. Exponential curves were fit to each stimulation and the average time constant for the 30 stimulations is shown as a single circle. Matlab code for producing all these plots is given in the **Supplementary material**.

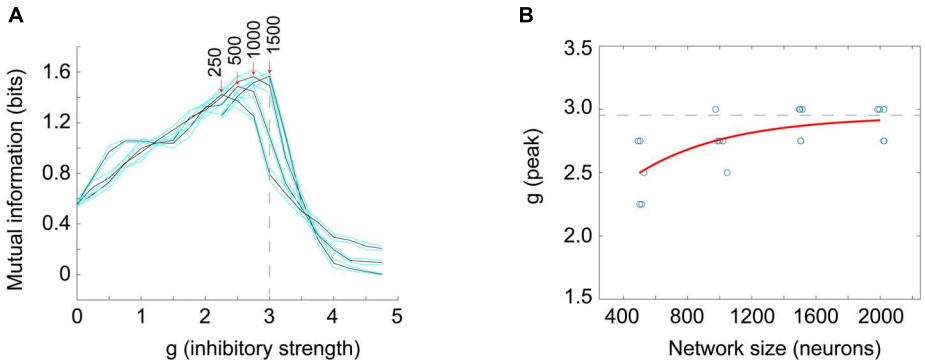

FIGURE 7
The peak in the mutual information coincides with the peak in the time constant. **(A)** Mutual information between the response and the stimulus was measured in Brunel models of different sizes (250, 500, 1,000, and 1,500 neurons shown) as the inhibitory strength, g, was varied. Stimuli consisted of eight different numbers of neurons (e.g., 0, 125, 250, 375, ... for $N = 1{,}000$ neuron model) randomly activated at one time; the average number of neurons active at time steps 3 through 5 after the stimulus was taken as the response. Black curves show mutual information for each model; cyan curves show one standard deviation. Five models of a given size were run 30 times each to produce each data point; more details are in the **Supplementary material**. Peak mutual information values for each model size are indicated by red arrows. Note that as model size increases, peaks become taller and move toward $g = 3$. Dashed vertical line is at $g = 3$ for reference. **(B)** The value of g at which mutual information peaks is plotted against model sizes ($N = 500$, 1,000, 1,500, 2,000 shown). Blue circle tokens were jittered slightly to improve visibility. An exponential fit to these data gives an asymptotic value of $g = 2.952$, with 95% confidence bounds at 2.637 and 3.268. This is within experimental error of the peak in the time constant found for the Brunel model with 8,000 neurons ($g = 2.99$) shown in **Figures 6B,C**. This agreement of peak values in mutual information and time constant duration is what would be expected for a second order phase transition and supports the hypothesis that the Brunel model has a critical point. It also supports the criticality hypothesis. Matlab code for producing all these plots is given in the **Supplementary material**.

Touboul and Destexhe, 2017), and later showed that it could satisfy the exponent relation (Destexhe and Touboul, 2021). This model suggests that the signatures of criticality observed in neuronal experiments may be produced by a simple process, like a random walk, that is passed through a threshold. In other words, the criticality that has been claimed to exist in living neuronal networks may not be the result of collective interactions among neurons. If true, this would contradict the criticality hypothesis mentioned earlier, which claims that optimal information processing is emergent near the critical point and depends on interactions between neurons.

My response will consist of five parts. (A) First, we will cover some details of their unconnected model and its external noise source. (B) Second, to understand the contributions of external noise, we will examine how the behavior of the Brunel model changes when it is driven by *uncorrelated* random noise. (C) Third, we will examine how the behavior of the Brunel model changes when it is driven by *correlated* random noise.

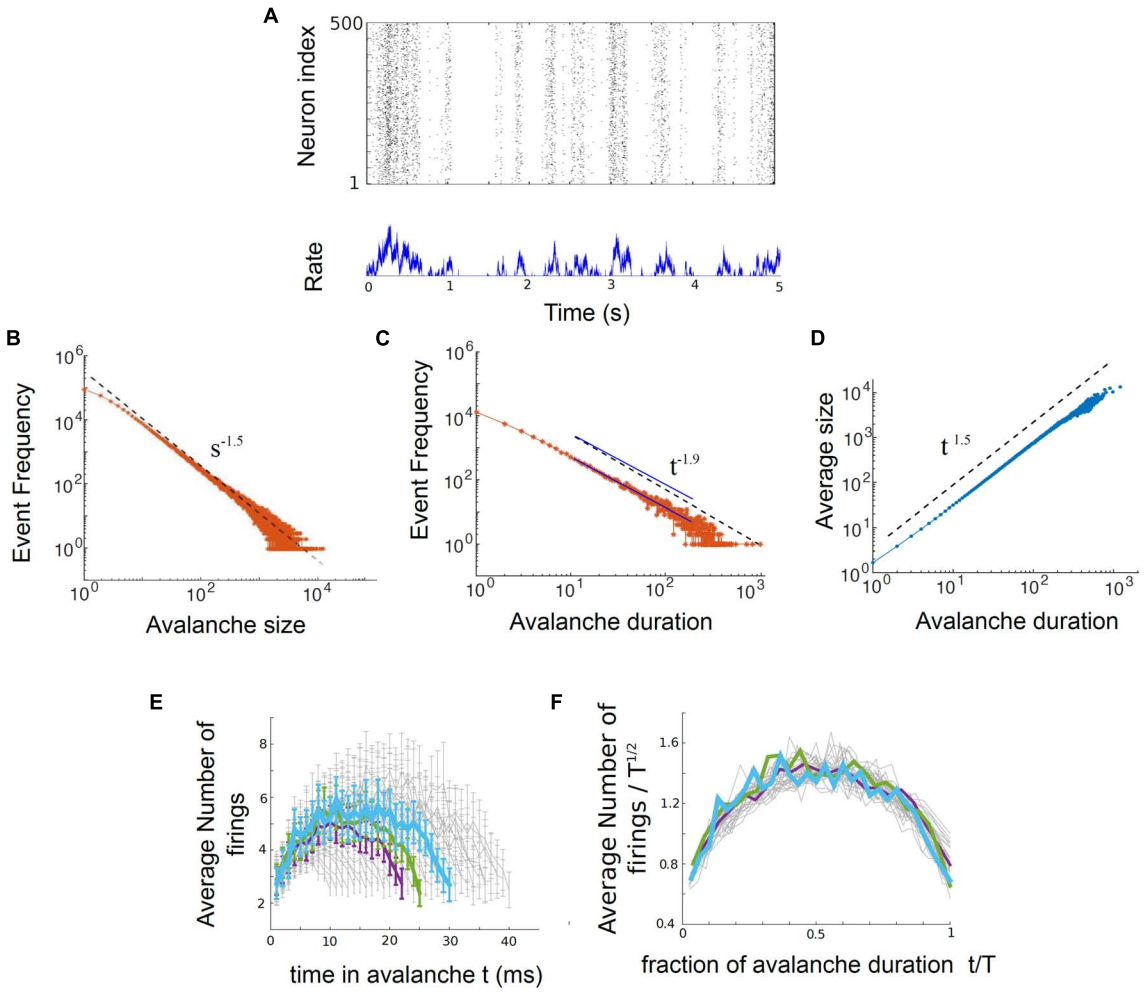

FIGURE 8
The output of the Ornstein-Uhlenbeck model implemented by Touboul and Destexhe (2017). **(A)** A raster plot of spiking activity. Neuron number is on the *y*-axis, and time is on the *x*-axis. Each dot represents a spike from a model neuron. The summed activity of all the neurons in each time bin is plotted below to show how firing rate changes with time. Here it is in the synchronous irregular (SI) phase. **(B)** Distribution of avalanche sizes for the model approximately follows a power law with exponent −1.5. **(C)** Distribution of avalanche durations approximately follows a power law with exponent −1.9. The two blue lines are parallel and are shown as an example of a slope that would be slightly shallower than the one found by Touboul and Destexhe (2017). **(D)** Average avalanche size for a given duration, plotted against avalanche duration, approximately follows a power law with exponent 1.5. **(E)** Average avalanche shapes, for durations of 10–40 time steps (ms) of the model. **(F)** Avalanche shapes collapse well for exponent of $\gamma = 1.5$, as expected. Figure adapted from Touboul and Destexhe (2017).

These two types of drive produce materially different behaviors, although both degrade information processing. (D) Fourth, we will examine the properties of the correlated noise itself and show that it can be tuned to produce power laws and even avalanche shape collapse, something that cannot be shown for uncorrelated noise. This will explain how even a network with no internal connections can show signatures of criticality. (E) Fifth, we will draw three distinctions between the signatures of criticality produced by correlated noise and those produced by a connected network of neurons. Connected networks transmit information well, have emergent criticality that depends on connections, and show long-range temporal correlations. In contrast, disconnected networks transmit information poorly if at all, do not display emergent criticality and show no long-range temporal correlations. We will show that the experimental data are consistent with connected network models but not with disconnected network models.

Understanding the disconnected model

Let us now turn to the model. It consists of an ensemble of neurons with no internal synaptic connections that is driven by external noise. This noise source is an Ornstein-Uhlenbeck process that we will explain more below. The model output

can be seen in **Figure 8**, taken from Touboul and Destexhe (2017). There, three power law plots are shown for avalanche size, duration, and size vs. duration. In addition, the average avalanche shapes show excellent collapse. While the exponents given from these power laws ($\tau = 1.5$, $\alpha = 1.9$, $\gamma = 1.5$) do not closely satisfy the exponent relation [$(1.9–1)/(1.5–1) = 1.8 \neq 1.5$], they are not too far off. A slightly shallower slope of $\alpha = 1.75$ for the avalanche duration plot, for example, would cause the exponent relation to be satisfied.

How does the Ornstein-Uhlenbeck process drive the population of neurons? It has a single variable, x, that zigs and zags across a threshold, as shown in **Figure 9A**. The equation governing the behavior of x is given in **Figure 9B**, and has two parts, one of which is random. The other part has the effect of constraining, or counteracting, the randomness. To turn the movements of this single variable into something that could represent a population of neurons, a threshold is introduced. Here, to prevent inaccuracies that can arise from setting the threshold too high (Villegas et al., 2019), we will set the threshold at zero. Whenever x crosses above the time axis, we can say that neurons become active. Whenever it is below the axis, there is no activity. The number of neurons activated is proportional to the height of x. For example, shortly before 20 time steps, x has a value of about 2. When multiplied by a proportionality constant of 3, this would mean that six neurons should be active at that time. Six neurons are randomly chosen out of the population and made active. When this is done for 128 neurons over about 800 time steps, you get the raster of activity shown in **Figures 9C,D**.

Clearly a very important part of this model is the random drive that activates the disconnected population. To better understand the role of random drive, let us return to the Brunel model. Recall that it can be tuned to a critical point when external drive is limited. Now we will examine the Brunel model dynamics when it is continually driven by two types of noise: uncorrelated and correlated. This will position us to better understand how the Ornstein-Uhlenbeck model can generate signatures of criticality, and how those signatures fail to match what is observed in experiments with living neurons.

Brunel model driven by uncorrelated random noise

Figure 10A shows how the mutual information curves from the Brunel model (shown previously in **Figure 7A**) change when uncorrelated noise is added, as Brunel originally proposed (Brunel, 2000). Increased noise decreases the mutual information; it also reduces the response entropy, as shown in **Figure 10B**. These results are consistent with the principle of quasicriticality (Williams-Garcia et al., 2014; Girardi-Schappo et al., 2020; Fosque et al., 2021), which describes how external drive will affect information processing functions in networks near the critical point.

Note also that by increasing external drive, we are moving through phase space along the path of the blue arrow shown in **Figures 3B**, **4**. But uncorrelated noise is not the only type of noise that we need to consider along this path. There is much research investigating the effects of correlated noise on neural networks (Lee et al., 1998; Cohen and Kohn, 2011). Let us explore this next.

Brunel model driven by correlated random noise

To produce a correlated noise source, I followed one of the models used by Touboul and Destexhe (2017) and drove the network with the output of a rectified coin flip. I will explain this mechanism more later, but for now it is enough to state that it is conceptually similar to the Ornstein-Uhlenbeck process mentioned earlier. The total number of neurons that could be activated in a 1,000 neuron model was varied among these values: 10, 100, 500, and 1,000. By increasing the number of neurons that could be activated, we could increase the relative strength of the external drive. Again, this would be moving along the blue arrow in phase space, as shown in **Figures 3B**, **4**.

When correlated noise like this is added to the Brunel model, we also see a decline in mutual information (**Figure 11A**). This is expected, as random background unrelated to the stimulus will alter the input patterns to the network, making the response variability go up. Interestingly, strong correlated noise does not always reduce the response entropy (or information capacity), in contrast to what we observed when the model was driven by uncorrelated noise. This can be seen in **Figure 11B** by following the red curve produced by the $N = 1{,}000$ condition. Notice that this curve does not drop back down to the axis as the inhibitory strength g is increased beyond 3. Rather, it remains high, and is roughly 2.5 bits when $g = 4$. This is consistent with the findings reported by Touboul and Destexhe (2017) who noted that there was not a peak in the information capacity as the model was moved across a phase transition. As we pointed out earlier, though, there is a peak in the mutual information (**Figure 11A**), as predicted by the criticality hypothesis. Thus, mutual information does show a peak, even though information capacity does not clearly show one for high values of g.

Let us now explore the cause of this elevated response entropy. What will it look like if we disconnect the neurons from each other in the Brunel model, thus imitating what was done in the Ornstein-Uhlenbeck model used by Touboul and Destexhe (2017)? As shown in **Figure 11B** by the black curve, a disconnected model has nearly the same amount of response entropy as that found in a connected model (red curve). The difference between the curves is indicated by the small green arrow to the right of **Figure 11B**. Compare this to the red arrow, the response entropy produced by the connected model when 1,000 neurons are driven by correlated noise. From this we can conclude that nearly 90% of the response

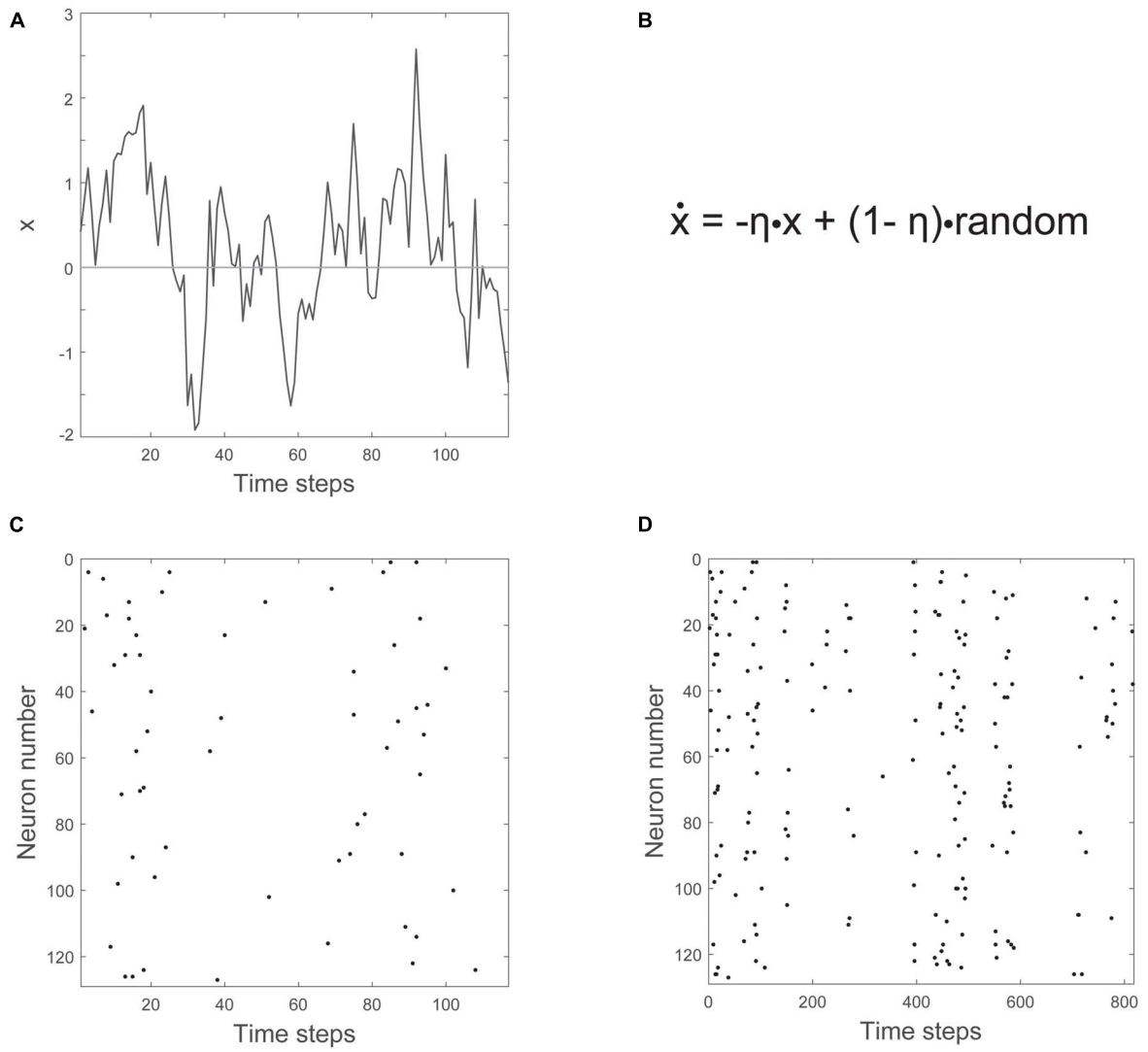

FIGURE 9
The Ornstein-Uhlenbeck model. **(A)** The variable x moves up and down across a threshold over time. The threshold is given by the horizontal line at zero. **(B)** The equation governing how x changes ($\dot{x}$) has negative feedback ($-\eta x$) and a random noise term ($+(1-\eta)\cdot$random). **(C)** Number of neurons firing is proportional to how far x is above threshold. **(D)** A zoomed out view of the raster plot, showing synchronous irregular (SI) activity.

entropy is caused by the external drive, and only about 10% of it is caused by interactions among the neurons within the network.

Because this external drive is so dominant, it deserves further scrutiny. What are the statistical properties of a rectified coin flip? We will turn to this in the next section.

Correlated random noise can show many signatures of a critical process

I will now explain the rectified coin flip process in more detail. We are all familiar with flipping a fair coin that has equal probability of landing heads (H) or tails (T). If we take this process and map it onto the number line, we could take one step forward (+1) for each head and one step backward (−1) for each tail. An example "avalanche" here could be a run like this: (H, H, H, T, T, T), as shown in **Figure 12A** (gray triangle). The process starts at the origin and returns there after an equal number of heads and tails have been flipped. The duration of this avalanche would be six, as there were six flips. The height of the avalanche at any given time is determined by the net excess of heads. In this case, it would be: (1, 2, 3, 2, 1, 0). The size of the avalanche would just be the sum of these numbers: 9. Let us introduce one last condition on this process–we will rectify it so that excursions from the origin that go negative will be made positive. This way,

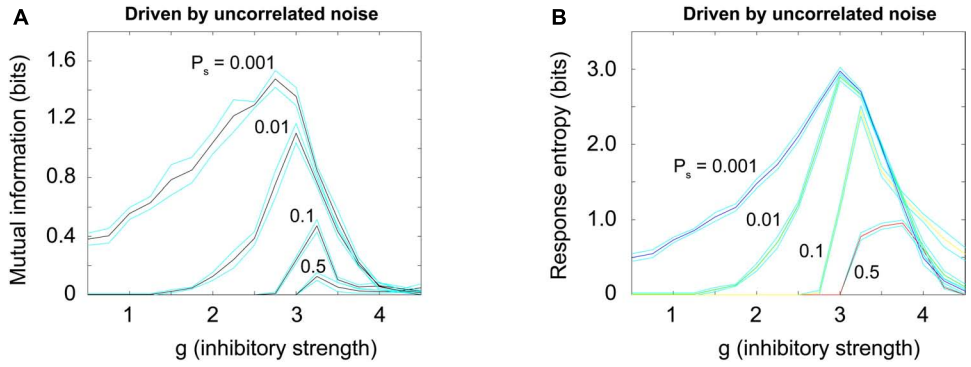

FIGURE 10
Random uncorrelated noise reduces mutual information and response entropy. **(A)** Mutual information was plotted for a Brunel model with 1,000 neurons, using the same procedures described previously, but now with varying amounts of externally generated uncorrelated noise. Noise was simulated by giving each neuron an independent probability of spontaneously firing, P_s, that varied (0.001, 0.01, 0.1, 0.5). This noise is uncorrelated because the activity in the randomly driven neurons was independent. Note that as uncorrelated noise is increased, the peak in mutual information declines. **(B)** Response entropy also declines as uncorrelated noise is increased. These results are consistent with the principle of quasicriticality (Williams-Garcia et al., 2014; Fosque et al., 2021). Matlab code for producing these plots is given in the **Supplementary material**.

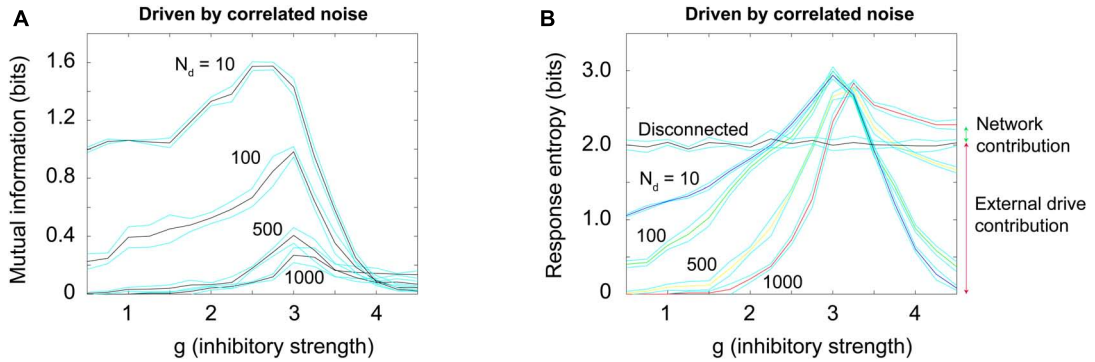

FIGURE 11
Random correlated noise reduces mutual information but *can increase* response entropy. **(A)** Mutual information was plotted for a Brunel model with 1,000 neurons, using the same procedures described previously, but now with varying amounts of externally generated correlated noise. Correlated noise was added by simultaneously driving varying numbers of neurons (N_d = 10, 100, 500, 1,000) with a rectified coin flip process (details described in text and in **Supplementary material**). This type of drive was also used by Touboul and Destexhe (2017) and Destexhe and Touboul (2021). Note that as this noise is increased, the peak in mutual information declines. **(B)** Response entropy, however, remains high near the peak (close to g = 3) for all numbers of neurons driven, and in the case of 1,000 neurons driven, it remains high even as g is increased beyond 3. This is consistent with the findings of Touboul and Destexhe (2017), who called the response entropy the "information capacity." Note however that the mutual information, shown in panel **(A)**, does decline as external drive increases, consistent with the critical brain hypothesis. Note further that the high response entropy is largely the result of external drive and not the network itself: The horizontal black curve shows the response entropy produced by a network with no internal connections, only receiving external drive. This curve is slightly below that produced by the Brunel model with its default setting of 10% connectivity (red curve). The difference between these is shown by the small green arrow to the right of the plot; the response entropy produced by the disconnected network is shown by the taller red arrow to the right. There is about an 11% difference between them, indicating that 89% of the response entropy can be accounted for by the external drive alone. Matlab code for producing these plots is given in the **Supplementary material**.

only the absolute value of avalanches will be considered. Now, what are the statistics of this process? Can it produce signatures of criticality?

In fact, it can. Analytic work has shown that the distribution of first return times to the origin of a fair coin flip follow a power law distribution (Kostinski and Amir, 2016). To probe this further, I simulated two billion coin flips and then plotted the resulting distributions, as shown in **Figures 12D–F**. They are all significantly better fit by power laws than by other distributions. Moreover, the exponents from these power laws satisfy the exponent relation, within an error of 2.9%. The exponent γ can be used to perform avalanche shape collapse, as shown in **Figure 12C**. All of these signatures of criticality are clearly satisfied.

In addition, the process is tunable: These signatures appear at the critical point, when the coin is exactly fair. They will

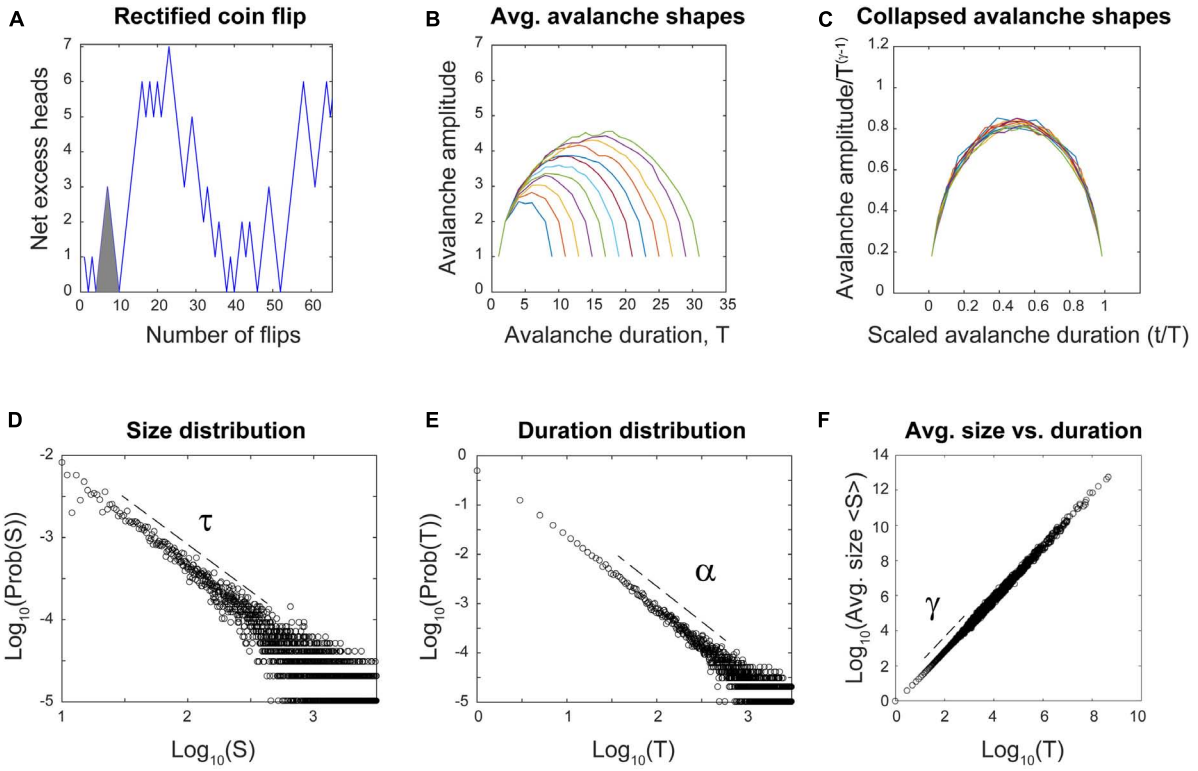

FIGURE 12
The reflected coin flip satisfies multiple signatures of criticality without any connections. **(A)** The reflected coin flip steps upward in y every time a head is flipped and downward for every tail. All negative excursions are reflected to produce only positive avalanches. Here, only 64 flips are shown; simulation had 2 billion flips. The gray triangle highlights an example run of six flips mentioned in the text. **(B)** Average avalanche shapes with durations from 8 to 32 are shown. **(C)** Average avalanche shapes are fractal copies of each other and show good collapse when rescaled using the exponent γ. **(D)** Avalanche size distribution followed a power law with exponent $\tau = 1.32$. Distribution was significantly better fit by truncated power law than by other distributions ($p = 0.786$). **(E)** Avalanche duration distribution followed a power law with exponent $\alpha = 1.49$. Distribution was significantly better fit by truncated power law than by other distributions ($p = 0.402$). **(F)** Average avalanche sizes plotted against durations follows a power law with exponent $\gamma = 1.50$. Using all three exponents, the error in fitting the exponent relation was 2.9%. Code for producing this simulation can be found in the **Supplementary material**. Dashed lines show approximate regions over which power laws were fit.

disappear when the coin is biased to produce more heads than tails. These biased conditions reveal the two phases–one where heads occur most often and another where tails occur most often. Perfect symmetry occurs only when the coin is exactly fair, and the signatures of criticality appear right at the point where this symmetry is about to be broken, at the transition between phases.

However, the coin flip does not show long-range temporal correlations as measured by the Hurst exponent: $H \approx 0.5$, indicating a memoryless process as we mentioned earlier. Still, many of the signatures of criticality we highlighted can be fulfilled by the coin flip.

This result suggests that a neural network model without internal connections and driven by an external source like a rectified coin flip could show some signatures of criticality. But these signatures would largely reflect the statistics of the noise source and not the network itself. To explore this situation further, we will next describe the differences between emergent and non-emergent criticality.

Emergent vs. non-emergent criticality

To adequately address this situation, it is necessary to first explain a key difference between the type of criticality we saw in the Brunel model and the signatures of criticality we saw in the coin flip model. This will require a short digression into degrees of freedom.

In describing any system, it is important to mention how many degrees of freedom it has. Briefly, the *degrees of freedom* are the number of parameters that would be needed to accurately specify the system. For example, in the coin flip model there was only one degree of freedom, given by the probability of getting heads. This could be for example $p = 0.500$ in a fair coin, or $p = 0.501$ in a biased coin. In the Brunel network model, the parameters included not only the relative strength of inhibition (g) and the relative frequency of external drive (ν_{ext}/ν_{thresh}), but also the list of all the connections made between the neurons. This list would include at least 100,000 more parameters (10% connection density × 1,000 neurons × 1,000 neurons = 100,000

connections). These examples illustrate the difference between systems with few degrees of freedom and those with many.

The criticality hypothesis as stated earlier assumes that the brain is a system with many degrees of freedom and that criticality emerges there as a result of interactions between neurons. Criticality in systems with many degrees of freedom is most often studied with the tools of *statistical mechanics*. In the example of the piece of iron, the spins in the lattice must be influencing their nearest neighbors. In the example of a neural network model, the neurons must be capable of stimulating each other through synapses. In these types of systems, when the interactions are reduced in strength or cut, the signatures of criticality are diminished or disappear. Power laws are destroyed and peaks in mutual information or temporal correlations are flattened. A way to probe this type of criticality is by observing what happens in the system when the connections are manipulated. An example of this is given in **Figure 11**, where the density of connections in the Brunel model is reduced. When they are, the model no longer produces a power law of avalanche sizes (**Figure 13A**); it no longer has a sharp peak in the time constant at the phase transition (**Figure 13B**); it no longer transmits information through the network (**Figure 13C**). Signatures of criticality in the Brunel model clearly depend on interactions within the ensemble; this criticality is therefore emergent. Other investigators have also recently noted that emergent criticality can be distinguished from external effects by tracking the mutual information (Nicoletti and Busiello, 2021; Mariani et al., 2022). This approach should be very fruitful in future studies.

In contrast, systems with few degrees of freedom may not have any connections at all. Signatures of criticality can still exist in these systems but can arise over time as a single unit interacts with itself. Activity in these systems is typically studied from the perspective of *dynamical systems*. For example, consider a single unit whose dynamics are given by the branching ratio, σ. If a small perturbation to the system grows over time ($\sigma > 1$), it is chaotic. If a small perturbation shrinks over time ($\sigma < 1$), it is damped and stable. Only when a small perturbation is neither amplified nor damped but relatively preserved ($\sigma = 1$) is the system poised near the critical point. For activity to arise in these systems, they need to be driven, and this often comes from an external source of randomness. This external drive is sometimes called a *latent variable* (Schwab et al., 2014). When internal connections are cut in systems like these, it does not affect signatures of criticality. It would make no difference in the Ornstein-Uhlenbeck model proposed by Touboul and Destexhe because there are no connections to begin with.

Which type of criticality is observed in living neural networks? Fortunately, there are numerous experiments that have addressed this through the application of pharmacological agents that disrupt synaptic transmission. If the non-interacting models with few degrees of freedom are correct, then this should have no effect on signatures of criticality. But if criticality emerges through the interactions of neurons in systems with many degrees of freedom, then these manipulations should disrupt signatures of criticality.

Let us now summarize results from a few of these experiments. Application of picrotoxin (PTX), a $GABA_A$ antagonist that blocks inhibitory synaptic transmission, causes disruption of power laws in acute cortical slices (Beggs and Plenz, 2003). In this experiment, when picrotoxin was washed out the activity returned toward a power law distribution. Shew et al. (2009) showed that application of AP5 and DNQX, which together block excitatory synaptic transmission, disrupted power laws in organotypic cortical cultures. When the $GABA_A$ antagonist bicuculline and the $GABA_A$ agonist muscimol were applied *in vivo*, they tuned cortical activity away from a critical point and into the supercritical and subcritical phases, respectively (Gautam et al., 2015; **Figure 14A**). Similar manipulations also cause cortical slice networks to move away from peak information capacity (**Figure 14B**) and peak information transmission (**Figure 14C**). These manipulations of criticality are not confined to chemical synapses, though, as even the gap junction blocker heptanol disrupts the quality of avalanche shape collapse in zebrafish larvae (Ponce-Alvarez et al., 2018), again moving the neural network away from a critical point. In addition, these findings extend to human patients; antiepileptic drugs reduce cortical connectivity and produce subcritical avalanche size distributions as well as a reduction in long-range temporal correlations (Meisel, 2020).

Taken together, these results consistently demonstrate that neuronal criticality is an emergent phenomenon that depends on collective interactions between neurons. Thus, low-dimensional models without interactions are inadequate for capturing the type of criticality that occurs in the neural systems just mentioned.

Are there any cases from biology that support the models with few degrees of freedom? Several studies have noted that a randomly varying external drive, when applied to an ensemble of units, can produce apparent signatures of criticality (Schwab et al., 2014; Priesemann and Shriki, 2018), much like what we discussed with the Ornstein-Uhlenbeck and coin flip models. Swarming animals like starlings and insect midges have been shown to have spatial correlations that scale with the size of the swarm, suggesting criticality (Cavagna et al., 2010). However, when swarms of midges were isolated from external perturbations like wind and light, these correlations disappeared (van der Vaart et al., 2020); this has not yet been tried with starlings (release them into a domed stadium?). This result suggests that at least in the case of midges, signatures of criticality may not be intrinsic to the swarm itself but rather produced by an extrinsic source.

Let us finally return to the issue of long-range temporal correlations. Recall that in the coin flip process the Hurst exponent was $H \approx 0.5$, indicating no temporal memory. Given that random walk models do not show emergent criticality or

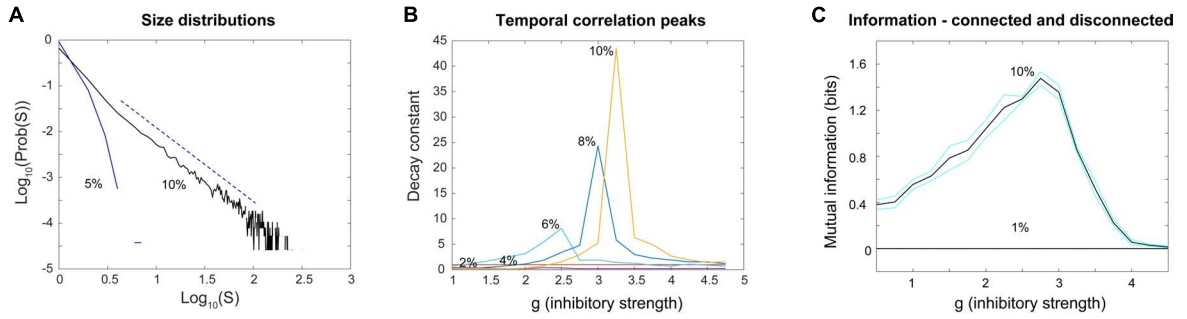

FIGURE 13
Power laws, peak decay constants and peak mutual information depend on connections between neurons in the Brunel model. **(A)** Avalanche size distributions deviate from power law form when connectivity between neurons is reduced. Black line shows power law distribution from the Brunel model when connectivity is set to the sparse default of 10%. It was statistically more similar to a truncated power law than other distributions (p = 0.238). Dashed line shows region over which power law scaling was found. Blue line shows downwardly curved distribution produced when connectivity is reduced to 5%. This was not statistically similar to a power law distribution (p = 0.076). **(B)** As connectivity is reduced from the default 10–2%, the time constant of temporal correlations drops and the peak near the phase transition point disappears. Note that as connectivity is increased, the peaks become taller and narrower, consistent with finite size effects observed in emergent criticality. Thus, temporal correlations in the Brunel model emerge from neuronal interactions near the critical point. **(C)** Mutual information shows a peak near g = 3 in the model when it has 10% connectivity, but this peak disappears completely when connectivity is reduced to 1%. Black lines are the average of five runs; cyan lines show one standard deviation. Each run of the model consisted of 30 networks constructed for each value of g. These figures demonstrate that criticality in the Brunel model emerges through the interactions among neurons. The code used for producing these figures is available in the **Supplementary material**.

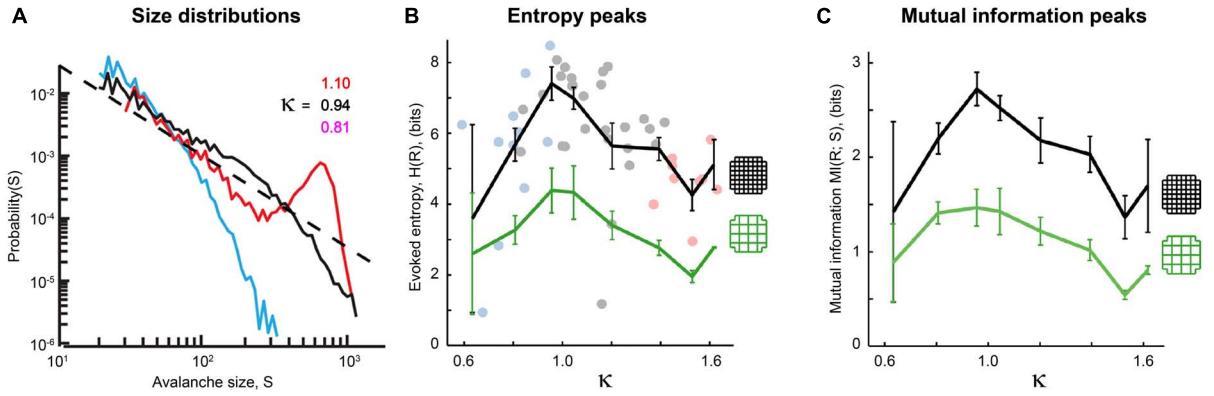

FIGURE 14
Power laws and peak information transmission depend on connections between neurons in living neural networks. **(A)** Avalanche size distributions recorded *in vivo* deviate from power law form when synaptic transmission is manipulated. Black line shows approximate power law distribution from an unmanipulated recording; dashed line has slope $\tau = -1.5$ for reference. Blue line shows downwardly curved distribution caused by enhancement of inhibitory synaptic transmission (application of muscimol). Red line shows distribution when inhibitory synaptic transmission is disrupted (application of bicuculline). The value of κ parameterizes how close a given distribution is to an ideal power law ($\kappa \approx 1$ if nearly critical, $\kappa > 1$ if supercritical, $\kappa < 1$ if subcritical). Adapted from Gautam et al. (2015). **(B,C)** Pharmacological manipulations that disrupt excitatory synaptic transmission (application of AP5 and DNQX, blue dots) or inhibitory synaptic transmission (PTX, pink dots) reduce the evoked entropy **(B)** and the mutual information **(C)** between the stimulus and the response. Gray dots show network responses where no manipulations were applied. Adapted from Shew et al. (2011). Cortical slice cultures were placed on a 60-electrode array and stimulated electrically with 10 different amplitudes. The distribution of network responses to each stimulus provided H(R| S), while the distribution of network responses provided H(R). Mutual information is calculated as MI(R;S) = H(R)−H(R| S). Note that MI peaks at κ = 1. The black curve shows results produced by all 60 electrodes, while the green curve shows results produced by a coarse-grained approach where four neighboring electrodes are grouped together into a super-electrode. In both conditions, manipulations that disrupt synaptic connectivity reduce response entropy and mutual information. These figures demonstrate that the type of criticality in these networks depends on connections between neurons and is therefore emergent.

long-range temporal correlations, it is worth asking if there are models that do. Even the simple Brunel model showed a spike in its time constant, when the network was connected and tuned to the critical point (**Figure 13B**). It is known that a population of neurons modeled as a critical branching process can produce avalanche distributions that follow power laws, the exponent relation and show good shape collapse (Friedman et al., 2012). However, critical branching by itself can

only produce short-range temporal correlations up to the length of the longest avalanche (Poil et al., 2008). But when neural network models include some type of homeostatic plasticity, over longer durations they can produce Hurst exponents up to $H = 1$, greater than the $H \approx 0.5$ seen in random walks (Poil et al., 2012). Perhaps the addition of a simple temporal feedback term would allow random walk models to show long-range temporal correlations also, but they would still fail to show emergent criticality that depends on connections between neurons.

To conclude this section, random walk models fail to capture emergent criticality, they fail to support information processing, and they fail to exhibit long-range temporal correlations, all of which are observed in neural experiments. Because there are models that do capture these features (Poil et al., 2012; de Candia et al., 2021), random walk models should be discarded.

Closing

The criticality hypothesis states that ensembles of neurons collectively interact to operate near a critical point. Near this point, they optimize multiple information processing functions simultaneously. The challenges to this hypothesis have taken several forms and have been met in different ways. Below is a summary of some recent challenges and how they have been addressed:

- An early objection was that many non-critical processes could produce power laws, so power laws alone were not sufficient to establish criticality. The field responded by developing additional ways to assess proximity to a critical point. These ways included the exponent relation, avalanche shape collapse, assessment of long-range temporal correlations and a better way of measuring the branching ratio. These methods are increasingly applied now and consistently show that many neural systems are operating near a critical point.
- A more recent objection is that even the well-known Brunel model of cortical networks does not show a peak in information capacity as it is tuned across a phase transition. In this paper, we saw that mutual information did show a peak, even if information capacity did not, when the Brunel model was decoupled from strong, correlated random drive. This result was consistent with the criticality hypothesis.
- Another recent objection is that even simple random walk processes like a coin flip can display signatures of criticality. This raises the possibility that signatures of criticality in living neural networks do not arise from collective interactions, but merely from external sources of randomness. While these simple models do produce many signatures of criticality and might be considered critical in some sense, they are unable to capture the type of criticality that emerges in neural networks through the interactions of many neurons. Because neuronal experiments show criticality produces a peak in mutual information, depends on synaptic transmission, and has long-range temporal correlations, these simple models are inadequate.

It is worth reviewing that in two of the objections, random noise played a key role. The peak in mutual information we observed in the Brunel model is suppressed in the presence of strong, external random drive (**Figures 10A**, **11A**). The recent principle of quasicriticality notes that increased external drive will push an intrinsically critical network slightly away from the critical point (Williams-Garcia et al., 2014; Fosque et al., 2021). And paradoxically, if all we have is a random walk or a coin flip, we can get some signatures of criticality (**Figure 12**), except for a peak in mutual information and the long-range temporal correlations. This highlights that apparent criticality can arise in two different ways–either intrinsically, through interactions among many units in an ensemble, or extrinsically, through a driving process or latent variable like a random walk. How then can we decide what type of system we have if both show some signatures?

Figure 15 shows a flow chart for this decision process, starting with the condition that we have some power law data in hand. To properly interrogate the system we must both analyze the data and perform causal interventions, as noted clearly by Priesemann and Shriki in their analysis of this situation (Priesemann and Shriki, 2018).

The first step is to determine if the data show more than just power laws. Do they support the exponent relation and show some type of scaling collapse? Can the process be tuned away from the point where these power laws are produced? Does the system show long-range temporal correlations? If most of these conditions are not satisfied, then the process under consideration is likely to be not critical. We discussed successive fractionation and the sum of many exponential distributions as examples of this category.

The second step is to determine if the signatures of criticality persist after the source of randomness is blocked. Note that this source of randomness can in theory arise from the system's internal dynamics, but in practice, experimental systems are often driven by external sources of randomness. If blocking this source, whatever its origins, removes signatures of criticality, then the system has few degrees of freedom. These systems are often studied within the framework of dynamical systems. Examples here include the coin flip, a random walk, the Ornstein-Uhlenbeck process when η is small, and possibly swarms of midges.

The third step is to determine if the signatures of criticality persist after internal connections are reduced or cut. If the connections were necessary, then we have a system with emergent criticality. It has many degrees of freedom and is

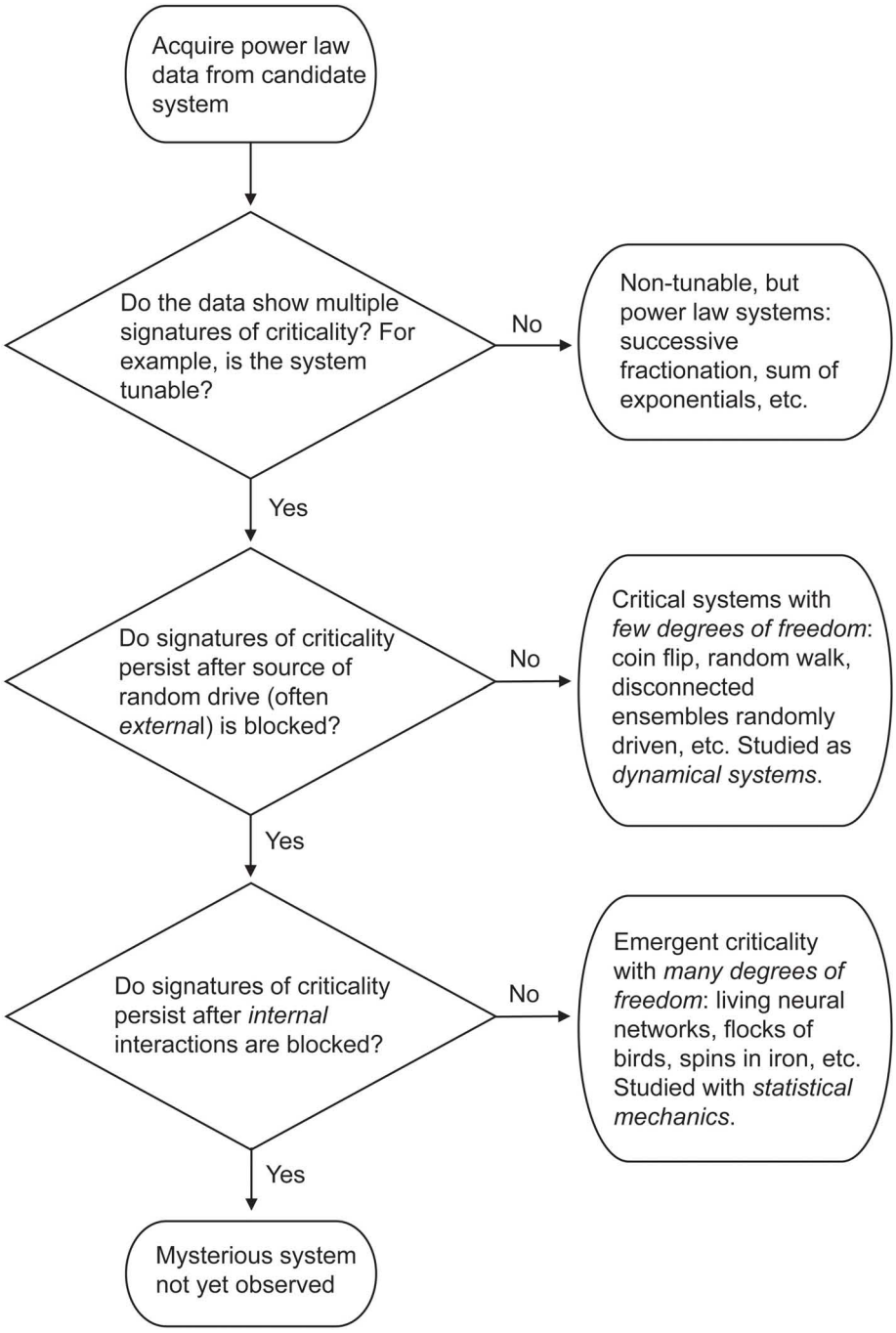

FIGURE 15
Flow chart describing classification of power law data described in this paper. For explanation, see text.

typically studied with the tools of statistical mechanics [but see Dahmen et al. (2019) for a powerful dynamical systems approach to ensembles]. Examples of such systems would include networks of neurons, spins in a piece of iron, or interacting water molecules poised between gas and liquid phases, and possibly murmurations of starlings.

If signatures of criticality persist even after sources of randomness and internal interactions are removed, then we are dealing with a novel type of system that has not to my knowledge been seen.

More broadly, this flow chart is part of a larger process: distinguishing things that are primarily driven by their

environment from things that are more autonomous and governed by internal dynamics. This process may eventually be refined to distinguish between things that are living and thinking generators of complexity from things that merely react to external inputs.

We have now come to the end of considering alternatives. Skeptical questions, far from being troublesome, are essential for us to clearly and correctly work through the implications of our experiments. Here, they force us to think carefully about what it means for a network of neurons to operate near criticality and what mechanisms could produce criticality. This in turn helps us to interpret the experiments we need to distinguish between competing models. Those who raise these questions are doing an essential service for science, helping the dialog to go further.

Author contributions

JB conceived of the study and wrote the manuscript.

Funding

This start of this work was supported by NSF grant 1513779 from the Robust Intelligence Program, and by an Indiana University Bridge grant; more recent portions of it were supported by NSF grant 2123781 from Expeditions in Computing.

Acknowledgments

The author was grateful for many helpful discussions with Gerardo Ortiz, Rashid Willaims-Garcia, and Ehren Newman and for the constructive feedback of the reviewers.

Conflict of interest

The author declares that the research was conducted in the absence of any commercial or financial relationships that could be construed as a potential conflict of interest.

Publisher's note

Supplementary material

The Supplementary Material for this article can be found online at: https://www.frontiersin.org/articles/10.3389/fncom.2022.703865/full#supplementary-material

References

Alstott, J., Bullmore, E., and Plenz, D. (2014). powerlaw: a Python package for analysis of heavy-tailed distributions. *PloS one* 9, e85777. doi: 10.1371/journal.pone.0085777

Scarpetta S., Apicella, I.I, Minati, L., and de Candia, A. (2018). Hysteresis, neural avalanches, and critical behavior near a first-order transition of a spiking neural network. *Physical Review E* 97, 062305. doi: 10.1103/PhysRevE.97.062305

Arviv, O., Goldstein, A., and Shriki, O. (2015). Near-critical dynamics in stimulus-evoked activity of the human brain and its relation to spontaneous resting-state activity. *Journal of Neuroscience* 35, 13927–13942. doi: 10.1523/JNEUROSCI.0477-15.2015

Bak, P. (1996). *How nature works: the science of self-organized criticality. 1996*. New York: Copurnicus*. doi: 10.1007/978-1-4757-5426-1

Beggs, J. M. (2008). The criticality hypothesis: how local cortical networks might optimize information processing. *Philos Trans A Math Phys Eng Sci* 366, 329–343. doi: 10.1098/rsta.2007.2092

Beggs, J. M., and Plenz, D. (2003). Neuronal avalanches in neocortical circuits. *J Neurosci* 23, 11167–11177. doi: 10.1523/JNEUROSCI.23-35-11167.2003

Beggs, J. M., and Timme, N. (2012). Being critical of criticality in the brain. *Front Physiol* 3, 163. doi: 10.3389/fphys.2012.00163

Bellay, T., Klaus, A., Seshadri, S., and Plenz, D. (2015). Irregular spiking of pyramidal neurons organizes as scale-invariant neuronal avalanches in the awake state. *Elife* 4, e07224. doi: 10.7554/eLife.07224.019

Bertschinger, N., and Natschlager, T. (2004). Real-time computation at the edge of chaos in recurrent neural networks. *Neural Comput* 16, 1413–1436. doi: 10.1162/089976604323057443

Bienenstock, E. (1995). A model of neocortex. *Network: Computation in neural systems* 6, 179–224. doi: 10.1088/0954-898X_6_2_004

Brunel, N. (2000). Dynamics of sparsely connected networks of excitatory and inhibitory spiking neurons. *Journal of computational neuroscience* 8, 183–208. doi: 10.1023/A:1008925309027

Carvalho, T. T., Fontenele, A. J., Girardi-Schappo, M., Feliciano, T., Aguiar, L. A., Silva, T. P., et al. (2020). Subsampled directed-percolation models explain scaling relations experimentally observed in the brain. *arXiv*. preprint*. doi: 10.3389/fncir.2020.576727

Cavagna, A., Cimarelli Giardina, A. I, Parisi, G., Santagati, R., Stefanini, F., and Viale, M. (2010). Scale-free correlations in starling flocks. *Proceedings of the National Academy of Sciences* 107, 11865–11870. doi: 10.1073/pnas.1005766107

Chialvo, D. R. (2010). Emergent complex neural dynamics. *Nature physics* 6, 744–750. doi: 10.1038/nphys1803

Chialvo, D. R., and Bak, P. (1999). Learning from mistakes. *Neuroscience* 90, 1137–1148. doi: 10.1016/S0306-4522(98)00472-2

Chialvo, D. R., Cannas, S. A., Grigera, T. S., Martin, D. A., and Plenz, D. (2020). Controlling a complex system near its critical point *via* temporal correlations. *Scientific reports* 10, 1–7. doi: 10.1038/s41598-020-69154-0

Cocchi, L., Gollo, L. L., Zalesky, A., and Breakspear, M. (2017). Criticality in the brain: A synthesis of neurobiology, models and cognition. *Progress in neurobiology* 158, 132–152. doi: 10.1016/j.pneurobio.2017.07.002

Cohen, M. R., and Kohn, A. (2011). Measuring and interpreting neuronal correlations. *Nature neuroscience* 14, 811–819. doi: 10.1038/nn.2842

Colombo, M. A., Wei, Y., Ramautar, J. R., Linkenkaer-Hansen, K., Tagliazucchi, E., and Van Someren, E. J. (2016). More severe insomnia complaints in people with stronger long-range temporal correlations in wake resting-state EEG. *Frontiers in physiology* 7, 576. doi: 10.3389/fphys.2016.00576

Dahmen, D., Grün, S., Diesmann, M., and Helias, M. (2019). Second type of criticality in the brain uncovers rich multiple-neuron dynamics. *Proceedings of the National Academy of Sciences* 116, 13051–13060. doi: 10.1073/pnas.1818972116

de Candia, A., . Apicella, A. I, and de Arcangelis, L. (2021). Critical behaviour of the stochastic Wilson-Cowan model. *PLoS computational biology* 17, e1008884. doi: 10.1371/journal.pcbi.1008884

De Carvalho, J. X., and Prado, C. P. (2000). Self-organized criticality in the Olami-Feder-Christensen model. *Physical review letters* 84, 4006. doi: 10.1103/PhysRevLett.84.4006

Destexhe, A., and Touboul, J. D. (2021). Is there sufficient evidence for criticality in cortical systems? *Eneuro* 8*. doi: 10.1523/ENEURO.0551-20.2021

Dunkelmann, S., and Radons, G. (1994). "Neural Networsk and Abelian Sandpile Models of Self-Organized Criticality," in *Proceedings of International Conference Artificial Neural Networks*, (Verlag: Springer).

Eurich, C. W., Herrmann, J. M., and Ernst, U. A. (2002). Finite-size effects of avalanche dynamics. *Physical review E* 66, 066137. doi: 10.1103/PhysRevE.66.066137

Finlinson, K., Shew, W. L., Larremore, D. B., and Restrepo, J. G. (2020). Optimal control of excitable systems near criticality. *Physical Review Research* 2, 033450. doi: 10.1103/PhysRevResearch.2.033450

Fontenele, A. J., de Vasconcelos, N. A. P., Feliciano, T., Aguiar, L. A. A., Soares-Cunha, C., Coimbra, B., et al. (2019). Criticality between Cortical States. *Phys Rev Lett* 122, 208101. doi: 10.1103/PhysRevLett.122.208101

Fosque, L. J., Williams-García, R. V., Beggs, J. M., and Ortiz, G. (2021). Evidence for quasicritical brain dynamics. *Physical Review Letters* 126, 098101. doi: 10.1103/PhysRevLett.126.098101

Freeman, W. J. (1987). Simulation of chaotic EEG patterns with a dynamic model of the olfactory system. *Biological cybernetics* 56, 139–150. doi: 10.1007/BF00317988

Friedman, N., Ito, S., Brinkman, B. A., Shimono, M., DeVille, R. E., Dahmen, K. A., et al. (2012). Universal critical dynamics in high resolution neuronal avalanche data. *Phys Rev Lett* 108, 208102. doi: 10.1103/PhysRevLett.108.208102

Gautam, S. H., Hoang, T. T., McClanahan, K., Grady, S. K., and Shew, W. L. (2015). Maximizing Sensory Dynamic Range by Tuning the Cortical State to Criticality. *PLoS Comput Biol* 11, e1004576. doi: 10.1371/journal.pcbi.1004576

Girardi-Schappo, M., Brochini, L., Costa, A. A., Carvalho, T. T., and Kinouchi, O. (2020). Synaptic balance due to homeostatically self-organized quasicritical dynamics. *Physical Review Research* 2, 012042. doi: 10.1103/PhysRevResearch.2.012042

Greenfield, E., and Lecar, H. (2001). Mutual information in a dilute, asymmetric neural network model. *Physical Review E* 63, 041905. doi: 10.1103/PhysRevE.63.041905

Haldeman, C., and Beggs, J. M. (2005). Critical branching captures activity in living neural networks and maximizes the number of metastable States. *Phys Rev Lett* 94, 058101. doi: 10.1103/PhysRevLett.94.058101

Hardstone, R., Poil, S.-S., Schiavone, G., Jansen, R., Nikulin, V. V., Mansvelder, H. D., et al. (2012). Detrended fluctuation analysis: a scale-free view on neuronal oscillations. *Frontiers in physiology* 3, 450. doi: 10.3389/fphys.2012.00450

Herz, A. V., and Hopfield, J. J. (1995). Earthquake cycles and neural reverberations: collective oscillations in systems with pulse-coupled threshold elements. *Physical review letters* 75, 1222. doi: 10.1103/PhysRevLett.75.1222

Hu, J., Zheng, Y., and Gao, J. (2013). Long-range temporal correlations, multifractality, and the causal relation between neural inputs and movements. *Frontiers in Neurology* 4, 158. doi: 10.3389/fneur.2013.00158

Ihlen, E. A. F. E. (2012). Introduction to multifractal detrended fluctuation analysis in Matlab. *Frontiers in physiology* 3, 141. doi: 10.3389/fphys.2012.00141

Kauffman, S. (1969). Homeostasis and differentiation in random genetic control networks. *Nature* 224, 177–178. doi: 10.1038/224177a0

Kelso, J. (1984). Phase transitions and critical behavior in human bimanual coordination. *American Journal of Physiology-Regulatory, Integrative and Comparative Physiology* 246, R1000–R1004. doi: 10.1152/ajpregu.1984.246.6.R1000

Kinouchi, O., and Copelli, M. (2006). Optimal dynamical range of excitable networks at criticality. *Nature physics* 2, 348–351. doi: 10.1038/nphys289

Klaus, A., Yu, S., and Plenz, D. (2011). Statistical analyses support power law distributions found in neuronal avalanches. *PloS one* 6, e19779. doi: 10.1371/journal.pone.0019779

Kostinski, S., and Amir, A. (2016). An elementary derivation of first and last return times of 1D random walks. *American Journal of Physics* 84, 57–60. doi: 10.1119/1.4930092

Laurson, L., Illa, X., Santucci, S., Tallakstad, K. T., Måløy, K. J., and Alava, M. J. (2013). Evolution of the average avalanche shape with the universality class. *Nature communications* 4, 1–6. doi: 10.1038/ncomms3927

Lee, D., Port, N. L., Kruse, W., and Georgopoulos, A. P. (1998). Variability and correlated noise in the discharge of neurons in motor and parietal areas of the primate cortex. *Journal of Neuroscience* 18, 1161–1170. doi: 10.1523/JNEUROSCI.18-03-01161.1998

Legenstein, R., and Maass, W. (2007). Edge of chaos and prediction of computational performance for neural circuit models. *Neural networks* 20, 323–334. doi: 10.1016/j.neunet.2007.04.017

Linkenkaer-Hansen, K., Nikouline, V. V., Palva, J. M., and Ilmoniemi, R. J. (2001). Long-range temporal correlations and scaling behavior in human brain oscillations. *Journal of Neuroscience* 21, 1370–1377. doi: 10.1523/JNEUROSCI.21-04-01370.2001

Lombardi, F., Herrmann, H. J., Perrone-Capano, C., Plenz, D., and De Arcangelis, L. (2012). Balance between excitation and inhibition controls the temporal organization of neuronal avalanches. *Physical review letters* 108, 228703. doi: 10.1103/PhysRevLett.108.228703

Lombardi, F., Herrmann, H. J., Plenz, D., and De Arcangelis, L. (2014). On the temporal organization of neuronal avalanches. *Frontiers in systems neuroscience* 8, 204. doi: 10.3389/fnsys.2014.00204

Lombardi, F., Shriki, O., Herrmann, H. J., and de Arcangelis, L. (2021). Long-range temporal correlations in the broadband resting state activity of the human brain revealed by neuronal avalanches. *Neurocomputing* 461, 657–666. doi: 10.1016/j.neucom.2020.05.126

Ma, Z., Turrigiano, G. G., Wessel, R., and Hengen, K. B. (2019). Cortical Circuit Dynamics Are Homeostatically Tuned to Criticality *In Vivo*. *Neuron 104(4)* 65, e654. doi: 10.1016/j.neuron.2019.08.031

MacLean, J. N., Watson, B. O., Aaron, G. B., and Yuste, R. (2005). Internal dynamics determine the cortical response to thalamic stimulation. *Neuron* 48, 811–823. doi: 10.1016/j.neuron.2005.09.035

Mariani, B., Nicoletti, G., Bisio, M., Maschietto, M., Oboe, R., Leparulo, A., et al. (2021). Neuronal avalanches across the rat somatosensory barrel cortex and the effect of single whisker stimulation. *Front. Syst. Neurosci.* 15.

Mariani, B., Nicoletti, G., Bisio, M., Maschietto, M., Vassanelli, S., and Suweis, S. (2022). Disentangling the critical signatures of neural activity. *Sci. Rep.* 12(1), 1–12.

Marshall, N., Timme, N. M., Bennett, N., Ripp, M., Lautzenhiser, E., and Beggs, J. M. (2016). Analysis of Power Laws, Shape Collapses, and Neural Complexity: New Techniques and MATLAB Support *via* the NCC Toolbox. *Front Physiol* 7, 250. doi: 10.3389/fphys.2016.00250

Martinello, M., Hidalgo, J., Maritan, A., Di Santo, S., Plenz, D., and Muñoz, M. A. (2017). Neutral theory and scale-free neural dynamics. *Physical Review X* 7, 041071. doi: 10.1103/PhysRevX.7.041071

Meisel, C. (2020). Antiepileptic drugs induce subcritical dynamics in human cortical networks. *Proceedings of the National Academy of Sciences* 117, 11118–11125. doi: 10.1073/pnas.1911461117

Meisel, C., Bailey, K., Achermann, P., and Plenz, D. (2017a). Decline of long-range temporal correlations in the human brain during sustained wakefulness. *Scientific reports* 7, 1–11. doi: 10.1038/s41598-017-12140-w

Meisel, C., Klaus, A., Vyazovskiy, V. V., and Plenz, D. (2017b). The interplay between long-and short-range temporal correlations shapes cortex dynamics across vigilance states. *Journal of neuroscience* 37, 10114–10124. doi: 10.1523/JNEUROSCI.0448-17.2017

Meisel, C., Olbrich, E., Shriki, O., and Achermann, P. (2013). Fading signatures of critical brain dynamics during sustained wakefulness in humans. *J Neurosci* 33, 17363–17372. doi: 10.1523/JNEUROSCI.1516-13.2013

Miller, S. R., Yu, S., and Plenz, D. (2019). The scale-invariant, temporal profile of neuronal avalanches in relation to cortical γ–oscillations. *Scientific reports* 9, 1–14. doi: 10.1038/s41598-019-52326-y

Mitzenmacher, M. (2004). A brief history of generative models for power law and lognormal distributions. *Internet mathematics* 1, 226–251. doi: 10.1080/15427951.2004.10129088

Schwab, D. J., Nemenman, I, and Mehta, P. (2014). Zipf's law and criticality in multivariate data without fine-tuning. *Physical review letters* 113, 068102. doi: 10.1103/PhysRevLett.113.068102

Nicoletti, G., and Busiello, D. M. (2021). Mutual information disentangles interactions from changing environments. *Physical review letters* 127, 228301. doi: 10.1103/PhysRevLett.127.228301

Nordlie, E., Gewaltig, M.-O., and Plesser, H. E. (2009). Towards reproducible descriptions of neuronal network models. *PLoS computational biology* 5, e1000456. doi: 10.1371/journal.pcbi.1000456

Papanikolaou, S., Bohn, F., Sommer, R. L., Durin, G., Zapperi, S., and Sethna, J. P. (2011). Universality beyond power laws and the average avalanche shape. *Nature Physics* 7, 316–320. doi: 10.1038/nphys1884

Petermann, T., Thiagarajan, T. C., Lebedev, M. A., Nicolelis, M. A., Chialvo, D. R., and Plenz, D. (2009). Spontaneous cortical activity in awake monkeys composed of neuronal avalanches. *Proceedings of the National Academy of Sciences* 106, 15921–15926. doi: 10.1073/pnas.0904089106

Poil, S.-S., Hardstone, R., Mansvelder, H. D., and Linkenkaer-Hansen, K. (2012). Critical-state dynamics of avalanches and oscillations jointly emerge from balanced excitation/inhibition in neuronal networks. *Journal of Neuroscience* 32, 9817–9823. doi: 10.1523/JNEUROSCI.5990-11.2012

Poil, S. S., van Ooyen, A., and Linkenkaer-Hansen, K. (2008). Avalanche dynamics of human brain oscillations: relation to critical branching processes and temporal correlations. *Human brain mapping* 29, 770–777. doi: 10.1002/hbm.20590

Ponce-Alvarez, A., Jouary, A., Privat, M., Deco, G., and Sumbre, G. (2018). Whole-Brain Neuronal Activity Displays Crackling Noise Dynamics. *Neuron 100(6)* 144, e1446. doi: 10.1016/j.neuron.2018.10.045

Priesemann, V., and Shriki, O. (2018). Can a time varying external drive give rise to apparent criticality in neural systems? *PLoS computational biology* 14, e1006081. doi: 10.1371/journal.pcbi.1006081

Priesemann, V., Valderrama, M., Wibral, M., and Van Quyen, M. Le (2013). Neuronal avalanches differ from wakefulness to deep sleep–evidence from intracranial depth recordings in humans. *PLoS computational biology* 9*. doi: 10.1371/journal.pcbi.1002985

Reed, W. J., and Hughes, B. D. (2002). From gene families and genera to incomes and internet file sizes: Why power laws are so common in nature. *Physical Review E* 66, 067103. doi: 10.1103/PhysRevE.66.067103

Sethna, J. P., Dahmen, K. A., and Myers, C. R. (2001). Crackling noise. *Nature* 410, 242–250. doi: 10.1038/35065675

Shew, W. L., Clawson, W. P., Pobst, J., Karimipanah, Y., Wright, N. C., and Wessel, R. (2015). Adaptation to sensory input tunes visual cortex to criticality. *Nature Physics* 11*. doi: 10.1038/nphys3370

Shew, W. L., and Plenz, D. (2013). The functional benefits of criticality in the cortex. *Neuroscientist* 19, 88–100. doi: 10.1177/1073858412445487

Shew, W. L., Yang, H., Petermann, T., Roy, R., and Plenz, D. (2009). Neuronal avalanches imply maximum dynamic range in cortical networks at criticality. *J Neurosci* 29, 15595–15600. doi: 10.1523/JNEUROSCI.3864-09.2009

Shew, W. L., Yang, H., Yu, S., Roy, R., and Plenz, D. (2011). Information capacity and transmission are maximized in balanced cortical networks with neuronal avalanches. *J Neurosci* 31, 55–63. doi: 10.1523/JNEUROSCI.4637-10.2011

Shriki, O., Alstott, J., Carver, F., Holroyd, T., Henson, R. N., Smith, M. L., et al. (2013). Neuronal avalanches in the resting MEG of the human brain. *Journal of Neuroscience* 33, 7079–7090. doi: 10.1523/JNEUROSCI.4286-12.2013

Spasojević, D., Bukvić, S., Milošević, S., and Stanley, H. E. (1996). Barkhausen noise: Elementary signals, power laws, and scaling relations. *Physical Review E* 54, 2531. doi: 10.1103/PhysRevE.54.2531

Spitzner, F., Dehning, J., Wilting, J., Hagemann, A., Neto, J., Zierenberg, J., et al. (2020). MR. Estimator, a toolbox to determine intrinsic timescales from subsampled spiking activity. *arXiv*. preprint*. doi: 10.1371/journal.pone.0249447

Tapiero, C. S., and Vallois, P. (1996). Run length statistics and the Hurst exponent in random and birth-death random walks. *Chaos, Solitons & Fractals* 7, 1333–1341. doi: 10.1016/0960-0779(96)00032-X

Timme, N. M., Marshall, N. J., Bennett, N., Ripp, M., Lautzenhiser, E., and Beggs, J. M. (2016). Criticality Maximizes Complexity in Neural Tissue. *Front Physiol* 7, 425. doi: 10.3389/fphys.2016.00425

Touboul, J., and Destexhe, A. (2017). Power-law statistics and universal scaling in the absence of criticality. *Physical Review E* 95, 012413. doi: 10.1103/PhysRevE.95.012413

van der Vaart, K., Sinhuber, M., Reynolds, A. M., and Ouellette, N. T. (2020). Environmental perturbations induce correlations in midge swarms. *Journal of the Royal Society Interface* 17, 20200018. doi: 10.1098/rsif.2020.0018

Villegas, P., di Santo, S., Burioni, R., and Muñoz, M. A. (2019). Time-series thresholding and the definition of avalanche size. *Physical Review E* 100, 012133. doi: 10.1103/PhysRevE.100.012133

Williams-Garcia, R. V., Moore, M., Beggs, J. M., and Ortiz, G. (2014). Quasicritical brain dynamics on a nonequilibrium Widom line. *Phys Rev E Stat Nonlin Soft Matter Phys* 90, 062714. doi: 10.1103/PhysRevE.90.062714

Wilson, H. R., and Cowan, J. D. (1972). Excitatory and inhibitory interactions in localized populations of model neurons. *Biophysical journal* 12, 1–24. doi: 10.1016/S0006-3495(72)86068-5

Wilting, J., and Priesemann, V. (2018). Inferring collective dynamical states from widely unobserved systems. *Nature communications* 9, 1–7. doi: 10.1038/s41467-018-04725-4

Wilting, J., and Priesemann, V. (2019). Between perfectly critical and fully irregular: A reverberating model captures and predicts cortical spike propagation. *Cerebral Cortex* 29, 2759–2770. doi: 10.1093/cercor/bhz049

Worrell, G. A., Cranstoun, S. D., Echauz, J., and Litt, B. (2002). Evidence for self-organized criticality in human epileptic hippocampus. *Neuroreport* 13, 2017–2021. doi: 10.1097/00001756-200211150-00005

Frontiers in
Neural Circuits

Explores the emergent properties of neural circuits - the brain's elementary modules

Part of the most cited neuroscience journal series, focuses on the anatomy, physiology, development and function of neural circuitry, exploring how plasticity shapes the architecture of the brain's elementary modules.

Discover the latest Research Topics

See more →

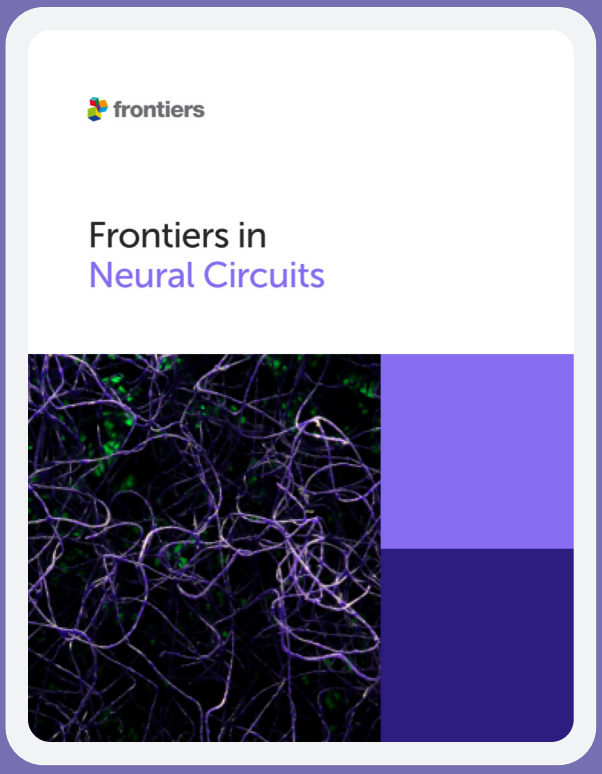

Frontiers

Avenue du Tribunal-Fédéral 34
1005 Lausanne, Switzerland
frontiersin.org

Contact us

+41 (0)21 510 17 00
frontiersin.org/about/contact